

# Spot Feeding Spheroidal Graphite Iron with Exothermic and Insulating Ram-Up Sleeves in Vertically Parted Moulds

PhD Thesis

$$P_{gas} + P_{shr} \rightarrow P = \frac{N_V = A \Delta T_{(\alpha)} \cdot 2\gamma L G S \frac{2}{\sqrt{\pi}} \left( \frac{T_m - T_0}{\rho_s H} \right)^{n-1 (\beta)}}{P_{amb} + P_{st} + P_{exp} + P_{\gamma} c_p (T - T_0)}$$

$$M_t = MEF \times M_g$$

C6H3N3O7

Nikolaj Kjelgaard Vedel-Smith  
October 2015



# **Spot Feeding Spheroidal Graphite Iron with Exothermic and Insulating Ram-Up Sleeves in Vertically Parted Moulds**

Efficiency, Microstructure, Dimensional Accuracy, Deformation,  
and Driving Force and Feeding Criteria Identification

DISSERTATION

To obtain the degree of doctor philosophiæ  
at the Technical University of Denmark,  
Department of Mechanical Engineering,

by

NIKOLAJ KJELGAARD VEDEL-SMITH

Ph.D. in Feeding of Cast Iron  
Born in Nykøbing Falster, Denmark.

*This dissertation has been approved by the supervisor:*

Associate Professor, Ph.D.  
Niels Skat Tiedje

*Supervisory Committee:*

Prof. Jesper Henri Hattel      Technical University of Denmark,  
(*Chairman*)                      Department of Mechanical Engineering

Prof. Attila Sándor Diószegi      Jönköping University,  
School of Engineering, Sweden

Dr. Karl Martin Pedersen      Siemens Wind Power A/s, Denmark

Copyright © 2015 by N.K. Vedel-Smith

**Published and Distributed by**

Technical University of Denmark,  
Department of Mechanical Engineering

Produktionstorvet,  
Building 427A  
2800 Kgs. Lyngby  
Denmark

**Digital Copy of the Dissertation**

[http://download.vedel-smith.com/PhD\\_Dissertation\\_Nikolaj\\_Vedel-Smith.pdf](http://download.vedel-smith.com/PhD_Dissertation_Nikolaj_Vedel-Smith.pdf)

**The PhD Defence Presentation**

<http://vedel-smith.com/PhD/PhD-Defence.html>

**Cover Images Description and Photographer**

Front Page	Formula graphics from the dissertation.	by Nikolaj Vedel-Smith
Part N and Chp 01	Mg treatment of SGI at the University Foundry.	by Kamran Mohaghegh
Part I and Chp 07	Close up of the CMM measurements of the disc castings.	by Flemming Jørgensen
Chp 13	Microstructure from the centre of the C10-M12 casting.	by Mathias K. Bjerre
Sup III Cover	CMM measurements of the disc castings.	by Flemming Jørgensen
Remaining	Images from the course of the project	by Nikolaj Vedel-Smith

**Printed in Denmark by**

STEP A/s  
Odense, 2017

All rights reserved. No part of the material protected by this copyright notice may be reproduced or used in any form or by any means, electronic or mechanical, including photocopying, recording, or by any information storage and retrieval system, without the prior permission of the author.

ISBN 78-87-7475-452-7

Author e-mail: [nikvs@mek.dtu.dk](mailto:nikvs@mek.dtu.dk)

*To Catharina, Luka, and Aya with Love* [1]



“TEN years from now, no one is going to care how quickly the books came out. The only thing that will matter, the only thing anyone will remember, is how good they were. That’s my main concern, and always will be.”

---

—George R.R. Martin  
*Official blog, (July 2007)*





# Abstract

## English

---

*Improvement of feeder technologies for energy savings in cast iron foundries* is not only the title of the project behind this dissertation; it is a good idea that can improve casting yield and reduce production cost, and in turn strengthening the foundries competitive advantage. The approach to solving feeding problems today is for a large part based on methodologies and know-how developed more than 50 years ago. This dissertation addresses the state-of-the-art as it is used presently in the foundries, reviewing the fundamentals of spot feeding cast iron.

THE findings presented in this dissertation is based on large-scale quantitative experiments with duplicates for statistical representation. The focus, as stated by the dissertation title, has been: '*Spot Feeding Spherical Graphite Iron with Exothermic and Insulating Ram-Up Sleeves in Vertically Parted Moulds*'.

THE application of spot feeders (ram-up sleeves) is investigated, showing that this new feeding approach can be used successfully to feed secluded sections in ductile cast iron (EN-GJS-500-7). The feeder efficiency is tested using a high Silicon (Si) ductile iron (EN-GJS-450-10). The limits for the examined feeder configurations are documented, showing that the exothermic feeder combinations managed the task successfully, while the insulating feeder combinations were insufficient.

IT is shown that the exothermic feeders do not influence the casting microstructure via comparing the microstructure of several colour etches samples from the castings, as well as the exothermic and insulating feeders.

THE thermal deformation related to the feeder combinations are investigated, and it is found that the thermal gradients created by the feeders could be signified by the deformation of the plane reverse side of the casting. The eutectoid phase transformation is found to be the governing factor. The main difference between the two alloys is that the pearlitic-ferritic EN-GJS-500-7 have twice as long a transformation interval as the fully ferritic EN-GJS-450-10. Knowledge of the deformation magnitude and variance can be used to reduce the machining allowance, subsequently reducing the melt cost and machining wear.

A series of different spot feeders with insulating or exothermic sleeves materials are investigated for three different modulus castings; 8 mm, 12 mm, and 15 mm. It is proved that the required feeder modulus does not scale linearly with the casting modulus. Additionally, it is shown that horizontal spot feeder can feed against gravity by optimising the interplay of forces created by the solidifying casting and the feeder itself.

THE investigation of the modulus relationship between the casting and the feeder leads to the formulation of a set of driving forces for feeding, accompanied by the pressure loss caused by the solidifying casting and the timing demanded by the feeding requirement. It is shown that the interplay of internal forces can drive a complete feeding process, but also that the frame of optimal function can be very narrow.

NUMERICAL simulation of casting processes and the prediction of porosities are addressed, and it is found that some castings and alloys can be reliably simulated concerning porosities. However, it is also found that for high Si alloy EN-GJS-500-14 the simulation setup cannot provide prediction that corresponds to the porosities found in the porosity analysis.

FINALLY, it is shown how multiple feeders can influence each other's performance even across solidified sections, and that two individual feeders that can retain a liquid connection can change the thermal gradients of the casting and the directions of solidification.

THE dissertation provides a new approach to feeding secluded sections, a new characterisation of the underlying feeding forces, and new knowledge about the thermal deformation effects caused and controlled by feeding.

# Resumé

## Dansk

*F*orbedring af efterføderteknologier til energibesparelser i jernstøberier er ikke kun titlen på projekter bag denne afhandling, det er også en god idé som kan forbedre udbyttet ved støbning og reducere produktionsomkostningerne, og derigennem styrke støberiernes konkurrenceevne. Den tilgang der er til at løse efterfødningsproblemer i dag er for en stor andel baseret på metoder udviklet for mere end 50 år siden. Denne afhandling adresserer state-of-the-art som det bliver brugt ude i støberierne, og giver et overblik over de grundlæggende teknikker til efterfødnings af støbejern.

RESULTATERNE præsenteret i denne afhandling er baseret på stor-skala kvantitative eksperimenter med duplikater for statistisk repræsentation. Fokus er som nævnt i titlen: “*Punktefterfødnings af duktilt støbejern med eksotermiske og isolerende ram-up sleeves i vertikalt delte forme*”.

ANVENDELSEN af punktefterfødere (ram-up sleeves) bliver undersøgt og viser at denne nye tilgang kan bruges til succesfuldt at efterføde isolerede sektioner i duktilt støbejern (EN-GJS-500-7). Efterfødereffektiviteten bliver testet med et høj-silicium (Si) duktilt støbejern (EN-GJS-450-10), og grænsen for de undersøgte efterføderkombinationer bliver dokumenteret, visende at de eksotermiske efterføderkombinationer klarede opgaven succesfuldt, mens de isolerende efterføderkombinationer var utilstrækkelige.

DET bliver vist at eksotermiske efterfødere ikke indvirker på mikrostrukturen af støbningerne via en sammenligning af en række farveætsede prøver fra hhv. støbningerne, samt fra de eksotermiske og isolerende efterfødere.

DEn termiske deformation forbundet med efterføderkombinationerne bliver undersøgt, og det viser sig at de temperaturegradienter skabt af efterføderne kunne genkendes via deformationen på den plane bagside af støbningen. Den eutektoid fasetransformation bliver identificeret som den styrende faktor, og den primære forskel mellem de to legeringer er at den perlitisk-ferritiske EN-GJS-500-7 legering har et dobbelt så langt transformationsinterval som den helt ferritiske EN-GJS-450-10 legering. Viden om deformationsstørrelsen og -afvigelsen kan bruges til at reducere bearbejdningstillægget, og deraf følgende reducere udgiften til smeltning og slitage af udstyr.

EN serie forskellige punktefterfødere med isolerende eller eksotermiske sleeve materialer bliver undersøgt for tre forskellige støbemoduler; 8 mm, 12 mm, and 15 mm. Det bliver bevist at den nødvendige efterfødermodul ikke skalerer lineært med emnemodulen. Ydermere bliver det vist at horisontale punktefterfødere kan efterføde imod tyngdekraften ved at optimere samspillet mellem de kræfter der skabes af det størknende emne og selve efterføderen.

**UNDERSØGELSEN** Undersøgelsen af modulforholdet mellem støbeemnet og efterføderen leder til formuleringen af et sæt af drivkræfter for efterfødningsproces, ledsaget af et tryktab forårsaget af den størknende emne og timingen krævet af efterfødningskræfter. Det bliver vist at samspillet af interne kræfter kan drive en hel efterfødningsproces, men også at processvinduet for optimal funktion kan være meget snævert.

**NUMERISK** simulering af støbeprocesser og forudsigelsen af porøsiteter bliver adresseret, og det bliver fundet at nogle støbninger og legeringer kan simuleres troværdigt med hensyn til porøsiteter. Dog bliver det også fundet at for høj-silicium (Si) legeringen EN-GJS-500-14 kunne simuleringssættet ikke levere forudsigelser der svarede til dem der er fundet i porositetsanalysen.

**SLUTTELIGT** bliver det vist hvordan flere efterfødere kan påvirke hinanden – endda på tværs af størknede sektioner, og at to efterfødere der kan bibeholde kontakt via smelte er i stand til at ændre temperaturgradienterne for en støbning samt størkneretningen.

**AFHANDLINGEN** giver en ny tilgang til efterfødningsproces af isolerede sektioner, en ny karakterisering af de underliggende efterfødningskræfter og ny viden om termiske deformationseffekters forårsaget og styret af efterfødningsproces.

# Preface

This dissertation is the final delivery of the Ph.D. project entitled; ‘*Improvement of Feeder Technologies for Energy Savings in Cast Iron Foundries*’. The project has been carried out at the Section for Manufacturing Engineering, in the Department of Mechanical Engineering, at the Technical University of Denmark. The project has transpired the period from January 2011 to October 2015. The present work has been performed under the supervision of Associate Professor Niels Skat Tiedje.

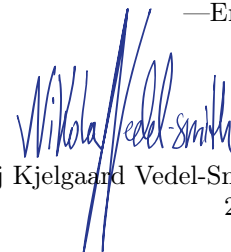
The project has been funded by the Danish Government via the Public Service Obligation (PSO) funds with the ELFORSK project. The Ph.D. project has comprised the cooperation of the following companies and institutions:

- Technical University of Denmark,  
Department of Mechanical Engineering
- Valdemar Birn A/s, Denmark
- DISA Industries A/s, Denmark
- MAGMA GmbH, Germany
- FOSECO Ltd., England

The collaboration has been involving all parties, and the project partners have all contributed valuable knowledge, assistance, education, enthusiasm, and engagement. The work, research, and results presented in this dissertation would not have been achievable without these companies, and the people behind.

The project has aimed to improve the performance and application of feeder technologies, particularly spot feeding. This unifying goal has been sought through demonstrations and documentation of the effects of different feeder solutions. Secondly, the project has aimed at communicating the results and doing so both via scientific publications in conference proceedings and journals, but also via presentation, demonstrations, and articles in foundry magazines with a broad spread audience. Finally, the author hopes the project will inspire renewed focus and research on the feeding of cast iron in particular and the improvement of the processing of cast iron in general. To the benefit of the environment, the foundries, and the customers.

—Enjoy



Nikolaj Kjelgaard Vedel-Smith  
2015



# Table of Contents

ABSTRACT	vii
PREFACE	xi
LIST OF FIGURES	xix
LIST OF TABLES	xxiii
LIST OF SUPPLEMENTS	xxv
ACKNOWLEDGEMENTS	xxvii
ABBREVIATIONS	xxix
NOMENCLATURE	xxx
TO THE READER	xxxvii

<b>N Introduction</b>	<b>1</b>
1 INTRODUCTION	<b>3</b>
<b>1.1 Casting Research</b>	<b>3</b>
1.1.1 Foundry Production	3
1.1.2 Novel Technologies	4
<b>1.2 Societal Relevance</b>	<b>5</b>
1.2.1 Advancing Foundry Technology	5
<b>1.3 Project Description</b>	<b>5</b>
1.3.1 Research Hypotheses	5
<b>References</b>	<b>11</b>
2 FEEDING REVIEW	<b>13</b>
<b>2.1 Introduction</b>	<b>13</b>
2.1.1 What is Feeding?	14
2.1.2 Other Functions of Feeders	14
<b>2.2 Porosity Defect Formation</b>	<b>14</b>
2.2.1 Shrinkage Porosities	15
<b>2.3 Seven Rules of Feeding</b>	<b>19</b>
2.3.1 Do Not Feed (Unless Necessary)	19
2.3.2 Heat-Transfer (Modulus)	20
2.3.3 Mass-Transfer (Volume)	21
2.3.4 Junction	21
2.3.5 Feed Path	23
2.3.6 Pressure Gradient	28

2.3.7	Pressure . . . . .	29
<b>2.4</b>	<b>Five Feeding Mechanisms . . . . .</b>	<b>30</b>
2.4.1	Liquid Feeding . . . . .	31
2.4.2	Mass Feeding . . . . .	31
2.4.3	Interdendritic Feeding . . . . .	32
2.4.4	Burst Feeding . . . . .	32
2.4.5	Solid Feeding . . . . .	33
<b>2.5</b>	<b>Advanced Feeding Methods . . . . .</b>	<b>34</b>
2.5.1	Ram-Up Sleeves . . . . .	34
2.5.2	Simulation and Optimisation . . . . .	34
2.5.3	Advanced Solidification . . . . .	34
<b>2.6</b>	<b>Summary . . . . .</b>	<b>34</b>
	<b>References . . . . .</b>	<b>35</b>
<b>3</b>	<b>PHYSICAL PHENOMENA AND THEIR SIMULATION . . . . .</b>	<b>39</b>
<b>3.1</b>	<b>Numerical Simulation . . . . .</b>	<b>39</b>
<b>3.2</b>	<b>Methodological Approach . . . . .</b>	<b>41</b>
<b>3.3</b>	<b>Parameters and Processes . . . . .</b>	<b>42</b>
3.3.1	Geometry . . . . .	42
3.3.2	Filling Simulation . . . . .	43
3.3.3	Heat Transfer . . . . .	43
3.3.4	Solidification . . . . .	45
3.3.5	Microstructure Modelling . . . . .	47
<b>3.4</b>	<b>Porosity Handling and Feeding . . . . .</b>	<b>50</b>
3.4.1	Thermal Expansion (Volume Change) . . . . .	51
3.4.2	Porosity Formation . . . . .	52
3.4.3	Criteria Functions . . . . .	54
3.4.4	Feeding Algorithms . . . . .	56
3.4.5	Feeders . . . . .	57
3.4.6	Feeding . . . . .	58
<b>3.5</b>	<b>Stress and Deformation . . . . .</b>	<b>58</b>
3.5.1	Irreversible Deformations . . . . .	60
3.5.2	Phase Transformations . . . . .	61
3.5.3	Dimensional Accuracy . . . . .	61
	<b>References . . . . .</b>	<b>61</b>
<b>I</b>	<b>Feeding Secluded Sections . . . . .</b>	<b>65</b>
<b>4</b>	<b>CASTING DESIGN AND TRIAL PLAN . . . . .</b>	<b>67</b>
<b>4.1</b>	<b>Trial Purpose . . . . .</b>	<b>67</b>
<b>4.2</b>	<b>Design of the Disc Casting . . . . .</b>	<b>68</b>
4.2.1	Alloys . . . . .	68
4.2.2	Feeder Options . . . . .	69
<b>4.3</b>	<b>Trial Setup and Configuration . . . . .</b>	<b>71</b>
4.3.1	Casting Sessions and Conditions . . . . .	71
4.3.2	Feeder Configurations and Properties . . . . .	71
<b>4.4</b>	<b>Production of Castings . . . . .</b>	<b>73</b>
<b>4.5</b>	<b>Temperature Measurements . . . . .</b>	<b>74</b>
	<b>References . . . . .</b>	<b>74</b>
<b>5</b>	<b>FEEDING EFFECT ANALYSIS . . . . .</b>	<b>75</b>
<b>5.1</b>	<b>Porosities Quantification . . . . .</b>	<b>75</b>
5.1.1	Sectioning of the Castings . . . . .	76



5.1.2	Preparation of Samples . . . . .	76
5.1.3	Liquid Penetrant Test . . . . .	77
5.1.4	Analysing the Castings . . . . .	77
5.1.5	Test Results . . . . .	78
5.1.6	Ultrasound Analysis . . . . .	80
5.1.7	X-ray Analysis . . . . .	81
5.1.8	Other Shrinkage Defects . . . . .	81
<b>5.2</b>	<b>Porosity Simulations . . . . .</b>	<b>83</b>
5.2.1	Setup and Assumptions . . . . .	83
5.2.2	Results . . . . .	84
	<b>References . . . . .</b>	<b>87</b>
<b>6</b>	<b>MICROSTRUCTURE ANALYSIS . . . . .</b>	<b>89</b>
<b>6.1</b>	<b>Introduction . . . . .</b>	<b>89</b>
<b>6.2</b>	<b>Macrostructure Analysis . . . . .</b>	<b>89</b>
6.2.1	Macro Etching . . . . .	90
<b>6.3</b>	<b>Analysis of the Macrostructure . . . . .</b>	<b>90</b>
<b>6.4</b>	<b>Microstructure Analysis . . . . .</b>	<b>90</b>
6.4.1	Colour Etching . . . . .	90
<b>6.5</b>	<b>Analysis of the Microstructure . . . . .</b>	<b>91</b>
6.5.1	Comparing the Castings . . . . .	91
6.5.2	Solidification and Microstructure . . . . .	91
6.5.3	Formation of Porosities . . . . .	95
	<b>References . . . . .</b>	<b>96</b>
<b>7</b>	<b>DEFORMATION MEASUREMENTS . . . . .</b>	<b>97</b>
<b>7.1</b>	<b>Quantifying Surface Shrinkage . . . . .</b>	<b>97</b>
7.1.1	Initial Deformation Analysis . . . . .	98
7.1.2	Deformation Prediction and Simulation . . . . .	98
7.1.3	Quantifying Measurement Results . . . . .	102
7.1.4	Setup, Equipment, and Procedure . . . . .	103
<b>7.2</b>	<b>Deformation Analysis . . . . .</b>	<b>104</b>
7.2.1	Deformation Characterisation . . . . .	105
7.2.2	Statistical Deformation Analysis . . . . .	109
7.2.3	Conclusions . . . . .	112
<b>7.3</b>	<b>Measurement Uncertainty . . . . .</b>	<b>113</b>
7.3.1	Data Validation . . . . .	113
7.3.2	Measurement Uncertainty . . . . .	117
7.3.3	Normalised Error Analysis . . . . .	119
7.3.4	Conclusions . . . . .	120
	<b>References . . . . .</b>	<b>121</b>
<b>8</b>	<b>THERMAL ANALYSIS . . . . .</b>	<b>123</b>
<b>8.1</b>	<b>Introduction . . . . .</b>	<b>123</b>
<b>8.2</b>	<b>Thermal Measurements . . . . .</b>	<b>123</b>
8.2.1	Numerical Simulation . . . . .	124
8.2.2	Cooling Curves . . . . .	124
<b>8.3</b>	<b>Thermal Analysis . . . . .</b>	<b>125</b>
8.3.1	Phase Transformation: Temperature . . . . .	126
8.3.2	Phase Transformation: Time . . . . .	130
8.3.3	Thermal Deformation Analysis . . . . .	130
	<b>References . . . . .</b>	<b>133</b>
<b>9</b>	<b>DISCUSSION . . . . .</b>	<b>135</b>

<b>9.1</b>	<b>Introduction</b>	135
<b>9.2</b>	<b>Purpose and Objectives</b>	136
<b>9.3</b>	<b>Experimental Setup</b>	136
9.3.1	Feeder Combination Analysis	136
9.3.2	Trial Plan	136
9.3.3	Thermal Measurements	136
9.3.4	Porosity Analysis	137
9.3.5	Numerical Simulations	138
9.3.6	Process Stability	140
9.3.7	Microstructure Analysis	140
9.3.8	Deformations Measurements	141
9.3.9	Thermal Analysis	142
<b>9.4</b>	<b>Porosity Analysis</b>	143
9.4.1	$\alpha$ -alloy (EN-GJS-500-7 (EN-GJS-500-7))	143
9.4.2	$\beta$ -alloy (EN-GJS-450-10 (EN-GJS-450-10))	143
9.4.3	Porosity Simulation	144
<b>9.5</b>	<b>Solidification and Microstructure</b>	146
<b>9.6</b>	<b>Thermal Deformation</b>	146
9.6.1	Surface Deformation Measurements	147
	<b>References</b>	150
<b>10</b>	<b>PART SUMMARY</b>	<b>153</b>
<b>10.1</b>	<b>Summary</b>	153
10.1.1	Experimental Setup	153
<b>II</b>	<b>Feeding Effect Quantification</b>	<b>155</b>
<b>11</b>	<b>CASTING DESIGN AND TRIAL PLAN</b>	<b>157</b>
<b>11.1</b>	<b>Trial Purpose</b>	157
11.1.1	Objectives	158
11.1.2	Casting and Pattern Design	161
<b>11.2</b>	<b>Scaling Error (M10 <math>\Rightarrow</math> M12)</b>	167
<b>11.3</b>	<b>Trial Description</b>	168
11.3.1	Alloy Composition	168
11.3.2	Choice of Feeders	168
<b>11.4</b>	<b>Trial Setup and Production</b>	171
11.4.1	Temperature Measurements	173
	<b>References</b>	174
<b>12</b>	<b>FEEDING ANALYSIS</b>	<b>175</b>
<b>12.1</b>	<b>Porosity Quantification</b>	175
12.1.1	Ultrasound Analysis	176
12.1.2	X-Ray Analysis	179
12.1.3	Weighing the Castings	179
12.1.4	Sectioned Castings	181
<b>12.2</b>	<b>Porosity Result Analysis</b>	186
12.2.1	Upper Feeder Only	187
12.2.2	Lower Feeder Only	190
12.2.3	Upper and Lower Feeders Together	190
12.2.4	Proportional Modulus Analysis	193
12.2.5	Puncture at the Pre-Feeder Neck	199
12.2.6	X-Ray Results Analysis	200
<b>12.3</b>	<b>Thermal Analysis</b>	202

12.3.1	Numerical Simulations . . . . .	202
12.3.2	Cooling Curve Analysis . . . . .	205
12.3.3	Thermal Gradients . . . . .	210
12.3.4	Fraction Liquid Analysis . . . . .	212
12.3.5	Geometric Solidification Analysis . . . . .	214
<b>12.4</b>	<b>Numerical Porosity Analysis . . . . .</b>	<b>221</b>
12.4.1	Simulation Setup and Calibration . . . . .	222
12.4.2	Porosity Simulation Results . . . . .	227
12.4.3	Sub Conclusions . . . . .	229
	<b>References . . . . .</b>	<b>229</b>
<b>13</b>	<b>DISCUSSION . . . . .</b>	<b>231</b>
<b>13.1</b>	<b>Introduction . . . . .</b>	<b>232</b>
13.1.1	Definition of Terms . . . . .	232
<b>13.2</b>	<b>Purpose and Objectives . . . . .</b>	<b>232</b>
13.2.1	Feeding Requirement and Modulus Relationship . . . . .	232
13.2.2	Grading the Feeder Efficiency . . . . .	233
13.2.3	Simulate Feeding of Secluded Sections . . . . .	233
13.2.4	Feeder Location . . . . .	233
13.2.5	Multiple Feeders . . . . .	234
13.2.6	Design for Analysis . . . . .	235
<b>13.3</b>	<b>Process Stability . . . . .</b>	<b>236</b>
13.3.1	Statistical Porosity Sum Analysis . . . . .	236
<b>13.4</b>	<b>Scalability of the Experiment . . . . .</b>	<b>239</b>
13.4.1	Scalability of the Castings . . . . .	239
13.4.2	Scalability of the Feeders . . . . .	240
13.4.3	Influence of Scaling Error . . . . .	242
<b>13.5</b>	<b>Shrinkage Defect Identification . . . . .</b>	<b>242</b>
13.5.1	Centreline Porosities . . . . .	243
13.5.2	Surface Shrinkage . . . . .	243
<b>13.6</b>	<b>Effects of Feeding Parameters . . . . .</b>	<b>244</b>
13.6.1	Feeder Modulus . . . . .	244
13.6.2	Sleeve Material . . . . .	246
13.6.3	Feeder Location . . . . .	248
<b>13.7</b>	<b>Solidification Behaviour . . . . .</b>	<b>251</b>
<b>13.8</b>	<b>Driving Forces . . . . .</b>	<b>252</b>
13.8.1	Graphic Explanation . . . . .	253
13.8.2	Volume Contraction . . . . .	254
13.8.3	Shell Compression . . . . .	254
13.8.4	Graphite Expansion . . . . .	255
13.8.5	Other Forces . . . . .	257
13.8.6	Pressure Loss . . . . .	257
13.8.7	Feeding Requirement . . . . .	260
13.8.8	Other Factors . . . . .	261
<b>13.9</b>	<b>Feeding Regimes . . . . .</b>	<b>265</b>
13.9.1	Initial Feeding . . . . .	266
13.9.2	Expansion Feeding . . . . .	266
13.9.3	Directional Feeding . . . . .	267
	<b>References . . . . .</b>	<b>267</b>
<b>14</b>	<b>PART SUMMARY . . . . .</b>	<b>269</b>
<b>14.1</b>	<b>Summary . . . . .</b>	<b>269</b>
14.1.1	Experimental Setup . . . . .	269

14.1.2	Porosity Quantification and Results . . . . .	270
14.1.3	Thermal Analysis . . . . .	270
14.1.4	Porosity Analysis . . . . .	271
14.1.5	Results Analysis and Discussion . . . . .	271
References	. . . . .	271
<b>III</b>	<b>Dissertation Summary</b>	<b>273</b>
15	CONCLUSION	275
15.1	<b>Introduction</b> . . . . .	275
15.1.1	Purpose and Objective . . . . .	275
15.2	<b>Conclusions</b> . . . . .	276
15.2.1	Feeding Guidelines . . . . .	278
15.3	<b>Impact</b> . . . . .	279
15.3.1	Energy Savings . . . . .	280
References	. . . . .	280
16	FUTURE WORK AND APPLICATION OF FINDINGS	281
16.1	<b>Technology Roadmap</b> . . . . .	281
16.2	<b>Spot Feeding</b> . . . . .	281
16.2.1	Applied Investigation in Production . . . . .	282
16.2.2	Pressurised Feeding . . . . .	282
16.2.3	Active Pattern . . . . .	282
16.3	<b>Thermal Deformation</b> . . . . .	282
16.4	<b>Feeding Forces</b> . . . . .	283
16.4.1	Pouring Temperature . . . . .	283
16.4.2	Active Cooling . . . . .	283
16.5	<b>Casting Production Statistics</b> . . . . .	284
16.5.1	Casting Research . . . . .	284
References	. . . . .	284
	BIBLIOGRAPHY	287
A	APPENDIX	295
Appendix A:	Colour Etching Guidelines for Picric Acid . . . . .	296
<b>IV</b>	<b>Supplements</b>	<b>299</b>
I:	Quantification of Feeding Effects of Spot Feeding Ductile Iron Castings Made in Vertically Parted Molds . . . . .	301
II:	Effect of Feeder Configuration on the Microstructure of Ductile Cast Iron . . . . .	315
III:	Thermal Distortion of Disc-Shaped Ductile Iron Castings in Vertic- ally Parted Moulds . . . . .	325
IV:	Feeding Against Gravity with Spot Feeders in High Silicon Ductile Iron . . . . .	337

# List of Figures

1.1	Production overview for cast iron . . . . .	4
1.2	Schematic of the ram-up sleeve function with the metal breaker core (compressor core) . . . . .	6
1.3	Cast iron casting, made in a vertically parted mould, using spot feeders to feed secluded sections . . . . .	8
2.1	Definition of shrinkage defects and the formation of microporosities . .	14
2.2	Solidification and porosity formation for different section sizes . . . . .	15
2.3	The stages of shrinkage cavity formation . . . . .	16
2.4	The stages of shrinkage porosity formation . . . . .	16
2.5	Geometry of the shrinkage porosity for a short freezing range alloy as a function of orientation . . . . .	16
2.6	Influence of pressure and gas content on mushy zone pore formation .	18
2.7	Nomogram for finding volume shrinkage % and shrinkage time ( $ST$ ) in % of solidification time, based on alloy composition and casting temperature . . . . .	22
2.8	Typical feeder yield for different geometries . . . . .	23
2.10	Feeding distance rules developed by Pellini . . . . .	24
2.9	Heuvers' circles and the use of integrated and detached padding . . . .	24
2.11	Endogenous and exogenous solidification based on alloy composition .	25
2.12	Melt flow from feeder to casting distinguished by solidification types .	26
2.13	Cross-section illustrating problems related to pressure gradients in the casting . . . . .	27
2.14	Division of liquid and solid shrinkage in comparison with a strong mould and a weak mould . . . . .	28
2.15	Correlation between cooling, solidification, and expansion of a SGI with a CEV of 4.35 . . . . .	29
2.16	Overview of the five feeding mechanisms . . . . .	30
2.17	Ferrostatic tension of the residual liquid, depending on freezing range regime . . . . .	31
2.18	Interdendritic feeding: Influence of eutectic solidification . . . . .	32
2.19	Solid Feeding: Zones of plastic deformation created by the tension of residual liquid contracting during solidification . . . . .	33
2.20	Ram-up sleeve application . . . . .	34
3.1	Comparison of Cartesian and Triangular meshes . . . . .	40
3.2	Illustration of cut-cells implementation in Solver5 . . . . .	41
3.3	Temperature profile across mould-metal interface as a function of Heat Transfer Coefficient (HTC) . . . . .	44
3.4	Comparison of the Scheil equation and the Lever rule . . . . .	46
3.5	Illustration of the solidification sequence of hypoeutectic SGI . . . . .	47
3.6	Illustration of the solidification sequence of hypereutectic SGI . . . . .	48

3.7	Illustration of the elementary volume element during solidification of eutectic SGI . . . . .	49
3.8	Temperature dependent volumetric thermal expansion of cast iron, $\alpha_V$ . . . . .	50
3.9	Temperature dependent volumetric thermal expansion, $\alpha_V$ , in MAGMASOFT 5.2.0 . . . . .	51
3.10	Dimensional variation during solidification . . . . .	52
3.11	Comparison of displacement during solidification for different graphite morphologies as a function of time in a rigid mould . . . . .	53
3.12	Comparison of displacement during solidification for different graphite morphologies as a function of Carbon Equivalent Value (CEV) . . . . .	53
3.13	Porosities in small cast iron casting with varying mesh cell size showing the relation between mesh cell size and porosity threshold value . . . . .	54
3.14	Illustration of the 1-dimensional mushy zone solidification with constant temperature gradient, $G$ , and isotherm velocity $R$ . . . . .	56
3.16	Influence of different degrees of constraints on contraction at different temperatures . . . . .	59
3.15	Influence of casting geometry and mould constraint on contraction . . . . .	59
4.1	Technical drawing of the disc casting including the gating system, mounted on the pattern plate . . . . .	69
4.2	Ram-up sleeve production overview . . . . .	69
4.3	Technical sectioned drawings of feeder sleeves . . . . .	72
4.4	Overview of castings from session three . . . . .	73
4.5	Setup of sleeves used in session three . . . . .	73
4.6	Placement of K- and N-element thermocouples for temperature measurements . . . . .	74
5.1	Sectioning of the castings. . . . .	76
5.2	Sectioned and planar ground sample from casting $\beta 11C$ . . . . .	77
5.3	Results of the porosity analysis. . . . .	79
5.4	Ultrasound analysis of casting without centre feeder, before the sectioning. . . . .	80
5.5	X-ray analysis of castings $\alpha 23A$ and $\alpha 00C$ . . . . .	82
5.6	Comparison of the feeders influence on temperature during solidification. . . . .	85
5.7	Comparison of four different trial setups. . . . .	86
6.1	Overview of sectioned casting $\alpha 11A$ etched with 1% Nital . . . . .	90
6.2	Overview of the different microstructures made visible by colour etching with Motz's picric acid . . . . .	92
6.3	Microstructures from castings $\alpha 23C$ and $\beta 23C$ . . . . .	93
6.4	Comparison of the first and second etching of the boss section (6) of the $\alpha 23C$ , $\alpha 11C$ , and $\beta 23C$ castings . . . . .	94
6.5	Porosity microstructures from the boss section (4) and the centre feeder section (6) . . . . .	95
7.1	Overview of the surface shrinkage analysis performed on the sectioned castings . . . . .	98
7.2	Comparison of the simulated total displacement of castings $\alpha 23$ and $\beta 23$ . . . . .	99
7.3	Comparison of the simulated displacement in the y-direction of castings $\alpha 23$ and $\beta 23$ . . . . .	100
7.4	Displacement in the y-direction of castings $\alpha 23$ magnified $\times 30$ . . . . .	101
7.5	Zeiss OMC 850 mechanical Coordinate Measurement Machine . . . . .	102
7.6	Deformation measurements of the pattern plates . . . . .	103
7.7	Two automated measurement programs for measuring the castings . . . . .	104

7.8	Measured casting topography amplified $\times 100$ . . . . .	105
7.9	Detailed measurement of one of the castings to prove or disprove the ripple effect . . . . .	109
7.10	Flatness values ( $f_v$ ) for each separate casting group, sorted by order of casting . . . . .	110
7.11	Flatness values ( $f_v$ ) for sorted groups . . . . .	111
7.12	Placement of the measurement points . . . . .	113
7.13	Box plot of all 17 castings sorted in the six groups . . . . .	114
7.14	Chi-Square ( $\chi^2$ ) test of complete dataset . . . . .	114
7.15	Thickness variation in mm from top to bottom, as sorted by height . .	116
7.16	Mean thickness in mm for each of the 17 castings . . . . .	119
8.1	Technical drawing of the disc casting including the gating system, mounted on the pattern plate . . . . .	124
8.2	Cooling curves from the trial castings. Comparison of Measurement Position (MP) 1 and 9 for the two castings . . . . .	125
8.3	Comparison of the cooling curves for castings $\tau 23A$ and $\tau 23B$ , and the numerical simulation $\tau 23$ (Sim) . . . . .	126
8.4	Simulated cooling curves for two alloy compositions— $\alpha$ and $\beta$ . . . . .	127
8.5	Phase Transformation Temperature: Austenite to ferrite phase transformation temperature intervals for all measured and simulated castings, for each of the nine MPs . . . . .	128
8.6	Phase Transformation Time: Austenite to ferrite phase transformation time intervals for all measured and simulated castings, for each of the nine MPs . . . . .	129
8.7	Thermal analysis summary . . . . .	131
8.8	Thermal gradients for the solidification and cooling of the casting viewed from both the front and the reverse side . . . . .	132
9.1	Overview of sectioned casting $\alpha 11A$ . . . . .	144
11.1	Illustration of the three different types of shrinkage observed during casting . . . . .	158
11.2	Pattern made by additive manufacturing in ABS plastics for DISAMATIC 2110 . . . . .	160
11.3	Scalable geometry for the modulus castings . . . . .	161
11.4	Solidification fraction against temperature . . . . .	163
11.5	Simulation overview of the different casting moduli combined with the different pre-feeder neck heights . . . . .	165
11.6	Ratio between $t_{close}$ and $t_{eut}$ for the different casting moduli with different pre-feeder neck heights . . . . .	165
11.7	Closing temperature ( $T_{close}$ ) at the casting centre for the different casting moduli with different pre-feeder neck heights . . . . .	166
11.8	Final pattern plates layout for the trial . . . . .	166
11.9	Technical drawing of the casting pattern including gating system . . .	167
11.10	Feedex HD V Series . . . . .	170
11.11	Insulating and exothermic versions of the selected Feedex HD V feeders	171
11.12	Thermocouple placement . . . . .	173
11.13	Setup of thermal measurement equipment . . . . .	173
11.14	Measurement Computing USB-5104 . . . . .	174
12.1	Porosity indications identified using ultrasound and marked with crayon	176
12.2	Control volumes for the porosity analysis . . . . .	178
12.3	Typical atmospheric punctures at the pre-feeder neck . . . . .	179

12.4	XYLON x-ray imaging machine used for the x-ray analysis . . . . .	179
12.5	Overview of x-ray images for M15 castings . . . . .	181
12.6	Sectioned castings cast without feeders . . . . .	182
12.6	Sectioned castings cast without feeders . . . . .	183
12.7	Sectioned castings cast with different feeder configurations . . . . .	184
12.7	Sectioned castings cast with different feeder configurations . . . . .	185
12.8	Overview of the Thermocouple (TC) setup and mould placement of castings 10A, 10B, 10C, and 17A . . . . .	186
12.9	Overview of the porosities size distribution based on feeder modulus for castings with upper feeder only . . . . .	188
12.10	Overview of the porosities size distribution based on feeder modulus for castings with lower feeder only . . . . .	190
12.11	Overview of the porosities size distribution based on feeder modulus for castings with both upper and lower feeder only . . . . .	192
12.12	Overview of the porosity distribution and size as a function of the proportional moduli for the upper and lower feeders . . . . .	195
12.13	X-ray images of the select castings stitched together to provide context and overview . . . . .	201
12.14	Simulation mesh from MAGMASOFT showing thermocouple placement	203
12.15	Comparison of the measured experimental cooling curves and the simulated cooling curves . . . . .	204
12.16	Comparison of the simulated cooling curves for six different feeder combinations . . . . .	207
12.16	Comparison of the simulated cooling curves for six different feeder combinations . . . . .	208
12.17	Temperature gradients for the M08, M12, and M15 castings without feeders . . . . .	211
12.18	Fraction liquid gradients for the M08, M12, and M15 castings without feeders . . . . .	213
12.19	Fraction liquid: Pre-feeder neck solidification . . . . .	216
12.20	Fraction liquid: M08 solidification . . . . .	218
12.21	Fraction liquid: M12 solidification . . . . .	219
12.22	Fraction liquid: M15 solidification . . . . .	220
12.23	Calibration simulation setups and their resulting porosity predictions for the benchmark casting, C10 . . . . .	223
12.24	Porosity results for feeder configurations C06, C10, and C19 . . . . .	226
12.24	Porosity results for feeder configurations C06, C10, and C19 . . . . .	227
13.1	Porosity Statistics: Benchmark castings without feeders . . . . .	237
13.2	Porosity Statistics: Castings with feeders . . . . .	238
13.3	Five major porosity types . . . . .	242
13.4	Driving Force, Volume Contraction: Overview of the pressure differ- ence created at the feeder and at the casting as a function of the volume contraction that occur during cooling and solidification . . . . .	253
13.5	Driving Force, Shell Compression: Overview of the pressure difference created at the feeder and at the casting as a function of the shell compression that occur during cooling and solidification . . . . .	255
13.6	Driving Force, Graphite Expansion: Overview of the pressure difference created at the feeder and at the casting as a function of the graphite expansion that occur during Solidification and cooling . . . . .	256
13.7	Driving Force, Pressure Loss: Overview of the pressure loss effect . . . . .	258
13.8	Driving Force, Feeding Requirement: Overview of the need for feeding	260



# List of Tables

4.2	Alloy Compositions for $\alpha$ (EN-GJS-500-7) and $\beta$ (EN-GJS-450-10) . . . . .	68
4.1	Casting Geometry in mm and moduli in mm . . . . .	68
4.3	Feeder overview . . . . .	70
4.4	Casting overview . . . . .	71
4.5	Feeder sleeve dimensions . . . . .	72
7.1	Topography overview . . . . .	107
7.2	Measurement calibration of reference artefact . . . . .	113
7.3	Individual distribution identification—Goodness of fit for $\alpha$ 23A . . . . .	114
7.4	Null hypothesis testing. . . . .	116
7.6	Analysis of Variance (ANOVA)—95 % confidence interval, rows . . . . .	116
7.5	Analysis of Variance (ANOVA)—95 % confidence interval, columns . . . . .	116
7.7	Significance index (b) . . . . .	117
7.8	Uncertainty data . . . . .	118
7.9	Uncertainty budget . . . . .	119
7.10	Uncertainty results . . . . .	119
7.11	Normalised error table . . . . .	120
7.12	Normalised error matrix . . . . .	121
11.1	Calculation of the feeder modulus required for each of the castings . . . . .	167
11.2	Alloy composition for the EN-GJS-500-14 alloy as measured at the beginning of each of the four sessions . . . . .	167
11.3	Overview of the selected feeders and the custom prototypes . . . . .	168
11.4	Overview of the chosen feeders from the Feedex HD V series . . . . .	169
11.5	Trial plan overview . . . . .	172
12.1	Overview of the ultrasound porosity analysis results . . . . .	180
12.2	Overview of the ultrasound porosity analysis results, sorted according to upper and lower feeder modulus . . . . .	194
12.3	Conversion table for $M^\infty$ . . . . .	194
12.4	Overview of the castings that had atmospheric punctures at the pre-feeder neck . . . . .	199
12.5	Modulus scaling ratios: Theoretical and recorded via numerical simulations . . . . .	208
12.6	Overview of parameter variation for numerical simulation of porosity probabilities . . . . .	224



# List of Supplements

The following list of supplements constitute the dissertation.

## Supplement I

page 301

---

### Quantification of Feeding Effects of Spot Feeding Ductile Iron Castings Made in Vertically Parted Molds

N.K. Vedel-Smith	Technical University of Denmark, Department of Mechanical Engineering
N.S. Tiedje	Technical University of Denmark, Department of Mechanical Engineering
J. Sällström	Foseco Sweden AB
K.T. Maza	Valdemar Birn A/S

Vedel-Smith was the main author. Tiedje contributed with review and evaluation. Vedel-Smith, Sällström, and Maza performed the experimental part.

Vedel-Smith presented the paper at the 2013 AFS conference in St. Louis, MO.

Paper was awarded the *Best Paper Award* at the 2014 AFS conference in Schaumburg, IL.

*Published*  
*AFS Proceedings 2013 © American Foundry Society, St. Louis, MO USA*

---

## Supplement II

page 315

---

### Effect of Feeder Configuration on the Microstructure of Ductile Cast Iron

N.K. Vedel-Smith	Technical University of Denmark, Department of Mechanical Engineering
N.S. Tiedje	Technical University of Denmark, Department of Mechanical Engineering

Vedel-Smith was the main author. Tiedje contributed with review and evaluation. Vedel-Smith performed the experimental part.

Vedel-Smith presented the paper at the 2014 TMS conference in San Diego, CA.

*Published*  
*Shape Casting: 5th International Symposium*  
*TMS Proceedings 2014 © The Minerals, Metals & Materials Society, San Diego, CA USA*  
*Edited by: Murat Tiryakioğlu, John Campbell, and Glenn Byczyski*

---

## Supplement III

page 325

---

### Thermal Distortion of Disc-Shaped Ductile Iron Castings in Vertically Parted Moulds

N.K. Vedel-Smith  
J. Rasmussen  
N.S. Tiedje

Technical University of Denmark, Department of Mechanical Engineering  
Technical University of Denmark, Department of Mechanical Engineering  
Technical University of Denmark, Department of Mechanical Engineering

Vedel-Smith was the main author. Tiedje contributed with review and evaluation. Vedel-Smith and Rasmussen performed the experimental part.

Additional material available online at <http://dx.doi.org/10.1016/j.jmatprotec.2014.11.025>

*Published*  
*Journal of Materials Processing Technology*

---

## Supplement IV

page 337

---

### Feeding Against Gravity with Spot Feeders in High Silicon Ductile Iron

N.K. Vedel-Smith  
N.S. Tiedje

Technical University of Denmark, Department of Mechanical Engineering  
Technical University of Denmark, Department of Mechanical Engineering

Vedel-Smith was the main author. Tiedje contributed with review and evaluation. Vedel-Smith performed the experimental part.

Vedel-Smith presented the paper at the 10<sup>th</sup> SPCI conference in Mar del Plata, Argentina, 2014.

*Published*  
*10<sup>th</sup> International Symposium on the Science and Processing of Cast Iron*  
*SPCI10, Mar del Plata, Argentina, 2014*

---

# Acknowledgements

First and foremost, my thanks and gratitude to my supervisor—Associate Professor Niels Skat Tiedje. It has been a privilege to work with you!

Thank you also to the rest of the foundry group, present and previous; Ugochukwu Chibuzoh Nwaogu, Elham Moumeni, Giovanni Luca Di Muoio, Kamran Mohaghegh, Emil Hovad, Jakob Skov Nielsen, Jakob Rasmussen, Robert Vedel Mackay, and Anette Fournais Kaltoft. You have all been a great help and support throughout the project. Many exciting and educating discussions have come of this collaboration.

My gratitude to the students I have supervised through the past years: Rune Engelberth Hansen, Sebastian Jan Hamdan, Mikkel Kolding, Morten Strange Blumenfeld, Tobias Theilman Rasmussen, Þóroddur Björnsson, David Hansen, and Jes Bandsberg Pedersen. Your efforts have been distinct, and your work with your projects yielded outstanding results. I have learnt many things, about teaching as well as academically, from working with you in your projects.

Special thanks to Professor Attila Diószegi and Sadaf Vazehrad at Jönköping University, School of Engineering, Sweden. I am grateful for your time and dedication to teaching me the art of colour etching, and for letting me use your facilities in Jönköping on more than one occasion.

Thank you to Casper Petersen for his help with, and introduction to, MatLab.

A great thank you to all the people that have been involved in the project. Thank you to MAGMA GmbH; with Marc Schneider and Jesper Thorborg, FOSECO Ltd.; with Jan Sällström, Christof Volks, and Ian Delaney, DISA Industries A/S; Niels Winter Rasmussen, Per Leif Larsen, and Charlie Brown, and Valdemar Birn A/S; with Kenneth Trøjborg Maza and Søren Krabbe Knudsen. Without you this project would never have come to be, nor been what it has become.

Thank you to ELFORSK and the PSO funds from the Danish Government for funding the project.

A thought of gratitude to Till Lindemann, Richard Z. Kruspe, Paul H. Landers, Oliver Riedel, Christian Lorenz, and Christoph Schneider for your ever-present and valued company during the time of writing.

Finally, my acknowledgement, gratitude, and love to my wife, Catharina. Without your tireless effort and acceptance, this dissertation would never have come to be. I am grateful that it did.



# Abbreviations

## General

---

ABS.....	Poly(Acrylonitrile Butadiene Styrene)
ADI.....	Alternating Directional Implicit
AMC.....	Automatic Mould Conveyor
AP.....	Aligned Porosities
ATAS.....	Adaptive Thermal Analysis System
BCC.....	Body-Centred Cubic
BCE.....	Before Common Era
CAD.....	Computer Aided Design
CCT-diagram....	Continuous Cooling Transformation-diagram
CEV.....	Carbon Equivalent Value
CMM.....	Coordinate Measurement Machine
CNC.....	Computer Numerical Control
CP.....	Non-Linear Clustered Indications
DoF.....	Degrees of Freedom
FCC.....	Face-Centred Cubic
FDM.....	Fused Deposition Modelling
FDM.....	Finite Difference Method
FEM.....	Finite Element Method

## General

---

FPC.....	Future Process for Casting
FVFD.....	Finite Volume Finite Difference Method
GP.....	Graphite Precipitation Coefficient
HPDC.....	High Pressure Die Casting
HTC.....	Heat Transfer Coefficient
LP.....	Linear Porosities
MEF.....	Modulus Extension Factor
MP.....	Measurement Position
MPE.....	Maximum Permissible Error
NPP.....	Normal Probability Plot
PP.....	Squeeze Plate
PPI.....	Pores Per Inch
SDAS.....	Secondary Dendrite Arm Spacing
SP.....	Swing Plate
SP.....	Non-Linear Isolated Indications
TC.....	Thermocouple
TTT-diagram....	Time-Temperature Transformation-diagram

## Elements

---

Al . . . . .	Aluminium	13
B . . . . .	Boron	5
Be . . . . .	Beryllium	4
C . . . . .	Carbon	6
Ce . . . . .	Cerium	58
Cr . . . . .	Chromium	24
Cu . . . . .	Copper	29
Fe . . . . .	Iron	26
H . . . . .	Hydrogen	1
K . . . . .	Potassium	19
La . . . . .	Lanthanum	57
Li . . . . .	Lithium	3
Mg . . . . .	Magnesium	12
Mn . . . . .	Manganese	25
Mo . . . . .	Molybdenum	42
N . . . . .	Nitrogen	7
Na . . . . .	Sodium	11
Ni . . . . .	Nickel	29
O . . . . .	Oxygen	8
P . . . . .	Phosphorus	15
S . . . . .	Sulphur	16
Si . . . . .	Silicon	14
Sn . . . . .	Tin	50

## Elements

---

Ta . . . . .	Tantalum	73
Te . . . . .	Tellurium	52
Ti . . . . .	Titanium	22
W . . . . .	Tungsten	74

## Alloys

---

ADI . . . . .	Austempered Ductile Iron
CGI . . . . .	Compacted Graphite Iron
LGI . . . . .	Lamellar Graphite Iron
SGI . . . . .	Spherical Graphite Iron
$\alpha$ -alloy	EN-GJS-500-7
$\beta$ -alloy	EN-GJS-450-10
$\tau$ -alloy	TC-castings EN-GJS-500-14

## Companies

---

Vald. Birn . . . . .	Valdemar Birn A/s
DISA . . . . .	DISA Industries A/s
DTU . . . . .	Technical University of Denmark
FOSECO . . . . .	FOSECO Ltd.
MAGMA . . . . .	MAGMA GmbH
PSO . . . . .	Public Service Obligation



# Nomenclature

$\alpha$	Sum of liquid and solid contraction	$\dot{T}_s$	Cooling rate at the solidus temperature
$\alpha$	Thermal expansion coefficient for the measurand	$\eta$	Viscosity
$\alpha_L$	Linear thermal expansion coefficient	$\gamma_{LG}$	Gas/liquid surface energy
$\alpha_V$	Volumetric thermal expansion coefficient	$\lambda$	Heat transfer coefficient [ $\text{W}/\text{m}^2\text{K}$ ]
$\beta$	Thermal expansion coefficient for the instrument	$\lambda_2$	Secondary dendrite arm spacing (SDAS)
$\beta$	Total solidification shrinkage ( $\beta = \rho_s - \rho_l/\rho_l$ )	$\mu$	Viscosity of the liquid metal
$\chi^2$	Normality test of experimental and theoretical distributions	$\mu_l$	Dynamic viscosity of the liquid
$\Delta H$	Change in Enthalpy during solidification	$\bar{\sigma}_R$	Average of the standard deviation for the reference
$\Delta h$	Latent heat of fusion	$\bar{\sigma}_S$	Average of the standard deviation for the sample
$\Delta L$	Change in length, $L$	$\bar{R}$	Average of the reference
$\Delta P$	Pressure drop across the mushy zone	$\bar{S}$	Average of the sample
$\Delta P_{cr}$	Critical pressure drop ( $\Delta P_{cr} = P_{liq} - P_{cr}$ )	$\rho C_p$	Specific heat content
$\Delta T$	Temperature change	$\rho$	Density [ $\text{kg}/\text{m}^3$ ]
$\Delta T$	Undercooling reached at recalescence	$\rho^\gamma$	Density of austenite
$\Delta T_f$	Alloy freezing range ( $\Delta T_f = T_{liq} - T_{sol}$ )	$\rho_l$	Density of the liquid
$\Delta T_L^g$	Undercooling relative to the graphite liquidus	$\rho_m$	Density of the mould
$\Delta V$	Volume change	$\rho_s$	Density of the solid
$\Delta x$	Elongation	$\rho_s$	Solid density of the metal
$\dot{\sigma}_\gamma$	Yield stress increment	$dp/dx$	Incremental pressure change per distance
$\dot{\epsilon}^{Pl}$	Plastic strain increment	$dR/dt$	Growth rate of the eutectic cell [ $\text{m}/\text{s}$ ]
$\dot{Q}$	Heat flow [ $\text{J}/\text{s}$ ]	$\sigma$	Standard deviation
$\dot{q}$	Heat flux (heat transfer rate per unit area) [ $\text{W}/\text{m}^2$ ]	$\sigma$	Stress
$\dot{T}$	Temperature increment ( $\dot{T} = dT/dt$ )	$\sigma^2$	Variance of individual data
		$\sigma_\gamma$	Yield stress
		$\sigma_m^2$	Variance of the average of $q$ data
		$\varepsilon$	Graphite expansion during solidification
		$\varepsilon$	Strain

$\varepsilon^{El}$	Elastic strain	$C2_T$	CMM x-axis coordinate value, measurement side two
$\varepsilon^{Pl}$	Plastic strain	$c_j$	Sensitivity coefficients
$\varepsilon^{Th}$	Thermal strain	$C_L$	Amount of gas dissolved in the liquid
$\varepsilon^{Tot}$	Total strain	$C_L$	Composition of liquid at the solid-liquid interface
$\varepsilon^{Tp}$	Transformation plasticity strain	$C_L^{max}$	Maximum solubility of Gas in the liquid
$\varepsilon^{Tr}$	Transformation strain	$C_m$	Specific heat of the mould
$\varepsilon_\gamma$	Displacement at the start of austenite shrinkage ( $T_{\gamma shr}$ )	$C_p$	Specific heat capacity [ $\text{J/kg K}$ ]
$\varepsilon_{Gr}$	Displacement at the start of graphite expansion ( $T_{Gr exp}$ )	$C_p$	Specific heat capacity [ $\text{J/kg K}$ ]
$\varepsilon_S$	Displacement at the end of solidification ( $T_S^\epsilon$ )	$C_S$	Composition of solid at the solid-liquid interface
$^\circ T_L$	Nominal liquidus temperature	$Crit$	Criterion number
$^\circ V$	Initial volume of the elementary domain	$D$	Characteristic distance [m]
$^\circ w_C$	Nominal carbon composition	$d$	Dendrite arm spacing
$^\circ w_C$	Nominal mass fraction of Carbon (C) in domain	$D^2$	Area of mushy zone
$^\circ w_{Si}$	Nominal silicon composition	$dN$	Number of graphite particles
$\Delta x$	Length of the mesh cell in the x direction	$E$	Young's modulus of elasticity
$\Delta y$	Length of the mesh cell in the y direction	$e$	Efficiency
$t_r$	Radius of the elementary volume at time $t$	$E_{Gen}$	Energy generated inside a given domain
${}^t V$	Volume of the previous elementary domain at time $t$	$E_{In}$	Energy added to a given domain
$A$	Area [ $\text{m}^2$ ]	$E_N$	Normalised error
$A$	Nucleation constant	$E_{Out}$	Energy subtracted from a given domain
$a$	Generic side length	$E_{Stored}$	Energy stored in a given domain
$a_j$	Half of variability band	$E_T$	Tangent modulus for mechanical strain
$A_n$	Inoculation amount constant	$F$	Force
$B$	Inoculation constant dependent on the inoculation quality	$f_L$	Fraction of remaining liquid
$b$	Measurement bias	$f_s$	Fraction solid
$C$	Mould-metal interface constant	$f_s$	Fraction solid
$C1_T$	CMM x-axis coordinate value, measurement side one	$f_v$	Flatness value
		$G$	Temperature gradient
		$g^\gamma$	Volume fraction of austenite in domain
		$g^l$	Liquid fraction in off-eutectic $V^{off}$
		$G_{cr}$	Critical temperature gradient at the solidus temperature

$g_{l,cr}$	Critical fraction liquid	$n$	Number of data used for evaluating the variance
$G_s$	Temperature gradient at the solidus temperature	$n_d$	Input multiplicity
$H$	Latent heat of the metal	$n_r$	Output multiplicity
$h$	Uncertainty budget safety factor	$N_V$	Number of eutectic cells per $\text{mm}^3$
$h_{ratio}$	Ratio between height and width of the generic casting	$P$	Uncertainty level
$K$	Permeability of the porous region being fed	$P_\gamma$	Pressure induced by surface tension on the pore
$k$	Equilibrium partition coefficient	$P_{amb}$	Ambient pressure applied on the mould
$k$	Spring constant	$P_{exp}$	Expansion pressure due to phase transformations
$k$	Thermal conductivity [ $\text{W}/\text{mK}$ ]	$P_{gas}$	Gas evolution
$k_a$	Coverage factor	$P_{mush}$	Sum of local pressure in the mushy zone
$K_m$	Thermal conductivity of the mould	$P_{shr}$	Negative pressure from resistance to shrinkage induced flow
$K_n$	Nucleation rate depend on Si content	$P_{st}$	Metallostatic pressure
$L$	Capillary flow length	$q$	Heat flow (heat flux) perpendicular to the surface [W]
$L$	Length	$q$	Number of data averaged
$L_{20}$	Length (thickness) of the casting at the chosen reference temperature.	$R$	Isotherm velocity
$M$	Modulus of the section [mm]	$R$	Radius of the capillary
$m$	Exponent	$R$	Reference
$M_c$	Modulus of the casting, or section of the casting	$r$	Radius of the pore
$M_c^{Vol}$	Casting modulus, volume criterion	$r^\gamma$	Outer radius of the austenite shell
$M_f$	Required feeder modulus to feed the casting, or section of the casting	$r^g$	Radius of the graphite nodule
$M_f^{Vol}$	Feeder modulus, volume criterion	$R_g$	Radius of the graphite nodule within the eutectic cell [m]
$M_g$	Geometric modulus	$R_{xy}$	Aspect ratio between the x and y directions.
$M_{neck}$	Modulus of the pre-feeder neck [mm]	$Re$	Reynolds Number
$M_t$	True modulus	$S$	The thickness of the solidified layer at a given time $t$
$MEF$	Modulus Extension Factor	$s$	Estimated standard deviation
$N$	Linear scale factor	$s^2$	Variance
$N$	Total number of graphite particles	$ST$	Shrinkage time [%]
$n$	Inoculation efficiency constant	$T$	Temperature [ $^\circ\text{C}$ ]
		$t$	Time [s]
		$T_0$	Initial temperature of an infinite mould

$T_{\gamma shr}$	Temperature at which austenite shrinkage starts	$T_{Sol}$	The solidus temperature of the alloy
$T_{close}$	Temperature at the thermal centre of the casting when the pre-feeder neck closes off	$t_{sol}$	Time in seconds for the pre-feeder neck to cool from the pouring temperature to a fraction solid of 100 % [s]
$t_{close}$	Time at the thermal centre of the casting when the pre-feeder neck closes off	$T_{start}$	Initial superheated temperature of the melt
$T_{EG}$	Equilibrium Iron-Graphite eutectic temperature [°C]	$t_s$	Solidification time [s]
$T_{EG}$	Eutectic temperature	$T_S^e$	Temperature at the end of solidification as indicated by the linear displacement analysis
$T_{ER}$	Temperature at the maximum recalescence during the eutectic solidification	$U$	Expanded uncertainty
$T_{eut}$	Temperature at the thermal centre of the casting when the casting reaches the eutectic arrest	$u$	Flow velocity of the metal feeding through the solidifying dendrite structure
$t_{eut}$	Time in seconds for the centre of the casting to cool from the pouring temperature to a eutectic temperature [s]	$u^2$	Variance (GUM)
$T_{EU}$	Temperature at the maximum undercooling during the eutectic solidification	$u_3$	Uncertainty in three dimensions
$T_E$	Temperature at the start of eutectic solidification	$u_l$	Liquid velocity in the mushy zone
$T_{Freeze}$	The freezing temperature of the alloy where the material has no flowability	$u_n$	Uncertainty component
$T_F$	Temperature at which the material is fully solidified	$V$	Volume
$T_f$	Melting point of the pure component [°C]	$v$	Velocity [m/s]
$T_{Gexp}$	Temperature at which graphite expansion starts	$V^{off}$	Volume of off-eutectic
$T_i$	Temperature at the metal-mould interface	$V_c$	Amount of melt the feeder (as a minimum) must be able to supply to the casting during solidification
$T_{LA}$	Temperature at the liquidus arrest	$V_f$	Total volume of the feeder
$T_{Liq}$	The liquidus temperature of the alloy	$V_f^{avbl}$	Volume of melt available for feeding
$T_L$	Temperature at the liquidus line intersection [°C]	$w_C$	Mass fraction of C
$T_{max}$	Maximum temperature reached during the recalescence—the eutectic arrest	$w_C^{\gamma/g}$	Mass fraction of C in the austenite surrounding the graphite nodule
$T_{min}$	Minimum temperature reached during initial undercooling	$w_C^{\gamma/l}$	Mass fraction of C in the off-eutectic austenite
$T_m$	Melting point of the metal	$w_C^{\gamma}$	Mass fraction of C in the austenite
		$w_C^E$	Eutectic carbon composition
		$w_C^g$	Mass fraction of C in the graphite
		$w_C^l$	Mass fraction of C in the liquid
		$W_{Si}$	Weight percent of Si
		$w_{Si}^E$	Eutectic silicon composition
		$x, y, z$	Spatial dimensions [m].
		$x_{cr}$	Critical spatial distance

M <sup>∞</sup>	Proportional modulus factor describing the ration between the feeder modulus and the casting modulus.	GF	Graphite Expansion, Feeder
*	Outliers	P-Value	Determines the appropriateness of rejecting the null hypothesis in a hypothesis test.
Ang	Angle of the valley direction	PL	Pressure Loss Factor
Cen	Height at the centre of the disc casting	Por	Indication of porosities
DF	Sum of Driving Forces	SC	Shell Compression, Casting
Dir	Direction of the valley of the disc casting	SF	Shell Compression, Feeder
Dist	Distance of the valley	SV	Side view of the sectioned disc casting
FR	Feeding Requirement, Casting	VC	Volume Contraction, Casting
GC	Graphite Expansion, Casting	VF	Volume Contraction, Feeder
		Vol	Volume of the valley



# To the Reader

Dear reader,

The dissertation you are reading is the embodiment of the work and effort encompassed in the Ph.D. project entitled; '*Improvement of Feeder Technologies for Energy Savings in Cast Iron Foundries*'. The project has required many long nights and weekends, but has also yielded many profound and awarding discoveries; scientific as well as personal.

## Structure of the Dissertation

---

The dissertation is divided into five parts: **N**, **I**, **II**, **III**, and **IV**.

The scope of the dissertation is framed in the introductory part—**Part N**: Introduction, from page 1. This part covers the project description and theoretical background of the research.

The first part—**Part I**: Feeding Secluded Sections, from page 65 and onward—focus on proving and documenting that secluded sections can be fed using spot feeders and providing a quantifiable scale of the feeding efficiency of the different insulating and exothermic feeders. Examination of the feeder sleeve material's influence on the casting's microstructure is also provided here. Additionally, the part also addresses thermal deformation and how this is governed by the thermal influence of the different feeder combinations.

The second part—**Part II**: Investigate the fundamental rules of spot feeding without the aid of gravity. Three different modulus castings are examined using a series of varying spot feeders and their proportional feeding efficiency. The results are subsequently used to develop a description of the driving forces governing the feeding regime. Additionally, the castings are simulated, and the porosity prediction of the numerical simulations are evaluated. These results are found from page 155 and onward.

The third part—**Part III**: Dissertation Summary, from page 273 and onward—summarises and distils the findings presented in Part I and Part II into concise conclusions, followed up by an outlook on the future work. This part provides the essence of the dissertation.

Finally, the four published articles that constitute part of the work of the dissertation is supplemented in the fourth part—**Part IV**: Supplements, from page 299 and onward. Each of the supplements can be read by themselves and stands alone without the support of the dissertation. Each provides a select view of a given topic.







# Part N

## Introduction

- Introduction 1
- Feeding Review 2
- Physical Phenomena 3  
and their Simulation

“I N the beginning there was nothing . . .  
... which exploded.”

—Terry Pratchett  
*Lords and Ladies*





# Chp 01 Introduction

## Background of the Work and Project Description

### Introduction

<b>1.1 Casting Research</b> . . . . .	<b>3</b>	1.2.1 Advancing Foundry Technology . . .	5
1.1.1 Foundry Production . . . . .	3	<b>1.3 Project Description</b> . . . . .	<b>5</b>
1.1.2 Novel Technologies . . . . .	4	1.3.1 Research Hypotheses . . . . .	5
<b>1.2 Societal Relevance</b> . . . . .	<b>5</b>	<b>References</b> . . . . .	<b>11</b>



**I**NTRODUCES the reader to the background of the project and research. The project description for the research that constitute the dissertation is described, and the overall project objectives are detailed.

Keywords: . . . . Introduction, Background, Project Overview. Chapter findings reported in: . . . . . Not reported directly.

### 1.1 Casting Research

**C**ASTING is one of the oldest production methods known to man. The first Copper (Cu) castings were made more than 7000 years ago, and cast iron castings date as far back as 600 BCE [2]. Casting then was considered a witchcraft because the process was a mystery. While casting today is not considered witchcraft, many of its secrets remain a mystery waiting to be solved.

Casting is by many considered an old-fashioned way to produce goods, which, considering its history is true in some way. That casting is an old discovery does, however, not make it backwards or outdated. Casting research is one of the oldest classical engineering disciplines, and it has developed alongside the industrialisation of civilisation.

Casting research moves the boundaries of what can be made and what is feasible to produce. Research in metallurgy, casting methods, and foundry process equipment supports the industry, which in turn support the companies they supply. Improving the performance and complexity of casting, cast iron or other alloys, improve the lifetime and performance of all the machinery and product that use cast parts.

#### 1.1.1 Foundry Production

Casting is also a technology for the future. In 2009

---

Before Common Era (BCE), Carbon Equivalent Value (CEV), Fused Deposition Modelling (FDM), High Pressure Die Casting (HPDC), Silicon (Si)

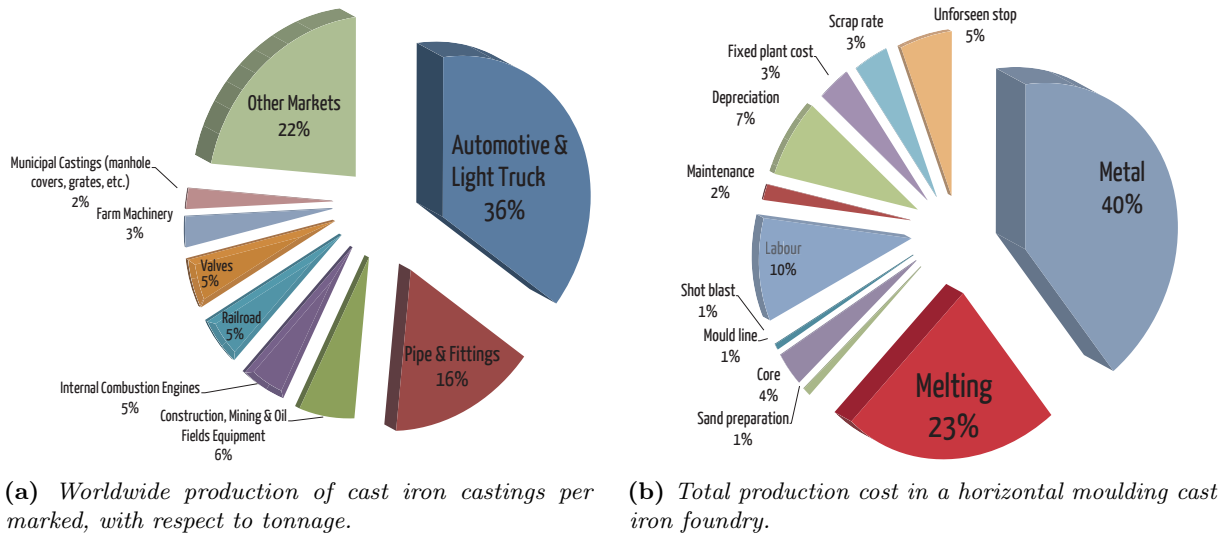


**Figure 1.1:** Production overview for cast iron. [3]

the American Foundry Society estimated that the worldwide production of ductile cast iron would grow to 23 million tonnes in 2010 [4]. Cast iron is today used in a wide range of different product and industries. See fig. 1.1a. This widespread use is because of cast iron, and other cast alloys, provide a unique combination of mechanical properties, production cost, the scale of production, and availability. Castings are produced worldwide and are not limited to low wage countries and partly because modern foundries are not particularly labour intensive, as seen in fig. 1.1b. Note, however, that fettling, machining, and other connected tasks may be labour intensive if not automated.

Foundries compete on price, naturally. However, the key to delivering the best-priced castings is often knowledge and know-how. Understanding of the process limitations and possibilities yield the best-priced quotes, enabling the foundry to make a profit while offering competitive prices. Reducing scrap and increasing the casting yield are important business parameters. Though scrap castings can be remelted and reused, the cost of melting is significant as seen in fig. 1.1b. For vertical moulding line foundries, the relative cost of melting is even higher as other production costs are reduced [3].

### 1.1.2 Novel Technologies

Technological development is a constant endeavour, also in the casting industry. All other industrial production technologies today have emerged since

the invention of casting, and these technologies exist alongside each other fulfilling different parts of the market. Metal casting is not the ideal choice for all products. Sometimes injection moulded plastics or sheet metal formed parts is the optimal choice. Casting, however, remains relevant and up to date by embracing new technologies. Hybrid technologies that combine High Pressure Die Casting (HPDC) and sheet metal forming have been shown by Joop [5] and an even closer integration of numerical simulations are being developed to improve the prediction of mechanical properties to benefit casting design, as shown by Olofsson [6].

The newest addition to the manufacturing toolbox is additive manufacturing, which by some experts is predicted to open a new era of industrialisation [7]. There is no doubt that additive manufacturing offers a new and novel solution to the production of a wide range of problems and complications that are not easily solved with traditional production technologies. Subsequently, additive manufacturing will expand into the existing market, as well as open new markets.

This new technology should, however, not be viewed as a competition to the foundry industry. While additive manufacturing may replace the production of highly specialised castings, the production of large volume castings will remain a casting technology for any foreseeable future. What is more interesting is the industry's adaptation of these emerging and maturing technologies. Additive manufacturing is today used in many foundries around

the world, and additive manufacturing especially developed for casting processes is not uncommon. FDM is used to manufacture patterns for green sand casting [8], and some companies like voxeljet GmbH and ExOne GmbH specialise in printing sand cores and moulds directly to enable extremely complex castings [9, 10]. Also, investment casting uses additive manufacturing on an industrial scale today [11].

## 1.2 Societal Relevance

---

THE project aims at reducing the consumption of electrical energy in the heaviest part of energy consumption in the Danish foundries. This energy reduction will take place by advancing the knowledge of spot feeding for use in Danish and foreign iron foundries; In Europe alone, it is expected to potentially save as much as 300 GWh per annum. This corresponds to a reduced CO<sub>2</sub> emission of 195 000 tonnes annually, assuming an average EU27 CO<sub>2</sub> emission of 650  $\frac{\%}{\text{kWh}}$  electricity. The Danish CO<sub>2</sub> emission is slightly lower at 412  $\frac{\%}{\text{kWh}}$  electricity [12]; Corresponding to 4.3% of the annual energy consumption of the Danish capital of Copenhagen, excluding transport [13].

The energy and environmental benefits will only be achieved when and if the foundries embrace the improvements offered by the findings of this project. Fortunately, as energy costs for melting are a very high production cost in cast iron foundries, the foundries themselves should have a strong incentive to use these new methods. As process stability is essential in this respect, it is also an objective to demonstrate to the foundries that these new feeding approaches work, and how they are best used in practice.

### 1.2.1 Advancing Foundry Technology

---

The work presented in this dissertation aim at improving the production of cast iron components. As described, the casting industry and technologies are competing and evolving. Knowledge and implementation of new technologies and methods are what drives the competitive edge for the foundries. Foundries in Denmark and other high wage countries survive by supplying their customers with know-how in the design and construction process, and by being able to produce castings that other foundries elsewhere cannot.

The research performed as part of this project is directed at improving the understanding of cast iron production, particularly regarding spot feeding. Providing the foundries with knowledge about feeding and feeding effects helps them improve their casting yield, reduce their scrap, and sometimes improve the mechanical properties of the castings as well. Another important aspect is to simply enable the foundries to produce complex castings that they have previously not been able to produce without loss due to too high scrap rates.

## 1.3 Project Description

---

THE feeder technology, which is used in most foundries today was developed in the first half of the 20<sup>th</sup> century. At a time where analysis methods and process technology was very different from what it is today. Though the techniques have improved through the years, the basic approach remains unchanged. It is the aim of the project to prove the application of spot feeders, also called ram-up sleeves, as these can aid high-efficient production in modern foundries. This new application must have support in a thorough analysis of the underlying feeding mechanisms that influence the efficiency of the spot feeder, as well as the spot feeder's influence on casting microstructure, dimensional accuracy, and casting deformation. Building on this the driving forces propelling the feeding and the feeding criteria will also be analysed.

### 1.3.1 Research Hypotheses

---

The project work presented in this dissertation is based on seven discrete hypotheses—some formulated at the initiation of the project, some formulated from discoveries made during the project. The hypotheses are listed below:

**Hypothesis 1** Spot feeders can (effectively) feed secluded sections located away from the parting line in vertically parted moulds

**Hypothesis 2** The location and amount of porosities can successfully be predicted via numerical simulation when spot feeding Spherical Graphite Iron (SGI)

**Hypothesis 3** Exothermic sleeve materials do not significantly influence the casting microstructure

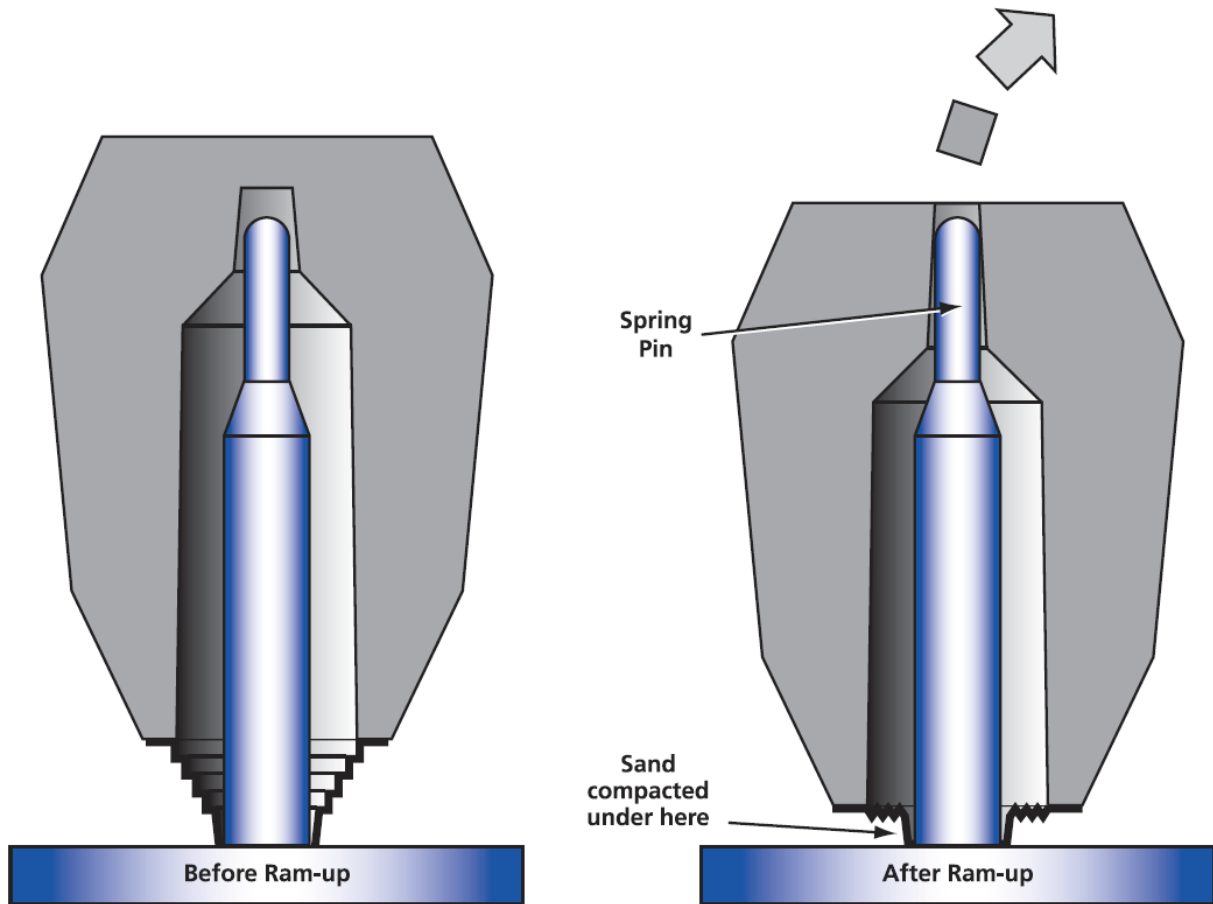


**Figure 1.2:** Schematic of the ram-up sleeve function with the metal breaker core (compressor core). Here shown for a FEEDEX VSK sleeve before and after moulding [14].

**Hypothesis 4** Thermal deformation is significantly influenced by spot feeders and can (to some degree) be controlled by choice of feeders

**Hypothesis 5** The side feeder modulus necessary to feed SGI is *not* a linear function of the casting module, and traditional methods overestimate the feeder size

**Hypothesis 6** Multiple smaller feeders can, for elongated sections, provide better feeding of a single casting section than a single large feeder

**Hypothesis 7** The feed material movement in spot feeding can be described by the sum of driving forces

Each of the hypotheses will be elaborated in the following sections, describing the background, relevance, and novelty of each of the research questions. The conclusions on the research hypotheses are presented in chapter 15, on page 275.

**Hypothesis 1:** Spot feeders can (effectively) feed secluded sections located away from the parting line in vertically parted moulds

This hypothesis is addressed in chapter 5, on page 75 and chapter 9, on page 135.

**Background** Sleeves have been used for more than three decades to prolong the solidification time and increase the yield of feeders. Ram-up sleeves with metal breaker cores were introduced for horizontal mould in the mid-00s [15]. The metal breaker core, or compressor core, was developed with two distinct goals: (1) Prevent crushing of the sleeves during moulding, and (2) ensure sufficient compaction of the sand between the feeder sleeve and the casting. This development allowed spot feeders to be used in high-pressure moulding operations, which are

the conditions used for moulding vertically parted moulds. The principle is shown in fig. 1.2 on page 6.

The idea with spot feeders is to offer foundries a type of feeder perpendicular to the moulding direction. For vertically parted moulds, however, this type of feeder becomes a type of side feeder with two distinct properties: (1) It can be mounted in positions otherwise inaccessible by traditional feeder approaches, and (2) it is without the aid of the pressure height available for top mounted feeder and to some extent traditional side feeders. An example of a casting with secluded sections is shown in fig. 1.3 on the following page.

**Relevance** The application of spot feeders to secluded sections in vertically parted moulds is of great interest as it can provide foundry engineers with a new way to access these troublesome areas, as it has been achieved with horizontally parted moulds where the spot feeders were placed in the cope. However, turning the feeder 90° and placing it below the top of the casting significantly changes the mode of operation for the feeder. The ferrostatic pressure will at best be negated if the feeder is placed at the very top of the casting. In most cases, however, the feeder has to overcome a significant pressure height to transport the melt into the casting. A means of transport that normally is aided by gravity.

**Novelty** The project aims to answer *if spot feeding of castings in vertically parted moulds is possible or not*, and if possible, under which conditions. Before the research comprised in present dissertation, the application of ram-up sleeves as spot feeders has not been investigated for vertically parted moulds. The work preceding this project was limited to closed tests performed by FOSECO Ltd.

**Hypothesis 2:** The location and amount of porosities can successfully be predicted via numerical simulation when spot feeding SGI

This hypothesis is addressed in chapter 7, on page 97, chapter 9, on page 135, chapter 12, on page 175, and chapter 13, on page 231.

**Background** Numerical simulations provide important process information for the foundry engineers during the design of the casting and the casting

layout. In this respect, the reliability of the simulation results is important. If the simulations show porosities that are not there in the castings, unnecessary efforts may be wasted on removing the non-existing porosities predicted by the simulations. On the other hand, if the simulations predict a sound casting, but porosities remain in the actual castings, then the porosity criteria cannot be used as a measure by which parameters or factors to optimise the casting layout.

**Relevance** Simulations approximate the real world, which is sufficient as long as the simulations provide useful information about the process in question. However, as simulations become more advanced and complex and have to encompass a vast range of process parameters, as eg for simulation of casting processes, it is no longer a trivial task evaluating if a casting effect, as eg porosity formation, can be simulated satisfactorily under specific conditions. Delimitations relating to the assumptions in the equations and the modelling setup can be analysed. However, as the feeding process itself is a complex process involving multiple different physical effects, so does the numerical model encompasses multiple interacting factors depicting the same physical effects. Hence, without an exhaustive knowledge of the underlying physics determining the outcome of the feeding and porosity formation, the outcome of the simulated reality cannot be guessed either. A shortcut to establishing the validity of the simulated porosity predictions is based on empirical knowledge—comparing castings and simulations.

**Novelty** As the application of spot feeders to the secluded section for castings made in vertically parted moulds is a novel approach to solving this type of feeding problems, no empirical basis exists on which a comparison between a state-of-the-art numerical simulation software can be benchmarked against. The work presented in this dissertation strives to establish the first benchmark for the comparison of the simulated and the actual porosities for spot feeders in vertically parted moulds.

**Hypothesis 3:** Exothermic sleeve materials do not significantly influence the casting microstructure

This hypothesis is addressed in chapter 6, on page 89 and chapter 9, on page 135.

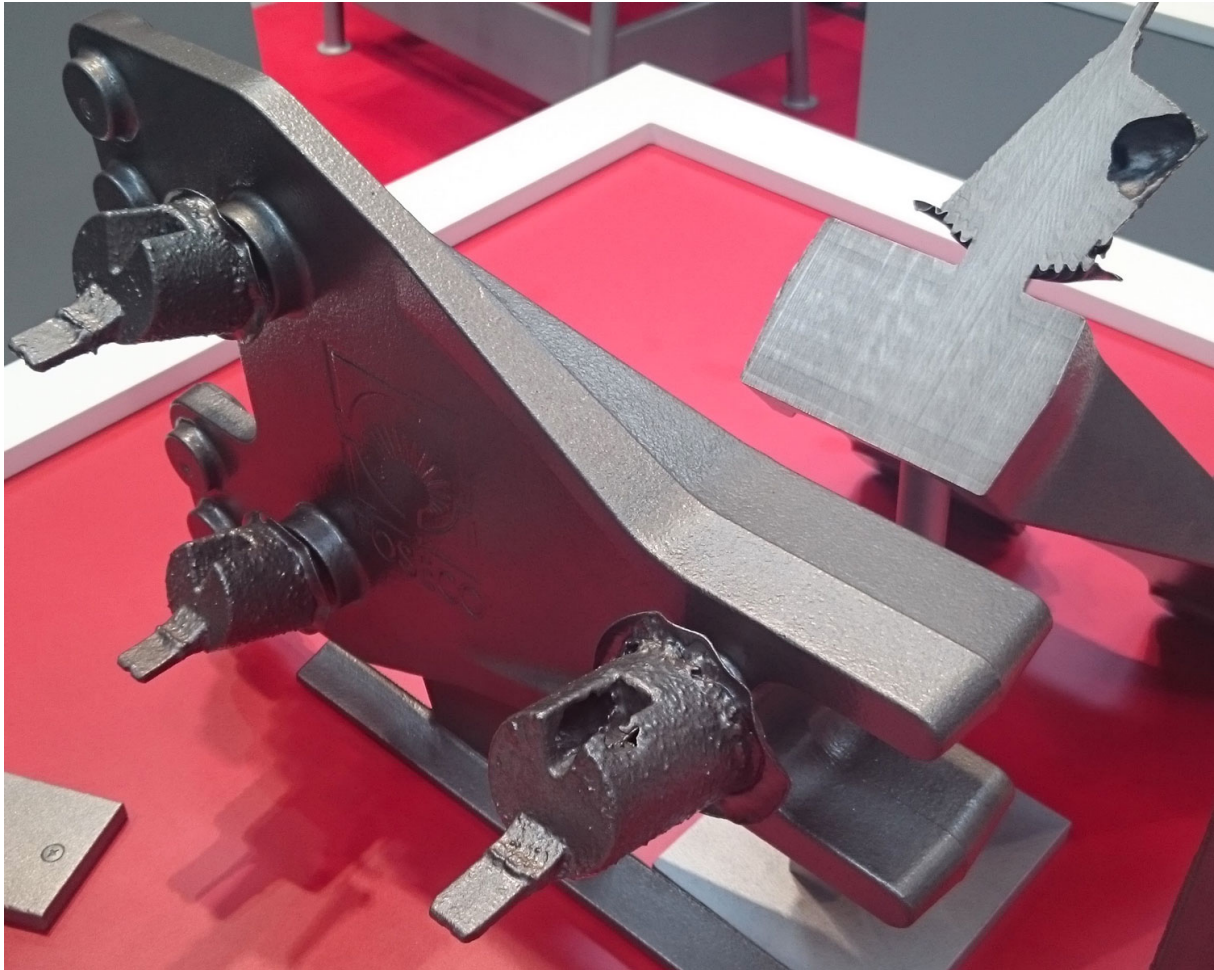


**Figure 1.3:** *Cast iron casting, made in a vertically parted mould, using spot feeders to feed secluded sections. Note that the tilted sleeves are a new option developed to increase the pressure height. Shown by FOSECO Ltd. at GIFA 2015.*

**Background** Some foundries are reluctant to use exothermic sleeves for two reasons: They fear (1) that the heat of the exothermic material will change the microstructure of the castings resulting in reduced strength and solidification related defects, and (2) that unburnt exothermic material is recycled with the return sand potentially ending up causing defects in subsequent castings. Only the first part is addressed in this dissertation. The feared microstructural changes are speculated by be related to excessive heat provided by the exothermic sleeve and by the fluoride used in the exothermic sleeve material [16]. Additionally, some foundries have expressed concern that the metal breaker core will act as a chill, resulting in microstructural changes

in the casting [15].

**Relevance** Microstructural changes are in this case unwanted. If exothermic feeder sleeves can cause changes to the casting microstructure, then it is important to document the nature and range of the change. If the exothermic sleeves do not influence the casting microstructure, then this is also important to document so that foundries can use these feeders without fearing unwanted microstructural changes to their castings.

**Novelty** No previous publications have addressed the correlation between exothermic feeder sleeves and the microstructure of the cast iron castings.



**Hypothesis 4:** Thermal deformation is significantly influenced by spot feeders and can (to some degree) be controlled by choice of feeders

This hypothesis is addressed in chapter 7, on page 97, chapter 8, on page 123, and chapter 9, on page 135.

**Background** Precision is an increasingly important parameter in cast components. As castings are influenced by the thermal fields created by the feeders, the choice of feeder become relevant concerning high precision parts as well as reduction of machining allowance. Danish foundries are today producing goods with a cast tolerances of 0.2 mm—equivalent to the average grain size of the green sand [17, 18].

**Relevance** The need for machining is often a determining factor with regards to the foundries making a profit on a given component. Hence, reduced or completely omitted machining allowance have a significant impact on the profitability of a casting for the foundry. The ability to control the casting process to a level where machining is rendered needless due to the high precision of the as-cast component is a considerable competitive advantage for a foundry, compared to cost related to casting the component with machining allowance and subsequently machining the required tolerances. Reduced or omitted machining allowance is an advantage for both the foundry and their customers, as well as an environmental advantage.

Note that many other process parameters play a great role regarding the deformation of cast iron castings and the ultimate dimensional accuracy that can be delivered. However, the thermal field introduced by the feeders is a link in the chain—a chain that must be controlled largely to reduce or negate the need for machining allowance.

**Novelty** Casting deformation is not a new discovery. The novelty of the present study is the correlation between feeder configuration, alloy composition, and the resulting deformations. The influence of the pearlite formation on the deformation variance of the castings is also new, and explain the observed differences between the low and high Si alloys.

**Hypothesis 5:** The side feeder modulus necessary to feed SGI is *not* a linear function of the casting module, and traditional methods overestimate the feeder size

This hypothesis is addressed in chapter 12, on page 175 and chapter 13, on page 231.

**Background** A traditional foundry approach to feeder design dictates that the feeder modulus must be 1.2 times larger than the modulus of the casting section it is feeding as reported by Karsay [19]. Kotas reports this 20% increase as a safety factor [20]. Though, both Chvorinov and Hansen et al have shown that the basic modulus approach is neither shape- nor size-independent [21, 22], the approach to feeder design is still based on an assumption that bigger is always better—or in other words that the feeder just needs to be large enough, then the porosities will eventually go away. Though the foundries design specialised moulded feeders for many castings, especially for castings of less than approximately 200 kg the 1.2 rule prevails.

**Relevance** Larger than necessary feeders benefit nobody. In fact, too large feeders may cause different types of casting defects, including porosities. Thus, knowledge about the scalability of feeders is important for the foundry engineers to choose the best solutions. Given that the typical (and maybe logical) action against porosities is to increase the feeder size, knowledge about the non-linear performance of cast iron feeders is very significant. Potentially the foundries in some cases should consider to reduce the feeder size instead, or even completely remove the feeder in question, to strengthen the performance of other feeders.

**Novelty** The increased graphite expansion concerning casting modulus is described by Brown [23], and Karsay also describes how large cast iron castings can be made sound completely without the use of feeders [19]. Note, however, that the requirements listed by Karsay entail requirements for both pouring temperature, that the casting modulus is at least 2.5 mm, a high CEV, a strong mould, and more. Hence, Karsay's solution is a specialised case, though it shows the non-linearity of cast iron.

The novelty of the work presented here is the investigation of castings with much smaller moduli than described by Karsay, as well as free from most of the restrictions suggested in the same article [19]. Karsay addresses the casting and its *self-feeding* abilities and finds that it is self-feeding because of its large modulus and substantial graphite expansion. The present research focuses on the modulus scaling of the feeders and the non-linear performance of

scaled feeder moduli, and show that larger feeders (including a higher graphite expansion) are not always preferable.

**Hypothesis 6:** Multiple smaller feeders can, for elongated sections, provide better feeding of a single casting section than a single large feeder

This hypothesis is addressed in chapter 12, on page 175 and chapter 13, on page 231.

**Background** Feeding of castings is often designed around the seven rules formulated by Campbell [24]. Central to this approach is rule two—heat-transfer (modulus) rule—which describes that the feeder must solidify later than the casting section it is feeding. Based on this, a typical solution is to opt for a single large feeder. This single large feeder option allows for as large a modulus as possible concerning both heat-transfer and mass-transfer (rule 3), while still optimising for casting yield.

The deciding rule is often the heat-transfer rule. If, however, the heat-transfer in a specific configuration is *not* the deciding rule, then a division of the feeder into two or more feeders may be advantageous, as this allows for feeding system designs that prioritise other feeding criteria. For example the feed path (rule 5). This single restricting parameter may be the case for some feeding scenarios (regimes) using sleeved feeders. Especially for spot feeding castings made in vertically parted moulds, as these depend on the internal forces to move the melt from the feeder into the casting, but also for extending the reach of the feeding system in the case of elongated geometries.

**Relevance** The interaction of multiple feeders with each other is important to understand the mechanisms controlling feeding as many parameters influence the process. At least the six physical aspects defined in the seven rules of feeding—rule 1 is a non-physical aspect: Do not feed (if not necessary)—and the five feeding mechanisms, both described by Campbell [24, 25], are identified physical parameters determining the function of a feeding system. Thus, knowledge about the interaction of multiple feeders is relevant for the understanding of which underlying feeding phenomena are dominant.

Additionally, overly large single feeders can cause other problems as prolonged solidifications, which can force a slowdown of production, or for large

castings graphite flotation or degeneration. Though the latter will be most pronounced within the feeder, the prolonged solidification of the casting itself may yield the same issues.

**Novelty** The application of multiple feeders is not a new thing, and multiple feeders are often placed around the rim of circular casting sections. This work represents two novelties. The first novelty is the application of multiple feeders to a casting geometry accessible for a single central feeder. In this case a bar geometry, as opposed to a ring geometry where the centre point is part of the mould or core. The second novelty is the vertical application of the feeders where the two feeders experience significantly different pressure height.

**Hypothesis 7:** The feed material movement in spot feeding can be described by the sum of driving forces

This hypothesis is addressed in chapter 12, on page 175 and chapter 13, on page 231.

**Background** The movement of the melt, or more precisely the feed material, is a result of the forces acting on the melt in the casting and the feeder. For traditional top mounted feeders, gravity is the dominant force as long as the feeder is properly vented. For spot feeders used in vertically parted moulds, gravity is no longer a constant force drawing the melt into the casting. Instead, the feeders depend on the internal forces created by the casting and the feeder, as well as the interplay of these forces.

**Relevance** It is important to know the order and magnitude of the internal forces moving the melt, as these can be used to design feeding systems that intentionally make use of these forces to transport feed material from the feeder into the casting. On the other hand, it is also important to know poorly designed feeding systems can increase the number of porosities due to unintentional combinations of the driving forces. In this respect, the description of the melt movement based on driving forces can be an essential tool for analysing and designing feeding systems. While the driving forces descriptions are valid for both top mounted and side mounted feeders, the use is particularly relevant for side-mounted feeders as they lack the direct interaction of the gravitational driving force.

Novelty The need for venting to equalise with atmospheric pressure is well known, and Campbell lists both pressure gradient and pressure (rule 6 and 7) in his seven rules of feeding [24]. The novelty of the driving force approach presented in this dissertation is that it encompasses the major pressure drivers influencing the melt. The novelty also lies in that it describes how to map these driving forces as they shift between positive and negative relative pressure—between moving the melt from the feeder into the casting and vice versa. This analysis has been possible because gravity as a driving force was negated by the horizontal application of the spot feeders.

## References

- [1] Lars Gierke. *Instrumentarium zur Planung und Umsetzung von Zulieferer-Hersteller-Netzwerken*. Peter Lang GmbH, Eurpäischer Verlag der Wissenschaften, Frankfurt am Main, 1999. ISBN: 3-631-34507-0.
- [2] Doru Michael Stefanescu. “Introduction to the Science and Engineering of Cast Iron”. In: Presented at the Metallurgy, Solidification, and Modelling of Cast Iron Castings, Jönköping, Sweden, 2013.
- [3] DISA Industries A/S, *Internal Report*. . Data.
- [4] *Worldwide Casting Tonnage Slowed by Recession*. <http://www.afsinc.org/content.cfm?ItemNumber=7613>. Data.
- [5] David Joop. “Fabrication of Hybrid HPDC-Structures with Perforated Sheet Metal Inserts”. In: Presented at the International MAGMASOFT User Meeting , Potsdam, Germany, 2014.
- [6] Jakob Olofsson. *Simulation of Microstructure-based Mechanical Behaviour of Cast Components*. School of Engineering, Jönköping University, 2014. ISBN: 978-91-87289-04-0.
- [7] David Bue Pedersen. *Additive Manufacturing Multi Material Processing and Part Quality Control*. DTU Mechanical Engineering, 2012. ISBN: 978-87-7475-384-1.
- [8] *Sand Casting With PolyJet and FDM Patterns*. <http://www.stratasys.com/solutions-applications/digital-manufacturing/tooling/sand-casting-Production>.
- [9] *Additive Manufacturing for Metal Casting*. <http://www.voxeljet.de/en/services/Production>.
- [10] *Additive Manufacturing for Metal Casting*. <http://www.exone.com/Services/3D-Printing-Services>. Production.
- [11] *Additive Manufacturing for Investment Casting*. <http://envisiontec.com/castable-materials/>. Production.
- [12] *CO<sub>2</sub>-emission per kWh*. <http://www.ens.dk/info/tal-kort/statistik-nogleletal/nogleletal/danske-nogleletal>. Data.
- [13] Kim Vedel Pedersen. *Elforsyning - Opgaver og cases*. Dansk Energi, 2010. ISBN: 978-87-91326-07-3.
- [14] Foundry Practice by FOSECO Ltd. “The Application of Compressor Core Technology for Feeding Systems in a Mass Iron Automotive Foundry”. In: 248 (2008), pp. 1–3.
- [15] Foundry Practice by FOSECO Ltd. “An Advanced Breaker Core System with Enhanced Knock Off Properties for High Pressure Moulding Applications”. In: 244 (2006), pp. 1–7.
- [16] Jörg Daier et al. *Manual of Casting Defects—Incidence and Avoidance of Defects Attributable to Moulding Sands*. 3rd ed. S&B Industrial Materials GmbH, 2011.
- [17] *Application Manual: DISAMATIC MK2, Sand moulding System*. Manual. 1995.
- [18] AFS Molding Methods & Materials Division. *Mold & Core Test Handbook*. 4th ed. American Foundry Society, 2014.
- [19] Stephen I. Karsay. “Rising Methods for Gray and Ductile Iron Castings”. In: *Int. Cast Met. J.* 5.4 (1980), pp. 45–51.
- [20] Petr Kotas. *Integrated Modeling of Process, Structures and Performance in Cast Parts*. DTU Mechanical Engineering, 2011. ISBN: 978-87-90416-54-6.
- [21] N Chvorinov. “Solving Feeders and Sink-heads”. In: *Proceedings of the 30th International Foundry Congress*. 1963.

- [22] PN Hansen, PR Sahn and E Flender. “How to Select and Use Criterion Functions in Solidification Simulation”. In: *Transactions of the American Foundrymen’s Society*. 101 (1993), pp. 443–446.
- [23] John R. Brown. “FOSECO Ferrous Foundryman’s Handbook”. In: FOSECO International Ltd., 2000. Chap. 19, pp. 296–310.
- [24] John Campbell. *Casting Practice - The 10 Rules of Casting*. Linacre House, Jordan Hill, Oxford OX2 8DP, 30 Corporate Drive, Burlington, MA 01803: Elsevier Butterworth-Heinemann, 2004. ISBN: 0 7506 4791 4.
- [25] John Campbell. *Castings, 2nd Ed.* Linacre House, Jordan Hill, Oxford OX2 8DP, 30 Corporate Drive, Burlington, MA 01803: Elsevier Butterworth-Heinemann, 2003. ISBN: 0 7506 4790 6.



## Feeding Review

### Methods and Mechanisms for Feeding Cast Iron

## Feeding Review

<b>2.1 Introduction</b> . . . . .	<b>13</b>	<b>2.4 Five Feeding Mechanisms</b> . . . . .	<b>30</b>
2.1.1 What is Feeding? . . . . .	14	2.4.1 Liquid Feeding . . . . .	31
2.1.2 Other Functions of Feeders . . . . .	14	2.4.2 Mass Feeding . . . . .	31
<b>2.2 Porosity Defect Formation</b> . . . . .	<b>14</b>	2.4.3 Interdendritic Feeding . . . . .	32
2.2.1 Shrinkage Porosities . . . . .	15	2.4.4 Burst Feeding . . . . .	32
<b>2.3 Seven Rules of Feeding</b> . . . . .	<b>19</b>	2.4.5 Solid Feeding . . . . .	33
2.3.1 Do Not Feed (Unless Necessary) . . . . .	19	<b>2.5 Advanced Feeding Methods</b> . . . . .	<b>34</b>
2.3.2 Heat-Transfer (Modulus) . . . . .	20	2.5.1 Ram-Up Sleeves . . . . .	34
2.3.3 Mass-Transfer (Volume) . . . . .	21	2.5.2 Simulation and Optimisation . . . . .	34
2.3.4 Junction . . . . .	21	2.5.3 Advanced Solidification . . . . .	34
2.3.5 Feed Path . . . . .	23	<b>2.6 Summary</b> . . . . .	<b>34</b>
2.3.6 Pressure Gradient . . . . .	28	<b>References</b> . . . . .	<b>35</b>
2.3.7 Pressure . . . . .	29		



THIS chapter presents a review of the requirements that must be fulfilled to successfully produce cast iron castings. The chapter deals with the seven feeding rules in logical order, and step by step describe the basis of the different requirements and how they can be accommodated.

Keywords: . . . . . Feeding, Riser, Feeding Rules, Modulus, Exogenous and Endogenous Solidification, Feeding Paths, Padding, Pressure Gradient, Junction, Ram-Up Sleeves.

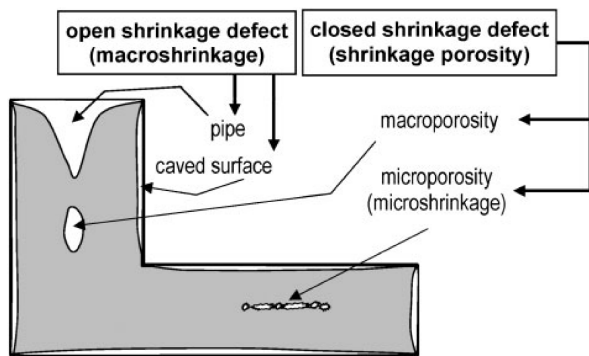
Chapter findings reported in: . . . . . Not reported directly.

## 2.1 Introduction

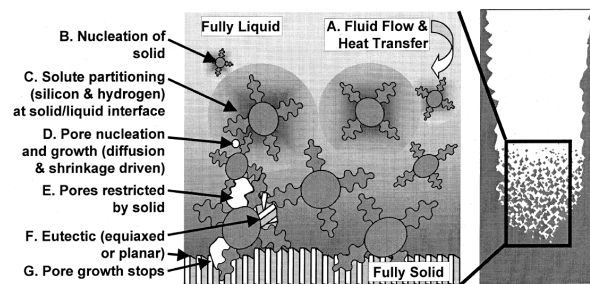
AS stated in section 1.1, on page 3, metal casting is one of the oldest methods of manufacturing known to man. Cast iron, as the first composite material manufactured, was first made more than 2500 years ago as reported by Stefanescu [28, 29].

While a basic understanding of feeding, metallurgy, or casting was not at hand at the time, our ancestors have unwittingly fought against porosities and

Aluminium (Al), Carbon (C), Carbon Equivalent Value (CEV), Compacted Graphite Iron (CGI), Hydrogen (H), Lanthanum (La), Lamellar Graphite Iron (LGI), Modulus Extension Factor (MEF), Nitrogen (N), Spherical Graphite Iron (SGI), Silicon (Si)



(a) Definition and classification of shrinkage defects. Courtesy of Stefanescu [26].



(b) Illustration of the physical processes involved in formation of microporosities. Courtesy of Lee et al [27].

**Figure 2.1:** Definition of shrinkage defects and the formation of microporosities.

other feeding-related casting defects from the very beginning. Hence, the feeding of cast iron can be said to be an ancient problem which we are still trying to understand to its fullest.

### 2.1.1 What is Feeding?

Feeding (also called risering) is an integral part of most gravity castings. Feeding is a compensation for the volume shrinkage that liquid metals undergo as they cool and solidify. Thus, a feeder is a reservoir of molten metal that supplies the casting with melt as the metal in the casting contracts due to liquid and solidification shrinkage.

A feeder does not prevent the metal from shrinking; rather it supplies liquid metal to an area that is contracting. This supply of melt requires a path between the feeder and the spot that requires feeding to conduct the flow of metal. Often the feeder must provide enough excess heat to sufficiently keep the feeding path open for the required time and secure that solidification progresses towards the feeder. Additionally, the feeder must provide a large enough quantity of liquid metal when it is needed. The feeder must close off from the casting in a way that the shrinkage in the feeder is not allowed to reach into the casting. This restriction is achieved by the design of the connecting part between the casting and the feeder, named the feeder neck.

Besides providing the casting with liquid metal at the right time and location, a feeder may also support the casting process by heating a local area, hence changing the direction of solidification and the local microstructure.

### 2.1.2 Other Functions of Feeders

Feeders fulfil other functions than supplying melt to the casting. Campbell describes that the ferrostatic pressure delivered by the pressure height of the feeder help increase the ductility of the casting and that this pressure also assists in preventing blow defects from forming [24]. For castings with poorly designed gating systems, or for melts with high amounts of slag, feeders provide a flow-off for the impurities, collecting these defects in a part that is removed from the casting afterwards and thus removing the defects. Additionally, feeders have been shown to influence the dimension of the castings by changing the ferrostatic pressure, but also solely by changing the temperature gradients found in the casting during solidification, as described by Vedel-Smith et al [30, 31].

## 2.2 Porosity Defect Formation

An important aspect of feeding, is the formation of shrinkage porosities—or preventing that it happens. As shrinkage porosities are invariably linked to feeding or the lack thereof, knowledge about feeding can be obtained by understanding how porosities are formed.

Porosities originate in the conditions and parameters of the casting process; alloy composition, purity of melt, filling conditions, gas in the melt, thermal gradients, casting geometry, volume contraction, and graphite expansion to name a few.

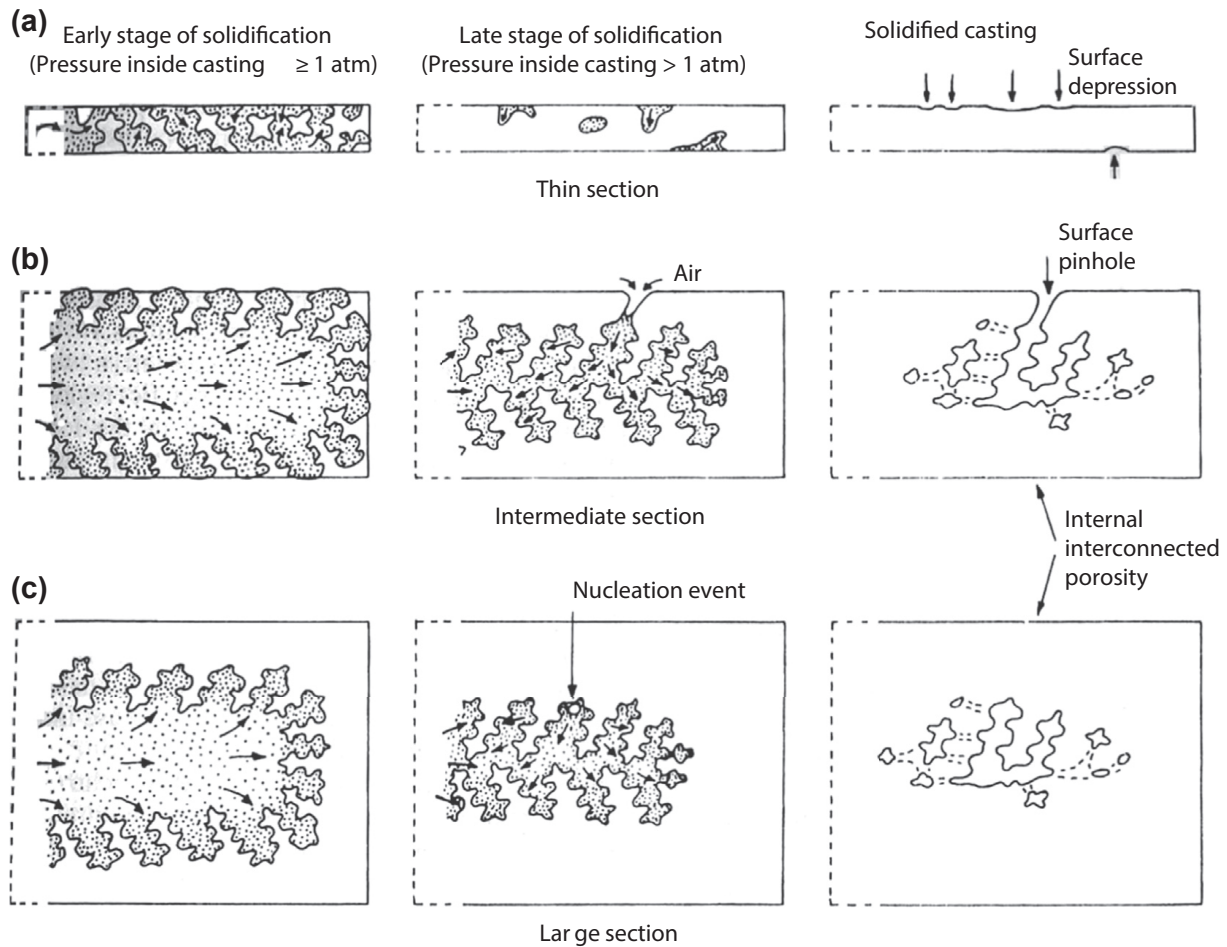


**Figure 2.2:** Solidification and porosity formation for different section sizes. Courtesy of Campbell [25].

The formation of porosities is an integral part of the process where all parameters are interconnected.

Lee et al categorise porosities as either macroporosities or microporosities and suggest that their cause is related to either volume shrinkage or gas formation [27]. Lee et al though, goes on to state that the above definitions are not this hard in reality. Note also, that Lee et al's work was on Al-Si alloys. However, the definition is also useful for cast iron. Stefanescu provides an illustration of how macro and microporosities are located in the casting—see fig. 2.1a on page 14 [26]. Lee et al's description of the formation of microporosities is shown in fig. 2.1b on page 14.

As this is not a review on casting defects in general, only the basic porosity formations typically found in cast iron will be discussed. For a more complete and hands-on list of casting defects, the reader is referred to the IKO Manual of Casting De-

fects [16]. The present review of porosity formations will address porosities formed because of volume shrinkage and gas evolution, as well as filling related defects respectively.

### 2.2.1 Shrinkage Porosities

Shrinkage porosities are related to the volume contraction of the metal during cooling and solidification, which for cast iron is complicated by the volume expansion caused by graphite precipitation. The volume change properties of cast iron are further discussed in section 3.4.1, on page 51. For now, it should be known that the metal contracts, and if not fed, will form different types of shrinkage porosities depending on the alloy, casting geometry, and cooling conditions.

Figure 2.2 illustrate how three different section sizes solidify and form porosities. The thin section

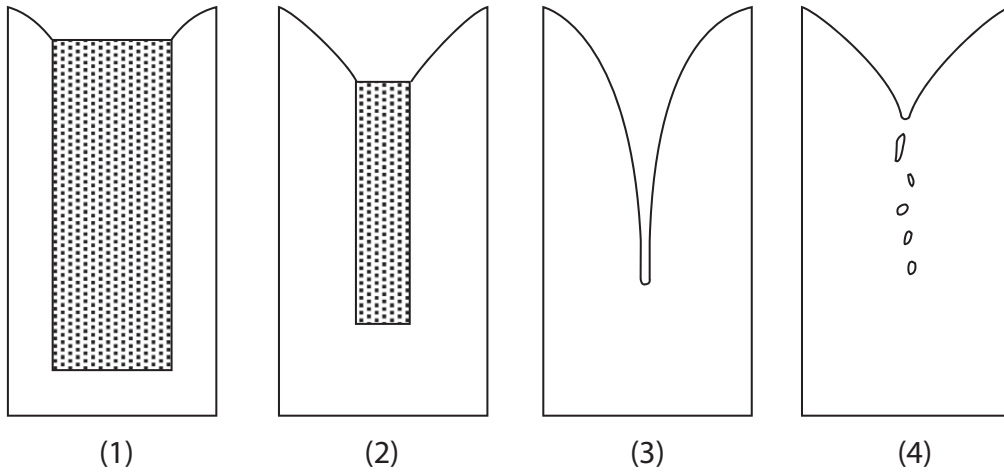


**Figure 2.3:** The stages of shrinkage cavity formation. Courtesy of Campbell [25].

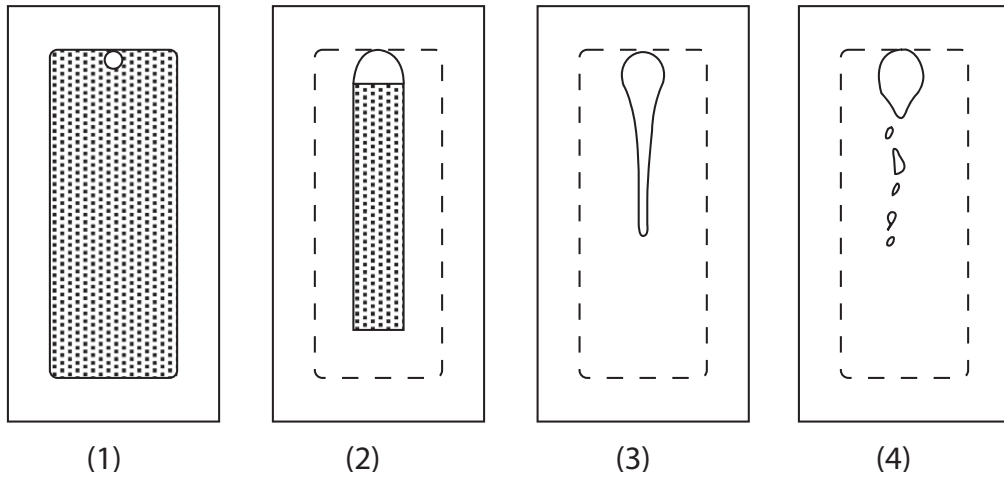


**Figure 2.4:** The stages of shrinkage porosity formation. Courtesy of Campbell [25].

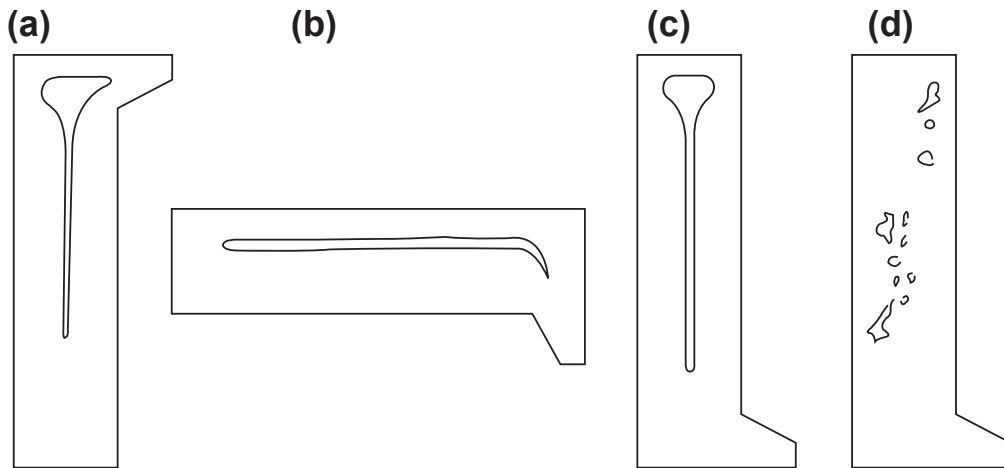


**Figure 2.5:** Geometry of the shrinkage porosity for a short freezing range alloy as a function of orientation. (a-c) show the effect of different casting orientations, and (d) shows irregular and chaotic porosity locations, which are often related to entrapped air or other gas porosities. Courtesy of Campbell [25].



(a) undergoes a rapid cooling with a shallow thermal gradient across the casting. This results in a uniform temperature distribution across the section as it solidifies, leaving the shrinkage on the outside of the casting as an example of solid feeding. The intermediate section (b) forms a shell. However, the residual melt remains in contact with the surface until the tension in the melt reaches a critical level and draws in air to relieve the pressure difference. The large section (c) on the other hand, builds the same tension in the residual melt, here, however, the melt is no longer in contact with the surface. This lack of surface contact allows the tension in the melt to build further, and at some point, an impurity will nucleate a rupture that releases the tension and forms an internal porosity.

The formation of an internal porosity is driven by the tension in the melt as it contracts. Hence, impurities in the melt—oxide films, inclusions, elevated gas content—can all initiate a rupture opening a shrinkage porosity.

#### Porosity Types

To reduce the ambiguity of the terminology often used, Stefanescu defines *shrinkage cavities* as shrinkage defects open to the atmosphere, and *shrinkage porosities* as closed porosities without access to atmospheric pressure [26]. Shrinkage cavities are formed as a consequence of metal contraction during solidification and cooling and are independent of the amount of gas dissolved in the melt and do not require a point of nucleation for the pore to initiate and grow. On the other hand, shrinkage porosities are dependent on pore nucleation and the gas content in the melt.

Figure 2.3 on page 16 shows the shrinkage cavity formation in an ‘open’ solidification that creates a shrinkage pipe into the casting. The cavity, or pipe, grows as more and more melt solidifies. This shrinkage formation is also called a primary shrinkage pipe. The scattered and disconnected pores located below the primary shrinkage pipe were originally connected to the primary shrinkage pipe, and hence, can be considered part of the same feeding problem.

Figure 2.4 on page 16 shows how a closed cavity will form a similar shrinkage porosity as seen with the open shrinkage cavity formation. The porosity will nucleate, possibly at the site of a melt impurity, and will form an internal pipe comparable to the open shrinkage cavity formation. Additionally, the enclosed shrinkage porosity will also form scattered

and disconnected pores below the primary shrinkage pipe.

Note that the shape of the shrinkage and the related pores are governed by the thermal gradients of the casting, and hence, is greatly influenced by the geometry of the casting. Thus, complex castings may have shrinkage cavity and porosity formations that are difficult to interpret. Additionally, also the orientation of the casting will influence the placement and shape of the porosities. See fig. 2.5 on page 16.

Pipe shrinkage occurs in all alloys [26], however, alloys exhibiting a wide mushy zone may allow for deformation of the mushy zone resulting in curved surfaces, also known as surface shrinkage. The phenomenon is shown in fig. 2.1a on page 14 and explained in section 2.4.5, on page 33. Other alloys exhibit a narrow mushy zone resulting in an early shell forming during solidifications. Consequently, the shrinkage defects are seen as a combination of closed shrinkage porosities (macro- and microporosities), plastic deformation of the solid shell, or the formation of a large number of vacancies in the lattice structure [26, 32]. The characteristic of the mushy zone is related to the endo- and exogenous solidification properties of the alloy, as described in section 2.3.5, on page 26.

#### Shrinkage Porosity Formation

Microporosities that are formed as a function of shrinkage are often caught by the dendritic structure of the solidifying melt. Thus, the dendrite structure influences the geometry of the pore, resulting in non-spherical porosities of sizes of a few to hundreds of micrometres [26].

The tension of the remaining melt will draw in feed material as long as the forces acting upon the melt allow this. However, towards the end of solidification, the tension in the melt will increase as shrinkage from other parts of the casting also draws in the melt. At the same time, the melt viscosity increases, increasing the cohesiveness of the melt, but also its flow resistance. To make matters worse for feeding, the feeding paths into the mushy zone also closes off by the reduced size of the still liquid capillary paths, with increased flow resistance as a result. The mushy zone capillaries may also be blocked by particles floating in the melt—eg graphite nodules (with or without an austenite shell), equiaxed dendrites, or inclusions. Thus, in some cases, the melt cohesiveness is overpowered by the

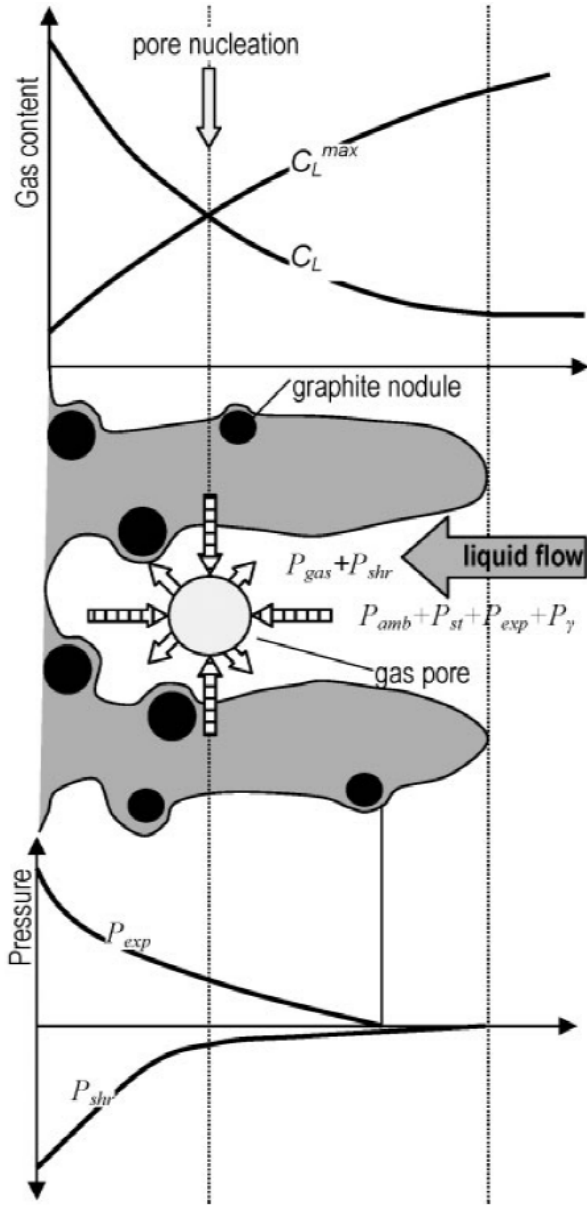


**Figure 2.6:** Influence of pressure and gas content on mushy zone pore formation.  $C_L$  is the amount of gas dissolved in the liquid,  $C_L^{max}$  is the maximum solubility of gas in the liquid,  $P_{gas}$  is the gas evolution,  $P_{amb}$  is the ambient pressure on the mould,  $P_{st}$  is the metallostatic pressure,  $P_{exp}$  is the expansion pressure due to phase transformations, and  $P_{\gamma}$  is the pressure induced on the pore by surface tension. Courtesy of Stefanescu [26].

forces acting on the melt, resulting in a rupture of the melt, creating a pore.

A further discussion on melt cohesiveness is found in section 13.8.8, on page 262. The flow of melt into the interdendritic and mushy zone is further

described in section 2.4.3, on page 32 and section 3.4.3, on page 54.

Alternatively, if the formed shell is weak as described above, the shell will yield to the tension before the melt, resulting in surface shrinkage [25, 26]. However, the formation of curved surfaces, or surface shrinkage, will consequently reduce the number of microporosities formed as a function of shrinkage.

Stefanescu structures the pressures acting as this to determine if a pore will develop or not [26]:

$$P_{gas} + P_{shr} > P_{amb} + P_{st} + P_{exp} + P_{\gamma} \quad (2.1)$$

where  $P_{gas}$  is the gas evolution,  $P_{shr}$  is the negative pressure from resistance to shrinkage induced flow,  $P_{amb}$  is the ambient pressure applied to the mould,  $P_{st}$  is the metallostatic pressure,  $P_{exp}$  is the expansion pressure caused by phase transformations, and  $P_{\gamma}$  is the pressure induced by the tension acting on the surface of the pore. The sum of local pressures makes up the mushy zone:

$$P_{mush} = P_{amb} + P_{st} + P_{exp} - P_{shr} \quad (2.2)$$

Equation (2.1) shows that the gas evolution,  $P_{gas}$ , and the resistance to shrinkage induced flow,  $P_{shr}$ , are the driving forces for pore formation. According to Stefanescu [26], the nucleation of pores is governed by the relationship between the maximum solubility of gas in the melt,  $C_L$ , and the amount of gas in the melt,  $C_L^{max}$ . See fig. 2.6. The stability of the pore after it is formed is given by [26]:

$$P_{\gamma} = \frac{2\gamma_{LG}}{r} \quad (2.3)$$

where  $\gamma_{LG}$  is the gas/liquid surface energy, and  $r$  is the radius of the pore. The equation shows that a minimal initial radius of the pore results in an enormous surface tension, making it unlikely that homogeneous nucleation will occur. However, impurities in the melt can help nucleate the pore as described by Stefanescu [26], allowing for a heterogeneous pore nucleation instead. This relationship also shows why melt treatment and melt purity is of great importance concerning porosity formation.

While inclusions in the melt can act as nucleation sites for pores, the amount of dissolved gas in the melt also influence the pore formation. The gas solubility in the metal changes as the melt cools and solidify. Hence, if more than a critical amount of gas is dissolved in the liquid this is expelled as

the temperature drops below the critical point. For Hydrogen (H) the solubility in commercial grade LGI and SGI is 8 ppm in the liquid, but only 4 ppm during solidification. For Nitrogen (N) the solubility values are 150 ppm and 80 ppm respectively [33, 34]. It should also be noted that the combined solubility of H and N is even lower.

The gases dissolved in the melt originate from the melting procedure, where cupola furnaces have been shown to introduce less H and N during melting when compared to induction furnaces [33, 34]. Also, the amount and purity of the steel scrap used for charge material is vital concerning the N level, as well as preheating of the charge material reduces the H level by removing moisture from the material before melting.

For SGI the Magnesium (Mg) treatment produces a process which can be compared to degassing of light metals.

According to Diószegi et al the gas absorption is controlled by the following phenomena; *gas diffusion* to the surface, chemical *reaction rate* on the surface, and *diffusion* of atoms from the gas/liquid interface into the melt [34]. While the diffusion of gas to the surface is considered quick, both the reaction rate on the gas/liquid surface and the diffusion of gas atoms in the liquid are limiting factors. Consequently, the size of the gas/liquid interface is of great importance to the amount of gas absorbed by the melt.

Thus, the initial treatment of the charge material and melting is not the only origin of the gases in the melt; the mould filling should also be taken into consideration. Hence, turbulent filling conditions promoting a turbulent flow will increase the gas/liquid surface area and increase the absorption of gas into the melt.

#### Other Defects

Another issue regarding the mould filling is air entrapment, though cast iron in green sand moulds is not typically prone to these defects [35]. Air entrapment primarily occurs in moulds with limited permeability and for skin forming alloys. Similarly, while steel alloys and light metal alloys are known to form oxides and bi-films, these types of defects are rare in cast iron [24, 35]. Pinholes, on the other hand, is a defect associated with cast iron [16, 35], especially if the gas content of the melt is critically high. Hence, the reduced solubility of gases in the metal as it cools and solidifies form holes on the surface of the casting when the limited permeability mould retains the gas inside the mould cavity.

## 2.3 Seven Rules of Feeding

---

POROSITIES, however, they may be formed, are unwanted in castings. Thus, castings are equipped with feeders to solve the problem with porosities and other related defects. The design of these feeders, to deliver the sound castings, require the consideration of a series of different aspects of the casting process.

Professor John Campbell formulated seven rules of feeding in his book ‘*Casting Practice—10 Rules of Casting*’ [24]. The seven areas that must be considered regarding feeding are listed below:

1. Do not feed (unless necessary)
2. Heat-transfer (modulus)
3. Mass-transfer (volume)
4. Junction
5. Feed path
6. Pressure gradient
7. Pressure

The rules should be used as a checklist when designing the casting layout and if possible also when designing the component itself. It should also be understood that the rules in many cases are inter-dependent, meaning that changes regarding one rule will influence the function of the feeder concerning another rule. Hence, optimising the construction of the feeder becomes an iterative process looping over the rules multiple times. However, the geometry of the casting itself, the gating system, the melt treatment, the pouring temperature, the mould conditions, all influence the performance of the feeders. Thus, changes to any of these should at least be considered with respect to the performance of the feeders.

### 2.3.1 Do Not Feed (Unless Necessary)

---

Campbell argues that this is the most important of all the feeding rules [24]. It serves no purpose to feed a casting, or section of a casting, that does not require it to fulfil its functionality. In some cases, a feeder can easily cause problems that would never have arisen without the feeder. While many cast iron castings require feeding, some thin-walled castings and some large SGI castings can be made without. The thin-walled castings are still subject to shrinkage, albeit the high cooling rate of the section forces the shrinkage to occur on the surface

of the casting. Hence, in some respects the changes in pattern geometry that allows for this external surface shrinkage act as the feeder. For the large, bulky SGI castings a different effect is used—namely the graphite expansion. Campbell [24] reports that many large SGI castings today are cast completely without feeders and Fournalakidis [36] have made a study of the conditions required to produce sound castings without the use of feeders.

It is also important to consider the need to eliminate all porosities. The primary function of feeders is to prevent porosities. However, if the function of the casting is not compromised by the presence of porosities at select locations, then the feeder is only an added production cost.

### 2.3.2 Heat-Transfer (Modulus)

The modulus criterion was first described by Nicolas Chvorinov in 1940 [37]:

$$\begin{aligned} t_s &= C \times M^2 \\ &= C \left( \frac{V}{A} \right)^2 \end{aligned} \quad (2.4)$$

where  $t_s$  is the solidification time,  $V$  is the volume of the section,  $A$  is the area of the cooling surface of the section, and the ratio between these two is defined as the modulus  $M$ .  $C$  is a constant which is dependent on both the casting material and the mould material.  $C$  is in some of the literature referred to as  $B$ . This method is still widely used in the foundries to calculate the required feeder size. Jelínek and Elbel recently presented new data for the mould constant for non-quartz sand mould [38]. An advanced approach has been proposed by Tiryakioğlu et al [39]. Different combinations of shapes and volumes can produce the same geometrical modulus. Tiryakioğlu et al [39] confirms that Chvorinov's rule yields accurate results for cooling time for both castings of the same shape and castings of the same volume. Tiryakioğlu's approach also yields comparable results for castings with the same modulus, but with different shapes.

M.C. Flemings published his method in 1974 in 'Solidification Processing' [40].

$$S = \frac{2}{\sqrt{\pi}} \underbrace{\left( \frac{T_m - T_0}{\rho_s H} \right)}_{(\beta)} \underbrace{\sqrt{K_m \rho_m C_m}}_{(\gamma)} \sqrt{t} \quad (2.5)$$

where  $S$  is the thickness of the solidified layer at a given time  $t$ .  $T_m$  is the melting point of the metal, and  $T_0$  is the initial temperature of an infinite mould.  $H$  is the latent heat of the metal,  $\rho_s$  is the solid density of the metal and  $\rho_m$  of the mould.  $K_m$  is the thermal conductivity of the mould, and  $C_m$  is its specific heat of the mould.

Subsequently, the  $\alpha$ -term is the potential that drives the cooling, the  $\beta$ -term is the energy stored in the melt, and the  $\gamma$ -term is the cooling power of the mould.

The heat-transfer criterion relates to the ratio between the modulus of the casting (or isolated section) and the feeder. Increasing the latent heat of the feeder is one way of securing the correct ratio between the two, however, using chills to increase the cooling rate of the casting can also increase the cooling rate of the casting by increasing the cooling power of the mould. In principle, the modulus is unchanged as the cooling surface is the same. However, the cooling power of the mould has changed. Feeder sleeves made from either an insulating or an exothermic material are also used in many foundries today. The sleeve materials are designed to retain the heat in the feeder, thus allowing for a geometrically smaller feeder to fulfil the heat-transfer criterion. For the same reason, they are sometimes known as mini risers. Different sleeve materials have different heat-transfer properties. It was described by Brown [23] as a MEF that multiplied with the geometric modulus ( $M_g$ ) gives the thermal (or true) modulus ( $M_t$ ) of the feeder.

$$M_t = \text{MEF} \times M_g \quad (2.6)$$

Note that the MEF is a relative value describing the insulating properties of the sleeve material relative to the insulating properties of the mould.

Casting designers should consider the temperature distribution in the casting because of the filling conditions. Most castings today are gated from the bottom to provide a stable, less turbulent filling. This bottom-gating will help float unwanted inclusion to the feeders at the top, but will also deposit the coldest of the melt in the feeders. If this proves to be a problem, it can often be solved by slightly increasing the modulus of the feeder.

Additionally, the temperature of the poured melt must also be considered. Temperatures above 1500 °C are often required during the initial melt treatment to secure a proper de-slagging of the melt. Typical pouring temperatures are in the range of

1350 °C to 1420 °C, depending on casting conditions and casting and gating geometry. A higher pouring temperature will entail a more substantial liquid shrinkage in the casting. However, a higher pouring temperature will also enable the casting to stabilise its temperature before solidification, so that high modulus sections will stay warm longer than low modulus sections [41]. This temperature stabilisation also results in a decreased undercooling and thus affect both nucleation and graphite growth as stated by Chen et al. [42].

### 2.3.3 Mass-Transfer (Volume)

Using feeder sleeves (or other methods) to prolong the cooling of the melt in the feeder it is possible to construct a feeder that will fulfil the heat-transfer criterion but may still be too small. The third feeding requirement is that the feeder must be able to supply the casting with enough melt to compensate for the liquid and solidification contraction that occurs. For cast iron, the required volume changes significantly with respect to alloy type. The volume shrinkage is dependent on alloy composition, melt treatment, and cooling rate. While other alloys as aluminium and steel have greater shrinkage and require larger feeders, these alloys are not as process sensitive as cast iron when it comes to how much the alloy will shrink.

To determine the required size of a feeder, it is necessary to first consider the volume shrinkage of the casting ( $V_c$ ).  $V_c$  is the amount of melt the feeder (as a minimum) must be able to supply to the casting during solidification. The feeder will be cooling and solidifying at the same time as the casting. Hence a percentage of the melt in the feeder will solidify in the feeder before it can be fed to the casting. This ratio is called the efficiency,  $e$ , of the feeder and is defined as:

$$e = \frac{V_f^{avbl}}{V_f} \quad (2.7)$$

where  $V_f$  is the total volume of the feeder and  $V_f^{avbl}$  is the volume of melt available to feed the casting. The term ‘available’ is used (as opposed to **eg** liquid) because the melt must not only be liquid but also movable by the collected sum of forces acting on the melt during the feeding process.  $e$  then becomes the efficiency of the feeder, describing the feeding yield.

A feeder is meant to feed the contraction in the casting caused by the liquid and solidification

shrinkage of the metal. However, the metal in the feeder undergoes the same contraction as the casting. Hence, this must be taken into account as well when determining the required feeder size. While the thermal gradients of the casting (including feeders) and the solidification microstructure influence the local shrinkage, a good approximation can be achieved by assuming that feeders and casting will display the same amount of contraction. Hence:

$$\begin{aligned} e \times V_f &= \alpha(V_f + V_c) \\ V_f &= \frac{\alpha V_c}{e - \alpha} \end{aligned} \quad (2.8)$$

where  $\alpha$  is the sum of liquid and solidification contraction for the particular alloy.

However, cast iron behaves differently than most other metal regarding solidification and shrinkage. As the cast iron solidifies graphite precipitates, creating an expansion that counters the contraction caused by cooling. Brown calls this shrinkage time,  $ST$ , and it denoted the percentage of the total solidification time and is alloy dependent. Equation 2.9 shows the reduced volume requirement for feeding a given cast iron alloy, at given process conditions:

$$M_f^{Vol} = M_c^{Vol} \times 1.2 \sqrt{\frac{ST}{100}} \quad (2.9)$$

where  $M_f^{Vol}$  is the volume criterion for the feeder modulus, and the  $M_c^{Vol}$  is the same for the casting.  $ST$  is the shrinkage time in percent of the total solidification time. The shrinkage time can be found using fig. 2.7 on the following page.

The continuous removal of melt from the feeder during solidification creates a piping effect that subsequently results in a ‘shrinkage cavity’ reaching the top of the feeder (if adequately vented) along the direction of feeding. If the heat-transfer criterion is fulfilled, but not the mass-transfer criterion, then the shrinkage cavity will ‘grow’ into the casting. The geometry of the shrinkage cavity in the feeder is very dependent on the feeder geometry itself, and hence directly influence the yield of the feeder. Figure 2.8 on page 23 shows how shrinkage cavities develop for different feeder geometries and how this affects the yield of the feeders.

### 2.3.4 Junction

The junction problem is related to castings that have a bulky design with a high modulus and thus

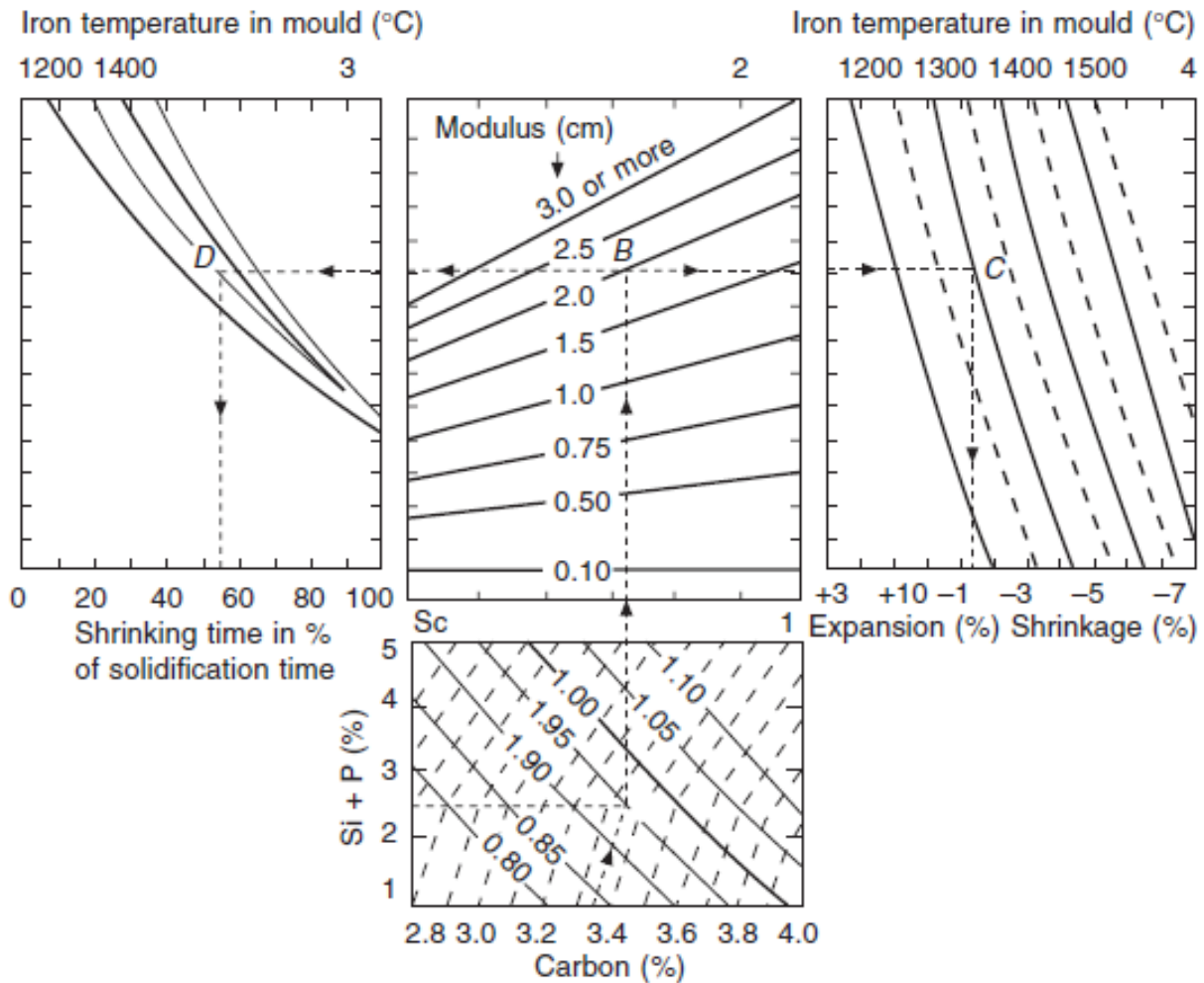


**Figure 2.7:** Nomogram for finding volume shrinkage % and shrinkage time in % of solidification time, based on alloy composition and casting temperature. Example with C: 3.35 wt%, Si: 2.5 wt%,  $M = 20$  mm,  $T = 1300$  °C, which gives shrinkage = 1.6% and  $ST = 55.0$ %. Courtesy of Brown [23].

displays a solidification progression similar to the feeder itself. If the casting (or section) is close to cubic or spherical, the volume- and mass-transfer criterion may not be sufficient to ensure a sound casting. The issue is the location of the shrinkage cavity. The location of the last to freeze melt, and thus also the porosities, is determined by the hotspot of the casting. If the casting has a bulky design that cools slowly, then the hotspot will often end up at the junction between the casting and the feeder, even though feeder can provide both enough heat and mass.

One solution is to increase the size of the feeder. If made large enough, the casting hotspot with the last to freeze melt will be drawn all the way into the feeder. This methodology, however, results in

feeders with a poor yield. Traditionally the modulus of a cast iron feeder will be made 1.2 times larger than the modulus of the casting it is feeding [23]. Depending on the geometry and the type of junction, the factor may have to be increased to  $M_f > 1.33 \times M_c$  for L-type junctions, and  $M_f > 2 \times M_c$  for T-type junctions [24].

An alternative is to increase the cooling of the heavy casting. This approach can be achieved with chills or cooling fins. Which of the solutions that are best suited for a given casting depends on the casting geometry, the casting conditions, the mould type and size, and the requirements for removal of the cooling fins afterwards. This alternative solution may provide a better total yield than the

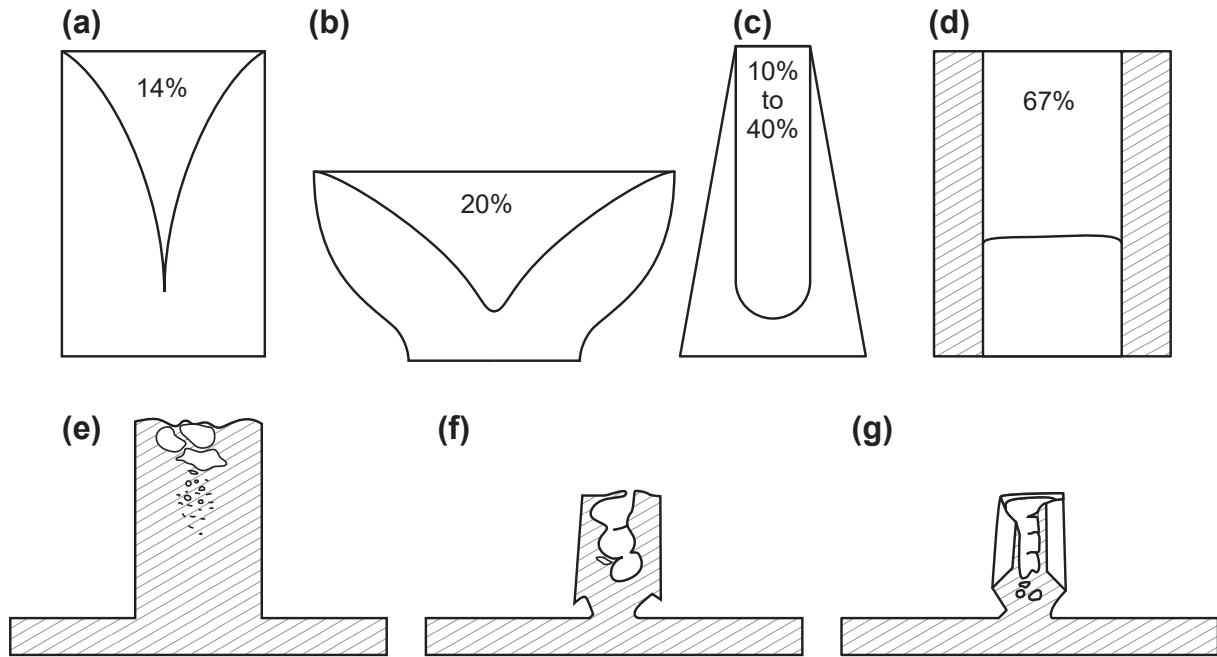


**Figure 2.8:** Typical feeder yield for different geometries. The top row shows (a) a cylindrical feeder, (b) a hemispherical feeder, (c) a reverse taper feeder head, and (d) a feeder with exothermic sleeves. The bottom row shows a ductile iron plate with (e) a cylindrical sand feeder, (f) an insulated feeder, and (g) an exothermic feeder. Courtesy of Campbell [24].

large feeder, albeit still not as good as for castings that inherently do not have this problem. Herein also lies the best way to improve the yield, namely to redesign the casting to avoid this type of heavy sections (if possible). Smaller sections will cool faster obtaining better strength and may thus in some cases, perform as well as the more massive constructions. On the other hand, it is not always (for various reasons) possible to change the design of the casting itself. In these cases, a reduced yield can be unavoidable.

Casting designers should take into consideration the migration of the castings hotspot (or hotspots) during the solidification process. Elmquist et al. [43] described how the hotspot, and thus the last to freeze melt and the porosities could move around inside the casting as a function of the different cooling rates of the different geometries. In moulds that contain more than one casting, the different castings may influence the migration of the hotspot in the other castings. This non-symmetric layout may lead to situations where only some of the castings display porosity defects in a critical area. In principle, this can also be used (deliberately or unwittingly) to keep sections warm longer as an effect of nearby castings. Vertically parted moulding lines have the

castings placed consecutively, and the heat from one mould will at some point penetrate the adjacent mould. However, only large castings were expected to still require feeding at the time when it is affected by the heat from the previous mould (depending on mould thickness). In general, dependence on heat flux from other sources that cannot be controlled is not advisable.

### 2.3.5 Feed Path

It has been determined that the feeder must provide both heat and mass in large enough quantities to feed the casting. However, both of these criteria would be useless if there is no feed path between the feeder and the section that must be fed. The casting must solidify towards the feeder. As it is not possible to feed melt through a section that has already solidified (or are about to in some cases), it is crucial to ensure this directional solidification towards the feeder.

#### Modulus Gradient Criterion

Traditionally, designers have used Heuvers' circles to determine if the casting geometry fulfilled the feed

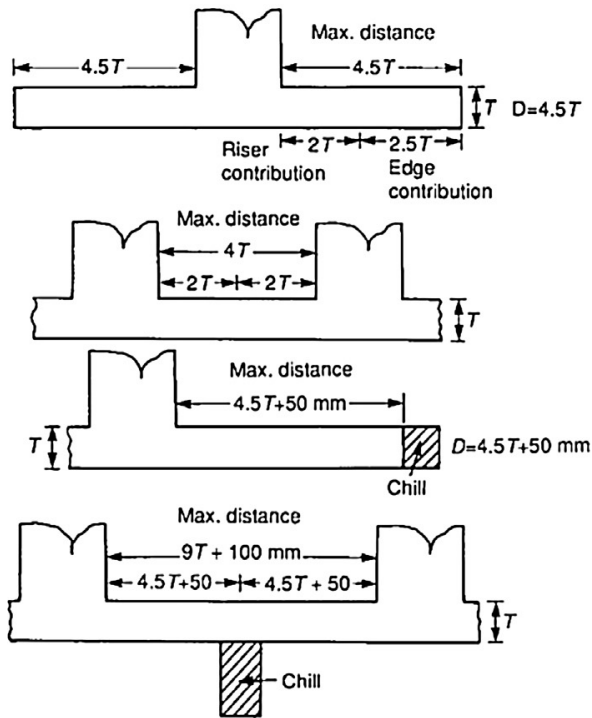


**Figure 2.10:** Feeding distance rules developed by Pellini for steel bars and steel plates cast in green sand moulds. Courtesy of Campbell and Pellini [24, 44].

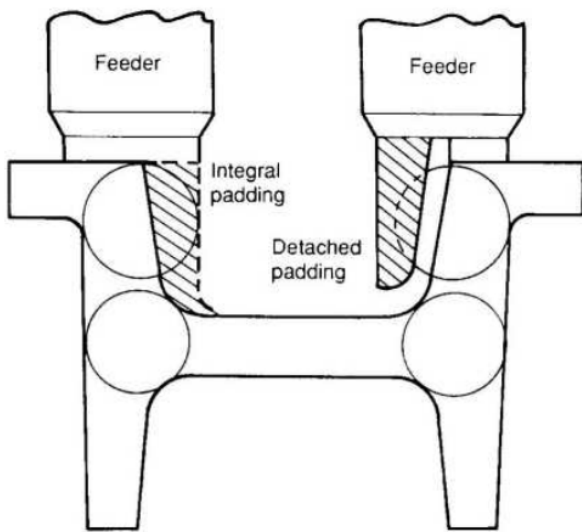


**Figure 2.9:** Use of 'Heuvers' circles' and the use of integrated and detached padding. Courtesy of Campbell [24].

path criterion. See fig. 2.9. The method is simply to draw the largest possible inscribed circle of each section of the casting. The larger the diameter of

the circle, the larger the modulus, and the later the section will solidify. The principle states that the circles must increase in diameter towards the feeder, creating a gradient in the modulus of the sections. The method provides a quick estimate of feeding path issues when inspecting technical drawings or sections of castings. However, the user must be aware that the method provides a 2D estimation of a 4D problem. The geometry itself is of course 3D, albeit changes in local temperature gradients over time must also be taken into consideration for a complete analysis. The complex geometries that are required for many castings today may be difficult to evaluate accurately without a numerical simulation. Moreover, temperature gradients from the filling of the mould also influence this phenomenon, complicating it even further.

The first attempt at a solution should be to orient the casting as favourably as possible in the mould, allowing the modulus gradient to develop from small sections at the bottom towards the more massive sections and the feeders at the top. Often other considerations intervene with the orientation of the casting in the mould. Part draft and cores must be respected, and in some cases, a particular orientation is favoured because it will eliminate or reduce the need to use cores, fettling, and machining.

The second approach should be to consider multiple feeders or alternative locations for the feeders. With the goal of optimising the casting yield, it can be advantageous to use fewer large feeders, thus more efficiently fulfilling the heat-transfer criterion. However, for castings with secluded sections, it is sometimes unfeasible or impossible to ensure a feeding path to these sections by merely increasing the feeder modulus. In these cases, local side feeder or ram-up sleeves may provide the best possible casting yield. Such feeding methods were shown by Vedel-Smith et al [30] that these feeders could be used to feed secluded sections.

The third approach should be to influence the feeding path by changing the cooling rate of the different sections. This can be accomplished in two ways; 1) increase the cooling of the sections that have too high a modulus by, e.g. including cooling fins or chills, or 2) to increase the modulus of the sections close to the feeder that have too small a modulus by either integral or detached padding of the section. If the customer allowed the padding to remain on the casting, this would be advantageous as subsequent removal of the padding would not be required. Alternatively, a solution with detached



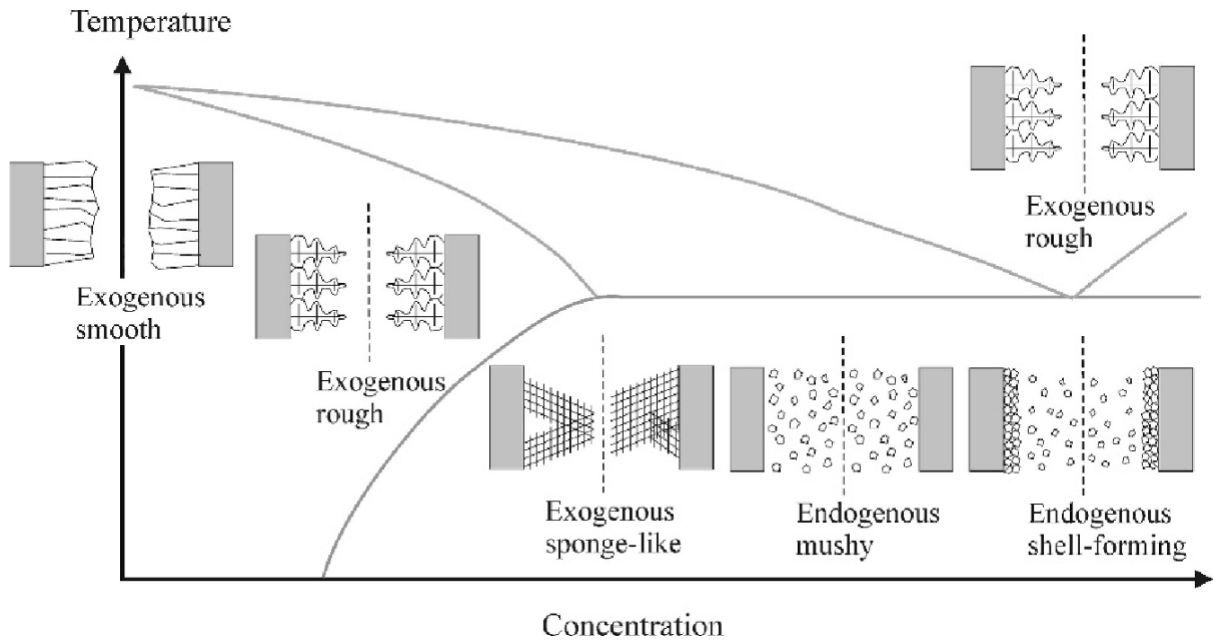


Figure 2.11: Endogenous and exogenous solidification based on alloy composition. Courtesy of Körner [45].

padding may be used if the casting geometry allows for this. See fig. 2.9 on page 24.

The order of the second and third approaches is not essential, and the casting designer should choose the solution that gives the best overall yield and a stable process.

#### Feeding Distance

Where the modulus gradient criterion ensures that the solidification of the casting is directional towards the feeder by evaluating the different sections, the feeding distance criterion targets the individual sections. Pellini [44] described the connection between the geometry of the casting and the distance at which a feeder could successfully feed a range of different geometries. Additionally, the work also describes how chills can improve the feeding distance by securing a directional solidification towards the feeder. See fig. 2.10 on page 24.

While these rules are widely used, they represent two limitations regarding feeding distances in cast iron. First, the feeding distance rules all describe horizontal feeding of simple geometries, and secondly, the basis of Pellini's research was steel castings.

**Feeding Path Geometry** A significant part of the castings made today has an elementary geometry; e.g. bars, plates, tubes, rails, and similar basic

shapes. For these castings, the geometries of Pellini's experiments are very suitable. However, many castings have a geometrical complexity beyond Pellini's experiments. Even though these 'complex' castings can be subdivided into basic shapes, they challenge the assumption made by Pellini in his experiments.

For example; how should the feeding distance be calculated for the casting in fig. 2.9 on page 24? Should the feeding distance be calculated as a U-shape from feeder to feeder, or will the vertical sections act as an extension of the feeders, so the only the horizontal section need to be considered? This approach does not take into account the effect of the lower vertical sections, which will draw melt towards them as the metal cools and solidifies. Likewise, it does not consider the increased pressure height due to the elevation of the feeders. Finally, the natural convection of the melt is significantly changed, in comparison with a bar or a plate, resulting in a changed solidification pattern.

Some alloys have equiaxed dendritic crystals forming in the melt during solidification. As these are heavier than the surrounding melt, the crystals will sink to the bottom and thus close off one part of the casting. Other alloys will solidify with columnar dendrites growing from the walls, slowly blocking the path. For the casting in fig. 2.9 on page 24 the feeding path of different alloys would be differ-

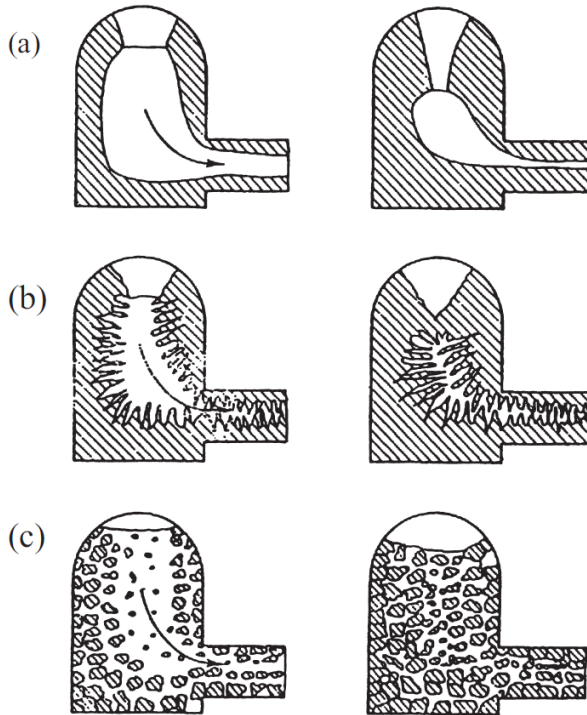


**Figure 2.12:** Melt flow from feeder to casting distinguished by solidification types: (a) smooth shell, (b) dendritic, and (c) mushy. Courtesy of Petrič [46].

ent. Pellini's experiments with steel alloys are not descriptive for all, if any, cast iron alloys.

**Endogenous and Exogenous Solidification** Feeding distances do exist in cast iron as well as in steel castings. However, the feeding distance is not the same for both alloys. Steel displays a far larger volume shrinkage than cast iron because of the graphite expansion in cast iron. The special volume change during solidification and cooling of cast iron caused by the graphite expansion also complicate the prediction of feeding distance. As described above, alloys with different chemical compositions will solidify differently—in the literature alloys are characterised as exogenous or endogenous according to how the solid phase nucleates and grows during solidification. See fig. 2.11 on page 25.

Exogenous solidification is found in pure and eutectic alloys and is promoted by a slow cooling rate. The solidification initiates as columnar growth at the mould interface and grows towards the casting centre. Exogenous solidification is divided into three sub-types: smooth-shell solidification, dendritic solidification, and spongy-layer solidification [46].

Endogenous solidification is typical in hypo- and hypereutectic alloy compositions. The off-eutectic compositions also entail solidification across a temperature range. Consequently, the shell forming at the mould interface is slow while equiaxed dendrites will form locally throughout the volume of the casting. Endogenous solidification is subdivided into two sub-types: mushy and shell-forming [46]. However, the solidification will cause changes in the composition of the remaining melt, hence forcing a change of the prevailing sub-type to the dormant sub-type as solidification progresses.

The phenomenon is dependent on the cooling rate. Increased cooling will promote shell-forming. However, cast iron will reach the metastable solidification that occurs if the cooling rate becomes high enough, which will significantly influence the solidification of the casting and derived material properties. Equally important is also the graphite growth in the solidifying melt. Depending on the iron type (LGI, CGI, or SGI) the graphite flakes or nodules will influence the growth of the dendrites and the composition of the melt. For the same reason, inoculation has a direct influence on the feeding properties of the solidifying alloy. Besides the inoculations influence on graphite expansion, the nucleation also affects the constitutional undercooling and thus the manner of the early solidification. Note also that the effects of inoculation regarding graphite precipitation are different for LGI and SGI respectively. Over-inoculation of LGI will promote shrinkage and porosities as described by Elmquist et.al. [43], while a better inoculation will improve the precipitation and subsequent expansion of graphite in SGI castings, thereby reducing the need for feeding as described by Chen et al [42, 47]. Finally, inoculation will limit undercooling during solidification, reducing metastable solidification.

Regarding feeding, it is optimal to have a shell formed, but with limited dendrite growth towards the centre as this will close off the feeding path. An equiaxed solidification towards the centre is often favourable. The rare earth element La is sometimes used in the treatment of SG irons [36, 48, 49], either as an alloying element or as part of the melt treatment. La promotes equiaxed grains (endogenous solidification). It restricts columnar growth and lowers the viscosity of the melt, improving the melt flow through the feeding path of the casting [48].

The freezing range, and ultimately the alloy composition, play a vital role in determining the solidification mechanism. Albeit the endogenous

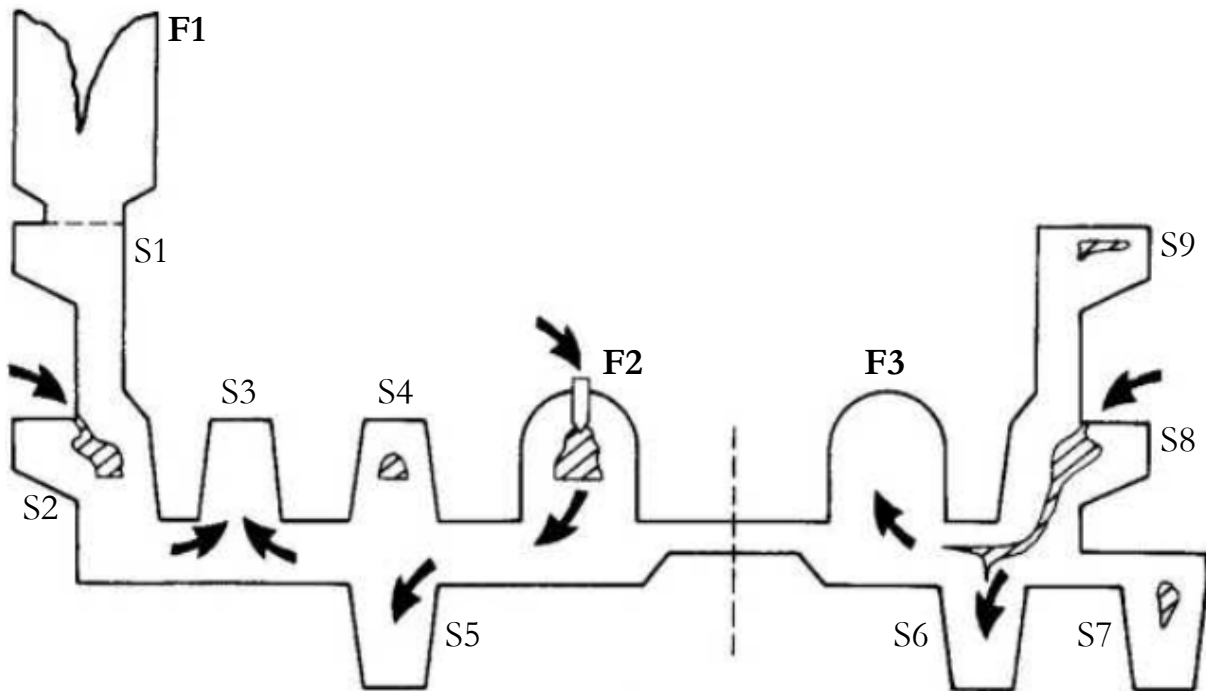


**Figure 2.13:** Cross-section illustrating problems related to pressure gradients in the casting. Arrows indicate the melt flow direction in relation to the feeders (**F**) and the casting sections (**S**). Courtesy of Campbell [24].

vs. exogenous solidification describes the solidification microstructure and the freezing range describes the extent of the temperature range from the first to last to freeze melt, the two are interdependent as a consequence of both being dependent on the chemical composition of the alloy.

The performance of the two basic types of solidification microstructures shown in fig. 2.11 on page 25 (endogenous with a long freezing range or exogenous with a short or long freezing range) is difficult to classify in equally simple terms. Different alloys perform well regarding feeding distance with short and long feeding ranges. Endogenous alloys can be shell-forming, hence allowing the equiaxed solidifying melt to be transported near the centre of the casting. However, if the formed shell is not strong enough, the walls will collapse inward providing so-called 'solid feeding'. As the walls collapse, they will also close off any further feeding through the section.

While the equiaxed grains of the endogenous solidification will flow with the melt, the dendrites formed during exogenous solidification will be attached to the walls of the casting, forcing the melt to flow through the structure. Both solidification

structures can hinder the flow of the melt: The endogenous melt flow can be compared to pouring a liquid with a high viscous resistance (or liquid filled with grains) through a clean pipe. Hence, the liquid itself provide the primary resistance. On the other hand, exogenous melt flow is similar to pouring a liquid with a low viscosity through a clogged pipe. The primary resistance comes from the inside structure of the pipe. See fig. 2.12 on page 26.

**Feeding Distance Breaking Point** Finally, it should be noted that the feeding distance might be significantly shortened if the feeding distance is exceeded and porosities are formed. It seems that the castings will resist the formation of porosities up until a certain point. If this point is exceeded, the porosities will spread further back than the original 'breaking point' [24]. The phenomenon seems allegorical to tearing cloth or paper. Initially, the paper will resist, but when the tear finally appears all the forces will be focused at this point instantly creating a tear of some length. As impurities and defects can act as crack initiation points, proper de-slugging of the melt before casting may help prevent porosities caused by breaking the feeding distance.

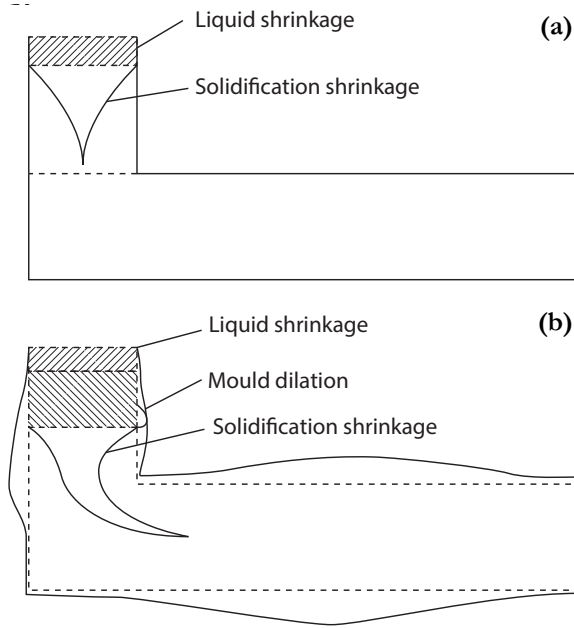


**Figure 2.14:** Division of liquid and solid shrinkage in comparison with (a) a strong mould and (b) a weak mould. Courtesy of Campbell [24].

### 2.3.6 Pressure Gradient

Complying with the previous requirements, it has been secured that enough liquid metal is available at the end of solidification and that the path to transport the melt from the feeder to the section where it needs is open. The pressure gradient requirement relates to the forces needed to move the melt along the feeding path. The necessary force again relates to the layout of the casting, the temperature and viscosity of the melt, and the condition of the feeding path.

The two main principles for securing a sufficient pressure gradient throughout the casting are pressure height and ventilation. The feeder F1 in fig. 2.13 on page 27 is located as the topmost part of the casting; hence, gravity provides sufficient force to move the melt into section S1. As S2 is located below S1, the pressure gradient requirement is satisfied for this section. However, the lack of compliance with the feed path requirement prevents the melt from F1 to feed S2. Likewise, it is important to note that the pressure gradient provided by the elevated location of F1 is negated as soon as the thin-walled section between S1 and S2 closes off. The pressure gradient effect of F1 will diminish as soon as the thin-walled section begins to solidify due to the flow resistance through the section.

The primary pressure that acts on the liquid metal in gravity castings is the atmospheric pressure. As with all other fluids, forces can be transferred relatively lossless from one surface to another. Hence, the combined pressure of the atmosphere and the height of the liquid melt of the casting, including feeders and gating system, is transferred from the open surface to the melt. This effect will help feed sections with poor feeding paths, as the pressure will force the melt through the solidifying path. However, the same thing will happen to the pressure path. As eg the in-gate solidifies, the atmospheric pressure is acting on the gating system, as well as the static pressure of the melt height, is prevented from acting on the casting as the solidified section can only transfer the force by solid deformation. Thus, as the feeding path must be kept open long enough to move the melt into the solidifying section, the pressure path must also be kept open long enough to move the melt through the feeding path.

If a feeder is unvented, it will form a solid outer shell, creating a vacuum that will hold the melt inside the feeder preventing the gravitational force from drawing the melt into the casting. The difference between a vented (F2) and unvented feeder (F3) is shown in fig. 2.13 on page 27. Venting is done by securing that the melt continues to have contact with air, which often, in turn, is achieved by creating a local hotspot using a Williams wedge or Williams core [23]. Likewise, a local hotspot at the corners of S2 and S2 are also venting these sections, resulting in open porosities. The problem for the two sections, though, is, in this case, insufficient feeding and not the local hotspot.

Casting designers should also remember that the density of liquid iron-carbon alloys is  $6.8 \text{ g cm}^{-3}$  to  $7.1 \text{ g cm}^{-3}$ , depending on melt temperature and wt% of C [50]. While the most significant impact of the weight of the dense liquid is seen during filling, the effect on feeding must also be taken into account, especially when feeding sections like S3, S4, and S9. For these sections to be sound, the ferrostatic pressure of the melt must be maintained from the part of the casting that provides the local pressure height, until the melt in the section is solidified enough that shrinkage and porosities will not evolve.

One method to optimise feeder yield and to secure the local ferrostatic pressure on the melt is so called active feeding. The technique was first patented in the mid-1800s for steel castings and is a method for pushing on the melt with pressurised air or an inert

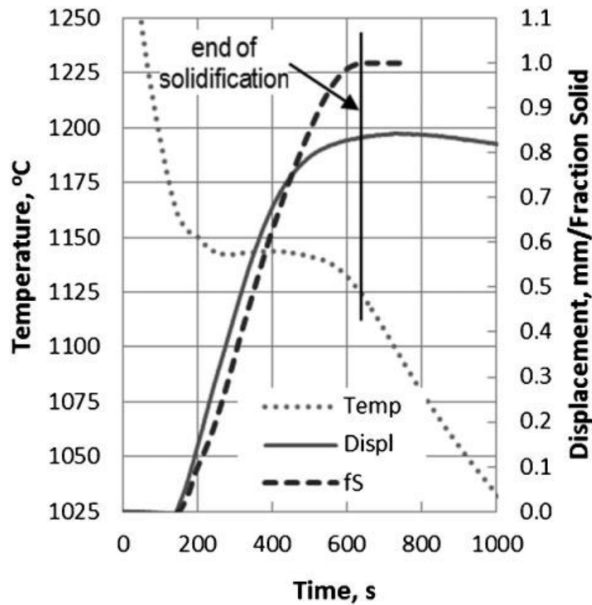


**Figure 2.15:** Correlation between cooling, solidification, and expansion of a SGI with a CEV of 4.35. Courtesy of Alonso [53].

gas [51]. It is argued that especially alloys with extended freezing range benefit from this technique, as the extra pressure help move the melt through the mushy zones of the casting. Promising applications using the method have been demonstrated for cast iron [52]; however, the technique is not widely used, possibly because the technique requires additional equipment installed in the foundry.

### 2.3.7 Pressure

Finally, yet importantly, the pressure in the melt must be available to suppress the nucleation and growth of porosities as well as deformation of the surface.

Surface deformation, or surface shrinkage, is most prominent in endogenous mushy alloys that do not form a stable shell early in the solidification process. If the internal vacuum of the casting, aided by the atmospheric pressure on the outside of the newly formed shell, is stronger than the newly formed shell, then the shell will deform inward, reduce the internal porosities, but create indents on the surface. Depending on the temperature distribution in the casting and size and location of those above mentioned internal and external forces, the surface shrinkage may be local or distributed across a large area.

What complicates this requirement for cast iron is the precipitation of graphite, which creates both a primary and a secondary graphite expansion in the solidifying casting.

Prof. Campbell expresses it as follows: “The successful feeding of cast irons is perhaps the most complex and challenging feeding task compared to all other casting alloys as a result of the curious and complicating effect of pressure. The effects are most dramatically seen for ductile irons.” [24]

What complicates the cast iron solidification is that the melt in the mould will: 1) shrink as it cools towards the solidifications temperature, then 2) as the alloy begins the solidify it will contract even further, followed by 3) the primary graphite expansion occurring at the eutectic temperature (or earlier for hypereutectic alloys), after this expansion the casting will 4) shrink as it cools towards the austenite to ferrite transformation temperature, where 5) the second graphite expansion takes place, before the casting eventually cools and shrinks until room temperature.

It is important to understand that the temperature where these phase transformations occur is dependent on alloy composition (which shifts towards eutectic compositions as the melt solidifies), on inoculation, and on cooling rate. Hence, different sections of the casting will undergo these phase changes at different intervals; consequently, push the remaining melt or solidified metal back and forth in the casting. Thus, it becomes important to control where these forces are directed. The graphite expansion can be large and powerful enough to deform the mould itself if it is not strong enough, resulting in serious issues with feeding and tolerances [24]. See fig. 2.14 on page 28. Khalil-Allafi et al [54] have examined the direct influence of mould hardness on the feeding need and found that increased mould hardness improves the impact of the graphite expansion thereby reducing porosities.

These changes in expansion and subtraction of the volume of the melt and solid, and subsequent suction and pressure can be used to transport the melt from the feeders into the casting against gravity as shown by Vedel-Smith et al [55]. However, the required combination of melt volume, feeder and casting modulus, alloy composition, inoculation efficiency, cooling rate, and mould strength call for some measure of caution. The foundry must have a stable process with great sand, melt, and process control. If this is not the case, feeders that rely on the internal melt forces to move the melt (eg low

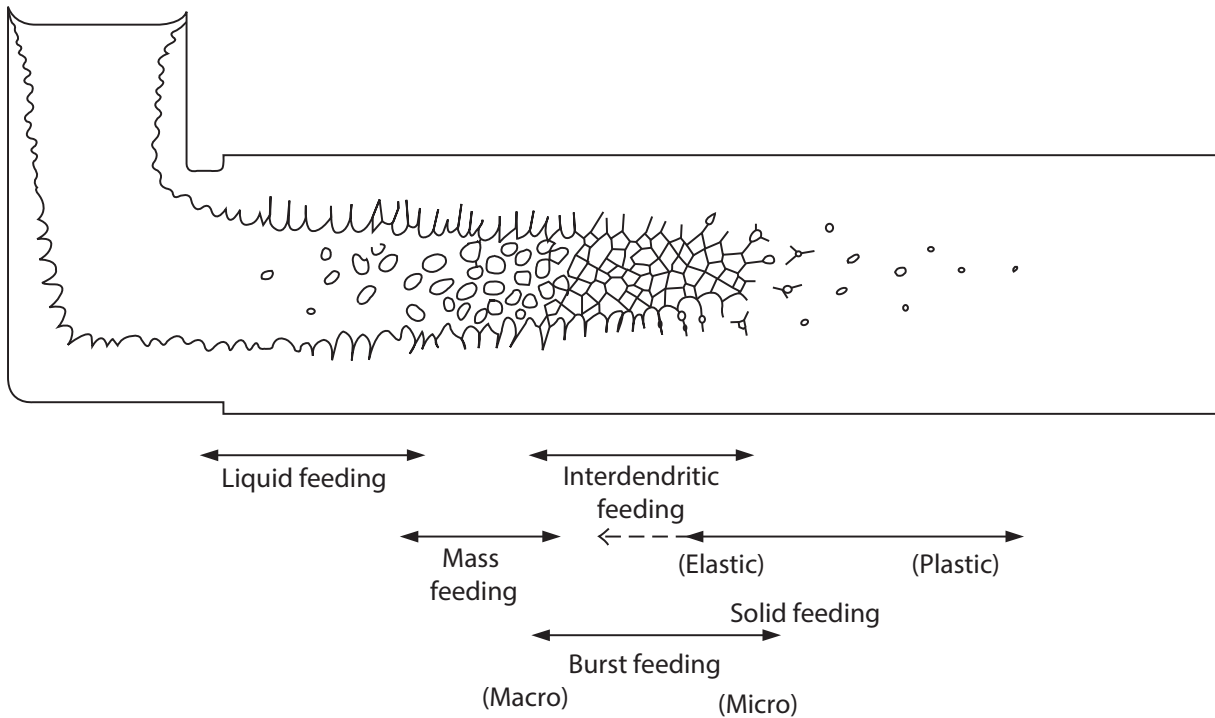


**Figure 2.16:** Overview of the five feeding mechanisms. Courtesy of Campbell [25].

placed ram-up sleeves) is not advisable, as minor changes in a single one of these areas may cause trouble.

Successful feeding of cast iron castings is strongly dependent on controlling the time and sequence of the graphite expansion. See fig. 2.15 on page 29. Alonso et al [53, 56] have made a detailed study of the growth kinetics of the graphite expansion in LGI, CGI, and SGI. Alonso et al [53, 56] show that some cast iron alloys can have a graphite expansion so large that the metal will expand during solidification. This extensive graphite expansion, however, is not necessarily the sought after effect. A large expansion during solidification will dilate the mould (if weak), or push away the remaining melt (if strong) if it comes too early. This is supported by the modelling made by Chen et al [57, 58]. The main factors influencing the graphite expansion in Alonso's experiment was the wt% C and the wt% Mg. Note that the Mg must be active to influence the nucleation of graphite. It should also be noted that Alonso's experiment does not examine the subsequent secondary graphite expansion, and hence no correlation is drawn between the sizes of the primary and the secondary graphite expansions.

## 2.4 Five Feeding Mechanisms

IN addition to the seven rules of feeding Campbell lists five mechanisms of feeding in his book 'Castings' [25], a subject also addressed by Professor Stefanescu in his book on the 'Science and Engineering of Casting Solidification' [29]. The five mechanisms that must be considered regarding feeding are listed below, and shown in fig. 2.16:

1. Liquid feeding
2. Mass feeding
3. Interdendritic feeding
4. Burst feeding
5. Solid feeding

These five mechanisms of feeding are directly linked to several of the feeding rules, as the same underlying phenomena govern them both. In that sense, the rules and the mechanisms are alike. However, their approach to feeding is different. The feeding rules are a series of descriptions detailing which actions can be taken to improve feeding. The mechanisms are an explanation of the ways the casting can, or cannot, counter the volume shrinkage experienced during cooling and solidification. The

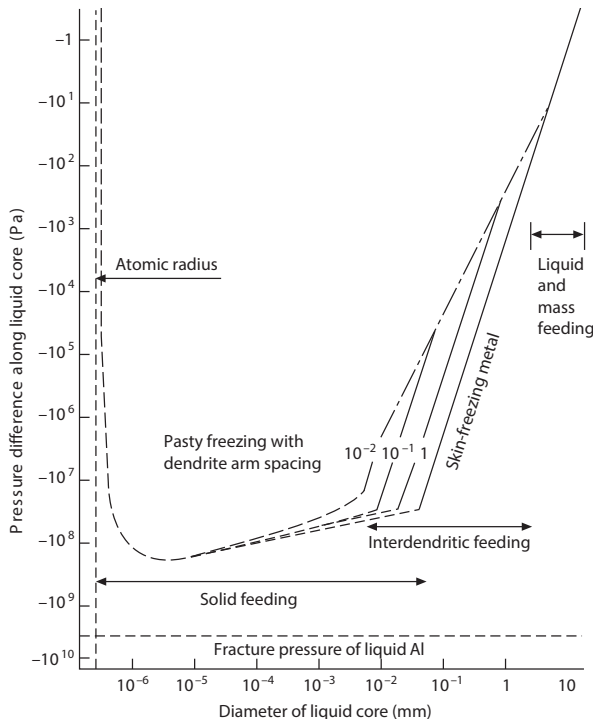


**Figure 2.17:** *Ferrostatic tension of the residual liquid, depending on freezing range regime for a 20 mm Al cylinder. Courtesy of Campbell [25].*

five feeding mechanisms address the movement and solidification of the melt feeding the casting.

The five mechanisms progress from liquid to solid feeding, including three intermediate states; mass, interdendritic, and burst feeding.

### 2.4.1 Liquid Feeding

Liquid feeding is, in some respects, the simplest form of feeding. As the name implies, this feeding mechanism treats the movement of 100% liquid, non-solidified melt from a reservoir to the feed area, a recess or a cavity in an immediate deficiency of melt, through a path of the non-solidified melt. Hence, the melt flow is as unobstructed as possible. Note that the superheat of the melt may influence the viscosity of the melt. A superheated melt may flow easier and longer due to the reduced viscosity and the greater thermal energy stored in the melt, which will in turn also postpone the initiation of the solidification, enabling the melt to flow further.

The melt flow is governed by the pressure difference in the melt, and the pressure drop from the reservoir and the feed area. The pressure drop

occurs as a function of the contracting of the cooling and solidifying casting, creating tension in the melt. However, the cooling casting is also contraction inwards, reducing the internal volume as the internal solidification of the casting is still undergoing. Hence, depending on the geometry of the casting, the cooling rate, the alloy solidification scheme (long or short freezing range), a pressure build-up occur in the remaining melt.

Campbell calculated the pressure of the remaining melt for a 20 mm in diameter infinite casting [25]. See fig. 2.17. Campbell reports that the tension of the melt is minimal and do not play a significant barrier against feeding. Additionally, the calculations do not take into consideration the thermal gradient of the solidified shell. Hence, the counter pressure from the contracting casting is even greater than depicted in fig. 2.17. In some cases the contraction of the casting can even exceed the internal tension, resulting in a combined positive melt pressure. In these special cases, the casting squeezes the melt, pushing it into other feed areas.

### 2.4.2 Mass Feeding

Mass feeding is the first of the intermediate feeding mechanisms and was initially named by W.A. Baker in 1945. Mass feeding encompasses a movement of a semi-liquid/semi-solid slurry from a reservoir to a feeding area. This material transport occurs when solidified precipitates, grains, or dendrites, are moved by a surrounding melt.

The higher the fraction solid, the more difficult it is to move the melt. A significant fraction of solid will more easily entangle and resist the movement of the melt. This entanglement again relates to the width of the feeding path vs. the size and shape of the solid particles. For small thin-walled sections, a few solid particles may be enough to block the flow, while more massive sections may have open feeding path more than 100 particles across [25]. This effect, again, relates to the alloy composition and melt treatment. Grain refinement, or inoculation in cast iron, help control the size and distribution of the particles found in the melt and thus aid mass feeding by reducing the particle size.

Note that in some cases the solid particles carried by the melt may become a barrier of its own when encountering a too narrow feed path. The particles will then plug the feeding path preventing further liquid or mass feeding.

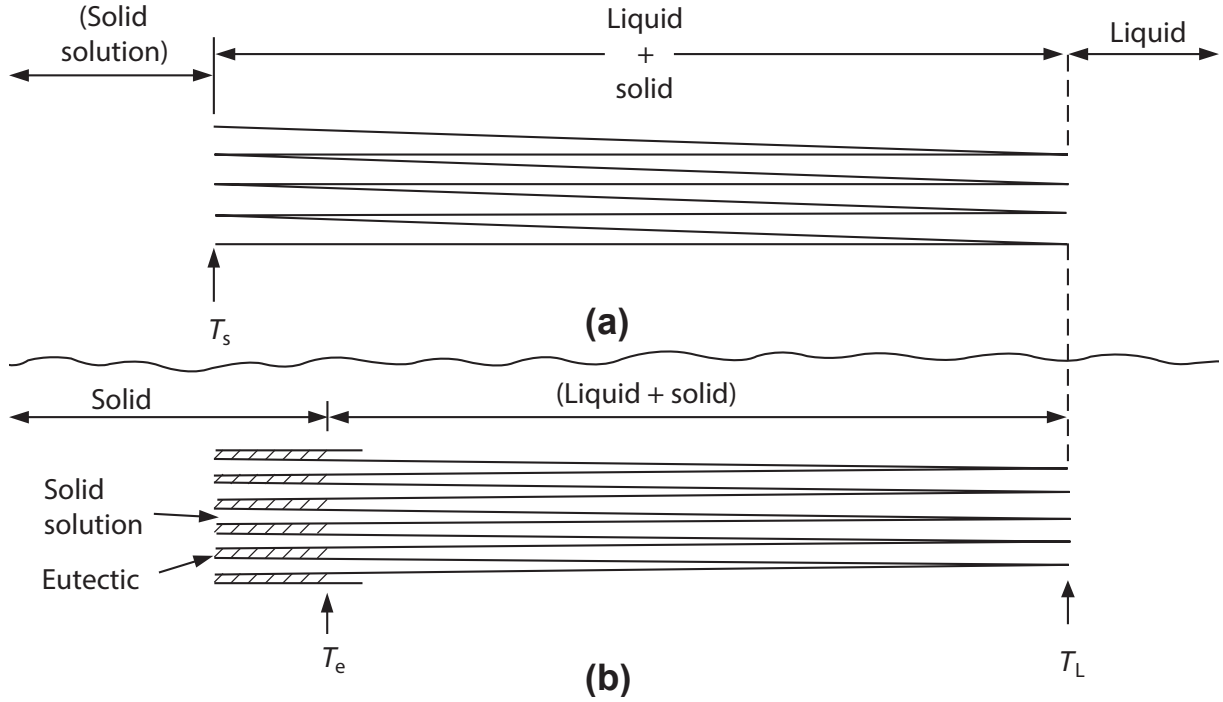


**Figure 2.18:** *Interdendritic Feeding: Influence of eutectic solidification. (a) The feeding path is tapered by the growth of dendrites, resulting in increasing pressure loss when nearing the solid solution. (b) Same situation, however, with a build-up of eutectic melt in between the dendrites, ensuring an isothermal solidification from that breaks the tapering of the feeding paths. Courtesy of Campbell [25].*

### 2.4.3 Interdendritic Feeding

At the point where the feeding path is obstructed by dendrites growing into the melt or equiaxed dendrites moved there by mass feeding, the residual melt can still (to some degree) flow through the network of dendrite arms. This phenomenon was called ‘interdendritic feeding’ by N.P. Allen in 1932.

The flow of melt through the capillary channels between the dendrite arms is governed by the pressure difference of the two sides. However, the pressure drop across the network of small capillary feeding paths can be significant and is controlled by several different factors. Campbell derive the following equation to describe the pressure drop:

$$\Delta P = 32\eta \left( \frac{\alpha}{1-\alpha} \right) \frac{\lambda^2 L^2 d^2}{R^4 D^2} \quad (2.10)$$

where  $\Delta P$  is the pressure drop across the mushy zone,  $\eta$  is the viscosity of the melt,  $\alpha$  is the coefficient of thermal expansion of the liquid,  $L$  is the length of the capillary flow through the mushy zone,  $d$  is the dendrite arm spacing,  $R$  is the radius of the capillaries and  $D^2$  is the mushy zone area the melt must travel through. The actual flow resistance

may be even higher than predicted by eq. (2.10), as this assumes straight channels and aligned flow.

Additionally, eq. (2.10) shows that the governing factor is the capillary radius,  $R$ . Narrow capillaries can present significant pressure differences,  $\Delta P$ . This pressure-drop explains the benefit of a eutectic melt when feeding through the interdendritic network of capillary channels. See fig. 2.18. The uniform solidification temperature of the eutectic melt creates an isothermal plane across the dendrite capillaries, creating the effect of a regular solidification front moving through the dendrite network. The specific solidification temperature of the eutectic melt and the latent heat of solidification enable the effect.

### 2.4.4 Burst Feeding

Burst feeding is the third of the intermediate feeding mechanisms. It occurs only under specific conditions and can be very difficult to predict and control. Burst feeding happens when a feeding barrier has been created, eg a dam of particles moved by mass feeding, and the resistance of the barrier is then



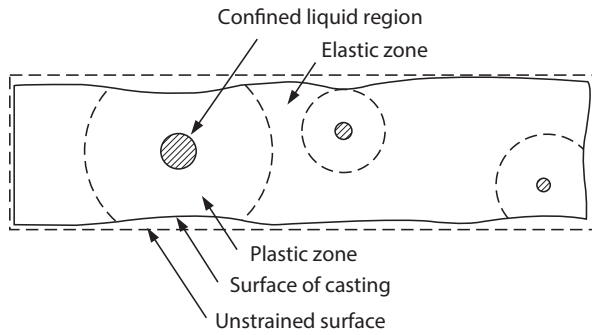


**Figure 2.19:** *Solid Feeding: Zones of plastic deformation created by the tension of residual liquid contracting during solidification. Courtesy of Campbell [25].*

overcome by the pressure difference, resulting in a burst of melt flowing into the previously cut off feeding area.

A curious phenomenon about burst feeding is that the feeding barrier gains strength as the casting cools and possibly more particles get entangled in the barrier. However, the pressure difference working to overcome the barrier will also increase as the casting cools. Hence, the occurrence of burst feeding is decided by the magnitude of both barrier and the pressure difference, but also of the rate of change of the two as the casting cools.

Note that the barrier may only be a partial barrier, allowing for interdendritic feeding to pass through. This effect will reduce the pressure difference and thus limit the likelihood of the barrier breaking.

In the early twentieth century, this process was aided manually by ramming an iron rod up and down in the open feeder to break through the feed barriers. The feeder would then be topped up as needed [25]. This practice was mainly used for large iron castings and could go on for hours.

#### 2.4.5 Solid Feeding

Solid feeding, or self-feeding, is the final mechanism the casting can use to prevent the formation of porosities. However, solid feeding differentiates itself from the other feeding mechanisms in one significant aspect: The casting itself collapses on the porosity, transferring the volume difference to the casting surface. See fig. 2.19.

As with the other feeding mechanisms, the driving force is the pressure difference, in this case between the feed area and the outside of the casting. The mechanisms also depend on the strength of the bar-

rier, in this case, the solidified part of the casting, which in turn depends on temperature. If the pressure difference is significant enough and the casting weak enough, the pressure difference will deform the casting to fill the internal volume deficit. This deformation can occur as either plastic deformation of the material or creep flow. Hence, the period these conditions are upheld also influence the outcome, as especially the creep mechanism is known to be time dependent.

Additionally, the solidification regime of the alloy and the cooling conditions play an important role regarding the strength of the casting during and just after ended solidification. Likewise, note that the geometry of the casting also has a significant influence on the strength of the casting shell. Large flat surfaces have the least inherent geometrical resistance. The section thickness is also essential as shown in fig. 2.2 on page 15.

Part of the pressure difference driving the solid feeding may come from the external pressure. However, the internal tension may by itself be powerful enough to drive the feeding. This solid feeding effect is seen as vacuum cast castings also display surface shrinkage, or surface sinks, as a function of solid feeding. Note that the melt quality plays an essential role as the rupture of the residual liquid, releasing the tension and creating a porosity, is often directly linked to impurities in the melt [25].

A way to relieve the tension in the melt as it contracts is to provide a liquid connection to a feeder that in turn can provide an adequate ferrostatic pressure. Hence, an open feeding path with limited pressure loss and a sufficient ferrostatic pressure provided by the feeder may prevent a significant part of the surface shrinkage.

It should be noted that solid feeding reduces the internal tension of the residual melt, thus indirectly limiting the castings ability to drive the other feeding mechanisms, as all mechanisms are pressure driven. Hence, the mechanisms that succeed first will automatically reduce the likelihood of the other mechanisms also occurring. This behaviour can explain some of the relatively significant differences in porosities observed in otherwise identical castings—it is essential which feeding mechanism is initiated. Subsequently, a situation can be imagined, where the cooling of the casting surface will strengthen the castings mechanical properties, prevent solid feeding, allow the internal tension to develop further, and enable one of the liquid feeding mechanisms. In short: cooling may further feeding.

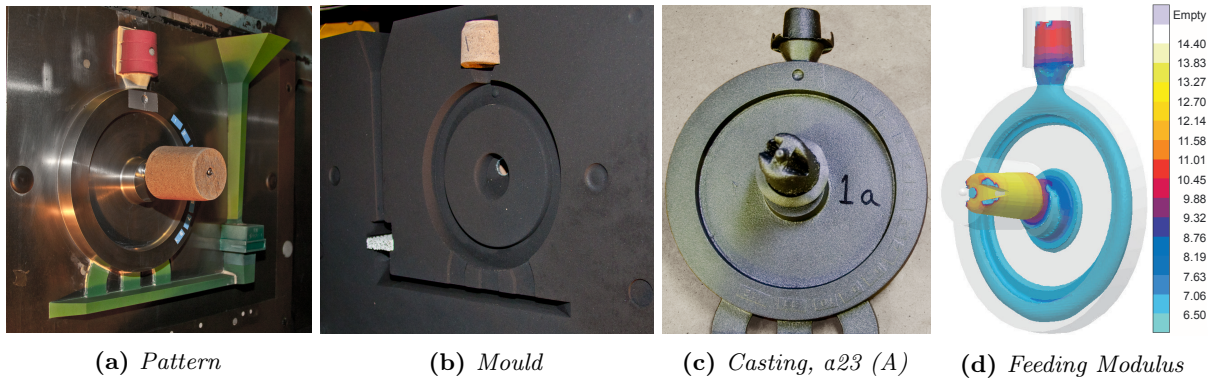


**Figure 2.20:** Ram-up sleeve application. (a) the pattern with a ram-up sleeve mounted at the centre, (b) a ram-up sleeve moulded in at the centre, (c) casting after shot blasting, and (d) numerical simulation of the feeding modulus for the casting.

## 2.5 Advanced Feeding Methods

NEW methods and approaches to feeding (both cast iron and other metals) are regularly developed. Feeding is a continued focus for metallurgists, foundrymen, and the casting buyers as a lot of energy and money can be saved by improving feeding.

### 2.5.1 Ram-Up Sleeves

Ram-up sleeves are traditional insulating or exothermic feeder sleeves mounted with a metal breaker core. The system enables the feeder to be placed away from the mould parting line and can thus be used to feed secluded sections, that would normally be unreachable due to the feed path requirement. Figure 2.20 shows the application of a ram-up sleeve on a vertically parted moulding line.

### 2.5.2 Simulation and Optimisation

Numerical simulation of castings is an integral part of many foundries today and can be an invaluable help when evaluating casting defects and improving the overall casting design. Simulations help visualise many of the ‘hidden’ causes for porosities and other feeding defects. Using simulations to optimise processes and secure a robust process is a logical development. Work has already been done towards automatically generated feeders, based on feeding rules. Tavakoli and Davami have published a series of articles on their work towards topologically optimised feeders for steel castings [59–61]. Similar methods may someday be possible for the optimisation of cast iron feeders as well.

### 2.5.3 Advanced Solidification

Advanced methods to reduce or eliminate the need for feeding have also been investigated. Muumbo et al [62] investigated the effect of casting cast iron as a semi-solid slurry under pressure. By this method, they greatly reduce the porosities in the castings. The semi-solid slurry reduced the shrinkage of the alloy, as there is no liquid shrinkage. However, the results presented by Muumbo et al also show that pressure is also required to achieve a porosity-free casting. These findings are supported by Sobczak et al [63] who present a comprehensive analysis of the influence of pressure on the solidification of metals. If the pressure is high enough, instantaneous solidification can occur, eliminating the need for feeding. While this is an interesting approach to feeding, the pressures required are not compatible with sand moulds, and the methods remain a curiosity more than a viable feeding solution for cast iron.

## 2.6 Summary

FEEDING of cast iron is a complex process that becomes more and more demanding as the casting geometries increase in complexity, the material property requirements become higher, and the foundries require smaller feeders and reduced scrap to make a profit. However, it is important to understand that the seven rules of feeding represent not only particular requirements that must be fulfilled but also potential areas for improvement. Similarly, the five feeding mechanisms provide an understanding

of the underlying processes of feeding and porosity formation and can be used together with the seven feeding rules to analyse feeding situations in depth.

As some alloys become demanding due to strength or ductility requirements, resulting in an alloy with a tendency to close off the feeding paths, an option may be to circumvent the problem by using eg ram-up sleeves to feed the closed-off section directly.

Increased control of the process parameters in the foundry is a way to stabilise and optimise the casting production. A stable process is essential, as useful optimisation is not possible if the influencing parameters continuously change—especially if the changes are unknown or unrecorded.

## References

- [16] Jörg Daier et al. *Manual of Casting Defects—Incidence and Avoidance of Defects Attributable to Moulding Sands*. 3rd ed. S&B Industrial Materials GmbH, 2011.
- [23] John R. Brown. “FOSECO Ferrous Foundryman’s Handbook”. In: FOSECO International Ltd., 2000. Chap. 19, pp. 296–310.
- [24] John Campbell. *Casting Practice - The 10 Rules of Casting*. Linacre House, Jordan Hill, Oxford OX2 8DP, 30 Corporate Drive, Burlington, MA 01803: Elsevier Butterworth-Heinemann, 2004. ISBN: 0 7506 4791 4.
- [25] John Campbell. *Castings, 2nd Ed*. Linacre House, Jordan Hill, Oxford OX2 8DP, 30 Corporate Drive, Burlington, MA 01803: Elsevier Butterworth-Heinemann, 2003. ISBN: 0 7506 4790 6.
- [26] DM Stefanescu. “Computer Simulation of Shrinkage Related Defects in Metal Castings—A Review”. In: *International Journal of Cast Metals Research* 18.3 (2005), pp. 129–143.
- [27] PD Lee, A Chirazi and D See. “Modeling Microporosity in Aluminum-Silicon Alloys: A Review”. In: *Journal of Light Metals* 1.1 (2001), pp. 15–30.
- [28] Doru Michael Stefanescu. “Modeling of cast iron solidification- The defining moments”. In: *Metallurgical and Materials Transactions A-Physical Metallurgy and Materials Science* 38A.7 (2007). Symposium on Solidification Modeling and Microstructure Formation held at the 2006 TMS Annual Meeting, San Antonio, TX, MAR 13-16, 2006, 1433–1447. ISSN: 1073-5623. DOI: {10.1007/s11661-007-9173-y}.
- [29] Doru Michael Stefanescu. *Science and Engineering of Casting Solidification, 2nd ed*. Springer Science+Business Media, LLC, 233 Spring Street, New York, NY 10013, USA: Springer, 2009. ISBN: 978-0-387-74609-8.
- [30] Nikolaj Kjelgaard Vedel-Smith et al. “Quantification of Feeding Effects of Spot Feeding Ductile Iron Castings made in Vertically Parted Molds”. English. In: *AFS Proceedings* (2013).
- [31] N. K. Vedel-Smith and N. S. Tiedje. “Effect of Feeder Configuration on the Microstructure of Ductile Cast Iron”. English. In: *TMS Proceedings—Shape Casting: 5th International Symposium 2014* (2014), pp. 113–120.
- [32] David A. Porter, Kenneth E. Easterling and Mohamed Y. Sherif. *Phase Transformations in Metals and Alloys*. 3rd ed. CRC Press, Taylor & Francis Group, 6000 Broken Sound Parkway NW, Suite 300, Boca Raton, FL 33487-2742, 2009. ISBN: 978-1-4200-6210-6.
- [33] Attila Diószegi et al. “Defect Formation at Casting of Gray Iron Components”. In: (2009).
- [34] Attila Diószegi, Tobias Björklind and Zoltán Diószegi. “Surface Turbulence at Flow of Gray Cast Iron”. In: *Key Engineering Materials*. Vol. 457. Trans Tech Publ. 2011, pp. 422–427.
- [35] R Monroe. “Porosity in Castings”. In: *AFS Transactions* 113 (2005), pp. 519–546.
- [36] Vasilios Fourlakidis. “A Study on Ductile Iron Production without the Use of Feeders”. In: *Science and Processing of Cast Iron IX*. Ed. by Nofal, A and Waly, M. Vol. 457. Key Engineering Materials. 9th International Symposium on Science and Processing of Cast Iron, Luxor, Egypt, Nov. 10-13, 2010. Central Metallurg Res & Dev Inst. 2011, 499–504. DOI: {10.4028/www.scientific.net/KEM.457.499}.
- [37] Nicolas Chvorinov. “Theory of the Solidification of Castings”. In: *Giesserei* 27 (1940), pp. 177–186.

- [38] P. Jelínek and T. Elbel. “Chvorinov’s Rule and Determination of Coefficient of Heat Accumulation of Moulds with Non-Quartz Base Sand”. In: *Archives of Foundry Engineering* 10.4 (2010), 77–82.
- [39] M. Tiryakioğlu, E. Tiryakioğlu and D.R. Askeland. “The Effect of Casting Shape and Size on Solidification Time: A New Approach”. In: *International Journal of Cast Metals Research* 9. (1997), 259–267.
- [40] Merton C. Flemings. *Solidification Processing*. New York: McGraw-Hill, 1974.
- [41] K. Weiß and C. Honsel. “New Algorithm to Calculate Liquid - Solid Shrinkage and Graphite Expansion”. In: *Solidification and Gravity IV*. Ed. by R. Roosz, M. Rettenmayr and Z. Gacsi. Vol. 508. Materials Science Forum. 4th International Conference on Solidification and Gravity, Miskolc Lillafured, Hungary, Sep.06-09, 2004. Univ Miskolc, Mat & Met Engn Fac, Phys Met & Metalforming Dept; Hungarian Acad Sci, Res Grp Mat Sci; NASA MSFC; HAS, Miskolc Comm; Hungarian Space Off; Assoc Hungarian Foundries. 2006, 509–514. ISBN: 0-87849-991-1.
- [42] Q.M. Chen, E.W. Langer and P.N. Hansen. “Influence of the Process Parameters on the Volume Change during the Eutectic reaction of SG Cast Iron: A Computer Simulation”. In: *Journal of Materials Science* 32.5 (1997), 1239–1248. ISSN: 0022-2461. DOI: {10.1023/A:1018592120197}.
- [43] Lennart Elmquist, Attila Diószegi and Tobias Björklind. “On the Formation of Shrinkage in Grey Iron Castings”. English. In: *Key Engineering Materials* 457 (2011), pp. 416–421.
- [44] W.S. Pellini. “Factors Influencing Riser Range and Feeding Adequacy—Part II”. In: *American Foundryman*. (1953), 62–71.
- [45] Carolin Körner. *Integral Foam Molding of Light Metals*. Berlin: Springer—Verlag Berlin Heidelberg, 2008. ISBN: 978-3-540-68838-9.
- [46] M. Petrič, J. Medved and P. Mrvar. “Effect of Grain Refinement and Modification of Eutectic Phase on Shrinkage of AlSi9Cu3 Alloy”. In: *Metallurgija* 50.2 (2011), 127–131. ISSN: 0543-5846.
- [47] Q.M. Chen, E.W. Langer and P.N. Hansen. “Stable Solute Boundary Layer for Liquid and Volume Change during Eutectic Solidification of Spheroidal Graphite Iron”. In: *Journal of Materials Science Letters* 16.4 (1997), 249–252. ISSN: 0261-8028. DOI: {10.1023/A:1018572211806}.
- [48] R. Siclari et al. “Micro-Shrinkage in Ductile Iron—Mechanism and Solution”. In: *Proceedings. 66th World Foundry Conference*. Istanbul. World Foundry Organisation. 2004, 863–873.
- [49] T. Skaland. “A New Method for Chill and Shrinkage Control in Ladle Treated Ductile Iron”. In: *Proceedings. 66th World Foundry Conference*. Istanbul. World Foundry Organisation. 2004, 975–986.
- [50] I. Jimbo and A.W. Cramb. “The Density of Liquid Iron-Carbon Alloys”. In: *Metallurgical Transactions B-Process Metallurgy* 24.1 (1993), 5–10. ISSN: 0360-2141. DOI: {10.1007/BF02657866}.
- [51] J.T. Berry, J. Shenefelt and R. Luck. “Pressurised Feeding Systems”. In: *International Journal of Cast Metals Research* 14.6 (2002), 365–370. ISSN: 1364-0461.
- [52] N.W. Rasmussen, R. Aagaard and P.N. Hansen. “Gating and risering in vertical green sand moulds”. In: *International Journal of Cast Metals Research* 14.6 (2002), 355–363. ISSN: 1364-0461.
- [53] G. Alonso. et al. “Kinetics of Graphite Expansion during Eutectic Solidification of Cast Iron”. In: *International Journal of Cast Metals Research* 27.2 (2014), 87–100. ISSN: 1364-0461. DOI: {10.1179/1743133613Y.0000000085}.
- [54] Jafar Khalil-Allafi and Behnam Amin-Ahmadi. “Effect of Mold Hardness on Microstructure and Contraction Porosity in Ductile Cast Iron”. In: *Journal of Iron and Steel Research International* 18.4 (2011), 44+. ISSN: 1006-706X.
- [55] Nikolaj Kjelgaard Vedel-Smith. “Feeding Against Gravity with Spot Feeders in High Silicon Ductile Iron”. In: *Science and Processing of Cast Iron X*. Vol. 10th International Symposium on the Science and Processing of Cast Iron, Mar Del Plata, Argentina, Nov.10-13, 2014. 2014,

- [56] G. Alonso et al. “Kinetics of Graphite Expansion during eutectic Solidification of Lamellar and Spheroidal Graphite Iron”. In: *AFS Proceedings 2014*. AFS Conference. Schaumburg, IL, USA. American Foundry Society. 2014, 1–12.
- [57] Q.M. Chen, E.W. Langer and P.N. Hansen. “Modelling Volume Change during Solidification of SG Cast Iron with Eutectic Composition”. In: *Scandinavian Journal of Metallurgy* 24.2 (1995), 48–62. ISSN: 0371-0459.
- [58] Q.M. Chen. “Influence of C, Si on Volume Change of SG Iron during Solidification—Computer Modelling for Hypereutectic and Hypoeutectic Compositions”. In: *Journal of Materials Science Letters* 16.15 (1997), 1288–1290. ISSN: 0261-8028. DOI: {10 . 1023 / A : 1018583110183}.
- [59] Rohallah Tavakoli and Parviz Davami. “Optimal Feeder Design in Sand Casting Process by Growth Method”. In: *International Journal of Cast Metals Research* 20.5 (2007), 288–296. ISSN: 1364-0461. DOI: {10 . 1179 / 136404607X268238}.
- [60] Rohallah Tavakoli and Parviz Davami. “Automatic Optimal Feeder Design in Steel Casting Process”. In: *Computer Methods in Applied Mechanics and Engineering* 197.9-12 (2008), 921–932. ISSN: 0045-7825. DOI: {10 . 1016 / j . cma . 2007 . 09 . 018}.
- [61] Rohallah Tavakoli and Parviz Davami. “Feeder Growth: A New Method for Automatic Optimal Feeder Design in Gravity Casting Processes”. In: *Structural and Multidisciplinary Optimization* 39.5 (2009), 519–530. ISSN: 1615-147X. DOI: {10 . 1007 / s00158-008-0340-6}.
- [62] A. Muumbo, H. Nomura and M. Takita. “Casting of Semi-Solid Cast Iron Slurry using combination of Cooling Slope and Pressurisation”. In: *International Journal of Cast Metals Research* 17.1 (2004), 39–46. ISSN: 1364-0461. DOI: {10 . 1179 / 136404604225020533}.
- [63] J.J. Sobczak, L. Drenchev and R. Asthanas. “Effect of Pressure on Solidification of Metallic Materials”. In: *International Journal of Cast Metals Research* 25.1 (2012), 1–14. ISSN: 1364-0461. DOI: {10 . 1179 / 1743133611Y . 0000000016}.



# Chp Physical Phenomena and their Simulation

## Numerical Simulation of Cast Iron

### Physical Phenomena and their Simulation

<b>3.1 Numerical Simulation</b> . . . . .	<b>39</b>	3.4.2 Porosity Formation . . . . .	52
<b>3.2 Methodological Approach</b> . . . . .	<b>41</b>	3.4.3 Criteria Functions . . . . .	54
<b>3.3 Parameters and Processes</b> . . . . .	<b>42</b>	3.4.4 Feeding Algorithms . . . . .	56
3.3.1 Geometry . . . . .	42	3.4.5 Feeders . . . . .	57
3.3.2 Filling Simulation . . . . .	43	3.4.6 Feeding . . . . .	58
3.3.3 Heat Transfer . . . . .	43	<b>3.5 Stress and Deformation</b> . . . . .	<b>58</b>
3.3.4 Solidification . . . . .	45	3.5.1 Irreversible Deformations . . . . .	60
3.3.5 Microstructure Modelling . . . . .	47	3.5.2 Phase Transformations . . . . .	61
<b>3.4 Porosity Handling and Feeding</b> . . . . .	<b>50</b>	3.5.3 Dimensional Accuracy . . . . .	61
3.4.1 Thermal Expansion (Volume Change) . . . . .	51	<b>References</b> . . . . .	<b>61</b>



**P**RESENTS the physical phenomena that lies behind the casting and feeding process, and correlate these phenomena to mathematical models, and related assumptions used to describe, simulate, and predict the properties and behaviour of castings.

Keywords: . . . . . Physical phenomena, Numerical Simulation, Feeding Algorithms, Enmeshment, Filling, MAGMASOFT, Heat Transfer, Solidification, Modelling, Lever Rule, Scheil, Thermal Expansion, Criteria Functions, Stress, Deformation, Phase Transformations

Chapter findings reported in: . . . . . Not reported.

### 3.1 Numerical Simulation

SINCE Müller's construction of his mechanised calculator in 1782 [65], through Babbage's conception of the analytical engine in 1834 [66], and Turing's formulation of his vision for mechanised computation in 1936 [67]; the development of automated problem solving has been ever developing.

Simulations are a useful tool to aid understanding of processes and phenomena. Simulations are used on many levels to solve casting related problems;

Alternating Directional Implicit (ADI), Aluminium (Al), Finite Difference Method (FDM), Finite Element Method (FEM), Finite Volume Finite Difference Method (FVFD), Heat Transfer Coefficient (HTC), Lamellar Graphite Iron (LGI), Magnesium (Mg), Nickel (Ni), Oxygen (O), Secondary Dendrite Arm Spacing (SDAS), Spherical Graphite Iron (SGI)

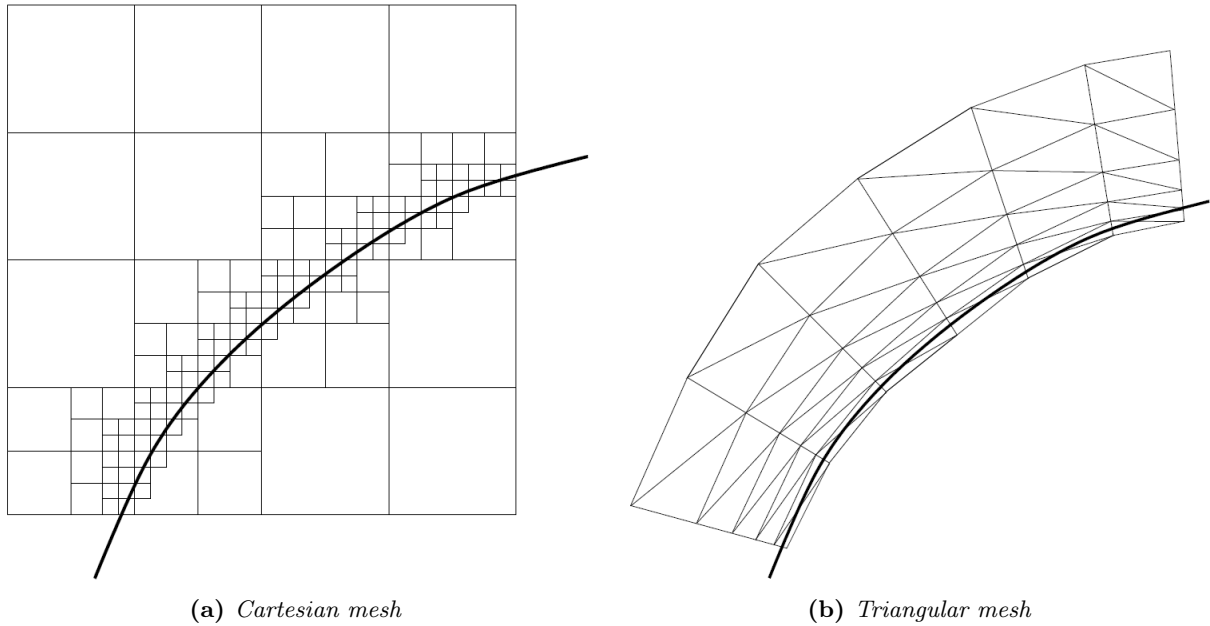


**Figure 3.1:** Comparison of Cartesian and Triangular meshes. MAGMASOFT uses Cartesian meshes while programs primarily using FEM often use Triangular meshes. Courtesy of Fidkowski [64].

from analytical phase-field modelling of interfaces at the smallest possible level to numerical simulations of full castings and whole castings processes and cycles. The main difference between the two approaches, analytical and numerical, is that analytical methods provide exact mathematical solutions while numerical methods provide approximations.

This difference is not the same as to say the analytical models cannot be inaccurate (nor that a numerical model cannot be precise). Often terms are deliberately excluded from an analytical model because the added accuracy of including the term does not justify the increased processing time. Numerical models make use of assumption to reduce processing time at the cost of mathematical accuracy. However, increased processing speed also allow more calculations to be performed expanding the subject of the simulation, improving the overall precision of the simulation.

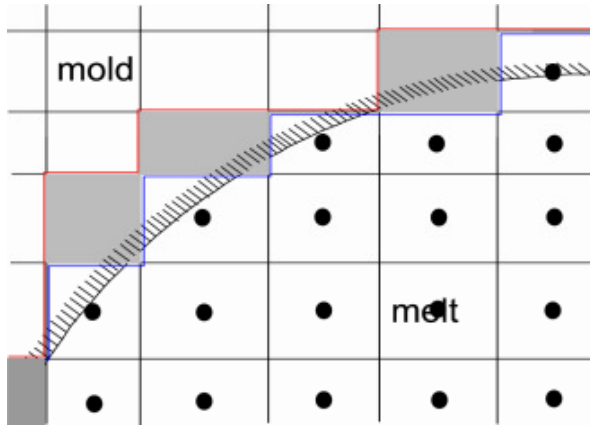
Numerical modelling is used for timely solutions to complex problems; hence, some mathematical inaccuracy is accepted to be able to solve complex problems as eg simulating the filling, solidification, and cooling of a whole casting. Analytically simulating an entire casting would be impossible as analytical systems are restrictive, and often require very simple (usually 1D) geometries, have restrictive boundary conditions, constant material prop-

erties, and a limited number of coupled phenomena [68]. Thus, many complex problems can only be solved numerically, as they have no known analytical solutions.

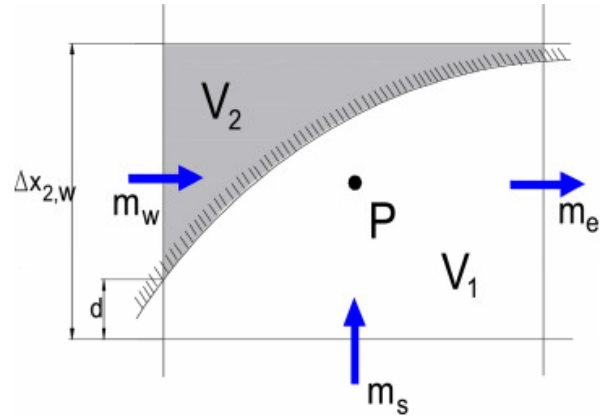
The primary requirement for a numerical simulation is; accurate enough results as soon as possible. Numerical simulations, as the ones provided by MAGMASOFT, are used for process understanding and process optimisation. MAGMA's approach to simulations is to model the physical phenomena as accurately as possible. Hence, the input to MAGMASOFT is the processing conditions and material data. Note that the accuracy of the simulations in most cases will be affected more by the simulation setup and material data than the capabilities of the numerical equations themselves.

It is important to assess and evaluate the potential sources of inaccuracy in the simulations to review the validity of the results. The solution performed by MAGMASOFT is, due to commercial considerations, confidential and not publicly available. Hence, note that the following sections are based on educated guesses, assumptions, and external references, unless referenced to the MAGMASOFT Manual itself [69]. This chapter is not a review on numerical modelling or casting simulation in general and should not be considered as such.





(a) Fluid domain mesh with cut-cells. Blue line indicate the standard solver mesh, and the red line the Solver5 mesh. Grey denote differences between meshes.



(b) 2D Cut-cell. Grey denote the mould volume.

**Figure 3.2:** Illustration of cut-cells implementation in Solver5 from the MAGMASOFT 5.2.0 manual [69].

### 3.2 Methodological Approach

**F**IRST step is to establish the fundamentals of how numerical simulations are solved. MAGMASOFT is based on Finite Volume Finite Difference Method (FVFD) to solve the governing partial differential equations [6, 70] and uses the Alternating Directional Implicit (ADI) method to achieve tridiagonal matrices for solving the equations [71]. The methods applied changes between implicit and explicit solutions to achieve the alternating effect. The methodological approach is important as it defines the possibilities and limitations of the solution. The applications of the ADI method allow for longer time steps to be used without reaching instability, which again increases the processing speed of the simulation.

The finite volume method, or control volume approach, is chosen because the equations exactly follow the underlying physics and the fluxes have more physical significance [70, 72]. While FVFD do not specify a particular type of mesh MAGMASOFT implement a rectangular Cartesian mesh to optimise the processing speed. MAGMASOFT allows for irregular mesh cell sizes, though if not used carefully this may decrease the processing speed, as irregular meshes require far more calculating effort. As MAGMASOFT does not allow for unstructured or triangular meshes, curved and round geometries are approximated by rectangular mesh cells as opposed to unstructured mesh cells as often used in FEM

meshes. See fig. 3.1 on page 40. For complex or curved geometries the rectangular mesh requires a high resolution to achieve an equally accurate representation of the geometry. However, the serrated edges do not introduce significant errors concerning heat transport and thermal gradients [71].

While the solidification is not significantly influenced by the serrated structure of the Cartesian mesh, the filling simulation is otherwise dependent on smooth surfaces. Thus, as a part of Solver5 which handles the filling simulation, MAGMASOFT has introduced the application of Cartesian cut-cells to improve the momentum, pressure, thermal energy, and free surface equation, as well as the venting model [69]. The cut-cell approach change how the mesh is generated to make use of the cut-cells. See fig. 3.2. The cut-cell approach is described further by Mingham et al, Ingram et al, and Fidkowski [64, 73, 74].

The cut-cell approach of the Solver5 is, however, even more sensitive to irregular meshes with cells of different aspect ratios than the standard solver [69]. The ‘Maximum Length Ratio of Neighbouring Elements’ and the ‘Maximum Aspect Ratio of an Element’ are the most important features. MAGMASOFT defines the aspect ratio as [69]:

$$R_{xy} = \frac{\Delta x}{\Delta y} \quad (3.1)$$

where  $R_{xy}$  is the aspect ratio between the x- and y-directions,  $\Delta x$  is the length of the mesh cell in the

x-direction, and  $\Delta y$  is the length of the mesh cell in the y-direction. MAGMASOFT recommends that the aspect ratio of a cell should not exceed 4 (at most 5) for the standard solver, and 3 (at most 4) for Solver5 [69]. In the same manner, the variation in length between two neighbouring elements in the same direction should also not exceed a given ratio. For the standard solver the ratio should be no larger than 3 (in exceptional cases 4), however, for the Solver5 the recommended maximum ratio is 2, albeit a limit of 1.75 would be even better [69]. These recommendations should be kept in mind when generating the mesh, as a good mesh quality is a prerequisite to obtaining good results. In this respect, the more uniform the mesh is, the better the results are going to be.

The advantages of FVFDMM according to Aagaard are as follows [71]:

- Quick mesh generation.
- Simple topology; global indexing in three dimensions.
- Line-by-line structure in the mesh; provide the possibility for using fast line-by-line solvers.
- The line-by-line solvers in the FVFDMM code simulate rapidly; often 10-100 times faster than the FEM applied to the same problem.
- Irregular boundaries approximated by serrated edges in the mesh do not produce significant errors, especially in regards to heat transfer calculations.
- Properties such as temperature are attached to the centres of the control volumes; No need for extra nodes or special formulations in the joint surfaces between different material domains.

Other significant points for the FVFDMM method is that the algebraic equations derived from the control volume approach ensure conservation on a discrete level, as well as globally (simulation domain) [70] and that it is well suited for heat transfer and fluid flow problems [6, 70]. It is less well suited for stress simulations, why MAGMASOFT uses FEM for these simulations.

A limitation of the numerical simulation, as well as analytical models, is that they can only approximate what is understood. The models cannot be better than our process understanding, and the accuracy of the simulations depend on how well

the physical phenomena are perceived and adapted mathematically. Note, however, that imperfect knowledge does not prevent very sound partial solutions. For instance, the nucleation and growth of nodular graphite are still debated. However, the thermal effects of nucleation and solidification are well-established. This dualistic basis is also valid for numerical simulation programs as MAGMASOFT. Physical phenomena are modelled only to a certain degree. For instance, it is expected that MAGMASOFT handles nucleation as a dispersed number of nuclei rather than a calculation of chemical potentials and local diffusion. The simplified algorithm is benchmarked against casting tests and analytical models to ensure that the outcome matches the microstructures and cooling curves of the test castings.

### 3.3 Parameters and Processes

As described in the previous section numerical simulations rely on assumptions; however the most significant source of inaccuracy is often the material and process data provided the model during simulation. Hence, great care should be taken when assigning properties during the simulation set up. The simulation cannot be better than the data provided.

In MAGMASOFT the parameters specify the starting conditions, which MAGMASOFT then processes chronologically starting with filling, followed by solidification, and optionally stress-strain calculations. This construction also means that all the processes are linked. The calculations of the first time step provide the data for the second time step and so forth. Hence, a change in eg pouring temperature will influence all the partial differential equations solved during the simulations, though only one time step at the time. Thus, the effect of the changed pouring temperature may, or may not, entail a significant change that affects the microstructure formation during solidification. The outcome depends on the heat loss during filling and cooling, as well as the absorption and heat transport of the mould.

#### 3.3.1 Geometry

The first step of setting up a simulation is to construct the geometry of the casting, mould, gating, feeders, chills, etc. While the simulations, as described by Aagaard is not particularly sensitive to

the serrated edges created by the Cartesian mesh [71], general inaccuracies in the Computer Aided Design (CAD)-model may pose problems. Often the part itself is modelled in great detail in the CAD-model, while the gating, feeders, and other casting process additions may be modelled simplified and inaccurate. As CAD-models are often not available for these features, an approximation may be the only solution; however, the operator should be aware of the accuracy restrictions imposed on the simulations as small geometrical changes can have great influence on the success of the casting setup.

The geometry of the casting and the mould also defines the boundaries of the simulations. The Cartesian mesh defines the flux between the control volumes; hence, the mesh itself determine the boundaries of the equations solved.

### 3.3.2 Filling Simulation

When the parameters are set up, and the geometry and mesh are defined, the simulations start with the simulation of the mould filling. The filling is, as well as solidification, based on the FVFD method, and is essential for providing an accurate representation of the temperature distribution throughout the metal and mould at the end of filling [75]. The model used by MAGMASOFT is based on the work by Lipinski et al [76, 77].

Besides the thermal gradients, the filling provides information on air entrapment, material age, mould erosion, and more. For cast iron, it is important to know that the fading of the inoculation begins with the filling simulation [71]. Note also that MAGMASOFT cannot simulate inclusions caused by parts of the green sand mould being torn off during filling; hence delicate geometries should be reviewed critically. Another limitation of the numerical simulation is the applications of different solvers. While the mesh and process data continue chronologically from the beginning of the filling to the end of cooling, the filling solver is separated from the solidification and stress solvers. Hence, the metal cannot begin to solidify before the filling is complete and the solidification solver is initiated. However, while the solidification simulation is decoupled during filling, MAGMASOFT, in Solver5, uses what is called variable viscosity. The variable viscosity is defined in the material data as a function of the temperature [69]. Hence, as the metal cools, it becomes less viscous resulting in poor flowability. At a given temperature the semi-liquid metal is said to freeze

and lose all flowability. MAGMASOFT defines the freezing temperature  $T_{Freeze}$  as [69]:

$$T_{Freeze} = T_{Sol} + 0.25(T_{Liq} - T_{Sol}) \quad (3.2)$$

where  $T_{Sol}$  is the solidus temperature of the alloy and  $T_{Liq}$  is the liquidus temperature. As an alternative to the  $T_{Freeze}$  defined in eq. (3.2) the freezing condition can also be expressed as a critical fraction solid,  $f_s$ , above which the flowability of the metal is zero [69].

It should be noted that, as the solidification is not coupled to the filling simulation, the latent heat of fusion is not included in the temperature calculation. This decoupled nature is most important for alloys with a large recalescence as eg cast iron.

### 3.3.3 Heat Transfer

At the end of filling the solidification solver is initiated. The primary driver for the solidification and cooling of the casting is the transport of heat away from the casting and to the ambient conditions outside the boundary domain. The governing assumption is that of energy conservation, where energy is conserved both locally in the transport between adjacent control volumes (mesh cells) as well as globally [71]:

$$E_{Stored} = E_{In} + E_{Gen} + E_{Out} \quad (3.3)$$

where  $E_{Stored}$  is the total amount of energy held in a given domain at a given time,  $E_{In}$  is the energy added to the domain,  $E_{Out}$  is the energy subtracted from the domain, and  $E_{Gen}$  is the energy generated inside the domain.

By the laws of thermodynamics, heat transport can occur by either conduction, convection, or radiation. Conduction and convection are considered concerning the internal heat transport of a single material. Conduction functions via diffusion or collision of particles within the body, where energy is always transferred from the higher state to the lower state. Convection requires movement within the thermal body, hence effectively limiting this mode of heat transfer to liquids and gasses. While conduction and convection both transfer heat inside a thermal body, radiation transmits the heat between different thermal bodies. In a casting, the radiation will transfer heat from the metal to the mould. This radiating heat transfer will cool the surface of the metal initiating conduction (and potentially also

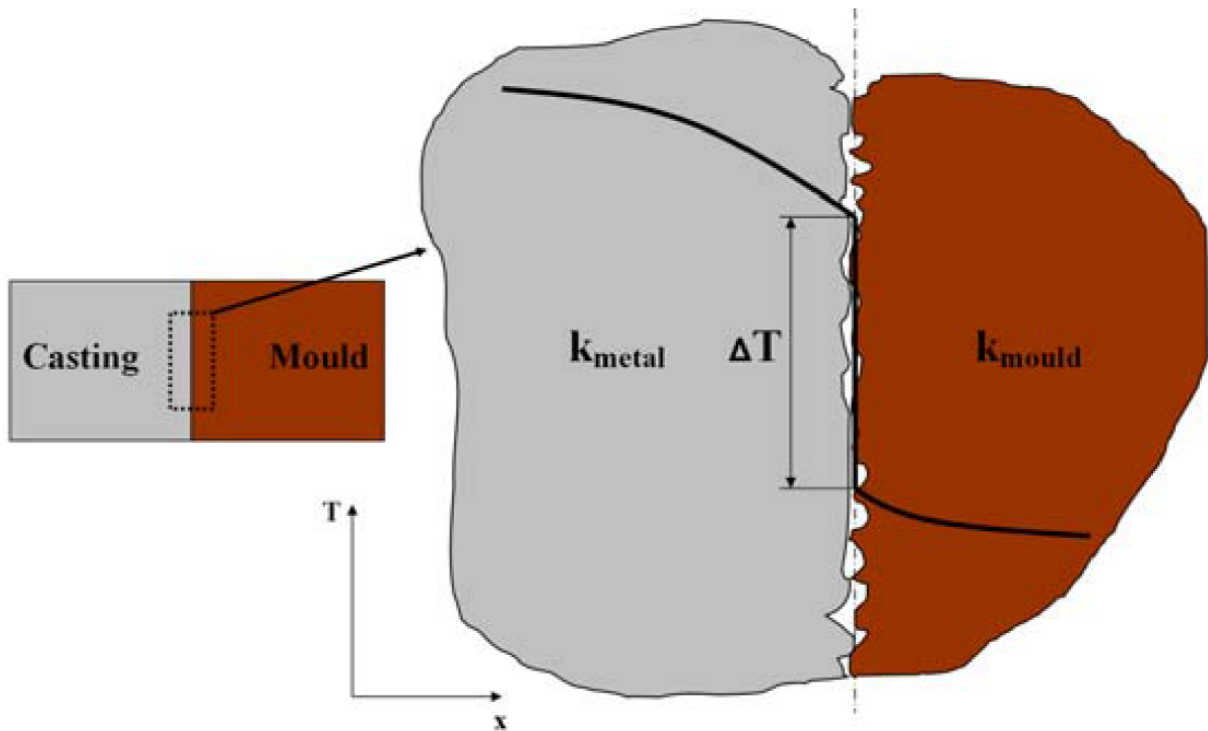


**Figure 3.3:** Temperature profile across mould-metal interface as a function of HTC. Courtesy of Kotas [20]

convection) to try to equalise the internal temperature difference. At the same time, the radiated heat will also heat the surface of the mould, which in turn will transport the heat towards the external ambient temperature via conduction. See fig. 3.3. The mathematical adaptations of these phenomena are elaborated in the following paragraphs.

#### Conduction

The thermal conduction is defined as the heat flow per unit area proportional to the temperature gradient, which can be written as:

$$q = -kA \frac{\partial T}{\partial x} \quad (3.4)$$

where  $q$  is the diffusive heat flow (heat flux) perpendicular to the surface,  $k$  is the thermal conductivity,  $A$  is the area of the surface,  $T$  is the temperature, and  $x$  is the descriptive space component perpendicular to the surface. Equation (3.4) is the fundamental Fourier's law of thermal conduction and the basis of eq. (3.6) on the facing page. Additionally, the equation also defines the thermal conductivity,  $k$  [20].

#### Convection

Convection is the only one of the three modes of heat transport that also transport mass. For the same reason, convection can also be forced by deliberately circulating the medium in question. While castings made in dies often use active cooling in the form of forced convection of a cooling medium (water or oil), the internal convection of the castings is free or natural convection [20]. Natural convection is created by the changes in density caused by differences in temperature. Hence, the cold and heavy material will sink downwards, while the hot a lighter material will rise towards the surface. As the material has moved to an area with a lower or higher temperature, the temperature difference will be reduced via conduction.

**Advection** While convection is the transport of material as a function of heat differences, the opposite, namely movement of the material (including the heat energy) can also occur as a function of other factors; eg volume contraction of the melt. This is particularly interesting with regards to feeding as the melt that is used to feed the casting also

transport heat energy inside the casting. This phenomenon is called advection.

$$q = -vA\rho C_p \frac{\partial T}{\partial x} \quad (3.5)$$

where  $q$  is the heat flow,  $v$  is the velocity of the melt flow,  $A$  is the area through which the melt flows,  $\rho$  is the density of the melt,  $C_p$  is the specific heat capacity of the melt, and  $x$  is the descriptive space parameter perpendicular to the cross-section area.

### Radiation (HTC)

MAGMASOFT has pre-calculated HTCs based on the properties of the two opposing materials and their radiation properties. The HTC is sometimes set as a constant neglecting the influence of varying temperatures [20]. This approximation is adequate for interfaces with little change in HTC during the cooling and solidification process, often related to poor heat transfer conditions. This poor heat transfer condition could be mould-metal contact in gravity sand casting, where the rough surface of the mould reduces the HTC at the beginning of the solidification. When the contraction of the metal creates a gap between the mould and the metal, this decrease in HTC can be neglected due to the already poor HTC [20]. See fig. 3.3 on page 44. However, MAGMASOFT offers a dynamic HTC for the metal which is supposed to provide more precise HTC values, especially at elevated temperatures. MAGMA calls this for a ‘temperature dependent HTC’. For cast iron the temperature dependent HTC is selected via the *TempIron* property [69].

As seen from eq. (3.4) on page 44 the thermal conductivity,  $k$ , is an important parameter. The heat conduction within a single material is described by  $k$ , however as the casting process comprises many different materials, heat needs to be transported from one material to another. For example from the melt to the mould and into the ambient surroundings. These heat transports between materials are handled by the Heat Transfer Coefficient (HTC), which depends on the two materials as well as their respective temperatures. The unit is  $W/m^2K$  [69].

In MAGMASOFT the transport is governed by Fourier’s differential equations. Including the temperature dependent material parameters the heat flow equations for conduction denotes as follows [75]:

$$\rho C_p \frac{\partial T}{\partial t} - \dot{q} = \frac{\partial}{\partial x} \left( \lambda \frac{\partial T}{\partial x} \right) + \frac{\partial}{\partial y} \left( \lambda \frac{\partial T}{\partial y} \right) + \frac{\partial}{\partial z} \left( \lambda \frac{\partial T}{\partial z} \right) \quad (3.6)$$

where  $\rho$  is the density,  $C_p$  is the specific heat capacity,  $T$  is the temperature in K,  $t$  is the time in seconds,  $\dot{q}$  is the heat flux (heat transfer rate per unit area),  $\lambda$  is the Heat Transfer Coefficient (HTC), and  $x, y, z$  denoted the dimensions.

Radiation is also what governs the heat release from the mould to the ambient surroundings. In MAGMASOFT 5.3 this can be simulated as ray-traced radiation, likely based on Maxwell’s equations [79]. This ray-tracing option, however, is an option specially intended for investment casting where the radiation from one part of the mould may reflect on other parts of the mould, thus heating it. For the DISA-mould setup in MAGMASOFT, which is used throughout this work, the mould is fictively placed in a moulding line with identical moulds before and after. This effect is achieved by transferring the heat from one side of the wall to the other side, simulating an infinite mould. It is possible that this mirroring of the heat transfer is delayed in one direction, corresponding to the cycle time, to give a more accurate simulation of the delay between mould fillings.

### 3.3.4 Solidification

Based on the heat transfers and extraction described in the previous section, MAGMASOFT applies two levels of numerical models to solve the solidification functions [75]. The first part is a macro model addressing the overall alloy composition and cooling rate. The latent heat of fusion is handled as a material parameter incorporated in  $\rho C_p$  for a fixed temperature interval where solidification occurs. The latent heat of fusion is released based on the composition, which determines the solidification path, and thus also the approach for its solution [71, 75]:

**Hypoeutectic** The Scheil equation is used to calculate the fraction of solid prior to eutectic solidification.

**Eutectic** The latent heat of fusion will be distributed as a mean value over the solidifying interval.

**Hypereutectic** The Lever rule is used to calculate the fraction of primary graphite forming in the melt before eutectic solidification.

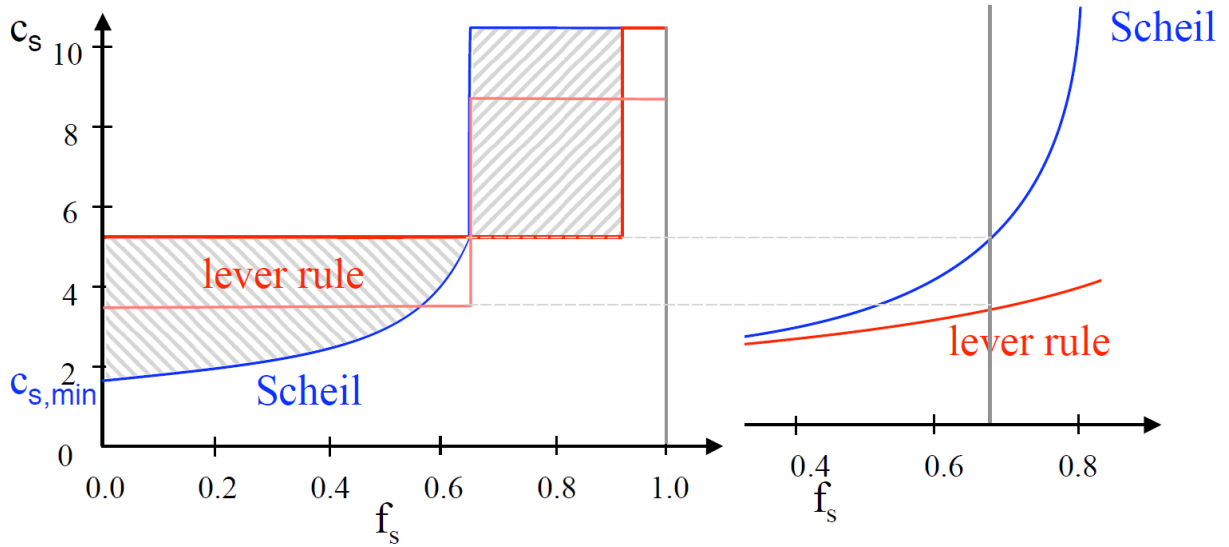


**Figure 3.4:** Comparison of the Scheil equation and the Lever rule. Courtesy of Rettenmayr [78]

Hence, the dendritic growth is governed by the Scheil equation [70]:

$$f_s = 1 - \left( \frac{T - T_f}{T_L - T_f} \right)^{\frac{1}{k-1}} \quad (3.7)$$

where  $f_s$  is the fraction of solid,  $T$  is the temperature,  $T_L$  is the temperature at the liquidus line intersection,  $T_f$  is the melting point of the pure component,  $k$  is the equilibrium partition coefficient as defined in eq. (3.9).

The precipitation of graphite is governed by the Lever rule, here written as the relationship between the composition of the fraction solidified,  $f_s$ , and the temperature,  $T$  [70]:

$$f_s = \frac{T - T_L}{(T - T_f)(1 - k)} \quad (3.8)$$

However, both approaches are based on a number of assumptions. The Scheil equation assumes [70]:

1. Total mixing in the liquid of the solvent rejected at the solidifying interface.
2. No diffusion redistribution in the solid phase formed.

Note, also, that the Scheil equation does not predict the distribution of eg the Iron (Fe)-C system correctly [70].

The Lever rule shares the first assumption with the Scheil equation, assumes the opposite of the second assumption above, and adds a third assumption [70]:

1. Total mixing in the liquid of the solvent rejected at the solidifying interface.
2. Total diffusion redistribution in the solid phase formed.
3. The liquidus and solidus lines are described by straight lines, so the partition coefficient  $k$  is constant.

where  $k$  is the equilibrium partition coefficient defined as:

$$k = \frac{C_S}{C_L} \quad (3.9)$$

where  $C_L$  is the composition of the liquid, and  $C_S$  is the composition of the solid—both at the solid-liquid interface. Note that the third assumption can be relaxed for numerical calculations.

The Scheil equation and the Lever rule are compared in fig. 3.4, showing the differences in concentration in the solid.

The second assumption, total diffusion in the solid, can only be satisfied for very long solidification times. As MAGMASOFT models microstructures and local compositions, this cannot be achieved by the methods mentioned above. This unresolved issue is solved by introducing a micro model considering solidification kinetics [75]. This micro model operates locally, possibly confined to the single mesh cell, and runs in the intermediary time steps of the macro model. The micro model determines the latent heat

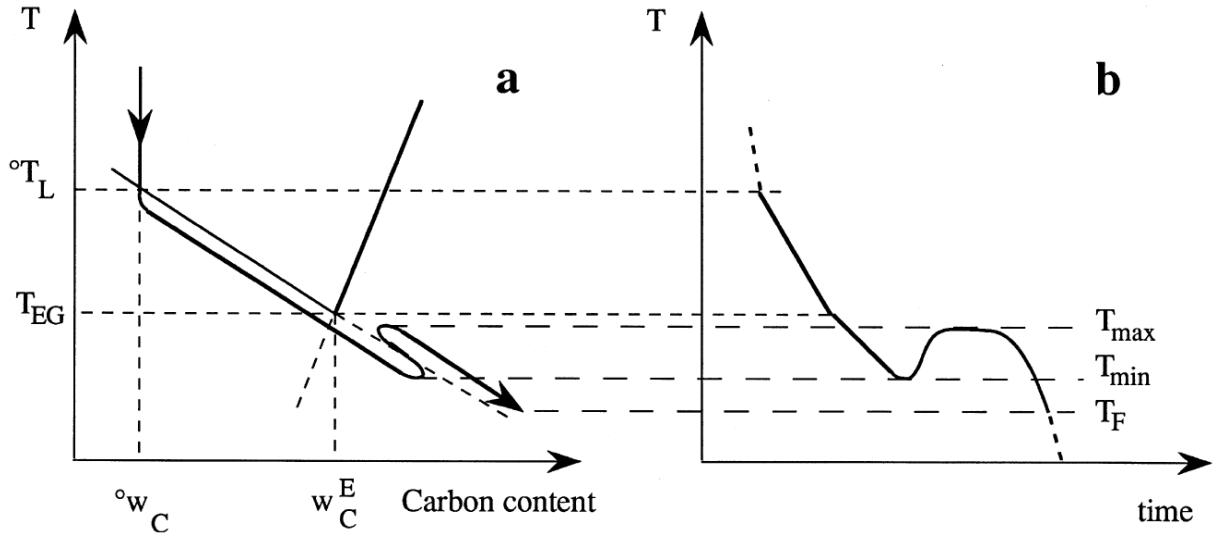


**Figure 3.5:** Illustration of the solidification sequence of hypoeutectic SGI. (a) The solidification path in the isopleth section  $w_{Si} = {}^\circ w_{Si}$ , and (b) the corresponding cooling curve.  ${}^\circ T_L$  is the nominal liquidus temperature,  $T_{EG}$  is the eutectic temperature,  ${}^\circ w_C$  is the nominal C composition of the alloy,  $w_C^E$  is the eutectic C composition,  ${}^\circ w_{Si}$  is the nominal Si composition of the alloy,  $w_{Si}^E$  is the eutectic Si composition,  $T_{max}$  is the maximum temperature reached during the recalescence (the eutectic arrest),  $T_{min}$  is the minimum temperature reached during the initial undercooling, and  $T_F$  is the temperature at which the material is fully solidified. Courtesy of Lesoult et al [80]

of fusion and uses this to determine the nucleation and growth of possible phases. The calculated latent heat of fusion is then applied as a source term for the macro model, which then calculate the temperature field for the next time step. This subroutine is repeated until the casting is completely solidified.

### 3.3.5 Microstructure Modelling

As the micro model calculates the primary austenite precipitation, the segregation of alloy elements is calculated based on either a modified Scheil model or the Lever rule [75], including back diffusion dependent on the diffusion rate of the atoms in the austenite. As solidification progresses differently depending on the state of the melt, if it is hypo-, eutectic, or hypereutectic, different models are needed to describe how solidification progresses.

#### Proeutectic Solidification of Hypoeutectic Cast Iron

For hypoeutectic compositions, the first to precipitate is austenite dendrites as the temperature of the melt reaches the austenite liquidus. The precipitation of austenite reduces the amount of Fe in the remaining liquid, which in turn is left with a composition closer to the eutectic composition. As the temperature drops and the compositions changes to

pass the graphite liquidus, then the graphite starts to precipitate, thus increasing the relative amount of Fe in the melt. This segregation is illustrated in fig. 3.5.

The nucleation and growth of austenite of hypoeutectic compositions has been described by Lesoult et al [80]:

Total mass balance:

$${}^\circ V \rho^l = {}^t V [\rho^l (1 - g^\gamma) + \rho^\gamma g^\gamma]$$

Carbon mass balance:

$${}^\circ V \rho^l {}^\circ w_C = {}^t V [\rho^l (1 - g^\gamma) w_C^l + \rho^\gamma g^\gamma w_C^\gamma] \quad (3.10)$$

where  ${}^\circ V$  is the initial volume of the elementary domain,  $\rho^l$  is the density of the liquid,  $\rho^\gamma$  is the density of the austenite,  ${}^t V$  is the volume of the previous elementary domain at time  $t$ ,  $g^\gamma$  is the volume fraction of austenite in the domain,  ${}^\circ w_C$  nominal mass fraction of C in domain,  $w_C^l$  mass fraction of C in the liquid, and  $w_C^\gamma$  mass fraction of C in the austenite.

The solution assumes that kinetic effects can be neglected, meaning that precipitation of austenite

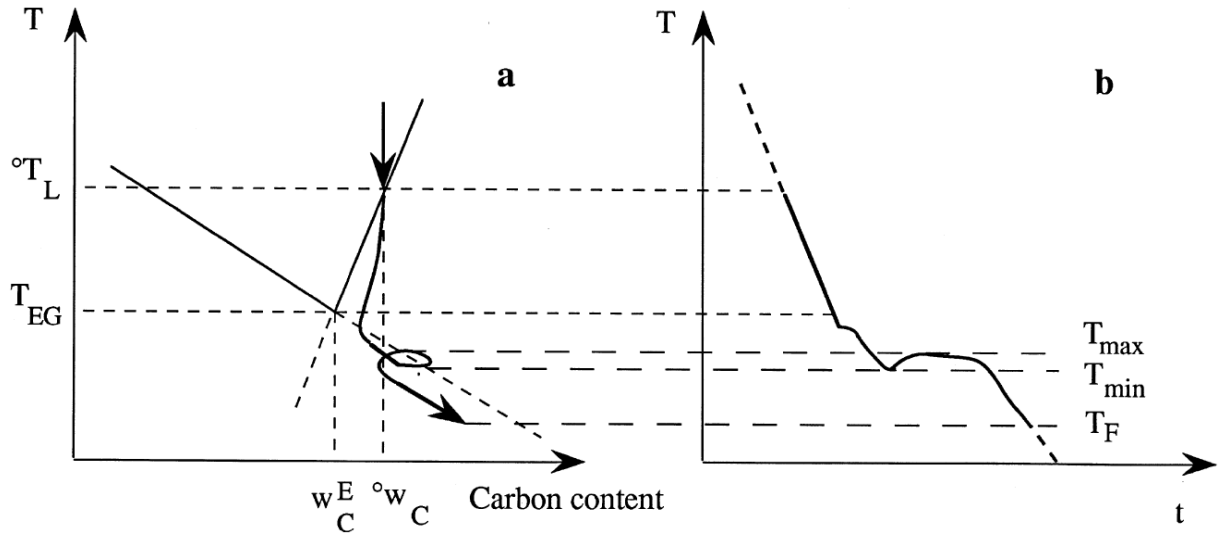


**Figure 3.6:** Illustration of the solidification sequence of hypereutectic SGI. (a) The solidification path in the isopleth section  $w_{Si} = {}^{\circ}w_{Si}$ , and (b) the corresponding cooling curve.  ${}^{\circ}T_L$  is the nominal liquidus temperature,  $T_{EG}$  is the eutectic temperature,  ${}^{\circ}w_C$  is the nominal C composition of the alloy,  $w_C^E$  is the eutectic C composition,  ${}^{\circ}w_{Si}$  is the nominal Si composition of the alloy,  $w_{Si}^E$  is the eutectic Si composition,  $T_{max}$  is the maximum temperature reached during the recalescence (the eutectic arrest),  $T_{min}$  is the minimum temperature reached during the initial undercooling, and  $T_F$  is the temperature at which the material is fully solidified. Courtesy of Lesoult et al [80]

will begin as soon as the temperature reaches the nominal austenite liquidus  ${}^{\circ}T_L$ . It is assumed that the dendrite growth proceeds at equilibrium conditions for both the melt-austenite interface and the coexisting austenite and liquid phases. Finally, the graphite precipitation between the austenite and liquid is assumed to obey the Lever rule.

#### Proeutectic Solidification of Hypereutectic Cast Iron

For hypereutectic alloys, the nucleation and precipitation of graphite start at the graphite liquidus. This early C precipitation results in a reduced C content in the melt until the temperature reaches the austenite liquidus, at which point the austenite will also precipitate and consequently re-increase the C content of the remaining liquid. This mechanism is illustrated in fig. 3.6.

The nucleation of graphite is strongly influenced by the inoculation, which controls both the number of eutectic cells and the required temperature for the growth of the cells. The nucleation model is empirically determined but originates from Oldfield's 1966 model which describes the relationship

between undercooling and the number of nuclei [68, 69, 81]:

$$N_V = A\Delta T^B \quad (3.11)$$

where  $N_V$  is the number of eutectic cells per  $\text{mm}^3$ ,  $A$  is a nucleation constant,  $\Delta T$  is the undercooling upon reaching recalescence, and  $B$  is an inoculation constant dependent on the inoculation quality. In Oldfield's original model  $B$  is fixed as 2 [81]. MAGMASOFT defines the inoculations as either 'Fair', 'Good', or 'Very Good', corresponding to different values of  $B$ . The three values can be fine-tuned by adjusting the treatment yield from 0% to 100% [69].

Oldfield's model is valid for steady state conditions, and with these limitations, describe the nucleation of mechanics of LGI. However, Oldfield's model is not valid for SGI which exhibit continuous nucleation throughout the solidification. For this Lesoult et al have developed an extended model describing the nucleation with consideration to continued reduction in the amount of liquid available for nucleation [80]:



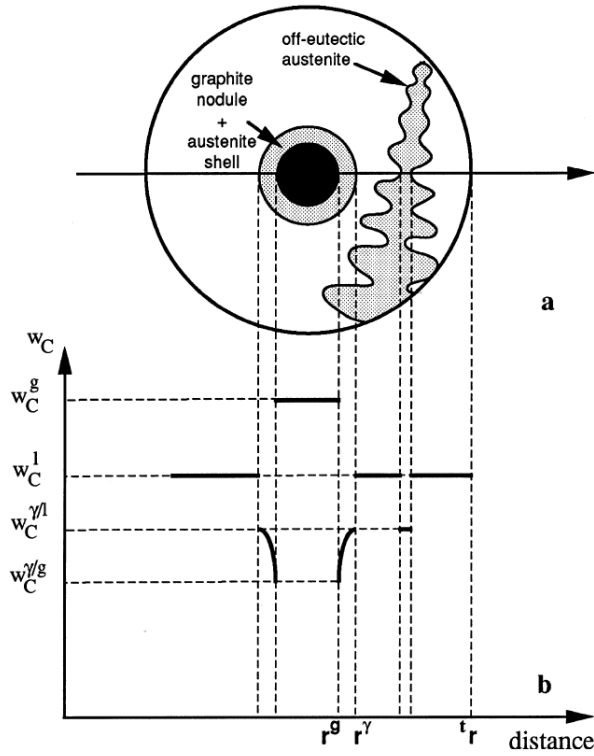


**Figure 3.7:** Illustration of the elementary volume element during solidification of eutectic SGI. Fig. (a) is a schematic illustration of the elementary volume including a graphite nodule with an austenite shell and an austenite dendrite surrounded by liquid. Fig. (b) shows the correlating concentrations of C along the horizontal line in fig. (a).  $r^g$  is the radius of the graphite nodule,  $r^\gamma$  is the outer radius of the austenite shell,  $t_r$  is the radius of the elementary volume at time  $t$ ,  $w_C$  is the mass fraction of C, where  $w_C^g$  is the fraction in the graphite,  $w_C^l$  is the fraction in the liquid,  $w_C^{\gamma^l}$  is the fraction in the off-eutectic austenite, and  $w_C^{\gamma^g}$  is fraction in the austenite surrounding the graphite nodule. Courtesy of Lesoult et al [80].

$$dN = A_n (\Delta T_L^g)^{n-1} (g^l V^{off}) \frac{d(\Delta T_L^g)}{dt} dt$$

$$\text{when } \frac{d(\Delta T_L^g)}{dt} > 0$$

and

$$dN = 0$$

$$\text{when } \frac{d(\Delta T_L^g)}{dt} < 0$$

(3.12)

where  $dN$  is the change in number of graphite particles (nodules) for the time step  $dt$ ,  $n$  is an inoculation efficiency constant,  $A_n$  is an inoculation amount constant,  $\Delta T_L^g$  is the undercooling relative to the graphite liquidus,  $g^l$  is the liquid fraction of off-eutectic volume,  $V^{off}$ . Thus,  $g^l V^{off}$  describes the volume of the remaining liquid and its limiting influence on nucleation sites as the solidification progresses. The expression  $g^l V^{off}$  is sometimes replaced with the fraction of remaining liquid,  $f_L$ , for simplicity [82, 83].

The total number of graphite nodules,  $N$ , is the sum of  $dN$  for the entire volume at the time  $t$ .

Note, however, that the inoculation efficiency and amount changes with time. The inoculation fades as soon as it is added to the melt, which is often done in the stream during filling. MAGMASOFT considers this fading, which is another reason for running the filling simulations beside the temperature fields. With respect to Lesoult's eq. (3.12) this can be simulated in a discrete model, and the values for  $n$  and  $A_n$  can be updated for each time step  $dt$ .

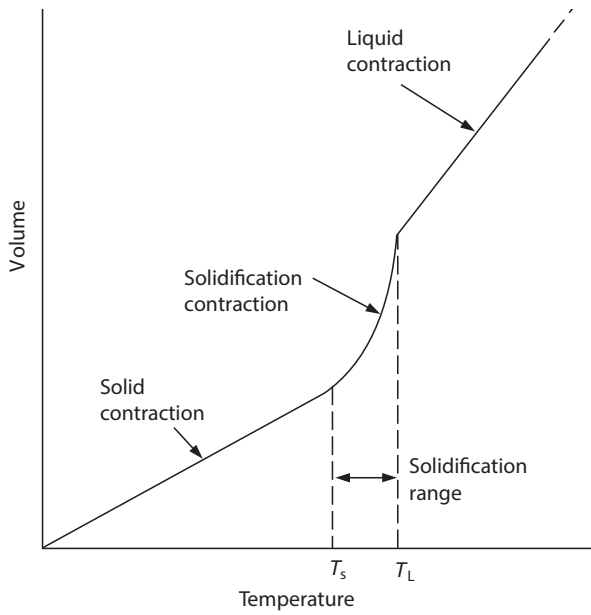
The conditions specified for the equation state that the nucleation becomes zero when the change in undercooling, concerning the graphite liquidus, becomes positive. This nucleation state can happen during recalescence, as this raises the temperature of the domain due to the heat of fusion. Alternatively, the graphite nucleation can stop during the initial deposition given that the growth rate of the free nodules is great enough [80].

MAGMASOFT handles the inoculation efficiency via a *graphite precipitation factor* which is a number between 1 and 10, where ten is the most abundant precipitation possible. The precipitation of graphite at the beginning of solidification is governed by the undercooling. The amount of late precipitation, however, is controlled by the precipitation factor and is physically governed by the composition and inoculation [69].

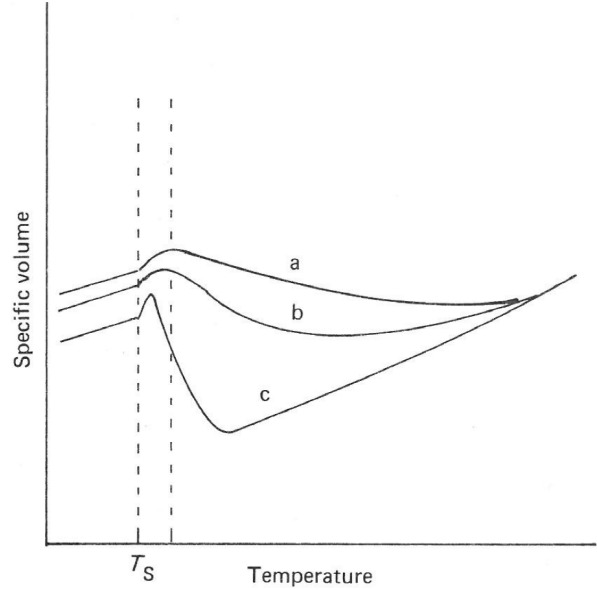
While Lesoult's eq. (3.12) for nucleation of graphite in SGI is a better and more accurate description of the physical process, it is also not well suited for numerical simulations of the type provided by MAGMASOFT. Thus, MAGMASOFT uses a modified version of Oldfield's eq. (3.11) on page 48 which was also used for nucleation of eutectic cells in LGI [69].

### Eutectic Solidification of Cast Iron

The eutectic solidification for LGI is handled on the basis of an equation originally derived by Wetterfall



(a) Illustration of the three different types of shrinkage observed during casting. Courtesy of Campbell [24].



(b) Illustration of the volume change for three types of LGI during solidification. The specific volume is  $m^3/kg$ . Courtesy of Elliott [84].

**Figure 3.8:** Temperature dependent volumetric thermal expansion of cast iron,  $\alpha_V$ .

et al [85] and later described by Aagaard [75]:

$$\frac{dR}{dt} = \frac{K_n}{R_g} (T_E - T) \quad (3.13)$$

where  $dR/dt$  is the growth rate of the eutectic cell,  $K_n$  is the nucleation rate dependent on the Si content,  $R_g$  is the radius of the nodule within the eutectic cell,  $T$  is the temperature, and  $T_E$  is the eutectic temperature. The equation taken into account the Si segregation and the concentration of Si at the interface between austenite and liquid [75].

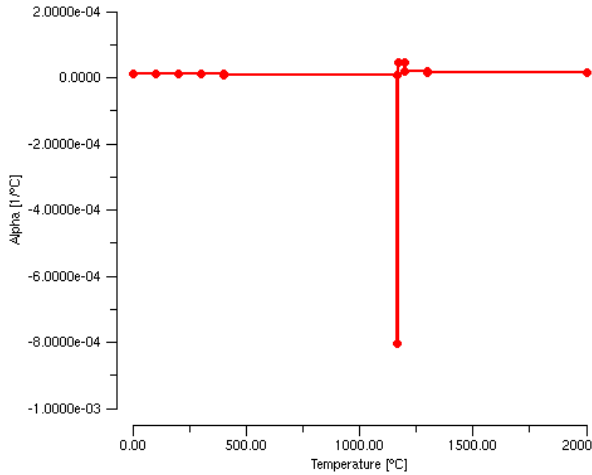
It is estimated that MAGMASOFT use a derivative of Wetterfall's eq. (3.13) for LGI. However, the eutectic solidification of SGI is much more complex and is driven by local diffusion kinetics. Figure 3.7 on page 49 shows the correlation between the C concentration and the formation of austenite dendrites and graphite nodules. The graphite and austenite grow simultaneously in the melt, and the model assumes an approximately homogeneous liquid regarding the C mass balance. Note, however, that Lesoult et al, contrary to this assumption for the model, expects some C build up in the liquid. They describes two ways to satisfy the increased C in the melt necessary to maintain the chemical equilibrium between the austenite and the liquid: (1) a build-up of C in the

liquid in front of the fast-growing eutectic austenite shells, and (2) a build-up of C around the growing off-eutectic dendrites and subsequent diffusion of the C back into the bulk liquid. A combination of the two methods can also be imagined.

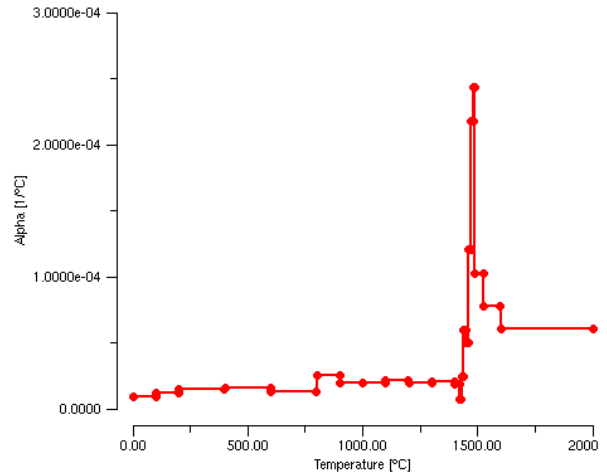
The mass balance equations describing the growth kinetics for the eutectic solidification of an elementary volume of SGI melt is derived by Lesoult et al, but will not be derived here. Lesoult et al describes the growth mechanisms and the subsequent mass balance equations, and the reader is referred to this work for further details [80], and for Lacaze et al's and Pedersen's publications for a numerical implementation [86–88].

### 3.4 Porosity Handling and Feeding

THE solidification and microstructure formation of the cast iron play a significant role in the shrinkage and feeding characteristics of cast iron. Depending on the alloy composition, melt treatment, and cooling conditions the contraction, expansion, and feeding characteristics may change significantly. Feeding of porosities in MAGMASOFT, as in real castings, can be divided into three steps: (1) the need for feeding (shrinkage), (2) the formation and



(a) *GJS-500 cast iron*



(b) *Steel, MAGMASOFT standard*

**Figure 3.9:** Temperature dependent volumetric thermal expansion,  $\alpha_V$ , in MAGMASOFT 5.2.0 [69].

location of porosities, and (3) the removal of porosities (feeding).

### 3.4.1 Thermal Expansion (Volume Change)

As cooling and solidification progresses the casting and the melt contracts creating shrinkage. This is illustrated in fig. 3.8a on page 50, and is the all dominating reason for having feeders, though not the only one, as described in chapter 2, on page 13. However, the design of the feeders is dependent on the amount of porosities, which depends on the thermal expansion (and contraction) of the alloy. The volume change (or shrinkage) of the casting can be described thus:

$$\frac{\Delta V}{V} = \alpha_V \Delta T \quad (3.14)$$

where  $V$  is the volume of the casting,  $\Delta V$  is the volume change,  $\Delta T$  is the temperature change, and  $\alpha_V$  is the volumetric thermal expansion coefficient for the given material for the given temperature interval.  $\alpha_V$  is defined by rearranging eq. 3.14:

$$\alpha_V = \frac{1}{V} \frac{dV}{dT} \quad (3.15)$$

As shown in fig. 3.8a on page 50, the liquid and solidification shrinkage both contribute to the reduction of the casting volume before complete solidification. Note, however, that the directional solidification may result in some parts of the casting being completely solidified while other parts are

still entirely liquid. Thus, the contraction of the first solidified metal may influence the contraction in as much as a solidified shell may reduce the internal volume, reducing the feeding requirement.

MAGMASOFT handles these variations by assigning specific values of  $\alpha_V$  for a given temperature  $T$ . Figure 3.9 shows MAGMASOFT's  $\alpha_V$  values for a standard GJS-500 iron and steel. Note that, for the GJS-500 in fig. 3.9a, the coefficient of thermal expansion is almost constant for the entire temperature range, except for the solidification range. This data means that MAGMASOFT considers the thermal expansion (or contraction) of the GJS-500 close to linear. For the range around the solidification, it should be noted that the coefficient of thermal expansion becomes negative, indicating an expansion as the alloy cools and solidifies. This behaviour is not the case with the steel in fig. 3.9b.

Additionally, it should be noted that MAGMASOFT use a single constant,  $\alpha_V$ , for the thermal expansion coefficient of the materials. Hence, it is assumed that the thermal expansion is isotropic with equal linear expansion in all three directions:

$$\alpha_V = 3\alpha_L \quad (3.16)$$

where  $\alpha_L$  is the linear thermal expansion coefficient.

Cast iron has a special volume change pattern during solidification when compared to other alloys. This is shown by Elliott for LGI in fig. 3.8b on page 50. SGI also displays a combination of contraction and expansion during solidification, though the

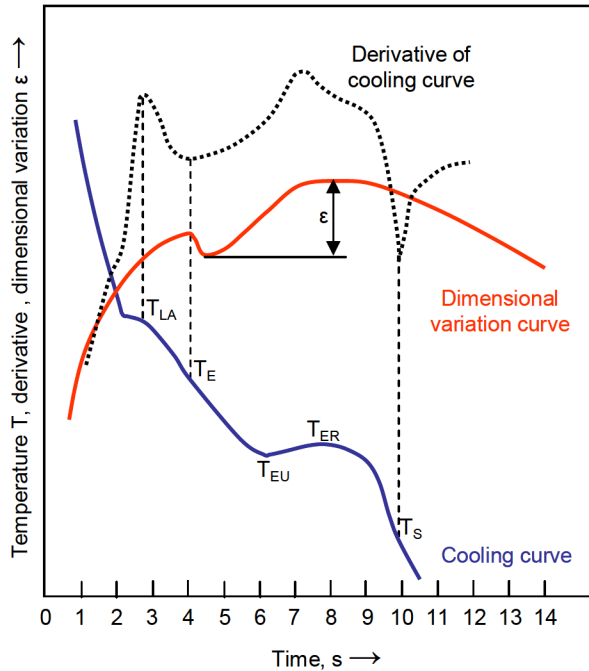


**Figure 3.10:** Dimensional variation during solidification.  $\epsilon$  is the graphite expansion,  $T_{LA}$  is the temperature at the liquidus arrest,  $T_E$  is the temperature at the start of eutectic solidification,  $T_{EU}$  is the temperature at the maximum undercooling during the eutectic solidification,  $T_{ER}$  is the temperature at the maximum recalescence during the eutectic solidification, and  $T_S$  is the temperature at the end of eutectic solidification. Courtesy of Stefanescu et al [91].

timing is more dependent on inoculation and other process parameters. This is illustrated by Stefanescu et al and Alonso et al in fig. 3.10 [53, 56, 89, 90]. Stefanescu et al goes on to show the measured difference in displacement between LGI, CGI, and SGI as shown in fig. 3.11 on the facing page. They also show the correlation between the graphite morphologies and the total displacement as well as the graphite expansion displacement respectively. See fig. 3.12 on the next page.

Comparing fig. 3.9a on page 51 and fig. 3.11 on the next page it is seen that MAGMASOFT has a greater positive  $\alpha_V$  value listed at the initiation of solidification. This relationship corresponds to a greater decrease in volume as the metal solidify and cool, which is also shown by all three curves in fig. 3.11. Following the positive  $\alpha_V$  value, the value turns negative as the solidification continues. As noted above, this corresponds to volume expansion as solidification and cooling continue; and also in accordance with the displacement graphs in fig. 3.11.

### 3.4.2 Porosity Formation

The formation of shrinkage porosities in castings is described in section 2.2.1, on page 17. The present section focus on the handling of porosities in MAGMASOFT. The total amount of shrinkage is determined by the volume contraction as described in section 3.4.1, on page 51. The shrinkage from the entire casting volume is distributed between the different mesh cells. MAGMASOFT calculate the shrinkage and material density of each phase, adding this up to the total shrinkage, which is calculated continually throughout the cooling of the melt [69].

The location of the porosities is determined by criteria functions and is described in section 3.4.3, on page 54. Each mesh cell has one of three states: (1) full—no loss of material, (2) empty—no remaining material, or (3) partially empty—a fraction of the mesh cell volume contains material. These states are fairly straightforward; however, MAGMASOFT use a threshold value to eliminate porosities of a size so small that it would be doubtful if the porosity prediction were correct or even detectable in a real casting. The porosity fraction threshold value is a trade secret; however, the effect can be observed when changing the mesh to a very fine structure. If the mesh count is sufficiently high, this can make the simulated porosities disappear because the total shrinkage in a given area of the casting is distributed over a greater number of cells, consequently reducing the absolute porosity fraction for the individual mesh cell [92]. See fig. 3.13 on page 54. From this, it can also be deduced that the threshold value is not percent based, but an absolute value. The value may be material specific, but it is also possible that it is a fixed value in iron module—MAGMAiron—or in MAGMASOFT in general.

Another factor influencing the amount of shrinkage is the potential mould dilation, as described in section 2.3.7, on page 29. MAGMASOFT includes this in the porosity estimation [69]; and offers three mould types, each with a different dilation:

- ‘Die’ (permanent mould)
- ‘Stable Mould’ (stable sand mould)
- ‘Weak Mould’ (weak sand mould)

with ‘Stable Mould’ as the standard.

The shrinkage developed in each of the mesh cells agglomerate into larger porosities—or rather

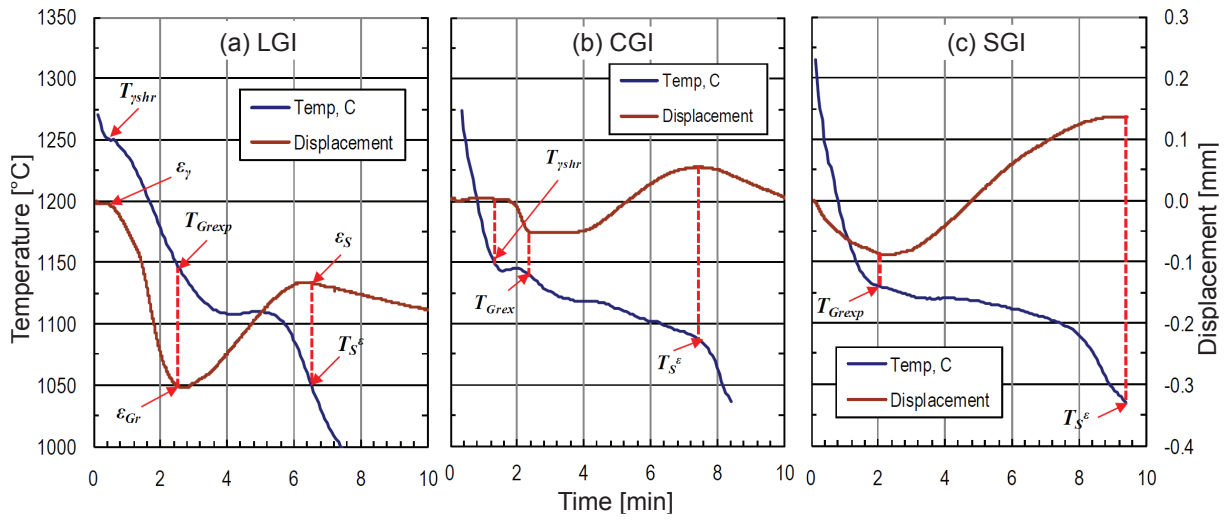
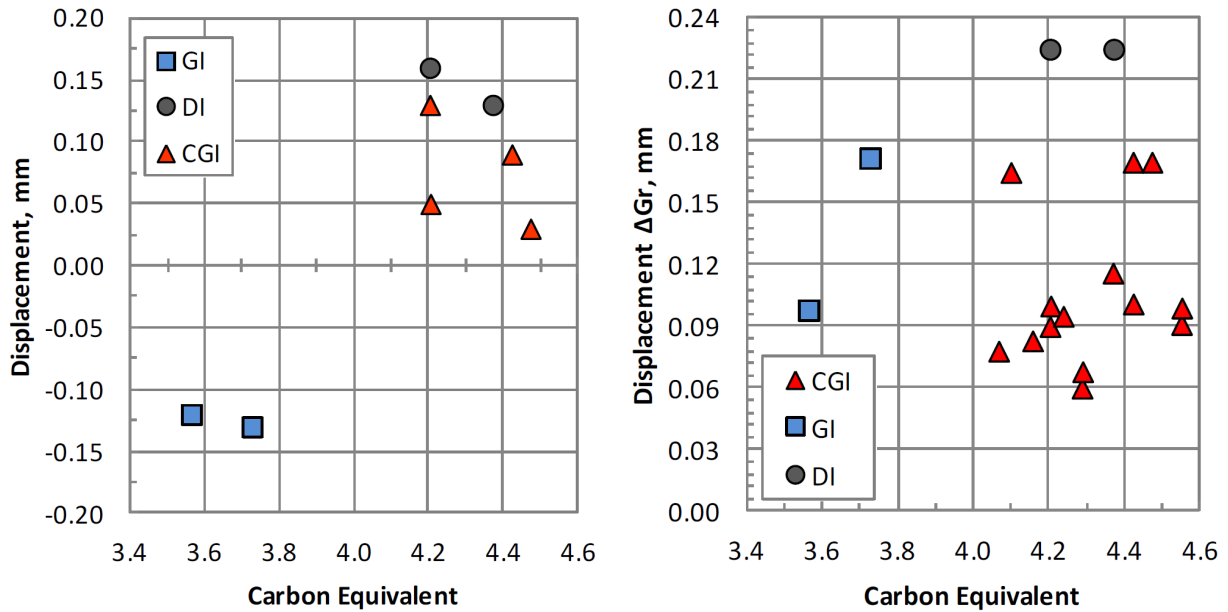


**Figure 3.11:** Comparison of displacement during solidification for different graphite morphologies as a function of time in a rigid mould.  $T_{\gamma shr}$  is the temperature at which austenite shrinkage starts,  $T_{Gr exp}$  is the temperature at which graphite expansion starts,  $T_S^e$  is the temperature at the end of solidification as indicated by the linear displacement analysis,  $\epsilon_{\gamma}$  is the displacement at the start of the austenite shrinkage,  $\epsilon_{Gr}$  is the displacement at the start of the graphite expansion, and  $\epsilon_S$  is the displacement at the end of solidification. Courtesy of Stefanescu et al [89].



(a) Total displacement, defined as the sum of austenite shrinkage ( $\Delta\gamma$ ) and graphite expansion ( $\Delta Gr$ ).

(b) Graphite expansion displacement, defined as the graphite expansion ( $\Delta Gr$ ) alone.

**Figure 3.12:** Comparison of displacement during solidification for different graphite morphologies as a function of CEV. Courtesy of Stefanescu et al [89].

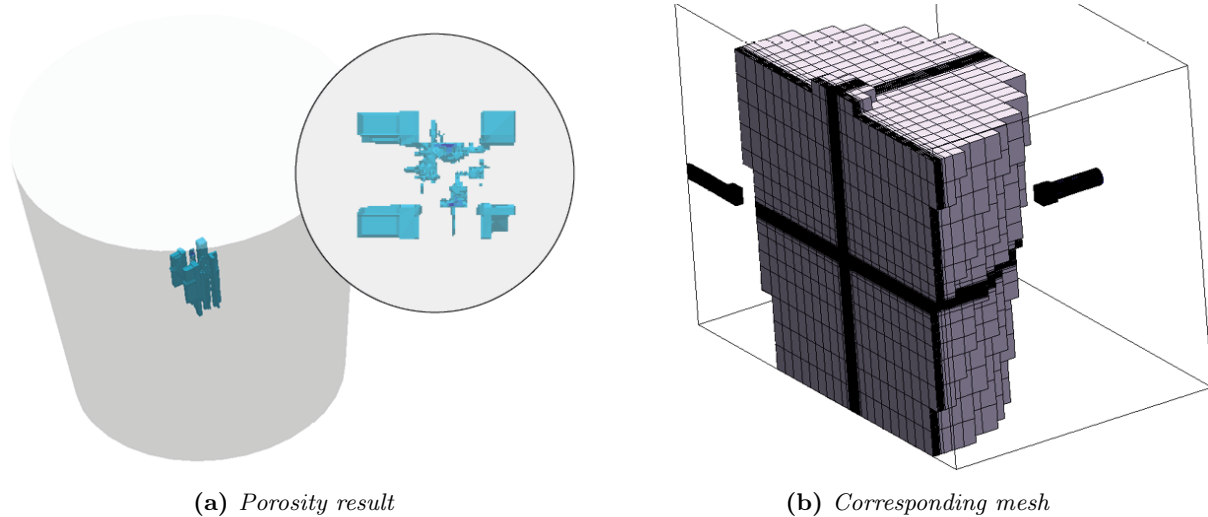


**Figure 3.13:** Porosities in small cast iron casting with varying mesh cell size showing the relation between mesh cell size and porosity threshold value. Courtesy of Vedel-Smith [92].

the melt around the porosities flow together thus pushing the voids in the melt together to larger entities. The melt flow in the casting is controlled by gravity and other factors influencing the internal pressure in the casting [69]:

- Primary Contraction
  - Liquid Contraction
  - Primary Austenite Contraction
- Secondary Contraction
  - Non-Interacting Growth of Graphite
  - Austenite at the End of Solidification
- Graphite Expansion
- Solidification Morphology
- Shell Forming, and
- External Pressure on the Solidifying Shell

MAGMASOFT can calculate the porosities in two different ways—as a final result after the end of the solidification simulation or progressively during the solidification simulation [69]. Both approaches make use of the same criterion function, however, for the progressive results to be calculated the required data have to be dumped from the simulation at regular intervals to be available for the post-processing of the results. While any casting manufacturer or casting buyer will only care about the porosities

present in the casting when it is fully solidified, it can be useful from an evaluation and development point of view to know-how and when the porosities develop within the casting. Especially for cast iron where porosities can first develop and grow, then diminish or disappear as the graphite expansion begins at the later stages of solidification.

### 3.4.3 Criteria Functions

In simulations, the material properties of castings—such as ultimate yield strength, mould erosion, hot and cold tearing, and porosity formation—are modelled using criteria functions [22, 70]. Criteria functions are in nature descriptions of process parameters that are expected to yield certain results, often defined as threshold values determining if the casting is sound or defect.

The first, and simplest, of these criteria functions was proposed by Bishop and Pellini in 1950 and simply described the correlation between the thermal gradient,  $G_s$ , and the formation of centreline porosities in steel castings [44, 93]. Bishop and Pellini defined a critical temperature gradient,  $G_{cr}$ , which the temperature gradient of the casting  $G_s$ , should be larger than to avoid porosities.

$$BP = G_s \gg G_{cr} \quad (3.17)$$

However, Bishop and Pellini’s criterion is both shape and size dependent, meaning that the critical

temperature gradient had to be established for each casting geometry [94].

Pellini's approach was improved in 1982 by Niyama et al who discovered that  $G_{cr}$  is proportional to  $1/\sqrt{\dot{T}_s}$  [95]:

$$\text{Niyama} = \frac{G_s}{\sqrt{\dot{T}_s}} \quad (3.18)$$

where  $\dot{T}_s$  is the cooling rate also at the solidus temperature. The Niyama criterion was later proved to be size-independent [22, 26, 70, 94], though the shape-dependence is still unresolved [22, 96].

A further development was made by Hansen and Sahm in 1988 whom included the flow velocity of the metal feeding through the solidifying dendrite structure,  $u$  [96]:

$$\text{HS} = \frac{G_s}{\sqrt{\dot{T}_s^{1/4} u^{1/2}}} \quad (3.19)$$

The HS criterion function has the significant advantage that it only requires one critical value for different geometries [22]. It has been shown to be size-independent and is also believed to be shape-independent [22]. At the same time, it is a weakness of the HS criterion function that it requires the knowledge of the feeding flow velocity through the dendritic structure. This information is difficult, at best, to obtain experimentally, but should today be part of what MAGMASOFT calculate as part of its feeding algorithm, though most likely through other empirically based macro models and not found in actual interdendritic flow simulation.

The flow velocity is related to the pressure drop experienced by the melt, as it has to feed through the interdendritic structure. Campbell derived function eq. (2.10) on page 32 to describe this phenomenon. His derivation is based on the work of Piwonka and Flemings, and address capillary flow [25]. For eutectic and hypereutectic cast irons it may be better to use Darcy's law of flow through a porous medium to describe the feeding flow, as these alloys do not form dendrites but solidify as a grainy structure [68, 70]:

$$\frac{dp}{dx} = \frac{\mu(1-f_s)}{K} v \quad (3.20)$$

where  $dp/dx$  is the incremental pressure change per distance,  $\mu$  is the viscosity of the liquid metal,  $f_s$  is the fraction of solid,  $K$  is the permeability of the porous region being fed, and  $v$  is the velocity of the

liquid metal. Note that  $v$  is equal to  $u$  in eq. (3.19), thus Darcy's law can be used to find the feeding velocity required for the HS criterion function.

The independence of shape and scale is important for the universality of the criteria functions. Hansen et al made a review of the most common criteria functions and determined their independence of both shape and size respectively [22], which has also been elaborated by Hattel et al [70]. Hansen et al define the following equation for evaluating the dependence of a range of different criteria functions:

$$\text{Crit} = \text{Crit}_0 N^m \quad (3.21)$$

where  $\text{Crit}$  is the criterion number,  $N$  is the linear scale factor, and  $m$  is an exponent. Thus, all criteria functions that have  $m = 0$  scale linearly and can be said to be independent of size. Hansen et al used this method to evaluate a range of criteria function [70]:

**Size-Independent** Niyama [95], HS criterion [96], and Xue [97]

**Size-Dependent** LLC criterion (Lee, Chang, and Chieu) [98], GAP criterion (Gradient Acceleration Parameter) [99], Flender's hot tearing criterion [22], and Chvorinov's rule [37]

Note that Chvorinov's rule, as described in section 2.3.2, on page 20, is neither shape-, nor size-independent. The scaling evaluation using eq. (3.21) show, however, that Chvorinov's rule, eq. (2.4) on page 20, has an exponent value of  $m = 2$ . This means that by doubling the dimensions of a casting geometry, the solidification time,  $t_s$ , will increase four times [70]. This corresponds directly to Chvorinov's own revision of his rule in 1963 [21, 22]:

$$t_s = (t_s)_0 N^2 \quad (3.22)$$

where  $N$  is the same linear scaling factor as used by Hansen et al in eq. (3.21) [22].

Also the Niyama criterion, eq. (3.18), has been presented in a dimensionless form. Carlson and Beckermann derived the dimensionless Niyama criterion based on Darcy's law [100]:

$$\text{Ny}^* = \frac{G\lambda_2\sqrt{\Delta P_{cr}}}{\sqrt{\mu_l\beta\Delta T_f\dot{T}}} \quad (3.23)$$

where  $G$  is the temperature gradient,  $\lambda_2$  is the Secondary Dendrite Arm Spacing (SDAS),  $\Delta P_{cr}$

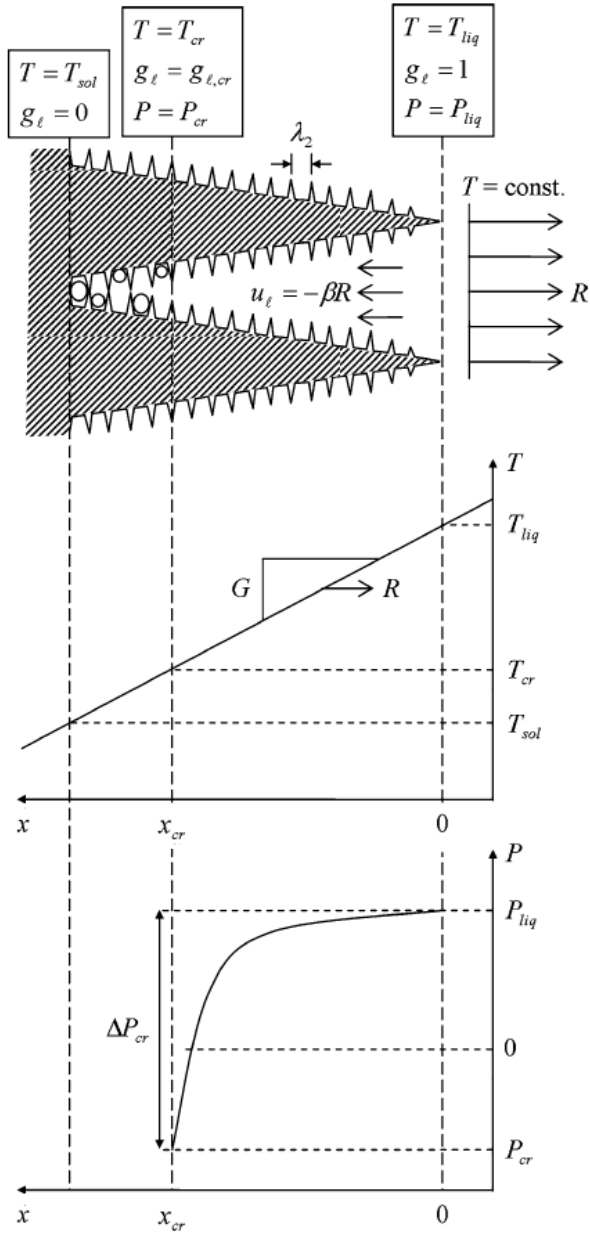


**Figure 3.14:** Illustration of the 1-dimensional mushy zone solidification with constant temperature gradient,  $G$ , and isotherm velocity  $R$ .  $T_{sol}$  and  $T_{liq}$  is the solidus and liquidus temperature,  $T_{cr}$  is the critical temperature  $g_l$  is the volume fraction of liquid and  $g_{l,cr}$  is the critical fraction liquid,  $P_{liq}$  and  $P_{cr}$  is the liquid and critical pressures respectively,  $x_{cr}$  is the critical spatial distance,  $\lambda_2$  is the SDAS,  $u_l$  is the liquid velocity in the mushy zone, and  $\beta$  is the total solidification shrinkage. Courtesy of Carlson and Beckermann [100].

is the critical pressure drop ( $\Delta P_{cr} = P_{liq} - P_{cr}$ ),  $\mu_l$  is the dynamic viscosity of the liquid,  $\beta$  is the

total solidification shrinkage ( $\beta = \rho_s - \rho_l / \rho_l$ )—with  $\rho_l$  and  $\rho_s$  being the density of the liquid and the solid respectively,  $\Delta T_f$  is the alloy's freezing range ( $\Delta T_f = T_{liq} - T_{sol}$ ), and  $\dot{T}$  is the temperature increment ( $\dot{T} = dT/dt$ ). See fig. 3.14.

Additionally, Carlson and Beckermann also show that for different criterion values it is valid for not only steel, but also for Al, Mg, and Ni alloys [100].

The Niyama criterion, dimensionless or not, is, however, not well suited to describing porosity formation in cast iron. Cast iron, unlike the above-mentioned alloys, does not solidify exogenously, and eutectic and hypereutectic irons do not form dendrites. While cast irons of both hypoeutectic, eutectic, and hypereutectic compositions form mushy zones that require feeding, the different flow properties, thermal gradients, and the graphite expansion are significantly different from eg steel or Al alloys.

Tavakoli defines that the criteria functions must be modelled at the same spatial scale as phenomena they are meant to describe [94]. Hence, macro porosities should be modelled using macro models, and micro porosities using micro models respectively. At the same time, Tavakoli also stresses that alloy solidification is a multiscale phenomenon that involves both macro, meso, micro, atomic, and sub-atomic (electronic) scales [94].

While a wide range of different criteria functions have been developed since Bishop and Pellini introduced their temperature gradient criterion, a large part of these functions are defined based on the same basic parameters: Temperature gradient,  $G_s$ , square root of cooling rate,  $\sqrt{\dot{T}}$ , feeding velocity,  $u$  or  $v$ , and solidification speed,  $V_s$  [70]. Thus, while the porosity criterion function for cast iron in MAGMASOFT is not based on the Niyama criterion, it may be based on a modified version of the HS criterion function or another function using the same (but not limited to) criteria parameters as the more basic functions presented here. Here it should also be noted that the porosity predictions in MAGMASOFT, as with most other criteria functions, indicate a *probability* for porosities in a given area, *not a certainty* [69].

### 3.4.4 Feeding Algorithms

For the iron module MAGMASOFT offers two different algorithms for calculating feeding—‘Standard’ and ‘Extended’—where the extended option is the default [69]. The extended feeding algorithm considers the porosity formation factors listed in the



previous section. The standard feeding algorithm is presumably based on more straightforward criteria functions focusing on thermal gradients and fraction solid.

The feeding algorithms determine the movement of feed material within the casting. Hence, the algorithms change how MAGMASOFT calculate the transport of melt within the feeders and the casting during solidification. While the standard approach for generating the porosity result is after the end of the solidification simulation, the feeding algorithms are active during models running as part of each time step in the solidification simulation.

An essential parameter for the feeding flow is the ‘Feeding Effectivity’, which defines the threshold for when it is no longer possible to feed through a section that has solidified a given percentage [69]. The feeding effectivity is a material property defined as a value between 0% to 100%, where 0% is no feedability, and 100% is full feedability, meaning that it is possible to feed through the material until it is completely solidified.

For cast iron the feeding effectivity must be set to 100% [69]. The reason for this is that the iron module calculates the feeding efficiency for the material based on the nucleation modelling, hence a user-defined feeding efficiency of less than 100% will influence this calculation in an unintended way. The feeding effectivity also defines the following solidification criteria [69]:

- FSTime
- Hot Spot FSTime
- Porosity
- Soundness

MAGMASOFT also offers a feature called ‘Active Feeding’, which allow the user to define externally applied pressure within the feeders. This feature, though, is not available for with MAGMAiron at present [69].

### 3.4.5 Feeders

MAGMASOFT request that the user defines the individual parts of the casting; pouring cup, runner, gating, feeder, feeder neck, feeder sleeve, etc. MAGMASOFT, however, does not specify for what purpose these parts need to be defined. With respect to the feeders, it was previously the case that the feeder neck was used to control the melt flow between the

feeder and the casting, and that the flow was only allowed to pass from the feeder into casting, and not from the casting and into the feeder. This scenario seems a reasonable simplification for most feeder applications in most alloys; however, for cast iron, the variation in displacement shown in figs. 3.10 and 3.12 on page 52 and on page 53 challenge this assumption, and MAGMASOFT now allow for the melt flow to pass both ways through the feeder neck.

The material properties characterise the feeder sleeves. For the commercial sleeves provided via the FOSECO Pro Module, these material data are disclosed. However, for the insulating sleeves this is handled via the thermal conductivity,  $\lambda$ , and the specific heat capacity,  $C_p$ , with the thermal conductivity as the governing parameter defining the insulating power of the material.

The thermal conductivity and the specific heat capacity is also of importance for the exothermic sleeves. The exothermic sleeves, however, display a release of chemical potential that will reheat the melt and keep it heated for an extended period. It is not known if this behaviour is modelled via the same material parameters as are available for other materials, however, if it is, this is likely done via the specific heat content,  $\rho C_p$ . In MAGMASOFT the specific heat content is more than just the product of the density,  $\rho$ , and the specific heat capacity,  $C_p$  [69]. The release of latent heat,  $\Delta h$ , is incorporated into the parameter as a function of the temperature,  $T$ , and the fraction solid curve,  $f_s$ :

$$\text{Rho} * C_p = \rho C_p + \left| \Delta h \frac{df_s}{dT} \right| \quad (3.24)$$

Hence, the definition of latent heat can be used to define a heat release from the material at a given temperature. It is possible to determine the initial temperature of the sleeve material, and this is often set to 20 °C. Thus, use of the specific heat content requires some special adaptation that does not require the same amount of energy to be put into the sleeve material during heating, as is released afterwards.

Another aspect is the way in which the latent heat is released. Physically the exothermic material will ignite from the centre and outwards, hence the heat release and temperature will rise as the process progresses. Similarly, some locations will burn out before others depending on the order of ignition and access to O, resulting in a fading heat release towards the end. For the simulation of exothermic feeder

sleeves, Sutaria and Ravi assume the exothermic material to be a perfect heat source—meaning a uniform heat release throughout the combustion [101].

Besides the parameters mentioned above, the HTC is also a parameter of some importance. As the standard for both exothermic and insulating sleeves the HTC, between the melt and the sleeve, is handled by the temperature dependent HTC (TempIron). Meanwhile the HTC between the sleeve, the sand mould, and breaker core respectively is controlled by a constant HTC of  $800 \text{ W/m}^2\text{K}$  [69].

The pre-defined feeder sleeves and breaker cores in the FOSECO Pro Module are locked macros where the subentries cannot be edited or scaled. Likewise, no stress data are defined in the FOSECO Pro Module. Thus, the filters, sleeves, and breaker cores in this database cannot partake in stress calculations [69].

The potential reheating of the melt also raise the question of remelting. It is perceivable that a feeder with a smaller melt volume may cool and form a solid shell before the heating of the exothermic feeder sleeve reaches the temperature at which the material is ignited. In this case, the heat from the exothermic sleeve will initially remelt the solidified shell before it can heat the remaining melt in the feeder. It is unclear if the macro model supports remelting, and if it does, then if the nucleation model would provide a different result for the second nucleation. It is likely, however, that this scenario is eliminated by defining the ignition temperature of the exothermic material above the liquidus temperature of the alloy type that the feeder is designed to be used with.

### 3.4.6 Feeding

So in relation to the previous sections, what is feeding in the sense of numerical simulations? It is *just* a calculation of the defined boundary conditions. The calculation is based on different parameters and criteria functions; however, MAGMASOFT is not moving any melt around as a part of a feeding micro-model. The simulation setup—material properties, geometry, pouring temperature, alloy composition, filling, etc.—describe the casting process including the feeding regime. As with real castings, the virtual castings of numerical simulations are made porosity-free by adjusting the parameters as described in the feeding review in chapter 2, on page 13.

## 3.5 Stress and Deformation

**M**ATHEMATICAL modelling of stress and strain in casting processes is not a simple matter. It involves a series of different phenomena, including; solidification, phase transformations, shrinkage-dependent interfacial heat transfer, mould distortion, temperature and time-dependent plasticity, hydrostatic pressure from the liquid, and potential crack formation [70]. The coupled 3-dimensional thermomechanical analysis have to determine which of these matter for the situation at hand, and how to implement these phenomena to accurately describe the stress/strain-development in the casting. The stress/strain analysis implemented in MAGMASOFT is a so-called semi-coupled analysis as the thermal analysis is performed first, as part of the solidification simulations, as this information is subsequently used for the mechanical stress/strain analysis [70].

For castings, the stresses originate from the thermal history of the casting and the constraints of the mould. The stresses induced by thermal changes in the material is called *thermal stresses* [70], and is closely coupled with the casting geometry and the constraints enforced by the mould. This correlation between casting geometry and mould constraint is shown in fig. 3.15 on the facing page. As illustrated, the more constrained the casting is, the less it will contract, consequently increasing the stresses within the casting. However, this contraction is not linear over the entire temperature range, as the solid-state phase transformations act as stress relief but also a significant volume change. See fig. 3.16 on the next page.

A constraint preventing free contraction of the casting will introduce strain,  $\varepsilon$ , into the casting. Note that the thermal strain,  $\varepsilon^{Th}$ , cannot produce stress by itself, but only in combination with some kind of constraint resulting in elastic strain,  $\varepsilon^{El}$ . The relationship describing the total strain,  $\varepsilon^{Tot}$ , is defined as [70]:

$$\varepsilon^{Tot} = \varepsilon^{El} + \varepsilon^{Th} \quad (3.25)$$

Thermal contraction can, based on eq. (3.25), yield three types of outcome; (1) deformation only (free contraction:  $\varepsilon^{El} = 0$ ), (2) stress only (totally restrained:  $\varepsilon^{Tot} = 0$ ), or (3) a combination of the previous two. Case number three is almost always the outcome in reality. Case one does not produce any stress as the material elastically yields to the thermal strain. In case two, however, the material

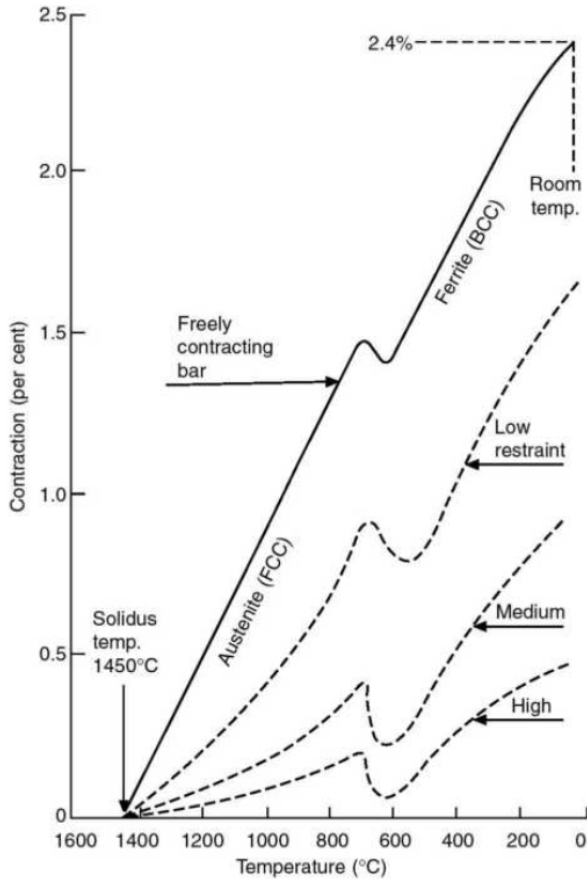


**Figure 3.16:** Influence of different degrees of constraints on contraction at different temperatures. Here for a steel casting in a green sand mould. Courtesy of Campbell et al [25].

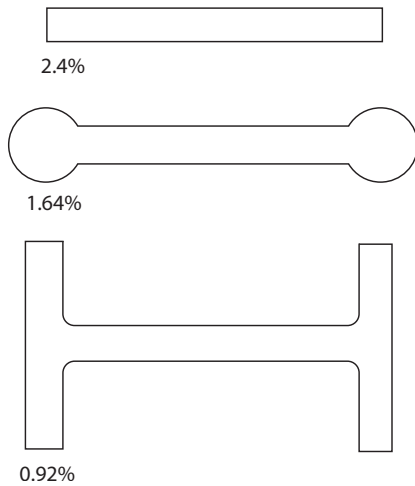


**Figure 3.15:** Influence of casting geometry and mould constraint on contraction. Courtesy of Campbell et al [25].

holds firm by matching the thermal strain with an equal amount of stress. Or more precisely, the thermal load promote elastic strain which in turn causes the stress in the material [70].

As shown in section 3.4.1, on page 51 there exist a direct correlation between temperature and expansion. This volume change is the basis for strain to arise in the first place, and can be expressed as [70]:

$$\varepsilon^{Th} = \alpha_L \Delta T \quad (3.26)$$

where  $\varepsilon^{Th}$  is the thermal strain,  $\Delta T$  is the temperature interval, and  $\alpha_L$  is the linear thermal expansion coefficient for  $\Delta T$ .  $\alpha_L$  is the 1-dimensional equivalent of  $\alpha_V$  expressed in eq. (3.14) on page 51. Equation (3.26) is valid for a constant  $\alpha_L$ .

The direct correlation between thermal expansion and thermal strain is unsurprising as strain can be defined as the relative elongation (or displacement in the 3-dimensional implementation). This can be expressed as [70]:

$$\varepsilon = \frac{\Delta L}{L} \quad (3.27)$$

where strain,  $\varepsilon$ , is defined by the original length of the object,  $L$ , and the change in length,  $\Delta L$ , which again can be described as the slope of a line defined by the length along one axis,  $x$ , and the change in length along another axis,  $u$ :

$$\varepsilon = \frac{\partial u}{\partial x} \quad (3.28)$$

where the partial definition is used to describe the time-dependent increment.

When a material is under strain it can respond either by deforming (potentially breaking) or by a corresponding but opposing stress,  $\sigma$ . Stress can be seen as a force acting on the cross-sectional area, balancing out the strain the material is exposed to:

$$\sigma = \frac{F}{A} \quad (3.29)$$

Having defined stress as force per area,  $\sigma = F/A$ , the force,  $F$ , can be defined by Hook's law:

$$F = k\Delta x \quad (3.30)$$

where  $F$  is the external force (opposite of the spring force),  $k$  is the spring constant, and  $\Delta x$  is the elongation of the material. An elastic strain is defined

by the materials ability to totally recover when unloaded, combining eq. (3.30) on page 59 with eq. (3.29) on page 59, stress can be redefined as [70]:

$$\sigma = E\varepsilon^{El} \quad (3.31)$$

where  $E$  is Young's modulus of elasticity which describe the relationship between stress and strain;  $E = \sigma/\varepsilon$ .

Combining eq. (3.31) with eq. (3.28) on page 59 and eq. (3.29) on page 59 yields:

$$F = EA \frac{\partial u}{\partial x} \quad (3.32)$$

which yield the force,  $F$ , that corresponds to  $E$  of the given material, and the cross-sectional area,  $A$ , of the geometry for a partial increment. In correlation with Newton's second law of mechanics for a stationary body,  $\sum F = 0$ , eq. (3.32) yields the necessary force exerted on the body to deform it corresponding to  $\partial x$ . Reversely this is the same force the mould needs to exert on the casting body to prevent a deformation of  $\partial x$ .

### 3.5.1 Irreversible Deformations

While the mechanisms described above may yield linear deformations, these deformations are per definition reversible. At low temperatures, the linear relationship and deformation reversibility is a good approximation of most metals stress/strain behaviour. These assumptions, however, are not valid for high stress levels or elevated temperatures [70], where the material behaviour become inelastic.

All materials have a limit at which they yield when subjected to a sufficient amount of stress. This limit is called yield stress,  $\sigma_\gamma$ , and denote the shift from the elastic strain,  $\varepsilon^{El}$ , (reversible), to plastic strain,  $\varepsilon^{Pl}$ , (irreversible). How a material behaves when loaded beyond its yield stress is very material dependent, but the elasto-plastic behaviour is also strongly dependent on the temperature.

Assuming ideal plasticity—meaning that the yield stress,  $\sigma_\gamma$ , is constant for all strain values,  $\varepsilon$ —mechanical strain,  $\varepsilon^{Mech}$  can be defined as the sum of elastic and plastic strain:  $\varepsilon^{Mech} = \varepsilon^{El} + \varepsilon^{Pl}$ . Combined with eq. (3.25) on page 58 this yields:

$$\varepsilon^{Tot} = \varepsilon^{El} + \varepsilon^{Pl} + \varepsilon^{Th} \quad (3.33)$$

In metals, the material properties are related to the microstructure, grain boundaries, and dislocations in the material [32]. When the material is

strained, the grain boundaries will reposition until the vacancies capture the dislocations in the lattice structure, thus reducing the material's plasticity in turn for deformation or elasticity (strain hardening).

For casting processes, the thermal history of the casting significantly influence the stress/strain development and the resulting deformations. At increased temperatures the material is softened, and reversely it is hardened at decreased temperatures. Thus, the yield stress needs to be defined as a function of both temperature and plasticity,  $\sigma(T, \varepsilon^{Pl})$ , to adequately describe thermal deformation for irreversible loads at elevated temperatures [70]:

$$\dot{\sigma}_\gamma = \frac{\partial \sigma_\gamma}{\partial T} \dot{T} + \frac{E E_T}{E - E_T} \dot{\varepsilon}^{Pl} \quad (3.34)$$

where  $\dot{\sigma}_\gamma$  is the yield stress increment,  $\dot{T}$  is the temperature increment,  $E$  is the Young's modulus of elasticity,  $E_T$  is the tangent modulus of mechanical strain, and  $\dot{\varepsilon}^{Pl}$  is the plastic strain increment. The dot denotes an increment and is understood as differentiation with respect to a monotonically increasing parameter. The tangent modulus,  $E_T$ , is defined as:

$$E_T = \frac{d\sigma}{d\varepsilon^{Mech}} \quad (3.35)$$

Equation (3.34) shows that when only the temperature is varying, then the stress will remain the same, while the casting will deform as a consequence of thermal expansion (or contraction) and plastic deformation. Equation (3.34) also yields that there must be a balance between the temperature,  $T$ , and the plastic strain,  $\varepsilon^{Pl}$  [70]:

$$\dot{\varepsilon}^{Pl} = \frac{E_T - E}{E E_T} \frac{\partial \sigma_\gamma}{\partial T} \dot{T} \quad (3.36)$$

when the yield stress increment,  $\dot{\sigma}_\gamma$ , is set as zero.

Equation (3.36) yields additional information about the thermo-elasto-plastic deformation of castings [70]: (1) as the tangent modulus,  $E_T$ , is smaller than Young's modulus,  $E$ , the yield stress decreases with increasing temperature, and (2) the mechanical strain increment,  $\dot{\varepsilon}^{Mech}$ , and the plastic strain increment,  $\dot{\varepsilon}^{Pl}$  are equal to the elastic strain increment,  $\dot{\varepsilon}^{El}$ , is zero (assuming that Young's modulus,  $E$ , is equal for both temperature states).

Note that, while thermoplastic mechanisms dominate some thermomechanical problems, thermoelastic properties (eg Young's modulus,  $E$ , and the thermal expansion coefficient,  $\alpha$ ) cannot be neglected as they also significantly influence the result [70].

### 3.5.2 Phase Transformations

The solutions so far all address the stress/strain development in the solid; however, castings undergo at least one, and often multiple, phase transformation on the road from liquid to room temperature. While it is beyond the scope of this text to derive the mathematics behind calculating stresses in a solidifying slab, it should be noted that this theorem exists and is used in numerical simulations [70]. Stress can only be analysed in the solidified material as the liquid cannot resist deformation and hence cannot develop stress or strain. Including the mould that contains the melt, the system comprises three zones (plastic, elastic, and plastic), where the two boundaries in-between are non-stationary.

For cast iron, the stresses developed during the solidification are partially erased by the eutectoid transformation. However, the eutectoid phase transformation introduces new stresses into the casting. Furthermore, the thermal gradients developed by the phase transformations also influence the stress creation.

Denis et al has described the correlation of physical phenomena and the strain development for carbon steel [102]. While some of the strain mechanisms are known from basic stress/strain descriptions as related in the previous section, Denis et al had to expand on eq. (3.37) to adequately describe the total strain,  $\varepsilon^{Tot}$ , for solid state phase transformations [102]:

$$\varepsilon^{Tot} = \varepsilon^{El} + \varepsilon^{Pl} + \varepsilon^{Th} + \varepsilon^{Tr} + \varepsilon^{Tp} \quad (3.37)$$

where  $\varepsilon^{El}$  is the elastic strain,  $\varepsilon^{Pl}$  is the plastic strain, and  $\varepsilon^{Th}$  is the thermal strain which is described above. The new terms are  $\varepsilon^{Tr}$  which is transformation strain, and  $\varepsilon^{Tp}$  which is the transformation plasticity strain.

### 3.5.3 Dimensional Accuracy

The result of the deformation mechanisms described in the previous sections all come together, with the sum of the stress and strain resulting in the casting deformations seen at room temperature. The difference between the pattern and the casting at ambient temperature, except the expected linear pattern makers shrinkage, can be difficult, but vital to predict. Such prediction allows changes to the pattern; compensating for the deformations to reduce machining allowance and reducing costs. Addressing machining allowance by changing the pat-

tern to accommodate for deformations is, however, not new idea.

Working with grey cast iron and steel, Jackson [103] showed why casting precision was more than just a distance between a finite number of working faces, but more importantly also a concern with regards to eliminating excess machining and grinding. Jackson's paper also discussed the influence of alloy composition, casting geometry, and thermal gradients on the dimensional variation of the castings. Demonstrating that free linear contraction was inversely related to the section modulus, Mkumbo et al [104] also reported a correlation between the modulus and shape of the casting and modelled how flanges affected this. Likewise, Motoyama et al [105] examined the effect of flanges and showed how residual stress and distortion develop during solidification and cooling of the casting, and that these were affected by the casting geometry and the strength of the sand mould.

The idea of counteracting distortion by modifying the pattern geometry was suggested by Kang et al [106] who also proposed machining allowance as a parameter for distortion reduction. This preemptive approach requires precise measurements and an understanding of the casting's dimensional change and surface finish. As part of the development of a better model for a sand surface element, Chang and Dantzig [107] described how the green sand mould itself was deformed by the contraction of the casting, and how that left the casting unconstrained by the mould. Subsequently, Nwaogu et al [108] described how to characterise the surface of ductile iron castings, and provide some guidance as to which types and sizes of surface roughness can be expected with and without coating.

Mkumbo et al [104] also showed that ductile iron, even with a higher CEV, displayed greater contraction than grey iron, and variations in dimensional change between pearlitic and ferritic alloys were demonstrated by Sosa et al [109]. They worked with Austempered Ductile Iron (ADI) to show that a ferritic microstructure displayed greater dimensional stability than a pearlitic microstructure and that a pearlitic-ferritic structure was even more prone to dimensional change.

## References

- [6] Jakob Olofsson. *Simulation of Microstructure-based Mechanical Behaviour of Cast Components*. School of

- Engineering, Jönköping University, 2014. ISBN: 978-91-87289-04-0.
- [20] Petr Kotas. *Integrated Modeling of Process, Structures and Performance in Cast Parts*. DTU Mechanical Engineering, 2011. ISBN: 978-87-90416-54-6.
- [21] N Chvorinov. “Solving Feeders and Sink-heads”. In: *Proceedings of the 30th International Foundry Congress*. 1963.
- [22] PN Hansen, PR Sahn and E Flender. “How to Select and Use Criterion Functions in Solidification Simulation”. In: *Transactions of the American Foundrymen’s Society*. 101 (1993), pp. 443–446.
- [24] John Campbell. *Casting Practice - The 10 Rules of Casting*. Linacre House, Jordan Hill, Oxford OX2 8DP, 30 Corporate Drive, Burlington, MA 01803: Elsevier Butterworth-Heinemann, 2004. ISBN: 0 7506 4791 4.
- [25] John Campbell. *Castings, 2nd Ed*. Linacre House, Jordan Hill, Oxford OX2 8DP, 30 Corporate Drive, Burlington, MA 01803: Elsevier Butterworth-Heinemann, 2003. ISBN: 0 7506 4790 6.
- [26] DM Stefanescu. “Computer Simulation of Shrinkage Related Defects in Metal Castings—A Review”. In: *International Journal of Cast Metals Research* 18.3 (2005), pp. 129–143.
- [32] David A. Porter, Kenneth E. Easterling and Mohamed Y. Sherif. *Phase Transformations in Metals and Alloys*. 3rd ed. CRC Press, Taylor & Francis Group, 6000 Broken Sound Parkway NW, Suite 300, Boca Raton, FL 33487-2742, 2009. ISBN: 978-1-4200-6210-6.
- [37] Nicolas Chvorinov. “Theory of the Solidification of Castings”. In: *Giesserei* 27 (1940), pp. 177–186.
- [44] W.S. Pellini. “Factors Influencing Riser Range and Feeding Adequacy—Part II”. In: *American Foundryman*. (1953), 62–71.
- [53] G. Alonso. et al. “Kinetics of Graphite Expansion during Eutectic Solidification of Cast Iron”. In: *International Journal of Cast Metals Research* 27.2 (2014), 87–100. ISSN: 1364-0461. DOI: {10 . 1179 / 1743133613Y . 0000000085}.
- [56] G. Alonso et al. “Kinetics of Graphite Expansion during eutectic Solidification of Lamellar and Spheroidal Graphite Iron”. In: *AFS Proceedings 2014*. AFS Conference. Schaumburg, IL, USA. American Foundry Society. 2014, 1–12.
- [64] Krzysztof Jakub Fidkowski. *A Simplex Cut-Cell Adaptive Method for High-Order Discretizations of the Compressible Navier-Stokes Equations*. Massachusetts Institute of Technology, Department of Aeronautics and Astronautics, 2007.
- [65] *Die Rechenmaschine des Johann Helfrich Müller aus Darmstadt*. <http://www.fbi.fh-darmstadt.de/fileadmin/vmi/darmstadt/objekte/rechenmaschinen/mueller/index.htm>. History.
- [66] *The Analytical and Difference Engines*. <http://www.computerhistory.org/babbage/>. History.
- [67] Alan Mathison Turing. “On computable numbers, with an application to the Entscheidungsproblem”. In: *J. of Math* 58.345-363 (1936), p. 5.
- [68] Jonathan A Dantzig and Michel Rappaz. *Solidification*. EPFL press, 2009.
- [69] *MAGMASOFT 5.2 by MAGMA GmbH*. [http://www.magmasoft.com/en/solutions/MAGMA\\_5.html](http://www.magmasoft.com/en/solutions/MAGMA_5.html). Program. 2014.
- [70] Jesper Henri Hattel et al. *Fundamentals of Numerical Modelling of Casting Processes*. Polyteknisk Forlag, 2005. ISBN: 978-87-502-0969-0.
- [71] Richard Aagaard. *Ductile Iron—Solidification Shrinkage Simulation*. DTU, Institute of Manufacturing Engineering, 1997.
- [72] *Autodesk Inc., Finite Element vs Finite Volume*. <http://knowledge.autodesk.com/support/cfd/learn-explore/caas/CloudHelp/cloudhelp/2015/ENU/SimCFD-Learning/files/GUID-12A9AED8-2047-4D3A-BC80-82BE9CF47517-htm.html>.
- [73] CG Mingham and DM Causon. “High-Resolution Finite-Volume Method for Shallow Eater Flows”. In: *Journal of Hydraulic Engineering* 124.6 (1998), pp. 605–614.

- [74] David M Ingram, Derek M Causon and Clive G Mingham. “Developments in Cartesian Cut Cell Methods”. In: *Mathematics and Computers in Simulation* 61.3 (2003), pp. 561–572.
- [75] Richard Aagaard et al. “Simulation vs. Reality of an Industrial Ductile Iron Casting”. In: *Transactions of the American Foundrymen’s Society* 104 (1996), pp. 659–667.
- [76] M. Lipinski, W. Schaefer and S. Andersen. “Modeling of Combined heat and Fluid Flow for Determination of Filling Sequence for Real Complex shaped Castings”. In: *Modeling of casting, welding and advanced solidification processes. TMS, Warrendale, PA* (1991), pp. 185–211.
- [77] D.M. Lipinski, W. Schaefer and E. Flender. “Numerical Modelling of the Filling Sequence and Solidification of Castings”. In: *The Minerals, Metals & Materials Society(USA)*, (1993), pp. 389–396.
- [78] *Scheil or Lever Rule*. Presentation by Markus Rettenmayr, Friedrich-Schiller-University Jena, Institute of Materials Science and Technology. 2008.
- [79] MAGMASOFT 5.3 by MAGMA GmbH. [http://www.magmasoft.com/en/solutions/MAGMA\\_5.html](http://www.magmasoft.com/en/solutions/MAGMA_5.html). Program. 2015.
- [80] G Lesoult, M Castro and J Lacaze. “Solidification of Spheroidal Graphite Cast Irons—I. Physical Modelling”. In: *Acta materialia* 46.3 (1998), pp. 983–995.
- [81] W Oldfield. “A Quantitative Approach to Casting Solidification: Freezing of Cast Iron”. In: (1966).
- [82] Karl Martin Pedersen and Niels Tiedje. “Nucleation and Solidification of Thin Walled Ductile Iron—Experiments and Numerical Simulation”. In: *Materials Science and Engineering: A* 413 (2005), pp. 358–362.
- [83] K.M. Pedersen and N.S. Tiedje. “Undercooling and Nodule Count in Thin Walled Ductile Iron Castings”. In: *International Journal of Cast Metals Research* 20.3 (2007). 5th Decennial International Conference on Solidification Processing, University of Sheffield, Sheffield, England, Jul. 23-25, 2007, 145–150. ISSN: 1364-0461. DOI: {10.1179/136404607X239816}.
- [84] Roy Elliott. *Cast Iron Technology*. Butterworth-Heinemann, 1988.
- [85] S E Wetterfall, H Fredriksson and M Hillert. “Solidification Process of Nodular Cast Iron”. In: *Journal of the Iron and Steel Institute* 210.5 (1972), pp. 323–333.
- [86] J Lacaze, M Castro and G Lesoult. “Solidification of Spheroidal Graphite Cast Irons—II. Numerical Simulation”. In: *Acta materialia* 46.3 (1998), pp. 997–1010.
- [87] J Lacaze. “Solidification of Spheroidal Graphite Cast Irons—III. Microsegregation Related Effects”. In: *Acta materialia* 47.14 (1999), pp. 3779–3792.
- [88] Karl Martin Pedersen. *Simulation and Microstructure of Thin Walled Ductile Cast Iron*. DTU Mechanical Engineering, 2006. ISBN: 87-91035-42-2.
- [89] DM Stefanescu et al. “Use of Combined Liquid Displacement and Cooling Curve Analysis in Understanding the Solidification of Cast Iron”. In: *Transactions of the American Foundrymen’s Society* 120 (2012), pp. 365–374.
- [90] G. Alonso. et al. “Understanding Graphite Expansion During the Eutectic Solidification of Cast Iron Through Combined Linear Displacement and Thermal Analysis”. In: *International Foundry Research* 66.4 (2014), 2–12.
- [91] Doru M Stefanescu. “Solidification and Modeling of Cast Iron—A Short History of the Defining Moments”. In: *Materials Science and Engineering: A* 413 (2005), pp. 322–333.
- [92] Nikolaj Kjelgaard Vedel-Smith. “Obtaining Comparable Simulation and Thermal Measurement Results in Sand Moulds”. In: Presented at the Nordic MAGMASOFT User Meeting , Svedala, Sweden, 2012.
- [93] H.F. Bishop and W.S. Pellini. “The Contribution of Risers and Chill-Edge Effects to Soundness of Cast Steel Plates”. In: *AFS Transactions* 58 (1950), pp. 185–197.
- [94] Rouhollah Tavakoli. “On the Prediction of Shrinkage Defects by Thermal Criterion Functions”. In: *The International Journal of Advanced Manufacturing Technology* 74.1-4 (2014), pp. 569–579.

- [95] E Niyama et al. “A Method of Shrinkage Prediction and its Application to Steel Casting Practice”. In: *Int. Cast Met. J.* 7.3 (1982), pp. 52–63.
- [96] PN Hansen and PR Sahm. “How to Model and Simulate the Feeding Process in Casting to Predict Shrinkage and Porosity Formation”. In: *Modeling and Control of Casting and Welding Processes. IV* (1988), pp. 33–42.
- [97] X. Xue. *M.Sc. Thesis from Shenyang Research Institute of Foundry, Shenyang, China.* Shenyang Research Institute of Foundry, Shenyang, China, 1985.
- [98] YW Lee, E Chang and CF Chieu. “Modeling of Feeding Behavior of Solidifying Al-7Si-0.3 Mg Alloy Plate Casting”. In: *Metallurgical transactions B* 21.4 (1990), pp. 715–722.
- [99] RM Pillai, V Panchanathen and UD Mallya. “Chilled Influence on Feeder Dimensions of Long-Freezing-Range Aluminum Alloys”. In: *AFS Trans* 86 (1978), pp. 103–112.
- [100] Kent D Carlson and Christoph Beckermann. “Prediction of Shrinkage Pore Volume Fraction Using a Dimensionless Niyama Criterion”. In: *Metallurgical and Materials Transactions A* 40.1 (2009), pp. 163–175.
- [101] Mayur Sutaria and B Ravi. “Computation of Casting Solidification Feed-Paths using Gradient Vector Method with Various Boundary Conditions”. In: *The International Journal of Advanced Manufacturing Technology* 75.1-4 (2014), pp. 209–223.
- [102] S Denis, S Sjöström and A Simon. “Coupled Temperature, Stress, Phase Transformation Calculation”. In: *Metallurgical Transactions A* 18.7 (1987), pp. 1203–1212.
- [103] R.S. Jackson. “Factors Determining Dimensional Accuracy of Castings”. English. In: *The British Foundryman* 56 (1963), pp. 332–336.
- [104] C. S. E. Mkumbo et al. “Linear Contraction of Grey Iron Sand Castings”. English. In: *Applied Mathematical Modelling* 14.6 (2002), pp. 225–234.
- [105] Yuichi Motoyama et al. “Dynamic Measurements of the Load on Castings and the Contraction of Castings During Cooling in Sand Molds”. English. In: *Journal of Materials Processing Technology* 213.2 (2013), pp. 238–244.
- [106] J. W. Kang et al. “Evaluation of Distortion of Castings”. English. In: *International Journal of Cast Metals Research* 24.3 (2011), pp. 228–232.
- [107] Anthony Chang and Jonathan Dantzig. “Improved sand surface element for residual stress determination”. English. In: *Applied Mathematical Modelling* 28.6 (2004), pp. 533–546.
- [108] U. C. Nwaogu, N. S. Tiedje and H. N. Hansen. “A Non-Contact 3D Method to Characterize the Surface Roughness of Castings”. English. In: *Journal of Materials Processing Technology* 213.1 (2013), pp. 59–68.
- [109] A. D. Sosa, M. D. Echeverría and O. J. Moncada. “Machining and Heat Treatment Effects on Distortion and Residual Stresses in an Industrial Application of ADI”. English. In: *ISIJ International* 44.7 (2004), pp. 1195–1200.





# Part I

## Feeding Secluded Sections

Casting Design and Trial Plan	4
Feeding Effect Analysis	5
Microstructure Analysis	6
Deformation Measurements	7
Thermal Analysis	8
Discussion	9
Part Summary	10

“THE successful feeding of cast irons is perhaps the most complex and challenging feeding task compared to all other casting alloys as a result of the curious and complicating effect of pressure. The effects are most dramatically seen for ductile irons.”

---

—Prof. John Campbell  
*Castings Practice: The Ten Rules of Castings*





# Casting Design and Trial Plan

## Experimental Procedures and Techniques

### Casting Design and Trial Plan

---

4.1 Trial Purpose . . . . .	67	4.3.1 Casting Sessions and Conditions . . .	71
4.2 Design of the Disc Casting . . . . .	68	4.3.2 Feeder Configurations and Properties	71
4.2.1 Alloys . . . . .	68	4.4 Production of Castings . . . . .	73
4.2.2 Feeder Options . . . . .	69	4.5 Temperature Measurements . . . . .	74
4.3 Trial Setup and Configuration . . . . .	71	References . . . . .	74

---



THE chapter gives a run-through of the trial setup including a detailed description of the different feeders that have been tested during the trials and of the casting geometry. The chapter also contains an overview of the alloys that have been cast during the trials, as well as the feeder combinations for the basis for following chapters.

Keywords: . . . Trial Plan, Casting Geometry, Ram-Up Sleeves, Feeder Dimensions, Production Setup, Thermocouple Setup.

Chapter findings reported in: . . . Supplement I, on page 301  
 Supplement II, on page 315  
 Supplement III, on page 325

---

### 4.1 Trial Purpose

---

THE purpose of these trial series was to prove that SGI castings with an isolated section could be produced soundly on vertically parted moulding systems in a manner that would be feasible for foundry production applications. As part of this proof, the trial was designed to show and quantify the effects of different feeder sleeve materials as well as different feeder geometries. Additionally, it was a goal for the trail to show the types of casting defects that would be found in the castings

if sufficient feeding was not provided.

Later it also became a trial purpose to prove that other, more demanding, SGI-alloys could be feed via the ram-up sleeves. It became a purpose to find the limitations of the ram-up sleeves used in the trials. Both of the alloys was later tested for microstructural changes caused by the feeders used in the trial series.

---

Adaptive Thermal Analysis System (ATAS), Carbon (C), Copper (Cu), Modulus Extension Factor (MEF), Phosphorus (P), Pores Per Inch (PPI), Spherical Graphite Iron (SGI), Silicon (Si), Tellurium (Te)

**Table 4.2:** Alloy Compositions for  $\alpha$  (EN-GJS-500-7) and  $\beta$  (EN-GJS-450-10) [wt%].

Alloy	C	Si	Mn	P	S	Mg	Cu	CEV
$\alpha$	3.67	2.73	0.50	0.015	0.005	0.049	0.025	4.60
$\beta$	3.35	3.48	0.34	0.017	0.003	0.046	0.010	4.50
$\tau$	3.20	3.71	0.27	0.044	0.028	0.048	0.081	4.44

**Table 4.1:** Casting Geometry in mm and moduli in mm.

Section	T.Rim	U.Sec	Boss	L.Sec	B.Rim
Height	27.5	55	55	55	27.5
Thickness	20	10	30	10	20
Modulus	6	5	9	5	6
Feed Modulus	7	6	11	6	7

Finally, it was a goal of the trial to cast a series of castings in production conditions in an operating foundry. The series had to include multiple castings of the same configuration in order to prove that the results of the single feeder configuration could be repeated. It would also provide statistical data for determining the variation of the production as well as the feeders. These repeated castings would subsequently be used to assess the process stability and dimensional accuracy of the castings concerning alloy composition and feeder configuration.

## 4.2 Design of the Disc Casting

THE disc casting was designed to imitate casting components with isolated high modulus sections that were difficult to feed via traditional solutions for vertically parted moulds. The casting consisted of a central boss (modulus = 9 mm), separated from an outer ring (modulus = 6 mm) by a thin-walled section (modulus = 5 mm). See fig. 4.1 on the next page. The down sprue was designed to use a  $15 \times 50 \times 50$  mm 10 PPI foam filter.

The dimensions of the different sections of the casting are shown in table 4.1 and fig. 4.1 on this page and on the next page. The pouring weight was  $\sim 8$  kg and the castings themselves weighed  $\sim 4$  kg. The pouring time was  $\sim 3.5$  s.

The feeders used in the trials were selected based on the feed modulus shown in table 4.1. The feed modulus was calculated based on the modulus of the individual casting section using Chvorinov's law of modulus [37]. The following equation was used:

$$M_f = 1.2 \times M_c \quad (4.1)$$

where  $M_f$  is the required modulus of the feeder to feed the given section,  $M_c$  is the geometrical modulus of the casting, and 1.2 is an empirical size factor for the feeder traditionally used in foundries. See section 2.3.2, on page 20.

### 4.2.1 Alloys

The trial casting was cast with three different SGI-alloys during the project. The three alloy compositions are found in table 4.2. Table 4.5 on page 72 shows the pouring temperature and the order in which the different alloys were cast. The alloy compositions were determined using optical emission spectroscopy.

The  $\alpha$ -alloy is a traditional, commercial production grade of SGI and is widely used in the industry. It is defined by the European standard—EN 1563:2012-3 *Founding: Spheroidal Graphite Cast Irons* [110], classified as an EN-GJS-500-7-grade. The  $\alpha$ -alloy displayed a moderate graphite expansion for a SGI-alloy. The EN-GJS-500-7-grade is often used for non-hydraulic car and truck components.

The  $\beta$ -alloy is also a traditional production grade of SGI as defined by EN 1563:2012-3 [110] and classified as an EN-GJS-450-10-grade. The EN-GJS-450-10-grade is often used for hydraulic components. The main differences between the  $\alpha$  and  $\beta$ -alloys were the lower C and higher Si content of the  $\beta$ -alloy. The changed alloy composition increased the elongation of the material due to a higher percentage of ferrite in the final casting. However, the low C, high Si also decreased the graphite expansion and increased the overall shrinkage of the metal. Hence, the  $\beta$ -alloy required more feeding than the  $\alpha$ -alloy to produce sound castings.

Finally, the  $\tau$ -alloy was made to resemble the  $\beta$ -alloy as much as possible. However, some differences in alloy composition exist. The  $\beta$ -alloy is a standard grade for the foundry, Valdemar Birn A/s, and was produced as part of a large-scale production. Similar large-scale production conditions were not present at the Technical University of Denmark (DTU) where the  $\tau$ -alloy was prepared. The main differences between the  $\beta$ -alloy and the  $\tau$ -alloy are the slightly lower C content and a higher Si content for the  $\tau$ -alloy, but also an increased Sulphur (S)-, P- and Cu-content.

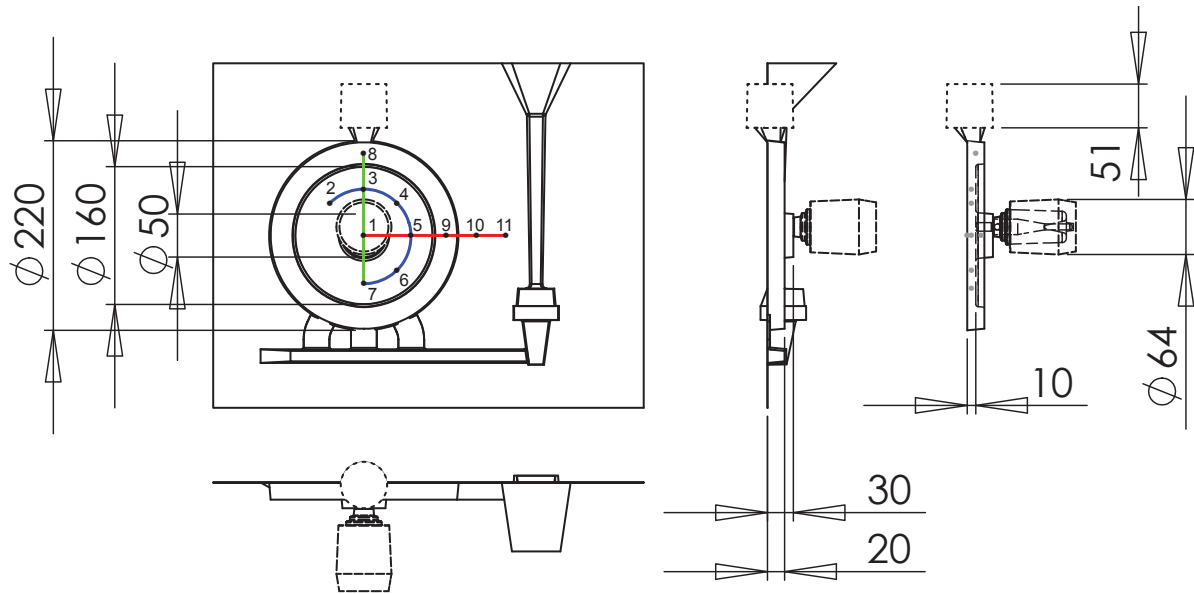


**Figure 4.1:** Technical drawing of the disc casting including the gating system, mounted on the pattern plate. The short dashed line indicates the pattern to mount the top feeder, and the long dashed line indicates the centre feeder. Numbers indicate thermocouple locations.

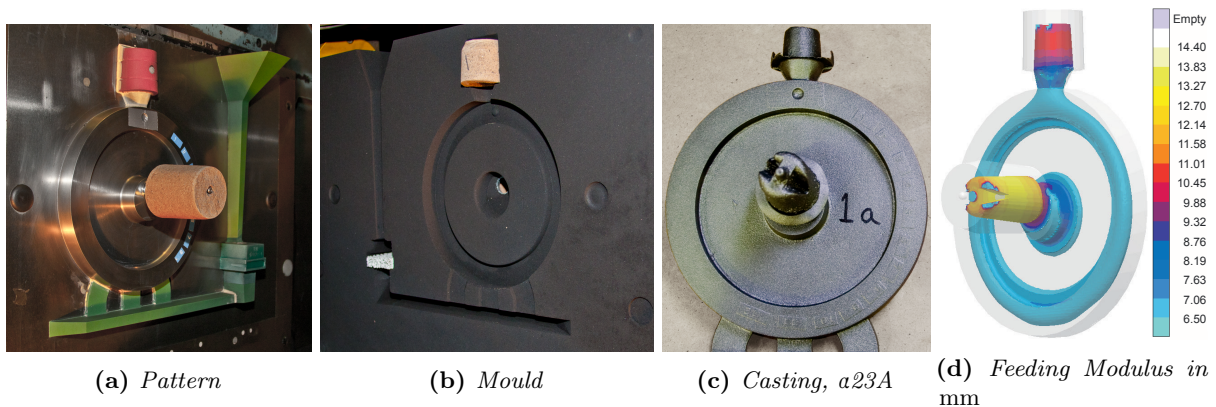


**Figure 4.2:** Production overview; (a) the pattern with a ram-up sleeve mounted at the centre, (b) the mould with a top feeder sleeve mounted at the top, a ram-up sleeve moulded in at the centre, and a 10 PPI foam filter mounted at the bottom of the down sprue, (c) casting a23A after shot blasting, and (d) numerical simulation of the feeding modulus of the different sections of the casting.

#### 4.2.2 Feeder Options

The pattern was made to provide three types of feeders for the casting. See figs. 4.1 and 4.2. The top feeder was at the parting line where a cavity was made by the pattern. The feeder sleeve could be inserted into the cavity after moulding. The installation of the feeder sleeve could be done either by hand or automatically by using the core setter. The feeder neck for this feeder was determined by

the pattern.

The second feeder option was a moulded in ram-up sleeve placed at the centre boss. The ram-up sleeves were mounted on a specially designed pin and were then moulded into the green sand mould. This design required that the pin and ram-up sleeves be mounted normal to the pattern plates. Hence, the ram-up sleeves have a horizontal orientation when mounted. The pin has a small spring-loaded

**Table 4.3:** Feeder Overview [23].

### Top Feeder

T#	ID	Type	Shape	Vol [mm <sup>3</sup> ]	Surface [mm <sup>2</sup> ]	M <sub>g</sub> [mm]	MEF [ ]	M <sub>t</sub> [mm]	Brand	Diss.
1	2	E/I	○	30.304	4.064	7.5	1.3	10	Kalminex 2000 ZP 3.5/5K	α23
2	2	E/I	○	30.304	4.064	7.5	1.3	10	Kalminex 2000 ZP 3.5/5K	α22
3	2	E/I	○	30.304	4.064	7.5	1.3	10	Kalminex 2000 ZP 3.5/5K	α21
4	1	Ins	○	30.304	4.064	7.5	1.2	9	Kalmin S KSP3.5/5K	α13
5	1	Ins	○	30.304	4.064	7.5	1.2	9	Kalmin S KSP3.5/5K	α12
6	1	Ins	○	30.304	4.064	7.5	1.2	9	Kalmin S KSP3.5/5K	α11
7	2	E/I	○	30.304	4.064	7.5	1.3	10	Kalminex 2000 ZP 3.5/5K	α23 Sul
8	1	Ins	○	30.304	4.064	7.5	1.2	9	Kalmin S KSP3.5/5K	α13 L
9	1	Ins	○	30.304	4.064	7.5	1.2	9	Kalmin S KSP3.5/5K	α12 L
10	2	E/I	○	30.304	4.064	7.5	1.3	10	Kalminex 2000 ZP 3.5/5K	α20
11	0									α02
12	0									α00
13	2	E/I	○	30.304	4.064	7.5	1.3	10	Kalminex 2000 ZP 3.5/5K	β23
14	1	Ins	○	30.304	4.064	7.5	1.2	9	Kalmin S KSP3.5/5K	β11
15	2	E/I	○	30.304	4.064	7.5	1.3	10	Kalminex 2000 ZP 3.5/5K	β23 s
16	1	Ins	○	30.304	4.064	7.5	1.2	9	Kalmin S KSP3.5/5K	β11 s
17	2	E/I	○	30.304	4.064	7.5	1.3	10	Kalminex 2000 ZP 3.5/5K	β22 s
18	2	E/I	○	30.304	4.064	7.5	1.3	10	Kalminex 2000 ZP 3.5/5K	β20
19	2	E/I	○	30.304	4.064	7.5	1.3	10	Kalminex 2000 ZP 3.5/5K	τ23TC

### Centre Feeder

T#	ID	Type	Shape	Vol [mm <sup>3</sup> ]	Surface [mm <sup>2</sup> ]	M <sub>g</sub> [mm]	MEF [ ]	M <sub>t</sub> [mm]	Brand	Diss.
1	3	Exo	○	69.025	8.042	8.6	1.40	12	Feedex HD1 GK4/7KW/33MH	α23
2	2	E/I	○	69.025	8.042	8.6	1.28	11	Kalminex SDP7/7K/33MH	α22
3	1	Ins	○	69.025	8.042	8.6	1.28	11	Kalmin 250 FE P4/7KL/33MH	α21
4	3	Exo	○	69.025	8.042	8.6	1.40	12	Feedex HD1 GK4/7KW/33MH	α13
5	2	E/I	○	69.025	8.042	8.6	1.28	11	Kalminex SDP7/7K/33MH	α12
6	1	Ins	○	69.025	8.042	8.6	1.28	11	Kalmin 250 FE P4/7KL/33MH	α11
7	3	Exo	○	69.025	8.042	8.6	1.40	12	Feedex HD1 GK4/7KW/33MH	α23 Sul
8	3	Exo	○	122.145	11.432	10.7	1.31	14	Feedex HD1 CUSTOM	α13 L
9	2	E/I	○	122.145	11.432	10.7	1.22	13	Kalmin 250 CUSTOM	α12 L
10	0									α20
11	2	E/I	○	69.025	8.042	8.6	1.28	11	Kalminex SDP7/7K/33MH	α02
12	0	0								α00
13	3	Exo	○	69.025	8.042	8.6	1.40	12	Feedex HD1 GK4/7KW/33MH	β23
14	1	Ins	○	69.025	8.042	8.6	1.28	11		β11
15	3	Exo	○	28.000	3.500	8.0	1.38	11	Feedex HD1 CUSTOM	β23 s
16	1	Ins	○	28.000	3.500	8.0	1.13	9	Kalmin 250 CUSTOM	β11 s
17	2	E/I	○	28.000	3.500	8.0	1.25	10	Kalminex CUSTOM	β22 s
18	0									β20
19	3	Exo	○	69.025	8.042	8.6	1.40	12	Feedex HD1 GK4/7KW/33MH	τ23TC

ball that holds the ram-up sleeve in place while the pattern plates move and as the moulding chamber is filled with sand. The ram-up sleeves used a specially designed breaker core made of steel. These breaker cores were made to collapse and thus achieve two things: (1) Prevent the ram-up sleeve from being crushed as the mould compacts, and (2) to help compact the sand properly between the ram-up sleeve and the pattern. The feeding modulus of the

ram-up sleeves could be changed by using different sleeves materials. Likewise, the geometry of the ram-up sleeves could be changed. The used feeders are listed in table 4.3.

The third feeder option provided by the pattern was to mount a ram-up sleeve at the top of the outer ring, just below the top feeder. The same ram-up sleeves that could be mounted at the centre boss could also be mounted at the top of the outer

**Table 4.4:** *Casting Overview.*

T#	C#	Dup.	Alloy	Pouring Temp.	Casting Date	Session	Diss.	AFS	TMS	JMPT
1	12	A,B,C	$\alpha$	1401(5) °C	2011-05-30	1	$\alpha$ 23	$\alpha$ 1	$\alpha$ 1	$\alpha$ 23
2	11	A,B,C	$\alpha$	1401(5) °C	2011-05-30	1	$\alpha$ 22			$\alpha$ 22
3	10	A,B,C	$\alpha$	1401(5) °C	2011-05-30	1	$\alpha$ 21			$\alpha$ 21
4	9	A,B,C	$\alpha$	1401(5) °C	2011-05-30	1	$\alpha$ 13			$\alpha$ 13
5	8	A,B,C	$\alpha$	1401(5) °C	2011-05-30	1	$\alpha$ 12			$\alpha$ 12
6	7	A,B,C	$\alpha$	1401(5) °C	2011-05-30	1	$\alpha$ 11	$\alpha$ 2	$\alpha$ 2	$\alpha$ 11
7	6	A,B	$\alpha$	1401(5) °C	2011-05-30	2	$\alpha$ 23 Sul			
8	5	A,B	$\alpha$	1408(5) °C	2011-05-30	2	$\alpha$ 13 L			
9	4	A,B	$\alpha$	1408(5) °C	2011-05-30	2	$\alpha$ 12 L			
10	3	A,B,C	$\alpha$	1408(5) °C	2011-05-30	2	$\alpha$ 20	$\alpha$ 3	$\alpha$ 3	$\alpha$ 20
11	2	A,B,C	$\alpha$	1408(5) °C	2011-05-30	2	$\alpha$ 02	$\alpha$ 4		$\alpha$ 02
12	1	A,B,C	$\alpha$	1408(5) °C	2011-05-30	2	$\alpha$ 00	$\alpha$ 5		$\alpha$ 00
13	13	A,B,C	$\beta$	1392(5) °C	2012-01-24	3	$\beta$ 23	$\beta$ 1	$\beta$ 1	$\beta$ 23
14	14	A,B,C	$\beta$	1392(5) °C	2012-01-24	3	$\beta$ 11	$\beta$ 2	$\beta$ 2	$\beta$ 11
15	15	A,B,C	$\beta$	1392(5) °C	2012-01-24	3	$\beta$ 23 s			$\beta$ 23 s
16	16	A,B,C	$\beta$	1392(5) °C	2012-01-24	3	$\beta$ 11 s			$\beta$ 11 s
17	17	A,B,C	$\beta$	1392(5) °C	2012-01-24	3	$\beta$ 22 s			$\beta$ 22 s
18	18	A,B,C	$\beta$	1392(5) °C	2012-01-24	3	$\beta$ 20	$\beta$ 3	$\beta$ 3	$\beta$ 20
19	19	A,B	$\tau$	1385(5) °C	2014-05-21	4	$\tau$ 23TC			

ring. This option was only used at the beginning of the project. The trial was designed to show how a similar casting with a secluded section could be feed on a vertically moulding line. Most foundries would choose to feed this section with a parting line feeder, and thus the same was chosen for these trials. Instead, the placeholder for the top feeder would be removed from the pattern for the few trial combination that required this setup.

### 4.3 Trial Setup and Configuration

THE setup of the first trial was decided in close collaboration with FOSECO Ltd. and was partly based on an initial test casting at the university foundry at DTU. The second trial series was planned based on the result of the first trial series. Thus, the feeder combinations for this trial series was deliberately selected to elaborate on the results and findings of the first series.

#### 4.3.1 Casting Sessions and Conditions

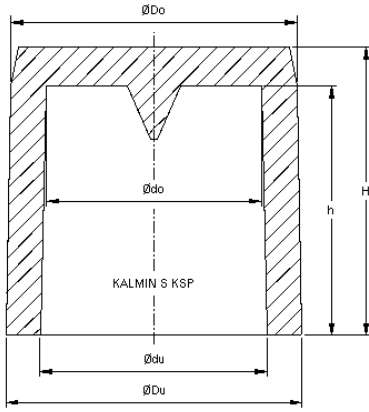
The trials were conducted at Valdemar Birn A/s. All castings, except no. 19 A and B, were cast on the same DISAMATIC 230A using the same machine settings for all castings. See table 4.5 on the following page. As two different alloys were used for the trial, the castings were made on two different dates—June 2011 and January 2012. The June 2011 trial series used the EN-GJS-500-7-alloy, and the January 2012

trial series used the EN-GJS-450-10-alloy. The trial series in June 2011 was divided into two sessions cast approximately one hour apart. This approach was used to enable continuously casting of the different casting configurations; which again was done to secure a uniform pouring temperature for all castings. As only half of the total number of castings could be stored on the moulding line, between the moulding chamber and the pouring station, the trial series was divided into two sessions. The trial series in January 2012 was cast in one session. Finally, a fourth session was cast at the foundry at DTU in May 2014. For this trial series a DISAMATIC 2110 was used. The focus of the trial series was thermal measurements of the solidification of the different sections of the casting. The alloy used for this trial series was the  $\tau$ -alloy, made to be as similar as possible to the EN-GJS-450-10 (EN-GJS-450-10)-alloy used for the third session cast in January 2012.

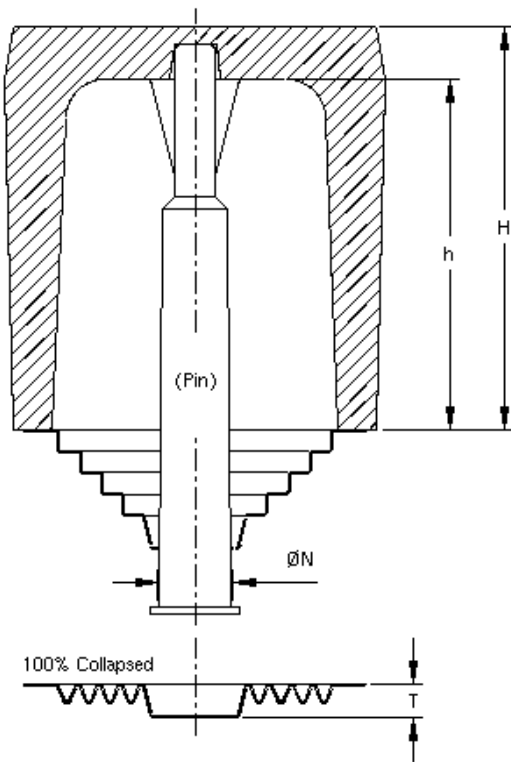
All moulds had a mould thickness of 250 mm for both the DISAMATIC 230A and the DISAMATIC 2110.

#### 4.3.2 Feeder Configurations and Properties

The castings shown in table 4.5 on the next page represent a range of different feeder configurations—different top feeder solutions and different centre feeder solutions. Table 4.3 on page 70 shows which top and centre feeders were used for the different castings. Some of the feeders were commercial



(a) Top feeder sleeve, here for Kalmin S. Kalminex sleeve is geometrically identical.



(b) Ram-up sleeve, here Feedex. The custom sleeves are made to match this design. The metal breaker core is shown on the sleeve for moulding, and at the bottom as 100 % collapsed state.

**Figure 4.3:** Technical sectioned drawings of feeder sleeves.

**Table 4.5:** Feeder Sleeve Dimensions

	du [mm]	Du [mm]	do [mm]	Do [mm]	h [mm]	H [mm]
Top feeder sleeves	35.0	53.0	30.5	49.0	39.5	49.5
Ram-up sleeves	41.5	59.0			64.0	76.0

products that could be bought off the shelf, while others were custom feeders made especially for these trial series. The first column shows the trial no. which can be used to cross-reference between the tables.

The last column shows the systematic name for the casting. This naming scheme is used throughout the dissertation to reference the individual castings. The name reads as follows: alloy ( $\alpha$ ,  $\beta$ , or  $\tau$ ), top feeder ID (0,1,2), centre feeder ID (0,1,2,3), and centre feeder comment (special feature). Thus,  $\beta 23s$  indicate the EN-GJS-450-10-alloy, with a Kalminex 2000 ZP 3.5/5K top feeder sleeve made of a combination material with both insulating and exothermic properties, and a small Feedex HD1 GK4/7KW/33MH centre feeder.

Table 4.3 on page 70 also show the melt volume, cooling surface area, geometrical modulus ( $M_g$ ), MEF, and true modulus ( $M_t$ ) of the different feeders. These feeder properties provide a correlation between melt volume, heat capacity, and feeding ability. Some of the properties were listed in the FOSECO Sleeve Database released in connection with MAGMASOFT [111], other properties have been calculated based on the properties listed in aforementioned database in combination with calculations of cooling times for the different feeder types. The correlation between  $M_g$  and  $M_t$  via MEF is shown in the following equation:

$$M_t = \text{MEF} \times M_g \quad (4.2)$$

The MEF combine both the thermal properties of the material and the geometry of the sleeve into a single factor. Thus, the MEF is not solely a material parameter, which is seen by the variation in MEF in table 4.3 on page 70. Note also, that the MEF is a factor relative to the properties of the surrounding mould. More information about the MEF is found in section 2.3.2, on page 20. The MEF values listed in table 4.3 on page 70 are found based on cooling solidification times simulated with MAGMASOFT 5.1.0 [111, 112]. This approach was chosen as includes both material and geometrical properties, as well as allow for the simulation and calculation of MEF values for the custom feeder sleeves. FOSECO Ltd. do not list the MEF values directly in their material; however, the values can be calculated from the given data for geometry and modulus, though only for the commercially available sleeves [113].





**Figure 4.4:** Overview of castings from session three. The missing casting, 15B, was incompletely filled during casting and was thus discarded.



**Figure 4.5:** Setup of sleeves used in session three. Numbers correspond to trial numbers in tables 4.3 and 4.5 on page 70 and on page 72.

#### 4.4 Production of Castings

As described, the castings were cast in four different sessions on three different dates. The experimental approach for the three sessions cast at Valdemar Birn<sup>A/s</sup> is described in this section. The

fourth session, cast at DTU, is described in section 4.5, on the next page.

The pattern plate with the disc geometry, see fig. 11.2 on page 160, was mounted on the squeeze plate. The plain pattern plate was mounted on the swing plate. The pattern plates were made for a DISAMATIC 2110 (500 × 400 mm), and was thus mounted in a cassette system to fit the larger moulding chamber of the DISAMATIC 230A (600 × 480 mm).

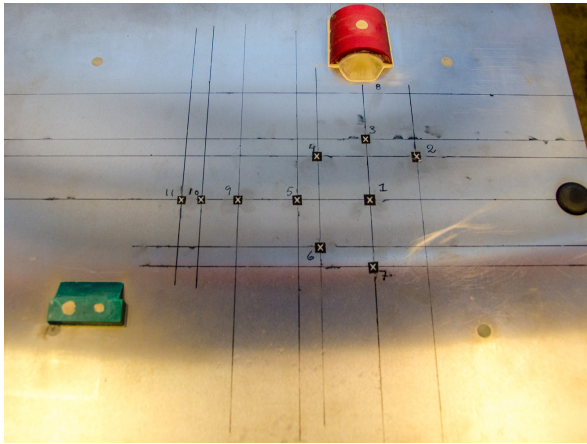
All feeders and sleeves were numbered and arranged in order of use before the experiment, see fig. 4.5.

For sessions 1 and 2 Dymo-labels were mounted on the casting geometry on the pattern plate, thus moulding an individual marker into each casting. For session 3 the casting numbers were imprinted into the sand mould itself.

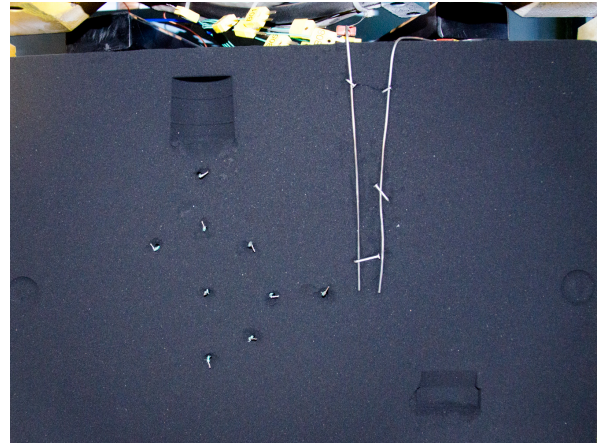
The moulding of the castings was done in sessions to be able to cast continuously to minimise the potential temperature drop. Pouring was done from a heated pouring station, and in-stream inoculation was used. The pouring temperature was measured twice for each casting session, and ATAS-analysis was performed for sessions two and three [114].

The castings were transported through the cooling tunnel with the production goods. The cooling time before shake-out was ~1 h. At the shake-out station, the trial castings were separated from the other production goods and moved to a container to cool to room temperature. After the castings were cooled, they were cleaned using shot blasting.

Finally, the castings were sorted, marked with casting number and duplicate letter, and photo documented. See fig. 4.4.



(a) Marking of location for the placement of the thermocouples on the reverse side pattern.



(b) Thermocouples mounted in the mould. The N-elements are the vertical metal rods.

**Figure 4.6:** Placement of K- and N-element thermocouples for temperature measurements.

## 4.5 Temperature Measurements

THE fourth session of castings was not cast at Valdemar Birn  $\frac{A}{S}$ . Instead, the two castings were cast at the university foundry at DTU to allow for detailed temperature measurements from the casting and mould. The temperature measurements were made to document the thermal gradients present in the casting during solidification. The two castings both have the same feeder combination as trial casting no. 1, 7, and 13—Kalminex top feeder and Feedex centre feeder. See table 4.3 on page 70.

The locations of the thermocouples were marked on the reverse side pattern plate using Dymo-labels. See fig. 4.6a. The Dymo markers imprinted the thermocouple location in the mould. A hole was punched through the mould using a 3.5 mm metal rod. After the holes had been punched, the thermocouples were guided through the mould from the opposite side. Here the thermocouple cables were assembled and guided to the top of the mould. See fig. 4.6b. Then the thermocouples were carefully placed to be at the centre of the individual section, and the moulds were pushed together.

In total 22 thermocouples were used. 11 in each of the two identical castings—nine in the casting itself and two in the mould. See fig. 4.1 on page 69. Additionally, two quick cups were cast and recorded. One standard and one with  $\tau_e$  for white solidification. The thermal measurements were recorded using DasyLab at a sample rate of 100 Hz [115].

## References

- [23] John R. Brown. “FOSECO Ferrous Foundryman’s Handbook”. In: FOSECO International Ltd., 2000. Chap. 19, pp. 296–310.
- [37] Nicolas Chvorinov. “Theory of the Solidification of Castings”. In: *Giesserei* 27 (1940), pp. 177–186.
- [110] *Founding: Spheroidal Graphite Cast Irons*. Norm. 2012.
- [111] MAGMASOFT, FOSECO *Sleeve Database*. [http://www.magmasoft.com/en/solutions/MAGMA\\_5.html](http://www.magmasoft.com/en/solutions/MAGMA_5.html). Database. 2012.
- [112] MAGMASOFT 5.1 by MAGMA GmbH. [http://www.magmasoft.com/en/solutions/MAGMA\\_5.html](http://www.magmasoft.com/en/solutions/MAGMA_5.html). Program. 2012.
- [113] *Mail correspondence with Christof Volks, International Product Manager—Feeding Systems*, FOSECO International Limited, 2015. Mail correspondence.
- [114] *ATAS MetStar*, by Novacast Systems AB. <http://novacast.se/products/atasmeststar/>. Adaptive Thermal Measurement System.
- [115] *DasyLab by Measurement Computing*. <http://www.dasylab.com/>. Program.

## Feeding Effect Analysis

Quantification of the Experimental Results and Numerical Simulations

### Feeding Effect Analysis

<b>5.1 Porosities Quantification</b> . . . . .	<b>75</b>	5.1.7 X-ray Analysis . . . . .	81
5.1.1 Sectioning of the Castings . . . . .	76	5.1.8 Other Shrinkage Defects . . . . .	81
5.1.2 Preparation of Samples . . . . .	76	<b>5.2 Porosity Simulations</b> . . . . .	<b>83</b>
5.1.3 Liquid Penetrant Test . . . . .	77	5.2.1 Setup and Assumptions . . . . .	83
5.1.4 Analysing the Castings . . . . .	77	5.2.2 Results . . . . .	84
5.1.5 Test Results . . . . .	78	<b>References</b> . . . . .	<b>87</b>
5.1.6 Ultrasound Analysis . . . . .	80		



**Q**UANTIFICATION and analysis of the trial castings with respect to porosity defects. The chapter also covers numerical simulation setup, results, and analysis with respect to thermal gradients and porosity prediction.

Keywords: . Sectioning of Castings, Liquid Penetrant Testing, Porosity Results Overview, Numerical Simulations, Porosity Prediction, Graphite Precipitation Coefficient.

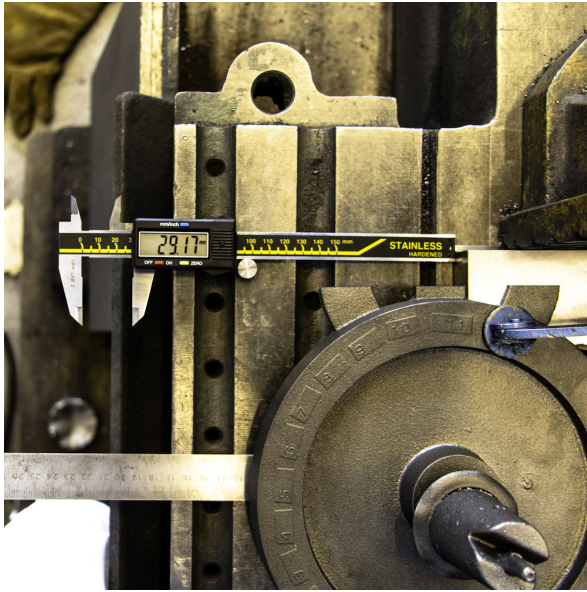
Chapter findings reported in: . . . Supplement I, on page 301  
 Supplement II, on page 315  
 Supplement III, on page 325

### 5.1 Porosities Quantification

THE trial castings were produced as described in chapter 4, on page 67. Identifying and quantifying the size, location, and amount of porosities could be achieved in different ways. However, as the geometry as-cast was not well suited for any porosity analysis, the castings had to be sectioned and adapted for analysis. As the investigations required destructive measured to be taken, it was important to conduct the experiments in the right order to obtain as much information as possible.

Priority is to analyse the amount and location of porosities in close connection with the feeders. It was decided that this was best investigated by sectioning the castings through the vertical centreline, thus exposing the centre of both the top and centre feeder, as well as the sections they are meant to feed. The exposed surface could then be analysed using

Aligned Porosities (AP), Computer Aided Design (CAD), Computer Numerical Control (CNC), Non-Linear Clustered Indications (CP), Finite Difference Method (FDM), Graphite Precipitation Coefficient (GP), Heat Transfer Coefficient (HTC), Linear Porosities (LP), Pores Per Inch (PPI), Silicon (Si), Non-Linear Isolated Indications (SP)



(a) A caliper was used to position each casting accurately to ensure the cutting line was placed correctly.



(b) All castings were first sectioned through the vertical centreline.

**Figure 5.1:** Sectioning of the castings. A special mount was made to fasten the castings during the cutting process. A ~10 mm thick slice was cut from each casting.

the liquid penetrant method. The visual inspection of a casting surface (sectioned or not), will however only find porosities with a connection to the analysed surface. Thus, other methods were required to ensure that the porosities found via the liquid penetrant tests were representative for the castings. To aid the analysis, a standardised penetrant test procedure was used.

For these reasons it was chosen to start by sectioning the castings through the vertical centreline, thus enabling a direct visual analysis of the casting at the sectioned plane.

Ultrasound analysis requires an even reverse side of the casting; else the unevenness would interfere with the echo rendering the analysis difficult at best. Ultrasound could be used for all other sections than the boss with an attached feeder. The feeders themselves hindered the analysis. As the boss was the main point of interest for the porosity analysis, it was important that this part of the casting could be analysed. Thus, for a select number of castings, the feeders were removed and the surface area where the feeders had been was ground plane to ensure a clean and undisturbed surface without interfering geometries influencing the ultrasound analysis.

X-ray analyses are strongly dependent on the variance in the absorption of the x-rays. Thus, non-

uniform section thicknesses can be difficult to analyse simultaneously. However, removing the feeders, especially the centre feeder, a foreshadowing of the boss section is prevented. Consequently, selected castings were subsequently x-ray imaged and analysed to confirm the results from the ultrasound analysis.

### 5.1.1 Sectioning of the Castings

All castings in sessions 1-3 were sectioned. The sectioning was done using a cold saw. The cold saw prevented changes to the microstructure due to friction heating from the cutting process. Additionally, the long blade of the cold saw, combined with the mounting of the castings, ensured that the cuts were straight. See fig. 5.1.

### 5.1.2 Preparation of Samples

The cutting process left the sectioned pieces with straight cut sides, but with cutting marks. All sample pieces were plane ground to provide as smooth and uniform a surface as possible. This step was done to eliminate potential errors and disturbances that may have arisen if the unplanned samples had been used for the penetrant test.

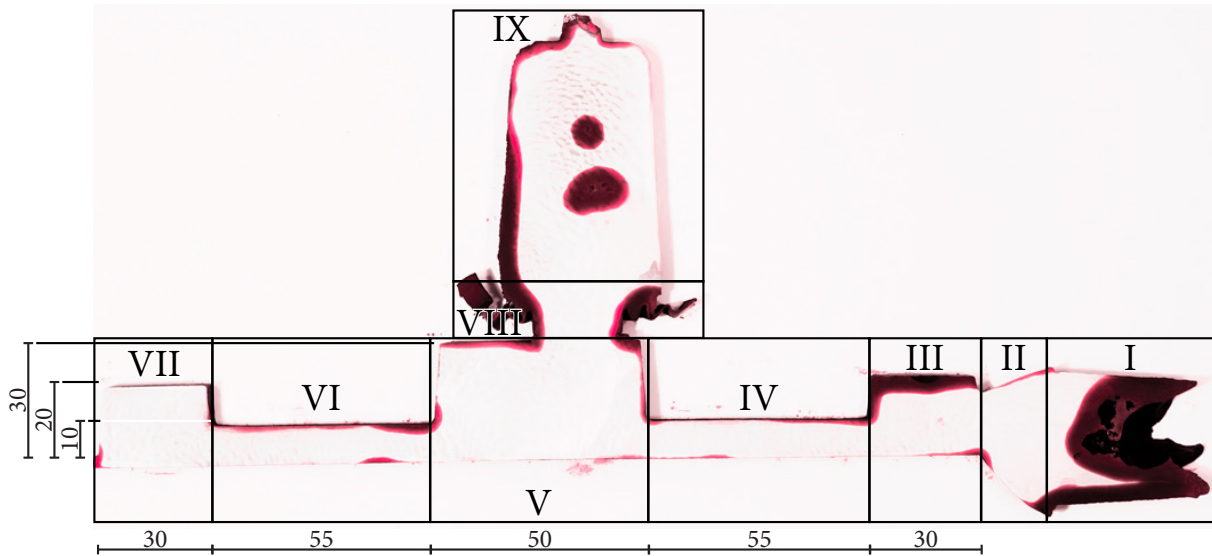


**Figure 5.2:** Sectioned and planar ground sample from casting  $\beta 11C$ .

After the pieces had been ground plane they were all etched in oxalic acid dihydrate—approximately 25 g and 500 ml water per casting. The pieces were etched at 20 °C for 24 h. The etching was done to etch away any material that might have been smeared over any porosities by the plane grinding process. In most cases, a penetrant test would be performed on the production piece as it is, without any grinding and etching preparations. However, it was chosen to include this procedure for the trial to obtain as detailed and unobscured porosity indications as possible.

### 5.1.3 Liquid Penetrant Test

The liquid penetrant test was conducted according to EN1371-1:2011 Founding: Liquid Penetrant Testing—Sand, Gravity Die, and Low Pressure Die Castings [116]. The penetrant test process consists of four steps: (1) the sample was cleaned with the specified aerosol spray cleaner, (2) the sample was thoroughly covered with dye penetrant, also administered via aerosol spray, then the sample was allowed to rest for 5-10 min., after which (3) the sample was thoroughly cleaned once more using the same aerosol spray cleaner, and finally (4) the re-cleaned sample was sprayed with a white developer that draws out any remaining dye penetrant.

As the development of the penetrant test was continuous, all castings were photo-documented within 20 min. of the development. This procedure al-

lowed for penetrant analysis to be performed at a later time. Additionally, the photo documentation also allowed for multiple people to each perform an individual analysis of the porosity indications.

### 5.1.4 Analysing the Castings

The sectioned casting samples were divided into nine separate areas to analyse and quantify the results of the liquid penetrant test. See fig. 5.2. Each area was analysed separately and in correspondence to the standard [116].

The standard classifies porosities according to type and size. All porosities found during this analysis were classified as either non-linear isolated indications (SP) or non-linear clustered indications (CP). The two other, more severe categories described by the standard, were linear porosities (LP) and aligned porosities (AP). The classification type was then appended with a number indicating the size of the porosity—eg SP1. The SP-classification ranges from SP01, SP02, SP03, SP1, SP2, SP3, SP4, and SP5. The CP-classification cover the same ranges, but only up to CP3.

The red edges seen in fig. 5.2 were found on all castings. The colouring on the edges did not indicate porosities. It was the result of small amounts of dye penetrant located at the sides of the samples after the second cleaning. However, the false positive at the edges could in principle have obscured true positives, if they were located near the edges

of the sample. The risk of this phenomena was considered unlikely due to the solidification direction from the mould-metal interface and inwards into the melt towards the thermal centre.

### 5.1.5 Test Results

The photos of the treated samples were reviewed by three different people, each assigning a classification to each of the nine areas of the sample. This triplicate analysis was done for all castings within the first three sessions. Recording all found porosities in a data-sheet; it was possible to sort the data according to several different parameters—eg casting vs amount of porosity, or areas vs amount of porosity. See fig. 5.3 on the next page.

#### Structuring the Results

First, the porosities were sorted according to casting and area, and then plotted for porosity size. See fig. 5.3a on the facing page. The graph shows an even distribution across the 12 different  $\alpha$ -alloy castings (blue). The six different  $\beta$ -alloy castings (red) also displayed a uniform distribution of porosities, but with an increase in porosities over the  $\alpha$ -alloy.

Secondly, the porosity data for each area were grouped. Hence, the location of porosities could be analysed. See fig. 5.3b on the next page. The graph shows that three areas had no porosities—areas II, IV, and VI. These areas were the top feeder neck (II), the upper thin-walled section (IV), and the lower thin-walled section (VI). Thus, it was not surprising that these areas were without porosities. However, the analysis showed that they could be left out of the continued analysis.

An area that displayed porosities was the lower section of the outer ring (VII). This area was located just above the ingate. In total four of the 51 castings had a defect in this area. Analysing each of the four defects in detail,  $\alpha$ 21B and  $\beta$ 20C have regular but very small porosity defects.  $\alpha$ 13B was slightly larger and located directly above the ingate.  $\beta$ 20A was assessed to be an inclusion defect more than a porosity defect. See section 2.2.1, on page 17. However, although three of the porosities were genuine, they were excluded from the continued analysis. This exclusion was because the porosities were estimated to be related to an imperfect gating system, and not related to the efficiency of the different feeder combinations. The porosities near the ingate are discussed further in section 5.2.2, on page 84 as part of the numerical simulation analysis.

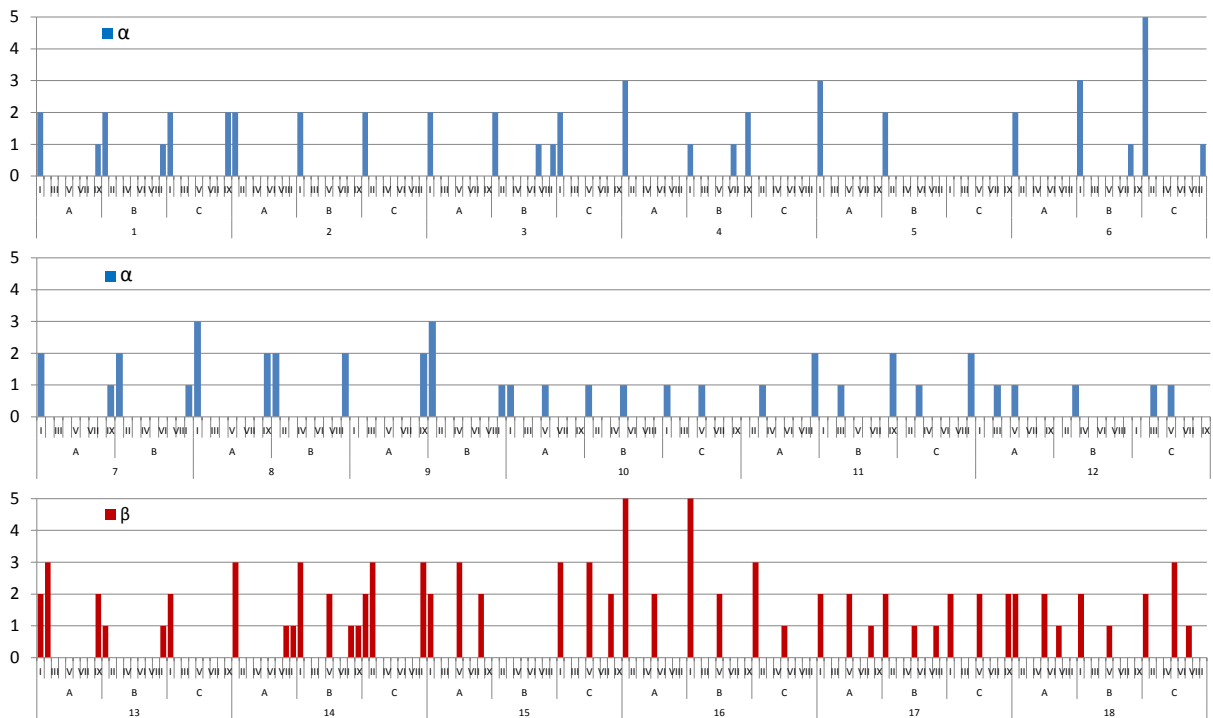
Having excluded the areas without porosities, and area VII, the next step was to evaluate which areas would be expected to yield porosities. The graph shows that areas I and IX have a significant number of registered porosities. Again, as these areas were the top feeder (I) and the centre feeder (IX), respectively, these results were also expected. Porosities found in the feeders provide information in the functioning of the individual feeder type, for the given conditions. However, to simplify the analysis to the degree that could provide a general overview, the feeder areas (I,IX) were excluded from the analysis.

#### Castings no. 1-9 — $\alpha$ -alloy with both feeders

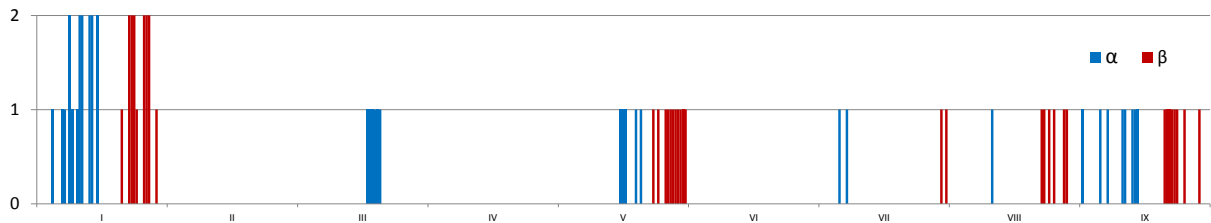
The remaining areas were sorted according to casting and area vs type and size of the porosities. See fig. 5.3c on the facing page. The first nine castings displayed only one porosity defect in any of the three analysed areas. That was casting no. 6 ( $\alpha$ 11B) area VIII which had an SP1 porosity. Area VIII was the feeder neck of the centre feeder, so the porosity is not within the casting itself. However, the feeder neck was still an interesting area to analyse. Porosities in this area indicated that the feeder was close to the limit of its capability. Had more castings shown porosities in this area, then a revised feeding solution should be considered. In this case, however, the feeder neck porosity was a single defect for the first group of castings, and should not be taken as an indication that the feeder had reached its limit. Local variations in the location of porosities occur as reported by Kainzinger [117]. It should be noted that all castings in this groups were sound. On the other hand, the variation in porosity locations was an indication of the process robustness and variation.

#### Castings no. 10-12 — $\alpha$ -alloy without feeders

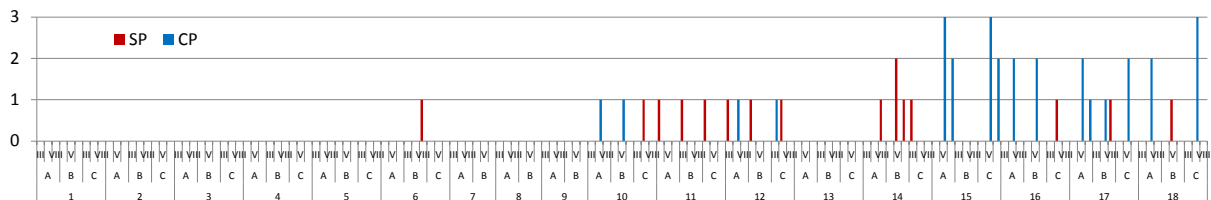
The next series of castings of interest were the reference castings—no. 10-12. These three casting groups were all cast without either the top feeder, the centre feeder, or without any of the two feeders. Casting group no. 10 ( $\alpha$ 20), which was cast with the top feeder, but without the centre feeder, showed porosities at the boss (V) for all three castings. Casting group no. 11 ( $\alpha$ 02), which was cast without the top feeder, but with the centre feeder, showed porosities at the upper ring (III) for all three castings. Finally, the last group, no. 12 ( $\alpha$ 00), cast without the top



(a) Quantification of the porosities size found each of the nine different areas for each of the castings.  $\alpha$ -alloy (blue) on the top two graphs, and  $\beta$ -alloy (red) on the bottom graph. The graph does not distinguished between types (SP or CP) of porosities.



(b) Porosities sorted according to area but not casting. The graph show which of the nine areas have porosities.  $\alpha$ -alloy (blue) and  $\beta$ -alloy (red). 0 = no porosities, 1 = limited porosities, and 2 = substantial porosities. The graph does not distinguished between types (SP or CP) of porosities.



(c) Porosities sorted according to casting and area, for the areas III, V, and VIII. Type distinguished by colour; non-linear isolated indications SP (red), and non-linear clustered indications CP (blue). Porosity size-scale is the same as fig. 5.3a.

**Figure 5.3:** Results of the Porosity Analysis



**Figure 5.4:** *Ultrasound analysis of casting without centre feeder, before the sectioning.*

and the centre feeder, had porosities at the upper ring (III) in all three cases and porosities at the boss (V) in two of three cases.

Comparing the results from the first series of castings with the series of reference castings; it was concluded that sound castings could not be produced without both feeders being used at the same time.

#### Castings no. 13-18 — $\beta$ -alloy

All the  $\beta$ -alloy castings displayed porosities in one or more of the three selected areas, except the three castings in group no. 13. Group no. 13 used an insulating-exothermic top feeder and an exothermic centre feeder; the same feeders as used in group no. 1. Casting group no. 14 used an insulating top feeder and an insulating centre feeder. The same as group no. 6. However, while group no. 6 had only a single small porosity defect, group no. 14 had porosity defects in all three castings. Hence, it was concluded that the insulating feeder sleeves were sufficient for the  $\alpha$ -alloy, but not for the  $\beta$ -alloy.

The groups from no. 15-17 used scaled down ver-

sions of the centre sleeves. None of these castings was without porosities. No. 15B did not fill completely and was thus never part of the analysis. The types of porosities found in these three casting groups were also more severe than the porosities mentioned above. Most of the porosities were classified as CP2 or CP3.

Finally, the group of reference castings, no. 18, all displayed porosities at the boss (V). This result was similar to the identical feeder configuration for the  $\alpha$ -alloy, although the porosities were larger for the  $\beta$ -alloy castings.

#### 5.1.6 Ultrasound Analysis

The castings without centre feeder were analysed with ultrasound as part of a quick initial analysis of the castings. See fig. 5.4. However, the main analysis was conducted as described above. Hence, as the castings were sectioned before the main ultrasound analysis, each casting part has the casting number written on it, as well as designated if it was the left or right part. One would believe that the



left or right part would be self-evident, however, with all other parts cut off, the castings were simple geometries without strong indications of up or down, left or right. Thus, as the ultrasound analysis was performed by an experienced operator at Valdemar Birn A/s, it was ensured that left and right was not mixed up by mistake.

The ultrasound operator was also given a document with an illustration of the two sectioned casting parts and a commentary field for each of the 24 castings. The operator was instructed to draw in all the porosities, as he would typically mark them on the casting itself. The commentary field was used for remarks about the type of porosities, clarifications about locations, and other comments.

In total 24 castings, divided between eight different feeder configurations, were ultrasound tested. The eight different configurations were; 01 ( $\alpha$ 23), 06 ( $\alpha$ 11), 10 ( $\alpha$ 20), 11 ( $\alpha$ 02), 12 ( $\alpha$ 00), 13 ( $\beta$ 23), 14 ( $\beta$ 11), 18 ( $\beta$ 20). All groups encompassed duplicates A, B, and C, though the left part of casting  $\beta$ 20B was missing.

The analysis showed an excellent correlation with the results from the liquid penetrant test, listed in fig. 5.3 on page 79. Casting groups  $\alpha$ 23 and  $\alpha$ 11 were found to be utterly free of porosities. Remember that the porosities recorded for these two groups were located in the feeders, and for  $\alpha$ 11B in the feeder neck (VII), which have all been cut from the castings before the ultrasound analysis.

The  $\alpha$ 20 groups showed porosities at the boss section (V) for all three castings, precisely as indicated by the liquid penetrant test. Group  $\alpha$ 02 was found to have porosities at the top part of the ring (III) for all three castings, as was also found in the liquid penetrant test. For casting  $\alpha$ 02C, however, the ultrasound analysis showed the porosity as off centre, located in the left part of the casting. Thus, the porosity found in the same section, using the liquid penetrant test, seems to have been lost as part of the sectioning.

The  $\alpha$ 00 casting group without feeders was found to have porosities at both the top part of the ring (VII), as well as at the boss section (V), for all three castings. These results also match the results from the liquid penetrant test, except for porosity at the boss section (V) for  $\alpha$ 00B, which was not found in the liquid penetrant test.

Of the casting groups cast with the high Si  $\beta$ -alloy, group  $\beta$ 23 corresponded perfectly with the liquid penetrant test results and showed no porosities.

The next group cast with the  $\beta$ -alloy, group  $\beta$ 11, was found to have small porosities near the surface

of the boss section (V), where the porosities in  $\beta$ 11B was a bit deeper than the two other castings. The liquid penetrant test showed porosities at the boss section (V) for casting  $\beta$ 11B. The location of the porosities near the surface may have been obscured by the bleeding of the edges, as described in section 5.1.4, on page 77.

Finally, casting group  $\beta$ 20 showed porosities at the boss section (V) for all three castings, matching the results of the liquid penetrant test. The ultrasound results, however, did not reveal the porosities in the bottom ring (VII) discovered for both  $\beta$ 20A and  $\beta$ 20C with the liquid penetrant test.

In summary, the ultrasound results showed a good correlation with the previously recorded porosity results based on the liquid penetrant test. A few variations were found; however, these do not significantly change anything for the overall results as revealed by the liquid penetrant test.

### 5.1.7 X-ray Analysis

---

A few of the castings selected for ultrasound analysis was also analysed using x-ray imaging. These were castings  $\alpha$ 23A,  $\alpha$ 20C,  $\alpha$ 00C, and  $\beta$ 11B. See fig. 5.5 on the following page. The results of the x-ray analysis corresponded with the ultrasound analysis.  $\alpha$ 23A showed no signs of porosities,  $\alpha$ 20C showed porosities at the centre boss section (V),  $\alpha$ 20C showed porosities at both the ring section (III) and the boss section (V), while  $\beta$ 11B showed porosities near the surface of the boss section (V). The only porosity found in the x-ray analysis, which was not also found by the ultrasound analysis and liquid penetrant test, was the small porosity in the ring section of casting  $\alpha$ 00C, as marked on the right-hand side of fig. 5.5b on the next page.

Thus, the x-ray analysis has further confirmed the results of the liquid penetrant test and the ultrasound analysis.

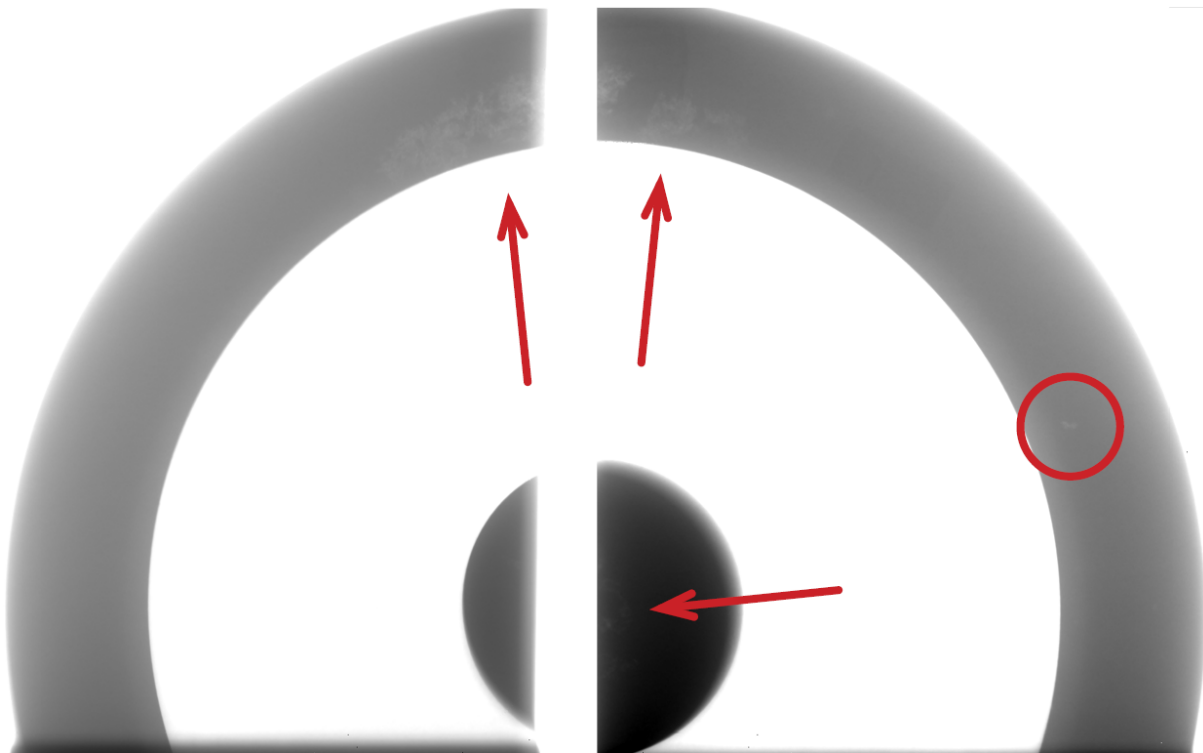
### 5.1.8 Other Shrinkage Defects

---

In addition to the internal porosities that have been quantified and analysed in section 5.1.5, on page 78, external shrinkage was also a possibility. However, external shrinkage—or surface shrinkage—cannot be identified using either ultrasound, x-ray, or liquid penetrant tests. The surface shrinkage requires detailed measurements and model comparisons to determine the existence and amount of surface shrinkage. Surface shrinkage was not included in the



(a) X-ray of casting a23A.



(b) X-ray of casting a00C. Arrows indicate location with porosities. The circle mark a small porosity located away from the cross-section.

**Figure 5.5:** X-ray analysis of castings a23A and a00C. a23A was cast with an exothermic-insulating feeder at the top, and an exothermic feeder at the centre. a00C was cast without feeders.

analysis in section 5.1.5, on page 78; however an investigation of the surface shrinkage and deformation can be found in chapter 7, on page 97.

## 5.2 Porosity Simulations

**M**ATCHING the simulations of the castings to the results of the trials provided a better understanding of both processes—numerical simulation and casting.

Most of the 19 trial combinations have been simulated using a commercial numerical simulation software—MAGMASOFT 5.1 and 5.2 [69]. Only trial combinations no. 7-9 have not been simulated. Most simulated castings were simulated multiple times with different setups.

### 5.2.1 Setup and Assumptions

All simulations were set up to match their respective castings conditions as precisely as possible. In most cases existing projects have been copied to a new version to preserve all settings, ensuring that only specifically changed parameters were different from previous versions of the simulation. This approach allowed for multiple iterations, examining the effect and influence of multiple parameters.

#### Geometry Modelling

The casting geometry, including the pouring cup, down sprue, filter holder, runner, and ingate, were loaded from an external CAD-file. The CAD-file used to CNC-machine the pattern was also used for the simulations. Additionally, also the pin for the ram-up sleeves was imported from CAD-files. The remainder of the geometries used during the simulations were modelled in MAGMASOFT itself.

The top feeder sleeves were imported from the build-in FOSECO sleeve database [111]. The two top feeder sleeves used during the trials—Kalmin S KSP 3.5/5K and Kalminex 2000 ZP 3.5/5K—were both available in the database. These were used without modifications.

Only one of the centre feeder sleeves were a standard FOSECO product—namely the Feedex HD1 GK4/7KW/33MH. This standard feeder was used for trial combinations no. 1, 3, 13, and 19. Trial combination no. 7 used the standard sleeve, but lined with sulphur. Trial combinations no. 2, 5, and 11 used the same geometry but with the Kalminex material. Trial combinations no. 3, 6, and 14 used

the same geometry but with the Kalmin S material. See table 4.3 on page 70.

As the custom sleeves were not available in the database, the feeder geometry was imported separately and assigned material properties according to the sleeves materials that already existed in the sleeve database. This work-around was necessary because the sleeves from the database are locked entities that cannot be edited, as described in section 3.4.5, on page 57.

The trial combinations no. 15-17 used a scaled-down centre feeder sleeve. Again the imported geometry of the standard feeder was used as it was not locked. The CAD-geometry was scaled to match the size of the custom feeders used during the trials. The sleeve material was again changed between the exothermic Feedex-material, the insulating-exothermic Kalminex-material, and the insulating Kalmin S-material.

The 10 PPI Sedex foam filter that was used during the trials was selected in the FOSECO filter database in MAGMASOFT [118].

**Thermocouples** For all simulations, except trial combination no. 19, eight thermocouples were placed at select locations in the casting and inside the feeders themselves. The thermocouples were located;

- In the casting
  - at the centre of the boss,
  - at the centre thin-walled section between the top feeder and the boss,
  - at the centre of the upper ring section just below the top feeder.
- In the feeders
  - inside the top feeder,
  - inside the centre feeder.
- In the mould, 25 mm behind the casting
  - behind the upper ring,
  - behind the upper thin-walled section,
  - behind the boss.

The cooling curves obtained from these virtual thermocouples were used in the analysis of the simulation results, the trial castings, and in the comparison of these.

For trial combination no. 19, 11 thermocouples were included in the simulation; nine thermocouples in the casting itself, and two in the mould. See fig. 4.1 on page 69.

The cooling curves were used as part of the simulation results analysis. A more thorough comparison of the measured and the simulated cooling curves is found in section 8.2.2, on page 124.

### Mesh Generation

The mesh generation was divided into two parameter sets: ‘Standard’ and ‘Advanced’. The mould and the gating system were assigned the standard mesh setting. This setting used equidistant mesh cells of 5 mm and allowing for three subdivisions. All other geometries, including the casting, feeders, and filter, were assigned equidistant mesh cells of 1.5 mm and allowing for three subdivisions. The equidistant approach to the mesh generation was chosen because MAGMASOFT is based on the Finite Volume Finite Difference Method (FVFD) [6, 70], as described in chapter 3, on page 39.

These settings generated meshes with between 2.5 million cells and 3.6 million cells, depending on the size and shape of the feeders.

### Process Parameter Definitions

**Material Definitions** The different trials were simulated using the temperatures given in table 4.5 on page 72. The simulations used the standard settings for bentonite green sand provided by Magmsoft, and the initial sand temperature was set to 40 °C. The initial temperature of the feeder sleeves was set to 20 °C.

The trial combinations were simulated using both the standard GJS-500 material data available with MAGMASOFT, but also using custom material datasets calculated with JMatPro [119]. In all cases, the alloy compositions obtained via the optical emission spectrometry were used. See table 4.2 on page 68.

**Heat Transfer Definitions** The standard temperature dependent HTC (TempIron) was used, as this was adjusted according to the temperature of the two materials. However, investigations using a constant HTC were also performed. Eventually, it was chosen to use the dynamic build-in HTC for the simulations. An explanation of the different HTC types is given in section 3.3.3, on page 43.

The castings have been simulated with a filling time of 3.5 s and using a *stable mould*, as described in section 3.4.2, on page 52. The influence of mould stability is further elaborated in section 2.3.7, on page 29.

**Melt Treatment** The melt treatment settings influenced the simulation outcome the most. The melt treatment at Valdemar Birn  $\alpha$ s was excellent; hence this was reflected in the settings as inoculation method was set as *Very Good* with a treatment yield of 80 %. The graphite precipitation was set on a scale from 1 to 10, with 1 = minimal graphite expansion and 10 = full potential graphite expansion. Several different graphite precipitation coefficients were simulated and analysed. Comparing the simulations with the results of the porosity analysis from the trials, a graphite precipitation of 8 was chosen as the most accurate setup for the  $\alpha$ -alloy. Likewise, a graphite precipitation coefficient of 6 was chosen for the  $\beta$ -alloy; however, a setting of 6.5 would have been more accurate. MAGMASOFT only allow integers to be used.

**Solidification and Cooling** As the production of the trial castings was different from a standard DISAMATIC production, a few adaptations were needed for the solidification and cooling setup. The simulations used *Production Rate/Shake out Time* with a moulding time of 120 s and a production rate of 10. The shake-out time was set to 3600 s.

As the castings were removed at the shake-out station they did not undergo any additional controlled cooling, nor were they sent through a cooling drum. MAGMASOFT, however, require a time set for these phases, so they were set to 1 s.

## 5.2.2 Results

The porosity analysis showed a good correspondence with the porosity defects found in the trials. The overview given in fig. 5.7 on page 86 shows that alloy, feeder configuration, and graphite precipitation all made a significant difference.

### Graphite Precipitation

The rows in fig. 5.7 on page 86 represent three different graphite precipitation coefficients. Higher coefficient utilises more of the potential graphite expansion, thus limiting porosities. However, the analysis showed significant differences between the location of the porosities as the graphite precipitation changes.

The  $\alpha$ 23 casting with insulating-exothermic top feeder and exothermic centre feeder displayed few changes to the amount and location of the porosities, regardless of the graphite precipitation coefficient.

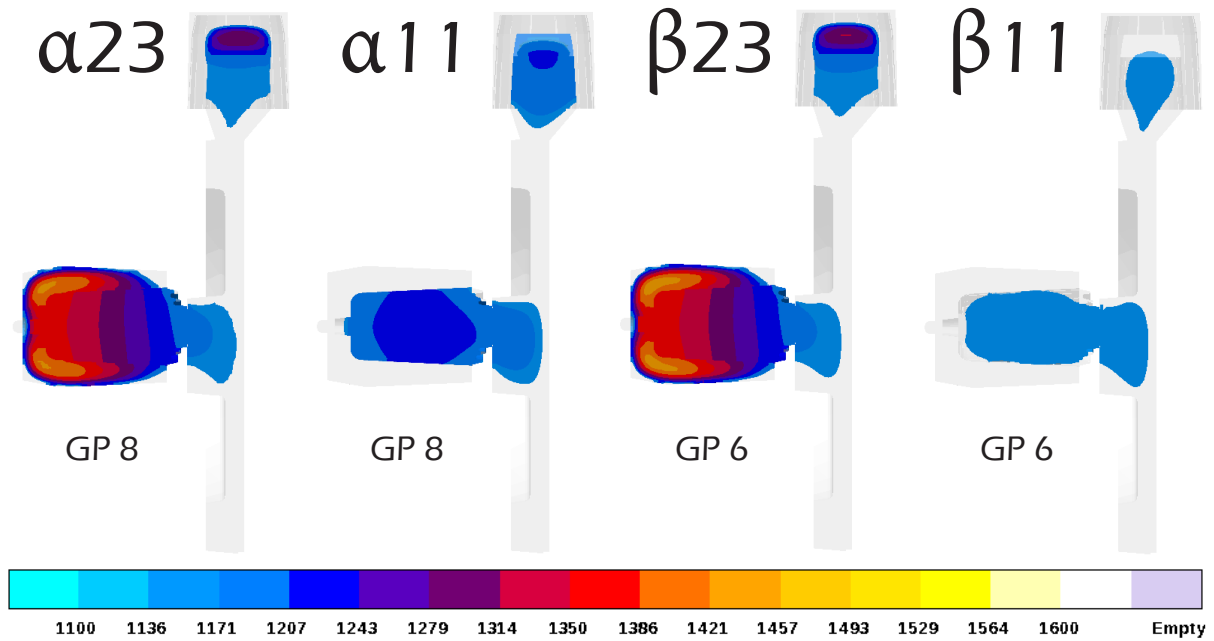


**Figure 5.6:** Comparison of the feeders influence on temperature during solidification for four different trial setups ( $\alpha 23$ ,  $\alpha 11$ ,  $\beta 23$ , and  $\beta 11$ ). The first two simulated with a GP of 8. The other two with a coefficient of 6. The results are shown in x-ray mode at 85% solidified. The scale is 1100°C to 1600°C.

However, the  $\beta 23$  displayed a significant increase in the porosity probability as the coefficient decreased. A probability for porosities in the boss was present for a coefficient of 7, albeit it was not present for either a coefficient of 6 or 8. The porosity predictions moved and merged into larger porosity probabilities close to the lower outer ring and in the centre feeder.

A similar effect of the graphite precipitation coefficient was found for the  $\beta 11$ , which had an insulating top feeder and an insulating centre feeder. Again, the porosity probabilities were seen to merge and grow. However, for the  $\beta 11$ , as opposed to the  $\beta 23$ , the porosities move upward toward the boss. A similar effect was found for  $\alpha 11$ , where the merging porosities also moved towards the boss.

The movement and merging of the porosity probabilities changed with changing graphite precipitation coefficient. However, the feeder type influenced the direction of the porosity movement. Thus, the exothermic centre feeder of  $\beta 23$  apparently ‘pushed’ the porosity closer to the lower ring section. Both of the simulations using the insulating centre feeder sleeves appear to draw the merging porosities towards the boss and the centre feeder.

Note that porosities were only observed for four

of the castings in area VII, as described in section 5.1.5, on page 78, while the numerical simulation of both  $\alpha 11$ ,  $\beta 23$ , and  $\beta 11$  indicate a probability for a porosity forming in this area. The porosity prediction indicated by MAGMASOFT are probabilities, hence a risk that a porosity will form in this area, not a certainty that it will form. Additionally, Kainzinger showed that porosities form within a defined thermal area sums up to the probabilistic area when comparing multiple castings; though the exact location of the porosity within the single area is still difficult to predict [117]. As a consequence other porosities may have been form in the vicinity of the ingate, but missed by the porosity analysis. The latter is not unplausible as the chosen method of analysis views a single sectioned plan of the casting only. This limited sample size, though, can also be said to apply for the porosities at the other areas. Another possibility may be that the numerical simulation was setup in a way, especially with the mesh at the ingate, the made the simulation results influenced more by the filling of the mould.

The prediction of porosities in MAGMASOFT is based on criteria functions, though the exact criteria used by MAGMASOFT is not known, as described in section 3.4.3, on page 54.

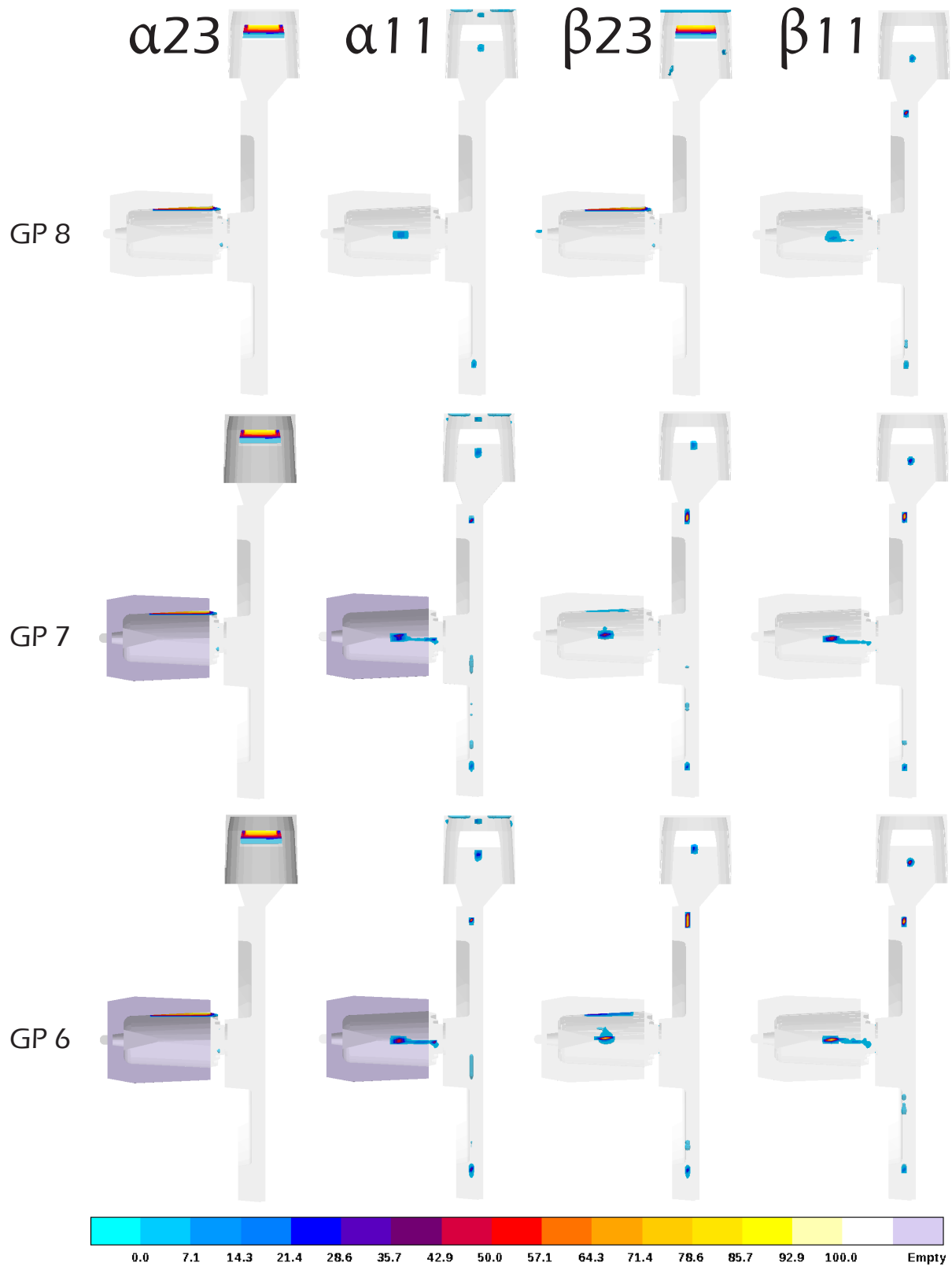


**Figure 5.7:** Comparison of four different trial setups ( $\alpha 23$ ,  $\alpha 11$ ,  $\beta 23$ , and  $\beta 11$ ), simulated with three different graphite precipitation coefficients (GP 6 to 8). The comparison shows the influence of graphite precipitation (6 to 8), alloy ( $\alpha$  or  $\beta$ ), and the application of feeders.  $\alpha$ - and  $\beta 23$  had insulating and exothermic top feeder and exothermic centre feeder.  $\alpha$ - and  $\beta 11$  had insulating top and centre feeder. The simulation results are shown in x-ray mode and sectioned through the vertical centreline. Scale indicates probability of porosities in %.

## Alloy and Feeder Configuration

Analysing the influence of the two different alloys—EN-GJS-500-7 (EN-GJS-500-7)  $\alpha$ -alloy and EN-GJS-450-10  $\beta$ -alloy—it was found that the high Si  $\beta$ -alloy was influenced more by the variance in graphite precipitation than the low Si  $\beta$ -alloy. The  $\alpha$ 23 displayed no changes for any of the three GP levels, which indicate that the prolonged solidification of the exothermic feeders allows for a more extended and more complete precipitation, releasing a more significant part of the potential graphite expansion. The fact that the simulation predicts an almost porosity-free casting for all three GP levels indicate that the combination of the prolonged solidification of the exothermic feeders, even with the low graphite expansion factor of GP 6, was enough to yield an almost porosity-free casting. The only remaining porosity probability at the centre feeder neck is not formed due to lack of graphite expansion potential.

The same alloy with the lower modulus insulating feeders showed a considerable variation between the GP 7 and 8, though the continued step to the GP 6 assembled rather than increased the number of porosities predicted, as mentioned in section 5.2.2, on page 84.

It is concluded that the  $\alpha$ -alloy contains a more substantial graphite expansion potential, which can be used with a high enough modulus feeder. It can also be concluded that there are two influencing factors; (1) the graphite expansion potential, and (2) the ability to use the full potential. The  $\alpha$ 23 castings had both the potential and the ability to feed the casting. The  $\alpha$ 11 castings had the same potential for each of the three GP levels, as the alloy was the same, but the total of the potential and the ability was not a sufficient to remove all porosity probabilities from casting simulation. The analysis shows that the  $\alpha$ 11 with a GP of 8 fares better than the castings with a lower GP level. This difference between the alloys is because of the reduced ability to utilise the potential of the graphite expansion.

The same correlation is also governing the castings simulated with the  $\beta$ -alloy. The  $\beta$ 23 with a GP level of 8 yields almost no porosities, which correspond well with the results from the porosity analysis. See fig. 5.3 on page 79. Note that the simulation does not predict any significant porosities at the feeders, though porosities were found in these areas in the sectioned castings. The simula-

tions with GP levels of 6 and 7 yield more credible amount of porosities when comparing the feeder areas with porosity analysis results. Note, however, that these two levels also predict porosities at other areas, which at least was not found in the porosity analysis—neither for the liquid penetrant test, ultrasound analysis, nor x-ray imaging.

The final casting simulation,  $\beta$ 11, confirmed the combined influence of the graphite expansion potential and the ability to utilise it.

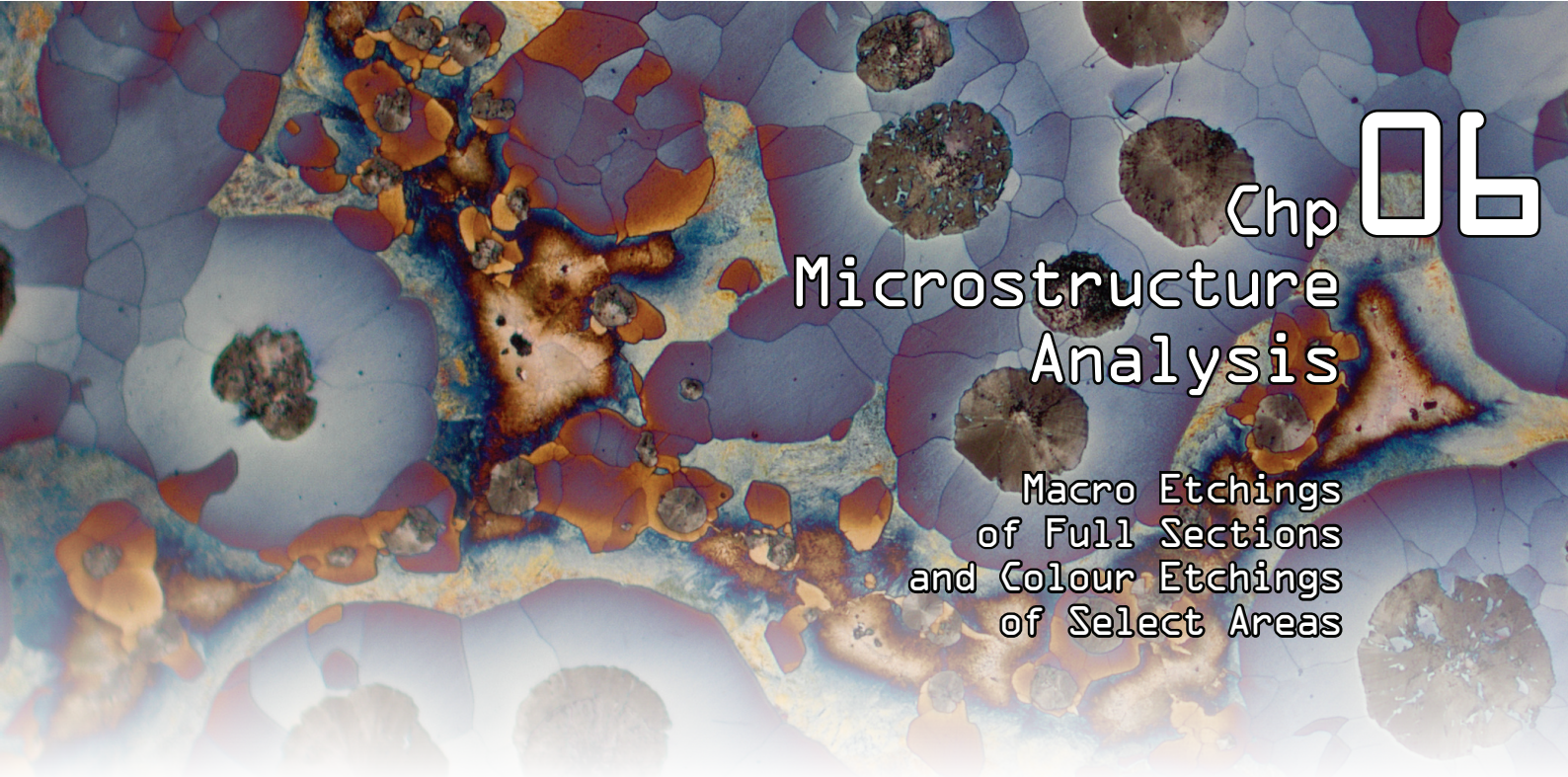
Finally, it should be noted that the exothermic feeders showed indications of liquid shrinkage at the upper part of the feeders. This liquid shrinkage was observed for both the top and the centre feeders. The effect was most pronounced for the  $\alpha$ -alloy, though it was also found in the  $\beta$ -alloy simulations. It is proposed that the exothermic effect itself cause this effect. The feeders sleeves have the same temperature as the surrounding mould when they are filled with the melt. For the insulating feeders, this instant chill may be enough to form a shell that remains throughout the remainder of the solidifications. This shell-forming is not advantages as the encapsulated melt will be more difficult to move due to the vacuum effect of the feeders as described in section 2.3.6, on page 28. The problem can be helped by the application of a William's wedge as described in the same section. It is likely the that exothermic feeders experience the same shell-forming and encapsulation shortly after the filling of the feeder. However, where the insulating and insulating-exothermic feeders retain the shell, the heat transferred to the metal by the exothermic sleeve material remelts the shell, ensuring that the entire melt volume in the feeder remains liquid for a prolonged period. The simulations indicate that the prolonged period is sufficient to manifest liquid shrinkage at the top of the feeder.

## References

- [6] Jakob Olofsson. *Simulation of Microstructure-based Mechanical Behaviour of Cast Components*. School of Engineering, Jönköping University, 2014. ISBN: 978-91-87289-04-0.
- [69] MAGMASOFT 5.2 by MAGMA GmbH. [http://www.magmasoft.com/en/solutions/MAGMA\\_5.html](http://www.magmasoft.com/en/solutions/MAGMA_5.html). Program. 2014.

- [70] Jesper Henri Hattel et al. *Fundamentals of Numerical Modelling of Casting Processes*. Polyteknisk Forlag, 2005. ISBN: 978-87-502-0969-0.
- [111] MAGMASOFT, FOSECO *Sleeve Database*. [http://www.magmasoft.com/en/solutions/MAGMA\\_5.html](http://www.magmasoft.com/en/solutions/MAGMA_5.html). Database. 2012.
- [116] *Founding: Liquid Penetrant Testing—Sand, Gravity Die, and Low Pressure Die Castings*. Norm. 2011.
- [117] Paul Kainzinger. “Utilizing Casting Simulation for the Fatigue Design of Wind Turbine Components”. In: Presented at the International MAGMASOFT User Meeting , Hannover, Germany, 2012.
- [118] MAGMASOFT, FOSECO *Filter Database*. [http://www.magmasoft.com/en/solutions/MAGMA\\_5.html](http://www.magmasoft.com/en/solutions/MAGMA_5.html). Database. 2012.
- [119] *JMatPro by Sente Software Ltd*. <http://www.sentesoftware.co.uk/jmatpro.aspx>. Program.





# Microstructure Analysis

Macro Etchings of Full Sections and Colour Etchings of Select Areas

## Microstructure Analysis

<b>6.1 Introduction</b> . . . . .	<b>89</b>	<b>6.5 Analysis of the Microstructure</b> . . . . .	<b>91</b>
<b>6.2 Macrostructure Analysis</b> . . . . .	<b>89</b>	6.5.1 Comparing the Castings . . . . .	91
6.2.1 Macro Etching . . . . .	90	6.5.2 Solidification and Microstructure . . .	91
<b>6.3 Analysis of the Macrostructure</b> . . . . .	<b>90</b>	6.5.3 Formation of Porosities . . . . .	95
<b>6.4 Microstructure Analysis</b> . . . . .	<b>90</b>	<b>References</b> . . . . .	<b>96</b>
6.4.1 Colour Etching . . . . .	90		



**M**ACRO- and microstructure analysis of the  $\alpha$ - and  $\beta$ -alloys. The chapter covers the initial macro etchings of the sectioned casting samples, and follow-up with a description of the process of colour etching using picric acid. The chapter is concluded with a short analysis of the formation of the observed porosities.

Keywords: . . . . . Macro Etching, Colour Etching, Picric Acid, Segregation, Feeding Effects, Porosities, Si.

Chapter findings reported in: . . . Supplement II, on page 315  
Supplement III, on page 325

### 6.1 Introduction

**T**HE previous chapters have shown that the disc castings, depending on alloy composition, produce a varying amount of porosities. The entire sectioned plane of the casting was macro etched, and selected areas (called sections) were cut out and colour etched. This was done to analyse the microstructure of the two different alloys used in the experiment; the low Si  $\alpha$ -alloy (EN-GJS-500-7), and the high Si  $\beta$ -alloy (EN-GJS-450-10). The alloy composition influence the segregation and solidification of the castings, and in turn the feeding efficiency.

### 6.2 Macrostructure Analysis

**T**HE macrostructure analysis was conducted for three purposes: (1) to confirm that the  $\alpha$ -alloy castings were ferritic-pearlitic and that the  $\beta$ -alloy castings were fully ferritic, (2) it should show the macrosegregation of the  $\alpha$ -alloy castings to indicate solidification patterns, and (3) to aid in identifying the sections of interest for further investigation.

Lamellar Graphite Iron (LGI), Manganese (Mn), Phosphorus (P), Spherical Graphite Iron (SGI), Silicon (Si)

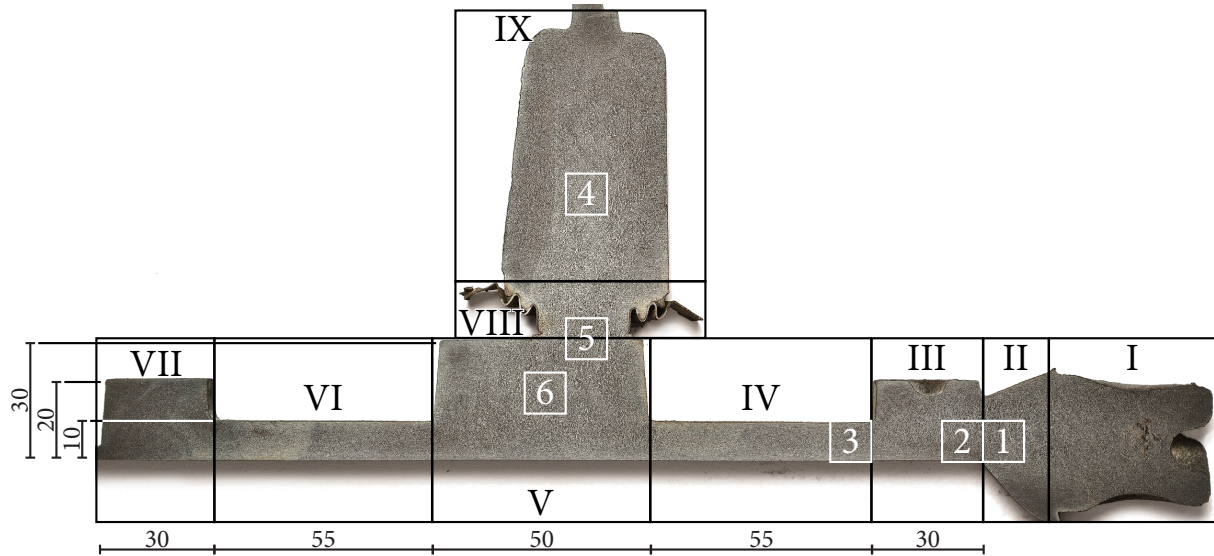


**Figure 6.1:** Overview of sectioned casting a11A. Etched with 1% Nital for ~600s. The casting is divided into nine non-overlapping sections (Roman numerals) for quantification and analysis of porosities. Six sections (Arabic numerals) of 10 x 10 mm were cut and color etched. All measurements are in mm.

### 6.2.1 Macro Etching

Following the liquid penetrant test, all the sectioned casting samples were planar ground once more. The newly ground samples were then etched in a 1 % Nital etchant—99 ml Ethyl alcohol and 1 ml Nitric acid ( $\text{HNO}_3$ ). Each sample was etched for ~600s at 20°C. After etching the castings were cleaned with ethanol and left to dry in a convection oven at 110°C for ~1800s. The macro etched castings were analysed using a magnifying glass.

One of the macro etched castings,  $\alpha$ 11A is seen in fig. 6.1.

### 6.3 Analysis of the Macrostructure

THE Nital etching of the high Si  $\beta$ -alloy had little or no effect. This outcome was as expected; but confirmed that all the  $\beta$ -alloy castings were indeed fully ferritic, with very little or no amount of pearlite.

The analysis of the pearlitic-ferritic  $\alpha$ -alloy showed evenly distributed pearlite in all areas of the castings. Dendrite structures were visible to the naked eye in areas I, II, III, V, VIII and IX. See fig. 6.1. Areas IV, VI and VII did not have visible dendritic structures. All  $\alpha$ -castings showed clear signs of directional dendrite growth across areas I, II and III. The dendrites in areas V, VIII and IX did not show a clear direction of solidification.

Based on the investigation of the macrostructure of the  $\alpha$ -alloy castings, six areas were selected for further analysis. The amount was chosen as a compromise between the regions of interest to the study, the number of castings that had to be included in the analysis, and the number of samples that reasonably could be etched and analysed. The six areas chosen are shown in fig. 6.1 and was selected based on the area related to the feeding paths of the top and centre feeder.

### 6.4 Microstructure Analysis

THE selected sections were cut from the selected castings, and the samples were all mounted and polished. In total nine castings were analysed, divided by two sessions. Initially, castings  $\alpha$ 23C,  $\alpha$ 11C, and  $\beta$ 23C were etched and analysed for all six sections. Subsequently castings  $\alpha$ 23C,  $\alpha$ 11C,  $\alpha$ 20C,  $\alpha$ 00C,  $\beta$ 23C,  $\beta$ 11C,  $\beta$ 23sC,  $\beta$ 11sC,  $\beta$ 22sC, and  $\beta$ 20 were etched and analysed for selected sections.

#### 6.4.1 Colour Etching

The samples were colour etched with picric acid—50 ml Distilled water, 10 g Sodium hydroxide (NaOH), 40 g Potassium hydroxide (KOH) and 10 g Picric Acid ( $\text{C}_6\text{H}_3\text{N}_3\text{O}_7$ ). This etchant was first

proposed by Motz in 1988 [120], albeit other similar picric etchants have also been developed [121]. After mixing the mounted and polished pieces were etched at 105 °C. Most pieces required an etching time around 330s, but some required more.

Each piece was analysed in an optical microscope after etching and then etched again if the etching was not fully developed. This approach was to prevent over-etching of the samples. An over-etched sample had to be polished anew and etched again. The etching process has a narrow window between not fully developed and over-etched. Thus, the etching time should be controlled within this window. Timing the submersion of the sample is simple; however, the required etching time depends on the sample size, if it is mounted, and the age of the etchant. This hard to control process means that, even for similarly sizes and mounted samples, the required submersion time changes as the etchant ages and becomes in-reactive. For large samples it may not be possible to achieve an acceptable etching on the entire sample; either the centre will be under-developed, or the edges will be over-etched.

Motz's picric etchant is interesting concerning cast iron because it is sensitive to Si segregation. Combined with Si's affinity with austenite this etchant can reveal austenite patterns in the cast iron microstructure. For the  $\alpha$ - and  $\beta$ -alloy this is particularly interesting as the main difference between the two alloys is the Si-content. Note that Motz's picric etchant is also capable of showing P segregations, though the P content of both the  $\alpha$ - and  $\beta$ -alloys was low. See table 4.2 on page 68. Another aspect of the picric based colour etchants is that they are more sensitive to grain orientation and other segregation effects, compared with eg Nital etchant. As a result grains and segregation effects become visible on the etched sample.

The colours, or tint, comes from an optical interference phenomenon, where the thickness of the thin film layer on top of the sample changes the refraction of the light. Subsequently, the thickness of the thin film layer determines the reflected tint. The etchant colours different sections of the sample in different tints based on the growth rate of the thin film. Thin films of  $<0.04\ \mu\text{m}$  are too thin to create an optical tint. Thin films of  $\geq 0.5\ \mu\text{m}$  are too thick to provide colourisation [121]. Thin films between  $0.04\ \mu\text{m}$  to  $0.5\ \mu\text{m}$  is where the etchant tints the sample; hence the etching time should be adjusted, as best possible, accommodate this. Reproducing the same etching, even of the same sample, requires

skill and practice which is also a challenge regarding automation of the process.

Note of warning: Picric acid must be handled with extreme care as it is carcinogenic and toxic in case of both inhalation and skin contact. Additionally, picric acid is also explosive by stroke, friction, fire or ignition.

A detailed guide for colour etching cast iron with picric acid is found in appendix A, on page 296. For further information, the reader is referred to the work of Vazehrad et al [121, 122].

## 6.5 Analysis of the Microstructure

DIFFERENT etchants can enhance different microstructural elements in a range of different ways [123, 124]. Hence, it is important to illustrate which parts of the etched sample is which phase. See fig. 6.2 on the next page.

### 6.5.1 Comparing the Castings

Comparing the microstructures of the  $\alpha$ - and  $\beta$ -alloys it was seen that the  $\beta$ -alloy display a greater nodule count. All three castings displayed good nodularity in all of the etched sections. The thin-walled section (3) showed directional solidification from the edge and towards the centre of the section. Dendrites were found in sections 3, 4, 5 and 6 for the  $\alpha 23\text{C}$ ,  $\alpha 11\text{C}$ , and  $\beta 23\text{C}$  castings. See fig. 6.3 on page 93. Dendrites were not identified in the etchings of section 1 and 2.

$\alpha 23\text{C}$  and  $\beta 23\text{C}$  with the exothermic feeder sleeves contained a significant fraction of low Si eutectic segregation in section 6.  $\alpha 11\text{C}$  with the insulating sleeves, showed a substantial fraction of low Si eutectic segregation in sections 3, 4 and 5. Furthermore, sections 4 and 5 for castings  $\alpha 23\text{C}$  and  $\beta 23\text{C}$  showed an alignment of the graphite nodules according to the dendritic structure, while the same section for  $\alpha 11\text{C}$  was less orderly and displayed a more substantial fraction of non-linearised nodules. For section 6 none of the three castings showed a high degree of linearised nodules.

### 6.5.2 Solidification and Microstructure

The greater nodule count in the  $\beta$ -alloy cannot be contributed to the difference in alloying elements. Increased Mn content can increase the nodule count, but the  $\beta$ -alloy has a lower Mn content than the  $\alpha$ -alloy, and should thus have a lower nodule count.

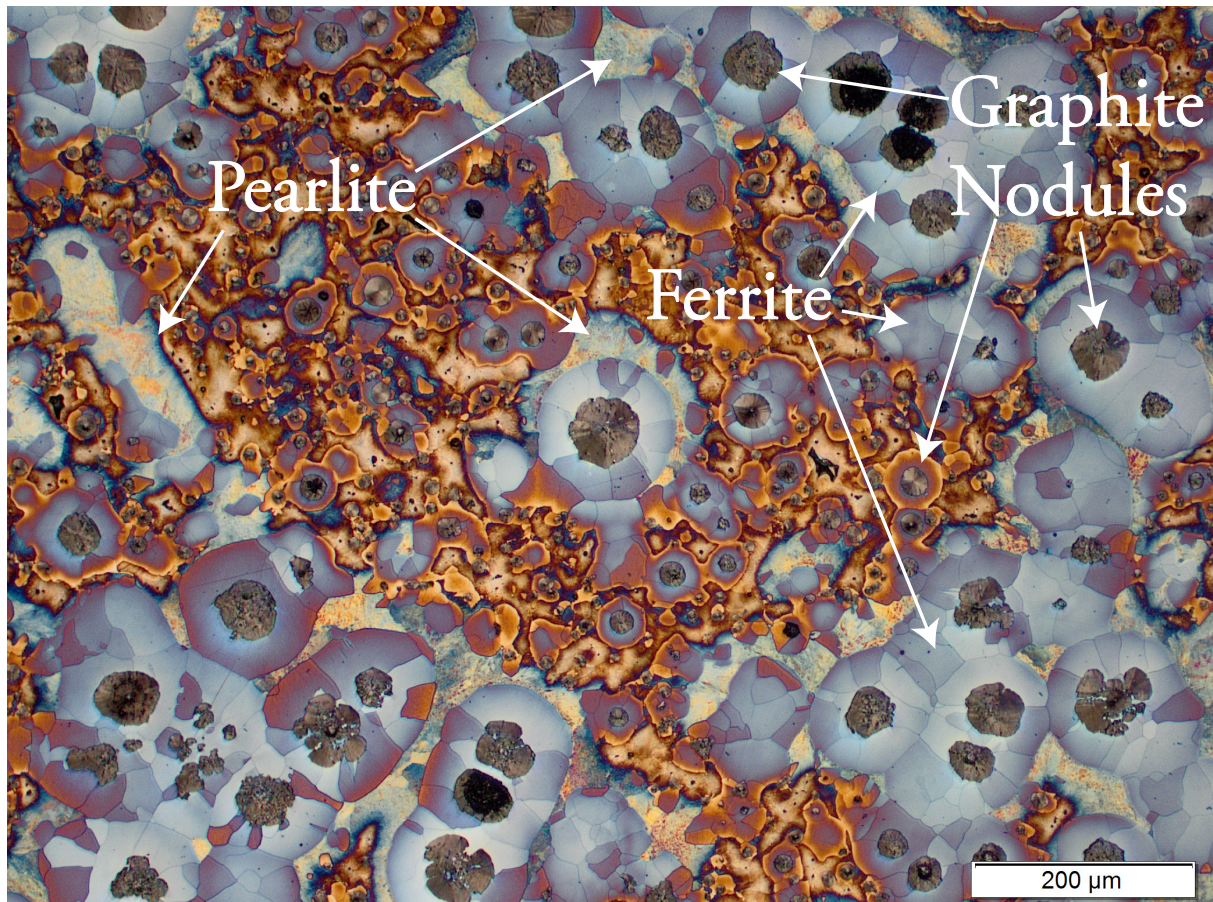


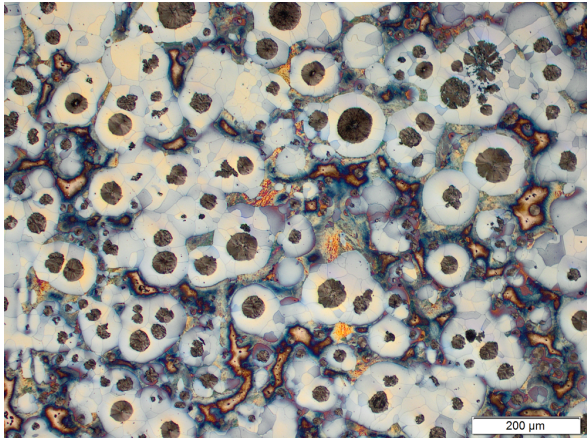
**Figure 6.2:** Overview of the different microstructures made visible by colour etching with Motz's picric acid. Pearlite, ferrite, and graphite nodules are located in the microstructure. The areas with bluish tint are high on Si. The low Si areas have an orange-brown tint, and these areas are the last to freeze.

However, the two alloys were cast at different dates, and the inoculation procedure may have changed in between. It is also reasonable to assume that different inoculations settings were deliberately used due to the demand for a 95 % ferritic structure in the  $\beta$ -alloy castings.

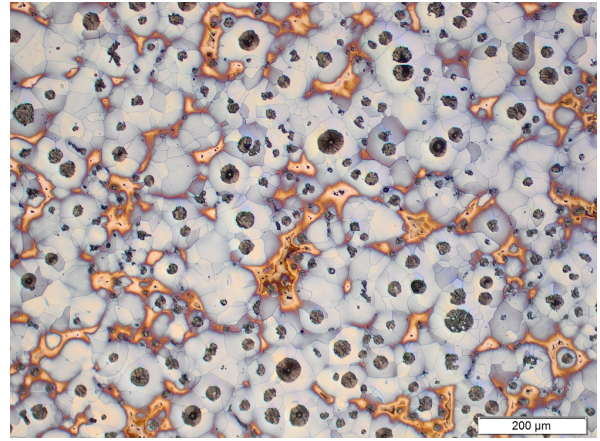
The castings with the exothermic feeder sleeves ( $\alpha$ 23C and  $\beta$ 23C) both showed a significant fraction of low Si eutectic solidifying in between the nodules at the boss (6). The insulating sleeves showed the opposite effect, having low Si eutectic at the feeder neck and in the feeder itself. In supplement II on page on page 315 it was speculated that this phenomenon might be explained by the delayed graphite expansion of the exothermic feeders. The boss section (V) would have expanded and squeezed out part of the low Si eutectic, after which the graphite expansion in the feeder (IX) would push back the last to freeze melt—the low Si eutectic.

However, as is also mentioned in the supplement II, the etchings are very sensitive to etching time, and the lack of brown areas in section 6 of  $\beta$ 11C may be due to under-etching, and that additional etchings should be performed and analysed before conclusions were made. See fig. 6.4 on page 94. Hence, the subsequent etchings showed that the observed effect was indeed related to etching time rather than a solidification effect.

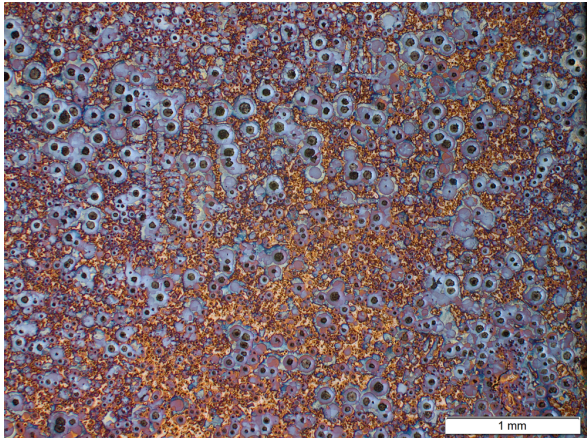
In supplement II, on page 315, it was also speculated that the higher tendency to shrink could be found in the fact that the  $\beta$ -alloy had an improved inoculation procedure. Elmquist et al had previously shown that over-inoculation could increase the primary graphite expansion in LGI and potentially cause increased shrinkage [43]. It was later found that over-inoculation influences SGI differently. For highly inoculated SGI, the increased



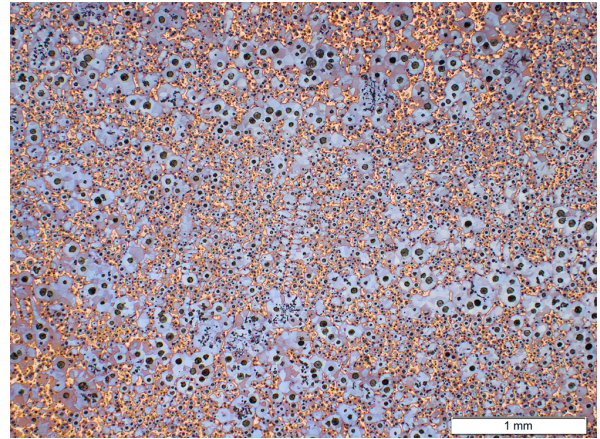
(a)  $\alpha$ -alloy; microstructure from section 3 [ $\times 10$ ]



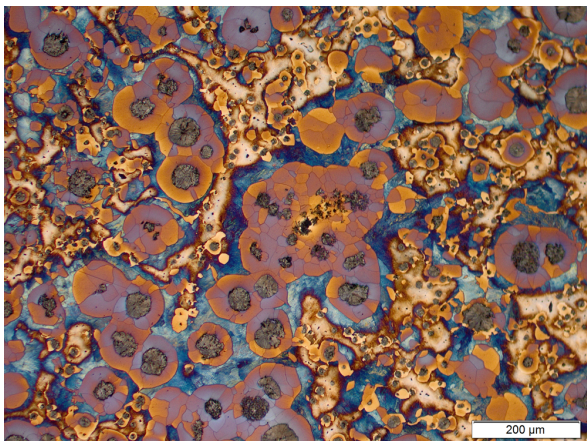
(b)  $\beta$ -alloy; microstructure from section 3 [ $\times 10$ ]



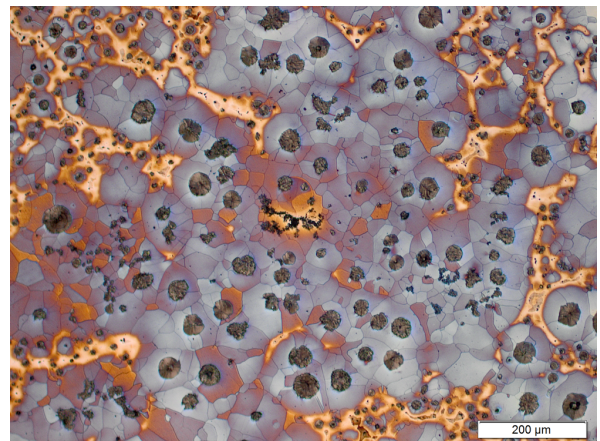
(c)  $\alpha$ -alloy; microstructure from section 4 [ $\times 2.5$ ]



(d)  $\beta$ -alloy; microstructure from section 4 [ $\times 2.5$ ]

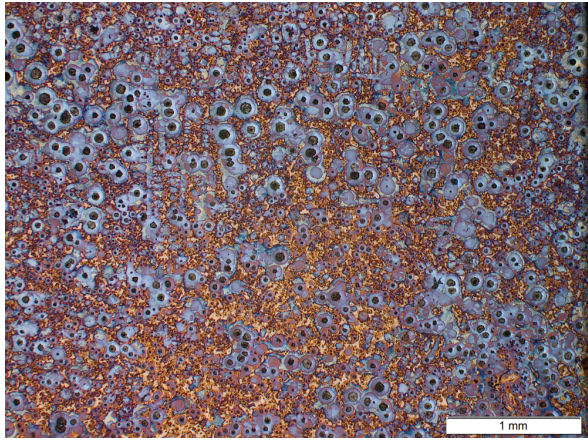


(e)  $\alpha$ -alloy; microstructure from section 4 [ $\times 10$ ]

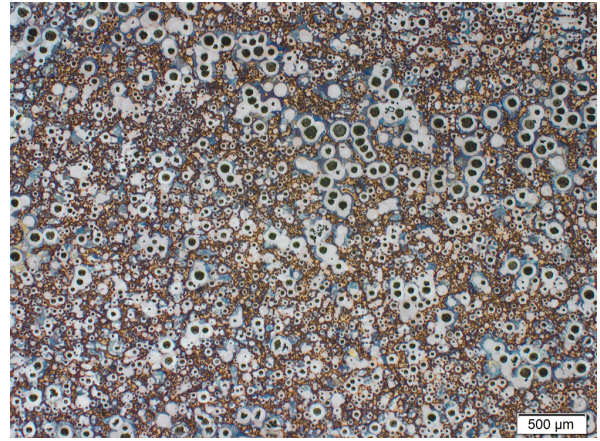


(f)  $\beta$ -alloy; microstructure from section 4 [ $\times 10$ ]

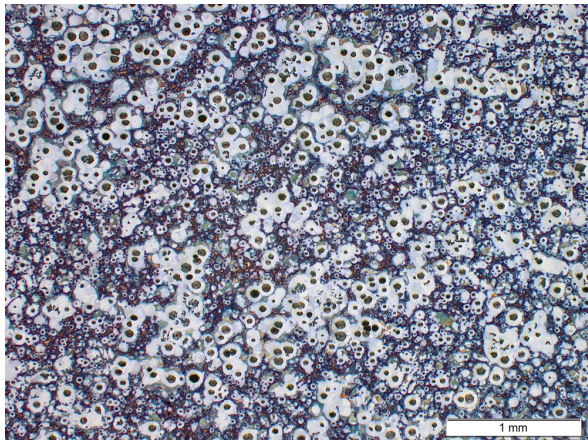
**Figure 6.3:** Microstructures from castings  $\alpha 23C$  (a,c) and  $\beta 23C$  (b,d). Both castings were made with an insulating-exothermic top feeder and an exothermic centre feeder. Microstructures (a) and (b) were from the thin-walled section at the vertical centre line just below the upper ring. Microstructures (c), (d), (e), and (f) were from the centre of the boss section.



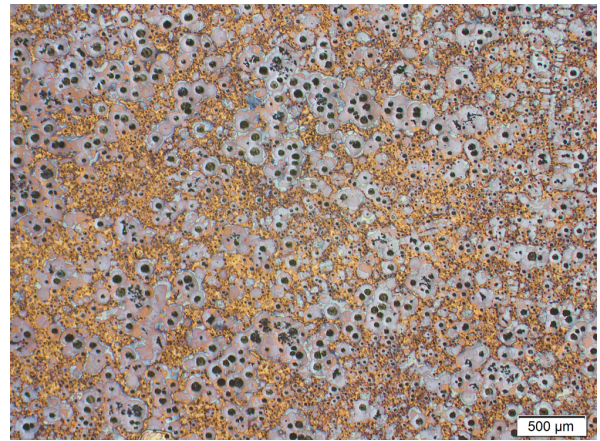
(a)  $a_{23}C$ , section 6, first etching [ $\times 2.5$ ]



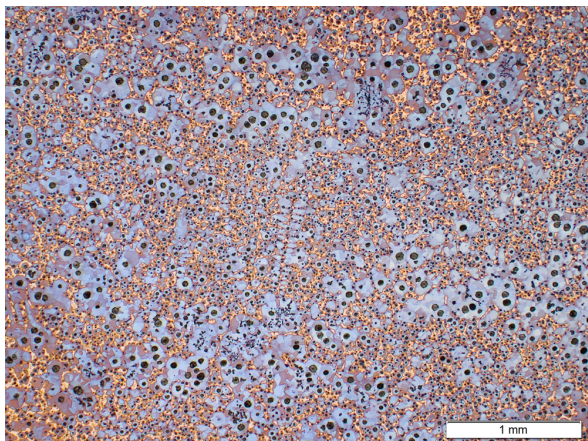
(b)  $a_{23}C$ , section 6, second etching [ $\times 2.5$ ]



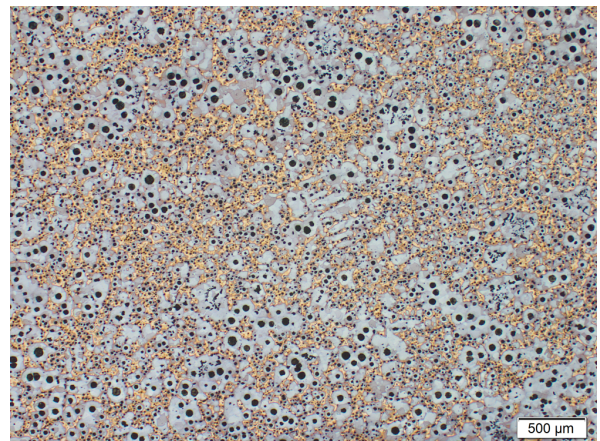
(c)  $a_{11}C$ , section 6, first etching [ $\times 2.5$ ]



(d)  $a_{11}C$ , section 6, second etching [ $\times 2.5$ ]

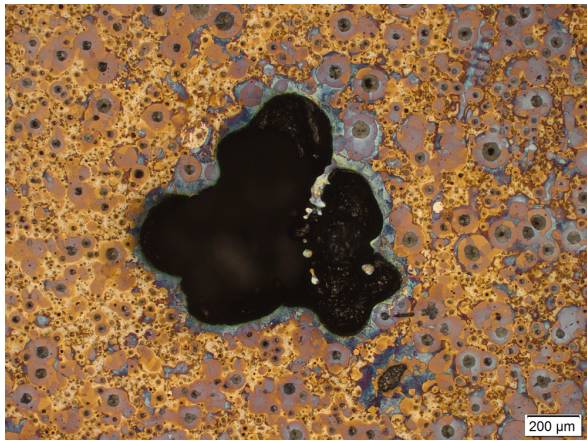


(e)  $\beta_{23}C$ , section 6, first etching [ $\times 2.5$ ]

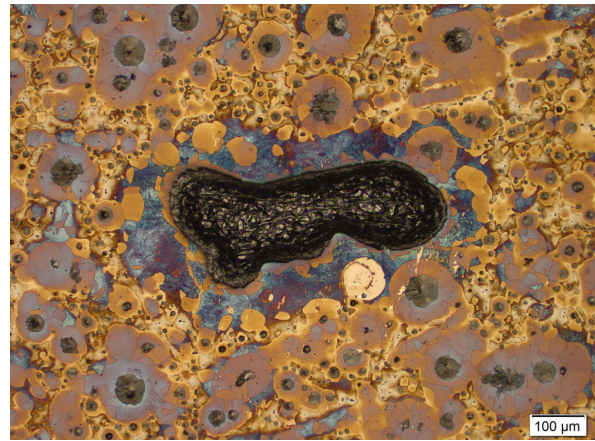


(f)  $\beta_{23}C$ , section 6, second etching [ $\times 2.5$ ]

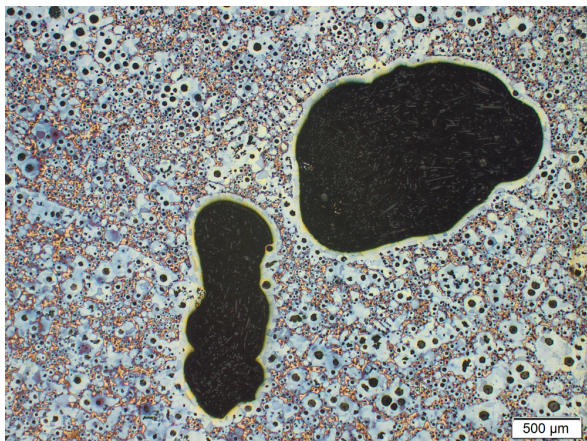
**Figure 6.4:** Comparison of the first and second etching of the boss section (6) of the  $a_{23}C$ ,  $a_{11}C$ , and  $\beta_{23}C$  castings. First etching on the left, and second etching on the right.



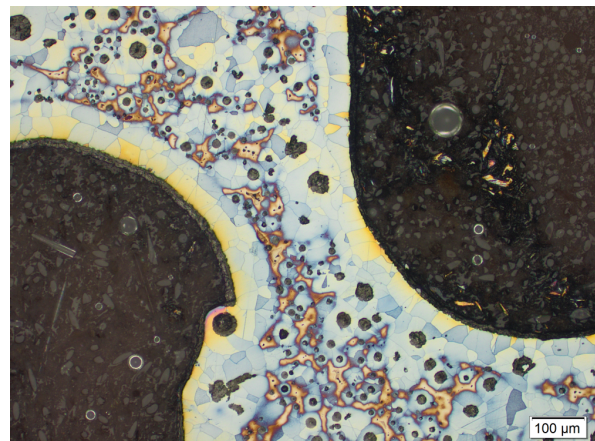
(a) a20B, section 6 [ $\times 5$ ]



(b) a20B, section 6 [ $\times 5$ ]



(c)  $\beta 11C$ , section 4 [ $\times 2.5$ ]



(d)  $\beta 11C$ , section 4 [ $\times 10$ ]

**Figure 6.5:** Porosity microstructure from the boss section (4) and the centre feeder section (6).

nodule count caused by the inoculation eases the precipitation of graphite from the melt, which in turn reduces the constitutional undercooling. The constitutional undercooling subsequently limits the distance the graphite excreted from the austenite at the eutectoid phase transformation had to travel; which increases the likelihood that the graphite will precipitate to the existing nodules, rather than form pearlite [42]. The formation is described in detail in section 8.3.1, on page 126.

While under-inoculation will result in a decreased graphite expansion, over-inoculation can advance the occurrence of the graphite expansion resulting in a decreased expansion later in the process. Additionally, if the mould and solidified shell of the casting cannot contain the expansion from the graphite, the effect may cause dilation of the mould

cavity and subsequently result in massive porosities. Mould dilation is shown in fig. 2.14 on page 28. The subject is discussed further in section 13.8.7, on page 261.

Thus, the colour etchings of the six different areas of each of the various castings show no indication that the material of the exothermic sleeves has any influence on the casting microstructure, except what would be expected by an increased modulus and prolonged solidification time.

### 6.5.3 Formation of Porosities

Comparing the formation of porosities for the two different alloys, it was found that the 'shell' formed around the cavity was different. See fig. 6.5. The  $\alpha$ -alloy showed porosities completely surrounded by

pearlite, while the high Si  $\beta$ -alloy had a similar type of shell, but fully ferritic.

The smooth shell indicates that the porosities were formed in the melt before final solidification. One suggestion, made by Campbell, is that these types of porosities are caused by bi-films in the melt [24]. Bi-films, however, is not as common in cast iron as in light metals. The porosities can also be explained as the gas porosities, which have possibly nucleated on inclusions in the melt, as described in section 2.2.1, on page 17. The shape of the porosities indicates that they are formed in the semi-solidified mushy zone, as their irregular shapes suggest that the surrounding melt has been structured enough to shape the porosities. These irregular shapes are opposed to gas porosities formed in the entirely liquid melt which is often very close to spherical. The porosities are sized in the range between micro- and macroporosities. Hence, if they have formed as interdendritic porosities as described by Stefanescu and Carlson and Beckermann [26, 100], then they have grown significantly from there. This growth mechanism, however, is possible as gas in the melt can more easily expand an existing pore, rather than create a new, as long as the diffusion distance for the gas is not too long.

In any case, the colour etchings do not reveal the cause of the porosity formation. However, it is almost certain that a rupture has occurred in the melt as an effect of tension that overloaded the cohesiveness of the melt, weakened by impurities or not. This phenomenon is described in section 2.2.1, on page 17 and discussed further in section 13.8.8, on page 262.

## References

- [24] John Campbell. *Casting Practice - The 10 Rules of Casting*. Linacre House, Jordan Hill, Oxford OX2 8DP, 30 Corporate Drive, Burlington, MA 01803: Elsevier Butterworth-Heinemann, 2004. ISBN: 0 7506 4791 4.
- [26] DM Stefanescu. “Computer Simulation of Shrinkage Related Defects in Metal Castings—A Review”. In: *International Journal of Cast Metals Research* 18.3 (2005), pp. 129–143.
- [42] Q.M. Chen, E.W. Langer and P.N. Hansen. “Influence of the Process Parameters on the Volume Change during the Eutectic reaction of SG Cast Iron: A Computer Simulation”. In: *Journal of Materials Science* 32.5 (1997), 1239–1248. ISSN: 0022-2461. DOI: {10.1023/A:1018592120197}.
- [43] Lennart Elmquist, Attila Diószegi and Tobias Björklind. “On the Formation of Shrinkage in Grey Iron Castings”. English. In: *Key Engineering Materials* 457 (2011), pp. 416–421.
- [100] Kent D Carlson and Christoph Beckermann. “Prediction of Shrinkage Pore Volume Fraction Using a Dimensionless Niyama Criterion”. In: *Metallurgical and Materials Transactions A* 40.1 (2009), pp. 163–175.
- [120] J. M. Motz. “Microsegregations easily unnoticed influencing variable in the structural description of cast materials”. In: *Prac.Met.* 25.6 (1988), pp. 285–293.
- [121] Sadaf Vazehrad, Jessica Elfsberg and Attila Diószegi. “Study on microstructure in cast iron using color etching and electron microprobe analysis”. English. In: *Materials Characterization* (2015). DOI: {10.1016/j.matchar.2014.09.008}.
- [122] Sadaf Vazehrad. *A Study on Factors Influencing the Microstructure and Shrinkage Porosity Formation in Compacted Graphite Iron*. School of Engineering, Jönköping University, 2014. ISBN: 978-91-7595-275-8.
- [123] Françoise Condet and Alain Reynaud. *Metallographic Atlas of Cast Iron*. ETIF, 2007.
- [124] Janina M. Radzikowska. *Metallography and Microstructures of Cast Iron*. ASM International.



## Deformation Measurements

### Casting Deformation and Measurement Uncertainty

#### Deformation Measurements

<b>7.1 Quantifying Surface Shrinkage</b> . . . . .	<b>97</b>	<b>7.2.3 Conclusions</b> . . . . .	<b>112</b>
7.1.1 Initial Deformation Analysis . . . . .	98	<b>7.3 Measurement Uncertainty</b> . . . . .	<b>113</b>
7.1.2 Deformation Prediction and Simulation	98	7.3.1 Data Validation . . . . .	113
7.1.3 Quantifying Measurement Results . . . . .	102	7.3.2 Measurement Uncertainty . . . . .	117
7.1.4 Setup, Equipment, and Procedure . . . . .	103	7.3.3 Normalised Error Analysis . . . . .	119
<b>7.2 Deformation Analysis</b> . . . . .	<b>104</b>	7.3.4 Conclusions . . . . .	120
7.2.1 Deformation Characterisation . . . . .	105	<b>References</b> . . . . .	<b>121</b>
7.2.2 Statistical Deformation Analysis . . . . .	109		

» DESCRIPTION of surface shrinkage and the methods to detect this type of casting defects. The chapter covers the measurement setup and results from the CMM measurements alongside the analysis of the casting deformation. The analysis is assisted by a complete uncertainty budget for the measurements.

Keywords: . . . . . Deformation Measurements, CMM, Uncertainty Budget, Statistical Evaluation of Deformation, Casting Thickness Variation.

Chapter findings reported in: . . . Supplement I, on page 301  
 Supplement II, on page 315  
 Supplement III, on page 325

#### 7.1 Quantifying Surface Shrinkage

AS shrinkage of the metal during solidification can cause internal porosities in the casting, the same process can also cause external shrinkage or surface shrinkage. Whether or not this happens, depends on the shell forming abilities of the casting, as described in section 2.2.1, on page 17. The quantification of the internal porosities was described in chapter 5, on page 75.

The external shrinkage, though, cannot be quantified using the same methods as were used to quantify the internal porosities.

The internal shrinkage defects can be identified

---

Computer Aided Design (CAD), Coordinate Measurement Machine (CMM), Computer Numerical Control (CNC), Degrees of Freedom (DoF), Maximum Permissible Error (MPE), Normal Probability Plot (NPP)

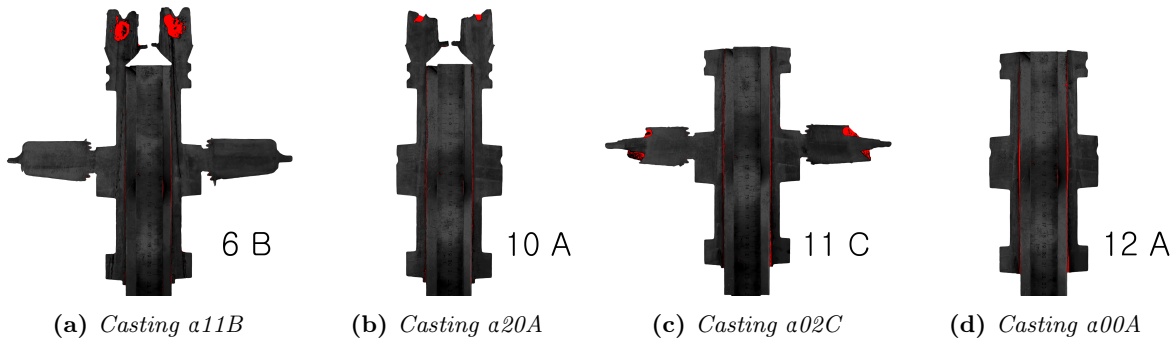


**Figure 7.1:** Overview of the surface shrinkage analysis performed on the sectioned castings. Subfigures (a) to (d) shows the different feeder combinations. The analysis show shrinkage/deformation (red), however, precise quantification was not possible to achieve based on these images. The images were processed using a digital image filter to enhance the contrast between the casting and the area with surface shrinkage. It is the digital filter that gives the black and red colours to the images.

as porosities, smaller or larger, within a material that should be solid or fully dense. External shrinkage defects are otherwise difficult to identify and quantify. The external shrinkage defects appear as differences between the geometry that should have been, and the actual geometry. In this case the geometry that should have been was not the CAD-geometry of the pattern, the shape of the mould before casting, nor even the mould after casting.

Surface shrinkage is defined as the volumetric difference between the actual casting and an identical casting without surface shrinkage. The reference casting geometry is defined as the casting would look without any deformation—de facto a scaled-down version of the pattern, scaled down according to the solid shrinkage of the material from the solidus temperature to 20 celsius. The CAD-geometry allowing for pattern makers shrinkage.

The reference casting geometry, though, cannot be cast without special control of the solidification and cooling of the casting. The solidification sequence and phase transformations during cooling and the subsequent residual stresses is what creates the deformations in the castings. See section 3.5, on page 58.

In practice, comparing the casting's geometry with the geometry of the CAD-model partly solves the comparison problem. However, it is essential to keep in mind that the filling, cooling, solidification, solid-state phase transformation, and shake-out all influence of the casting geometry. Thus, smaller or larger deformations found on the casting were not surface shrinkage but rather the result of the overall process itself.

### 7.1.1 Initial Deformation Analysis

It was found that  $\alpha 00B$  had no porosities at the sectioned plane at the boss area, despite that no feeders were used for this casting. The surface of the reverse side of the casting, however, had a clear indentation at the boss. Later ultrasound analyses, however, also showed that porosities could indeed be found in the boss section.

Still, the force of the contracting melt was stronger than the already solidified shell; hence shrinkage of the contracting melt was compensated by a collapse of the casting's volume rather than by internal porosities. As described in chapter 2, on page 13 the alloy composition influence the shell forming of the casting, and thus also the tendency to have shrinkage defects internally or externally.

Initially, all of the sectioned castings were mounted alongside a straight line and photo documented. The images were then enhanced digitally and the castings analysed. See fig. 7.1. The investigation showed that all of the casting surfaces had sunken in at the otherwise plane reverse side of the casting. On the other hand, the investigation gave no accurate measure to the amount of deformation or how it was distributed across the casting. Another type of deformation measurement was needed, and a better understanding of the deformation mechanisms governing the casting.

### 7.1.2 Deformation Prediction and Simulation

Having established that the reverse surface of the castings all curved inward, with the reverse side of

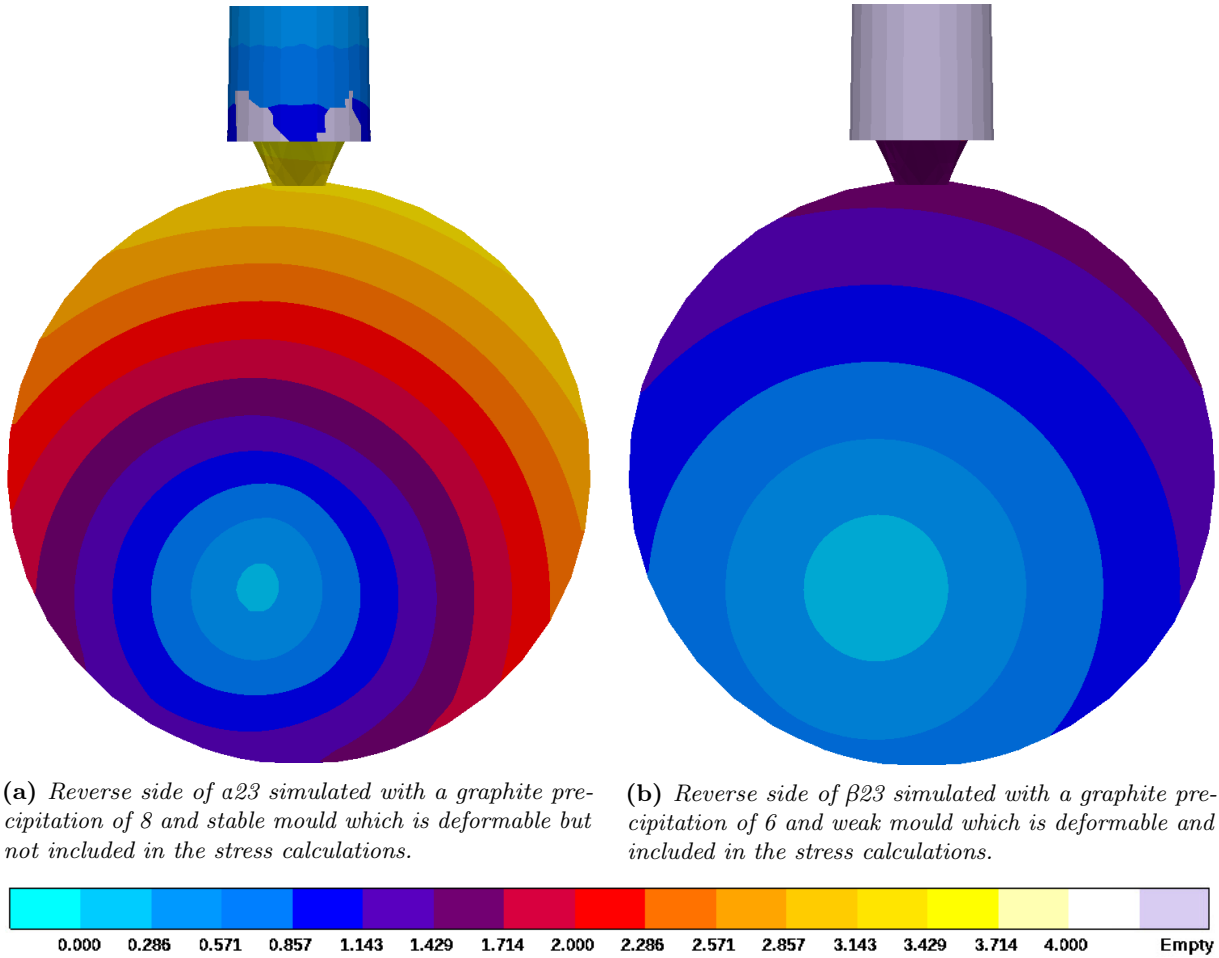


**Figure 7.2:** Comparison of the simulated total displacement of castings a23 and  $\beta$ 23. The displacement is relative to the global coordinate system used during the simulation. The gating system was also included in the simulation, though not shown here. Scale in mm.

the boss section as the, lowers area, it was sought to establish how the casting geometry was expected to look after solidification, cooling, and resulting phase transformations.

It was expected that the thermal centre at the front of the casting would weaken this side of the casting. The thermal centre was created by a combination of the outer ring, the centre boss, and if present, the centre feeder. All three sections and feeders heat the front of the casting—where the reverse side is entirely free of similar heat centres.

The thermal strain,  $\epsilon^{Th}$ , reacting on casting during solidification and cooling, is constrained by the mould, in turn building a corresponding stress,  $\sigma$ , within the casting. The amount of stress and deformation is dependent on the firmness of the constraint. See section 3.5 on page 58. Some constraint

may come from the geometrical interlocking of the overhang of the outer ring. However, besides this, the casting geometry is only constrained by the gating system and possibly the feeders. In this case the feeder is assessed to provide a minimum of constraints to the casting. Remaining is the firmness of the mould itself, which also play a role. Green sand moulds are considered as a type of mould that provides a minimum of rigidity [125]. This limited rigidity is in part related to the drying out of the sand, as a consequence of the heat from the melt.

To confirm the expectation of a forward folding of the disc casting, as a consequence of the thermal fields, the deformation of the castings were simulated using MAGMASOFT. The simulations were set up the solutions space within which the castings were produced—meaning that the extremes were

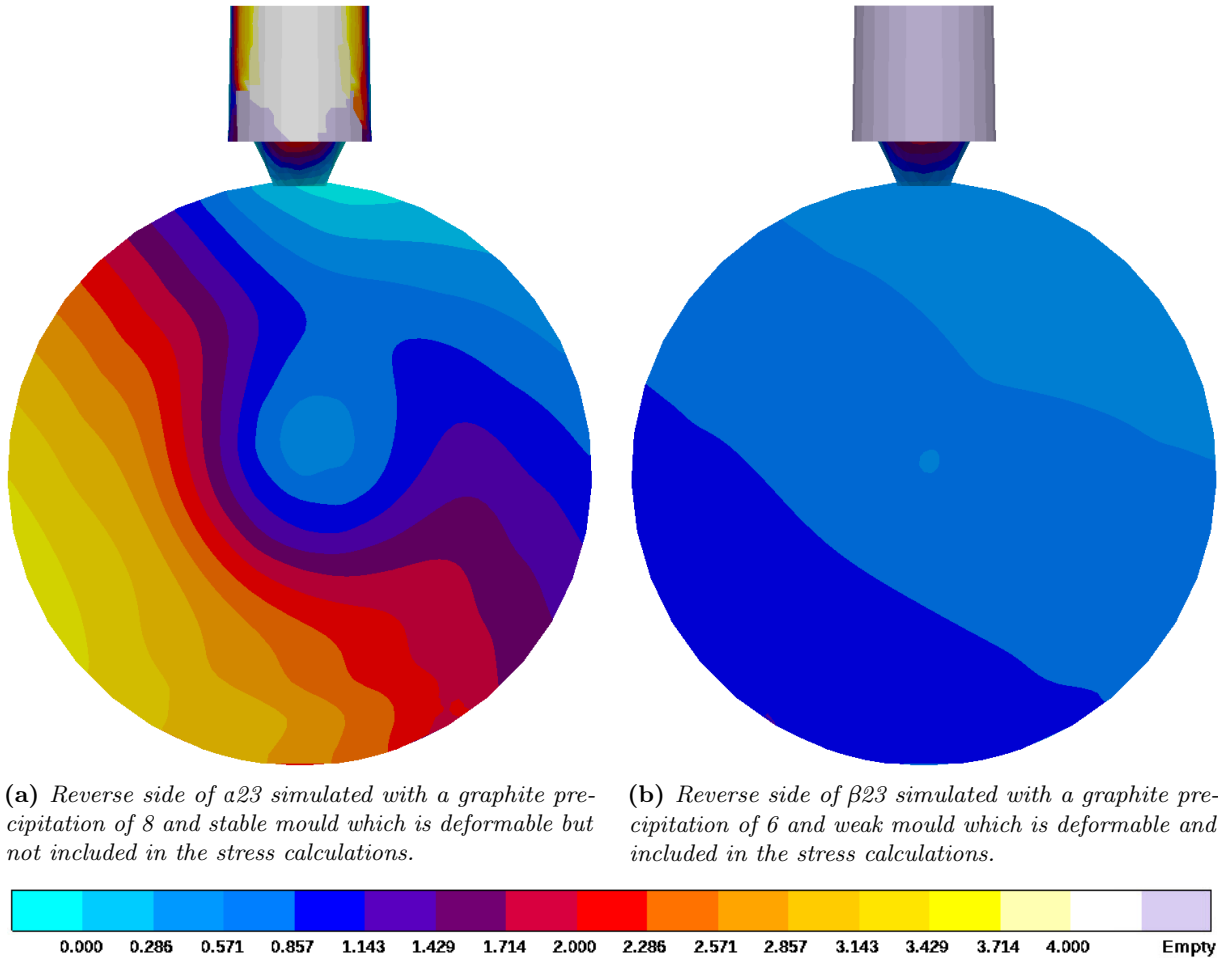


**Figure 7.3:** Comparison of the simulated displacement in the  $y$ -direction of castings  $\alpha 23$  and  $\beta 23$ . The displacement is relative to the global coordinate system used during the simulation. The gating system was also included in the simulation, though not shown here. Scale in mm.

simulated to ensure that no combinations would yield an inward curving reverse side of the casting. The parameters analysed were; alloy ( $\alpha$ - or  $\beta$ ), stable or weak mould, and stress simulation of the mould itself or not. The results are presented in fig. 7.2 on page 99, which shows the total displacement of the two castings— $\alpha 23$  and  $\beta 23$ —at ambient temperature. Total displacement means the sum of displacements in all three spatial directions ( $x,y,z$ ). Note that the displacement is relative to the overall location of the CAD geometry—corresponding to the pattern—with reference to the global coordinate system used in the simulation. Hence, the displacement shown in the simulations include pattern makers shrinkage as well as the displacement of the gating system.

Figures 7.2a and 7.2b on page 99 show the dis-

placement in mm relative to the global coordinate system, as viewed from the reverse side of the casting. Note that the reverse side of the casting is set up as part of the  $x$ - $z$  plane; thus the displacement shown is relative to the original reverse surface from the pattern, with origo at the centre of the casting. The figures show that for both simulations, an area at the lower left corner has remained in the same place as at the beginning of solidification. All other parts of the casting have contracted towards this location. That the centre of contraction is not the centre of the castings is due to the gating system, which is not shown in the figure. The gating system has, though, been included in the simulations.

The deformation in the  $x$ - and  $z$ -directions, however, make the analysis of the deformation of the reverse side itself difficult. Thus, fig. 7.3 shows the

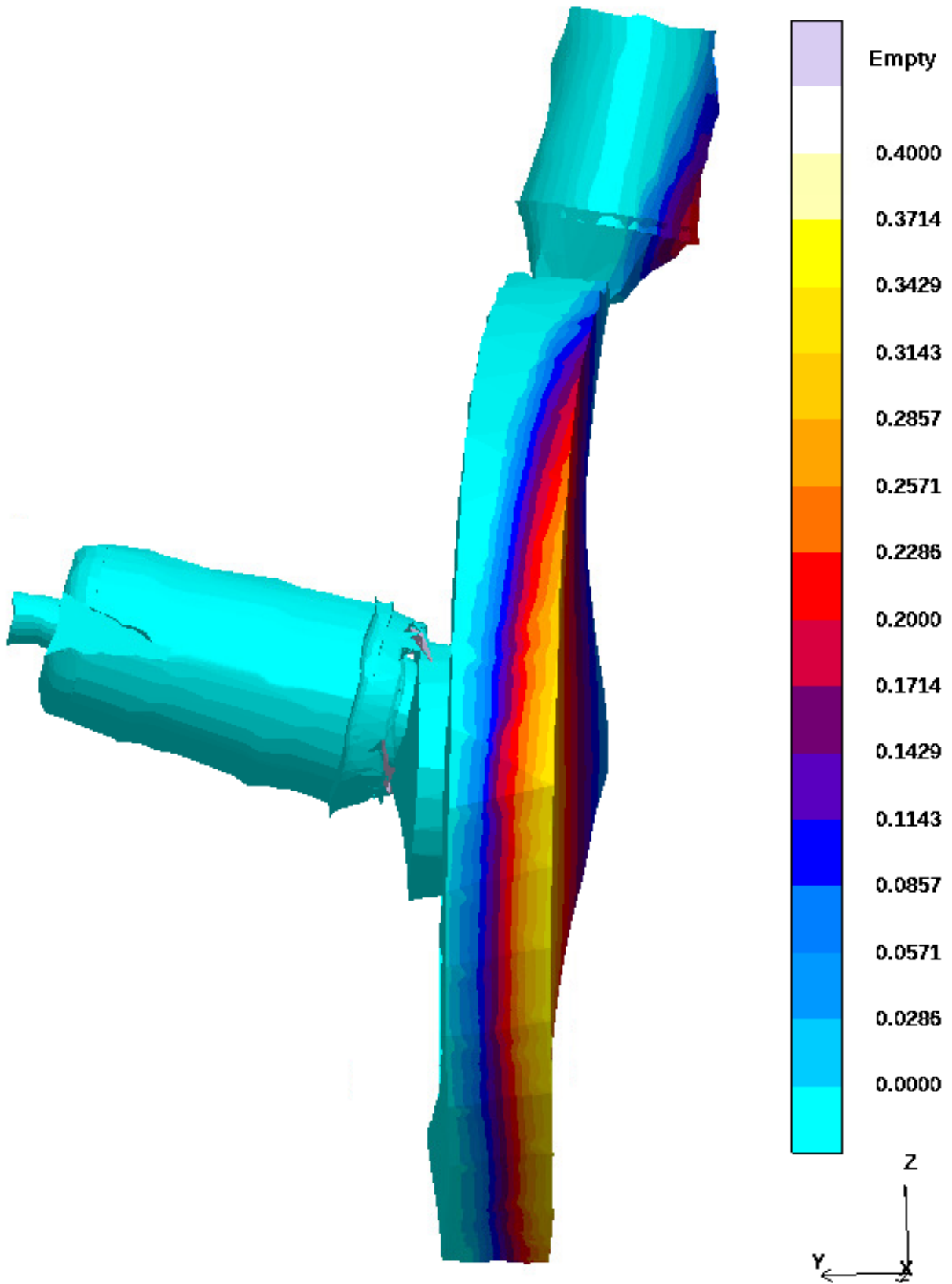
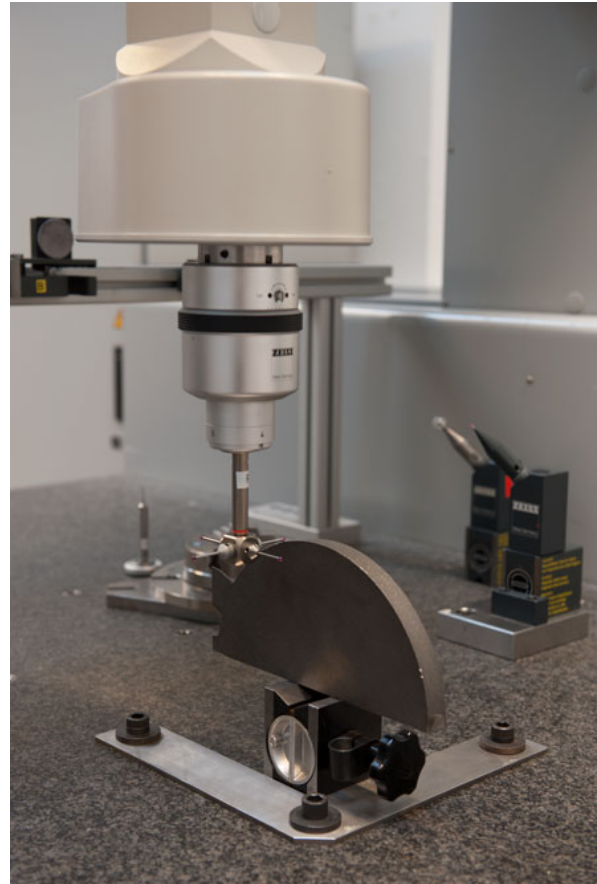


**Figure 7.4:** Displacement in the y-direction of castings a23 magnified  $\times 30$ . Scale in mm.



(a) Overview of the CMM.



(b) Close up of the measurement setup.

**Figure 7.5:** Zeiss OMC 850 mechanical Coordinate Measurement Machine (CMM) [126].

same casting simulations as in fig. 7.2 on page 99, though only showing the displacement in the  $y$ -direction. Note also, that the scale of fig. 7.3 is ten times smaller than the scale in fig. 7.2. Figure 7.3 on page 100 shows that the castings are bending forward at the lower left corner and that the thermal centre at the boss location to some extent changes this pattern.

Comparing the simulations with the deformations found in fig. 7.1 on page 98, the two do not match up. The simulations show the centre of the casting as the highest point if the casting, together with the upper right corner. The initial deformation analysis of the castings showed that top and bottom were the high points on the reverse side of the casting, with the centre as a valley. The deformation of the simulated casting is seen in fig. 7.4 on page 101 that shows the same simulation as in 7.3a, but viewed from the side and magnified  $\times 30$ . This figure shows how the outer ring, as well as the centre of the

reverse side, are deformed as a consequence of the stress and strain developed during cooling and phase transformations.

Additionally, the simulations also showed that this deformation of the simulated castings was overall the same for both alloys, and for both stable and weak moulds. It should, however, be noted that, while the overall direction of deformations remained the same, the magnitude of the deformation was significantly influenced by these changes.

### 7.1.3 Quantifying Measurement Results

Having established that the deformations on the reverse side of the castings could not be explained by the simulated thermal deformation of the castings, the next step was to obtain more precise measurements of the deformation and potential surface shrinkage.

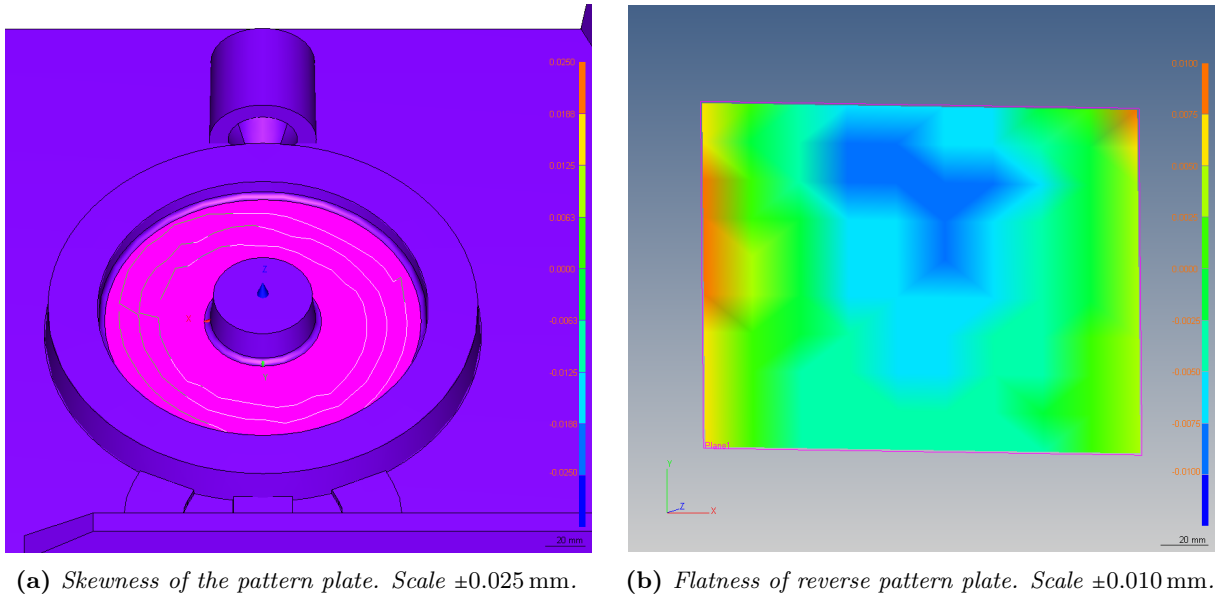


**Figure 7.6:** Deformation measurements of the pattern plates.

To quantify the surface shrinkage of the castings, it was decided to measure the reverse surface of the castings using a CMM. This CMM measurement approach was chosen to provide deformation and surface shrinkage data with a level of detail and repeatability that would allow for comparison of the different castings. Additionally, the pattern plates themselves were also measured to ensure that the deformation was not contributed by partly or entirely by any inaccuracy in the pattern plates.

#### 7.1.4 Setup, Equipment, and Procedure

All measurements were acquired using the same calibrated Zeiss OMC 850 mechanical CMM [126, 127], running the same automated measurement program. See fig. 7.5 on page 102. The CMM was located in a climate controlled room, kept at 20(2) °C.

Each measurement point was stored as a 3D coordinate referenced to a local Cartesian coordinate system, defined by a few measurement at the start of the automated measurement program.

The measurements were performed with a 3 mm probe. The probe size was chosen so it would act as a mechanical filter against the general surface roughness. The typical ranges of surface roughness were described and characterised by Nwaogu et al [108].

#### Reference Measurement of the Pattern Plates

To eliminate that any of the deformations measured could be contributed to inherent geometries in the patterns, both the swing plate (SP) and the squeeze plate (PP) were mapped using the same CMM as for the casting measurements. The measurements were automated.

The front pattern was manufactured by inserting a CNC-milled model made of steel into a steel plate. This approach allows for a smaller block of steel to be machined, hence saving both material and machine time. However, the measurement of the pattern plates showed that model had a small skewness, or tilt, towards the side with the down sprue. See fig. 7.6a. When this measured skewness was compared with the CAD-model plate itself and the measurements of the plate, it was observed the skewness was not an inaccuracy of the CNC-milled model, but rather an imperfect mounting of the model in the steel plate. The size of the skewness was, however, a factor of 10 to 20 times smaller than the size of the deformations measured on the castings.

The reverse pattern plate was a flat plane surface and has been measured to have a flatness value ( $f_v$ ) of 16.4  $\mu\text{m}$ . See fig. 7.6b. The flatness value ( $f_v$ ) is a simple measure of the maximum height difference found on a surface—it is the difference between the highest point measured and the lowest point measured.

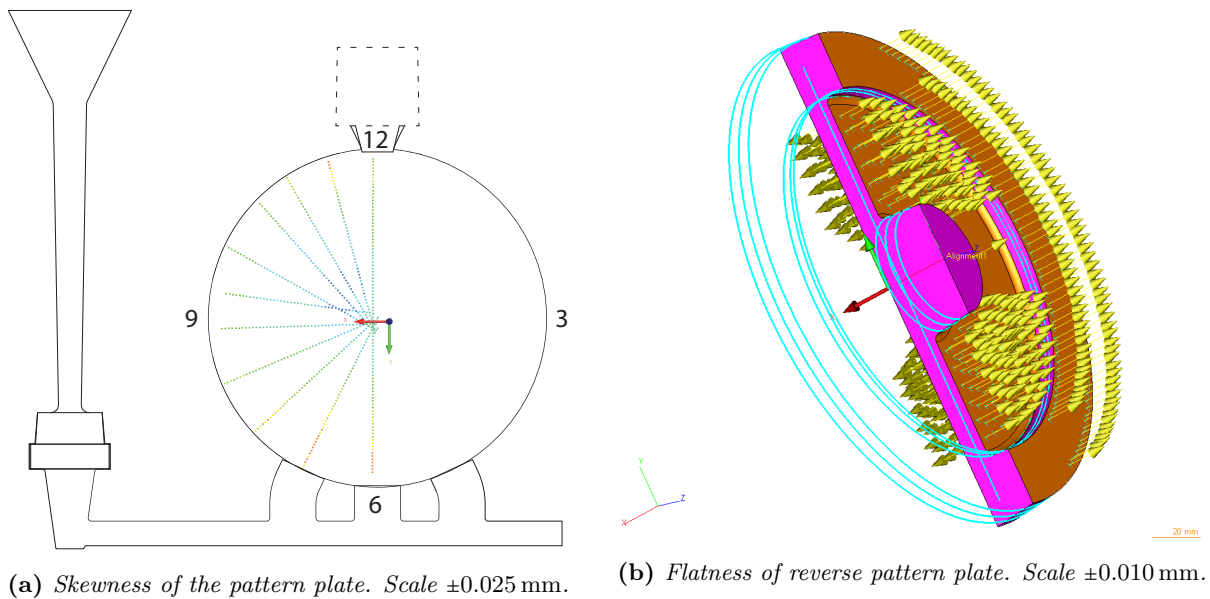


**Figure 7.7:** The two automated measurement programs for measuring the castings.

### Measurement Programs

The castings were measured twice, using two different automated measurement programs. See fig. 7.7. The first program, fig. 7.7a, was a series of lines of measurement points (MP) from the centre (boss) towards the ring. The program was designed to provide a relatively high resolution from the centre and outward with a reasonable distance between each of the lines.

The resolution of the measurement points—not the accuracy of the measurement itself—have a significant influence on the running time of the automated measurement program. While the machine handles the measurements automatically, some considerations must be taken concerning the machine time. Additionally, additional measurements that are not used or useful do prolong not only the measurement time but also the subsequent data analysis. The automated measurement program is shown in fig. 7.7a had a duration of approximately 20 min.; and a few minutes for the operator to take down the measured sample, save the data, mount the new sample, and restart the program. In total more than 20 hours of active machine time. The data from the first measurement program are analysed in section 7.2, on the current page.

The second measurement program was devised base on the analysis of the data from the first measurement program. The program was designed to address some of the shortcomings of the first program—

overall deformation of the casting and thickness of the sections. See fig. 7.7b. This second program encompasses more measurement points than the first. Where the first program measured only the flat reverse surface of the casting, the second program measured four flat surfaces and three cone geometries. The program had a duration of approximately 60 min. For this reason only 17 selected castings were measured with this program.

Additionally, the feeders had to be removed from the castings before the measurement to allow full access for the probe. Some areas, though, had to be excluded from the measurement program because some of the castings had markings that would obscure the measurement. An example of this was the numbers imprinted into the castings during the casting trial for identification. These markings were not a natural part of the deformation or geometry of the casting. Part of the data from the second measurement program is analysed in section 7.3, on page 113.

## 7.2 Deformation Analysis

THE analysis of the deformation of the reverse, plane side of the casting was divided into two separate analyses. First, a visual analysis was made, identifying and characterising the features describe the castings' deformation. The second analysis used



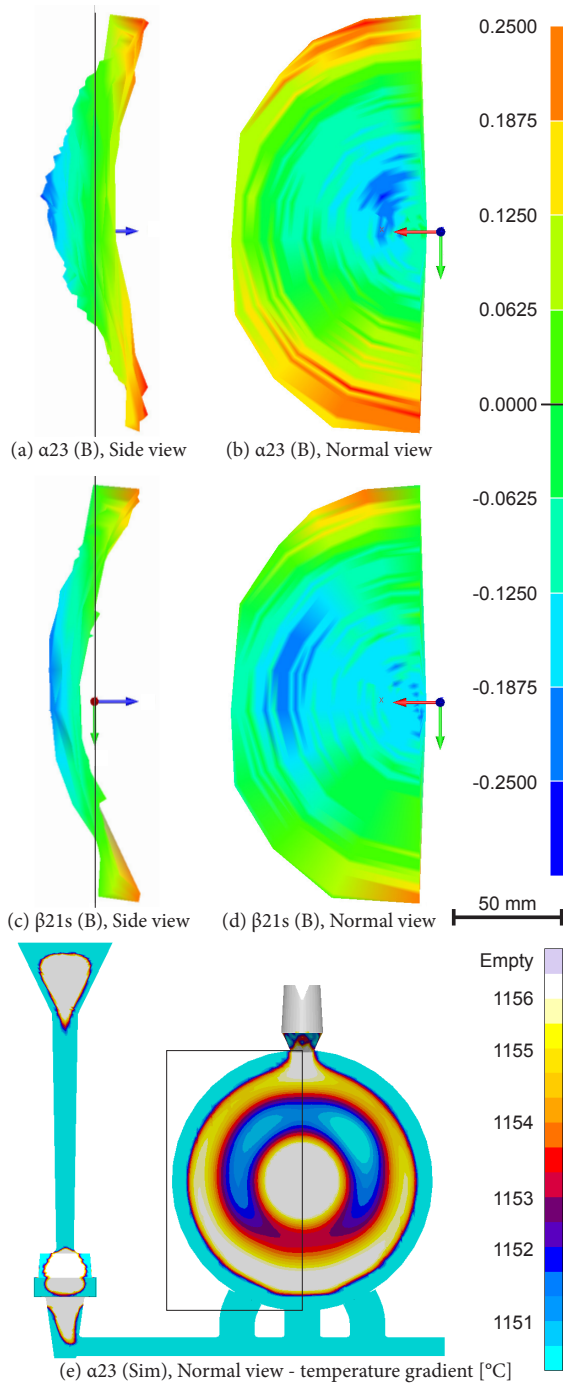


**Figure 7.8:** Measured casting topography amplified  $\times 100$ . Scale in mm. Sub-figures (a) and (b) are the same casting, a23B, viewed perpendicular to the measured surface. Sub-figures (c) and (d) are the same, but for casting  $\beta 21sB$ . The black horizontal line on (a) and (c) indicates the mean of the measured values (0.0000 on the scale) for the respective casting. (b) shows a mean (M) centre area, and (d) shows a low (L) centre area. (e) show the thermal gradients at 50% solidified for a23. The black box frame the area viewed in (b) and (d).

the simplified flatness value ( $f_v$ ) to describe and compare the castings statistically.

### 7.2.1 Deformation Characterisation

The measured coordinates obtained from the automated measurement program was illustrated as a coloured surface, amplifying the deformation. The colours provide a plus-minus scale—meaning that the scale was centred on 0.0000 mm as a mean value (green). The positive (high) areas have colours shifting towards red, while the negative (low) have colours shifting towards blue.

In addition to the colour scale, Calypso (the measurement program used with the Zeiss OMC 850 CMM) [128], was able to present the measurements as a 3D surface or topographic image. Amplifying the deformation by  $\times 100$ , the curvature of the surface became visible and easier to analyse. See fig. 7.8.

The measurement data of all the castings were illustrated using the same setup and depicted as both perpendicular to the surface and from the side, as seen in 7.8. This combination of perpendicular views aided primarily by the colour scale and a side view taking advantage of the amplified deformation provided a basis for the characterisation and analysis of the casting deformation.

The analysis of the 18 different alloy and feeder configurations, comprising in total 46 measured castings, showed that the casting deformation could be described based on: (1) the crescent shape of the casting (viewed from the side), (2) the height of the centre area (boss area), and (3) the shape, size and direction of the ‘valley’ (low area indicated by blue). The quantified results of the analysis are found in table 7.1 on page 107.

The basic idea behind the description of the casting deformation features was to subdivide the features into simple descriptions that could easily be quantified with as little bias as possible. The features should be the characteristics that were found (or at least can be described by their absence) for all castings in the examined population. The subdivision of the features allows for a more thorough comparison of the individual features, as they can be analysed individually.

### Casting Crescent ( $f_v$ and SV)

When the 3D topography of the castings measurements are viewed from the side (SV), the high top and bottom part of the casting make the topography appear like a crescent moon. See figs. 7.8a and 7.8c. However, the middle of the casting varies between a high (H), mean (M), or low (L) position. For instance, the crescent of castings  $\alpha$ 23B shown in fig. 7.8a was characterised as high (H), because of the middle part, near the blue arrow, is markedly above the black vertical mean line. For comparison the  $\beta$ 21sB casting shown in fig. 7.8c was characterised as low (L). Again this is because of the middle part, near the coordinate arrows, curves markedly below the black vertical mean line.

Of the 40 castings analysed and listed in table 7.1 on the facing page two were designated as high (H), nine were designated as low (L), and the remaining 29 were designated as mean (M). Nine of the 15 groups had the same designation for all three castings in the group. No group varied across all three designations.

The flatness values ( $f_v$ ) are listed in table 7.1 on the next page for comparison. No correlation was found between the height of the crescent shape and the flatness value,  $f_v$ , of the casting.

### Centre Area Height (Por and Cen)

The centre area was analysed using the view perpendicular to the surface. Again the analysis characterises the height of the selected area, here the area of the casting above the boss, and characterise it as high (H), mean (M), or low (L). This local area was of particular interest because it could be linked directly to the analysis of the porosities found in the boss in chapter 5, on page 75.

As the shape of the area could not be evaluated based on an absolute value due to the varying deformation of the different castings, it was instead evaluated according to its height in comparison to the surrounding casting. For example  $\alpha$ 23B in 7.8b was characterised as mean (M) because the area at the boss was higher than the area just outside the boss area. On the other hand,  $\beta$ 21sB was characterised as low (L) because the boss area was as low (or lower) as the surrounding area. The analysis used the same scale as for the shape of the crescent.

Of the 40 analysed castings none were designated as high (H), 17 as mean (M), and 23 as low (L). All groups were designated the same; meaning that either the group was low or it was mean. No group

had a combination of low and mean. Most of the  $\alpha$ -alloy castings were mean (M), while most of the  $\beta$ -alloy castings were low (L).

The porosities in the boss, found in the analysis in chapter 5, on page 75, was designated as a simple present or not—(Y) for yes porosities were found, or (N) for no porosities were found.

Comparing the results of the analysis of the centre area with the porosity analysis for the underlying section (the boss), it was found that all 17 areas that were classified as mean (M) were also porosity-free. Of the 23 areas that were classified as low (L) 19 had porosities. Of the remaining seven castings that were classified as low (L), three was from the  $\alpha$ 02 group which had a centre feeder, but not two feeders. This was an indication that the top feeder did influence the solidification and deformation of the centre boss to some degree despite the separation of the thin-walled section. The final three castings classified as low (L) at the centre area were all found in a group where porosities were found in at least one of the other castings with the same feeder configuration. Due to the nature of the liquid penetrant test, it is possible that these three castings have porosities that were just not found in the porosity analysis. Three of these—namely  $\alpha$ 00B,  $\beta$ 11A, and  $\beta$ 11C—was subsequently discovered by the ultrasound analysis to have porosities at the boss section away from the sectioned line. These subsequent results leave only casting  $\beta$ 23sC, which was not selected for the additional ultrasound analysis.

Note that a relatively small variation in surface height—here  $\approx 0.1$  mm—between two areas, could be used as a good indication of the presence of porosities.

### Casting Valley (Dir, Ang, Vol, and Dist)

The description of the valley—the blue area in figs. 7.8b and 7.8d—was the most complex of the three casting deformations characteristics that were chosen to evaluate the castings. As the valley displayed more variation than the previous two descriptions, it was decided to subdivide the description into four individual characteristics.

**Direction (Dir)** It was found that the valleys of the different castings had different directions. By drawing a line through the middle of the valley from the boss to edge of the casting, this line acted as the hour hand of a clock. Hence, if a clock face

**Table 7.1:** *Topography Overview; where  $f_v$  is the flatness value measured, SV is a low, mean, high evaluation (L,M,H) of the central area of the crescent, Por indicates porosities (Y = yes—porosities were found, N = no—porosities were not found) in the boss as described in chapter 5, on page 75, Cen is a low, mean, high evaluation (L,M,H) of the boss area at the centre, Dir is an time indication of the direction of the valley, Ang is an angle degree width indication for the valley, Vol is a 1-3 scale volume indication for the valley, and Dist is a x/3 indication of the distance the valley reaches from the centre.*

Grp	Id	$f_v$	SV	Por	Cen	Dir	Ang	Vol	Dist
$\alpha 23$	A	0.486	M	N	M	10:30	75°	2	2/3
	B	0.502	H	N	M	11:00	65°	2	1/3
	C	0.479	M	N	M	10:30	75°	2	2/3
$\alpha 22$	A	0.359	M	N	M	10:00	75°	1	2/3
	B	0.337	M	N	M	10:00	65°	1	2/3
	C	0.364	M	N	M	10:00	75°	2	2/3
$\alpha 21$	A	0.367	M	N	M	10:30	75°	1	2/3
	B	0.316	M	N	M	10:30	65°	1	2/3
	C	0.424	L	N	M	10:00	90°	2	3/3
$\alpha 13$	A	0.520	M	N	M	09:00	75°	3	3/3
	B								
	C								
$\alpha 12$	A	0.375	M	N	M	09:30	65°	1	2/3
	B	0.428	L	N	M	09:30	75°	2	3/3
	C								
$\alpha 11$	A	0.335	M	N	M	10:00	65°	1	2/3
	B					10:30	50°	1	2/3
	C								
$\alpha 20$	A	0.406	M	Y	L	09:30	65°	2	2/3
	B	0.371	L	Y	L	10:00	65°	2	2/3
	C	0.383	M	Y	L	09:30	65°	2	2/3
$\alpha 02$	A	0.505	M	N	L	11:00	65°	2	1/3
	B	0.530	M	N	L	11:00	65°	2	2/3
	C	0.505	M	N	L	11:00	65°	2	1/3
$\alpha 00$	A	0.915	L	Y	L	09:30	75°	3	3/3
	B	0.969	L	Y	L	09:30	75°	3	3/3
	C	0.820	L	Y	L	09:30	75°	3	3/3
$\beta 23$	A	0.415	M	N	M	10:00	65°	2	2/3
	B	0.388	H	N	M	10:30	50°	1	1/3
	C	0.395	M	N	M	10:30	65°	1	1/3
$\beta 11$	A	0.412	M	Y	L	10:30	65°	2	2/3
	B	0.409	M	Y	L	10:30	65°	2	2/3
	C	0.396	M	Y	L	10:30	75°	2	2/3
$\beta 23s$	A	0.452	L	Y	L	10:00	75°	2	2/3
	B								
	C	0.487	L	N	L	09:30	75°	2	2/3
$\beta 12s$	A	0.430	M	Y	L	10:00	65°	2	2/3
	B	0.437	M	Y	L	10:00	75°	2	2/3
	C	0.424	M	Y	L	10:00	65°	2	2/3
$\beta 21s$	A	0.396	M	Y	L	10:30	65°	2	2/3
	B	0.423	L	Y	L	10:00	65°	2	3/3
	C	0.403	M	Y	L	10:30	65°	2	2/3
$\beta 20$	A	0.358	M	Y	L	09:30	65°	1	2/3
	B	0.398	M	Y	L	10:00	65°	1	2/3
	C	0.351	M	Y	L	09:30	65°	1	2/3

was superimposed on figs. 7.8b and 7.8d, the line through the middle of the blue area acted as an hour hand, indicating the direction of the valley as time. See fig. 7.7a on page 104.

For  $\alpha 23B$  in fig. 7.8b this was 11:00 h and for fig. 7.8d this was 09:30 h. All castings were within the interval between 09:00 h and 11:00 h. Seven of the 15 groups had all valleys pointing in the same direction. The eight remaining groups had a maximum deviation of 30 min.

There was minimal variation in the direction of the valley within each group. This limited variation indicates a relationship between the feeder configuration and direction of the valley. If the identical feeder combinations are compared for the two alloys, it is found that: (1) for groups  $\alpha 23$  and  $\beta 23$  four castings have a valley direction of 10:30 h, one at 10:00 h, and one at 11:00 h. (2) for groups  $\alpha 11$  and  $\beta 11$  four castings have a valley direction of 10:30 and one at 10:00. And, (3), for groups  $\alpha 20$  and  $\beta 20$  four castings had a valley direction of 09:30 h and two at 10:00 h.

The feeder choice influences the direction of the valley. However, the influence was not a simple shift between two feeders. The direction of the valley was not directly drawn towards or pushed away from the feeders.

For comparison, the casting group without any of the two feeders— $\alpha 00$ —all three castings had a direction of 09:30 h. Hence, this valley direction was the natural direction for the casting when not influenced by feeders. The addition of the top feeder in group  $\alpha 20$  yielded that one of the three castings had a valley direction of 10:00 h. The two others remained at 09:30 h. The valley had turned, marginally at best, towards the location of the top feeder. On the other hand, the group with only the centre feeder,  $\alpha 02$ , had three castings with a valley direction of 11:00 h, indicating that the centre feeder had pushed the direction of the valley towards the top of the casting.

The above data suggest that the centre feeder had the prime influence on the direction of the valley. However, if groups  $\alpha 23$ ,  $\alpha 22$ , and  $\alpha 21$  that all have the exothermic-insulating top feeder are compared with groups  $\alpha 13$ ,  $\alpha 12$ , and  $\alpha 11$  that all have the insulating top feeder, it is seen that lower modulus feeder manages to push the valley downwards. At least for groups  $\alpha 13$  and  $\alpha 12$ , while  $\alpha 11$  was unchanged compared to  $\alpha 21$  and the other groups with the exothermic-insulating top feeder.

**Angle (Ang)** The valleys of the different castings also displayed varying width. As the valley geometry was similar to a piece of a pie-chart, the angle was used to describe the size of the valley. Like the direction, the angle of the valley was viewed starting at the boss. The most narrow valleys were  $\alpha 11C$  and  $\beta 23B$  with an angle of  $50^\circ$ , while the widest was  $\alpha 21C$  with an angle of  $90^\circ$ . These three castings, however, are the only castings that displayed an angle outside the interval of  $65^\circ$  to  $75^\circ$ .

Analysing the three groups with one or zero feeders, it was found that groups  $\alpha 20$ ,  $\alpha 02$ , and  $\beta 20$  which had only the top feeder or only the centre feeder, all had valleys with an angle of  $65^\circ$ . However, the group  $\alpha 00$  which was cast with any of the two feeders comprised only castings with a valley angle of  $75^\circ$ .

The analysis of the castings with feeders removed indicates that the feeders reduce the angle of the valley. However, for the castings with both the top and the centre feeder all have the same angle of  $65^\circ$  or an even more substantial angle of  $75^\circ$ . Except for the two castings that were  $50^\circ$  and the one that was  $90^\circ$ . Thus, one feeder will reduce the angle of the valley, while two feeders displayed a less definitive behaviour.

**Distance (Dist)** The area of the valley was only in part described by the angle of the pie section. It was found that the length of the valleys varied as well. Some castings had valleys that reached from the centre boss all the way to the edge of the casting at the outer ring. Others reached less than half the way from the centre to the edge. The length of the valleys was described as the distance reached from the centre towards the edge. As it was a subjective evaluation where the end of the valley was found, three equally spaced distances were chosen as categories— $\frac{1}{3}$ ,  $\frac{2}{3}$  and  $\frac{3}{3}$ .

Five of the castings had a valley that reached only  $\frac{1}{3}$  of the distance from the boss towards the edge. These were  $\alpha 23B$ ,  $\alpha 02$  (A,C), and  $\beta 23$  (B,C). The first is shown in figs. 7.8a and 7.8b. Some connections were found between the castings that displayed this short valley distance. Three of the five belong to the groups with an exothermic centre feeder. The other two had an exothermic-insulating centre feeder but had no top feeder to counter or change the influence of the centre feeder. This lack of a top fee indicates that a dominant centre feeder would favour a short valley. However,  $\alpha 13B$  which

also had a similar feeder configuration was found to have a valley distance of  $\frac{2}{3}$ .

Seven of the castings had a valley that reached all the way to the edge of the casting. Three of these were found in the group without any feeder— $\alpha 00$ . The remaining four belonged to four different groups— $\alpha 21C$ ,  $\alpha 13B$ ,  $\alpha 12B$ , and  $\beta 21sB$  respectively. The last is found in figs. 7.8c and 7.8d.

Eight of the casting groups were found to have the same valley distance for all of the group's castings.

**Volume (Vol)** The direction was used to describe the location of the valley, and the angle and distance have been used describe shape and size of the area of the valley. However, none of these describes the size of the valley itself. Defining a depth for the valley would, together with the angle and distance describe a volume, albeit this description was found to be inaccurate. The reason for this was the depth of the valleys were far from uniform. For some valleys, most of the area would have the same depth, but other valleys comprised both higher and lower areas within the area that was classified as the valley. Thus, to give a truthful description of the displacement, a volume description was chosen.

A simple three grade system was chosen to ease the evaluation and the subsequent analysis—1, 2, and 3—where 1 represents the smallest volume, 2 a mean, and 3 the most substantial volume.

Four of the 15 groups were evaluated as having variations in the valley volume; also meaning that 11 of the 15 groups had identical volumes for all the castings in the group. All castings in the group without feeders— $\alpha 00$ —were classified as having significant volume valleys. The only other casting with the same classification was  $\alpha 13B$ . No direct correlation was found between the volume of the valley and the presence of porosities in the boss.

#### Scale, Resolution, and Ripples

The precision of the results and the analysis can be affected by several factors. The precision of the measurements themselves is described in section 7.3, on page 113. However, other simpler factors may also influence the results and conclusions.

**Scale** The range of the scale illustrating the casting deformation influenced the perception of the deformation. As a large part of the analysis was a visual evaluation this influence should be considered and addressed.

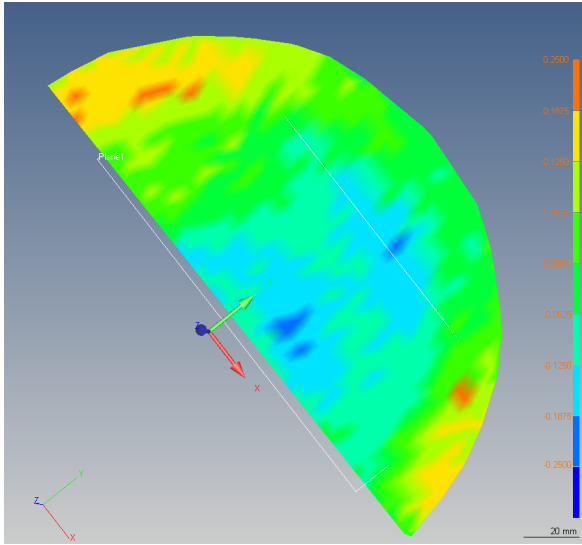


**Figure 7.9:** Detailed measurement of one of the castings to prove or disprove the ripple effect.

A scale ranging from  $\pm 0.2500$  mm was used for all topographic images used in the analysis. This uniform scale ensures comparable images for the analysis. Additionally, before the scale was chosen, different scales were viewed and tested. A narrower scale would provide greater detail close to the mean value (0.0000 mm). However, it would also cut off the highest and lowest area as out of range.

A broader range would only be useful for the castings that displayed a deformation great enough. Hence, the range was set to the scale the just included most of the castings. The flatness value ( $f_v$ ) listed in table 7.1 on page 107 show which castings was affected by the set range—this was all castings with a  $f_v$  above 0.5000 mm. De facto only group  $\alpha 00$  was significantly affected by the threshold value, as they were the only ones that displayed a more significant deformation. For the same reason, these castings were also analysed with a broader scale to support the findings of the standard scale.

**Resolution and Ripples** Besides the resolution (precision) of the CMM itself, the resolution of the points of the automated measurements program influenced the topographic representation of the casting deformations. The topographic image was made by the Calypso software [128] by connecting the different measurement points (MPs) into a surface. However, the program had no information about the casting between the different MPs. Even more so, as the MPs in the automated program was ar-

ranged as in a polar grid, the distance between the points were small close to the point of origin at the boss, but the distance between the lines of points would grow towards the edge. See fig. 7.7a on page 104.

Additionally, the colour scale was displayed as steps rather than a gradient. This serrated display of data meant that measurements within as specified range was given a single uniform colour representing the entire range. This representation was the most correct, as gradient colours in between MPs would be interpretations describe by either a simple or an advanced algorithm. In any case, the gradients would be interpretations by the program, and potentially false. On the other hand, the colour step approach also has shortcomings. It was, for instance, not possible to see if two points that have the same colour was 0.0624 mm apart in height, or only 0.0001 mm. The same goes for two adjacent colours. Two MPs of different colours may be as little 0.0001 mm apart, or as much as 0.1249 mm apart.

The initial analysis identified ‘ripples’ in the casting deformation measurements. These were reported in [30]. The ripples were consistent and present for all castings and was also present at different scales settings. However, the ripples differentiated between the different castings which lead to the belief that wavy effect would be contributed to the similar shape of the casting and the subsequent solidification progression.

To confirm or dismiss this effect, a new measurement was made using a different automated measurement program. This time with a higher resolution (MP density) and with a Cartesian distribution as opposed to the radial polar coordinates used for the original measurement program. The topographical image of the new measurement is seen in fig. 7.9.

The new measurement setup showed that the ‘ripples’ was an effect caused by the MP coordinate setup of the original program, and not an effect present in the castings.

## 7.2.2 Statistical Deformation Analysis

Visual inspection, characterisation, and analysis of the castings was a time consuming and partly a subjective evaluation process. As the measurement programs were automated, the evaluation could also be. The features evaluated in the previous section could be described as threshold values for different MPs; a build in evaluation of the surrounding MP

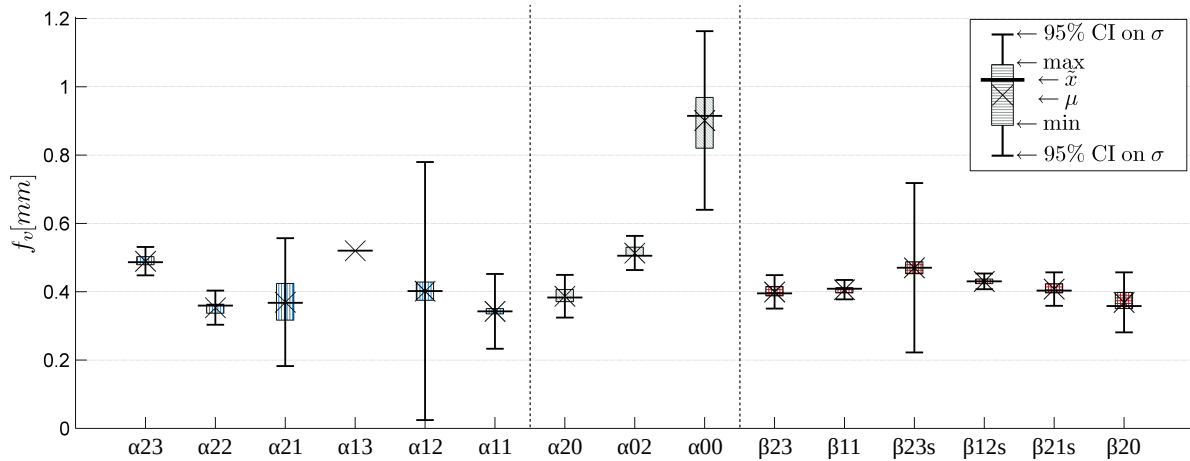


**Figure 7.10:** Flatness values ( $f_v$ ) for each separate casting group, sorted by order of casting. Group  $\alpha13$  consist of one casting, groups  $\alpha11$ ,  $\alpha12$ , and  $\beta23s$  consist of two castings. The remaining 11 groups all consist of three castings.

values. This form of evaluation, though, require a large effort to both develop and program. Hence, it would only be needed for high volume parts with very high tolerance and production requirements.

Some of these challenges could be solved by using optical 3D scanners. They provide a complete measurement of the part far faster than a CMM could do, and without the need for a pre-made program to guide the measurement process. This scanner technology, though, do not in itself provide a statistical representation of the cast part.

#### Information within the Flatness Value ( $f_v$ )

A simple representation of the of a plane surface was the so-called flatness value. This value represented the surface as a distance between the highest and lowest points measured on the surface, regardless of where these points were measured. This value, again, was an extremely simple measure for an entire casting, and using this measure without the knowledge gained through the casting deformation analysis described in section 7.2.1, on page 105 would be like an art critic reviewing paintings in the dark.

A simple measurement value was required to be able to perform a statistical analysis. It may be said that the  $f_v$  was a simple, single value in itself to represent an entire casting surface. This value, though, represents the difference between two points, but also the knowledge that all the other measurements represented values in between these two points. The uncertainty of this one value

representation was that the distribution of points within the range was unknown.

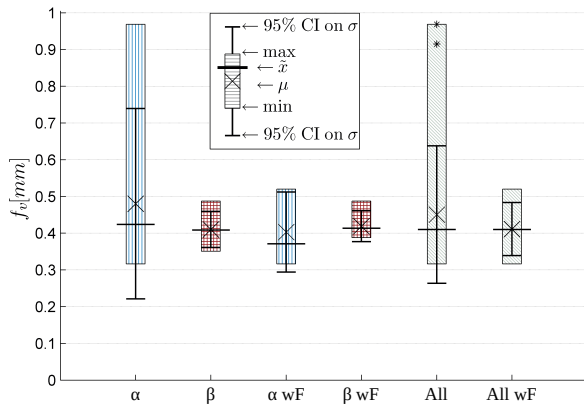
#### Statistical Representation of $f_v$

The  $f_v$  of the different castings can be grouped according to the selected process parameters, allowing for process variations to be determined and outliers to be identified.

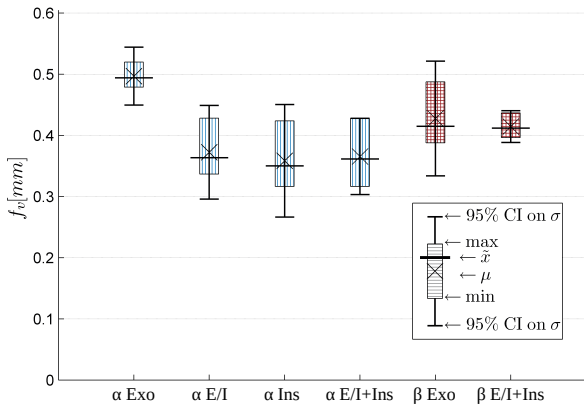
The  $f_v$  were represented as box plot graphs. See figs. 7.10 and 7.11 on this page and on the next page.  $\times$  indicated the average of the group,  $—$  indicated the median of the group, the boxes themselves showed the spread of the group from min. to max. value, the whiskers (or error bars) indicated a 95% confidence interval assuming a Gaussian distribution. Outliers were defined as  $> 3 \times \sigma$  (the standard deviation) and was indicated by  $*$ . Outliers were only found in fig. 7.11a on the facing page. The Gaussian (or student's t) distribution was chosen because of the small population size.

The  $f_v$  for each of the castings are listed in table 7.1 on page 107.

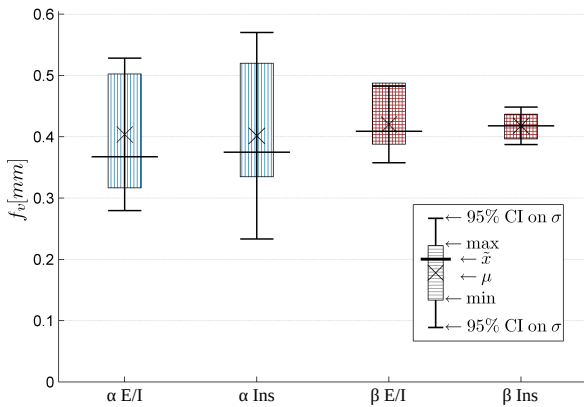
**Group Overview** Sorting the different castings according to the feeder configurations and alloys provide an overview of the different castings groups that were analysed in section 7.2.1, on page 105. See fig. 7.10. The confidence interval was strongly dependent on the number of samples of each group. As each group comprised only three castings, the 95% confidence interval naturally entail a significant range increase compared to the variation found



(a) Flatness values ( $f_v$ ) for all  $\alpha$ -castings, all  $\beta$ -castings, all castings, and all castings with two feeders (wF).



(b) Flatness values ( $f_v$ ) for each alloy ( $\alpha, \beta$ ) and sorted by centre feeder.



(c) Flatness values ( $f_v$ ) for each alloy ( $\alpha, \beta$ ) and sorted by top feeder.

**Figure 7.11:** Flatness values ( $f_v$ ) for sorted groups.

within the group. A narrower confidence interval would require a larger population. A sizeable statistical population is seldom found for research castings; however, measurement of castings that are part of a production in a foundry can quickly provide a population size raised above the statistical limitations of a small population.

The groups that were missing one casting showed a greater confidence interval. These are groups  $\alpha 21$ ,  $\alpha 12$ , and  $\beta 23s$ . Group  $\alpha 00$  showed a similar confidence interval, albeit this was related to the actual instability of the process without feeders, as this group did contain three castings. Finally, group  $\alpha 13$  displayed no confidence interval because only one casting remained in this group.

The group overview was divided into three groups based on the casting sessions. The first session (blue) were the EN-GJS-500-7-alloy castings with two feeders. The second session (grey) were the EN-GJS-500-7-alloy configurations that were cast with one or no feeders. The third session (red) were cast with the EN-GJS-450-10-alloy.

Analysing the groups it was found that the  $f_v$  for all castings were within the range 0.316 mm for  $\alpha 21B$  to 0.530 mm for  $\alpha 02B$ , with the exception of group  $\alpha 00$ , which ranges from 0.820 mm for  $\alpha 00C$  to 0.969 mm for  $\alpha 00B$ . These results indicated that the feeders helped minimise and stabilise the casting deformation. The analysis also indicated that one feeder, top or centre, was enough to achieve the stabilising effect, and that little or no additional minimisation or stabilising of the casting deformation was gained by two feeders, as compared to only one.

**Influence of Alloy** Sorting the castings according to alloy; it was found that the pearlitic-ferritic  $\alpha$ -alloy (EN-GJS-500-7) displayed a more significant variation in  $f_v$  as compared to the fully ferritic  $\beta$ -alloy (EN-GJS-450-10). See fig. 7.11a. However, it must be noted that the feeder configurations and the number of castings for each of the two alloys were not identical. Hence, when the castings without two feeders were separated from the alloy groups, it was found that the repeatability of the  $\alpha$ -alloy was significantly improved.

The alloy groups with two feeders both comprise 14 castings. It was found that the pearlitic-ferritic  $\alpha$ -alloy displayed a smaller average deformation than the fully ferritic  $\beta$ -alloy. However, the fully ferritic  $\beta$ -alloy displayed a much smaller variance (range) of

the deformation compared to the pearlitic-ferritic  $\alpha$ -alloy. In other words, the  $\beta$ -alloy was more predictable and had greater reproducibility.

Examining the different groups shown in fig. 7.10 on page 110 individually it was found that the pearlitic-ferritic  $\alpha$ -alloy casting groups themselves did not display a higher variance than the groups cast with the fully ferritic  $\beta$ -alloy. However, the variation between the different groups was more significant, resulting in a greater overall variance for this alloy. The pearlitic-ferritic  $\alpha$ -alloy was influenced more by the changes in feeder configuration than the fully ferritic  $\beta$ -alloy.

The population size matter; as discovered when all castings were grouped. See the two grey box plots on the right on fig. 7.11a on page 111. The *All* group was the only group that included outliers, as previously defined as  $> 3 \times \sigma$ . Only the two most 'deviant' casting in group  $\alpha 00$  were characterised as outliers when all 40 castings were analysed together. When analysed in its alloy group of 23 castings, the population size was too small to identify these castings as outliers. This example demonstrated the vulnerability of small population statistics. However, while this showed that the casting analysis had limitations, it did not render the analysis invalid. The limited populous statistics by nature have a wider uncertainty span, which was exactly what was shown in the graphs.

In short, the analysis requires a larger sample size, or more significant deviation, to identify outliers within the sorted groups.

**Influence of Top and Centre Feeder** By sorting the castings according to the different feeders—first centre feeder then top feeder as seen in figs. 7.11b and 7.11c on page 111—the effect of the different feeders were illustrated.

While five of the six groups in fig. 7.11b on page 111 were statistically indistinguishable from each other, the first group ( $\alpha$  Exo) was found to be statistically different from groups  $\alpha$  E/I,  $\alpha$  E/I+Ins, and  $\beta$  E/I+Ins with a 95% confidence interval. The lower value of the  $\alpha$  Exo interval was 0.450 mm, while the upper range of the confidence interval of the other groups is just below this value with 0.449 mm, 0.428 mm, and 0.440 mm respectively. Additionally, group  $\alpha$  Ins overlapped the confidence interval by the smallest possible margin by an upper value of 0.451 mm.

The exothermic centre feeder with a modulus of 12 mm was statistically distinguishable from the

exothermic-insulating centre feeder with a modulus of 11 mm. Regardless of alloy. Additionally, it was also almost distinguishable from the purely insulating centre feeder with a modulus of 11 mm.

On the other hand, the  $\beta$  Exo group that also comprised the exothermic centre feeder displayed both a greater deformation and a more substantial variation than the other groups, and could not be distinguished from the other groups. Note also that the  $\alpha$  Exo showed the least variance of the four pearlitic-ferritic groups.

When the castings were sorted according to the top feeder type, as seen in fig. 7.11c on page 111, it was found that the four groups could not be distinguished in statistical terms. However, the variance of the pearlitic-ferritic  $\alpha$ -alloy was higher than that for the fully ferritic  $\beta$ -alloy. The range of the 95% confidence interval covered a range of 0.249 mm and 0.337 mm for the two  $\alpha$ -alloys, while the  $\beta$ -alloy groups covered 0.126 mm and 0.061 mm. Again the fully ferritic  $\beta$ -alloy display less variance, though the average deformation for the  $\beta$ -alloy was slightly higher than the pearlitic-ferritic  $\alpha$ -alloy.

Comparing the two graphs, figs. 7.11b and 7.11c on page 111, it was found that for both the top and the centre feeder the pearlitic-ferritic  $\alpha$ -alloy was most stable, meaning that it showed the least amount of variance, with the high modulus feeders. This effect was most significant for the centre feeder. The effect, however, was found to be the opposite for the fully ferritic  $\beta$ -alloy. In this case, the low modulus feeders showed the least amount of variance. This changing effect indicates that the feeders influence on casting repeatability and stability was strongly dependent on the alloy type.

### 7.2.3 Conclusions

The deformation of the plane, reverse side of the trial casting was analysed, classified, and characterised. The analysis was divided into two different approaches—a descriptive characterisation of features and a statistical representation of the deformation.

#### Deformation Classification

A series of different features were identified and described for all the castings. The variation in the deformation for the different castings were classified, listed and analysed. It was found that the deformation features could be linked to the different feeder configurations and alloys.



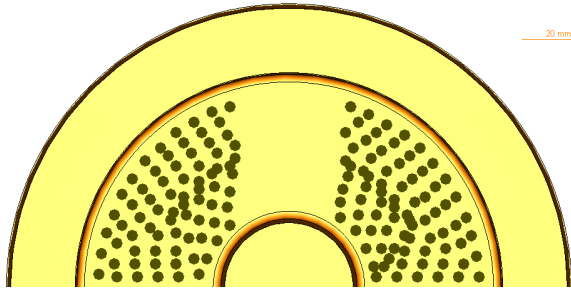


**Figure 7.12:** Placement of the measurement points. There are 155 points on the front, opposed by 155 other points on the reverse side of the casting. The top of the casting is left, bottom right.

**Table 7.2:** Measurement calibration of reference artefact—10 mm gauge block.

Measurement 1	9.9979	mm
Measurement 2	9.9990	mm
Measurement 3	9.9978	mm
Measurement 4	9.9988	mm
Measurement 5	9.9989	mm
Average	9.9985	mm
Standard Deviation ( $\sigma$ )	0.0006	mm
Variance	3.37E-07	mm <sup>2</sup>
Certified Value	10.00028	mm
Systemic Error	-0.00180	mm

A good correlation between a local low area at the boss and the presence of porosities were found.

The scale and resolution of the measurements were examined, and it was found that the ripple effect was created by the location of the measurement points in combination with the manner the topographic images were produced.

#### Statistical Representation and Analysis

The flatness value  $f_v$  was used to condense information of the deformation of the plane, reverse side of the casting into a single comparable value. It was analysed how the  $f_v$  retain some overall information of the deformation as it represents the min. and max. values measured on the surface, thus also conveying the information that all other values lie within this range.

It was found that some groups could be distinguished statistically even with relatively small sample populations.

It was established that the pearlitic-ferritic  $\alpha$ -alloy displayed a smaller average deformation; however, it was also found that the fully ferritic  $\beta$ -alloy displayed less variance. Hence, pattern adaptations

to counter casting deformation would be easier to accomplish accurately for a fully ferritic alloy.

Finally, it was also found that the modulus of the feeders influenced the two alloys differently. While the high modulus exothermic feeders tended to increase both deformation and stability for the pearlitic-ferritic  $\alpha$ -alloy, the same feeders tended to decrease the stability for the fully ferritic  $\beta$ -alloy.

## 7.3 Measurement Uncertainty

As the surface deformation measurements were expanded it became important to secure the validity of the measurements. Thus, it was even more important to show that the effect of changing process parameters is statistically significant. The thickness of the thin-walled section was chosen, as the variation in thickness would provide insight into the alloys and feeders influence on the feeding ‘through’ the thin-walled section. Also, by choosing only the thin-walled section, variations related to the modulus of different sections could be eliminated.

The thickness was calculated by finding the distance between the two vector coordinates. The centre area was excluded from the automated measurement program due to identification markings in this area, which will produce measurement errors if measured. See figs. 7.7b and 7.12 on page 104 and on this page.

### 7.3.1 Data Validation

The first part of the analysis was to validate the data, and if systematic errors are found to correct the data before any further analysis was performed. A box plot of the data for each of the 17 castings that were part of this analysis is seen in fig. 7.13 on the next page.

#### Systematic Error of the Measurement Machine

The thickness of the thin-walled section of the castings which was analysed here was  $\sim 10$  mm. Thus, to identify the systematic error of the machine itself for this particular measurement range, a certified reference artefact—a 10 mm gauge block—was measured five times. See table 7.2.

The systemic error was found to be  $-1.8 \mu\text{m}$ . Usually, the complete dataset should be corrected for this systematic error. In this analysis, this correction is not performed because the systematic error

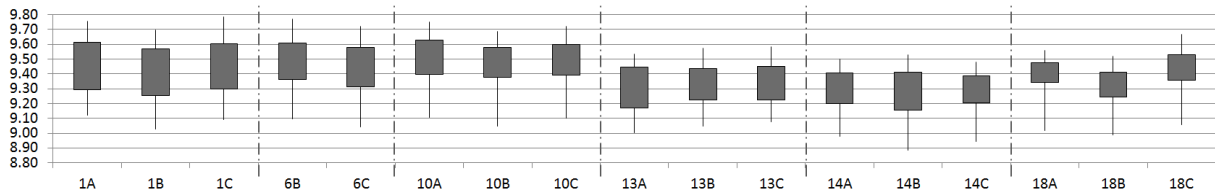


Figure 7.13: Box plot of all 17 castings sorted in the six groups, showing thickness in mm.

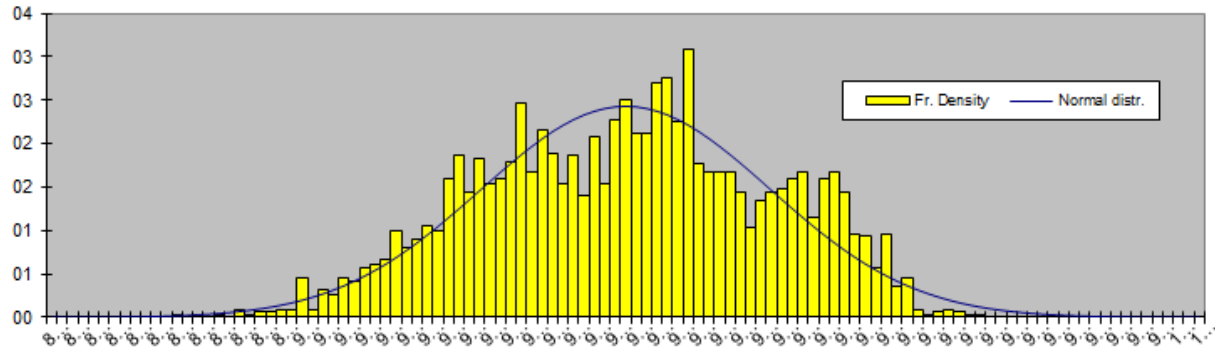


Figure 7.14: Chi-Square ( $\chi^2$ ) test of complete dataset.

Table 7.3: Individual Distribution Identification—Goodness of Fit for a23A.

Distribution	Result		Front		Reverse	
	AD	P	AD	P	AD	P
Normal	35.507	<0.005	3.689	<0.005	1.028	0.010
3-Parameter Lognormal	56.148	*	2.835	*	0.936	*
2-Parameter Exponential	94.784	<0.010	18.004	<0.010	20.514	<0.010
3-Parameter Weibull	56.625	<0.005	2.696	<0.005	0.759	0.034
Smallest Extreme Value	37.266	<0.010	4.621	<0.010	2.359	<0.010
Largest Extreme Value	37.304	<0.010	2.841	<0.010	1.139	<0.010
3-Parameter Gamme	50.056	*	2.678	*	0.900	*
Logistic	32.509	<0.005	3.795	<0.005	1.336	<0.005
3-Parameter Loglogistic	52.943	*	2.975	*	1.180	*

is negligible compared to the population deviation which is roughly 50 times greater. Moreover, the analysis performed here is a relative comparison of different production setups. A correction of the dataset should be made to compensate for this measurement error if absolute values were required.

#### Outliers and Frequency Distribution

Using Chauvenet's criterion no outliers were found. Thus the entire population was found to be significant, and no data were excluded from the dataset as being measurement errors. It should be noted, however, that the Chauvenet's criterion is less effective in finding outliers as a result of the different process parameters included in the dataset.

Following, it was validated that the data were not normally distributed. Some types of data ana-

lyses are strongly dependent on normally distributed data; thus a distribution analysis was required to validate the continued measurement analysis.

First, a frequency distribution test and a  $\chi^2$  (Chi-Square) analysis were performed. The analysis showed that the experimental  $\chi^2$ -value of 252.97 was outside the range of the theoretical  $\chi^2$ -interval from 81.13 f to 138.65 for a 95 % confidence level. The density frequency is displayed in fig. 7.14, and show that the data were not normally distributed. This abnormal data distribution was also supported by the NPP which was hyponormal.

**Risk Assessment** The analysis encompasses a low risk of the first kind ( $\alpha$ ) of incorrectly rejecting the null hypothesis—meaning that the data is normally distributed. By accepting this assumption, it can be stated with a 95 % confidence level, that does contain systematical effects (or measurement accidents). Traditionally a higher risk (eg 15 % to 20 %) would be chosen to obtain a more robust proof of the null hypothesis. The consequences of wrongfully rejecting the null hypothesis were small in this particular analysis of significant parametric effects; thus the low first-order risks and high second-order risks were accepted.

The first-order risk of 5 % was low, though not as low as required for statistical certainty for vital components. In this case, the risk was *not* set

in relation to failing to meet a requirement of a cast product but preferably assessed according to the validity of the scientific research. The results may be used to reduce the machining allowance of castings, reducing the melt required, saving energy and money. However, if the machining allowance were reduced too much, the entire casting would be scrap with additional losses. As only an incorrect rejection of the lower end of the distribution would result in a machining allowance that was too small, the de facto first order risk is only half, namely 2.5%. Thus the requirements for validity of the results strengthen the need for a low-risk assessment.

**Individual Distribution Identification** As the data are not normally distributed an ‘Individual Distribution Identification’-analysis was performed using Mini-TAB [129]. This analysis was initiated to evaluate if the data distribution would match other statistical distribution types when it was proven not to match the normal distribution.

In this analysis, the data columns were analysed separately—here for casting  $\alpha 23A$ . See table 7.3 on page 114. First, the thickness was the result of two opposing datasets subtracted from each other. Evaluating the Anderson-Darling (AD) statistic and P-value not a single one of the distributions was found to match. As the resulting dataset consists of two separate measurements, the analysis was extended to encompass each of the two sets separately. This subsequent data analysis showed that the front of the casting was a better match for all of the distributions, compared with the combined results, though it was still not a distribution match in the statistical sense. Finally, the reverse side of the casting was even closer to matching the different distributions. The 3-Parameter Weibull was the best match as indicated by the lowest AD statistic and highest P-value.

### Null Hypothesis

The data was validated assuming a null hypothesis of *no systematic differences* between the thickness of *all* the castings. Tests were performed to reject the null hypothesis with a given confidence interval for both the complete dataset and the individual groups concerning; both for the average and the variance of the data. The results are shown in table 7.4 on the next page.

For both null hypothesis tests encompassing all datasets, it was found that a majority of the values

were outside the boundaries. This result means that the null hypothesis could be rejected, and with a 95% confidence level state that there were systematic differences between the measured thicknesses of the castings.

Refocusing the null hypothesis to state that there were *no systematic differences* between the casting of each *group*, it was found that the *average hypothesis* with a 95% confidence level rejected this hypothesis for groups  $\alpha 23$  and  $\beta 20$ , meaning that these groups displayed signs of systematic differences. The remainder of the groups were with a 95% confidence interval upholding the null hypothesis and thus display no systematic differences within the groups.

Additionally, the *variance hypothesis* was rejected for groups  $\beta 23$  and  $\beta 11$ , each with a single casting outside the acceptable interval.

Often the hypothesis test would be calculated with a confidence level of 80%. Here the higher confidence level was accepted for two reasons; the higher confidence level still reject the hypothesis and as there was no operator influence on the measurements the type B risk was limited. Additionally, the considerations described in section 7.3.1, on page 114, are also valid here.

### Analysis of Variance

An Analysis of Variance (ANOVA) was performed to determine if there were systematic differences between the different columns of data. The analysis was performed assuming that only a single factor was under control. Thus the analysis was based on eq. 7.1.

$$\begin{aligned}
 SS_{TC} &= \sum_{J=1}^k \sum_{i=1}^n (x_{ij} - \bar{x}_{\bullet\bullet})^2 \\
 &= \sum_{J=1}^k \sum_{i=1}^n (x_{ij} - \bar{x}_{\bullet j})^2 + n \sum_{J=1}^k (\bar{x}_{\bullet j} - \bar{x}_{\bullet\bullet})^2 \\
 &= SS_W + SS_B
 \end{aligned} \tag{7.1}$$

Though there were 17 different columns (one for each casting that was part of the analysis), the DoF for the examined factor was only five because there were only six different production setups as part of the population. The variance ration of 46.80 was greater than the upper limit of the 95% confidence interval of the corresponding Fisher distribution, which was 2.22 See table 7.5 on the next page.

**Table 7.4:** Null Hypothesis Testing - **bold** are outside boundaries

	Group $\alpha_{23}$			Group $\alpha_{11}$		Group $\alpha_{20}$			Group $\beta_{23}$			Group $\beta_{11}$			Group $\beta_{20}$		
	(A)	(B)	(C)	(B)	(C)	(A)	(B)	(C)	(A)	(B)	(C)	(A)	(B)	(C)	(A)	(B)	(C)
All	<b>9.453</b>	9.398	<b>9.445</b>	<b>9.479</b>	<b>9.436</b>	<b>9.499</b>	<b>9.465</b>	<b>9.474</b>	<b>9.297</b>	<b>9.325</b>	<b>9.332</b>	<b>9.289</b>	<b>9.272</b>	<b>9.277</b>	9.388	<b>9.312</b>	<b>9.428</b>
Group	9.453	<b>9.399</b>	9.446	9.480	9.437	9.500	9.465	9.475	9.298	9.326	9.332	9.290	9.273	9.277	9.389	<b>9.313</b>	<b>9.428</b>
All	<b>0.030</b>	<b>0.030</b>	<b>0.028</b>	0.024	0.024	0.024	0.022	0.021	0.022	<b>0.015</b>	<b>0.016</b>	<b>0.016</b>	0.024	<b>0.016</b>	<b>0.014</b>	<b>0.014</b>	0.017
Group	0.030	0.030	0.028	0.024	0.024	0.024	0.022	0.021	<b>0.022</b>	0.015	0.016	0.016	<b>0.024</b>	0.016	0.014	0.014	0.017

Average Null Hypothesis Test								Variance Null Hypothesis Test							
	All	$\alpha_{23}$	$\alpha_{11}$	$\alpha_{20}$	$\beta_{23}$	$\beta_{11}$	$\beta_{20}$		All	$\alpha_{23}$	$\alpha_{11}$	$\alpha_{20}$	$\beta_{23}$	$\beta_{11}$	$\beta_{20}$
No. of samples avg.	155	155	155	155	155	155	155	No. of samples for Var.	155	155	155	155	155	155	155
Average	9.387	9.432	9.457	9.479	9.318	9.280	9.376	Expected Variance	0.021	0.030	0.024	0.022	0.018	0.019	0.015
Average $\sigma$	0.013	0.014	0.013	0.012	0.011	0.011	0.011	Expected v	154	154	154	154	154	154	154
Confidence level	95 %	95 %	95 %	95 %	95 %	95 %	95 %	Confidence level	95 %	95 %	95 %	95 %	95 %	95 %	95 %
Lower boundary	9.361	9.405	9.433	9.456	9.297	9.258	9.356	Lower boundary of $s^2$	0.017	0.023	0.019	0.018	0.014	0.015	0.012
Upper boundary	9.412	9.460	9.482	9.503	9.339	9.301	9.397	Upper boundary of $s^2$	0.026	0.037	0.029	0.028	0.022	0.023	0.019

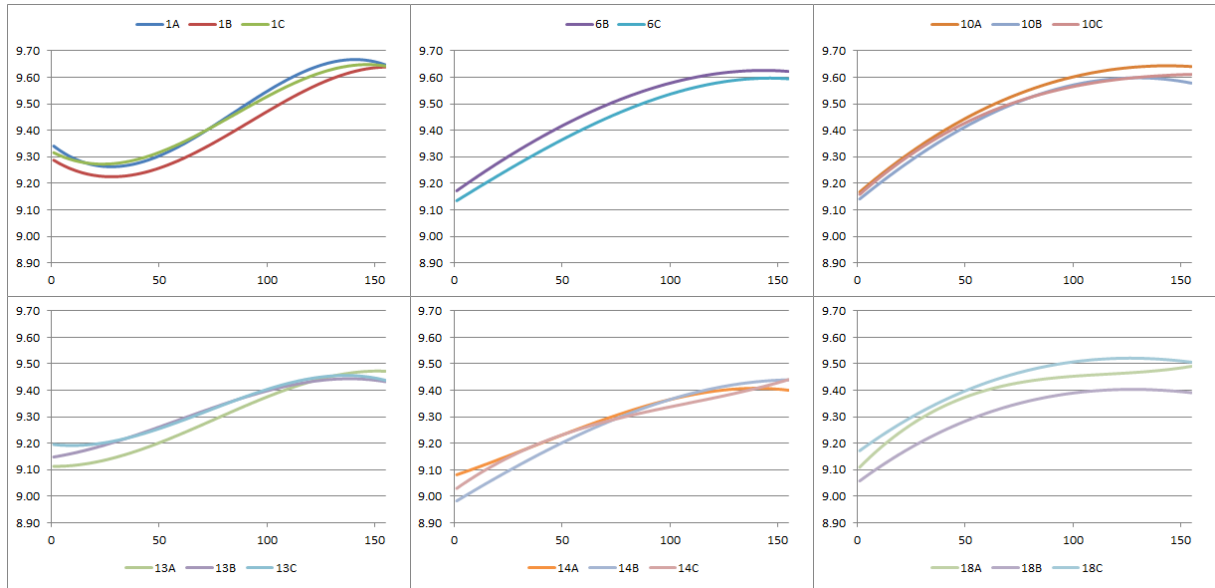


**Figure 7.15:** Thickness variation in mm from top ( $x=1$ ) to bottom ( $x=155$ ), as sorted by height. Described by  $3^{rd}$  degree polynomial equations derived from the regression trend.

**Table 7.6:** Analysis of Variance (ANOVA)—95 % confidence interval, Rows

Variation cause	DoF	Variance	Variance Ratio	F Max
Examined factor	154	3.07E-01	32.11	1.20
Random errors	2480	9.55E-03		
Total	2634			

**Table 7.5:** Analysis of Variance (ANOVA)—95 % confidence interval, Columns

Variation cause	DoF	Variance	Variance Ratio	F Max
Examined factor	5	9.86E-01	46.80	2.22
Random errors	2629	2.11E-02		
Total	2634			

As all measurements were performed by an automated measurement program and thus can be compared point by point, a single factor ANOVA for this event was also analysed. This point-by-point analysis gave 154 DoF, and with the confidence interval kept at 95 % it was found that the variance ratio of 32.11 was also outside the upper limit of the Fisher distribution of 1.20. See table 7.6.

For both of the analysed cases above it was concluded, with a 95 % confidence interval, that there were systematic differences between the different process parameters and between the different measurement points. As the assessment of the previous confidence intervals, the 95 % confidence interval was chosen based on the relative requirement for a

**Table 7.7:** Significance Index ( $b$ ):  $>1$  indicate a systematic slope for the regression trend line.

	$\alpha 23$			$\alpha 11$			$\alpha 20$			$\beta 23$			$\beta 11$			$\beta 20$		
	A	B	C	B	C	A	B	C	A	B	C	A	B	C	A	B	(C)	
Height	10.12	9.05	8.82	11.45	13.35	11.91	11.31	11.02	10.40	8.75	7.39	9.13	11.68	10.03	7.20	7.95	6.74	
Width	0.66	0.79	1.13	1.15	0.86	0.40	0.70	0.72	1.19	0.89	1.72	0.68	0.59	0.20	0.26	0.44	0.27	
Point	0.18	0.17	0.06	1.21	0.99	1.26	1.23	1.59	0.96	1.57	1.37	1.74	1.47	1.33	2.60	2.28	3.20	

low risk of incorrectly rejecting the hypothesis, as well as the balancing of the risk of the second kind.

### Regression Evaluation

In the previous sections, it has been concluded that the data with a high probability displayed systematic differences. To better understand the nature of this difference regression analysis was used to evaluate if the data for each thickness measurement (column) was systematic for both height, width, and time respectively.

**Difference in Height** Sorting the data according to height and analysing the 17 resulting significance indexes for  $b$ , it was found that all 17 are strongly significant; meaning that for all castings there was a significant change in thickness from top to bottom. See table 7.7.

**Difference in Width** The significance becomes more diverse as the data are sorted data concerning the width of the castings. The slope of the trend lines are close to 1 for all 17 castings; thus we conclude that the effect was smaller than for the height. This concluded, some castings show a significant slope— $\beta 23C$  with as much as 1.72—indication that the variation in thickness from the centre towards the edge may be systematic. The control measurement of the pattern showed a skewness or sloping, of the disc as it was mounted on the plate. The height difference within the area examined in this analysis was  $\approx 10 \mu\text{m}$ . Thus, one can argue that the skewness of the pattern was the reason that some of the castings showed a significant trend across the width of the casting. However the skewness of the pattern only account for  $\frac{1}{10}$  of the difference in thickness that is measured when sorting according to width, so the effect has greater relation to other effects than the skewness of the pattern itself. There was no significant skewness of the pattern from top to bottom.

**Difference in Measurement Time** Systematic influences were found for some castings when sort-

ing the data according to the measurement sequence (Point). Others displayed no significant slope. Rather than viewing this way of sorting the data as changes over *time*, it should be viewed as a combined effect of height and width. The points were measured sequentially in half circles, starting from the outside and moving inwards, every half cycle pass started closest to the ingate and moved towards the top. Considering the effect of thermal expansion during the hour-long measurement routine, in a climate controlled laboratory, the significance displayed by some castings cannot be contributed to the time passed during the measurement of the casting. Note, though, that the slopes of the different castings were reasonably similar within all six groups. Thus, it was possible to relate the changes displayed by the regression slopes to the process changes between the groups.

To evaluate how the castings compared with respect to the top to bottom deformation, the regression was used to find a 3<sup>rd</sup> degree polynomial equation for each of the castings. See fig. 7.15 on page 116. The figure shows that both the magnitude and the curve of the deformation were comparable for all six casting groups.

Additionally, the changes in process parameters were also visible in the results. Groups  $\alpha 23$  and  $\beta 23$  both use exothermic centre feeders, and both displayed an S-shaped thickness curve. The four other groups all displayed a simpler single bend curve. Comparing the two alloys, groups  $\alpha 23$ ,  $\alpha 11$ , and  $\alpha 20$  (top three graphs) versus  $\beta 23$ ,  $\beta 11$ , and  $\beta 20$  (bottom three graphs), it was found that thought the curves are comparable in shape; the three groups at the bottom (EN-GJS-450-10) are all slightly thinner than the three groups displayed on top (EN-GJS-500-7).

### 7.3.2 Measurement Uncertainty

To assess the measurement uncertainty of the thickness measurements a certified reference artefact was measured five times under the same conditions, using the same machine and operator as for the castings. The reference artefact chose—a

**Table 7.8: Uncertainty Data**

Measuring Instrument			
Factor	Information	Value	
Bias	Expanded	3.04	$\mu\text{m}$
	Uncertainty of the average of at a confidence level of	5 95 %	meas.
Repeatability	Standard Deviation	5.81E-04	$\mu\text{m}$
Resolution		$\pm 0.1$	$\mu\text{m}$
Temperature sensitivity	Declared	1.15E-05	$^{\circ}\text{C}^{-1}$
Measurement Complex			
Factor	Information	Value	
Reproducibility	Standard Deviation	6.23E-03	$\mu\text{m}$
Ambient Conditions			
Factor	Information	Value	
Temperature	Mean Value	20	$^{\circ}\text{C}$
	Variability Interval	$\pm 2$	$^{\circ}\text{C}$
Measurand			
Length $C1_T$ of the manufact at temperature T		9.66130	$\mu\text{m}$
Length $C2_T$ of the manufact at temperature T		0.21265	$\mu\text{m}$
Number of measurement averaged		5	
Factor	Information	Value	
Temperature	Handbook	1.15E-05	$^{\circ}\text{C}^{-1}$

10 mm gauge block—was the one closest to the measured value of the castings. The data used to calculate the measurement uncertainty can be found in table 7.8. As the primary influence on uncertainty for the castings was the temperature fluctuations in the measurement laboratory; thus eq. 7.2 was used to specify the measurement complex:

$$\begin{aligned}
 L_{20} &= C1_T [1 + (\alpha - \beta)(20 - T)] \\
 &\quad - C2_T [1 + (\alpha - \beta)(20 - T)] \\
 L_{20} &= (C1_T \pm \text{Bias} \pm \text{Repr}) \\
 &\quad [1 + (\alpha \pm \Delta\alpha - \beta \pm \Delta\beta)(20 - T \pm \Delta T)] \\
 &\quad (C2_T \pm \text{Bias} \pm \text{Repr}) \\
 &\quad [1 + (\alpha \pm \Delta\alpha - \beta \pm \Delta\beta)(20 - T \pm \Delta T)]
 \end{aligned} \tag{7.2}$$

#### Measurement Complex Values

$L_{20}$  is the length (thickness) of the casting at the chosen reference temperature  $T = 20^{\circ}\text{C}$ . The  $C1_T$  and  $C2_T$  values are the readings for the x-axis coordinate for the two-point measurements, one on each side of the manufact respectively. The two

space coordinates were measured as part of the same measurement program, but each of the two points is measured approx. 30 min. apart. The thermal expansion of the measurand,  $\alpha = 1.15 \times 10^{-5}$ , was a textbook value for pearlitic ductile cast iron in the interval between  $20 - 100^{\circ}\text{C}$  as listed in the Ductile Iron Data handbook [130]. The same thermal expansion is declared for the instrument,  $\beta = 1.15 \times 10^{-5}$ , by the manufacturer. This duplicity of thermal expansion coefficients is coincidental and due to the similarities in materials between the probe and the examined castings and should not be mistaken for being from the same source. The ambient temperature and variability interval is certified for the measurement laboratory.

#### Type A Uncertainty: Statistical Methods

The first and second variables are the bias of the measurement instrument for which the MPE of the CMM provided by the manufacturer was used. The MPE for 3D measurements was used because it was not possible to document that the two opposing measurements points were exactly opposite each other. The MPE was thus calculated as  $u_3 = 3.0 \mu\text{m} + \frac{L}{250}$ , where  $L$  is the measured distance in mm [131].

In the third line, the standard deviation of the five repeated measurements of the  $\alpha 23A$  manufact gives the reproducibility of the measurement complex as  $6,23 \times 10^{-6}$  m, calculated as the average of the standard deviation of each of the five samples divided by the square root of the number of samples. Since the statistical input based was used in less than ten measurements, the addition to the uncertainty budget was multiplied by a safety factor,  $h$ . In this case of the safety factor used was  $h = 1.4$  because it was based on five measurements as described by both De Chiffre and the ISO/DTR 14253-2 [127, 132]. The use of reproducibility also eliminated the need to evaluate the repeatability and the resolution of the instrument separately; though the data are still listed in table 7.8 to provide information on the measurement instrument.

#### Type B Uncertainty: Non-Statistical Methods

The fourth and fifth lines represent the thermal deformation coefficient of the measurand and the thermal sensitivity of the instrument itself. Both the measureand  $\alpha = 1.15 \times 10^{-5}$  m [130] and the instrument  $\beta = 1.15 \times 10^{-5}$  m [131] have the same thermal sensitivity as stated above.

**Table 7.9: Uncertainty Budget**

Variable $x_j$			Statistical						Non Statistical				Par. Est.					
Symbol	Value	Note	$U_j$	$P_{dj}$	$n_{dj}$	$k_{dj}$	$h$	$s_j$	$a_j$	$k_a$	$n_j$	$n_d$	$n_r$	$u^2(x_j)$	$c_i = \frac{\delta y}{\delta x}$	$u_j^2(y)$	$\frac{u_j^4(y)}{n_j}$	
$C1_T$	0.0966130	Bias	3.04E-06	95 %	100	2.0	1.0	1.5E-06		3	5	5	1	1.2E-11	1.0E+00	1.2E-11	2.8E-23	
$C2_T$	0.0021265	Bias	3.04E-06	95 %	100	2.0	1.0	1.5E-06		3	5	1	1	1.2E+11	-1.0E+00	1.2E-11	2.8E-23	
		Repr	6.23E-06	95 %	100	2.0	1.4	4.4E-06		3	9	1	1	1.9E-11	1.0E+00	1.9E-11	4.2E-23	
$\alpha$	1.15E-05	Table		95 %	100	2.0	1.0	0.0E+00	2.0E-06	3	30	1	1	1.3E-12	0.0E+00	0.0E+00	0.0E+00	
$\beta$	1.15E-05	Table		95 %	100	2.0	1.0	0.0E+00	2.0E-07	3	30	1	1	1.3E-14	0.0E+00	0.0E+00	0.0E+00	
T	20	Estim.		95 %	100	2.0	1.0	0.0E+00	2.0E-00	2	30	1	1	2.0E+00	0.0E+00	0.0E+00	0.0E+00	
$y = L_{20}$	0.00944865	m																

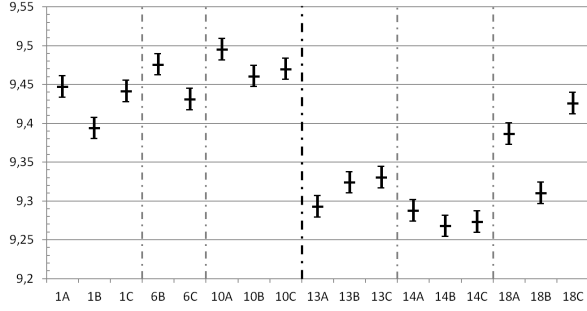


**Figure 7.16: Mean thickness in mm for each of the 17 castings, showing the expanded uncertainty of 13.75  $\mu\text{m}$ .**

**Table 7.10: Uncertainty Results**

Variance of $y$ , $u^2(y)$	4.3E-11	9.7E-23
Standard Uncertainty of $y$ , $u(y)$	6.5E-06	
Degrees of Freedom of $y$ , $n(y)$	18	
Confidence Level	95 %	
Coverage Factor (Student t)	2.1E+00	
Expanded Uncertainty $U(y)$	1.4E-05	m
	13.75	$\mu\text{m}$

The sixth and final line concerns the ambient temperature during measurement. The certified variability interval was  $\pm 2^\circ\text{C}$  and naturally change in a sinusoidal pattern, allowing for the use of a U-shaped distribution denominator as coverage factor— $k_a = 2$  as reported by De Chiffre and Barbato [127, 133].

#### Expanded Uncertainty

The uncertainty budget is found in table 7.9. Repeatability and resolution were not used, as reproducibility was available for the analysis. The expanded measurement uncertainty was found to be  $\pm 13.75 \mu\text{m}$  for a 95 % confidence interval. This measurement uncertainty was estimated to be entirely acceptable for measurements displaying significant changes in the range in  $1/10$  of a mm. The use of the results in comparison to each other, and not as

absolute values, lessen the requirement for a narrow expanded measurement uncertainty.

Figure 7.16 shows how most of the castings can be distinguished from one another when allowing for the expanded measurement uncertainty of  $\pm 13.75 \mu\text{m}$ . The figure does not show that there were dimensional differences in the castings based on the variation of the production parameters. However, it does show that variations between the different castings were significant enough to be distinguished even when allowing for the expanded measurement uncertainty.

The most substantial single contribution to the expanded uncertainty was the reproducibility; however, the bias of the measurement instrument was the most significant. This significance was because it counted twice, once for each of the two opposing space points. On the other hand, the uncertainty budget also shows that the influence of thermal variation during the measurement has no statistical influence on the readings. The influences of thermal change were for all three variables so small that they could be eliminated from the budget by the sensitivity evaluation.

### 7.3.3 Normalised Error Analysis

Having established that there were systematic differences between the different castings, and that was not contributed to by the expanded measurement uncertainty, a method was needed to evaluate to which degree two castings were different. For this purpose the normalised error was used. See eq. 7.3.

$$E_N = \frac{\bar{R} - \bar{S}}{2\sqrt{\bar{\sigma}_R^2 + \bar{\sigma}_S^2}} \quad (7.3)$$

where  $E_N$  is the normalised error,  $\bar{R}$  and  $\bar{S}$  is the average of the reference and sample respectively,  $\bar{\sigma}_R$  and  $\bar{\sigma}_S$  are the averages of the standard deviation for the reference and sample respectively, and

**Table 7.11:** Normalised Error Table—Values greater than  $\pm 1$  are considered statistically different. The greater the value, the greater the difference.

Cast	All	Top	Cen	$E_N$	Gr.	Cast	All	Top	Cen	$E_N$
$\alpha 23A$	a	2	3	-1.83		$\alpha 20A$	a	2	0	-3.33
$\alpha 23B$	a	2	3	-0.33	-1.27	$\alpha 11B$	a	1	1	-2.73
$\alpha 23C$	a	2	3	-1.65		$\alpha 20C$	a	2	0	-2.67
$\alpha 11B$	a	1	1	-2.73	-2.09	$\alpha 20B$	a	2	0	-2.34
$\alpha 11C$	a	1	1	-1.45		$\alpha 23A$	a	2	3	-1.83
$\alpha 20A$	a	2	0	-3.33		$\alpha 23C$	a	2	3	-1.65
$\alpha 20B$	a	2	0	-2.34	-2.78	$\alpha 11C$	a	1	1	-1.45
$\alpha 20C$	a	2	0	-2.67		$\beta 20C$	b	2	0	-1.34
$\beta 23A$	b	2	3	2.70		$\alpha 23B$	a	2	3	-0.33
$\beta 23B$	b	2	3	2.02	2.16	$\beta 20A$	b	2	1	-0.06
$\beta 23C$	b	2	3	1.76		$\beta 23C$	b	2	3	1.76
$\beta 11A$	b	1	1	3.17		$\beta 23B$	b	2	3	2.02
$\beta 11B$	b	1	1	3.36	3.36	$\beta 20B$	b	2	0	2.47
$\beta 11C$	b	1	1	3.55		$\beta 23A$	b	2	3	2.70
$\beta 20A$	b	2	1	-0.06		$\beta 11A$	b	1	1	3.17
$\beta 20B$	b	2	0	2.47	0.36	$\beta 11B$	b	1	1	3.36
$\beta 20C$	b	2	0	-1.34		$\beta 11C$	b	1	1	3.55

where 2 signify a sinusoidal distribution. For the calculations displayed in table 7.11 the average of the complete dataset acts as reference  $R$ . Values  $> \pm 1$  are characterised as significant.

Analysing the table on the right in table 7.11, which was sorted according to the  $N_E$ -value, it is seen that except for  $\alpha 23B$  and  $\beta 20C$ , all castings sort according to alloy. It was observed that the groups  $\alpha 23$ ,  $\alpha 20$ ,  $\beta 23$ , and  $\beta 11$  were fairly agglomerated. Groups  $\alpha 11$  and  $\beta 20$ , on the other hand, are scattered, indicating a less stable process.

#### Normalised Error Matrix

The normalised error table shows the  $N_E$ -value with a chosen reference—in this case, the average of all the castings. See table 7.12 on the next page. The matrix setup makes it possible to compare the castings with each other, showing the differences—in the form of the normalised error—between all the castings.

The main conclusion drawn from the matrix was that there was a significant difference between the two alloys. Additionally, the matrix can be used to analyse how individual castings compare with other castings. For example casting  $\beta 20C$  was not significantly different from castings  $\alpha 23$  (A,B,C), but was significantly different from the two other castings in its group—castings  $\beta 20$  (A,B). In the same way,  $\beta 23A$  was not statistically different from  $\beta 11$  (A,B,C), while  $\beta 23$  (B,C) were in all cases are. Groups  $\beta 11$  and  $\beta 20$  were significantly different as well, except for  $\beta 11A$  and  $\beta 20B$ . Finally, table 7.12 on the facing page shows that, in terms of thickness, there was little statistical difference between groups

$\alpha 11$  and  $\alpha 20$ , meaning that the added centre feeder did not significantly change the casting thickness for the EN-GJS-500-7 alloy.

### 7.3.4 Conclusions

First, it was established that the measurement equipment displayed a systematic error of  $-1.8 \mu\text{m}$ . The systematic error should normally be subtracted from all measurements. However, the systematic error was not corrected here because the magnitude of the error was considered negligible and the focus of the analysis was on comparability and not absolute values.

#### Data Validation

It has been validated that the data contain no outliers and that the dataset does not adhere to a normal distribution. In fact, only for the deformation of the reverse side of the castings, a 3 parameter Weibull distribution could be said to match the data. All other matches were outside the respective distribution boundaries.

Additionally, it was concluded with a 95 % confidence interval that the null hypothesis could be rejected and that there was statistical difference between the castings. The variance test showed that for both production parameters and measurement points were, with a 95 % confidence interval, different.

#### Uncertainty Measurement

An uncertainty budget was made for the thermal influence on the measurement accuracy and the different contributions to the expanded measurement uncertainty has been evaluated. The expanded uncertainty ( $U$ ) was found to be  $\pm 13.75 \mu\text{m}$ , and thus also greater than the systematic error. The influence of the expanded uncertainty was shown to be small enough not to mask the changes caused by the parameters of the casting setup for the chosen response variable—the casting thickness.

#### Production Parameter Analysis

It has been shown that some production changes result in statistically significant changes in the casting thickness, while parameter changes cannot be set apart from each other. The most significant process parameter was the change between alloys. The two alloys behave differently to a degree where



**Table 7.12:** Normalised Error Matrix—Values greater than  $\pm 1$  are considered statistically different. The greater the value, the greater the difference.

	$\alpha_{23A}$	$\alpha_{23B}$	$\alpha_{23C}$	$\alpha_{11B}$	$\alpha_{11C}$	$\alpha_{20A}$	$\alpha_{20B}$	$\alpha_{20C}$	$\beta_{23A}$	$\beta_{23B}$	$\beta_{23C}$	$\beta_{11A}$	$\beta_{11B}$	$\beta_{11C}$	$\beta_{20A}$	$\beta_{20B}$	$\beta_{20C}$
$\bar{S}$	9.45	9.40	9.45	9.48	9.44	9.50	9.46	9.47	9.30	9.33	9.33	9.29	9.27	9.28	9.39	9.31	9.43
$\bar{\sigma}_S$	0.01	0.01	0.01	0.01	0.01	0.01	0.01	0.01	0.01	0.01	0.01	0.01	0.01	0.01	0.01	0.01	0.01

	$\alpha_{23A}$	$\alpha_{23B}$	$\alpha_{23C}$	$\alpha_{11B}$	$\alpha_{11C}$	$\alpha_{20A}$	$\alpha_{20B}$	$\alpha_{20C}$	$\beta_{23A}$	$\beta_{23B}$	$\beta_{23C}$	$\beta_{11A}$	$\beta_{11B}$	$\beta_{11C}$	$\beta_{20A}$	$\beta_{20B}$	$\beta_{20C}$
$\alpha_{23A}$	0.00																
$\alpha_{23B}$	1.37	0.00															
$\alpha_{23C}$	0.19	-1.20	0.00														
$\alpha_{11B}$	-0.70	-2.15	-0.91	0.00													
$\alpha_{11C}$	0.45	-0.99	0.26	1.22	0.00												
$\alpha_{20A}$	-1.25	-2.69	-1.47	-0.59	-1.80	0.00											
$\alpha_{20B}$	-0.32	-1.79	-0.53	0.41	-0.83	1.01	0.00										
$\alpha_{20C}$	-0.58	-2.07	-0.80	0.14	-1.12	0.75	-0.28	0.00									
$\beta_{23A}$	4.25	2.76	4.12	5.31	4.02	5.89	4.97	5.33	0.00								
$\beta_{23B}$	3.74	2.14	3.59	4.87	3.48	5.50	4.50	4.89	-0.92	0.00							
$\beta_{23C}$	3.48	1.91	3.33	4.57	3.20	5.19	4.20	4.58	-1.12	-0.24	0.00						
$\beta_{11A}$	4.75	3.16	4.62	5.95	4.56	6.58	5.60	6.01	0.24	1.28	1.49	0.00					
$\beta_{11B}$	4.82	3.36	4.70	5.88	4.63	6.45	5.56	5.92	0.72	1.67	1.85	0.53	0.00				
$\beta_{11C}$	5.09	3.50	4.96	6.31	4.92	6.93	5.96	6.38	0.63	1.71	1.90	0.43	-0.15	0.00			
$\beta_{20A}$	1.90	0.30	1.71	2.89	1.50	3.53	2.48	2.84	-2.99	-2.29	-1.99	-3.55	-3.68	-3.97	0.00		
$\beta_{20B}$	4.15	2.53	4.00	5.33	3.92	5.97	4.96	5.37	-0.51	0.47	0.70	-0.83	-1.28	-1.27	2.79	0.00	
$\beta_{20C}$	0.71	-0.85	0.50	1.56	0.23	2.19	1.15	1.47	-4.15	-3.59	-3.28	-4.79	-4.79	-5.19	-1.40	-4.09	0.00

it can be said to be statistically significant in term of casting thickness.

The analysis shows that the exothermic centre feeder influenced the thickness at the top of the casting, as seen by the regression trend lines displayed in fig. 7.15 on page 116. The four other casting groups show a comparable curvature with decreasing thickness towards the top of the casting.

Finally, it was shown that the changes in the regression were significant for all castings when the data is sorted from top to bottom. A similar significance was not found when sorting the data according to width or measurement sequence.

## References

- [30] Nikolaj Kjelgaard Vedel-Smith et al. “Quantification of Feeding Effects of Spot Feeding Ductile Iron Castings made in Vertically Parted Molds”. English. In: *AFS Proceedings* (2013).
- [108] U. C. Nwaogu, N. S. Tiedje and H. N. Hansen. “A Non-Contact 3D Method to Characterize the Surface Roughness of Castings”. English. In: *Journal of Materials Processing Technology* 213.1 (2013), pp. 59–68.
- [125] Ugochukwu Chibuzoh Nwaogu. *New Sol-Gel Coatings to Improve Casting Quality*. DTU Mechanical Engineering, 2011. ISBN: 978-87-90416-82-9.
- [126] *Zeiss OMC 850 by Carl Zeiss AG and Schott AG*. [http://www.zeiss.co.uk/industrial-metrology/en\\_gb/metrology-solutions/machinery.html](http://www.zeiss.co.uk/industrial-metrology/en_gb/metrology-solutions/machinery.html). Instrument.
- [127] Leonardo De Chiffre. *Geometrical Metrology and Machine Testing: Textbook*. DTU Mechanical Engineering, 2011. ISBN: 978-87-7078-155-8.
- [128] *Calypso by Carl Zeiss AG*. [http://www.zeiss.dk/industrial-metrology/da\\_dk/produkter/software/calypso.html](http://www.zeiss.dk/industrial-metrology/da_dk/produkter/software/calypso.html). Program.
- [129] *MiniTAB 16 by Cleverbridge AG*. <http://www.minitab.com/en-us/>. Program.
- [130] Ductile Iron Data. *Ductile Iron Data - for Design Engineers*. Rio Tinto Iron & Titanium Inc., 1990.
- [131] Flemming Hjelmberg. *Calibration Certificate - Carl Zeiss OMC 850 3D Coordinate Measuring Machine*. Tech. rep. Brock and Michelsen A/S, Industriel Måleteknik, 2011.

- [132] *ISO/DTR 14253-2:1997(E): Geometrical Product Specifications (GPS)—Inspection by Measurement of Workpieces and Measuring Equipment—Part 2: Guide to the Estimation of Uncertainty of Measurement, in Calibration of Measuring Equipment and in Product Verification.* Norm. 1997.
- [133] Giulio Barbato, Alessandro Garmak and Gianfranco Genta. *Measurements for Decision Making: Measurements and Basic Statistics.* Società Editrice Esculapio, 2013. ISBN: 978-88-7488-575-6.



# Chp 08 Thermal Analysis

## Analysis of Thermal Gradients and Local Cooling Times

### Thermal Analysis

---

<b>8.1 Introduction</b> . . . . .	<b>123</b>	8.3.1 Phase Transformation: Temperature	126
<b>8.2 Thermal Measurements</b> . . . . .	<b>123</b>	8.3.2 Phase Transformation: Time . . . . .	130
8.2.1 Numerical Simulation . . . . .	124	8.3.3 Thermal Deformation Analysis . . . . .	130
8.2.2 Cooling Curves . . . . .	124	<b>References</b> . . . . .	<b>133</b>
<b>8.3 Thermal Analysis</b> . . . . .	<b>125</b>		

---

» THERMAL measurements of the cooling curves at select locations in the casting, supported by simulated cooling rates, and phase transformation analysis with respect to both transformation temperature and time. This thermal analysis is used to support and develop a proposed mechanisms explaining the observed casting deformation.

Keywords: . Thermal Measurements, Thermocouples, Cooling Rate, Cooling Curves, Phase Transformations, Deformations Mechanisms.

Chapter findings reported in: . . Supplement III, on page 325

---

### 8.1 Introduction

---

IT was theorised that the deformations described in chapter 7, on page 97, which were reported in supplements I and II, on page 301 and on page 315, were related to the thermal gradients in the casting during solidification and cooling.

It was decided to support the thermal analysis with thermal measurements at selected locations in the casting and in the sand near the casting. These measurements could then be used to verify the simulated data for the same positions, as well as validate the thermal data of the numerical simulations in

general. The thermocouples in the sand were used to verify the thermal properties of the mould.

### 8.2 Thermal Measurements

---

AS described in section 4.5, on page 74, the TC-castings (castings with thermocouples) were produced on a vertically parted moulding machine—DISAMATIC 2110—at the university foundry at DTU.

Body-Centred Cubic (BCC), Carbon (C), Face-Centred Cubic (FCC), Iron (Fe), Measurement Position (MP), Silicon (Si), Thermocouple (TC)

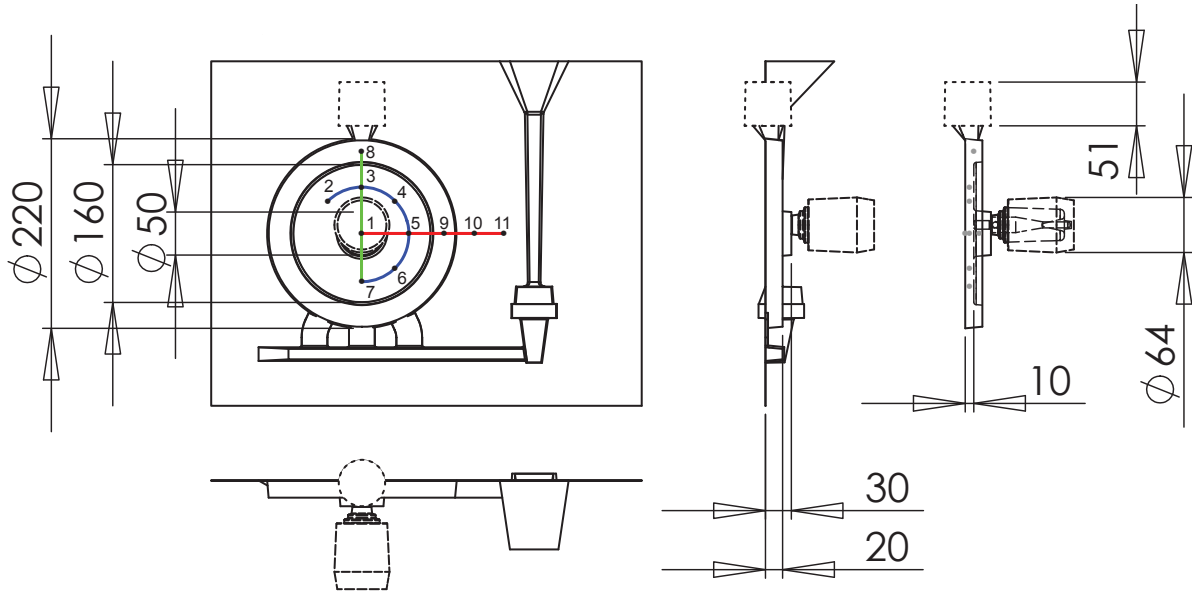


**Figure 8.1:** Technical drawing of the disc casting including the gating system, mounted on the pattern plate. The short dashed line indicates the pattern to mount the top feeder, and the long dashed line indicates the centre feeder. Numbers indicate thermocouple locations.

The poured weight and pouring time were identical to the process parameters for the other castings, as described in chapter 4, on page 67. The pouring temperature was 1385(5) °C.

Thermocouples 1-9 were type K and were placed inside the casting. Thermocouples 10 and 11 were type N and were placed in the mould. See figs. 4.6 and 8.1 on page 74 and on this page. Thermocouples 1-9 were mounted through the mould perpendicular to the reverse side of the casting. Thermocouples 10 and 11 were mounted vertically parallel to the mould parting line. The data were sampled at 100 Hz.

### 8.2.1 Numerical Simulation

Numerical simulations were made using MAGMASOFT 5.2 [69]. The simulations were set up to resemble the casting conditions in the best possible way. Another commercial simulation software, JMatPro [119], was used to calculate the thermo-physical properties of the  $\alpha$ - and  $\beta$ -alloys. These thermal datasets were used in the numerical casting simulation. The simulations with the  $\tau$ -alloy used the  $\beta$ -alloy dataset, albeit with  $\tau$ -alloy composition.

The simulations were used to (1) visually evaluate the thermal gradients of the casting during filling and solidification, and (2) export TC-measurement data at the 11 Measurement Position (MP) of the

trial TCs for comparison of the simulation and the trial measurements. The simulations were made with an equidistant mesh.

### 8.2.2 Cooling Curves

The cooling curves from the trial measurements were plotted and analysed using the second derivative of the cooling curve to identify the start and end points of the austenite to ferrite phase transformation, as seen in fig. 8.2 on the next page. The figure shows the measured cooling curves from MP 1 (boss) and 9 (right ring) as seen in fig. 8.1. The cooling curves show an excellent correspondence between the thermal measurements of the two castings in MP 9. The  $\tau$ 23A cooled slightly faster than  $\tau$ 23B for MP 1. The phase transformation from austenite to ferrite was identified using the second derivative of the cooling curves—the cooling acceleration. The cooling acceleration of the four cooling curves is shown as dashed lines below the cooling curves. The vertical dashed lines indicate the start and end of two of the four cooling acceleration curves and are linked to the right y-axis.

The same procedure was followed for the simulated cooling curves, albeit sixth-degree polynomial fits were used to describe the simulated cooling curves when derived. The latter was necessary due

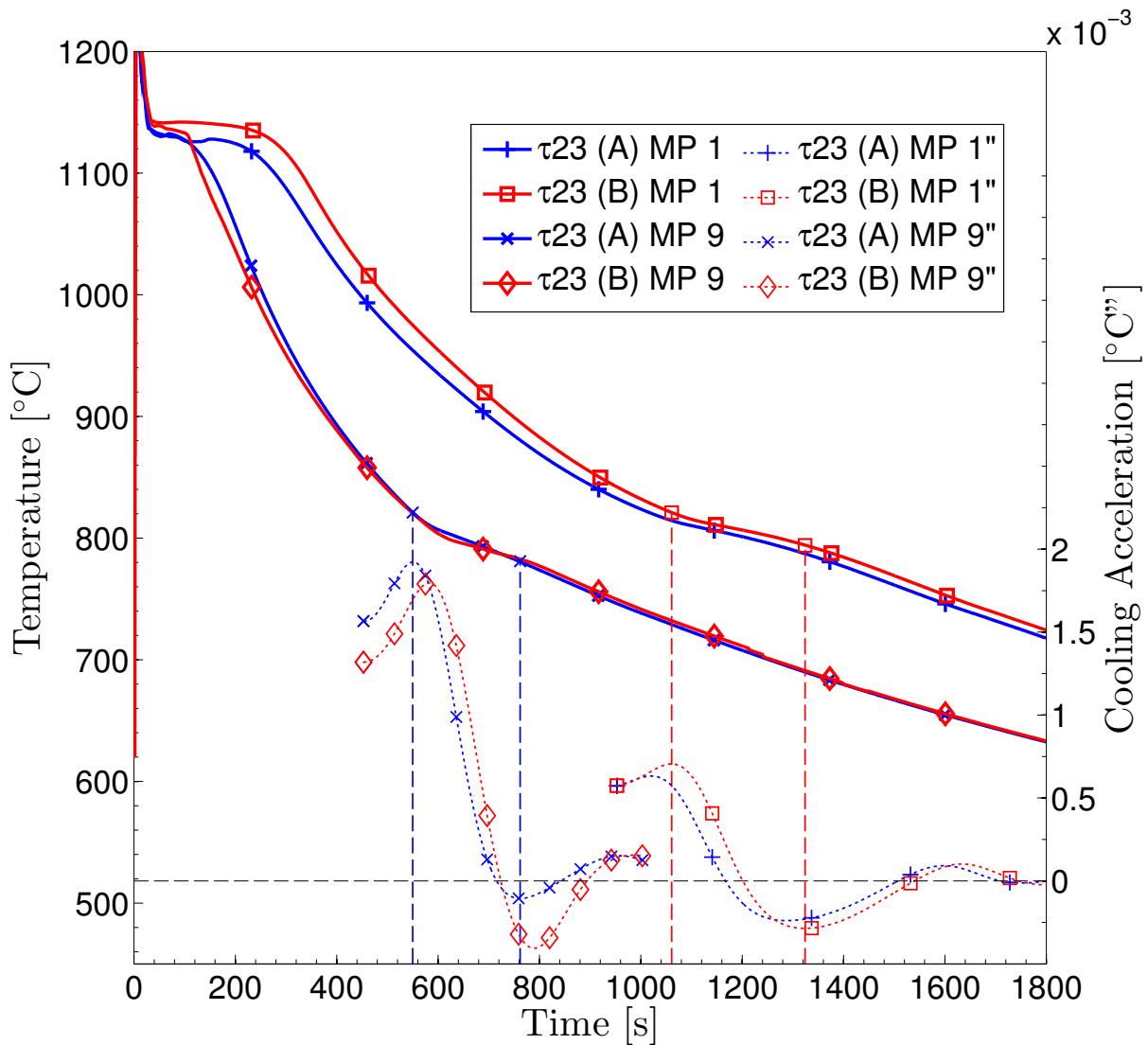


**Figure 8.2:** Cooling curves from the trial castings. Comparison of MP 1 and 9 for the two castings. The dashed lines show the second derivative of the cooling curves. The vertical lines show how the beginning and end of the austenite to ferrite phase transformation has been identified.

to time steps of the simulated data. An overview of the cooling curves for the two TC-castings and the numerical simulation with the same  $\tau$ -alloy is shown in fig. 8.3 on the next page. The figure shows the phase transformations for seven of the nine MPs, including the derived cooling curves and indication of the start and end of the phase transformations.

The analysis is partly based on the methods described in Labrecque and Gagné’s review on cooling curve interpretation for cast iron [134].

The derived cooling curves are shown in fig. 8.3 on the following page was used to find the start

and end of the austenite to ferrite phase transformation. These intervals were then plotted to show the transformation time for each of the MPs for the simulated and measured casting temperatures.

### 8.3 Thermal Analysis

HAVING measured, simulated, and extracted the thermal data from the two trial castings and the three simulated castings; the data were then organised according to phase transformation temperature and phase transformation time.

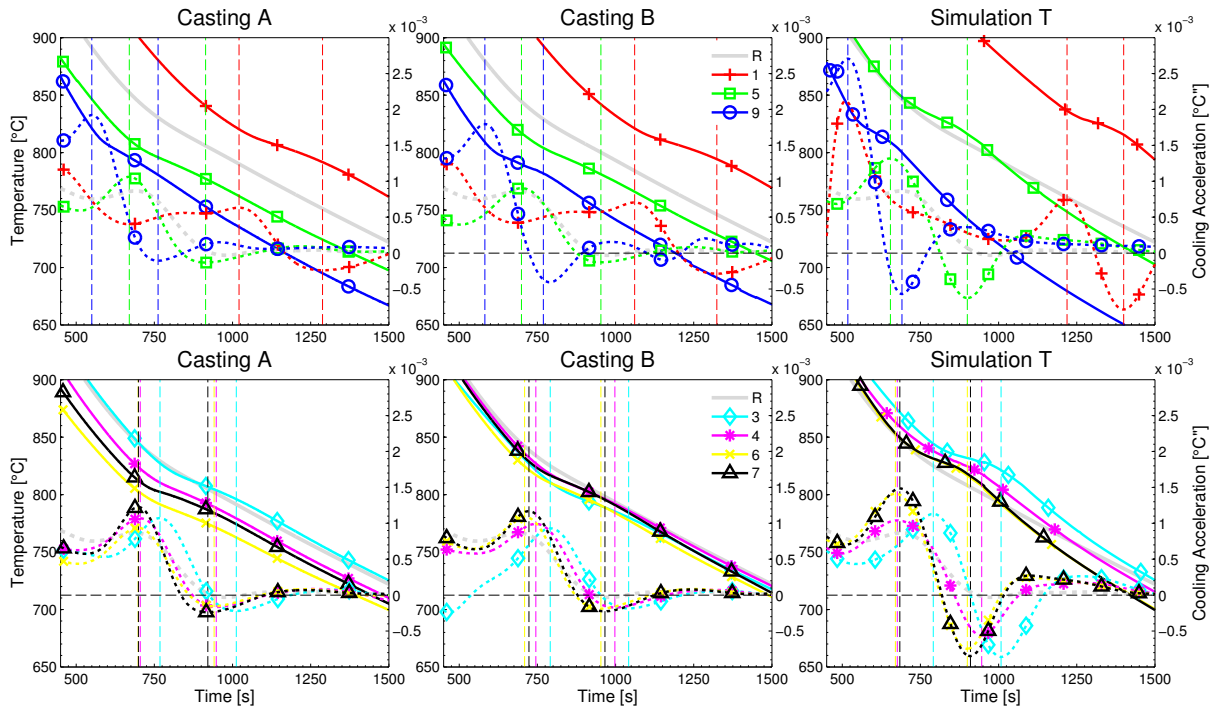


**Figure 8.3:** Comparison of the cooling curves for castings  $\tau23A$  and  $\tau23B$ , and the numerical simulation  $\tau23$  (Sim). The top row shows MPs 1, 5, and 9. The bottom row shows MPs 3, 4, 6, and 7. An overview of the MPs is found in fig. 8.1 on page 124. The full lines are the cooling curves (left y-axis), and the dashed lines are the second derivative of the cooling curves (right y-axis). The vertical dashed lines indicate the start and end of the austenite to ferrite phase transformation. The grey curve is a reference curve displayed on all six graphs to aid visual comparison. The reference curve is the average of all 9 in the casting MP measurements for the  $\tau23B$  casting.

### 8.3.1 Phase Transformation: Temperature

While graphs like fig. 8.3 are suitable to illustrate the methodology and compare general impressions, the figure is too information heavy to be useful for an in-depth data analysis. Hence, to compare and analyse the influence of geometry and alloy on the phase transformation duration and temperature, the data retrieved from the cooling curves had to be reorganised.

The phase transformation times and temperatures were extracted from the cooling curves and plotted as a box-plot for each of the nine MPs, see figs. 8.5 and 8.6 on page 128 and on page 129. Subsequently the information from 8.6 was summarised in fig. 8.7 on page 131.

Figure 8.5 on page 128 shows the temperature interval of the phase transformations. The difference in the temperature interval related to the Si content of the alloy. Increased Si increase the stable eutectic as well as the eutectoid temperatures of the alloy [135]. This metallurgical change explains

the increased phase transformation start temperatures of the high Si  $\beta$ - and  $\tau$ -alloy. Note however that the start temperatures were only significantly higher for MP 2-7 for the  $\beta$ -alloy. The  $\tau$ -alloy showed a higher start temperature even at MP 1, 8, and 9, though the difference was noticeably smaller at these locations. These measurements indicate that the Si content varies locally as a function of the Si segregations during solidification. The same phenomenon also explains the variation in start and end temperatures for MP 2-7 which are all located in the thin-walled section. Note though, that other effect may also play a part. It is not likely that the segregation of Si alone can cause this substantial an impact by itself.

Note that the blue box-plots show that the phase transformation temperature intervals for the pearlitic-ferritic  $\alpha$ -alloy were significantly longer than the high Si alloys ( $\beta$ ,  $\tau$ ). The main reason for this was the double phase transformation that included the formation of pearlite. The derived cooling curves in fig. 8.4 on the facing page show

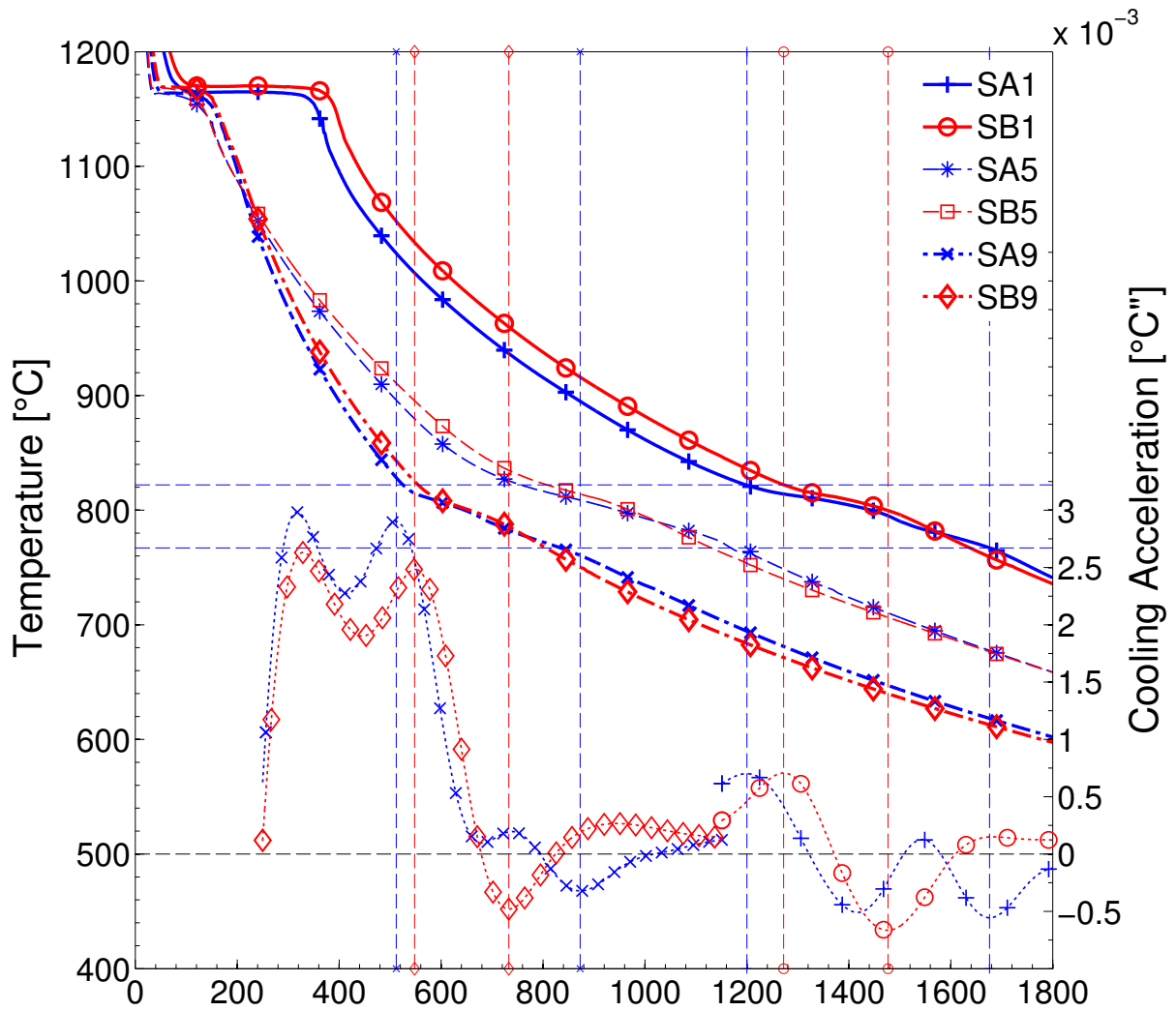


**Figure 8.4:** Simulated cooling curves for two alloy compositions— $\alpha$  and  $\beta$ . The full lines are the cooling curves, and the dashed lines are the second derivative of the cooling curves. The latter curves are linked to the y-axis on the right. The dashed vertical lines indicate the start and end of the phase transformation. The markers at the top and bottom of the vertical lines indicate which simulation they relate to. The intersections of the vertical lines with the cooling curves were used to establish the start and end temperature of the phase transformation. The horizontal dashed blue lines show the start and end temperature for the pearlitic-ferritic  $\alpha$ -alloy at MP 1. SA and SB are respectively the simulations of the  $\alpha$ - and  $\beta$ -alloy, here shown for MP 1, 5, and 9.

that the pearlitic-ferritic  $\alpha$ -alloy (blue) display two consecutive phase transformations. This double phase transformation occurs via the transformation of austenite to ferrite; which is tailgated by a pearlite formation. The C embedded in the FCC austenite lattice precipitates into the graphite as the FCC to BCC transformation occur [32]. This happens because the FCC austenite lattice can potentially hold as much as 2.04 wt% C, whereas the BCC structure of the ferrite lattice only holds 0.02 wt% C at 723 °C, and as little as 0.005 wt% C at 0 °C.

If the C content of the austenite is 0.8 wt% or above at the time of the phase transformation, the austenite will become supersaturated which results in a simultaneous growth of ferrite and cementite resulting in the formation of pearlite.

Hence, the austenite of the low Si  $\alpha$ -alloy contains 0.8 wt% C or more resulting in a subsequent austenite to pearlite reaction. This additional phase transformation prolongs the overall phase transformation as the austenite to ferrite is a more

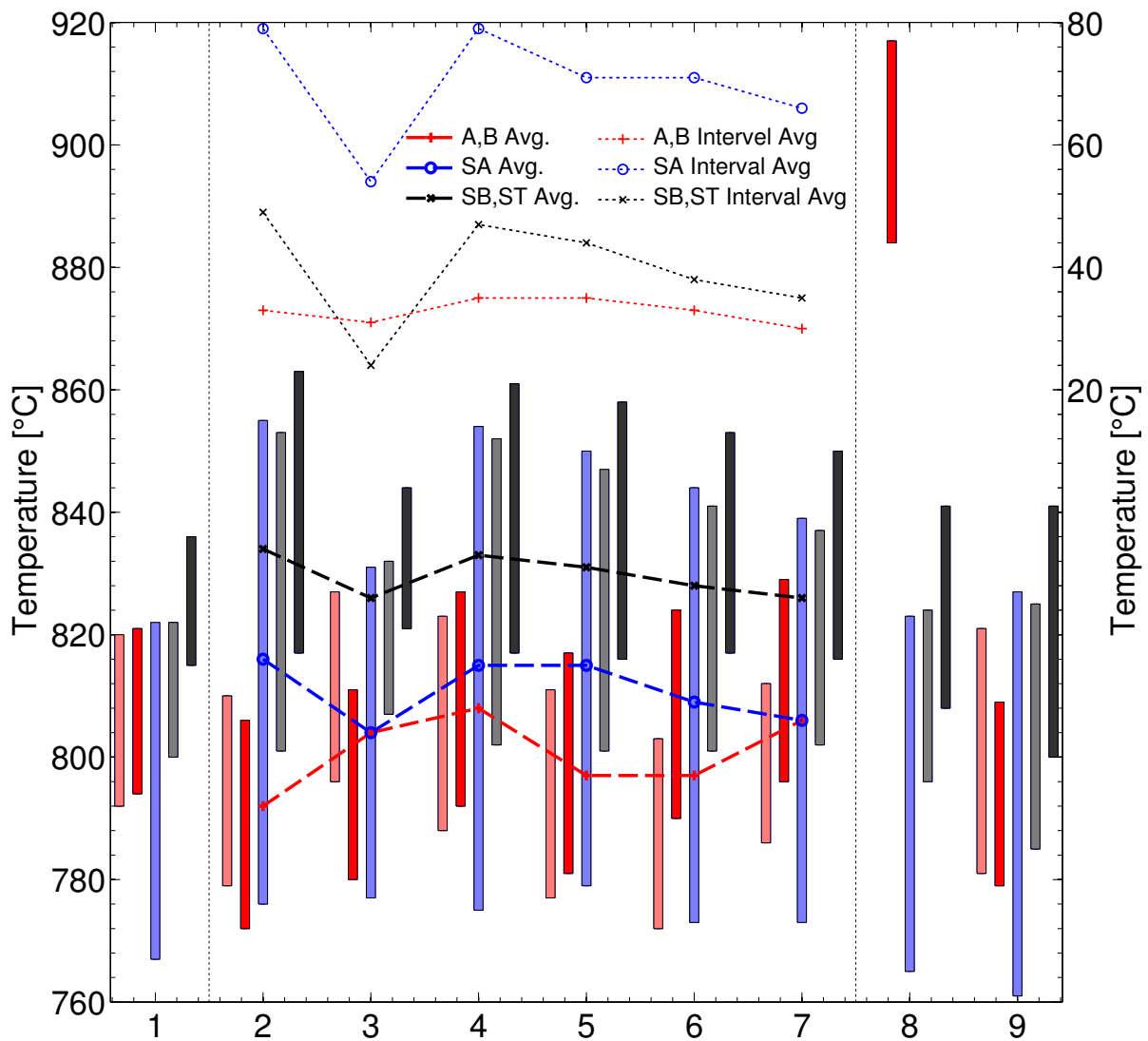


**Figure 8.5:** Phase Transformation Temperature: Austenite to ferrite phase transformation temperature intervals for all measured and simulated castings, for each of the nine MPs. The red bars represent the measured castings with the  $\tau$ -alloy. The blue is the simulation of the pearlitic  $\alpha$ -alloy, the grey is the simulation of the fully ferritic  $\beta$ -alloy, and the black is the fully ferritic  $\tau$ -alloy. The bars indicate the phase transformation interval, and the bold dashed lines indicate the mean phase transformation temperature for the three alloys for MP 2-7. The thin dashed lined at the top indicate the phase transformation interval duration for the three alloys for MP 2-7 and is linked to the right y-axis. A and B are the TC-castings, and SA, SB, and ST are the simulations of the three different alloys.

rapid transformation compared with the diffusion controlled pearlite growth. Note, however, that some of the C will precipitate from the austenite to nearby primary graphite. As a result, only the austenite that contains 0.8wt% C or more at the time when the diffusion distance becomes too great for the embedded C to reach a grain boundary or a primary graphite formation.

The result of the double phase transformation is seen by the prolonged duration of the phase transformation in fig. 8.5, and as the double ‘bump’ on the derived cooling curves in fig. 8.4 on page 127.

The key to understanding the variation of the temperature intervals is found in the solidification and segregation of the alloying elements. The cooling rate during solidification governs the segregation



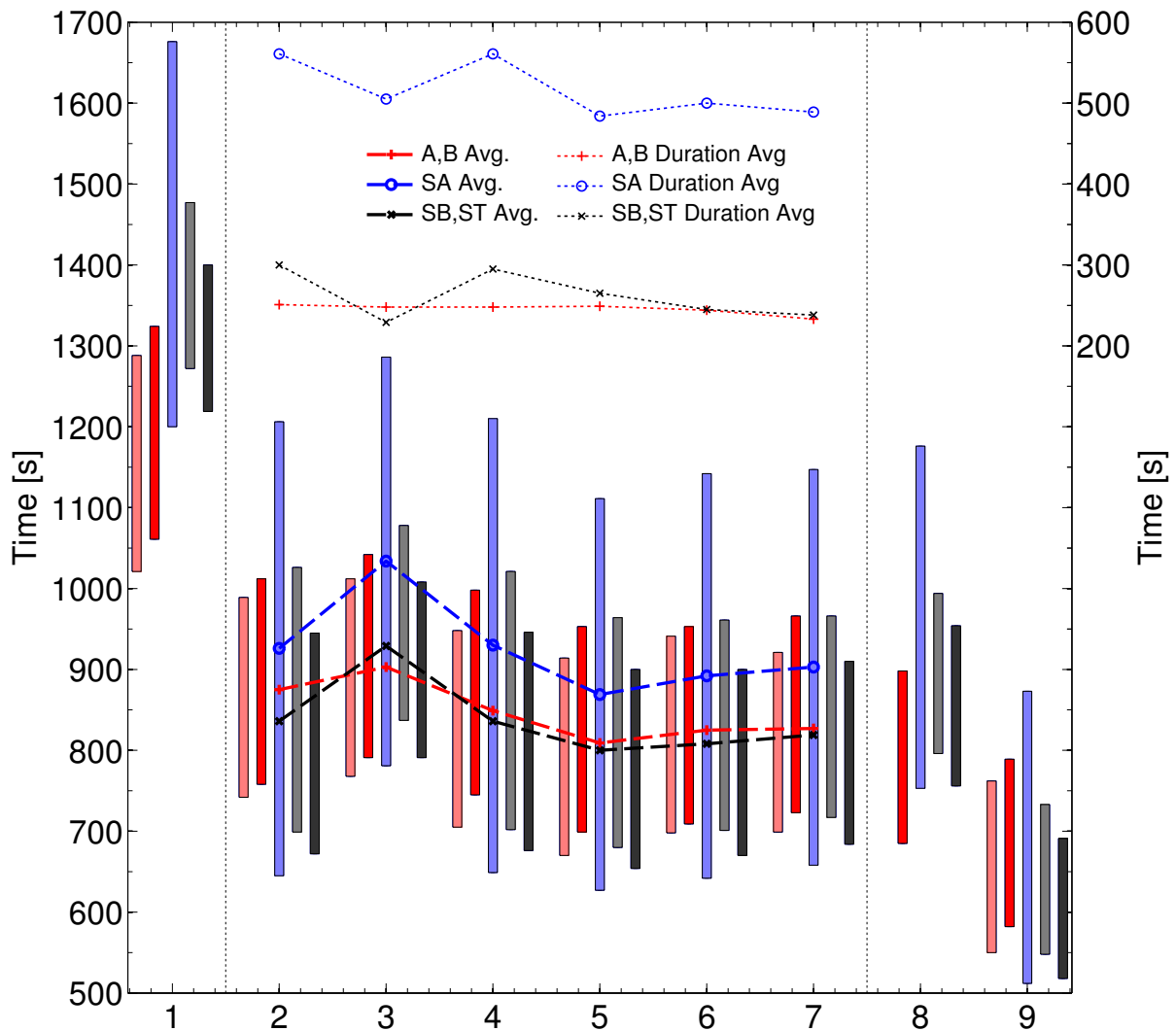


**Figure 8.6:** Phase Transformation Time: Austenite to ferrite phase transformation time intervals for all measured and simulated castings, for each of the nine MPs. The red bars represent the measured castings with the  $\tau$ -alloy. The blue is the simulation of the pearlitic  $\alpha$ -alloy, the grey is the simulation of the fully ferritic  $\beta$ -alloy, and the black is the fully ferritic  $\tau$ -alloy. The bars indicate the phase transformation interval, and the bold dashed lines indicate the mean phase transformation time for the three alloys for MP 2-7. The thin dashed lines at the top indicate the phase transformation interval duration for the three alloys for MP 2-7 and is linked to the right y-axis. A and B are the TC-castings, and SA, SB, and ST are the simulations of the three different alloys.

of different alloying elements. Si will segregate into the austenite, as reported by Vazehrad [122]; which in this respect presents two effects: (1) The Si will take up some of the volumes in the FCC structure, thus reducing the C content in the austenite, and as a result a more substantial primary graphite precipitation will occur. (2) The concentration of Si will be highest in the area with a high cooling rate as the first austenite will form here, and in turn, the Si will segregate into the austenite where it first

appears. Subsequently, the Si content of the residual melt will be reduced, which lowers both the eutectic and the eutectoid temperatures and increases the potential C content of the last to freeze austenite. Hence, the differences in temperature intervals can be seen as a reference to the solidification history of the casting.

The segregation effects of Si are nicely illustrated in the colour etched sample in fig. 6.2 on page 92.

The figure shows how the ferrite near the primary nodules are rich in Si, and how pearlite have formed at the edges of the high Si ferrite.

Comparing the transformation of the TC-castings and the simulated castings it was found that the curves in fig. 8.3 on page 126 show good correlation. However, the phase transformation temperatures vary with as much as 50 °C for MP 2. The temperature difference may partly be related to the calculation of the phase transformation in the numerical simulation. The calculated temperatures and transformation may be idealised as a result of the underlying assumption required to solve the equation within a reasonable time. Note, however, that the difference is much less for the larger modulus at MP 1. This reduced difference indicates that the effect is related to the cooling rate during either solidification or at the eutectoid transformation.

The thermal influence on the transformation temperatures for the simulated casting is confirmed by the duration of the interval, which is shown at the top of the graph with dashed lines. Note that the measured curve (red) is very flat, while both of the simulated curves show a significant reduction in the phase transformation interval for the MP 3. This position was right below the top feeder and was hotter than the other MPs in the thin-walled section.

Note also that the MP 8 for the  $\tau$ 23A did not provide any thermal measurement. The other TC-casting measurement at MP 8 displayed a very high phase transformation temperature. This increased temperature was considered a measurement error.

### 8.3.2 Phase Transformation: Time

---

The phase transformation times are shown in fig. 8.6 on page 129, and are set up in the same manner as with the phase transformation temperatures in fig. 8.5 on page 128. Compared with the transformation temperatures the transformation times are more uniform. The high Si alloys ( $\beta$ ,  $\tau$ ) showed a relatively short transformation duration, while the pearlitic-ferritic  $\alpha$ -alloy showed significantly longer phase transformation duration. In fact, the pearlitic-ferritic phase transformation was twice as long as the fully ferritic phase transformation. This prolonged transformation is shown by the dashed lined at the top of the graph, which indicates transformation duration for the three groups. Note that the duration graphs are linked to the right y-axis. Note also that the simulations (blue and black) predict

a variation around MP 3, while the measured temperatures (red) resulted in a very uniform phase transformation duration.

Figure 8.5 on page 128 shows at which temperatures the transformation occurs for the different MPs, while fig. 8.7 on the facing page shows the sequence between the different MPs. It is observed that MP 1 (the boss) showed the latest transformation, while MPs 2-8 showed almost the same start and end times. Note though that MP 3 goes through the phase transformation a little later than the rest of the group. Even later than the MP 8 in the ring on top of MP 3. Likewise, the ring on the right (MP 9) cooled even faster was the first MP to undergo the phase transformation. Note that the modulus of the ring is larger than the thin-walled section, and thus solidify later than the thin-walled section. Hence, the solidification and the eutectoid phase transformations progress differently. The solidification and cooling pattern of the casting show this very well. See fig. 8.8 on page 132.

### 8.3.3 Thermal Deformation Analysis

---

Figure 8.2 on page 125 shows that the difference between the cooling curves for two castings made under similar conditions was small. The two castings solidify and cool identically. The austenite to ferrite phase transformation was shifted 40 s, but the difference in the duration of the phase transformation was only 4 s. The duration of the phase transformations was within a 10 s time frame for six of the nine MPs. The largest measured difference was 25 s at MP 9.

The cooling and solidification times and temperatures were similar to both the measured and simulated results. In the trial castings and for the simulations it was found that the thin-walled section (MP 2-7) solidified before the ring (MP 8-9). However, after solidification, this changed so that the ring cooled faster than the thin-walled section. Thus, the ring was the first section of the casting to go through the austenite to ferrite phase transformation followed by the thin-walled section, and ending with the boss (MP 1). Figure 8.7 on the next page shows how long time it took before the MP was halfway through the austenite to ferrite phase transformation (full lines at the top). The duration of the phase transformation is also shown (dashed lines at the bottom). For the trial castings, the ring right below the top feeder also cooled faster than the thin-walled section. All three simulations

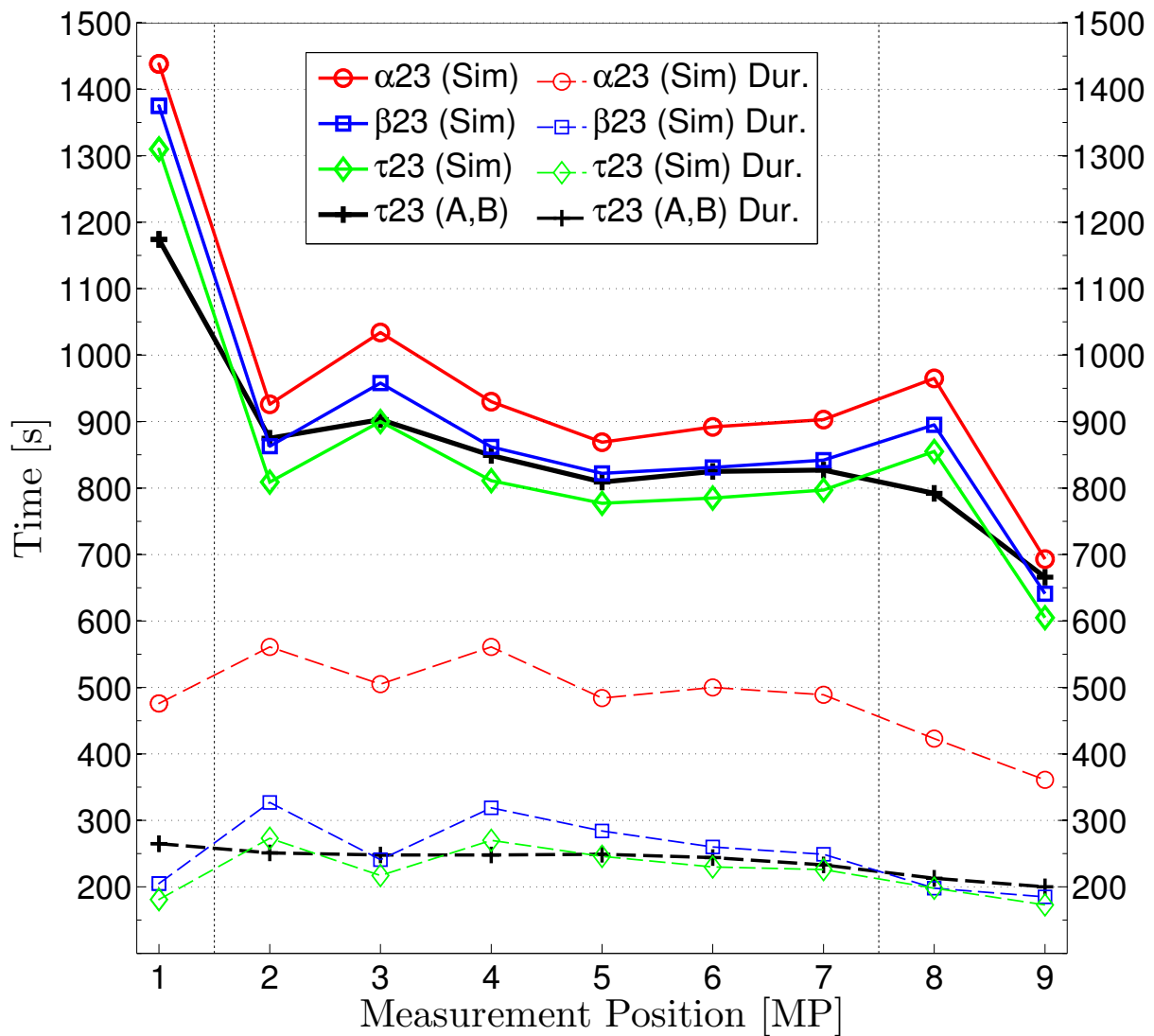


**Figure 8.7:** Thermal analysis summary. The full lines show the mean time of the austenite to ferrite phase transformation for all nine MPs inside the casting. The dashed lines show the duration of the phase transformation for each MP. The black lines marked with + display the average of the experimental measurements. The three other curves were obtained via numerical simulation.

showed a greater effect of the heat from the top feeder on the top part of the ring (MP 8) and on the top most part of the thin-walled section (MP 3).

The top feeder was also found to influence the duration of the phase transformation for the upper part of the thin-walled section (MP 2-4) for the numerical simulations. All three alloy simulations showed a prolonged phase transformation duration at MP 2 and 4, while the centre point between the two displayed a decreased duration of the phase transformation. See fig. 8.7. In comparison, the trial measurements did not show a similar effect.

The simulations showed an increased duration of the phase transformation at MP 2 and 4, and decreased duration close to the feeders at MP 1 and 3, although the duration at MP 8 was unaffected when compared to MP 9. The duration of the phase transformation was longest at the boss (MP 1). The thin-walled measurements (MP 2-7) was slightly shorter and all within an 18 s time frame. Finally, the fastest phase transformation was found for the ring (MP 8-9). Measurements and simulations showed that the eutectoid transformation begins at the ring and

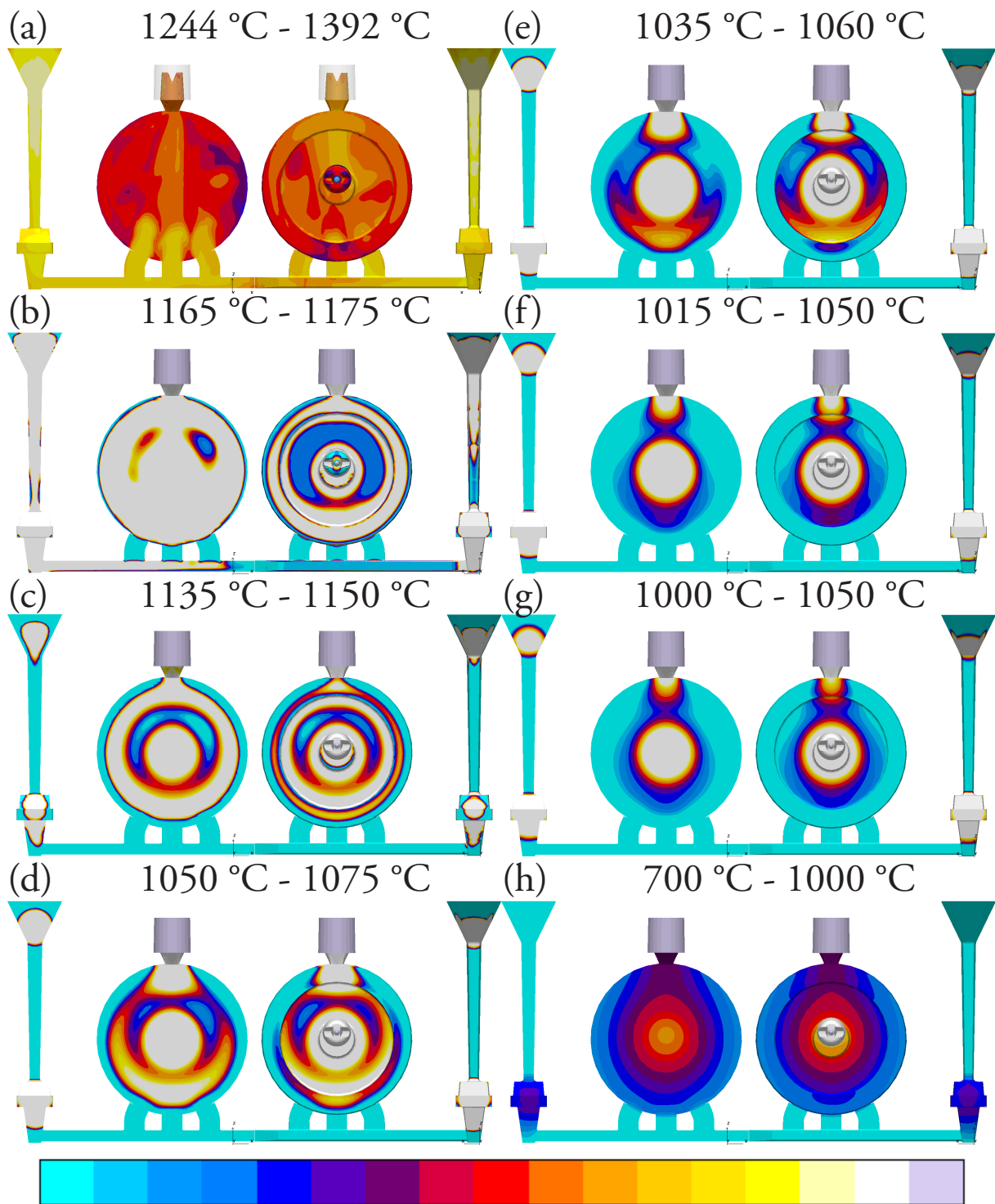


**Figure 8.8:** Thermal gradients for the solidification and cooling of the casting viewed from both the front and the reverse side. The temperature scale is adapted for each of the steps through the solidification and cooling to show the small but important thermal gradients that exist throughout the sequence. The simulation is for feeder combination  $\beta 23$  with a GP level of 6.

travels through the thin-walled section to the boss at the centre.

The duration of the phase transformation for the trial measurements (A,B) only varied by 80s from MP 1 to 9 in an almost linear fashion. The duration of the phase transformation of the high Si alloys ( $\beta, \tau$ ) simulations varied by 130s with peaks at MP 2 and 4. The pearlitic low Si alloy ( $\alpha$ ) varied by 200s and also showed peaks at MP 2 and 4. The duration of the phase transformation for the pearlitic-ferritic alloy ( $\alpha$ ) was found to be approximately twice as long as for both the trial measurements and the high Si alloy simulations. This prolonged duration was related to two-step phase transformation that was found for all MPs for the pearlitic-ferritic  $\alpha$ -alloy.

The temperature distribution in the casting during the solidification and cooling from 0% to 100% solidified was analysed. It was found that there was a non-uniform temperature distribution in the casting. This non-uniform distribution was particularly evident in the thin section of the plate and is illustrated in 7.8e on page 105. The figure shows two colder areas located at approximately 02:00 hrs and 10:00 hrs respectively. Those two regions remained 5 °C to 10 °C colder than the rest of the thin-walled section until 85% of the entire casting was solidified. The local solid-fraction was at this point 100% and the local temperature approximately 1050 °C. Since this temperature variation was observed during eutectic solidification, where that solidification interval was small, it means that there was a significant local variation in solid fraction and strength of the casting.

Likewise, it was found that the inside of the ring and outside of the boss, where the geometry retains the heat so that circular hotspots are formed, solidification was markedly slower than for the remaining casting. In these hotspots, the heat was retained on the front side of the casting, while on the reverse, flat, side cooling was more efficient. As a result, the

temperature gradient from one side of the casting was in the order of 10 °C over a distance of 10 mm. It was also found from the simulations that this picture was standard for all three alloys.

## References

- [32] David A. Porter, Kenneth E. Easterling and Mohamed Y. Sherif. *Phase Transformations in Metals and Alloys*. 3rd ed. CRC Press, Taylor & Francis Group, 6000 Broken Sound Parkway NW, Suite 300, Boca Raton, FL 33487-2742, 2009. ISBN: 978-1-4200-6210-6.
- [69] MAGMASOFT 5.2 by MAGMA GmbH. [http://www.magmasoft.com/en/solutions/MAGMA\\_5.html](http://www.magmasoft.com/en/solutions/MAGMA_5.html). Program. 2014.
- [119] JMatPro by Sente Software Ltd. <http://www.sentesoftware.co.uk/jmatpro.aspx>. Program.
- [122] Sadaf Vazehrad. *A Study on Factors Influencing the Microstructure and Shrinkage Porosity Formation in Compacted Graphite Iron*. School of Engineering, Jönköping University, 2014. ISBN: 978-91-7595-275-8.
- [134] C. Labrecque and M. Gagne. "Interpretation of cooling curves of cast irons: A literature review". In: *Transactions of the American Foundrymen's Society, Vol. 106*. Vol. 106. Transactions of the American Foundrymen's Society. 102nd Annual Meeting of the American-Foundrymen's-Society, Atlanta, GA, May 10-13, 1998. American Foundrymen's Society. 1998, 83–90. ISBN: 0-87433-195-1.
- [135] Conrad Vogel, Celia Juhl and Ernst Maahn. *Metallurgi for ingeniører*. Polyteknisk Forlag, 2009. ISBN: 978-87-502-0930-0.





# Chp 09

## Discussion

### Discussion

---

<b>9.1 Introduction</b> . . . . .	<b>135</b>	9.3.8 Deformations Measurements . . . . .	141
<b>9.2 Purpose and Objectives</b> . . . . .	<b>136</b>	9.3.9 Thermal Analysis . . . . .	142
<b>9.3 Experimental Setup</b> . . . . .	<b>136</b>	<b>9.4 Porosity Analysis</b> . . . . .	<b>143</b>
9.3.1 Feeder Combination Analysis . . . . .	136	9.4.1 $\alpha$ -alloy (EN-GJS-500-7) . . . . .	143
9.3.2 Trial Plan . . . . .	136	9.4.2 $\beta$ -alloy (EN-GJS-450-10) . . . . .	143
9.3.3 Thermal Measurements . . . . .	136	9.4.3 Porosity Simulation . . . . .	144
9.3.4 Porosity Analysis . . . . .	137	<b>9.5 Solidification and Microstructure</b> . . . . .	<b>146</b>
9.3.5 Numerical Simulations . . . . .	138	<b>9.6 Thermal Deformation</b> . . . . .	<b>146</b>
9.3.6 Process Stability . . . . .	140	9.6.1 Surface Deformation Measurements	147
9.3.7 Microstructure Analysis . . . . .	140	<b>References</b> . . . . .	<b>150</b>

---



**D**ISCUSSION of the validity of the experiment and the reported findings. The reproducibility of the experiment and castings is discussed, and the implications of the thermal deformations are addressed and explained.

Keywords: Discussion, Trial plan, Experimental setup, Thermal Deformation, Solidification, Microstructure, Flatness value

Chapter findings reported in: . . . Supplement I, on page 301  
 Supplement II, on page 315  
 Supplement III, on page 325

### 9.1 Introduction

---

As a lot of different findings, observations, and data have been presented in the previous chapters constituting the first part of the dissertation. This chapter will address and discuss the findings, strengths, and weaknesses of the experimental part. Additionally, this chapter will also address the correlation of between feeding defects

and thermal deformation of the castings.

Austempered Ductile Iron (ADI), Adaptive Thermal Analysis System (ATAS), Continuous Cooling Transformation-diagram (CCT-diagram), Carbon Equivalent Value (CEV), Coordinate Measurement Machine (CMM), Non-Linear Clustered Indications (CP), Graphite Precipitation Coefficient (GP), Lamellar Graphite Iron (LGI), Manganese (Mn), Spherical Graphite Iron (SGI), Silicon (Si), Non-Linear Isolated Indications (SP), Thermocouple (TC), Time-Temperature Transformation-diagram (TTT-diagram)

## 9.2 Purpose and Objectives

---

THE primary purpose of the first part was to demonstrate that spot feeders could be used to feed secluded section in castings on vertically parted moulding lines. Subsequently it became a priority to investigate the applicability of spot feeder to a more demanding alloy, and to identify the limit of the spot feeder performance. The latter with respect to yield optimisation and potential energy reduction. Part I has also addressed the influence of exothermic feeders on the casting microstructure.

The discovery of the thermal deformations opens an additional objective for this part of the dissertation. The aim was to explain the thermal influence from the feeders on the casting deformation. Understanding the underlying effect of thermal distortion of cast iron castings can potentially be used to reduce machining allowance, and thus reduce energy consumption and tool wear. However, a better understanding of the thermal influence on the casting, made by the feeder, would also help choose the optimal feeder based in a broader knowledge base.

## 9.3 Experimental Setup

---

THE casting was designed as a generic casting with a difficult to feed secluded section. The design included the possibility to place ram-up sleeve spot feeder at both the centre boss section and the top of the rim. Additionally, a traditional parting line feeder sleeve could be mounted on top of the casting. This setup allowed for a wide range of combinations of different feeders, varying both volume, shape, and sleeve material.

### 9.3.1 Feeder Combination Analysis

---

With respect to analysing if the ram-up sleeves were useful for a foundry using vertically parted moulding machines, it was assessed that combination of the parting line feeder at the top and the ram-up sleeve at the centre resembled the way such a casting would be produced on a vertical moulding line. So in this respect, the setup was well suited for the purpose.

The design that allowed for the removal of the different feeders was very successful. It was essential to show the influence of the two feeders by themselves, as well as obtain a reference casting without any feeders. The full influence of the two feeders would have been impossible to assess without references

cast without feeders. The castings cast with only the top feeder, only the centre feeder, or without both feeders showed that the castings could not be made soundly without the feeders.

The feeders analysed were chosen based on the modulus of the ring for the top feeder, and the modulus of the boss for the centre feeder. The feeder modulus for the insulating and insulating-exothermic sleeves was based on the classical approach of making the feeder 1.2 times larger than the section it is required to feed. Based on the moduli of the ring and boss sections shown in table 4.1 on page 68, this gave the feeder moduli listed in table 4.3 on page 70.

### 9.3.2 Trial Plan

---

The castings were cast in three different sessions at Valdemar Birn <sup>A/s</sup> (Vald. Birn), and a fourth session at the university foundry at DTU. It would have been advantageous if the castings at Vald. Birn could have been cast at the same date to ensure the greatest possible reproducibility of the casting conditions. However, it is assessed that the casting conditions were as similar as possible between the first and second sessions and the third session. However, the change in alloy between the two dates means that no direct reference can indicate which, if any, differences in casting conditions occurred between the two trial dates. It would have been advantageous to cast a few castings with the EN-GJS-500-7 alloy on the day of the trials with the EN-GJS-450-10 alloy. This additional casting would, however, not have been possible as the foundry changes the entire iron production to a given alloy. Hence, no EN-GJS-500-7 alloy melt could have been acquired. This said, there were no indications that the differences observed between the two different alloy castings were not related to the alloy properties.

An advantage of the division of the trials was that the session with the high Si  $\beta$ -alloy could be designed based on the findings of first trial sessions. A full factorial parameter examination is always the best for data completeness. However, as the trial plan had to provide useful data with a limited number of trial castings, only selected feeder and alloy combinations could be examined.

### 9.3.3 Thermal Measurements

---

The fourth and final session was cast at the university foundry at DTU. This naturally entailed



some process variations in relation to the full-scale foundry that Vald.Birn have at their disposal. However, the experiment with two castings with 11 thermocouples could not have been performed at Vald.Birn. Previously thermal measurements had been performed at Vald.Birn, as described by Aagaard [71]. However, modernisation of the foundry layout since the work of Aagaard made this approach impossible. Additionally, it would require that the moulding line was halted while the castings cooled. Because of these reasons, and because of the availability of the university foundry at DTU, it was decided to cast the TC-castings at this facility.

The casting condition of Vald.Birn could not be replicated in full at the university foundry. The trials at Vald.Birn was cast on a DISAMATIC 230A, while the trial series at DTU was cast on a smaller DISAMATIC 2110. Additionally, the stability of the sand production quality and stability at the university foundry cannot match that of an operating foundry. The alloy composition was slightly different from the  $\beta$ -alloy cast in session 3 of the Vald.Birn trial sessions. See table 4.2 on page 68. The differences in alloy composition and the other process parameters were assessed to not significantly influence the thermal performance of the casting, as compared with the  $\beta$ -alloy castings made at Vald.Birn.

It would however, had been advantageous to have thermal measurements from the trials at Vald.Birn to compare and validate the TC-castings but also the numerical simulations of the casting combinations. The only temperatures available from the first three casting session were the pouring temperatures and the ATAS curves made before the sessions [114]. Though these temperature measurements were sufficient to have a target pouring temperature for the fourth session, a thermal measurement from the casting itself would have been a bonus. Eventually, this leads to the development of the setup for thermal measurements that could function with the production facilities at Vald.Birn. See section 11.4.1, on page 173.

### 9.3.4 Porosity Analysis

---

The casting design did not allow for non-destructive porosity analyses of the centre boss. As part of the objective was to quantify the efficiency of the different feeder combinations, three different porosity analysis tools were used—liquid penetrant test, ultrasound analysis, and x-ray imaging. An import-

ant aspect was, however, to analyse the porosity distribution in and close to the feeder, hence favouring methods that allowed for the feeder to be analysed together with the casting. For this purpose, the liquid penetrant test was chosen for the primary analysis via sectioned castings, while the ultrasound and x-ray imaging was used a subsequent confirmation of the porosity findings made with this method.

The outcome of the porosity analysis will be discussed in detail in section 9.4, on page 143, however, the influence of the casting design concerning the possible analyses is discussed here. The limited application of non-destructive porosity tests resulted in the castings being sectioned before it was known that the surface deformation of the reverse side had to be investigated further. In this way, the geometry would have benefited if an initial porosity analysis could have been performed without sectioning the castings. The casting did, however, fulfil the criteria established at the time it was developed.

#### Liquid Penetrant Test

The liquid penetrant tests were performed as prescribed by the corresponding standard—EN1371-1:2011 Founding: Liquid Penetrant Testing—Sand, Gravity Die, and Low Pressure Die Castings [116]. The method has advantages and disadvantages. The advantages were that it is a well known and documented methods that can easily be referenced and with standard types of porosities which can be quantified based in categories. The tests were easy to perform, though the developed ‘porosity prints’ bleed and became obscured with time. This was fixed by photo-documenting the developed porosity prints following the development process. However, the porosities near the surface of the boss section for castings  $\beta$ 11A and  $\beta$ 11C, discovered by the subsequent ultrasound analysis, not the less showed that the bleeding edges indeed could potentially hide porosities. See section 5.1.6, on page 80.

The drawbacks of the liquid penetrant test type of porosity analysis are first and foremost that only the porosities that happen to lie in the sectioned plane can be discovered. The porosities that are found can be mapped and assessed precisely, and they provide solid evidence (no pun intended), that the porosities are there, and where they are located for that specific plane of examination. However, the possibility that porosities are located in all three spatial dimensions, while the analysis only took into

account a two-dimensional view, leaves the possibility that porosities are overlooked. However, the duplicates of the castings reduce the likelihood of accidentally sectioning three castings with porosities, and by happenstance not finding any of the porosities. Additionally, an increased amount of porosities will likewise also increase the change that some porosities are found.

Porosities located away from the sectioned plane cannot be detected. Additionally, improper cleaning of the castings before the final development of the penetrant may cause false positives. This is especially problematic near corners, edges, or other less easily accessible areas. Fortunately, these bleed effect often show up in an area where porosities would not naturally occur, which makes it easier to estimate if the marking is related to a porosity or an improperly cleaned scratch, edge, or corner.

The photo documentation was necessary to allow for all the castings to be analysed together, and to allow multiple views assist with the classification of the porosity size, type, and location. However, the scale of the printed photos of the penetrant treated castings was not 1:1. This was a known fact and compensation was made. However, this was an added uncertainty factor concerning the correct assessment of the porosity sizes.

#### Ultrasound and X-ray analysis

The ultrasound analysis and x-ray imaging were performed after the castings were sectioned and analysed with the liquid penetrant test. In addition to the sectioning of the castings, it was also necessary to cut off the feeders to ensure plane surfaces for the ultrasound analysis to work. Thus, these subsequent porosity analyses were excluded from analysing the feeders. The analysis of the casting geometry did, however, to a great extent confirm the porosity results obtained by the liquid penetrant tests. The ultrasound analysis additionally also found a few porosities which had not been revealed by the initial inspection, thus providing a more complete picture of the correlation between the feeder configurations and the formation of porosities. It should also be noted that the additional porosities discovered were found in the boss section of two castings that were expected to have porosities on account of the third casting in the group showing porosities in this area.

The x-ray imaging yielded a further confirmation of the porosities found in the two previous analyses, though it also yielded a single small porosity loc-

ated at the right side of the ring, which was not discovered by the ultrasound analyses. This porosity, however, was in casting  $\alpha 00C$  which was cast without any feeder and showed large porosities at both the boss section and the ring.

A weakness of the ultrasound and x-ray analyses is the limited number of castings examined by each of the methods. In total 24 castings, out of the 53 castings made, was tested, while only four out of the 24 ultrasound analysed castings were x-rayed. Thus, the two analyses serve as confirmation of the liquid penetrant tests but do not themselves provide a complete description of the porosities found in all castings. On the other hand, the castings selected for ultrasound and x-ray analysis respectively were chosen because these castings were the most interesting to examine—to prove the confirmation of the porosity-free castings actually being porosity-free, as well as examine the porosity formation away from the sectioning line.

#### 9.3.5 Numerical Simulations

---

The uncertainty related to the porosity findings of the liquid penetrant test, the ultrasound analysis, and the x-ray imaging was for a large part reduced by the numerical simulation porosity analysis shown in fig. 5.7 on page 86. Besides having the function of benchmarking the calibrating the MAGMASOFT setup; the porosity simulations also showed that the predicted porosities were located in the area covered by the sectioned plane. Moreover, it also showed that the number and size of porosities observed with the liquid penetrant test corresponded to the amount and location of the porosities predicted by the simulations.

Additionally, it was found that the calibrated simulation provided accurate simulations of the castings for most parameters. Some parameters, eg the porosity analysis, was found to be useful and relatively precise. Though the exact mathematics of the criteria functions used by MAGMASOFT is not known, it was found that the porosity probability estimates made by MAGMASOFT to a certain degree matched the porosities found in the castings via the three different porosity analyses.

The main issue was to calibrate the simulation setup to match the casting conditions, and particularly the setup of the alloy and melt treatment to match the porosity findings of the porosity analyses. Most important, though, it was possible to find a setup for each of the alloys that predicted to a

reasonable degree the amount and location of the porosities for the different feeder configurations.

It was assessed that the number and size of porosities corresponded to a GP level of 6.5, where only integers can be selected. However, reading and understanding the results provided by MAGMASOFT require an understanding of the casting process, and in no small degree is aided by an empirical knowledge of the processing conditions in the particular foundry. This is not to say that the simulations are not accurate, but more a question of all the process parameters that cannot be included in the simulation. As phase diagrams, CCT-diagrams, and TTT-diagrams require skill and knowledge to use, the same is true for numerical simulation results.

Hence, the process of simulating the casting and matching the simulations and results provided insight into the significant process variables, as these had to be identified and adjusted to match the simulations to the casting results.

The approach of matching the simulations to the observed results may appear backwards, especially with the approach that simulation is primarily used to aid the design and construction castings before the patterns are made. Note however, that as an external user, the standard setup developed as empirical knowledge by the foundry engineer at Vald. Birn was not available. This said the parametrical investigations required to develop a suitable standard simulation setup for this specific disc casting was an advantage in understanding the nature of the castings itself, as well as an opportunity to investigate the processing of MAGMASOFT.

A great challenge for the correct and precise prediction of porosities in castings is that porosities are the most notable outcome of the simulations for most operators. Other aspects, such as mechanical properties like the ultimate tensile strength, Young's modulus of elasticity, nodule count, pearlite amount, and potential white solidifications can also be tested and are sometimes tested as often as porosity analyses are made. However, porosities for many foundries act as a benchmark of the simulation setup, as all major process parameters influence the formation of porosities in one way or another. Be it pouring temperature, filling flow, heat transfer, sand composition, mould strength, alloy composition, microstructure formation, or contraction and expansion; all these factors influence the formation of porosities in the simulations as well as in the foundry. See chapter 3, on page 39. This, however, also muddle the picture somewhat, as many factors require fitting to an acceptable degree to set up

the simulations, with only an indirect correlation between the parameters and the outcome. Similarly, changes to the production conditions in the foundry, deliberate or not, also disrupts the picture; thus it is important that the calibration of the specific alloy is calibrated and that the calibration is kept updated.

Something that is not simulated by MAGMASOFT is inclusions and impurities in the melt. The assumption is that the melt is clear, and that the abrasion of the mould do not occur. As described in section 2.2.1, on page 17 the surface tension of the forming pore make it very difficult for a pore to form without a nucleating site, because the pore cannot overcome the very small radius of the sphere that forms the pore itself. As related in eq. (2.3) on page 18 by Stefanescu [26]:

$$P_\gamma = \frac{2\gamma_{LG}}{r}$$

where  $P_\gamma$  is the pressure induced by surface tension on the pore,  $\gamma_{LG}$  is the gas/liquid surface energy, and  $r$  is the radius of the pore.

Hence, impurities in the melt may change the formation of porosities in a way MAGMASOFT cannot predict. Note that this assumption requires both the presence of inclusions in the melt and that the melt is oversaturated with gasses as reported by Stefanescu and Diószegi et al [26, 33, 34].

As described in section 5.1.4, on page 77, four of the 51 castings analysed had porosities at the lower ring section (VII), some of which were analysed resemble inclusion defects. Viewing the porosity in fig. 5.7 on page 86, however, it is also noted the simulation setups with a graphite precipitation of both 6, 7, and 8 showed potential porosities in this area. For the  $\alpha$ -alloy, it was however assessed that the graphite precipitation of 8 was a more accurate description of the performance of the  $\alpha$ -alloy. Thus, an explanation for the porosities in the lower ring section (VII); which was not predicted with the high graphite precipitations, could be, that a melt impurity or other small inclusions have acted as a nucleation site for the porosities. Additionally, the porosity was also located in an area shown by the other simulations to be prone to forming porosities.

Whether or not the above theory for the formation of the porosities in the lower ring section is correct, it is essential to understand the porosities formed in the castings being analysed. As porosities formed for process conditions, as eg inclusion and melt impurities, that is not simulated

by MAGMASOFT, but can be found in the castings, will obscure the correlation between the simulated results and the analysed castings.

### 9.3.6 Process Stability

---

The repeatability of the castings was excellent, as was shown by both the porosity analysis in chapter 5, on page 75, and the thermal deformation analysis in chapter 7, on page 97.

Casting three duplicates of most of the castings allowed for an estimation of the process variation, even though three samples are a tiny population for statistical purposes. However, when all the castings were analysed together, sorted based on different trial parameters, a reasonable statistical representation could be achieved.

Based on the porosity and deformations findings, and the possibility to distinguish which feeder combination had been used, based on the deformation of the casting, indicate that the production process at Vald.Birn was very stable and controlled. Had the process stability and reproducibility not been this high, then other factors would have influenced the porosity formation and the thermal deformation of the castings, obscuring the effect of the investigated process parameters. Chapter 7, on page 97 showed how the different process parameters could be distinguished statistically based in the casting deformation alone, both for thickness of the thin-walled section and the surface shrinkage on the reverse side of the casting.

### 9.3.7 Microstructure Analysis

---

The initial macrostructure analysis provided information about the segregation of the pearlitic-ferritic casting and proved that the  $\beta$ -alloy castings were indeed fully ferritic. The Nital etching worked well considering the size of the samples. The sectioned castings were ground plane as this was the best surface quality that could be achieved. The size of the sectioned pieces made it impossible to use any of the traditional metallographic preparation equipment. However, the etching results showed that the acquired surface finish was adequate for the purpose. Additionally, the dissolved Nital etchant of just 1% Nitric acid ( $\text{HNO}_3$ ) prolonged the etching time, which made it easier to retain a stable process and achieve the same level of etching for all castings.

The photo documentation of the macro-etched castings served as an archive for later analysis. How-

ever, the etched castings themselves were used for the analysis, as this provided a better view of the macrostructure compared with the photos.

The colour etching of the microstructure was performed at the School of Engineering at Jönköping University in Sweden. This was a great opportunity as it was not possible to use the picric acid at the facilities at DTU. A drawback of this was however, that the samples to be analysed all had to be pre-selected and was limited to the number of samples that could be processed during the stay in Jönköping. As the analysis of the colour etched microstructures did raise questions that required further investigations, it was, fortunately, possible to borrow the facilities at Jönköping University once again. Hence, the selection of samples for the second etching was made based on the knowledge and questions raised by the first etching. This second etching was very valuable as it made it possible to disprove the speculations made about the last to freeze melt in supplement II on page on page 315.

Colour etching using picric acid has advantages and disadvantages. Among the advantages are that one etchant can reveal a range of different solidification and segregation effects. This provides information about the correlation of different effects, that would else require several different types of etchings to be made on the same sample, and then compared afterwards. Additionally, the reactivity of Motz's picric etchant with Si was ideal for a comparison of two alloys where the main difference in composition relates to the Si content [121].

A disadvantage of Motz's etchant, besides that it should be used with extreme care and safety, is that the process is arduous to control and automate. Hence, the successful etching of a sample relies on the skill and experience of the operator performing the etching. As described in section 6.4.1, on page 90, the tint is created by a thin-film on the surface of the samples, and the thickness of the thin film determine the colour of the tint. Hence, a prolonged etching of the sample will 'burn' the colours of the sample by having developed a too thick thin film across the different microstructures. What makes this difficult is that the microstructures with a high concentration of Si, which should have a blueish tint, become an orange-brown typically found in the last to freeze melt which is poor on Si. Hence, the optimum etching time is when the segregation differences are displayed with the greatest contrast.

If a sample is under-etched, the etching can be continued. If a sample is etched long enough for it to get ‘burnt’ then it can be polished and etched again. The challenging assessment is to etch the samples the exact right amount that can provide comparable etchings. This is difficult because there is no reference guide. Each alloy and even each sample contain different amounts of Si and have differences in the microstructure that makes the samples behave differently. Hence, it can be difficult to know how the sample should look when it is etched right. This was shown by the results presented in supplement II on page on page 315, where the variation in the degree of etching led to doubt about the amount of Si segregation in the exothermic centre feeder. The second etchings of the same samples proved that this was, with a high probability, an effect attributed to the etching of the samples rather than an effect of the solidification and segregation.

As with the numerical simulations, the setup, etching, and subsequent microstructure analysis of the colour etched samples require experience and know-how to perform and analyse afterwards. The possibility to re-etch samples of particular significance to prove or disprove the findings is a great asset.

The microstructure of the castings matched the section thickness that the samples were obtained from. The comparison of the microstructures in the feeders with insulating and exothermic sleeves respectively, showed that significant or distinguished differences in the microstructure could not be found.

### 9.3.8 Deformations Measurements

The numerical simulations can be used to verify the amount and location of porosities. MAGMASOFT can also provide information regarding thermal deformations caused by stress and strain developed during solidification and cooling. The numerical simulations cannot, at the moment, provide information about surface shrinkage caused by the thermal gradient during cooling and solidification. Hence, it was necessary to examine the castings to assess the influence of the feeder configurations on surface shrinkage, or thermal deformation.

The first step was to establish if any surface shrinkage occurred for these castings and these alloy at all. This was examined by documenting if the reverse side of the casting was as plane as the casting was designed, or not. See fig. 7.1 on page 98.

The investigation showed that the castings did show signs of surface shrinkage. However, this approach could not provide precise comparable results, and this particular approach only investigated the vertical centre line of the casting, not the surface as a whole. Thus, it was decided to measure the surface to enable a full analysis of the geometric difference between the casting and the pattern.

The deformation measurements were made using a calibrated CMM, and the measurement data was assessed for a reference artefact. Hence, the measurement data themselves were assessed to be valid within the expanded measurement uncertainty shown in table 7.10 on page 119. The roughness of the surface of the casting may potentially be of a magnitude to influence the measurement results. A 3 mm probe was used to limit the effect of the surface roughness. While a small probe can potentially measure either the valley between two peaks, or the top of one of the peaks, the larger probe (if large enough) is too large to reach the valley, and will thus measure close to the peak or on the peak itself. The probe size was assessed based on the work about casting surfaces by Nwaogu et al [108].

Additionally, if the probe measures a protrusion or large enough valley (defect) that the probe could reach the bottom, these data would show up as outliers that could be assessed manually and if need be discarded. Not such outliers were found, and no data were discarded.

A drawback of the deformation analysis was that only one half of the casting could be investigated as a whole, as the castings had all been sectioned for the porosity analysis before it was known that surface deformation measurements were required. Hence, the measurements only represent one half of the casting. Additionally, the sectioning of the casting itself may potentially have released some strain that deformed the casting. It would have been preferable if the castings had not been sectioned before the measurements were made. The potential release of deformation strain in the castings was, however, the same for all castings, and did not directly influence the deformation caused by thermal gradients during solidification.

As the simulations of the casting deformation in section 7.1.2, on page 98 show, the casting naturally ‘fold’ forward leaving a local maximum at the centre of the reverse side of the casting. This, however, does not match well with the geometries measured for any of the castings—they all curve inward leaving the centre area a local minimum.

### 9.3.9 Thermal Analysis

As described in section 9.3.3, on page 136, some of the process parameters from the trials at Vald.Birn could not be replicated at the university foundry at DTU, and no thermal measurement from the solidification and cooling of the castings were recorded during the sessions cast at Vald.Birn. However, it was assessed that the thermal data could be considered as representable for the thermal gradients present in the casting during solidification and cooling.

Another weakness of the thermal analysis was that only one feeder and alloy combination was examined. With the number of thermocouples placed in each mould, 11, the data acquisition equipment simply could not handle more than two castings at one time. Additionally, it was assessed that it was more important to examine the reproducibility of the thermal data, rather than examining two different feeder combinations. Casting two castings with the same feeder configuration would also provide information about the process stability of the thermal gradients in the casting. The thermal data from the experiment should then be used to validate the numerical simulation setup, which in turn could be used to simulate other feeder combinations.

A large part of the thermal analysis was based on the phase transformation intervals identified via the second derivative of the cooling curves from the thermal measurements and numerical simulations respectively. To obtain cooling acceleration curves without too much noise, the cooling curve data was smoothed using a Gaussian distribution filter. This approach will theoretically smooth the curve without obscuring or moving the underlying data too much. Unless the noise insulation has been perfect and the cooling curves are without fluctuations, the signal noise will be increasingly more visible in the data per derivation step. A typical approach to reducing signal noise is to mean several measurements into one. This however, requires a high enough sampling rate to retain a reasonable time step for the mean data. The experimental data was meant from the recorded sampling rate of 100 Hz to 1 Hz before the subsequent smoothing of the curves using the Gaussian distribution filter.

Note that these data operations can potentially shift the cooling curves, which in turn will shift the minimum and maximum of the derived curves. To ensure the data smoothing did not significantly alter the shape or position of the cooling curves, the smoothed curves were plotted together with the

original curves to assess if the transformation was acceptable or not.

The magnitude of the smoothing was greatest when applied to the original curve, as this reduced the small peaks that would create greater peaks for the derived curve. Hence, to limit the smoothing of the original curve, the Gaussian distribution filter was also used on the first derived curve, and subsequently for the second derivative as well. This was found to be the best method to ensure that the original curve was not changed too much, while still obtaining smooth cooling acceleration curves with identifiable local minimum and maximum. See fig. 8.2 on page 125.

The location of the minimum and maximum of the second derivative was found manually for all 22 cooling curves. Subsequently the location of the minimum and maximum was used to manually find the intersection points with the corresponding cooling curves, which provided the start and end temperatures for the phase transformations. The manual identification of the intersections may potentially have an inherent inaccuracy due to the human factor. However, the identification was performed with great care and with a magnified section of the graph to provide a large view of the local turning point or intersection. It is assessed that the inaccuracy is no more than  $\pm 2$  s and  $\pm 2$  °C for the manual identification of the intersections points. It is considered that the smoothing of the cooling curves and may have a significant influence, and the synchronisation of the cooling curves initiation in itself can shift the curve a few seconds. However, there is no indication that these potential inaccuracies should be systematic, and thus it is assessed that the presented time and temperature intervals are reliable within a few seconds and a few °C for each measurement. See figs. 8.5 and 8.6 on page 128 and on page 129. Note however, that there is an inaccuracy of the thermocouple measurement itself as well.

While the temperature measurements from the experiment showed some signal noise, the cooling curves obtained via the numerical simulations had another problem. To optimise the simulation time the calculations run close to the edge of stability. De facto this means that the data output sequence does not follow a fixed time step as described in chapter 3, on page 39. This in turn, when the steps become too small, will create noise in the derived curves. The reason is that when the time step becomes close to zero, any small change in temperature will go towards infinity. However, this cannot be solved by

smoothing the curves, as the underlying problem is the time step and not the recorded temperature.

To work around the problem, the cooling curves were interpolated using a 6<sup>th</sup> degree polynomial. Subsequently, the function could then be derived to find the first and second derivative. Some degree of inaccuracy will come from this. The original cooling curve and the extrapolated cooling curves were plotted together to assess the differences in the range of interest for the eutectoid phase transformations. Several fitting functions and settings were examined before the best fit was chosen for the continued analysis.

The thermal gradient analysis was based on the calibrated numerical simulation of the  $\beta$ 23 casting with a GP level 6. See fig. 8.8 on page 132. The thermal gradients shown in fig. 7.8 on page 105 is for the  $\alpha$ 23 casting, proving that the same phenomenon occurs for both the  $\alpha$ - and the  $\beta$ -alloy. The thermal gradients are small, which as a result require a very narrow temperature gradient scale to show these effects. There is some uncertainty as the gradient scales are of different intervals, and are all defined manually. Additionally, the interpretation of the figure is challenged by the same colours representing different temperature for each of the eight subfigures. The only constant is the order of the colours. Hence, the figure should be view as showing the trends and which areas are hot and cold, and not to estimate the absolute magnitude of the gradients.

In this case, the effect was discovered based on the observed deformations, which led to the theory of a thermal gradient resulting in differentiated solidification within the thin-walled section. However, if such a thing was not expected, it is unlikely that these effects would be discovered. For most simulations, the focus of the analyst, and thus also the displayed scale, are focused on the larger gradients in the casting. However, this investigation shows that these narrow field gradients do influence the solidification and subsequent deformation of the casting.

The overview shown in 8.8 illustrate the thermal gradients that are created in the early stages of solidification are retained until  $\sim 150^\circ\text{C}$  below the eutectic temperature. Figure 8.8a shows that the gradient is not related to the mould filling, which subsequently must mean that the gradient is related to the casting geometry, and the modulus of the feeders.

## 9.4 Porosity Analysis

---

THE porosity analysis showed that the ram-up sleeves worked successfully for all the  $\alpha$ -alloy castings. Porosities were observed, but only the feeder or feeder necks. Porosities in the feeder neck should off course be considered with care, as this would indicate that the safety margin for the chosen feeder was not great enough. The high Si  $\beta$ -alloy showed a significant increase in observed porosities.

An overview of the areas and sections is found in fig. 9.1 on the following page.

### 9.4.1 $\alpha$ -alloy (EN-GJS-500-7)

---

The casting porosity analysis showed almost no defects for the feeder combinations groups  $\alpha$ 23,  $\alpha$ 11, and  $\beta$ 23. The one defect identified in these nine castings was found in  $\alpha$ 23B area VIII and classified as an SP1 defect. It was a minimal non-linear porosity in the feeder neck of the centre feeder. Thus, all nine castings were sound for all categories according to the EN 1371-1:2011 [116].

Compared to the feeder combination groups  $\alpha$ 20,  $\alpha$ 02, and  $\alpha$ 00, which were cast with the same alloy as above, but cast without the top feeder, without the centre feeder, or without both feeders, all of these nine castings display SP1 or CP1 defects in one or more areas. Casting group  $\alpha$ 20 shows the effect of not using a spot feeder.  $\alpha$ 20A and B display SP1 defects at area V, while  $\alpha$ 20C display a CP1 defect in the same area. As the design of the casting was made to provoke this type of defects, this is not surprising, but it proves that both the exothermic and the insulating ram-up sleeves provide the conditions needed to produce defect-free castings. The spot feeder supply melt, heat, and pressure sufficient for the boss to be porosity-free. Note, also, that part of the pressure-effect is supplied by the casting itself, as described in section 13.8, on page 252.

Feeder combination group  $\alpha$ 02—centre feeder without the top feeder—displayed no defects in area V, but an SP1 defect in area III. This corresponds with the intention of the casting design. Likewise, feeder combination group  $\alpha$ 00 displayed SP1 or CP1 defects in area III and V respectively. The only exception was  $\alpha$ 00B, area V, which was found to be defect-free.

### 9.4.2 $\beta$ -alloy (EN-GJS-450-10)

---

The high Si  $\beta$ -alloy displayed more severe porosities than the  $\alpha$ -alloy. Only feeder combination group

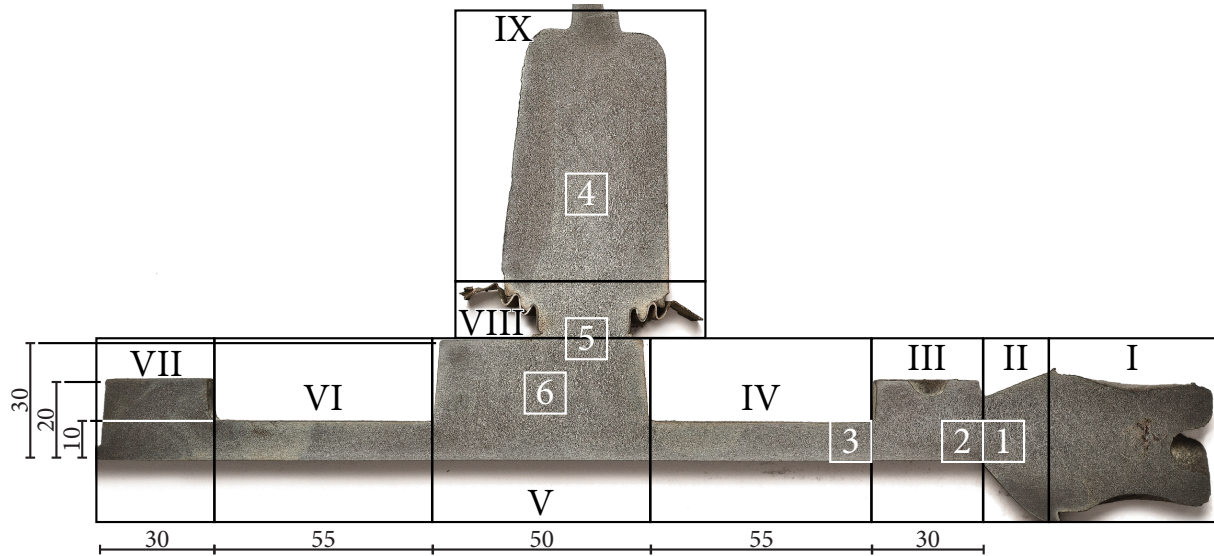


**Figure 9.1:** Overview of sectioned casting a11A. Etched with 1% Nital for ~600s. The casting is divided into nine non-overlapping sections (Roman numerals) for quantification and analysis of porosities. Six sections (Arabic numerals) of 10 x 10 mm were cut and colour etched. All measurements are in mm.

$\beta$ 23 was found to be defect-free. Feeder combination group  $\beta$ 23 used an insulating-exothermic top feeder sleeve and an exothermic centre feeder sleeve. Feeder combination group  $\beta$ 11 displayed defects at the boss section which were confirmed by the ultrasound analysis to be present for all three duplicates. Casting  $\beta$ 11A displayed an SP1 defect in area VIII—the feeder neck of the centre feeder. This defect was similar to the same area of casting  $\alpha$ 11B, which was cast with the same feeder configuration.  $\beta$ 11A, however, also had a small porosity near the surface of the boss. Hence, the  $\beta$ -alloy has shown that there is a functional difference between the insulating and exothermic feeders, where the extended  $M_t$  of the exothermic feeder sleeve, together with the changed shell-forming characteristics, mounted to a significant difference.

Finally, as a reference to feeder combination group  $\alpha$ 20, group  $\beta$ 20 examined the effect of castings cast without the centre feeder for the high Si  $\beta$ -alloy. As with group  $\alpha$ 20, the affected area was area V. The severity of the defects was slightly more pronounced than with the low Si A-alloy.

### 9.4.3 Porosity Simulation

After some adjustment of the process parameters, particularly the graphite expansion, comparable results were achieved between the porosities found in

the castings and the simulated predictions made by MAGMASOFT. The graphite expansion, as well as the general volume contraction and expansion during solidification, play a significant role in describing the feeding characteristics of cast iron. The graphite expansion is again linked with the microstructure and the nucleations and growth of graphite nodules. This, in turn, is again linked to the cooling conditions. All of these mechanisms are described in chapter 3, on page 39.

The cooling conditions and thermal calculations are considered accurate in MAGMASOFT. This is also confirmed by the cooling curves shown in figs. 8.2 and 8.4 on page 125 and on page 127. Note however, that the simulated cooling curves in fig. 8.4 on page 127 do not display the same drop off towards the end of solidification as is seen in the measured cooling curves shown in fig. 8.2 on page 125. The overall correlation between the simulated and measured cooling curves are otherwise considered good.

While the exact cause of this difference between the simulated and measured cooling curves at the end of solidification is not known, this part of the cooling curve is generally governed by the latent heat of fusion, which in turn is related to the nucleation and growth of graphite and austenite. Lasoult et al described a model for the nucleation of graphite in hypereutectic SGI in eq. (3.12) on page 49 [80]:



$$dN = A_n (\Delta T_L^g)^{n-1} (g^l V^{off}) \frac{d(\Delta T_L^g)}{dt} dt$$

when  $\frac{d(\Delta T_L^g)}{dt} > 0$

and

$$dN = 0$$

when  $\frac{d(\Delta T_L^g)}{dt} < 0$

where  $dN$  is the change in number of graphite particles (nodules) for the time step  $dt$ ,  $n$  is an inoculation efficiency constant,  $A_n$  is an inoculation amount constant,  $\Delta T_L^g$  is the undercooling relative to the graphite liquidus,  $g^l$  is the liquid fraction of off-eutectic volume,  $V^{off}$ . Thus,  $(g^l V^{off})$  describes the volume of the remaining liquid and its limiting influence on nucleation sites as the solidification progresses.

Lesoult et al's model is dependent on the undercooling and the recalescence caused by the heat of fusion overpowering the cooling power will terminate further nucleation of nodules. Additionally, Lesoult et al describes a separate kinetic growth model for the eutectic solidification [80].

It is not known if MAGMASOFT uses Lesoult et al's nucleation model, parts thereof, or a similar model. Most likely this is not the case. According to the MAGMASOFT manual a variation of Oldfield's original nucleation model is used as described in eq. (3.11) on page 48 [68, 69, 81]:

$$N_V = A \Delta T^B$$

where  $N_V$  is the number of eutectic cells per  $\text{mm}^3$ ,  $A$  is a nucleation constant,  $\Delta T$  is the undercooling reached during recalescence, and  $B$  is an inoculation constant dependent on the inoculation quality.

Oldfield's model, as opposed to Lesoult et al's model, will not terminate as soon as the cooling acceleration changes but will continue as long as the temperature difference is present as a driving force for nucleation. This may explain part of the difference in the temperature drop off at the end of solidification.

Returning to the graphite expansion, this difference in nucleation is important as the nucleation help determine the potential for particularly the large graphite expansion. Stefanescu et al and Alonso et al showed that cast iron, and in particular SGI, can have a significant graphite expansion at the end

of solidification to counteract the austenite shrinkage of the early solidification [53, 56, 89, 91]. See section 3.4.1, on page 51.

Additionally, Pedersen and Tiedje found that the measured curves showed initial eutectic undercooling, resulting in nucleation that controls and influence the subsequent solidification much more than was predicted by the model [136, 137], though the modulus of the casting examined by Pedersen and Tiedje was somewhat smaller than the moduli found in this casting.

To sum up, the nucleation model used in MAGMASOFT may not yield the correct amount of graphite nuclei at the end of solidification, which will, in turn, influence the graphite expansion and the porosity formation. This said, it is however likely that some of these factors are decoupled in the MAGMASOFT simulation, and thus not directly dependent on the graphite nucleation. The thermal expansion of the alloy is a fixed part of the material data in MAGMASOFT [69]. See fig. 3.9 on page 51. The graphite expansion factor is not directly a part of any of the nucleation models, though it should be noted that the inoculation amount and inoculation efficiency is part of Lesoult et al's model.

The above discussion is principal and is valid for SGI simulations in general. What makes it essential for the application of spot feeders, is that spot feeder, or ram-up sleeves, due to their placement is very dependent on the thermal contraction and expansion of the material during the solidification. Feeding without the aid of gravity requires that the pressure difference between the section being fed and the feeder must be in favour of moving the melt into the casting—and at the time when it is needed.

Stefanescu proposed eq. (2.1) on page 18, which is a non-equilibrium describing the formation of porosities [26]:

$$P_{gas} + P_{shr} > P_{amb} + P_{st} + P_{exp} + P_{\gamma}$$

where  $P_{gas}$  is the gas evolution,  $P_{shr}$  is the negative pressure from resistance to shrinkage induced flow,  $P_{amb}$  is the ambient pressure applied to the mould,  $P_{st}$  is the metallostatic pressure,  $P_{exp}$  is the expansion pressure caused by phase transformations, and  $P_{\gamma}$  is the pressure induced by the tension acting on the surface of the pore.

A success criterion for any feeder is that the porosities end up in the feeder rather than the casting. This can be rephrased to say that the feeder is designed to promote porosity formation in the feeder itself. Viewing Stefanescu's equation, it is seen

that the metallostatic pressure,  $P_{st}$ , help prevent the formation of porosities. However, as the spot feeder is placed level with the section it is feeding, as opposed to traditional feeders, this feeding advantage is eliminated. An advantage for the spot feeder, however, is the gas evolution,  $P_{gas}$ . As the solubility of the gasses in the melt is reduced, as the melt cools and solidify; the concentration of gas in the melt will be highest at the last region to freeze. Given that pores have not formed elsewhere beforehand and that the diffusion rate of the gas in the melt allows for a sufficient transport of gas to these late solidifying regions; a porosity may form. The negative pressure from resistance to shrinkage induced flow,  $P_{shr}$ , is unchanged concerning the function on traditional feeders.

The flow resistance is primarily governed by the thermal fields as these control the progress of solidification, as the alloy specific characteristics of the mushy zone. Similarly, the ambient pressure,  $P_{amb}$ , can also safely be assumed to be unchanged. The surface tension of the pore,  $P_{\gamma}$ , was discussed previously in relation to eq. (2.3) on page 18. It is unlikely that amount of inclusions and melt impurities are directly affected by the application of spot feeder rather than traditional parting line feeders. If this should be, it should relate to the sleeve material—insulating or exothermic—releasing particles into the melt which can act as nucleation sites for porosities. No evidence has been found to support this theory however, and if it were the case, the nucleation of pores within the feeder would in some cases be beneficial.

Having run through the terms in eq. (2.1) on page 18, the final parameter is the expansion pressure caused by phase transformations,  $P_{exp}$ , which closes the circle back to the discussion on how MAGMASOFT handles graphite expansion, volume change, and nucleation. The pressure development depends on the firmness of the mould, as described in section 2.3.7, on page 29 and section 3.4.2, on page 52. As green sand moulds are considered relatively weak, the sleeves encasing the spot feeders may themselves provide a firmer cavity for the expansion to exploit.

## 9.5 Solidification and Microstructure

THE colour etched microstructure analysis described in chapter 6, on page 89 showed that the two alloys solidified similarly, though the nodule

count for the high Si  $\beta$ -alloy was higher than the low Si  $\alpha$ -alloy. The colour etchings also confirmed that the  $\alpha$ -alloy was pearlitic-ferritic, while the  $\beta$ -alloy was close to fully ferritic.

The greater nodule count in the  $\beta$ -alloy cannot be contributed to the difference in alloying elements. Increased Mn content can potentially increase the nodule count by allowing a greater undercooling without white solidification [71]. However, the  $\beta$ -alloy have a lower Mn content than the  $\alpha$ -alloy, and should thus have a lower nodule count. Note however, that Si also promote graphite formation, so even though the Mn content has been lowered the Si content has been significantly increased. The two alloys were cast on different dates; hence it is possible that the inoculation procedure has changed in between, either with a new inoculant or by an increased amount.

The more significant tendency to shrink found in the  $\beta$ -alloy may be, in part, related to an improved nucleation, as has previously been shown in LGI by Elmquist et al [43]. A similar effect was also described for SGI by Chen et al [42] While under-inoculation will result in a decreased graphite expansion, over-inoculation can advance the occurrence of the graphite expansion resulting in a decreased expansion later in the process. Another phenomenon that influences the movement of the last to freeze melt, through the mushy zone is the thermal centre. The movement of the thermal centre during solidification—a so-called migrating hot spot—has been shown to play a significant role in the development and location of porosities, as described by Elmquist et al [43, 138].

Beside the pearlite content and the increased nodule count for the high Si  $\beta$ -alloy, the microstructure of the two alloys was alike for the different sections investigated. It was also found that the microstructure showed no significant differences between the exothermic and the insulating feeders. Hence, it was found that the exothermic feeder sleeves did not influence the microstructure itself.

## 9.6 Thermal Deformation

IDENTIFYING the cause of the thermal deformations, and how they are linked to the influence of the feeders, is important both for understanding the functioning and side effect of feeders, but also to be able to estimate, predict, and compensate for the deformations by changing the pattern.

The thermal deformation is linked to the material properties of the cast alloy. The total strain,  $\varepsilon^{Tot}$ , that is developed and released in the casting during solidification, cooling, and phase transformations define the shape of the final casting. Depending on the constraints placed on the casting, primarily by the mould, some of the strain may be made into stresses,  $\sigma$ , as the casting is prevented from deforming freely. The deformation of the casting also requires that the strain exceed the materials limits for the elastic strain,  $\varepsilon^{El}$ , enabling the plastic strain,  $\varepsilon^{Pl}$  to permanently deform the casting. These terms describe the strain caused by thermal volume contraction or expansion; however, the phase transformations also introduce volume changes as a function on the regrouping of atoms into new lattice structures [32]. This yields the transformation strain,  $\varepsilon^{Tr}$  and the transformation plasticity strain,  $\varepsilon^{Tp}$ . Together this yields eq. (3.37) on page 61 as described by Denis [102]:

$$\varepsilon^{Tot} = \varepsilon^{El} + \varepsilon^{Pl} + \varepsilon^{Th} + \varepsilon^{Tr} + \varepsilon^{Tp}$$

The final deformation is, through these factors, governed by the thermal gradients of the castings—defining the sequence and timing of the volume and phase change—and the internal pressures of the casting. Thus, some of the deformation can be referred to the overall geometry itself, and some to surface shrinkage and feeding. The geometry defined deformation is the deformation that would also occur if the casting was cast for instance in horizontal mould—deformation independent of orientation. The feeding dependent deformation, however, can be defined as the deformation dependent on the internal pressure on the casting. Note that these definitions liberate the two definitions from constraints of the thermal influence of the feeders, as this influence should, in theory, be the same whether or not the casting is cast in a vertical or horizontal mould. Subsequently, it should also be remarked that the thermal influence of the feeder and the potential metallostatic pressure it introduces will still influence deformation formation.

### 9.6.1 Surface Deformation Measurements

The topography of all of the 40 analysed castings was found to be similar. Feeder combinations group  $\alpha 00$  displayed a far greater distortion than the other 14 groups, but as shown in table 7.1 on page 107, the  $\alpha 00$  displayed the same valley direction and angle,

though the volume and distance of the valleys were more pronounced in the other 13 feeder combination groups. All 40 analysed castings displayed a valley with a centreline located between 09:00-11:00 hrs, with an angular width between 50°-90°. Almost  $\frac{3}{4}$  of the castings featured a valley reaching  $\frac{2}{3}$  of the distance from the centre to the edge of the ring. The last  $\frac{1}{4}$  were divided into two small groups either reaching all the way to the edge of the ring ( $\frac{3}{3}$ ) or only reaching a small distance outwards from the centre ( $\frac{1}{3}$ ). A similar pattern was found for the depth of the valleys. See fig. 7.11a on page 111.

Within each group of castings, it was seen that the direction of the valley varied not more than 30 minutes. For six of the groups, the valley ran in the same direction in all three castings. The total variation in the direction of the valley was within 1 hour and 30 minutes. This indicated that the direction of the valley was indeed influenced by the feeder combination and that it could be controlled by choice of feeder modulus. Likewise, there was an indication that for the pearlitic  $\alpha$ -alloy, that a high modulus centre feeder resulted in a more pronounced (larger) valley. This is in good agreement with the  $f_v$  measurements. On the other hand, no correlation between the range and the volume of the valley was found; meaning that a change in the area did not entail a change in valley depth. Hence, the volume of the valley was not constant.

The consistency of the castings, especially within each casting group, showed high reproducibility and indicated that production conditions were uniform. If the distortion had been variable, an effective adaptation to the pattern would be impossible, or in the best case have a limited effect. The consistency that has been demonstrated here may lead to an adaptation that not only reduces the machining allowance considerably but also counters the inherent distortion so that the cooled casting becomes much flatter than at present. Changing the pattern, however, requires either a sufficiently good optimisation simulation or an iterative trial and error development of the casting pattern. This is because the added and removed padding in various areas of the pattern also changes the thermal gradients and the strength of the sections, thus slightly affecting the distortion of the casting. Additionally, the casting deformation must be viewed as an interval, not an exact value, since variation will always occur—especially over time. A narrow confidence interval for the casting deformation indicates a stable pro-

duction and thus accordingly allow for a greater casting optimisation with smaller tolerances.

Though the analysis of the casting's topography showed consistency in the distortion between the different castings, it must also be noted that the graphical representation of the measured results was less well defined than the 0.1  $\mu\text{m}$  resolution of the CMM. The colour scale was discontinuous and comprises only nine colours from orange to blue as seen in fig. 7.8 on page 105.

As the geometric modulus ( $M_g$ ) of the casting was identical in all directions from the centre outward, the placement, range, size, and direction of the valley must be the product of the filling conditions and the thermal influence provided by the feeders. Alternatively, it could be an inaccuracy in the pattern itself. The flatness of the entire 400  $\times$  500 mm pattern was measured and found to have a  $f_v$  of 16.4  $\mu\text{m}$ —approximately 20-30 times smaller than deformations measured on the casting. Thus, pattern distortion was negligible.

#### Porosities

None of the 17 castings that were given the mean height indication (M) at the boss contained internal porosities. For the 23 castings designated low (L), 19 had internal porosities. Three of the four that were designated (L), but displayed no porosities were castings without the top feeder from the same group— $\alpha 02$ . The remaining casting was casting  $\beta 23sC$ , which was in a group with one other casting,  $\beta 23sA$ , which had porosities.  $\beta 23sC$  can thus also be said to be prone to porosities. Note here, that  $\beta 23sC$  was not one of the castings that was ultrasound analysed, so undiscovered porosities may be there away from the sectioned part examined by the liquid penetrant test. The porosities in the boss were all classified as small non-linear isolated porosities (SP) or non-linear clustered (CP) porosities as defined by [116].

#### Solidification and Deformation Sequence

The following mechanisms are proposed for solidification and deformation of the castings. The reverse, plane side of the casting was more uniformly cooled; it formed a solid shell that contracted uniformly during and immediately after solidification. On the front, there were areas—the inside of the ring and along the outside of the boss—that remained hot so that the strength was reduced locally. See fig. 8.8 on page 132.

The casting was initially pulled back as it solidified and cooled. As the hot areas on the front of the casting gained strength, additional stresses build up around the now relatively strong thin-walled section. At the point where the eutectoid transformation began, the temperature distribution in the casting had changed so that the ring now became the coldest part of the casting. As the transformation took place from the ring through the thin-walled section to the boss, further stresses build up, adding to the deformation. The shape of the reverse plane side was affected by the following four mechanisms.

(1) *Backwards Deformation:* The two sides were not equally stable. The hotspots created at the corners of the boss and ring remained hot for an extended period, thus postponing contraction and recovery of strength. This effect is illustrated by the feeding modulus in fig. 4.2d on page 69, showing the location of the last melt to solidify. The reverse plane side, on the other hand, was planar and cooled faster without less pronounced hotspots, and thus contract sooner and regain strength sooner than the front.

(2) *Location of the Valley:* The cold spot was pushed upward due to the bottom filling that heated the lower part of the mould more than the upper part. Because the ring had a greater modulus than the thin-walled section, the upper half of the thin-walled section was initially the coldest area of the casting. Again with the reverse planar side being colder than the front side. As the last volume of the mould to be filled was directly at the centre, the most abundant melt flow during filling was at the vertical centre line. This heated the vertical centre line more than the sides of the casting, creating a hotspot here, pushing the cold spot at the upper part of the thin-walled section towards the sides. Afterwards, this centre line hotspot was maintained by the top feeder. A hot top feeder will eventually counter the heating effect of the ingate, albeit the shift of the hotspot from below the boss to above the boss was only entirely in effect at the end of solidification. Thus the coldest area was where the valley would form. Reversing the argument, a valley at the centre thus indicate that this area was cold during solidification. This is supported by the correlation between low areas at the centre (Cen) and the porosities found inside the boss (Por) shown in table 7.1 on page 107.

(3) *Silicon (Si) Content:* A significant difference between the two alloys was the Si content. Si is a graphitizer and suppresses the formation of pearlite

[71, 139]. Although increased Si content leads to greater graphite expansion, and thus a potential for greater deformation, a side effect of Si was to increase the temperature for the transformation from austenite to ferrite, as described in Ductile Iron Data [130]. The higher temperature means that all parts of the casting had recovered less strength to withstand the graphite expansion. The higher temperature of the metal at the time of the transition made it softer and less likely to have built up unreleased stresses. The greater influence of Si, which, comes from its ability to suppress the formation of pearlite. The combined austenite to ferrite and pearlite phase transformation was shown to significantly increase the total duration of the transformation by comprising two consecutive phase transformations in the  $\alpha$ -alloy. See figs. 8.5 to 8.7 on page 128, on page 129 and on page 131.

(4) *Inoculation:* The  $\beta$ -alloy castings had a finer microstructure when compared to the  $\alpha$ -alloy castings, as described by Vedel-Smith and Tiedje [31]. Elmquist et al [43] reported that over-inoculation could advance the effect of the primary graphite expansion, but would in turn also lessen the effect of the secondary graphite expansion. For LGI this follows that over-inoculation could have caused increased shrinkage but also decreased deformation variation because the main graphite expansion occurred at a higher temperature and more uniformly. For SGI, however, Chen et al [42] reported that the increased nodule count ease the deposition of graphite excreted from the austenite and inhibit the formation of pearlite, which is mainly achieved by increasing the nodule count and thus reducing the required diffusion distance of the graphite to reach an existing graphite nodule. Hence, the effect reduces the possibility that oversaturated austenite will occur at the eutectoid temperature. Additionally better inoculation reduce the amount of undercooling during solidification limiting the formation of cementite and prompt a more uniform solidification.

#### Statistical Comparison of $f_v$

The variation in flatness within each group of castings was minimal compared to the total variation in the experiments. This showed that the experimental conditions were stable and uniform. The only group that was markedly different was  $\alpha 00$  which exhibited a distortion that was twice as large as that of the other 14 groups. See fig. 7.10 on page 110. The castings in group  $\alpha 00$  were significantly different from

all other castings. Applying at least one feeder to the casting, regardless of—whether it was applied to the top, the centre boss, or both—reduced the  $f_v$  in comparison to the castings without feeders. There was no statistically significant difference between the groups of castings to which feeders were applied.

As  $\alpha 00$  displayed the inherent deformation of the casting geometry itself, influenced only by the heated area at the in-gate; it was concluded that both feeders, together or separately, minimise the deformation of the casting. This reduced deformation is achieved by the changing cooling conditions, creating a temperature field that reduces thermal stress by allowing castings to maintain a more uniform temperature gradient during cooling.

**Influence of Alloy** Both materials were near-eutectic in composition. However, there were significant differences in how they responded to cooling. Most significantly, the high Si-alloy was less likely to form pearlite at the solid state transformation when cooled from 900 °C to 600 °C. It is known that this transformation is accompanied by a change in specific volume. The size of the volume change depends on the pearlite content in the finished casting, as described in Ductile Iron Data [130], so that the higher the pearlite content, the larger the volume change, even though the austenite to ferrite phase transformation would by itself cause a volume change.

Since the high Si  $\beta$ -alloy was a fully ferritic alloy, it would be less subject to deformation due to the reduced graphite expansion at the time of the solid-state phase transformation. On the other hand, pearlite formed in the low Si  $\alpha$ -alloy. The amount of pearlite will depend on local cooling conditions so that the pearlite content would vary between groups of castings and also between specific locations within the individual casting. As a result, it was seen that the high Si  $\beta$ -alloy castings that were pearlite free were also more consistent in their dimensions.

This means that with this alloy, and possibly also other fully ferritic alloys, it is easier to compensate for thermal deformation by modifying the pattern.

Regarding production, the correction should be aimed at the average deformation measured, adding a machining allowance to ensure that the confidence 95 % (or possibly 99 %) interval is covered. By adapting the tolerances required based on the reproducibility demonstrated in this dissertation, any traditional machining allowance as described by Angus [140] and defined by EN ISO 8062-3:2007 [141], specifying machining allowance for castings,

can be minimised considerably. This will only be feasible if sufficient process control and stability are achieved.

**Influence of Top and Centre Feeder** The feeders, besides fulfilling their primary job of feeding, alter the thermal gradients and subsequent pressure gradients of the casting. Vedel-Smith et al [30] showed that both the top and the centre feeders were required to produce sound, porosity-free castings. Regarding the deformation of the casting, it was not the actual feeding of melt to the casting that influences the final result, but the change in the thermal gradients of the casting. Thus, deformation could be changed and countered by increasing or decreasing the  $M_t$  of the feeder, providing  $M_t$  and the melt volume were still sufficient to provide adequate feeding.

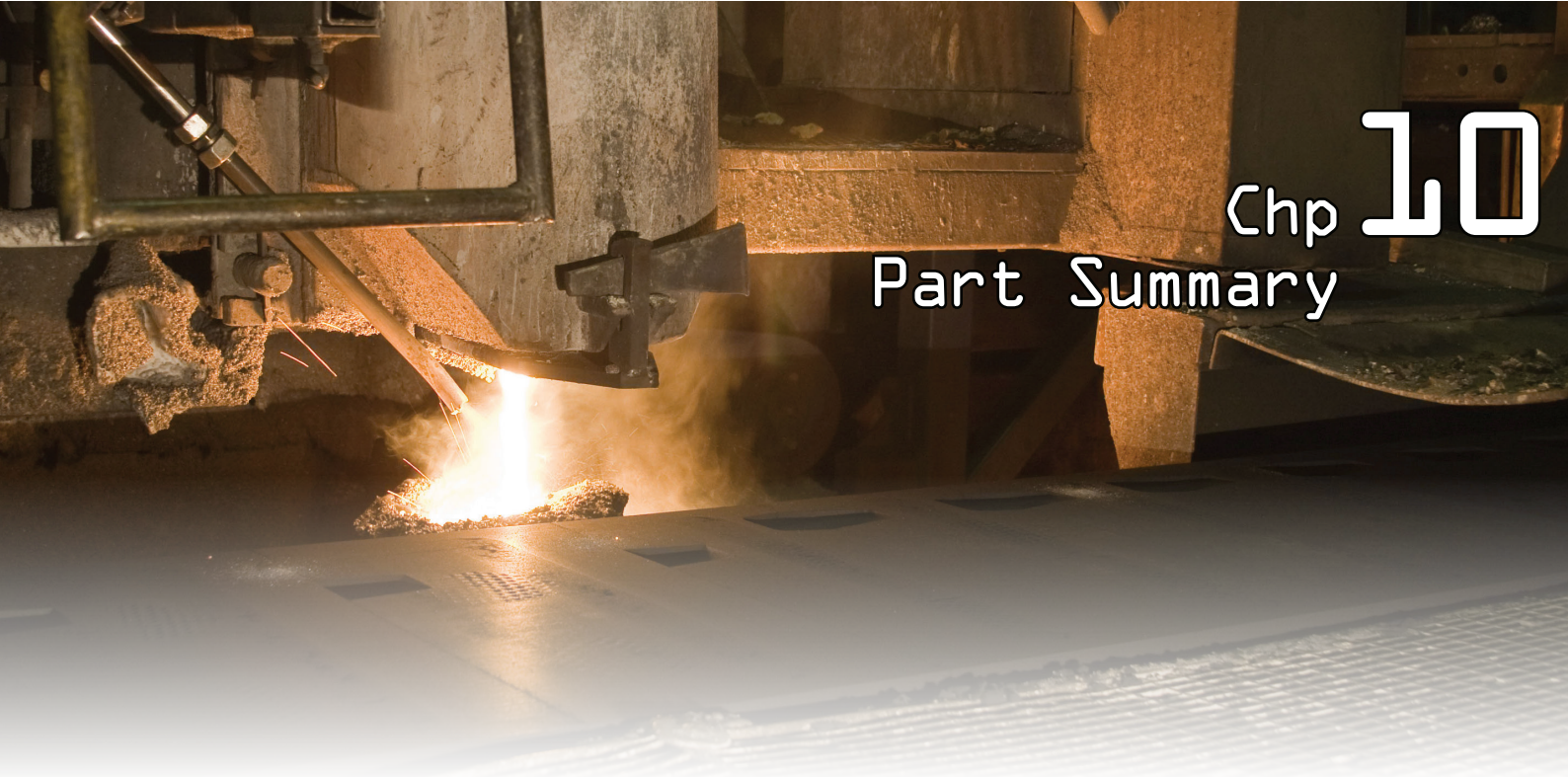
## References

- [26] DM Stefanescu. “Computer Simulation of Shrinkage Related Defects in Metal Castings—A Review”. In: *International Journal of Cast Metals Research* 18.3 (2005), pp. 129–143.
- [30] Nikolaj Kjelgaard Vedel-Smith et al. “Quantification of Feeding Effects of Spot Feeding Ductile Iron Castings made in Vertically Parted Molds”. English. In: *AFS Proceedings* (2013).
- [31] N. K. Vedel-Smith and N. S. Tiedje. “Effect of Feeder Configuration on the Microstructure of Ductile Cast Iron”. English. In: *TMS Proceedings—Shape Casting: 5th International Symposium 2014* (2014), pp. 113–120.
- [32] David A. Porter, Kenneth E. Easterling and Mohamed Y. Sherif. *Phase Transformations in Metals and Alloys*. 3rd ed. CRC Press, Taylor & Francis Group, 6000 Broken Sound Parkway NW, Suite 300, Boca Raton, FL 33487-2742, 2009. ISBN: 978-1-4200-6210-6.
- [33] Attila Diószegi et al. “Defect Formation at Casting of Gray Iron Components”. In: (2009).
- [34] Attila Diószegi, Tobias Björklind and Zoltán Diószegi. “Surface Turbulence at Flow of Gray Cast Iron”. In: *Key Engineering Materials*. Vol. 457. Trans Tech Publ. 2011, pp. 422–427.
- [42] Q.M. Chen, E.W. Langer and P.N. Hansen. “Influence of the Process Parameters on the Volume Change during the Eutectic reaction of SG Cast Iron: A Computer Simulation”. In: *Journal of Materials Science* 32.5 (1997), 1239–1248. ISSN: 0022-2461. DOI: {10.1023/A:1018592120197}.
- [43] Lennart Elmquist, Attila Diószegi and Tobias Björklind. “On the Formation of Shrinkage in Grey Iron Castings”. English. In: *Key Engineering Materials* 457 (2011), pp. 416–421.
- [53] G. Alonso. et al. “Kinetics of Graphite Expansion during Eutectic Solidification of Cast Iron”. In: *International Journal of Cast Metals Research* 27.2 (2014), 87–100. ISSN: 1364-0461. DOI: {10.1179/1743133613Y.0000000085}.
- [56] G. Alonso et al. “Kinetics of Graphite Expansion during eutectic Solidification of Lamellar and Spheroidal Graphite Iron”. In: *AFS Proceedings 2014*. AFS Conference. Schaumburg, IL, USA. American Foundry Society. 2014, 1–12.
- [68] Jonathan A Dantzig and Michel Rappaz. *Solidification*. EPFL press, 2009.
- [69] MAGMASOFT 5.2 by MAGMA GmbH. [http://www.magmasoft.com/en/solutions/MAGMA\\_5.html](http://www.magmasoft.com/en/solutions/MAGMA_5.html). Program. 2014.
- [71] Richard Aagaard. *Ductile Iron—Solidification Shrinkage Simulation*. DTU, Institute of Manufacturing Engineering, 1997.
- [80] G Lesoult, M Castro and J Lacaze. “Solidification of Spheroidal Graphite Cast Irons—I. Physical Modelling”. In: *Acta materialia* 46.3 (1998), pp. 983–995.
- [81] W Oldfield. “A Quantitative Approach to Casting Solidification: Freezing of Cast Iron”. In: (1966).
- [89] DM Stefanescu et al. “Use of Combined Liquid Displacement and Cooling Curve Analysis in Understanding the Solidification of Cast Iron”. In: *Transactions of the American Foundrymen’s Society* 120 (2012), pp. 365–374.

- [91] Doru M Stefanescu. “Solidification and Modeling of Cast Iron—A Short History of the Defining Moments”. In: *Materials Science and Engineering: A* 413 (2005), pp. 322–333.
- [102] S Denis, S Sjöström and A Simon. “Coupled Temperature, Stress, Phase Transformation Calculation”. In: *Metallurgical Transactions A* 18.7 (1987), pp. 1203–1212.
- [108] U. C. Nwaogu, N. S. Tiedje and H. N. Hansen. “A Non-Contact 3D Method to Characterize the Surface Roughness of Castings”. English. In: *Journal of Materials Processing Technology* 213.1 (2013), pp. 59–68.
- [114] *ATAS MetStar*, by Novacast Systems AB. <http://novacast.se/products/atasmeststar/>. Adaptive Thermal Measurement System.
- [116] *Founding: Liquid Penetrant Testing—Sand, Gravity Die, and Low Pressure Die Castings*. Norm. 2011.
- [121] Sadaf Vazehrad, Jessica Elfsberg and Attila Diószegi. “Study on microstructure in cast iron using color etching and electron microprobe analysis”. English. In: *Materials Characterization* (2015). DOI: {10.1016/j.matchar.2014.09.008}.
- [130] Ductile Iron Data. *Ductile Iron Data - for Design Engineers*. Rio Tinto Iron & Titanium Inc., 1990.
- [136] K.M. Pedersen and N.S. Tiedje. “Temperature Measurement During Solidification of Thin Wall Ductile Cast Iron. Part 1: Theory and Experiment”. In: *Measurement* 41.5 (2008), 551–560. ISSN: 0263-2241. DOI: {10.1016/j.measurement.2007.05.002}.
- [137] K.M. Pedersen and N.S. Tiedje. “Temperature Measurement During Solidification of Thin Wall Ductile Cast Iron. Part 2: Numerical Simulations”. In: *Measurement* 41.4 (2008), 341–348. ISSN: 0263-2241. DOI: {10.1016/j.measurement.2007.05.003}.
- [138] Lennart Elmquist and Attila Diószegi. “Shrinkage Porosity and its Relation to Solidification Structure of Grey Cast Iron Parts”. English. In: *International Journal of Cast Metals Research* 23.1 (2010), pp. 44–50.
- [139] R.W. Heine. “The Fe-C-Si Solidification Diagram for Cast Irons”. English. In: *AFS Proceedings* 94 (1986), pp. 391–402.
- [140] H.T. Angus. *Cast Iron - Physical and Engineering Properties*. Butterworth & Co (Publishers) Ltd., 1976.
- [141] *EN ISO 8062-3:2007: Geometrical Product Specifications (GPS)—Dimensional and Geometrical Tolerances for Moulded Parts—Part 3: General Dimensional and Geometrical Tolerances and Machining Allowances for Castings*. Norm. 2007.







## Part Summary

---

10.1 Summary . . . . .	153	10.1.1 Experimental Setup . . . . .	153
------------------------	-----	-------------------------------------	-----

---



**S**HORT summary of the investigations, results, and findings reported in part II.

Keywords: . . . . . Summary, Experimental Setup, Porosity Quantification, Thermal Analysis, Casting Deformation, Numerical Simulation.

Chapter findings reported in: . . . Supplement I, on page 301  
Supplement II, on page 315  
Supplement III, on page 325

---

### 10.1 Summary

---

The defined objective was: (1) to demonstrate if secluded sections could be fed using ram-up sleeves as spot feeders for vertically parted moulding lines, (2) show that the exothermic sleeve material did not influence the microstructure of the casting, (3) that feeders do influence the thermal deformation of the castings, and (4) that the formation of porosities can be prediction with the aid of numerical simulations. The efficiency of the feeders was examined, and the thermal deformation measured on the reverse side of the casting was documented and explained.

#### 10.1.1 Experimental Setup

---

A series of different feeders were selected for the chosen test casting. The spot feeders included

insulating, insulating-exothermic, and purely exothermic feeders. The first trial proved that secluded sections could indeed be fed with the application of spot feeder. To further examine the limits of the feeding ability, some of the same feeders combinations were also tested with the more porosity prone high Si  $\beta$ -alloy.

The castings were sectioned, and a liquid penetrant test was performed for all castings. The developed samples were photo-documented and analysed afterwards to quantify the size, type and locations of the porosities.

The porosity analysis showed that the  $\alpha$ -alloy performed very well, while the more demanding  $\beta$ -alloy was only found to be porosity-free for the high modulus exothermic feeders. The numerical simulations aided in this analysis and it was proposed that the

Coordinate Measurement Machine (CMM), Silicon (Si)

insulation feeder sleeves may have similar trouble as a traditional sand feeder, namely that a shell can form and develop a negative pressure that will keep some of the melt inside the feeder. The benchmark castings without either the top, or centre, or both feeders showed that the test casting could not be cast soundly without both feeders.

Additionally, it was found that the castings deformed differently based on the feeder combinations. The castings were measured using a CMM, and the flatness values  $f_v$  showed that the variation in deformation could be directly linked to the thermal gradients created by the feeders. Likewise, it was shown that the thickness of the thin-walled section of the casting was influenced by the feeder combinations and that the centre feeder could influence the thickness of the casting above its location. Hence, the effect was thermal and not ferrostatic.

The thermal analysis showed that the eutectoid phase transformation was significantly longer for the pearlitic-ferritic  $\alpha$ -alloy, as compared with the high Si  $\beta$ - and  $\tau$ -alloys. Using the second derivative of the cooling curves, it was shown that the subsequent transformation of the austenite to ferrite and austenite to pearlite influence the variance of the castings deformation. It was found that the av-

erage deformation showed little difference between the two alloys. However, the process stability of the high Si  $\beta$ -alloy was much greater than that of the  $\alpha$ -alloy.

The casting microstructures were colour etched and examined for differences in solidifications and segregation. Besides a higher nodule count for the  $\beta$ -alloy, the two alloys behaved similarly. It was also proved that the  $\alpha$ -alloy was pearlitic-ferritic and that the  $\beta$ -alloy was fully ferritic. A further analysis of the microstructures originating from feeders with exothermic and insulating sleeve materials was subsequently compared and analysed. This analysis showed that no significant difference in microstructure could be found between the feeders with different sleeve material.

Finally, the accuracy of the porosity prediction of the numerical simulations software, MAGMASOFT, was analysed. It was found that the simulations could be set up to match the porosities found in the porosity analysis, though this required some adjustment and calibration of the simulation setup. Most importantly, however, is that once the basic setup for the given alloy was achieved, the porosity prediction was relatively accurate and independent on the variations in feeder configuration.



# Part II

## Feeding Effect Quantification

Casting Design and Trial Plan 11  
Feeding Analysis 12  
Discussion 13  
Part Summary 14

“WE can lick gravity, but sometimes the paperwork is overwhelming.”

—Wernher von Braun





# Casting Design and Trial Plan

Experimental Procedures and Scalable Castign Design

## Casting Design and Trial Plan

---

<b>11.1 Trial Purpose</b> . . . . .	<b>157</b>	11.3.1 Alloy Composition . . . . .	168
11.1.1 Objectives . . . . .	158	11.3.2 Choice of Feeders . . . . .	168
11.1.2 Casting and Pattern Design . . . . .	161	<b>11.4 Trial Setup and Production</b> . . . . .	<b>171</b>
<b>11.2 Scaling Error (M10 ⇒ M12)</b> . . . . .	<b>167</b>	11.4.1 Temperature Measurements . . . . .	173
<b>11.3 Trial Description</b> . . . . .	<b>168</b>	<b>References</b> . . . . .	<b>174</b>

---



THE chapter describes the development of the casting trial as well as the casting itself. Weight is given to the pre-feeder development and how it ensure a controlled amount of liquid shrinkage. The feeders used for the trial are described, and the trial plan is presented. Additionally the thermal measurement setup is described.

Keywords: . . . Trial Plan, Casting Design, Pre-Feeder Design, Feeder Dimensions, Production Setup, Thermocouple Setup, Thermal Measurements.

Chapter findings reported in: . . Supplement IV, on page 337

---

### 11.1 Trial Purpose

---

SUPPORTED by the findings in Part I, the second phase of the research was focused on a general understanding of the feeding mechanisms. It was sought to find a manner by which the number and size of porosities could be quantified and used as a grading scale for the effectiveness of the feeding setup under investigation. As part of this, it was important to test the influence of the pressure height on the melt flow between the feeders and the casting. Additionally, it was important to device a test that was as comparable as possible between different

castings: moulding, sand conditions, casting temperature, alloy composition, and cooling conditions. If possible, the test setup should also be transferable so it could be used in other foundries under other conditions, while also yielding comparable results.

The trial was a quantitative study on feeding, rather than a qualitative approach. Hence, the trial design and structure were aimed at producing castings under as close to identical process conditions as possible; to provide a statistical comparison on the feeding efficiency of different feeder configurations

Poly(Acrylonitrile Butadiene Styrene) (ABS), Computer Aided Design (CAD), Modulus Extension Factor (MEF)

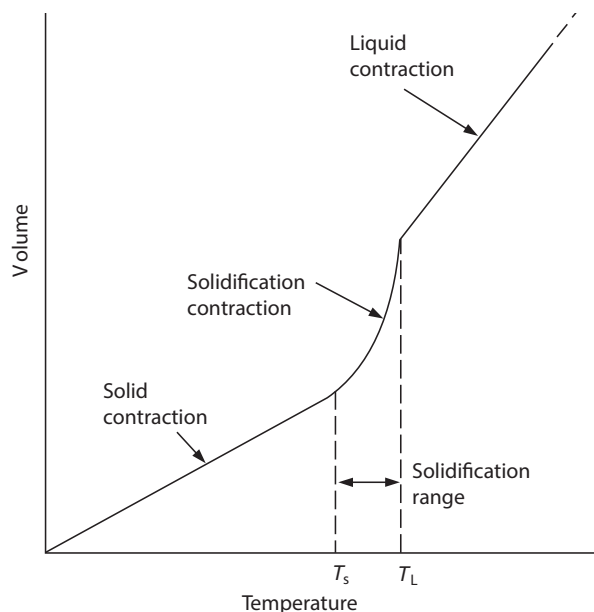


**Figure 11.1:** Illustration of the three different types of shrinkage observed during casting. Courtesy of Campbell [24].

for different modulus sections. The idea was that by producing a large number of castings with different feeder configurations, it would be possible to analyse the stepwise influence of the feeder modulus, rather than just analysing the extremes and assuming a linear relationship between these widespread moduli. Finally, the wide range of trial castings allowed for an analysis of the accuracy of simulated porosity predictions for different moduli castings and feeders. Again, with the duplicates as a statistical insurance against outliers.

### 11.1.1 Objectives

A list of six objectives was made for the casting design to address the above requirements:

1. Feedability and feeding requirement for different modulus sections
2. Grade the feeder efficiency
3. Simulate feeding of secluded sections
4. Importance of feeder location (pressure height)
5. Influence of multiple feeders
6. Designed for easy and accurate analysis

The idea with the six objectives is explained in the following sections.

### Feeding Requirement and Modulus Relationship

The trial setup should provide information on how similar feeding setups perform for different modulus sections. The feeder sizes are often determined by scaling the modulus of the casting section by  $\times 1.2$ , as described in section 1.3.1, on page 9. This factor assumes a linear relation between the size of the casting and the feeders; though this has been proved by both Chvorinov and Hansen et al not to be true [21, 22]. The work of Tiryakioğlu et al shows that the function can be modified to address these shortcomings between both shape and volume of the casting [39]. Large-scale castings illustrate these alterations to Chvorinov's original rule as they are known to be self-feeding and are often cast without feeders [142]. Additionally, the differences in cooling rate dictate different solidification patterns and following different feeding characteristics in each casting. See section 3.4.3, on page 54.

The casting design should be scalable to provide similar feeding conditions for different section sizes. Changing the geometry to achieve different modulus sections would influence the direct comparison of the different modulus sections, as described above. Thus, it was important that the shape of the casting was kept identical, regardless of scale.

### Grading the Feeder Efficiency

The castings with the EN-GJS-500-7 alloy in Part I showed that the grading scale must be adapted to the feeding efficiency interval covered by the castings—or expressed measurably: the number and size of porosities present in the different castings. The castings in Part I showed porosity for the reference castings without feeders. However, none of the castings that had both the feeder and the centre feeder displayed porosities in casting itself. This absence of porosities made it impossible to compare the efficiency of the different feeders. The only possible conclusion was that all configurations were sufficient.

To avoid a similar situation with this second trial, and to provide a grading scale on which to compare the different feeder configurations, a measure of the feeding efficiency was required. It was chosen to measure the number and size of remaining porosities in the castings. Porosities are often the direct result of insufficient feeding and can be measured and quantified via different well-known analysis methods.

To make a useful analysis it was required that the casting would produce porosities. If a casting were

made without porosities, the feeder configuration efficiency would be off the chart. Hence, no direct comparison could be made since it would not be possible to prove whether the configuration efficiency had been just efficient enough, or with a significant margin. For this reason, the trial was designed with the intent of always having some remaining porosities.

As the remaining porosities was a function of the relationship between the size (and efficiency) of the feeder configuration and the size (and need) for feeding by the casting; the adaptation of the grading scale was related to the modulus relationship between the casting and the feeder. This assessment of the porosities was approached from two different angles. First, the different feeders used for the trial was chosen to be no larger than complying with the above mentioned  $\times 1.2$  modulus size rule. Secondly, a casting alloy with a significant tendency to shrinkage was chosen for the trials—EN-GJS-500-14. Together these two prerequisites should secure a casting with porosities. The final choice of feeders is described in section 11.3.2, on page 168.

**Liquid Shrinkage** Another aspect of adequately grading the number and size of porosities was to secure the same initial amount of porosities for all castings. However, not all porosities are related to solidification shrinkage. Volume change also occurs in the cooling liquid, as illustrated in fig. 11.1 on page 158. The issue with liquid shrinkage was often solved by increasing the size of the feeders to hold a given amount of extra melt. However, to be able to compare the different feeder configurations correctly, a similar amount of porosities must be present in the casting before feeding every time.

The solution was to equip the casting with a unique ‘feeder’ designed—a pre-feeder—to handle only the liquid shrinkage. As the liquid shrinkage could vary depending on the pouring temperature, the pre-feeder was not limited by the amount of melt it could hold, but rather by the amount of melt it would feed to the casting before the solidification of the pre-feeder neck disabled further melt transport into the casting. A detailed description of the pre-feeder design and development can be found in section 11.1.2, on page 161.

### Simulate Feeding of Secluded Sections

In addition to providing a solidification shrinkage comparable for all castings, which was free from

(or with a similar limited amount of) liquid shrinkage, it was essential to have a casting that solidified similarly to a secluded section. Without the pre-feeder, the casting shrinkage tended to form on the top of the casting as a sinkhole or large surface deformation. The presence of the pre-feeder provided sufficient melt during the liquid cooling phase to avoid this and to secure the forming of a shell on the upper surface of the castings, ensuring a fully cast casting without surface shrinkage caused by liquid shrinkage.

Another significant effect of the pre-feeder casting design was the similarity to secluded sections. Liquid shrinkage is seldom an issue for secluded sections as these per definition are located away from the easily feed positions on the casting. Secluded sections have larger modulus than the sections connecting them to the nearest feeder so that the feeding path is cut off, as described in section 2.3.5, on page 23. Similar to the casting design used for these trials. Feeding these secluded sections may be achieved by side feeding, in which case the movement of the melt by other forces than gravity becomes essential for the functioning of the feeder itself.

### Feeder Locations

Side feeding castings can result in problems with insufficient ferrostatic pressure due to lack of feeding height. Hence, the influence of the ferrostatic pressure from the casting that the feeder has to overcome to transfer its melt to the casting, was an important parameter to classify for the efficiency of the feeders, as shown by eq. (2.1) on page 18 [26]. To evaluate this effect, two feeder locations were selected—at the very top of the casting near the pre-feeder, and at the very bottom of the casting near the ingate. These two locations—marked by U for upper and L for lower—provided the largest possible difference in pressure height. See fig. 11.2 on the next page.

As cylindrical spot feeders were used for the trials, the feeders themselves did not provide any feeding height. Hence, the average ferrostatic pressure acting against the feeder was equal to the ferrostatic pressure at the feederneck. Hence the ferrostatic pressure for the lower feeders scales along with the modulus of the casting. Consequently, the lower feeders of the high modulus castings had to overcome a higher ferrostatic pressure compared to the lower spot feeders of the small modulus castings.

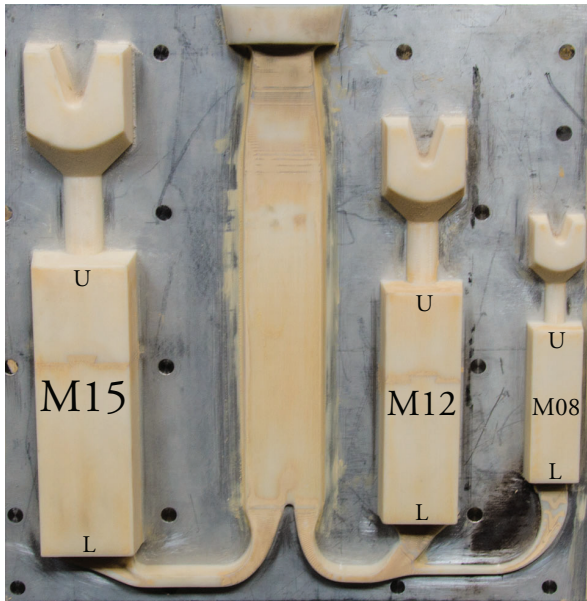


**Figure 11.2:** Pattern made by additive manufacturing in ABS plastics for DISAMATIC 2110. U indicate placement of Upper feeder, and L indicate placement of Lower feeder. Note the M12 pattern instead of the M10 used in the trial plan development.

In addition to providing a more realistic simulation of the feeding conditions found in secluded sections, the trial design with the side mounted spot feeders also provided insight into the relationship between gravity aided feeders and side feeders without any significant assistance from the ferrostatic pressure.

**Multiple Feeders** Having two locations for mounting spot feeders made it possible to examine the combined feeding efficiency of two feeders attached to the same section. The idea was to achieve a better understanding of the different feeder parameters as modulus and melt volume, while also providing a reference for the results of the castings that used only a single feeder. For instance, if two identical feeders could feed the casting better than a single feeder of the same type, it would indicate that the modulus was large enough to provide liquid melt for the casting, but that the melt reservoir of the feeder was too small to provide enough melt. See Rule 2 in section 2.3.2, on page 20 and Rule 3 in section 2.3.3, on page 21.

Two feeders located a distance apart could also be used to test feeding length, as performed by Pellini [44]. Pellini's experiments were performed on horizontal steel castings, and cannot be compared to

the trials described in the present research. However, Pellini's experiment is an essential reference for understanding the fundamentals of feeding.

Feeding length is determined by a combination of different factors. Assuming a basic geometry (eg a bar), feeding length is determined by alloy composition and cooling rate (exo- or endogenous solidification), and pressure gradients (feeding height). In the present trial, the distance between the feeders was a vertical distance, while Pellini's experiment examined a horizontal distance. Gravity will force the melt (and solidified austenite in the melt) towards the bottom, hence moving the porosities closer to the top feeder. However, if the alloy used did not solidify in an endogenous shell-forming manner, but instead in an exogenous way as with Pellini's steel castings, then it would be possible for the centre of the casting to close off for feeding before the areas closest to the feeders had completely solidified.

Though there can be several originating factors, the location of the porosities (top, middle, or bottom) relates to the manner of solidification and direction of solidification.

#### Design for Analysis

Finally, the casting should be designed to be analysis friendly. By making the casting square rather than a cylinder, several subsequent operations become faster, more comfortable, and more accurate. Ultrasound analysis requires a plane front and a plane reflection surface to provide useful and accurate results. The ultrasound waves moved through the casting and are reflected on the opposite side, moving back through the material to be recorded by the sensor. Imperfections in the material is recorded as a loss of sound. This loss of sound-reflection is how porosities are discovered. However, other features that disperse the sound waves will hinder the sound waves from returning to the sensor, and the porosities cannot be recorded. This disturbance could be an imperfection on the reflecting surface or merely a non-flat surface.

The square design had a similar advantage for the x-ray analysis. While x-rays move through the castings rather than reflect on the surface, the amount of the x-rays that reaches the detector is strongly dependent on the absorption of the material. This absorption is, in fact, the way x-rays can be used to identify porosities—areas that are less dense show up brighter on the x-ray image. For the same reason, it was essential to have a uniform casting thickness.



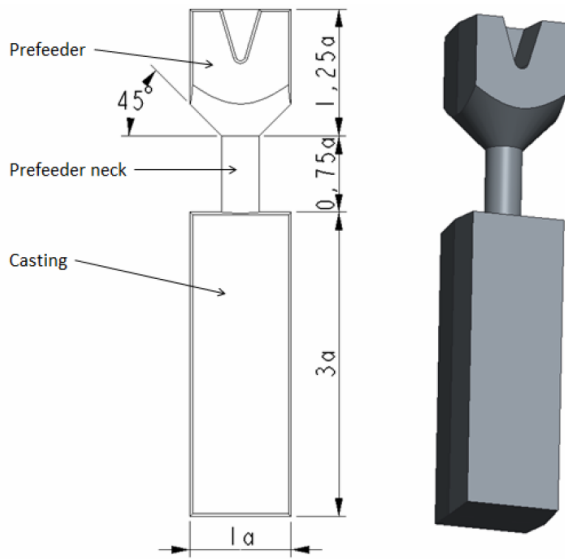


**Figure 11.3:** Scalable geometry for the modulus castings.

A cylinder would have been less dense towards the edges, resulting in either overexposed edges or underexposed centres.

Last, but not least, the square design allows for better and more comfortable clamping of the castings. Both for x-ray and ultrasound analysis; but also for subsequent cutting.

### 11.1.2 Casting and Pattern Design

Based on the trial and casting design considerations listed in section 11.1, on page 157, a casting design was developed. The development was performed through a few iterations, where the last two iterations were manufactured and tested to ensure that the performance of the design matched the intent of the design. The final development design is seen in fig. 11.2 on page 160.

The casting and pattern were developed in three steps, the casting, the pre-feeder, and the pattern layout, as described in the following section.

#### The Casting

The casting had to have as high a geometric modulus as possible, while providing an easy to analyse geometry, height to provide distance between the two feeder locations, and being as simple as possible. For these reasons a rectangular cuboid was chosen for the casting geometry. See fig. 11.3. Knowing the basic shape an equation was devised for the

modulus of the generic casting.

$$M_c = \frac{Volume}{Area} = \frac{a \times a \times ah_{ratio}}{4a \times ah_{ratio} + a \times a} \quad (11.1)$$

where  $M_c$  is the modulus of the casting,  $a$  is the generic side length, and  $h_{ratio}$  is the ratio between the height and the width of the casting. Note that the top surface of the casting, due to the presence of the pre-feeder, was assumed to be non-cooling, and was thus eliminated from the denominator.

8 mm, 10 mm, and 15 mm modulus sections were chosen for the three castings as the determining factor because these represented a range of section moduli found in castings produced on vertically parted moulding systems. Additionally, due to the constraints of fitting the pattern onto the 400 × 500 mm pattern plate for the DISAMATIC 2110, the height of the largest casting was limited to  $h_{ratio} = 3$ .

Having decided on the three moduli,  $a$  in eq. (11.1) was isolated providing the following equation for calculating the side lengths of the three castings.

$$a = M_c \frac{4ah_{ratio} + 1}{h_{ratio}} \quad (11.2)$$

A schematic of the casting design is seen in fig. 11.3.

#### The Pre-feeder

The pre-feeder was designed to compensate for liquid shrinkage independent of the pouring temperature. Its function was twofold: (1) A feeding function that must provide sufficient melt volume to counter the volume change in the casting due to liquid shrinkage, alongside the liquid volume shrinkage of the melt in the pre-feeder as well. Additionally, (2) the pre-feeder should be large enough to remain liquid for the necessary amount of time—the modulus requirement. Albeit, traditionally the modulus requirement prescribes that the feeder must stay liquid longer than the casting, while in this case the modulus requirement was used to secure that the pre-feeder provided a steady heat flux to provide a reference for the cooling conditions of the pre-feeder neck.

If the pre-feeder were significantly drained from melt during the liquid shrinkage, the cooling conditions of the pre-feeder neck would also change significantly, changing the point at which the pre-feeder neck closes off. Hence, the pre-feeder must be large enough to provide a stable heat flux regardless of the pouring temperature.

**Pre-feeder Neck** While the melt reservoir of the pre-feeder was constructed similar to a traditional feeder, the pre-feeder neck had to be constructed to close off as close to the beginning of solidification as possible, to eliminate the effects of liquid shrinkage on the casting. On the other hand, if the pre-feeder neck closed off to late, the pre-feeder would act as a regular feeder, removing the porosities and disturbing the trial results, while closing off to early result in a liquid shrinkage in the casting with additional porosities as a consequence. As one of the objectives of the trial design was to have porosities an early close off was favoured. As long as the remaining amount of liquid shrinkage in the casting could be kept identical regardless of the initial pouring temperature, this was not seen as a problem.

Thus, the design objective to construct a pre-feeder neck was defined as so:

The pre-feeder neck must be 95 % solidified ( $T_{sol}$ ) at the time ( $t$ ) when the temperature at the centre of the casting reaches the eutectic temperature ( $T_{eut}$ ).

The above definition entails an alloy dependency. The use of a eutectic (or near eutectic) alloy composition was assumed and for reference the eutectic temperature for the  $\alpha$ - and  $\beta$ -alloy from Part I was simulated using MAGMASOFT. The  $\alpha$ -alloy (EN-GJS-500-7) had a eutectic temperature ( $T_{eut}$ ) of 1165 °C, and the  $\beta$ -alloy (EN-GJS-450-10) had a eutectic temperature of 1170 °C. The 95 % fraction solid for the pre-feeder neck was assumed to be close enough to complete solidification that the mushy state of the remaining liquid would prevent further feeding through the pre-feeder neck section.

It was decided to use a cylindrical geometry for the pre-feeder neck because the pre-feeder neck design would not interfere with the requirements for a square design of the main casting, and because the cylinder was a basic shape that could easily be modelled analytically.

**Analytical Solution** Having decided that the pre-feeder neck have to be a cylindrical geometry, it was possible to express a relationship between the diameter of the pre-feeder neck ( $D_{neck}$ ) and the cooling time of the melt in the casting.

It was assumed that the casting and particularly the pre-feeder neck would experience small enough temperature gradients not to invalidate the use of the lumped analysis. The module law does not inherently consider the initial cooling time of the melt; however, it was assumed that the cooling characteristics displayed for solidification could be

adapted to cooling of the liquid as well. Additionally, the initial temperature of the melt was assumed to be uniform throughout the casting, pre-feeder, and pre-feeder neck.

As the two ends of the pre-feeder neck cylinder were assumed to be non-cooling surfaces, the expression reduces to a 1-dimensional solution that does not take the height of the neck into account. Likewise, the material constant for the mould reduces the expression as well, because the same mould material surrounds both the casting and the pre-feeder neck.

Hence, based on Chvorinov's modulus law described in eq. (2.4) on page 20, the ratio between the cooling time of the casting and the solidification time of the pre-feeder neck was defined as a ratio between the modulus of the pre-feeder neck and the modulus of the casting.

$$\frac{t_{sol}}{t_{eut}} = \frac{M_{neck}^2}{M_c^2} \quad (11.3)$$

where  $t_{sol}$  was the time in seconds for the melt in the pre-feeder neck to cool from the pouring temperature to a fraction solid of 100 %,  $t_{eut}$  was the time in seconds for the melt in the casting to cool from the pouring temperature to the eutectic temperature of the alloy, and  $M_{neck}$  and  $M_c$  were the moduli of the pre-feeder neck and the casting respectively. Note also that a complete solidification was used in the analytical approach, as opposed to the requirement defined previously and the later use of the numerical simulations.

As  $M_c$  was defined by the experiment,  $M_{neck}$  was isolated for the continued analysis.

$$M_{neck} = M_c \sqrt{\frac{t_{eut}}{t_{sol}}} \quad (11.4)$$

$t_{eut}$  and  $t_{sol}$  was then found analytically as a function of the pouring temperature, based on the heat flow from the casting and pre-feeder neck respectively. The heat flow was described in section 3.3.3, on page 43, while the cooling power of the mould was derived by b:

$$\begin{aligned} \dot{Q} &= -\rho V C_p \frac{dT}{dt} \\ &= A \sqrt{\frac{k_{mld} \rho_{mld} c_{p,mld}}{\pi t}} (T_i - T_o) \end{aligned} \quad (11.5)$$

where  $\dot{Q}$  is the heat flow in  $\text{J/s}$ ,  $\rho$  is the density,  $c_p$  is the specific heat capacity, and  $k$  is the heat conductivity.  $T_0$  is the ambient mould temperature, and

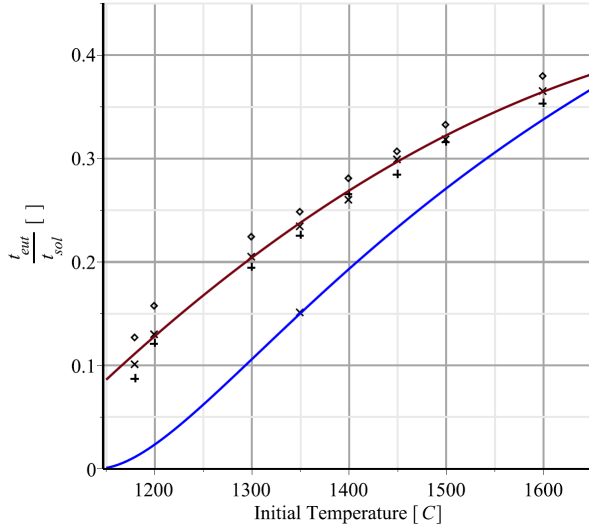


**Figure 11.4:** Solidification fraction against temperature—comparison of analytical model and correlated results of the numerical simulation.+ (M08), × (M10), and ◊ (M15). Blue line is the plot of eq. (11.9), and the red line is the correlation of numerical simulation in MAGMASOFT.

$T_i$  the temperature at the metal–mould interface. Additionally, the equation depends on the volume of the casting ( $V$ ) and the surface area between the casting and the mould ( $A$ ).

The cooling time for the casting was found by rearranging eq. (11.5) on page 162 with respect to the latter two factors, the  $V/A$  was substituted with the modulus  $M$  as described by Chvorinov [37]. See section 2.3.2, on page 20.  $\rho$  and  $c_p$  for both casting and mould are assumed to be constant. The heat transfer between metal and mould was assumed to be poor, hence  $T_i \approx T_{eut}$ .

$$t_{eut} = \frac{\rho^2 c_p^2}{4} \left( \frac{T_{start} - T_{eut}}{T_{eut} - T_0} \right)^2 \frac{\pi}{k_{mld} \rho_{mld} c_{p,mld}} M^2 \quad (11.6)$$

where  $T_{start}$  is the initial superheated temperature of the melt directly after pouring.

A similar derivation was made for  $t_{sol}$  using the following heat balance:

$$\begin{aligned} \dot{Q} &= \rho(-\Delta H) \frac{dV}{dt} \\ &= A \sqrt{\frac{k_{mld} \rho_{mld} c_{p,mld}}{\pi t}} (T_i - T_0) \end{aligned} \quad (11.7)$$

where  $\Delta H$  is the change in Enthalpy during solidification. Again  $V/A$  is substituted with  $M$  and

$T_i \approx T_{eut}$ . Additionally, eq. (11.6) was also substituted into the equation as it covers both the cooling of the liquid and subsequent solidification. This result in a version of Chvorinov’s rule that include superheat. Here derived for a 1-dimensional heat flow, but often used for more complex geometries as described by Fredriksson and Åkerlind [143].

$$t_{sol} = \left[ \frac{(-\Delta H) + c_p(T_{start} - T_{eut})}{\rho^2} \right]^2 \frac{\pi}{4(T_{eut} - T_0)^2 k_{mld} \rho_{mld} c_{p,mld}} M^2 \quad (11.8)$$

$t_{eut}$  in eq. (11.6) determine the time at which the pre-feeder neck should be solidified; determined by  $t_{sol}$  in eq. (11.8). Since the module,  $M$ , appears in both eq. (11.6) and eq. (11.8), it is possible to reduce the relationship to a dimensionless ratio. Subsequently, eq. (11.8) was reduced to:

$$\frac{t_{eut}}{t_{sol}} = \frac{c_p^2 (T_{start} - T_{eut})^2}{[(-\Delta H) + c_p(T_{start} - T_{eut})]^2} \quad (11.9)$$

This dimensionless analytical model for the time ratio is independent of the material parameters of the mould, the temperature difference between casting and mould, the density of the metal, and the module of the casting itself. Additionally,  $\Delta H$ ,  $T_{eut}$ , and  $c_p$  are all assumed constant. For further detail, the reader is referred to the technical report by Hansen [144].

The analytical model plotted as a function of different pouring temperatures ( $T_{start}$ ) is found in fig. 11.4.

**Numerical Solution** As the analytical model depends on a number of assumptions, a series of numerical simulations were made with MAGMASOFT to evaluate the validity of the model in the temperature range 1170 °C to 1600 °C. The extrapolation points shown in fig. 11.4 were found by dividing the measured  $t_{eut}$  at the casting centre with the  $t_{sol}$  for the pre-feeder neck. The result of the measurements for all three moduli castings is plotted in fig. 11.4. Subsequently, a 2<sup>nd</sup> degree polynomial correlation was fitted.

Both the analytical model and the numerical correlation showed that the initial pouring temperature did influence the closing time for the pre-feeder neck. Additionally, the comparison revealed two things. First, the analytical model and numerical simulation display a similar trend, though with an upward

shift in the numerical simulation results. However, both approaches indicate that a higher pouring temperature increases the time difference between the solidification of the pre-feeder neck and the cooling to the eutectic temperature of the casting.

For dimensioning the pre-feeder, the analytical model was chosen; because the analytical model presents the most conservative estimate of the two approaches. As the objective of the pre-feeder neck design was to eliminate variation resulting from varying pouring temperatures, some residual liquid shrinkage in the casting could be accepted; primarily, if the liquid shrinkage within the casting itself was kept at a similar amount for all relevant pouring temperatures. This design-safety was a better premise than accidentally feeding the casting via the pre-feeder.

Following the above premiss, a lowest expected initial temperature was chosen to be 1350 °C. This point is shown as a ×-sign on the blue line of the analytical model in fig. 11.4 on page 163.

Reverting to eq. (11.8) on page 163, the modulus of the pre-feeder neck was isolated. Subsequently, eq. (11.6) on page 163 was rearranged and inserted to establish a relationship between the module of the pre-feeder neck  $M_{neck}$  and the module of the casting  $M_{casting}$ .

$$M_{neck} = \frac{c_p(T_{start} - T_{eut})}{(-\Delta H) + c_p(T_{start} - T_{eut})} M_c \quad (11.10)$$

The equation describes the required ratio between the modulus of the pre-feeder neck  $M_{neck}$  and the module of the casting  $M_c$  required to secure that the pre-feeder neck solidifies when the casting reaches the eutectic temperature. Note that the expression is independent of the mould properties, density, and the temperature difference between the two geometries. The latter because a uniform initial temperature was a premise established at the beginning of the derivation.

**Pre-feeder Neck Height** The analytical solution derived in the previous section assumed that the pre-feeder neck was an infinite cylinder as the two ends were non-cooling surfaces. However, the presence of the pre-feeder and the casting influence the cooling time of the neck geometry. Hence, the height of the pre-feeder neck was not negligible and had to be considered separately as the analytical model did only include the diameter of the geometry.

Dimensioning the diameter of the cylindrical pre-feeder neck was based on the modulus of an infinite

cylinder, the diameter determined to be  $1/4 \times M_{neck}$  [24, 144], which was again be linked to the modulus of the casting in question—M08, M10, or M15.

The subsequent task was to determine how high the pre-feeder neck had to be to have a part in the middle that would solidify according to the 1D scenario modelled in the analytical model.

To estimate the required height of the pre-feeder neck the scalable geometry described in section 11.1.2, on page 161 was simulated using MAGMASOFT. The casting was simulated in three different sizes—M08, M10, and M15—all with five different pre-feeder neck heights—0.5a, 0.75a, 1.0a, 1.25a, and 1.5a. In total 15 different geometries, as seen in fig. 11.5 on the facing page. The simulation was made with two alloys—EN-GJS-500-7 and EN-GJS-450-10.

The simulation was set up to examine the solidification time at the middle part of the pre-feeder neck ( $t_{sol}$ ) and the cooling time to reach the eutectic temperature at the centre of the casting ( $t_{eut}$ ). The temperature at the thermal centre of the casting, at the time  $t_{sol}$  was recorded as  $T_{close}$ . Likewise, the temperature at the thermal centre at the time  $t_{eut}$  was recorded as the eutectic temperature  $T_{Eut}$ . However, as these two points cool at different rates (and numerical increments) an additional measurement point was chosen for reference of how close to the intended closing time the setup was. The third measured time was the time at the centre of the casting (same location as for  $T_{close}$ ), recorded at the time of solidification of the pre-feeder neck ( $t_{sol}$ ). This measurement was called  $t_{close}$ .

Plotting the ratio between  $t_{close}$  and  $t_{eut}$  it easily depicted if the pre-feeder neck closed off too late. If  $t_{close} > t_{eut}$  then the pre-feeder neck closed off too late. The simulation results for the different moduli castings, with different pre-feeder neck heights, are plotted for both of the two alloys in fig. 11.6 on the next page.

The graphs show that the four tallest pre-feeder necks solidify before the eutectic temperature was reached at the casting centre, but that the shortest (0.5a) closed off too late in all but one configuration. Additionally, the graphs also show that the shorter pre-feeder necks display a more uniform performance across the analysed temperature range. Hence, the more horizontal the lines were, the more uniform did the neck perform. The closer the lines were to the eutectic temperature, the closer the pre-feeder neck designs were to fulfilling the design cri-

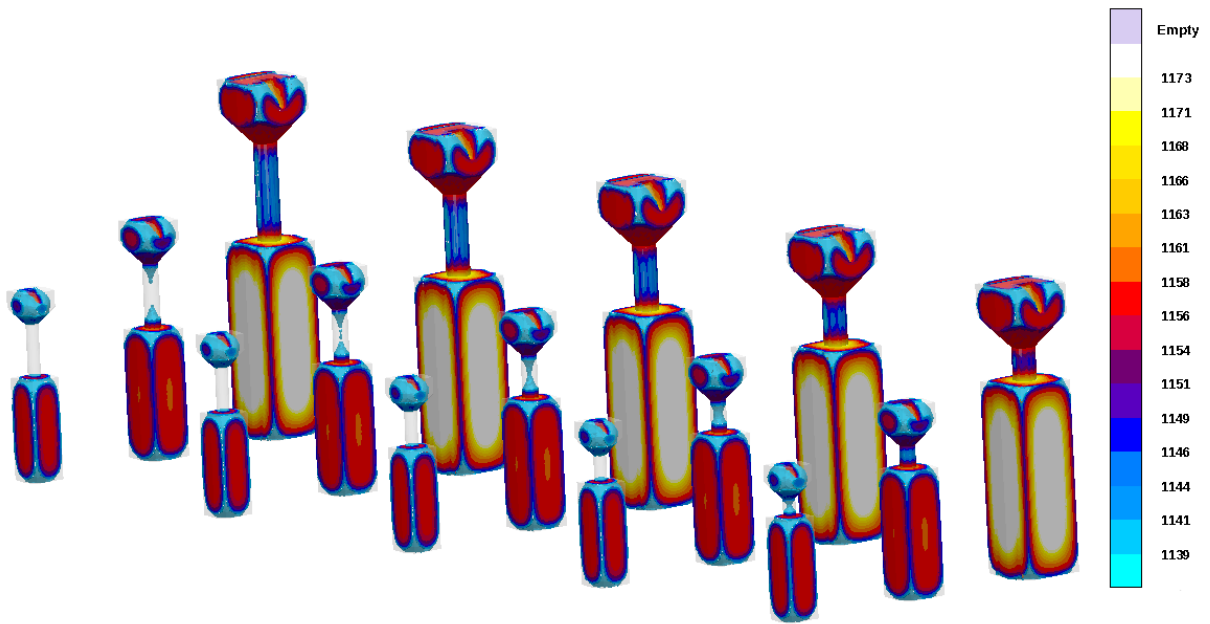


**Figure 11.5:** Simulation overview of the three different casting moduli (M08, M10, and M15) combined with the five different pre-feeder neck heights (0.5a, 0.75a, 1.0a, 1.25a, and 1.5a). Scale is 1130 °C to 1172 °C.

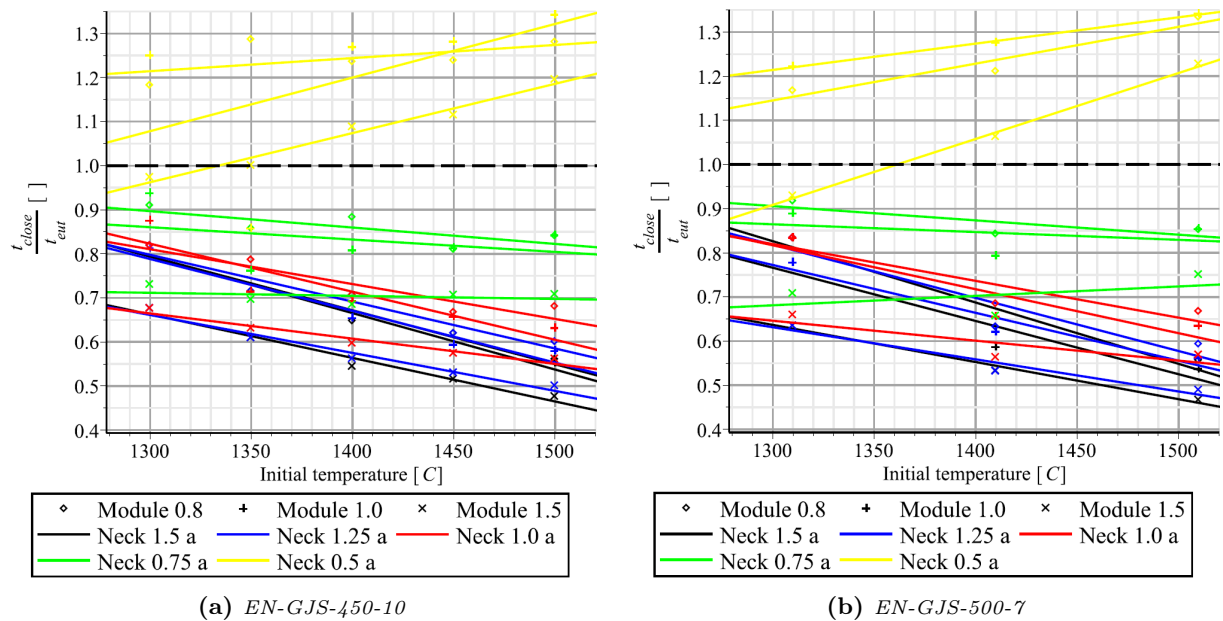
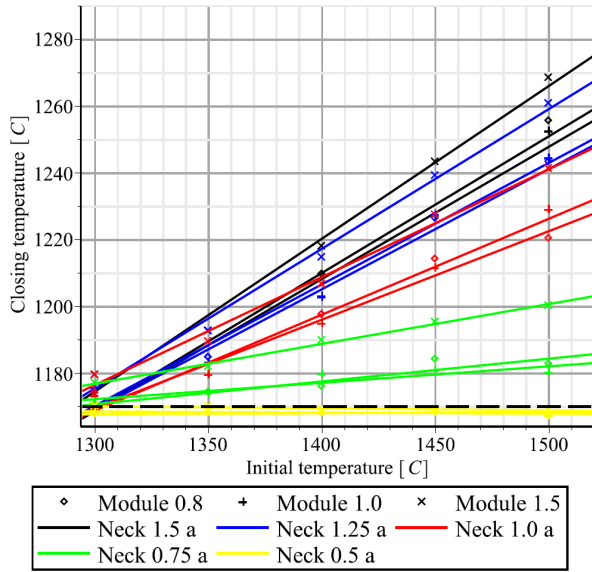


**Figure 11.6:** Ratio between  $t_{close}$  and  $t_{out}$  for the casting moduli M08, M10, and M15 with pre-feeder neck heights of 0.5a, 0.75a, 1.0a, 1.25a, and 1.5a, at different pouring temperatures. Ratios below 1 were acceptable.

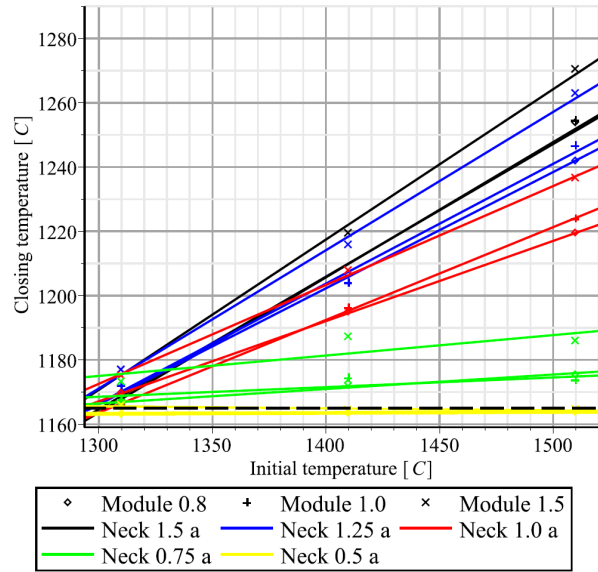
terion. Finally, the graphs show that the differences between the two alloys analysed were negligible.

Analysing the graphs, it was found that the pre-feeder neck with a height of 0.75a performed best for all of the conditions. The two tallest pre-feeder

necks (blue and black) were almost coincidental signifying that these are both long enough to negate the thermal influence of the neighbouring parts. However, the thermal influence of the neighbouring elements proved to help stabilise the performance

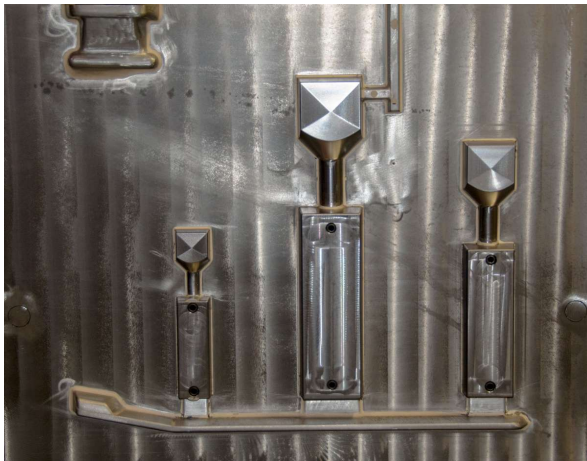


(a) EN-GJS-450-10

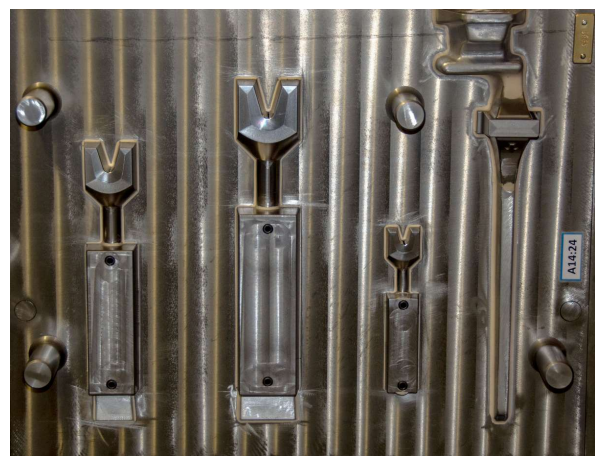


(b) EN-GJS-500-7

**Figure 11.7:** Closing temperature ( $T_{close}$ ) at the casting centre for the casting moduli M08, M10, and M15 with pre-feeder neck heights of 0.5a, 0.75a, 1.0a, 1.25a, and 1.5a, at different pouring temperatures.  $T_{close}$  above the eutectic temperature were acceptable.



(a) Pattern, swing plate (SP).



(b) Pattern, squeeze plate (PP).

**Figure 11.8:** Final pattern plates layout for the trial. Note the M12 size instead of the M10 used in the trial plan.

of the pre-feeder neck at elevated pouring temperatures. Thus, the optimal solution was too short to achieve the 1D solidification criterion at the middle part, and instead made use of the thermal influence of the casting and the pre-feeder to ensure a more uniform performance across the analysed temperature range. The maximum temperature difference between  $T_{close}$  and  $T_{eut}$  measured for 0.75a was less

than 30 °C.

To illustrate the influence of pouring temperature on the amount of residual liquid shrinkage in the casting, the temperature at the centre of the casting at the time of the pre-feeder neck close off was plotted as a function of the initial melt temperature. See fig. 11.7.

**Table 11.1:** Calculation of the feeder modulus required for each of the three modulus castings for each of the geometries. Moduli in mm.

(a) Planned moduli.				(b) Pattern moduli.				(c) Actual moduli.			
Factor	0.8	1.0	1.2	Factor	0.8	1.0	1.2	Factor	0.8	1.0	1.2
M08	6.0	8.0	10.0	M08	6.0	8.0	10.0	M08	6.0	8.0	10.0
M10	8.0	10.0	12.0	M12	9.6	12.0	14.4	M12	8.0	10.0	12.0
M15	12.0	15.0	18.0	M15	12.0	15.0	18.0	M15	12.0	15.0	18.0

**Table 11.2:** Alloy composition for the EN-GJS-500-14 alloy as measured at the beginning of each of the four sessions [wt%].

	CEV	C	Si	Mn	P	S	Mg	Cr	Ni	Mo	Cu	Sn	Pouring Temp.
I	4.60	3.31	3.91	0.31	0.015	0.003	0.051	0.047	0.021	0.001	0.09	0.004	1398(5) °C
II	4.57	3.31	3.81	0.31	0.015	0.003	0.045	0.046	0.023	0.001	0.09	0.005	1387(5) °C
III	4.54	3.35	3.61	0.25	0.015	0.004	0.042	0.051	0.026	0.001	0.06	0.005	1380(5) °C
IV	4.54	3.34	3.64	0.25	0.015	0.004	0.039	0.050	0.025	0.001	0.06	0.005	1361(5) °C
Avg	4.56	3.33	3.74	0.28	0.015	0.004	0.044	0.049	0.024	0.001	0.075	0.005	1382(5) °C

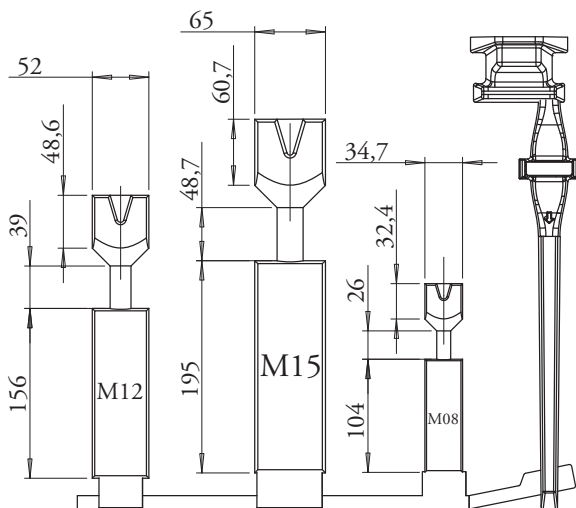


**Figure 11.9:** Technical drawing of the casting pattern including gating system. Note the M12 size instead of the M10 used in the trial plan. Measurement in mm.

### The Pattern

Having determined the scalable design of the casting and pre-feeder the pattern plate layout was created. However, the M10 casting pattern was erroneously manufactured as an M12 casting pattern. See section 11.2, on the current page.

The development pattern layout is shown in fig. 11.2 on page 160. This pattern was developed to fit the DISAMATIC 2110 at the university foundry. However, as the trials were to take place at Valde-

mar Birn <sup>A/s</sup>, it was chosen to let their application department build the pattern so that it would fit together with their production equipment.

The final pattern layout is shown in fig. 11.8 on page 166 and the dimension are shown in fig. 11.9. The patterns were designed to fit a DISAMATIC 230A, however they could also be fitted to a DISAMATIC 240A using a cassette system. The use of the standard pouring cup allowed for the automatic pouring system to be used during the trials, securing a more uniform mould filling.

## 11.2 Scaling Error (M10 ⇒ M12)

**B**ETWEEN the development of the trial plan and the development of the pattern plates, an error occurred. While the trial plan development focused on three modulus castings, M08, M10, and M15, the CAD-files used to manufacture both the development pattern, as well as the final trial pattern, had the modulus sizes of M08, M12, and M15.

This mistake was, however, not discovered at that time; hence the different feeder moduli used for the M12 castings were scaled to fit an M10 casting as described in section 11.3.2, on the next page. Thus, as a consequence, the M10/M12 castings did not scale according to the trial plan, or according to the feeder, modulus scaling used for the M08 and M15 castings.

Table 11.1 shows the difference between: (1) the planned feeder moduli setup (11.1a), (2) the feeder

**Table 11.3:** Overview of the selected feeders and the custom prototypes. True modulus ( $M_t$ ) in mm.

Sleeve	$M_t$
Feedex HD V 6	$\approx 6$
Feedex HD V 8	$\approx 7.5$
Feedex HD V 28	$\approx 9.5$
Feedex HD V 22	12
Feedex HD V 82	15
Feedex HD V 121	19
Kalmin 250 C2 V 6	$\approx 5$
Kalmin 250 C2 V 8	$\approx 6$
Kalmin 250 C2 V 28	$\approx 8$
Kalmin 250 C2 V 22	$\approx 10$
Kalmin 250 C2 V 82	$\approx 12$
Kalmin 250 C2 V 121	$\approx 16$

moduli that would have upheld the logic scaling for the patterns manufactured (11.1b), and (3) the actual feeder moduli that was used during the trial and which no longer scale linearly (11.1c).

The actual scaling factor of the M12 feeders, thus, mistakenly ended up being; 0.66, 0.83, and 1.00, rather than 0.8, 1.0, and 1.2. This scaling factor also meant that the scaling of the actual M12 feeders did not match the intended casting proportional feeder scaling, used for the M08 and M15 castings. Consequently, the M12 results had to be viewed in this context and part of the scalable linearity of the trial was lost.

## 11.3 Trial Description

THE experiment plan encompassed a series of castings using different feeders at different locations, as well as a decision on which alloy, or alloys, to examine.

### 11.3.1 Alloy Composition

It was chosen to use only one alloy for the trial. The two main reasons here fore was, that the alloy had to have sufficient shrinkage to provide a useful scale to evaluate the number and size of porosities, and because using a single alloy for the trial allowed for a broader range of feeders to be examined.

The alloy chosen was the EN-GJS-500-14 as this was available as part of the regular production at Valdemar Birn A/s. Additionally, the alloy was an alloy with a high shrinkage tendency and comparable to the previously examined  $\beta$ -alloy—EN-GJS-450-10.

The alloy compositions measured during the trials are shown in table 11.2 on page 167.

### 11.3.2 Choice of Feeders

The design and construction of the casting geometry and pre-feeding abilities were important features to ensure a repeatable and reliable comparison of the performance of the different feeders examined in the trial.

The feeders, however, had to be selected based on the moduli of the three casting sizes developed for the trial. As it had previously been decided to use the ram-up sleeve feeders due to the easy exchange between different feeders modulus sizes, as well as feeder geometries, locations, and even insulating properties.

#### Sleeve Material

Additionally, it was decided that the base selection of the feeders should be part of the ram-up sleeve feeders provided by FOSECO Ltd.. This decision ensured a ready supply of most of the feeders needed, as well as reduce the requirement for an expensive and timely prototype production. On the other hand, it was an integral part of the experiment to obtain a better understanding of the influence of modulus in comparison to the actual melt volume. Hence, it was decided to select the required feeders as one type, exothermic, and subsequently, produce an insulating version of these feeders for the trial.

In Part I an intermediate sleeve material was also investigated—the insulating-exothermic Kalminex material. However, because the insulating-exothermic material was very similar to the purely insulating material it was decided to limit the experimental setup to two sleeve materials—insulating and exothermic—as this would allow for a greater variety of size combination to be examined.

#### Feeder Moduli

As the moduli of the three castings had been decided to be M08, M10, and M15, the subsequent decision was to determine the feed modulus factors for the feeders. As the base requirement of the trial was to quantify the feeder efficiency based on the remaining porosities, the highest feed modulus was chosen to be  $1.2 \times M_c$ . See eq. 4.1 in section 4.2, on page 68. As the EN-GJS-500-14 alloy chosen for the trial was known to generate substantial porosities, this was the main feature for selecting this alloy. It was assumed that the traditional feed modulus factor of 1.2 would not completely feed the castings.



**Table 11.4:** Overview of the chosen feeders from the Feedex HD V series.

Casting	Factor	Mod [mm]	Vol [cm <sup>3</sup> ]	Name	Ins	no.	Exo	no.
M08/M10/M15	0.00	0	0	N/A				
<i>M08</i>	<i>0.75</i>	<i>6</i>	<i>6</i>	<i>SPECIAL</i>	<i>6I05</i>	<i>9</i>	<i>6E06</i>	<i>19</i>
M08	1.00	8	8.0	Feedex HD V 8	8I06	16	8E08	36
M08	1.25	10	28.0	Feedex HD V 28	28I08	12	28E10	32
M12	0.66	8	8.0	Feedex HD v 8	8I06		8E08	
M12	0.83	10	28.0	Feedex HD V 28	28I08		28E10	
M12	1.00	12	22.0	Feedex HD V 22	22I10	14	22E12	34
M15	0.80	12	22.0	Feedex HD V 22	22I10		22E12	
M15	1.00	15	87.0	Feedex HD V 82	82I12	7	82E15	17
M15	1.27	19	124.0	Feedex HD V 121	121I16	5	121E19	15
<b>SUM</b>						<b>63</b>		<b>153</b>

Additionally, the previously used 1.2 factor would also provide a reference to results presented in Part I as well as for foundrymen and instructional material addressing feeding of castings.

Consequently, two additional feed modulus factors were required, and it was decided to use 0.8 and 1.0 along with the 1.2 factor. This change provided a 1:1 feeding option with the 1.0 feed modulus factor. Subsequently, the 0.8 factor secured a linear progression of the factors tested. The planned feeder moduli are listed in table 11.1a on page 167, table 11.1b on page 167 lists the moduli that should have been used to oblige the M12 casting, and table 11.1c on page 167 shows the actual feeder moduli combinations for the M08, M12, and M15 castings. The moduli of the selected feeders are listed in table 11.3 on page 168.

#### Feeder Type

Following the decision of the feeder moduli to be used in the trial, a feeder type had to be chosen. FOSECO Ltd. provided a wide range of different feeder solutions. Some were natively designed to be used as ram-up sleeves; others could be fitted to the purpose. Feeders with the moduli listed in table 11.1 on page 167 could be found for a series of different feeder types. However, it was estimated that the more geometrically similar the feeders could be, the better. A greater geometrical similarity would eliminate variations in the results based on different feeder types and shapes. Hence, a single series of feeders were needed, which could provide the moduli mentioned above.

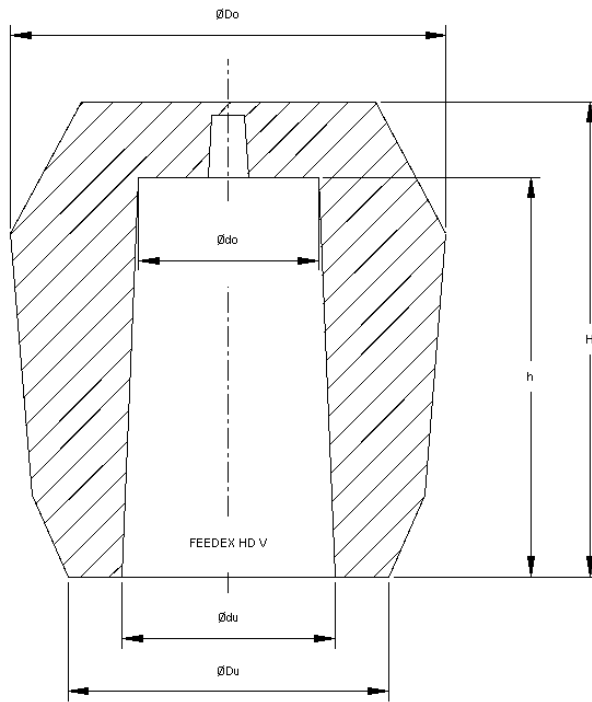
The series that best fitted the requirements was the Feedex HD V series. The feeders in the series are listed in fig. 11.10b on the following page. A feeder with an 18 mm modulus was not available within the selected series. Thus, the 19 mm modulus version was selected instead because the requirement of comparable geometries was preferred rather than having the exact feed modulus. The feeders used during the trials are shown in fig. 11.11 on page 171.

Additionally, it was also decided to retain the geometries of the different feeders, as selected from Feedex HD V series, also for the insulating sleeves. As the Feedex HD V series encompasses only exothermic sleeves, the insulating sleeves had to be produced as prototypes for the trials. The change in material also changed the Modulus Extension Factor (MEF), as described in eq. 2.6 in section 2.3.2, on page 20.

$$M_t = \text{MEF} \times M_g$$

As the exothermic sleeve material had a higher MEF compared with the insulating sleeve material, the resulting thermal (or true) modulus  $M_t$  of the prototyped insulating sleeves were lower than their geometrically identical exothermic counterparts. The trade name of the exothermic material is Feedex, and the trade name of the insulating material is Kalmin 250. The selected feeders with calculated  $M_t$  are shown in table 11.3 on page 168.

The chosen feeders; their properties, systematic name, and the amount that was used in the trials, is shown in table 11.4.



(a) Geometry overview of the Feedex HD V feeders.

size	modulus [cm]	volume [cm <sup>3</sup> ]	du [mm]	do [mm]	Du [mm]	Do [mm]	h [mm]	H [mm]
○ V 8	0.8	8	16	13	30	50.0	50	60
○ V 16	0.9	16	21	19	38	56.0	50	62
○ V 22	1.2	22	21	18	40	68.0	70	85
○ V 28	1.0	28	25	20	40	59.0	70	82
○ V 36	1.3	37	25	23	54	76.0	81	96
○ V 38	1.3	39	25	23	42	76.0	85	100
○ V 41	1.3	45	27	24	54	70.0	85	105
○ V 45	1.3	46	25	23	46	56.0	100	114
○ V 56	1.4	57	32	28	60	87.0	80	97
○ V 81	1.4	83	40	37	60	86.0	70	90
○ V 82	1.5	87	36	32	70	83.0	95	112
○ V 86 L	1.5	89	36	32	60	76.0	97	110
○ V 88	1.7	89	36	32	60	88.0	97	108
○ V 121	1.9	124	40	35	66	104.0	110	135
○ V 159	2.2	167	50	40	82	115.0	103	120
○ V 191	2.5	193	50	40	90	133.0	120	140
○ V 238	2.2	240	60	50	90	126.0	100	125
○ V 240	3.3	240	45	37	78	140.0	180	206
○ V 267	2.7	274	65	60	100	120.0	89	115
○ V 276	2.8	267	58	48	100	136.0	120	140
○ V 339	3.2	348	65	55	98	133.0	122	145
○ V 415	3.4	421	60	50	110	143.0	175	200
○ V 590	3.6	592	80	75	110	142.0	125	150
○ V 680	3.6	687	80	75	110	145.0	145	175
○ V 770	4.2	786	80	75	110	170.0	165	205
○ V 780	4.2	786	80	75	128	170.0	165	205
○ V 1140	4.5	1141	100	90	150	172.5	160	200
○ V 1480	4.8	1480	115	105	196	245.0	155	195
○ V 1650	4.8	1650	105	95	150	235.0	210	260
○ V 2565	6.0	2587	110	100	150	270.0	295	370

(b) Table overview of the different Feedex HD V sizes.

Figure 11.10: Feedex HD V Series.



**Figure 11.11:** *Insulating and exothermic versions of the selected Feedex HD V feeders, with the three sizes of metal breaker cores used for the trial.*

## 11.4 Trial Setup and Production

THE castings were produced at Valdemar Birn A/s in Holstebro as part of their running production. The trial was performed on a DISAMATIC 240A (750 × 600mm) moulding line, using a cassette system to mount the smaller pattern designed for a DISAMATIC 230A (600 × 480 mm). The moulding thickness was 300 mm. The castings were cast in four different sessions on two different dates in February and March 2014, with two sessions on each

date. The trial plan is shown in table 11.5 on the next page.

The patterns were mounted as shown in fig. 11.8 on page 166, and cast in the order described in table 11.5 on the next page starting at the top at each separate session. At the beginning of each combination, the mounting pins were mounted as shown on the right side of the table. Then the ram-up sleeve feeders were mounted on the pins, and the squeeze plate (PP) was moved to its end position.

**Table 11.5:** Trial plan overview. Trial number (#), Number of duplicates (No. ), Session number (S). Upper (U) and Lower (L) feeder for casting M08, M12, and M15 respectively. The feeders are listed by coded names, where the first number is the melt volume in the feeder in  $\text{cm}^3$ , and the E or I indicate if the material was exothermic or insulating, and the following number is the  $M_i$  in mm. The final number in parenthesis indicate the used breaker cores size. BKM 52/35, 58/33, and 64/33 indicate breaker core sizes and the numbers below indicate how many of which size of mounting pin had to be mounted at which location for the trial in question.

#	No.	S	M08			M12			M15		BKM 52/35	BKM 58/33	BKM 64/33
			U	L		U	L		U	L			
1	3	1,2,4											
2	3	3	6I05 (52)			8I06 (52)			22I10 (58)		2	1	
3	3	3	8I06 (52)			28I08 (58)			82I12 (64)		1	1	
4	3	3	28I08 (58)			22I10 (58)			121I16 (64)			1	
5	3	1	6E06 (52)			8E08 (52)			22E12 (58)		2	1	
6	3	1	8E08 (52)			28E10 (58)			82E15 (64)		1	1	
7	3	1	28E10 (58)			22E12 (58)			121E19 (64)			1	
8	2	1		6E06 (52)		8E08 (52)			22E12 (58)		2	1	
9	2	1		8E08 (52)		28E10 (58)			82E15 (64)		1	1	
10	4	1,2		28E10 (58)		22E12 (58)			121E19 (64)			1	
11	2	3	6I05 (52)	6E06 (52)	8I06 (52)	8E08 (52)	22I10 (58)	22E12 (58)		4	2		
12	2	3	8I06 (52)	8E08 (52)	28I08 (58)	28E10 (58)	82I12 (64)	82E15 (64)		2	2	2	
13	2	3	28I08 (58)	28E10 (58)	22I10 (58)	22E12 (58)	121I16 (64)	121E19 (64)			4	2	
14	2	4	8I06 (52)	6E06 (52)	28I08 (58)	8E08 (52)	82I12 (64)	22E12 (58)		3	2	1	
15	2	4	6I05 (52)	8E08 (52)	8I06 (52)	28E10 (58)	22I10 (58)	82E15 (64)		3	2	1	
16	2	4	6I05 (52)	28E10 (58)	8I06 (52)	22E12 (58)	22I10 (58)	121E19 (64)		2	3	1	
17	2	2	6E06 (52)	6E06 (52)	8E08 (52)	8E08 (52)	22E12 (58)	22E12 (58)		4	2		
18	2	2	8E08 (52)	8E08 (52)	28E10 (58)	28E10 (58)	82E15 (64)	82E15 (64)		2	2	2	
19	2	2	28E10 (58)	28E10 (58)	22E12 (58)	22E12 (58)	121E19 (64)	121E19 (64)			4	2	
20	2	2	8E08 (52)	6E06 (52)	28E10 (58)	8E08 (52)	82E15 (64)	22E12 (58)		3	2	1	
21	2	2	6E06 (52)	8E08 (52)	8E08 (52)	28E10 (58)	22E12 (58)	82E15 (64)		3	2	1	
22	2	2	6E06 (52)	28E10 (58)	8E08 (52)	22E12 (58)	22E12 (58)	121E19 (64)		2	3	1	

The swing plate (SP) closed the chamber, and the mould was shot and compacted. Subsequently, the mould was pushed to the mould line. Here the sequence was stopped, a ceramic filter was mounted, and then the next feeders for the next duplicate were prepared.

All moulds and subsequent the castings were marked using a punching tool. The mark was made in the sand mould when the ceramic filter was placed into the mould.

For the largest of the feeders, it was necessary to stop the cycle at the PP end position to ensure that the feeders were still positioned correctly after the pattern movement. This problem arose because the mounting pins were designed to handle several different feeder sizes to limit the required number of mounting pins and subsequent pin changing operations during the trial run. Unfortunately, this resulted in the largest of the feeders tending to drop the tip due to a too short mounting pin.

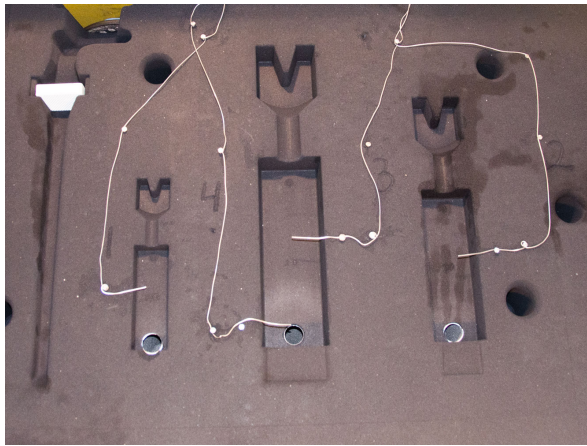
Like with the trials in Part I the moulding was done in sessions to allow for sequential casting without delay. This solution was chosen to ensure a more uniform pouring temperature for all of the

castings. In-stream inoculation of the melt was used. The pouring time without feeders was  $\sim 6$  s without feeders, and the total poured weight without feeders totalled  $\sim 16$  kg. Of this the feederless castings respectively;  $\sim 1.1$  kg for the M08 casting,  $\sim 3.7$  kg for the M12 casting, and  $\sim 7.3$  kg for the large M15 casting.

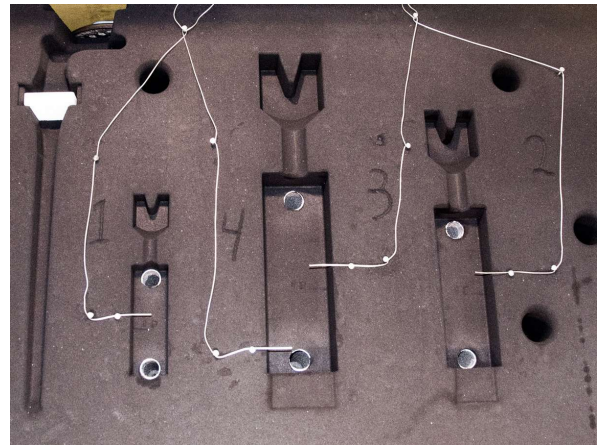
The castings cooled and solidified in the mould for  $\sim 1.5$  h before the castings reached the shake-out station, at which point the castings were recovered manually and allowed to air-cool to room temperature. The manual removal ensured that all feeders remained attached to the castings. Afterwards, the castings were cleaned by shot blasting.

Finally, the castings were sorted, marked for easy identification, and photo documented.

In total 69 castings of each of the three modulus sizes were made, totalling 207 different castings for the entire trial.

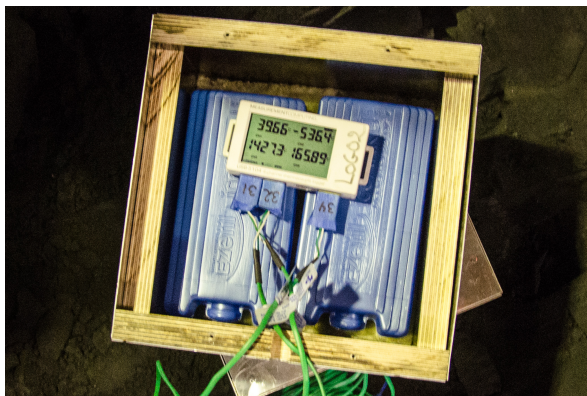


(a) *First mould.*

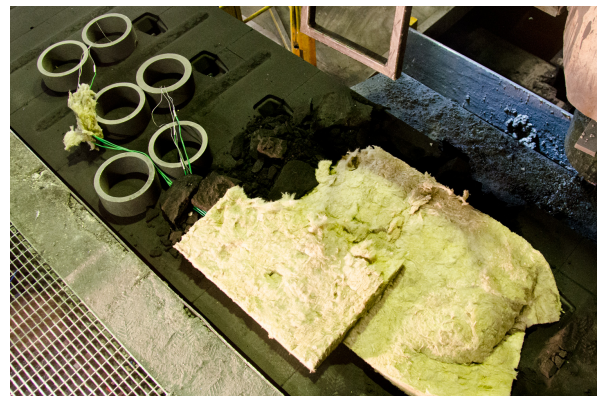


(b) *Second mould.*

**Figure 11.12:** *Thermocouple placement.*



(a) *Data-logger in insulated box before casting.*



(b) *Mounting and protection of the data-logger.*

**Figure 11.13:** *Setup of thermal measurement equipment.*

#### 11.4.1 Temperature Measurements

Temperatures were measured at the beginning of each session to assess the actual pouring temperature, and to provide a measure on the thermal variation that was part of the trial. However, these measurements do not provide information about the actual temperature of the casting during cooling. To obtain a better thermal description of the cooling of the casting from the pouring of the melt until shake-out thermocouples were placed in a mould and the temperature was measured as the castings moved along the cooling line.

Thermal measurements of this type could provide information to help calibrate the MAGMASOFT simulations better and provide information on the thermal effect of the feeders, as well as record the

cooling of the castings.

#### In-Production Thermal Measurements

As the cooling line was wholly encased at Valdemar Birn <sup>4</sup>/<sub>s</sub> it was not possible to follow the castings on either side of the line. Instead, it was decided to let the data logging equipment 'ride' along with the casting inside the cooling tunnel.

It was decided to use two USB-5104 4-channel thermocouple logger from Measurement Computing. See fig. 11.14 on the following page. They are compact and can log four channels plus the ambient temperature. The data-loggers are battery driven and can log with up to 1Hz. The temperature limitation was determined by which thermocouple type was used. Each channel could be programmed

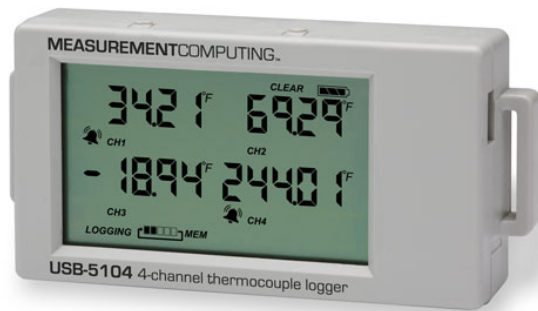


**Figure 11.14:** Measurement Computing USB-5104, 4-channel thermocouple data-logger.

separately. For this experiment, K-type elements were used.

The thermocouples were mounted on the vertical plane of the mould and fastened using core nails. Two times four thermocouples were mounted in trial C10 and C17 and cast immediately before the start of session 2. The feeder configuration is found in table 11.5 on page 172 and the alloy composition and pouring temperature in table 11.2 on page 167. The mounting of the thermocouples is shown in fig. 11.12 on page 173.

The USB-5104, like most other electronic equipment, had a maximum operating temperature of 70°C. The air temperature in the cooling tunnel was expected to rise above this threshold during the 1.5 h journey from the pouring station to the shake-out. Two insulated boxes were constructed to accommodate this issue. A data-logger was placed in each of the boxes along with cooling elements and padded with insulation. Due to the low roof clearance of the cooling tunnel, a few extra moulds were made, and the boxes were dug into these. See fig. 11.13 on page 173.

## References

[21] N Chvorinov. “Solving Feeders and Sink-heads”. In: *Proceedings of the 30th International Foundry Congress*. 1963.

- [22] PN Hansen, PR Sahn and E Flender. “How to Select and Use Criterion Functions in Solidification Simulation”. In: *Transactions of the American Foundrymen’s Society*. 101 (1993), pp. 443–446.
- [24] John Campbell. *Casting Practice - The 10 Rules of Casting*. Linacre House, Jordan Hill, Oxford OX2 8DP, 30 Corporate Drive, Burlington, MA 01803: Elsevier Butterworth-Heinemann, 2004. ISBN: 0 7506 4791 4.
- [26] DM Stefanescu. “Computer Simulation of Shrinkage Related Defects in Metal Castings—A Review”. In: *International Journal of Cast Metals Research* 18.3 (2005), pp. 129–143.
- [37] Nicolas Chvorinov. “Theory of the Solidification of Castings”. In: *Giesserei* 27 (1940), pp. 177–186.
- [39] M. Tiryakioğlu, E. Tiryakioğlu and D.R. Askeland. “The Effect of Casting Shape and Size on Solidification Time: A New Approach”. In: *International Journal of Cast Metals Research* 9. (1997), 259–267.
- [44] W.S. Pellini. “Factors Influencing Riser Range and Feeding Adequacy—Part II”. In: *American Foundryman*. (1953), 62–71.
- [142] Rio Tinto Iron & Titanium Inc. *Ductile Iron—The Essentials of Gating and Riser Design*. 770 Sherbrooke Street West - Suite 1800, Montréal (Québec) Canada: Rio Tinto Iron & Titanium Inc., 2000.
- [143] Hasse Fredriksson and Ulla Åkerlind. *Materials Processing during Casting*. English. Wiley, 2006, 434 blz. ; ISBN: 0470015136, 9780470015131.
- [144] Rune Engelbert Hansen. *Design of Experimental Method for Feeding*. Special Course. Technical University of Denmark, Department of Mechanical Engineering, 2013.



# Chp 12 Feeding Analysis

Quantification of the  
Experimental Results and  
Numerical Simulations

## Feeding Analysis

<b>12.1 Porosity Quantification</b> . . . . .	<b>175</b>	<b>12.3 Thermal Analysis</b> . . . . .	<b>202</b>
12.1.1 Ultrasound Analysis . . . . .	176	12.3.1 Numerical Simulations . . . . .	202
12.1.2 X-Ray Analysis . . . . .	179	12.3.2 Cooling Curve Analysis . . . . .	205
12.1.3 Weighing the Castings . . . . .	179	12.3.3 Thermal Gradients . . . . .	210
12.1.4 Sectioned Castings . . . . .	181	12.3.4 Fraction Liquid Analysis . . . . .	212
<b>12.2 Porosity Result Analysis</b> . . . . .	<b>186</b>	12.3.5 Geometric Solidification Analysis . .	214
12.2.1 Upper Feeder Only . . . . .	187	<b>12.4 Numerical Porosity Analysis</b> . . . . .	<b>221</b>
12.2.2 Lower Feeder Only . . . . .	190	12.4.1 Simulation Setup and Calibration . .	222
12.2.3 Upper and Lower Feeders Together .	190	12.4.2 Porosity Simulation Results . . . . .	227
12.2.4 Proportional Modulus Analysis . . .	193	12.4.3 Sub Conclusions . . . . .	229
12.2.5 Puncture at the Pre-Feeder Neck . .	199	<b>References</b> . . . . .	<b>229</b>
12.2.6 X-Ray Results Analysis . . . . .	200		

» QUANTIFICATION and analysis of the scalable modulus castings with respect to porosity sizes and locations. Porosities are quantified using ultrasound and x-ray imaging. The chapter also covers numerical simulation results and analysis with thermal and fraction liquid gradients.

Keywords: . . . . . Porosity Quantification, Ultrasound Analysis, X-Ray Analysis, Feeder Modulus vs. Porosities Graphs, Proportional Modulus Analysis, Numerical Simulations, Cooling Curves, Thermal Gradients, Fraction Liquid Gradients, Solidification Analysis.

Chapter findings reported in: . . Supplement IV, on page 337

### 12.1 Porosity Quantification

THE trial castings were produced as described in chapter 11, on page 157. The porosity analysis used in Part I—sectioning, grinding, and etching all the castings before performing a liquid penetrant test on each sectioned casting—was too time-

consuming to be useful in analysing all the castings produced for this second Part.

Additionally, the liquid penetrant test of a sec-

Aluminium (Al), Computer Aided Design (CAD), Modulus Extension Factor (MEF), Pores Per Inch (PPI), Silicon (Si), Thermocouple (TC)

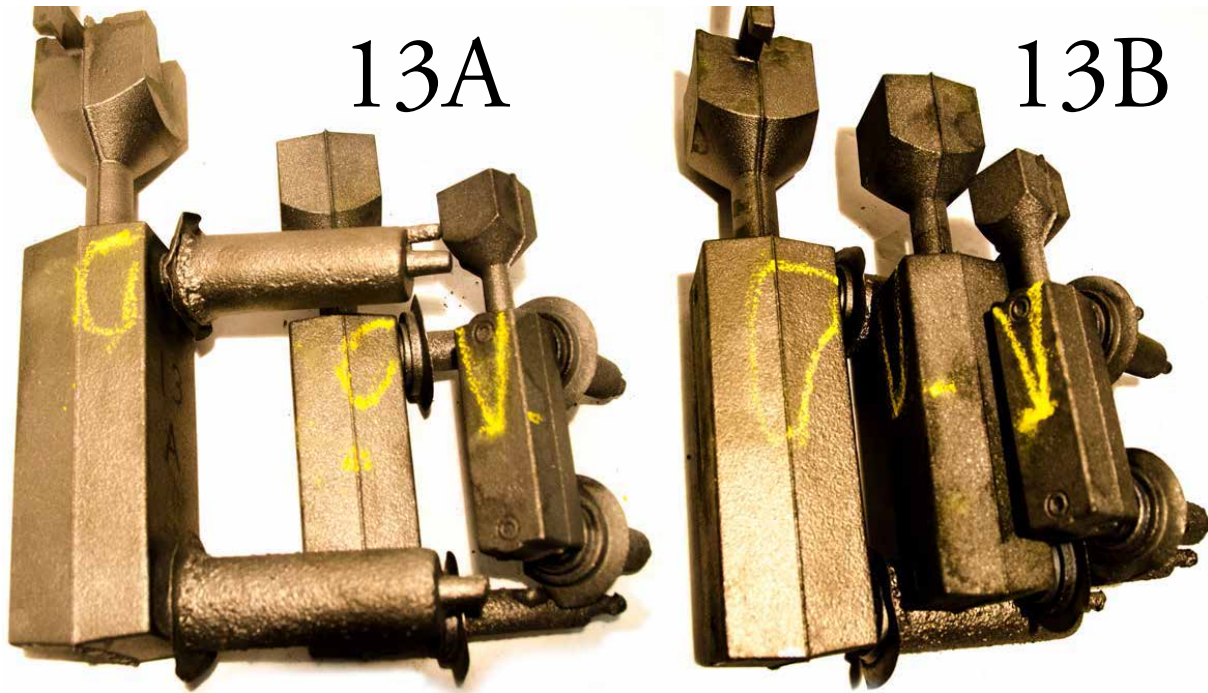


**Figure 12.1:** Porosity indications identified using ultrasound and marked with crayon by the operator. Note that both markings on the large M15 castings are classified as large (4) porosities. The porosity on the 13B-M15 casting is connected to a small (2) porosity at the middle control volume. Casting 13A-M12 shows a large porosity (4) at the top and a disconnected small (2) porosity at the middle control volume.

tioned casting has the disadvantage of only evaluating the plane at which the cut was made. For this reason, other methods were sought after.

To accurately quantify the porosities two things were essential: (1) establishing how large were the porosities, and (2) where were the porosities located. Hence, the analysis method used must provide a proper estimate of these two parameters for the entire volume of the casting, not just the sectioned plane. The methods must be reliable, repeatable, and relatively fast. As all 207 castings had to be analysed, it was decided to reserve the slow and labour intensive analyses for selected castings.

For these reasons, and because of the accessibility and expertise at Valdemar Birn A/s, it was decided that the bulk analysis and quantification should be performed by ultrasound analysis, that select castings would subsequently be x-ray imaged to support the analysis of the ultrasound examination, and other select castings should be sectioned.

Additionally, the application of non-destructive tests would preserve the castings for later examinations using other methods, destructive or non-destructive, if need be. Hence, only the sectioned castings would be eliminated from this.

### 12.1.1 Ultrasound Analysis

Ultrasound can be used to analyse a range of different material characteristics—eg material properties, elastic modulus, polymerisation in plastics, the density of ceramics, nodularity in cast iron, grain size in metals, and detection of particles and porosities and their distribution in the material, among other applications [145]. In this analysis, the ultrasound was used to analyse the size and distribution of porosities in the bulk of the material.

The porosity analysis was performed by moving a transducer over the surface of the casting. The transducer transmitted an ultrasound signal which was then recorded by the receiver—in this case, the transducer acted as a combined transmitter and receiver. This combined function also meant that the analysis was dependent on the reflection of the sound waves from the casting surface opposite the transducer. The surface of the casting was sprayed with a mixture of 5% machine oil and 95% water to ensure the required transmission of the sound from the transducer to the casting and back again.



The base signal was obtained when the sound travelled from the transducer to the reverse side of the casting and back to the transducer without any obstructions. The baseline is dependent on the material characteristics. For example ductile cast iron is a better sound conductor than grey cast iron, resulting in different baseline distances. Porosities and other impurities in the casting shatter the soundwave, reflecting part of the signal before it reaches the reverse side of the casting. This reflection provides a signal different from the baseline, identifying signal obstructions in the casting. The difference between the reflection of the obstruction and the reflection of the baseline indicate the depth and size of the obstruction.

The signal response time indicates the reflection distance directly below the transducer. By moving the transducer across the surface of the casting, the operator can detect where the signal obstructions (porosities) are located. The operator located the porosities and drew the edge of the defects directly onto the casting using a crayon, and thus created a projection of the porosity onto the outer surface of the casting. See Figure 12.1 on page 176.

The castings were analysed using a Karl Deutsch Digital-Echograph by an experienced operator.

The castings were analysed from two sides—the side with the feeders, and the parting line side. This approach ensured a ‘view’ of the porosities from two sides, thus increasing the reliability of the analysis as the results were confirmed by two separate measurements. Additionally, the two side approach allowed for a better 3D estimation of the porosities, as two projections, 90° apart, were available for the analysis.

All castings were photo-documented with the porosity indications drawn onto the castings for later analysis. See fig. 12.1 on page 176.

#### Defect Classification

The porosities had to be given quantifiable values and properties to enable a quantitative analysis of the feeding of the castings. The main property of the porosities was the size, albeit the location of the porosities was also an interesting property to quantify. Thus the scale was based on a notion similar to the definition presented by Lee et al [27], though with additional differentiation. See section 2.2.1, on page 17. Additionally, other observed phenomena were recorded to support the subsequent analysis.

**Porosity Size** The porosities were classified on an absolute scale from 0 to 4 where;

- 0 = no porosities,
- 1 = microporosities,
- 2 = small porosities,
- 3 = medium porosities, and
- 4 = large porosities.

Note that the scale is exponential, not linear and that the quantification of all porosities was performed by the same experienced operator. The scale was also the same for all three moduli castings, meaning that the porosity grading does not scale with casting modulus. The porosity values are absolute; hence eg a medium porosity is relatively more significant for the small M08 casting compared with the large M15 castings.

Note also that the scale displays a few inherent limitations. There is a lower limit to the size of porosities that can be detected by ultrasound analysis. Hence, very small intergranular porosities may have been undetected by the analysis. These possibly undetected porosities, however, do not significantly influence the validity of the analysis. The analysis quantifies the feeding efficiency of the different feeder configurations, and porosities so small that they cannot be detected by an ultrasound analysis will not alter the overall impression of the efficiency of a given feeder configurations. Additionally, porosities too small to be detected by non-destructive analyses would likewise not be large enough to cause the casting to be scrapped.

For the large porosities, the limitation of the scale is that the scale is open-ended. Hence, large porosities cover anything from large, over very large, to extremely large.

Another approach for estimating the total amount of porosities in the casting would be by weighing. This approach is addressed shortly in section 12.1.3, on page 179.

**Porosity Location** The next important parameter is to determine the location of the porosity by determining the size of the porosities,. It was chosen to divide the castings into three equally sized control volumes—top, middle, and bottom—and record the size of the porosities found in each of these control volumes for all of the castings. See fig. 12.2. Note

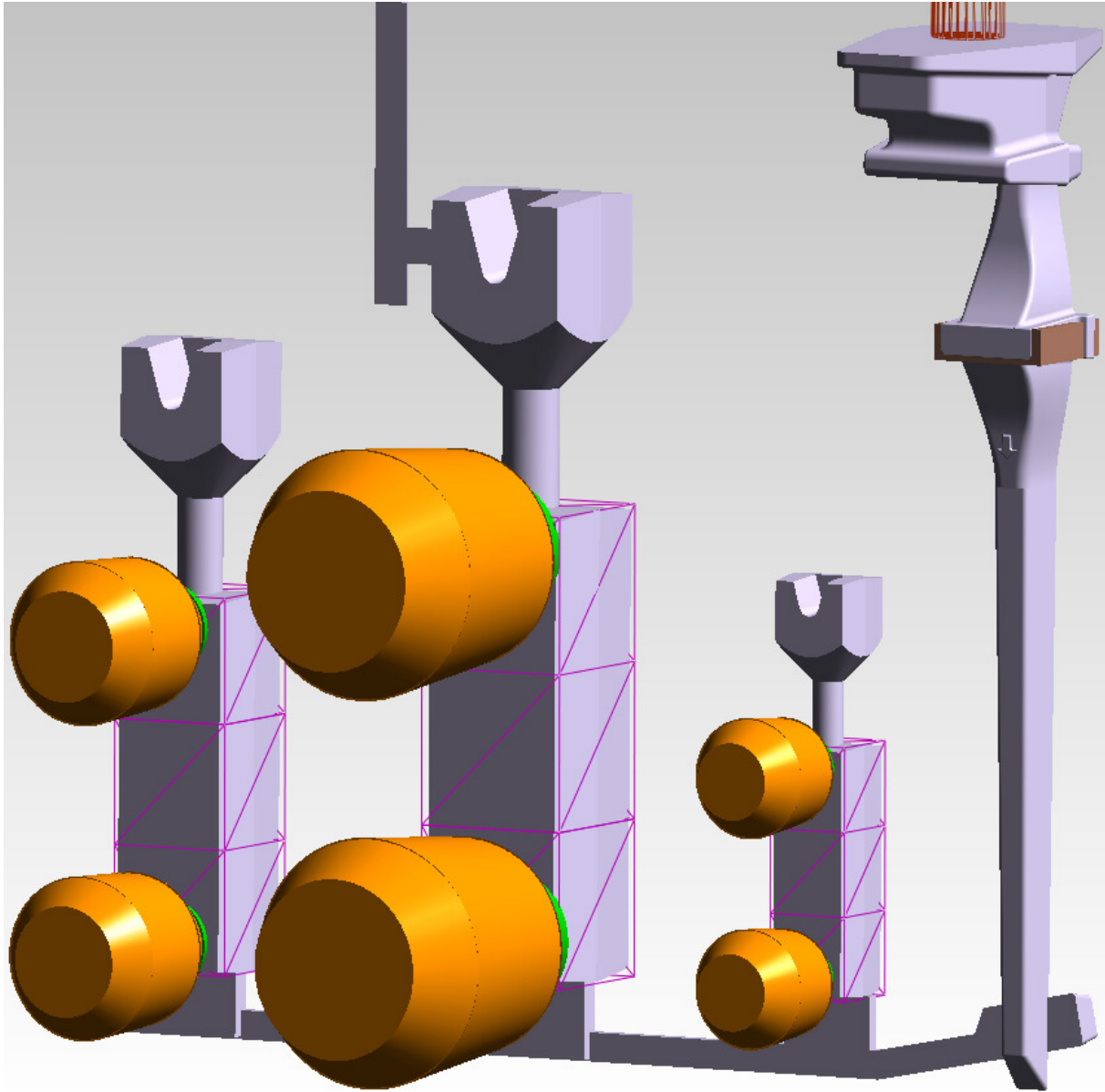


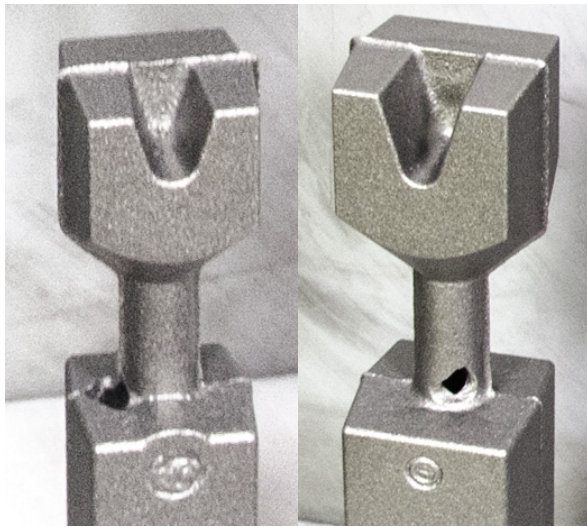
**Figure 12.2:** Control volumes for the porosity analysis. The three volumes that encase the castings themselves are designated as the top, middle, and bottom control volume.

that the three control volumes, as a result of the casting design, are all cubes with a side length of  $a$ , as described in section 11.1.2, on page 161, and shown in fig. 11.3 on page 161.

Another approach could have been to measure the distance from the bottom of the casting to the bottom of the porosity. For multiple porosities, this would require multiple measurements. This approach may provide a more accurate porosity location for the subsequent analysis, albeit an accurate

description of the large porosities would require an additional measurement—eg of the height of the porosity.

The volume approach was chosen because it reduced the number of measurements required, and because the location can, if need be, be evaluated using the imaged castings. Additionally, it was estimated that the volume approach provided an adequate level of information for a statistical comparison of the feeder configurations efficiency.



(a) M08: 01F

(b) M12: 01F

**Figure 12.3:** Typical atmospheric punctures at the pre-feeder neck.

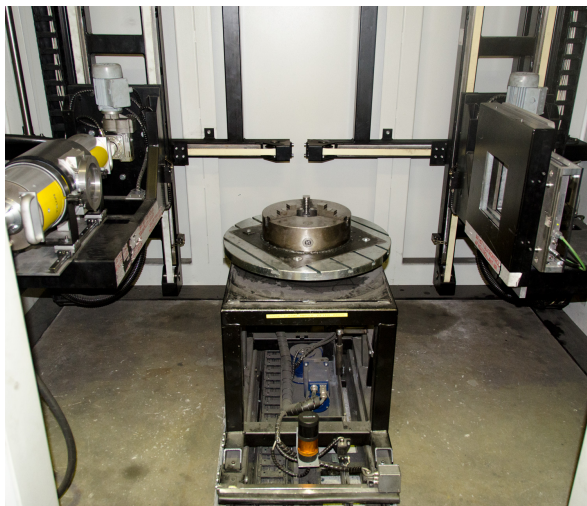


**Figure 12.4:** YXLON x-ray imaging machine used for the x-ray analysis. X-ray source on the left, turntable at the centre, and x-ray detector at the right [146].

**Other Observations** During the ultrasound analysis of the castings, other reoccurring features were observed. These were also recorded to support the porosity analysis.

**Connected or Disconnected** It was discovered that some castings had porosities that spanned two of the three predefined volumes—top, middle, and bottom. See fig. 12.1 on page 176. These porosities were recorded as the porosity size inside the specific

volume. For example, a porosity could cover both the top and the middle volume. The porosity size inside the top volume would then be assigned the top volume—eg 4 for a large porosity. Likewise, the porosity size inside the middle volume would be assigned a value based in the size of this part of the total porosity—eg this might be a 2 for a small porosity.

However, castings with porosities in adjacent volumes, which were not connected were also observed. Thus, it was necessary to indicate if the porosities were *connected* or *disconnected* across the volume boundaries. See table 12.1a on the following page, where connected porosities are indicated by *italic*.

**Puncture at the Pre-Feeder Neck** It was observed that some of the castings had an atmospheric puncture at the connection between the pre-feeder neck and the main body of the casting. See table 12.1a on the next page, where castings with an atmospheric puncture are marked as **bold** for the porosity size of the top control volume.

Two typical punctures are shown in fig. 12.3. The shown punctures are from castings without a feeder; however, no differences were observed between the atmospheric punctures that were found in casting with and without feeders.

### 12.1.2 X-Ray Analysis

Based on the results of the ultrasound analysis, select castings were analysed using x-ray imaging with a YXLON x-ray imaging machine [146]. See fig. 12.4. Note that the x-ray imaging was a simple method providing macroscale 2D images of select areas of the castings. The smaller M08 castings could be imaged in one frame, albeit the M12 and M15 could only be imaged in sections. The images of the different sections were stitched together to provide context to the images; again to provide a useful overview of the analysis. See fig. 12.5 on page 181.

### 12.1.3 Weighing the Castings

Another method for quantifying the number and size of porosities in the castings is to weigh them. The larger the porosities, the lighter the casting. This method yields some advantages; (1) the number and size of porosities is recorded as a value (weight), and (2) the method is free of subjective assessments



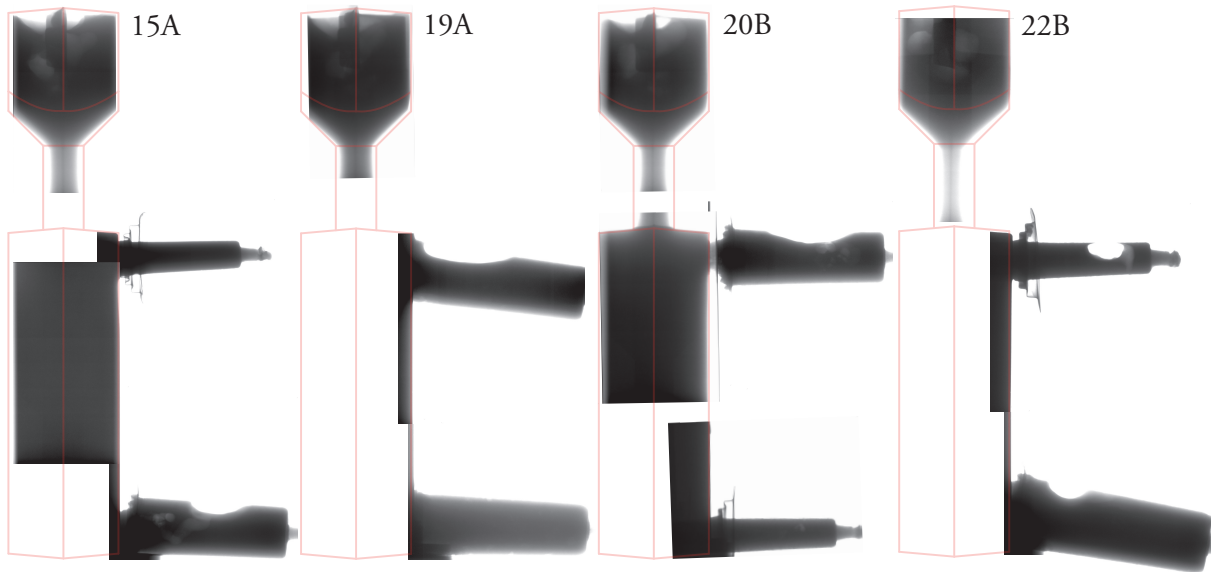


**Figure 12.5:** Overview of x-ray images for M15 castings, showing porosities in the pre-feeder and in the different ram-up sleeves feeders.

by an operator. On the other hand weighing the castings also entail a few disadvantages: (1) it is a destructive method that require the pre-feeder and other feeders to be separated from the casting, and (2) the accuracy of the method is greatly dependent on how identically the castings are cut and ground to leave the same amount of casting to be weighed for all castings. Burrs and excess edges may easily weigh the same as a medium sized porosity. Additionally, separate control volumes can be cut and measured; however, sectioning must be very precise to control the size of the volume. Some porosities will possibly also be located at the cutting plane and thus destroyed in the process.

As the method is destructive and would separate the feeders from the castings, it was decided to postpone this type of analysis until all other analyses were performed. Subsequently, the weighing porosity analysis has not been a part of the present porosity analysis.

#### 12.1.4 Sectioned Castings

In addition to the ultrasound and x-ray analyses, a selection of the castings was also sectioned through the vertical centreline—specifically the parting line of the mould. This approach allowed for a direct visual inspection of the porosities. A liquid penetrant test was not performed on the sectioned castings as it was assessed that the porosities were

plainly visible without the penetrant. Additionally, the tendency for the liquid penetrant to ‘bleed’ when applied to large porosities, obscuring the results, further dissuaded the application in this case.

An advantage of the sectioned castings compared the results of the ultrasound and x-ray analyses, was that direct visual inspection of the porosities was more natural to match with the results of the porosity predictions made by the numerical simulations.

Note that only M15 castings were sectioned, as these were the only one available at the time.

Figure 12.6 on the next page and on page 183 shows six different castings without feeders—benchmark castings. These castings show how the basic casting geometry solidify and form porosities without the application of feeders, but also testify to the process stability by showing the variation in porosities occurring as part of the production process itself.

The castings show a tendency to form a significant porosity right under the pre-feeder neck. This tendency is seen in all six castings. Additionally, casting 00B in fig. 12.6a on the next page also shows a porosity at the middle control volume, which was classified as a large (4) porosity. The porosity in the sectioned casting seem small for a ‘large’ porosity, but the sectioning only shows the plane that has been cut and may have removed a large part of the porosity by sectioning through it. The same can



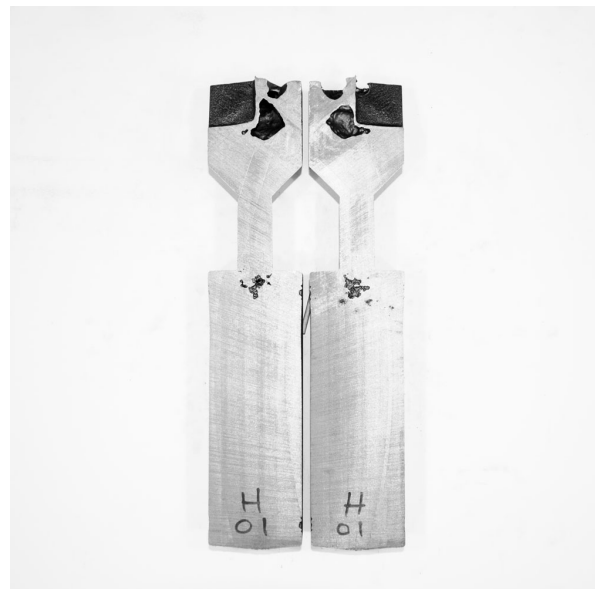
(a) 00B-M15 4:4:0



(b) 00C-M15 4:2:0



(c) 01A-M15 4:2:0



(d) 01H-M15 4:1:0

**Figure 12.6:** Sectioned castings cast without feeders. The numbers indicate the porosity size identified by the ultrasound analyses— $T:M:B$ . See table 12.1 on page 180.

be said for the other castings, where the porosities identified by the ultrasound analysis cannot be seen.

Figure 12.7 on page 184 and on page 185 show eight sectioned casting with various different feeder configurations. As expected, the size and distribution of the porosities vary much more between the

different casting groups than within the group of reference castings shown in 12.6. Note that particularly the castings in figs. 12.7b and 12.7e differentiate from the other castings in fig. 12.7, as well as the porosities observed in fig. 12.6.

The location and formation of the porosity in



(e) 1B-M15 4:2:0



(f) 03C-M15 4:1:0

**Figure 12.6:** Sectioned castings cast without feeders. The numbers indicate the porosity size identified by the ultrasound analyses— $T:M:B$ . See table 12.1 on page 180.

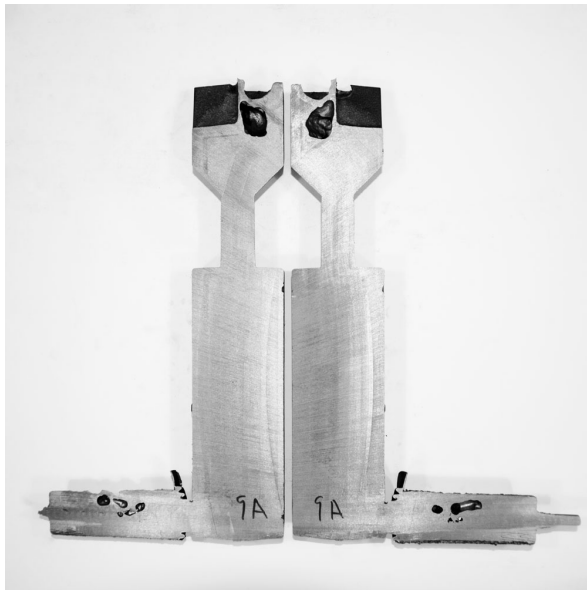
casting 10B in fig. 12.7b show clear signs of a casting defect aided by other factors than regular feeding. The same can be said of casting 16B in fig. 12.7e. Both porosities show formations that are distinctly different from the porosities observed in fig. 12.6, or in the feeder in fig. 12.7. The position of the porosities in the two castings also stray from the thermal centre of the castings, as is also illustrated in subfigure (d) in Figure 2.5 on page 16.

Note that casting 10B in fig. 12.7b has a blowhole on the right-hand side, indicating that some gas evolution has occurred. The session was halted right before the castings with feeder configurations C10, as to mount TCs in the moulds. Thus, castings 10B and 10C were the very first castings to be cast in the second session, while castings 10A and 17A with the TCs followed. As seen in fig. 12.8 on page 186. The designation A, B, and C is arbitrary as any order of casting is lost at the shake-out station. Consequently, the blowhole in 10B, which can also be found in almost the same spot in casting 10C, cannot be related to the presence of TCs. Viewing the cleanliness around the pouring cups, or lack thereof, in 12.8, indicate that the installation of the TCs indirectly may have caused inclusions.

That the 10B and 10C castings were the first castings to be cast after the extended pause may

have led to inclusions or other melt impurities to get into the melt and the casting; though a ceramic filter was used as described in chapter 11, on page 157. Alternatively, it is possible that the filter was not put in these two moulds by mistake, thus allowing for impurities and inclusions in the melt to get into the mould. Vald. Birn always uses filters due to the construction of the melt handling, which does not allow for de-slagging, which in turn give rise to problems with inclusion and impurities. A third option is that the inclusions have come into the mould via the vent.

Casting 16B in fig. 12.7e was cast as part of another session on another date. Furthermore, casting 16B had no TCs installed so this cannot be the cause of the unexpectedly large porosity in this casting, when compared with its sibling, casting 16A in fig. 12.7d. While the porosity in casting 16B, in general, is dissimilar to the porosity in casting 10B, they both display crescent shapes porosities hinting at some oxide bi-film opening, as described by Campbell [24]. The central part of the porosity is, however, very irregular in shape and does not resemble a gas porosity formed in the melt. A possibility is that impurities in the melt have caused weak spots in the melt, which as a result has ruptured as the tension in the melt at a later stage of



(a) 9A-M15 0:1:0



(b) 10B-M15 4:4:4



(c) 15B-M15 0:2:0



(d) 16A-M15 0:2:0

**Figure 12.7:** Sectioned castings cast with different feeder configurations. The numbers indicate the porosity size identified by the ultrasound analyses— $T:M:B$ . See table 12.1 on page 180.

solidification and feeding became too high. This theory is supported by the shape of the porosities which is substantially textured, as compared to the 10B porosities or the porosities in the pre-feeders, indicating that the melt was in a mushy, semi-solid state when the porosities formed, as shown in fig.

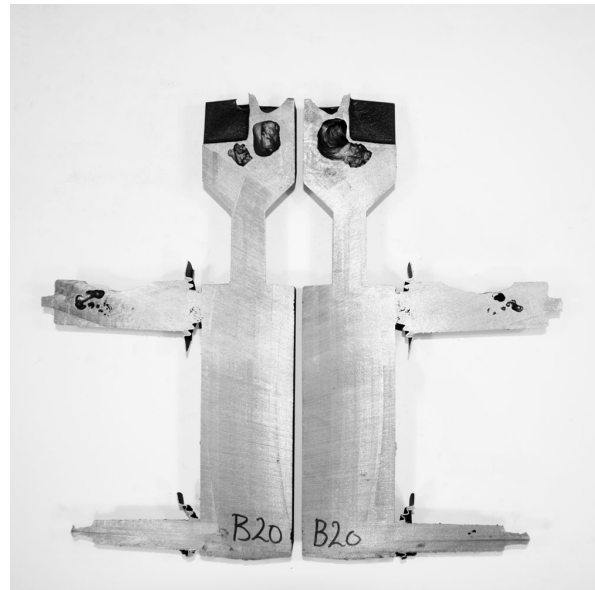
13.3c on page 242.

The porosities in the lower feeders of castings 9A, 15B, 21A, and 22B should also be noted. These show a smooth surface, indicating the surface tension was dominant at the time porosities were formed. This type of porosity formation may indicate that the

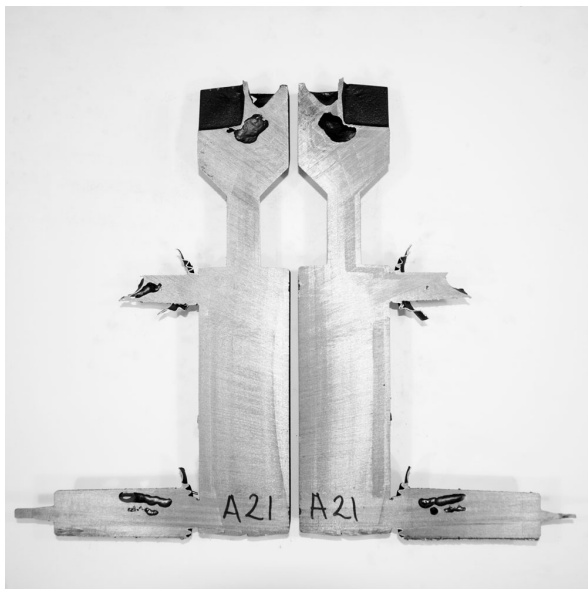




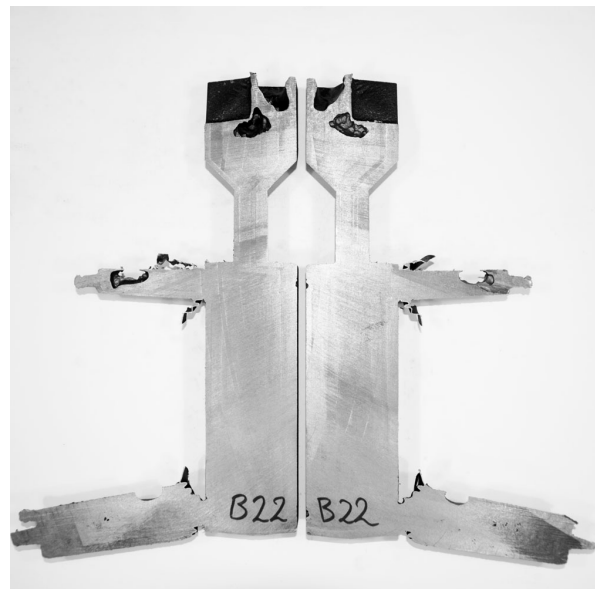
(e) 16B-M15 4:3:0



(f) 20B-M15 0:0:0



(g) 21A-M15 1:0:0



(h) 22B-M15 0:0:0

**Figure 12.7:** Sectioned castings cast with different feeder configurations. The numbers indicate the porosity size identified by the ultrasound analyses— $T:M:B$ . See table 12.1 on page 180.

porosities were formed in the not-to-mushy liquid. It is also likely that gas expelled from the solidifying melt have aided the formation of these porosities, though it is assessed that a rupture formed the porosities in the melt caused by too high a tension and that gas released as the solubility was lowered

afterwards found its way to these cavities in the melt.

Additionally, the sectioned castings visualise, in part, the size definitions of the porosities used in the ultrasound analysis in section 12.1.1, on page 176. Remember, though, that the sectioned casting only



**Figure 12.8:** Overview of the TC setup and mould placement of castings 10A, 10B, 10C, and 17A.

show the porosities that intersect with the section. Other porosities may be present away from the parting line or been initially located where the sectioning was made. Regardless of this, the sectioned castings do illustrate the exponential nature of the porosity scale used to quantify the size of the porosities, as described in section 12.1.1, on page 177.

## 12.2 Porosity Result Analysis

THE results of the ultrasound analysis are listed in table 12.1 on page 180. However, as causes and correlations can be difficult to extract from directly from the results table, subsequent data analysis and results illustrations have been made. Figure 12.9 on page 188 illustrate all the castings with either an

upper or a lower feeder. Figure 12.11 on page 192 illustrate the castings with both an upper and a lower feeder. The M08 castings are shown in red, the M12 castings are shown in blue, and the M15 castings are shown in green.

The graphs show the sum of porosities for the entire casting plotted as a function of the total sum of the moduli of both the upper and lower feeders used for the particular casting. For traditional gravity driven feeders the relationship would predict a reduction in the sum of porosities as the sum of the feeder moduli increases. This relationship would be valid from the point when the feeder was large enough to feed the casting, and until the feeder was large enough to prevent the porosities completely. Outside these boundaries, the relationship does not apply.

Contour plots are overlaid onto the scatterplot of the feeder moduli vs. the sum of porosities. Trend lines are used to illustrate the progressing of a set of data. However, due to the variation across the feeder combinations, the different trend line-type yielded a series of different trends; hence the choice of trend line became an interpretation in itself. For this reason, it was decided to use contour plots to illustrate the tendencies of the scatter data. Note that some scatter points are overlaying and that this is illustrated by the contour plot. Additionally, the less scattered the data, the denser the contour lines. Scattered data, on the other hand, disperse the contour lines, indicating a less stable process. Remember that the x-axis was predetermined as part of the experimental design, and that variation along this axis is a matter of experimental design rather than process stability.

Note that the feeder moduli used for insulating and exothermic feeder sleeves are different. The exothermic feeders have a higher feed modulus as the same sleeve geometry was used for both types, and the exothermic material has a greater MEF compared with the insulating material. Note also that the graphs do not show the location of the porosities in the castings, hence only displaying the porosity sum for all three control volumes—top, middle, and bottom.

### 12.2.1 Upper Feeder Only

The top row (a-c) of graphs in fig. 12.9 on the next page show all upper feeders, both insulating and exothermic. The second (d-f) and third (g-i) row represent the same data as in the top row but

differentiated between insulating and exothermic sleeves. Below each of the three casting moduli will be analysed separately, and subsequently compared.

#### M08 (12.9a)

Comparing the insulating (d) and the exothermic (g) feeder sleeves materials in fig. 12.9 on the following page, the insulating sleeves appeared to provide a more stable and uniform process. On the other hand, little if any feeding efficiency improvement were obtained by using a larger insulating feeder modulus.

**Insulating (12.9d)** Upgrading from a feeder with a modulus of 5 mm to a feeder with a modulus of 6 mm reduced the porosity sum from five to four for one of the three castings. The upgrade to feeder modulus 8 mm increased the porosity sum for two of the three castings from five to six, while the last casting had a porosity sum of four. Hence, increased feeder modulus, for the insulating sleeves, gives indications of increased porosities and decreased process stability.

**Exothermic (12.9g)** The exothermic feeder sleeves provided the least stable results; however, the lowest porosity sum for all M08 castings was found for the 6 mm exothermic feeder, displaying a porosity sum of three. This casting, 5C, showed no porosities at the top control volume. This behaviour was only observed in one other of the M08 castings, namely 19A. Instead of the top porosity, 5C was found to have a medium (3) porosity at the middle control volume. As the two other castings with the same feeder configuration were found to have a porosity sum of six, with four at the top control volume and two at the middle control volume, this behaviour was considered an anomaly.

The 8 mm feeder castings all had a porosity sum of eight. While this was stable, it was not an improvement regarding the number and size of porosities found in the benchmark castings without feeders.

For the 10 mm feeder castings, two of the three castings showed a porosity sum of four; while the last casting had a porosity sum of eight. This number and size of porosities indicated a tendency towards a better yielding, though less stable, feeding process. None of the castings in this group had any porosities at the middle control volume. However, the castings with a porosity sum of eight, 7C, displayed a large (4) porosity in the bottom control

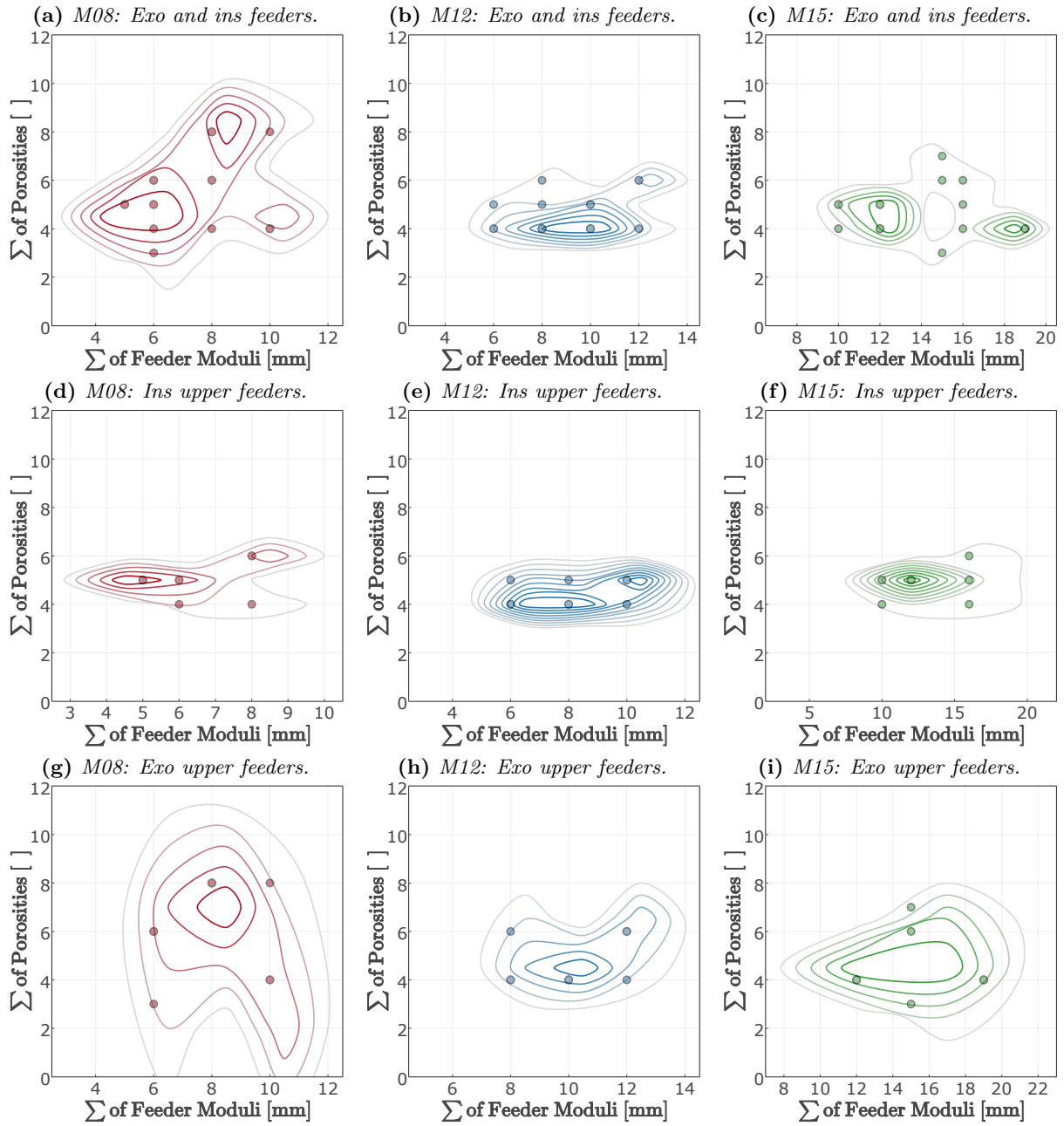


**Figure 12.9:** Upper feeder only: Overview of the porosities size distribution based on feeder modulus for castings with upper feeder only. Exo = exothermic feeder sleeves, and ins = insulating feeder sleeves.

volume. As the 10 mm was the largest modulus upper feeder used for the M08 castings and the only casting that did not show porosities at the middle volume, this indicates that the 10 mm upper feeder was large enough to significantly influence the solidification of the castings and the porosity formation.

#### M12(12.9b)

The M12 castings displayed less dispersion compared with the M08 castings. The combined graph (b) shows a baseline of castings with a porosity sum of four, but also that all feeder moduli had one or two castings with more porosities.

Note that the feeders used with the M12 castings were proportionally smaller compared with the M08 and M15 castings, as described in section 11.2, on page 167. Hence, decreased dispersion of the results may be related to the reduced influence of the size reduced feeders. Additionally, it should also be noted that the 6 mm feeder, with a proportional modulus of  $0.5M^\infty$  performs as well as the 10 mm feeder, and better than the 8 mm and 12 mm feeders.

**Insulating (12.9e)** The insulating feeder showed minimal variation between the different feeder configurations. The only small tendency was towards increased porosities for larger feeders. The small 6 mm and 8 mm feeders show a tendency towards reduced porosities, while the slightly larger 10 mm feeders were inclined towards slightly increased porosities. Again, note that all three feeders had a modulus smaller than the casting itself.

**Exothermic (12.9h)** The exothermic group was very similar to the insulating regarding stability and porosities. The exothermic group also displayed a baseline across all feeder moduli with a porosity sum of four. Like the insulating group, the exothermic group also showed a small tendency towards increasing porosities for the largest feeder modulus, the 12 mm. Note, though, that the exothermic feeders all were +2 mm larger than the insulating feeders. Hence, the 10 mm for the insulating feeders was the least favourable performer of its group, while 10 mm for the exothermic group it was the best performer.

#### M15 (12.9c)

The graph with the combined groups for the insulating and the exothermic feeders (c) can be subdivided into three groups. The first subgroup, the small modulus feeders 10 mm and 12 mm, showed porosity sums between four and five. Note, though that all the insulating 12 mm feeders resulted in a microporosity (1) at the middle control volume, while the same modulus feeder made with the exothermic material all were free of this porosity. The second subgroup, the medium modulus feeders 15 mm and 16 mm, displayed a large dispersion ranging from a porosity sum of three to seven. The last subgroup, the medium modulus feeders 19 mm, showed the same stable process with only porosities at the top control volume as was also found for the exothermic 10 mm feeders.

**Insulating (12.9f)** Analysing the insulating feeders separately, it was found that the group as a whole has a little variation, with the 12 mm feeder showing the most repeatable performance.

**Exothermic (12.9i)** The single best performance was observed for the casting 6A, with a modulus of 15 mm, albeit the performance of the group was dispersed. However, the group markedly had two castings, 6A and 6B, that displayed only small (2) porosities in the top control volume. The two other exothermic groups, 12 mm and 19 mm, both displayed stable processes with large (4) porosities in the top control volume.

#### Modulus Comparison (12.9a-12.9c)

Comparing the feeder performance across the three casting moduli, it is noted that the largest porosity sum was recorded for the smallest casting, M08. Remember that the porosity scale does not scale with the casting modulus, as described in section 12.1.1, on page 177. The M08 castings showed the largest dispersion, while the M12 castings were the most stable. Again, the reduced dispersion may be related to the proportionally smaller feeder used for the M12 castings.

**Insulating (12.9d-12.9f)** The insulating feeder groups were very uniform in their performance. However, none of the feeder configurations resulted in a significant reduction in porosities. For all three modulus castings, a slight increase in porosity sums was observed for increasing feeder modulus.

**Exothermic (12.9g-12.9i)** The exothermic groups showed more dispersed behaviour compared to the insulating groups. However, the castings with the smallest porosity sums were also found in the exothermic groups. Note that the feeder modulus proportional to the casting modulus was the differentiated modulus for the M08 and M15 castings. For M08 castings the 8 mm feeders were the most stable group with no variation in porosity sum. For the M15 castings, however, the opposite was true. Here the proportional feeder modulus, 15 mm, was the only group that showed any dispersion of the porosity sum. For the M12 castings, the best performance was recorded for the 10 mm feeder and increased dispersion and porosities for both the smaller 8 mm feeder and the larger 12 mm feeder.

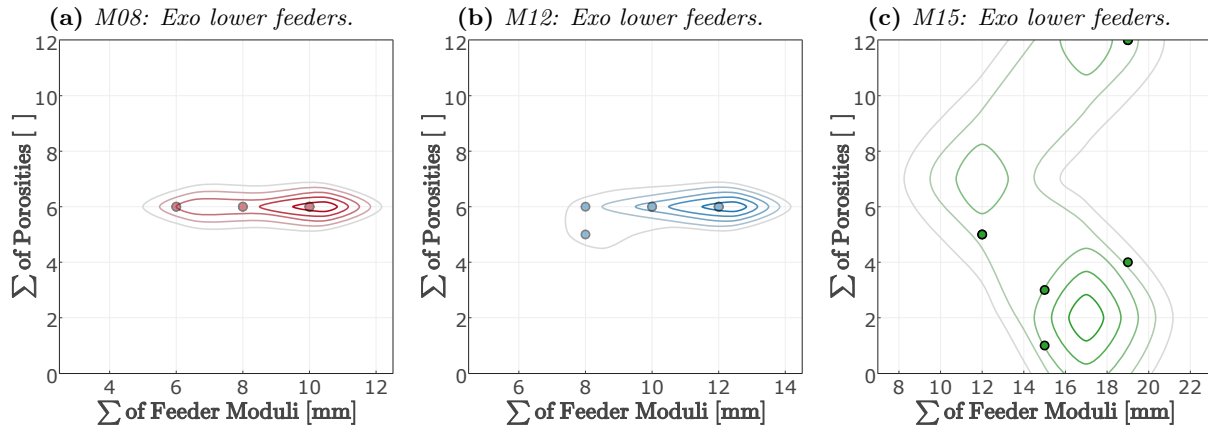


**Figure 12.10:** Lower feeder only: Overview of the porosities size distribution based on feeder modulus for castings with lower feeder only. Exo = exothermic feeder sleeves.

### 12.2.2 Lower Feeder Only

For the groups of castings with only a lower feeder there are no insulating feeder combinations, and subsequently, the combined group plots are also absent. See fig. 12.10. Note that the 10A casting was equipped with thermocouples and the temperature in the casting was measured during the solidification and cooling of the castings. See fig. 12.15 on page 204.

#### M08 (12.10a)

The M08 castings showed no variation in the results. All seven castings in the group had a porosity sum of six, distributed by four from the top control volume, and two from the middle control volume. The weight towards the 10 mm feeder in the contour plot is because there were three of these castings, while only two of the two other feeder moduli.

#### M12 (12.10b)

The M12 castings perform very stable and very similar to the M08 group. Only dispersion is the 8A casting that had a medium porosity (3) in the top control volume rather than a large (4) as all the other castings in the group. Remember that the 8 mm feeder that produced this improvement was  $6.66 M^\infty$  of the M12 casting, and thus the proportionally smallest bottom feeder analysed. Again the shift towards the 12 mm feeder in the contour plot relates to the number of castings.

#### M15 (12.10c)

While the M08 and M12 casting groups with only a bottom feeder showed almost no variation, the M15 casting group do. The castings with the 12 mm feeders perform similarly to the smaller modulus castings. The 15 mm feeders resulted in two castings without porosities at the top control volume. The middle control volume showed a microporosity (1) and a medium porosity (3) respectively, as the only porosities found in the two castings. These few and small porosities indicate that the proportional exothermic feeder located at the bottom of the casting manages to feed most of the casting. The largest feeder modulus, 19 mm, on the other hand, showed inferior results. The 10A casting showed small (2) porosities at the middle and bottom control volumes. However, the two other castings in the group had large (4) porosities in all three control volumes. This sum of porosities is more than double the sum of porosities found in the benchmark castings without feeders.

#### Modulus Comparison (12.10a-12.10c)

The graphs show that the M08 and M12 castings solidify comparably, while the larger M15 castings apparently solidify differently, changing the development of the shrinkage defects and feeding regime. The size increase of the casting alters the way the casting act together with the proportional feeders.

### 12.2.3 Upper and Lower Feeders Together

The scatter plots for the castings that have both an upper and a lower feeder are organised in the same way as for the scatter plots with a top feeder only.

See fig. 12.11 on the next page. The top row (a-c) shows the collected findings for each modulus casting, while the second row (d-f) shows the castings with an insulating upper feeder and an exothermic lower feeder, and row (g-i) shows the castings that had exothermic feeders at both the upper and lower position. Note that the x-axis denotes the sum of moduli of the two feeders. Note also that casting 17A was equipped with thermocouples and the temperature in the casting was measured during the solidification and cooling of the castings. See fig. 12.15 on page 204.

#### M08 (12.11a)

The contour plot show curves with low porosity sums at the small moduli sum, as well as the large moduli sum. The medium size moduli sum feeders showed larger total porosities than smaller and larger counterparts. All of the small moduli sum castings had a large (4) porosity at the top control volume, but no porosities at the middle control volume. Thus, a positive feeding effect was repeatedly achieved for all six castings with feeders that had a modulus of 5 mm or 6 mm. For the large moduli sum feeders, the sum of porosities was the same, albeit they were distributed differently. The 19A had small (2) porosities at the middle and bottom control volumes, while the 19B had small (2) porosities at the top and the middle control volumes.

**Insulating Upper Feeder (12.11d)** Most of the castings with insulating upper feeder had a stable performance with a large (4) porosity at the top control volume and a small (2) porosity at the middle control volume. Casting 12B, which had 8 mm feeders as both the upper and lower feeder position showed microporosities (1) at the middle control volume. However, a group of castings with small modulus feeder at both the upper and lower feeder position showed improved feeding performance. Hence, castings groups 11 and 15 both displayed castings without porosities at the middle volume. Note that the positive effect was only recorded for the smallest upper feeding modulus, 5 mm. The 6 mm insulating feeders did not show the same effect as removing the porosities at the middle control volume. Additionally, the combination of the smallest upper feeder, 5 mm, with a large lower feeder, 10 mm, did not yield the same positive results. Hence, the two feeders do influence each other's performance in a non-linear way.

**Exothermic Upper Feeder (12.11g)** The sum of porosities in castings with exothermic upper feeders was more dispersed than the castings with insulating upper feeders. The middle moduli sum group showed increasing porosities at the middle control volume. For example, the group C20 had a 8 mm upper feeder and a 6 mm lower feeder, resulting in large (4) porosities at both the top and middle control volume. However, the feeder combination with 6 mm upper feeder and a 6 mm lower feeder, as found in group C17, yielded a porosity-free middle control volume. Additionally, the reverse combination of a 6 mm upper feeder and a 8 mm lower feeder, as found in group C21, yielded small (2) porosities at the middle control volume.

Finally, in the same manner, as with the insulating upper feeders, group C22 illustrate that the combination of a small upper feeder, 6 mm, and a large lower feeder, 10 mm was not advantageous. This combination had medium (3) and large (4) porosities at the top control volume and large (4) porosities at the middle control volume.

#### M12 (12.11b)

The M12 castings displayed little variation across the different feeder combinations. Some dispersion in the porosity sum was found with a feeder modulus sum of 18 mm. The variation comes from groups C12 and C16. Group C12 used 8 mm insulating upper feeder, and a 10 mm exothermic lower feeder and yielded a reduction of the porosities at the middle control volume from a small (2) porosity to a microporosity (1). The same effect was achieved with casting 16B. It also had a small 6 mm insulating upper feeder, and a larger 12 mm exothermic lower feeder. However, casting 16A had a medium (3) porosity at the middle control volume. Additionally, groups C20 and C21 did not show the same reduction in the porosities of the middle control volume, as recorded for group C12 and casting 16B. Even though group C21 had the same feeder modulus combination as group C12, but with an exothermic upper feeder instead of the insulating upper feeder used in group C12.

The best feeding performance for the entire group was casting 11B, which had a small 6 mm insulating upper feeder and small 8 mm exothermic lower feeder. Hence, the feeder combination with the smallest sum of moduli also yielded the most significant porosity reduction.

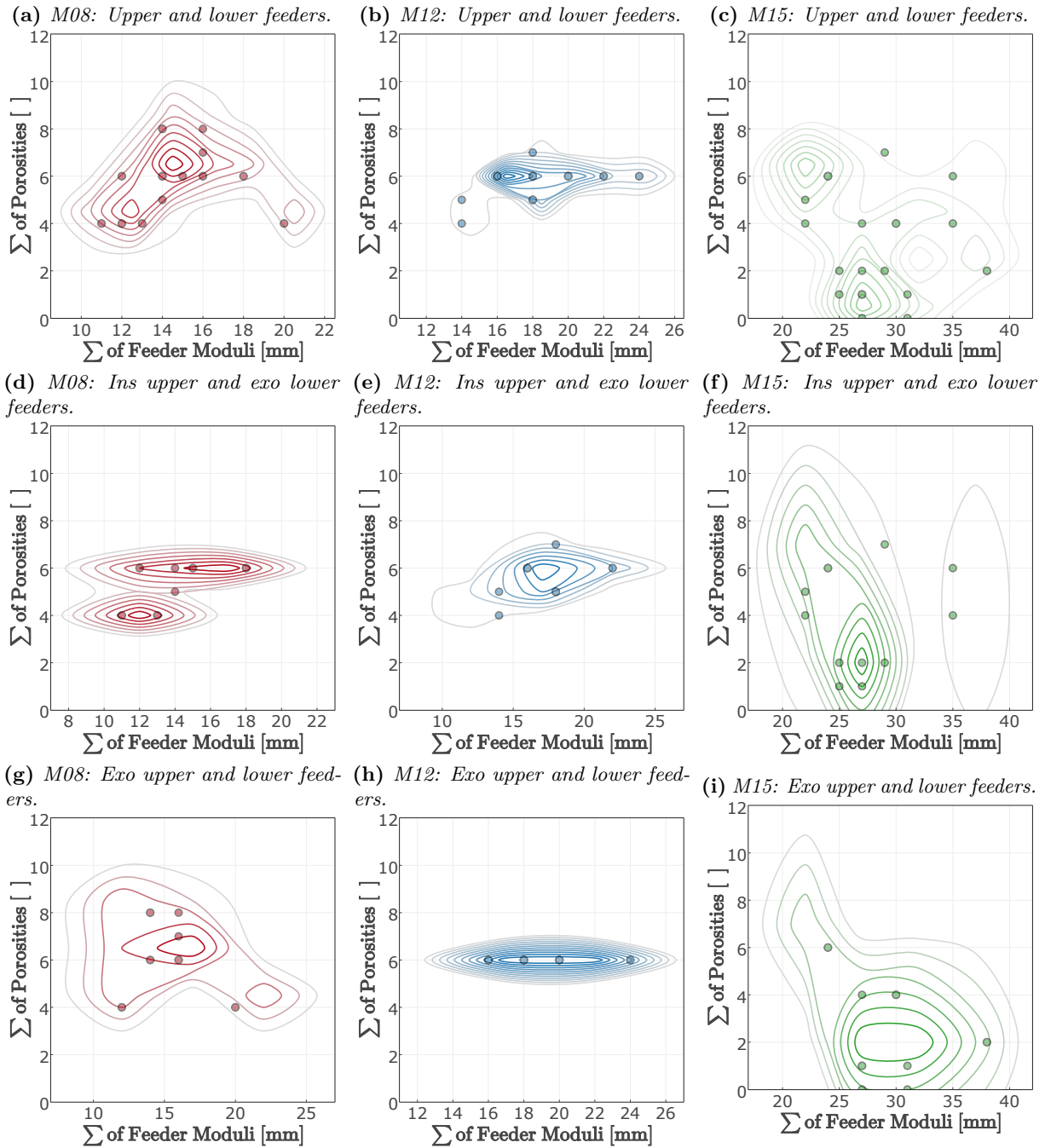


**Figure 12.11:** Upper and lower feeders together: Overview of the porosities size distribution based on feeder modulus for castings with both upper and lower feeder only. Exo = exothermic feeder sleeves, and ins = insulating feeder sleeves.

**Insulating Upper Feeder (12.11e)** In this case, the castings with the insulating upper feeder displayed the largest dispersion of results. The contour plot indicates a tendency towards larger porosities for larger sums of feeder moduli.

**Exothermic Upper Feeder (12.11h)** The group with exothermic upper and exothermic lower feeders was the most stable of all for the entire series. All 12 castings in the group had a large (4) porosity at



the top control volume and a small (2) porosity at the middle control volume. The feeders in this combination appear not to influence the number or size of porosities, positive or negative, found in the castings.

It could be argued that the absence of feeding relates to the scaling of the M12 casting and the analysed feeders. However, the insulating feeder with an even smaller modulus sum shows improved feeding, hence the proportionally smaller feeders cannot account for this feeding behaviour.

#### M15 (12.11c)

The large M15 castings behave markedly different than the M08 and M12 castings. The contour plot shows two concentrations of castings, but also a large population of dispersed castings. The castings the smallest feeders modulus sum are clustered together with porosity sums from four to six. The other cluster had the medium sum of feeder moduli ranging from 25 mm to 31 mm. The cluster showed castings that had a minimal porosity sum, and a few were even porosity-free. However, some of the feeder combinations also displayed great dispersion, eg group C16 which had casting 16A with a porosity sum of two, and casting 16B that had a porosity sum of 7. The castings with a large feeder modulus sum were more dispersed than their smaller counterparts. Group C13 that had a 16 mm insulating upper feeder and a 19 mm exothermic lower feeder had a porosity sum of four and six respectively. Group C19 that had a large 19 mm exothermic feeder as both upper and lower feeder displayed a small (2) porosity at the top control volume.

**Insulating Upper Feeder (12.11f)** Focusing on the group with insulating upper feeders and exothermic lower feeders, the contour plot shows a tendency towards larger feeders result in fewer porosities, albeit that group C13 with the 16 mm insulating upper feeder and a 19 mm exothermic lower feeder violate this trend.

**Exothermic Upper Feeder (12.11i)** The group with exothermic upper and exothermic lower feeders displayed the same trend as the insulating upper feeder, namely a correlation between larger feeder modulus sum and fewer porosities. As with group C13 for the insulating upper feeders, the largest feeder modulus sum showed a slightly larger porosity sum when compared with the best performing feeder combinations.

#### Modulus Comparison (12.11a-12.11c)

The small M08 castings were found to feed best for either small or large feeder combinations. The medium modulus sum feeders did not reduce the level of porosities below the amount found in the benchmark castings. The M12 castings were very stable with little dispersion among the results. This process stability may be explained by the different proportional feeder sizes used for this casting size. However, the only tendency observed was towards smaller feeders feeding better—and this was a limited effect. The M15 castings behaved very differently from the M08 and M12 castings. The best feeding performance was found for the medium feeder modulus sum, while the small and large feeder modulus sums had a less efficient performance. Additionally, the M15 castings showed a considerable dispersion of the results. Finally, the M15 castings also had a greater overall reduction in porosities when compared with M08 and M12 castings.

**Insulating Upper Feeder (12.11d-12.11f)** The M08 and M12 castings showed a little dispersion of the results, but generally with a trend of smaller feeder modulus sums resulting in fewer porosities in the castings. The M15 castings showed more dispersion but also the opposite tendency, namely that larger feeder modulus sum corresponds to fewer porosities.

**Exothermic Upper Feeder (12.11g-12.11i)** The M08 castings with exothermic upper feeders performed best with either small or large feeder modulus sums. However, the results are rather dispersed. The M12 castings were anything but dispersed. All 12 castings all had the same amount of porosities in the same control volumes. Finally, the M15 castings showed that some of the examined feeder combinations could produce sound porosity-free castings even though the experiment was designed to always produce porosities.

#### 12.2.4 Proportional Modulus Analysis

---

To further analyse the correlation between the different feeder combination and the proportional modulus of the feeders in relation to the castings on the size and location of the porosities, the data from table 12.1 on page 180 have been converted to proportional moduli and arranged according to upper and lower feeder modulus. See table 12.2.

**Table 12.2:** Overview of the ultrasound porosity analysis results, sorted according to upper and lower feeder modulus. The feeder moduli are shown proportional til casting modulus. # is the number of castings with the given feeder combination.  $\Sigma$  is the sum-average of porosity for all three control volumes.  $T$  is the average porosities in the top control volume,  $M$  is for the middle control volume, and  $B$  is for the bottom control volume.

(a) M08

Upper Feeder, $M^\infty$	#	M08				#	M08				#	M08				#	M08				
		$\Sigma$	T	M	B		$\Sigma$	T	M	B		$\Sigma$	T	M	B		$\Sigma$	T	M	B	
1.25	3	5.33	4.00	0.00	1.33	2	8.00	4.00	4.00	0.00	2	6.00	4.00	1.00	0.00	2	4.00	1.00	2.00	1.00	1.25
1.00	6	6.67	4.00	2.67	0.00	2	8.00	4.00	4.00	0.00	2	6.00	4.00	2.00	0.00	2	6.00	4.00	2.00	0.00	1.00
0.75	6	4.83	3.33	1.50	0.00	4	5.00	4.00	1.00	0.00	4	5.75	4.00	1.75	0.00	2	7.50	3.50	4.00	0.00	0.75
0.63	3	5.00	4.00	1.00	0.00	2	4.00	4.00	0.00	0.00	2	4.00	4.00	0.00	0.00	2	6.00	4.00	2.00	0.00	0.63
0.00	20	5.65	4.00	1.65	0.00	2	6.00	4.00	2.00	0.00	2	6.00	4.00	2.00	0.00	3	6.00	4.00	2.00	0.00	0.00
<b>0.00</b>					<b>0.75</b>					<b>1.00</b>					<b>1.25</b>						
Lower Feeder, $M^\infty$																					

(b) M12

Upper Feeder, $M^\infty$	#	M12				#	M12				#	M12				#	M12				
		$\Sigma$	T	M	B		$\Sigma$	T	M	B		$\Sigma$	T	M	B		$\Sigma$	T	M	B	
1.00	3	5.33	4.00	1.33	0.00	2	6.00	4.00	2.00	0.00	2	6.00	4.00	2.00	0.00	2	6.00	4.00	2.00	0.00	1.00
0.83	6	4.33	4.00	0.33	0.00	2	6.00	4.00	2.00	0.00	2	6.00	4.00	2.00	0.00	2	6.00	4.00	2.00	0.00	0.83
0.66	6	4.50	4.00	0.50	0.00	4	6.00	4.00	2.00	0.00	4	5.50	4.00	1.50	0.00	2	6.00	4.00	2.00	0.00	0.66
0.50	3	4.33	4.00	0.33	0.00	2	4.50	4.00	0.50	0.00	2	6.00	4.00	2.00	0.00	2	6.00	4.00	2.00	0.00	0.50
0.00	20	5.65	3.70	1.60	0.00	2	5.50	3.50	2.00	0.00	2	6.00	4.00	2.00	0.00	3	6.00	4.00	2.00	0.00	0.00
<b>0.00</b>					<b>0.66</b>					<b>0.83</b>					<b>1.00</b>						
Lower Feeder, $M^\infty$																					

(c) M15

Upper Feeder, $M^\infty$	#	M15				#	M15				#	M15				#	M15				
		$\Sigma$	T	M	B		$\Sigma$	T	M	B		$\Sigma$	T	M	B		$\Sigma$	T	M	B	
1.27	3	4.00	4.00	0.00	0.00	2	2.00	2.00	0.00	0.00	2	2.00	2.00	0.00	0.00	2	2.00	2.00	0.00	0.00	1.27
1.07	3	5.00	4.00	1.00	0.00	2	5.00	4.00	1.00	0.00	2	5.00	4.00	1.00	0.00	2	5.00	4.00	1.00	0.00	1.07
1.00	3	5.33	2.67	2.67	0.00	2	0.50	0.50	0.00	0.00	2	4.00	4.00	0.00	0.00	2	4.00	4.00	0.00	0.00	1.00
0.80	6	4.50	4.00	0.50	0.00	4	6.00	4.00	2.00	0.00	4	2.00	0.25	1.75	0.00	2	0.50	0.00	0.50	0.00	0.80
0.60	3	4.67	4.00	0.67	0.00	2	4.50	4.00	0.50	0.00	2	1.50	0.00	1.50	0.00	2	4.50	2.00	2.50	0.00	0.60
0.00	20	5.15	3.95	1.20	0.00	2	5.00	4.00	1.00	0.00	2	2.00	0.00	2.00	0.00	3	9.33	2.67	3.33	3.33	0.00
<b>0.00</b>					<b>0.80</b>					<b>1.00</b>					<b>1.27</b>						
Lower Feeder, $M^\infty$																					

**Table 12.3:** Conversion table for  $M^\infty$ .

M08		M12		M15	
$M_t$ [mm]	$M^\infty$	$M_t$ [mm]	$M^\infty$	$M_t$ [mm]	$M^\infty$
0.00	0.00	0.00	0.00	0.00	0.00
5.00	0.63	6.00	0.50	10.00	0.60
6.00	0.75				
8.00	1.00	8.00	0.66	12.00	0.80
		10.00	0.83	15.00	1.00
				16.00	1.07
10.00	1.25	12.00	1.00		
				19.00	1.27
<i>Italic = Ins</i>		<b>Bold = Exo</b>		<b><i>Bold-Italic = Both</i></b>	

The modulus of all the feeders have been converted to a proportional modulus,  $M^\infty$ .

$$M^\infty = \frac{M_f}{M_c} \quad (12.1)$$

where  $M^\infty$  is the proportional ratio between the modulus of the feeder,  $M_f$ , and the modulus of the casting,  $M_c$ .

The data for each of the three casting sizes have been arranged into separate subtables. Each of the three subtables comprises four subsequent subtables, each representing a proportional modulus for the lower feeder. Vertically in each of these sub-subtables are listed the average amount of porosities recorded for each of the castings with identical feeder combination, for each of the three control volumes, based on the corresponding proportional modulus of the upper feeder. The #-column shows the number of castings in the feeder combination group, and the  $\Sigma$ -column shows the sum of the porosities of the three control volumes. The data from table 12.2 are plotted in fig. 12.12 on the facing page. A conversion table can be found in table 12.3.

Analysing the bubble chart in fig. 12.12 on the facing page, it was found that the feeder combination does influence the number and size of the porosities in the castings. The bubble chart shows the average amount of porosities found for the different combinations. Likewise, the overlaid contour plot displays concentrations of porosities, thus indicating

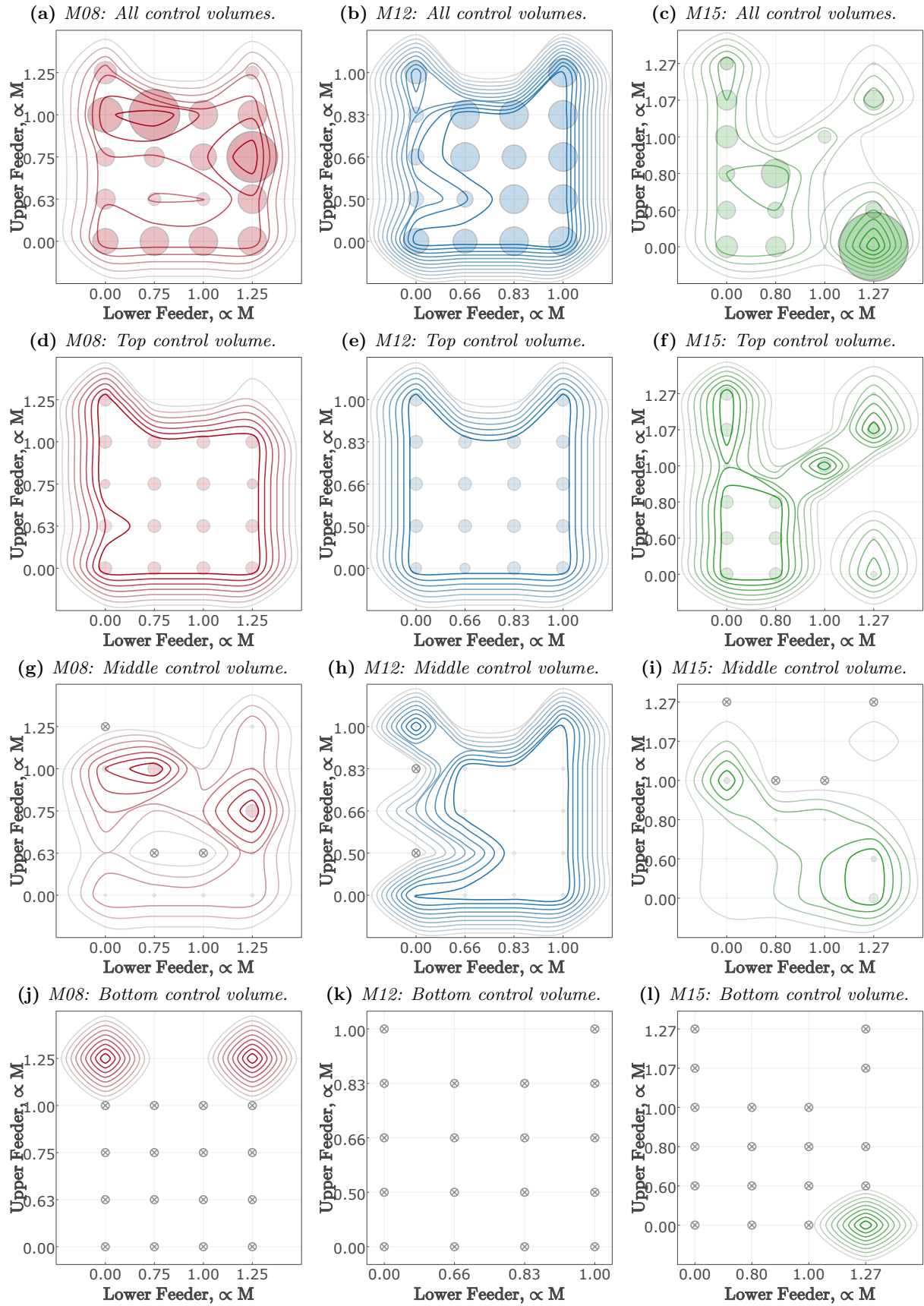


**Figure 12.12:** Overview of the porosity distribution and size as a function of the proportional moduli for the upper and lower feeders. The proportional modulus was found by dividing the feeder modulus with the modulus of the casting. Bubble size indicates porosity size—larger bubble = larger porosity. Fig. a-c shows porosities for the entire casting, while fig. d-f shows porosities for the top control volume only, fig. g-i shows porosities for the middle control volume only, and fig. j-l shows porosities for the bottom control volume only. Bubble sizes are not directly comparable between fig. a-c and fig. d-l.  $\otimes$  indicates combinations where no porosities were found.

trends in the feeding pattern. Note that insulating and exothermic feeders are not distinguished in the plot.

#### M08 (12.12a)

The plot shows two combinations that had a large number and size of porosities, as well as three combinations that had a low amount of porosities. However, the distribution of the porosities regarding the feeder combinations indicates that at least two different feeding mechanisms can be applied.

The  $0.63 M^\infty$  upper feeder combined with either the  $0.75 M^\infty$  or the  $1.00 M^\infty$  lower feeder yielded castings without porosities at the middle control volume. The same upper feeder with no lower feeder had a microporosity (1) at the middle control volume, while the combination with a large  $1.25 M^\infty$  lower feeder had small (2) porosities at the middle control volume. When the upper feeder was replaced by the slightly larger  $0.75 M^\infty$ , the result was large (4) porosities at the middle volume. Hence, the difference between feeding the middle control volume and increasing the porosities at the same control volume was minimal. Additionally, increasing the upper feeder from  $0.63 M^\infty$  to  $1.00 M^\infty$  with the same  $0.75 M^\infty$  lower feeder also changed the results from a porosity-free middle control volume to a control volume with a large (4) porosity.

The last feeder combination that resulted in a marked reduction of porosities was the one with two large feeders of  $1.25 M^\infty$  for both the upper and lower feeder. In this case, the porosity distribution was different, with a microporosity (1) at the top control volume, a small (2) porosity at the middle control volume, and a microporosity (1) at the bottom control volume.

The results show that two different feeding patterns can occur and that the two different approaches yield different porosity distributions as a consequence. Additionally, the plot also shows the marginal boundary between successful feeding and very unsuccessful feeding.

**Top Control Volume (12.12d)** The top control volume of the M08 castings had large (4) porosities for almost all of the castings. The  $0.75 M^\infty$  upper feeder with no lower feeder showed a small decrease of the average porosities. This reduction was caused by casting 5C in which no porosities were found in the top control volume; instead, it showed a medium (3) porosity at the middle control

volume. The two other castings in group C5 did not display this behaviour.

However, the feeder combination with the two large feeders displayed a top control volume with one casting, 19A, porosity-free at the top control volume, while casting 19B had a small (2) porosity in this volume.

**Middle Control Volume (12.12g)** The middle control volume displays the main difference between the castings. Two castings have large (4) porosities in this volume, which was also shown in the combined plot 12.12a. Note that the large upper feeder,  $1.25 M^\infty$  with no lower feeder was porosity-free in this volume.

**Bottom Control Volume (12.12j)** The bottom control volumes were porosity-free for all combinations except two. To illustrate the complexity of the feeding mechanisms the common denominator between the two castings with porosities at the bottom control volume, was that they had large  $1.25 M^\infty$  upper feeders. Hence, the feeder influence the solidification and porosity formation across the entire volume of the casting.

#### M12 (12.12b)

The M12 castings showed little variance between the different feeder combinations, which is also displayed at the plot for all three control volumes. A few combinations indicated reduced porosities. These were primarily castings without the lower feeder, as both the  $0.50 M^\infty$ ,  $0.66 M^\infty$ ,  $0.83 M^\infty$ , and  $1.00 M^\infty$  feeder ratios showed reduced porosities. The least effective of the four was the largest,  $1.00 M^\infty$ , which had only a small reduction in porosities. Additionally, the combination of a small  $0.50 M^\infty$  upper feeder and a small  $0.66 M^\infty$  lower feeder also yielded a reduction in porosities.

**Top Control Volume (12.12e)** The top control volume had very little variation. Castings 03B and 8A had respectively a small (2) and a medium (3) porosity in this control volume. All other of the 69 M12 castings had large (4) porosities in this control volume. The slight influence on the porosity average can be found in table 12.2b on page 194, however, it is not visible on the contour plot due to the averaging of the rounding of the data for making the contour plot.

**Middle Control Volume (12.12h)** The middle control volume displayed the main difference between the feeder combinations. Castings with a lower feeder of  $0.83 M^\infty$  or  $1.00 M^\infty$  had small (2) porosities at this control volume. The only exception was casting group C12 which had only microporosities (1) in this control volume. A small feeding effect was achieved with the  $0.50 M^\infty$  upper and the  $0.66 M^\infty$  lower feeder. Besides this, none of the feeder combinations with a lower feeder succeeded in feeding the middle control volume of the casting.

The castings with only an upper feeder were porosity-free in most cases for the  $0.50 M^\infty$  and  $0.83 M^\infty$  feeders, while the  $0.66 M^\infty$  performed almost as good with casting 5B as the only casting that had a small (2) porosity in this volume. The castings with the largest upper feeder,  $1.00 M^\infty$ , produces almost as many porosities as the benchmark castings without feeders.

The results show that feeding the middle part of the M12 castings were best done without a lower feeder and that the smaller upper feeders performed markedly better than the largest version.

**Bottom Control Volume (12.12k)** In all cases, for all feeder combinations, no porosities were found in the bottom control volume.

#### M15 (12.12c)

The large M15 castings were the ones most affected by the different feeder combinations. For the M12 castings, it was observed that the best feeding results were with a small or no lower feeder. For the M15 castings, the best feeding results were observed for the castings with large lower feeders of  $1.00 M^\infty$  or  $1.27 M^\infty$ , albeit the smaller  $0.80 M^\infty$  also provided one very effective and efficient combination.

The  $1.00 M^\infty$  upper feeder together with the  $0.80 M^\infty$  lower feeder yielded one porosity-free casting, 20B, and one with only a microporosity (1) at the top control volume, casting 20A. The upper feeders for this combination were exothermic. The same feeder combination with the one size smaller upper feeder of  $0.80 M^\infty$  yielded a porosity sum of six for the exothermic upper feeder, while the insulating upper feeders with the same modulus only had small (2) and microporosities (1) at the middle control volume. Thus, the boundary between successful feeding and poor feeding was narrow. Additionally, the same performance difference can be contributed to the differences in sleeve material, as the same modulus feeders yield very different feeding results.

The feeder combinations with a proportional modulus of  $1.00 M^\infty$  had a low porosity sum overall. The combinations either without an upper feeder, or with an upper feeder of  $0.60 M^\infty$  or  $0.80 M^\infty$  on average had small (2) porosities at the middle control volume, and no porosities at the top or bottom. In the case with no upper feeder, the feeding effect in the top control volume can only be contributed to the lower feeder. As previously seen, the boundaries between successful and unsuccessful feeding were very narrow. While the three aforementioned feeder combinations yielded no porosities at the top control volume, but small (2) porosities at the middle volume, the combination with a more extensive  $1.00 M^\infty$  upper feeder resulted in large (4) porosities at the top, but no porosities at the middle volume.

The castings with the largest lower feeder,  $1.27 M^\infty$ , yield anything but linear results. The castings without an upper feeder that performed very well with the slightly smaller  $1.00 M^\infty$  lower feeder, yield a porosity average of 9.33. See table 12.2c on page 194. Note that the largest possible score is 12 when the average of all three control volumes indicate large (4) porosities. This maximum score was the case for castings 10B and 10C, which was previously assessed to be caused by inclusions, as described in section 12.1.4, on page 181. Adding an upper feeder of  $0.60 M^\infty$  reduces the porosity sum below that of the benchmark castings, and an upper feeder of  $0.80 M^\infty$  was almost porosity-free. Casting 22A had a microporosity (1) at the middle control volume while casting 22B was completely free of porosities.

Increasing the proportional modulus of the upper feeder even further to  $1.07 M^\infty$  then again results in increased porosities. In this case with microporosities (1) at the middle control volume, but also with large (4) porosities at the top control volume. Increasing the proportional modulus of the upper feeder even further to  $1.27 M^\infty$  then again reduced the porosities to a porosity-free middle control volume and only small (2) porosities at the top control volume.

Again, as previously mentioned, two different feeding mechanisms seem to influence the castings changing the feeding pattern and the location of the porosities.

**Top Control Volume (12.12f)** Analysing the top control volume, it was found that the  $1.00 M^\infty$  up-

per feeder with no lower feeder, performed slightly better than the casting with only an upper feeder. Additionally, the same proportional modulus upper feeder,  $1.00 M^\infty$  with a small  $0.80 M^\infty$  lower feeder, resulted in an almost porosity-free top control volume.

The feeder combinations with the  $1.00 M^\infty$  lower feeder yielded few porosities for the top control volume except for the  $1.00 M^\infty$  upper feeder that performed very well for the smaller modulus versions of, the lower feeder. Additionally, the upper feeder of  $1.00 M^\infty$  then again yields very few porosities for the top control volume when the lower feeder was upgraded to the  $1.27 M^\infty$ . Equally good results were recorded for the large lower feeder in combination with the upper feeder of  $0.80 M^\infty$ , while the combinations without an upper feeder, or with the smallest upper feeder,  $0.60 M^\infty$  yielded some porosities.

**Middle Control Volume (12.12i)** The M15 castings showed few porosities at the middle control volume. The four combination with the largest upper feeders were all porosity-free. Note that this was the  $1.27 M^\infty$  upper feeder for the combinations without a lower feeder, and with the largest lower feeder,  $1.27 M^\infty$ . The two other porosity-free combinations, the  $0.80 M^\infty$  and  $1.00 M^\infty$  lower feeders, both had the  $1.00 M^\infty$  upper feeder. Additionally, both the castings without a lower feeder and the castings with the large  $1.27 M^\infty$  lower feeders showed micro-porosities (1) for the middle volume for the  $1.07 M^\infty$  upper feeder. However, the combination without a lower feeder and the  $1.00 M^\infty$  upper feeder had medium (3) porosities on average. Note that the  $1.07 M^\infty$  feeders were insulating while the  $1.00 M^\infty$  feeders were exothermic.

**Bottom Control Volume (12.12l)** All casting combinations were porosity-free for the bottom control volume, except the large  $1.27 M^\infty$  lower feeder without an upper feeder. This combination yielded two castings with large (4) porosities and one with small (2) porosities at this control volume.

#### Modulus Comparison (12.12)

To investigate the feeding mechanisms in the three different size (modulus) test castings, the data from the scatter plots in section 12.2.3, on page 193 was combined into the bubble charts in fig. 12.12

on page 195. It was observed that the three castings did not show the same feeding pattern. The small M08 castings were influenced by the feeders, but also revealed that two different feeding mechanisms seem to influence the porosity formation, resulting in complex non-linear patterns for optimal feeder combinations. The medium M12 castings were stable in their performance, which also meant that most feeder combinations had little effect on the number and size of porosities found in the castings. The absence of feeding effect may be related to the different proportionality of the M12 feeders. The combinations that did work, however, was the combinations without a lower feeder. The large M15 castings were more responsive to the to the feeder, and overall the porosity reduction was better for the large castings than for the smaller ones. Even for relatively smaller modulus feeders.

**Control Volume Porosity Distribution** The M08 and M12 castings had large (4) porosities for almost all casting for the top control volume. For these two casting sizes, the examined feeder sizes did no yield a suitable feeding solution for this control volume. The large M15 Castings performed markedly different than the scaled down versions. Several combinations yielded single castings that were porosity-free at the top control volume and other combinations that resulted in reduced porosities as well.

All three casting sizes had feeder combinations that resulted in porosity-free middle control volumes. However, of the nine combinations that resulted in a porosity-free casting at the middle part, only two are the same combination of more than one casting size. This feeder combination was the large  $1.25/1.27 M^\infty$  upper feeder with no lower feeder for the M08 and M15 castings. This correlation suggests a feeding mechanism that functions across the different modulus castings. The combination with a large upper feeder and no lower feeder for the M12 castings did yield fewer porosities than average, though it was not porosity-free. However, the largest of the M12 feeders was only  $1.00 M^\infty$ ; thus a more substantial  $1.20 M^\infty$  feeder might have yielded a result comparable to the porosity-free middle control volumes observed for the M08 and M15 castings.

Additionally, the dispersion of the successful feeder combinations indicates that different feeding mechanisms take place for the different casting sizes. This variation in feeding mechanisms is supported by the proportional modulus feeders being

**Table 12.4:** Overview of the castings that had atmospheric punctures at the pre-feeder neck. The castings are grouped according to different feeder criteria and the percentage of castings with atmospheric puncture is given. **Groups** refer to the group numbers listed in table 12.1 on page 180, **#C** lists the total number of castings in the group per modulus group, **#P** lists the number of castings with an atmospheric puncture for the same group.

	Groups	#C	M08		M12		M15		All	
			#P	%	#P	%	#P	%	#P	%
<b>All</b>	0-22	69	46	67 %	42	61 %	0	0 %	88	43 %
<b>No feeders</b>	0-03	20	18	90 %	9	45 %	0	0 %	27	45 %
<b>With feeders</b>	2-22	49	28	57 %	33	67 %	0	0 %	61	41 %
<b>With upper feeder</b>	2-7, 11-22	42	21	50 %	27	64 %	0	0 %	48	38 %
- Insulating	2-4, 11-16	21	19	90 %	14	67 %	0	0 %	33	52 %
- Exothermal	5-7, 17-22	21	2	10 %	13	62 %	0	0 %	15	24 %
<b>Without upper feeder</b>	8-10	7	7	100 %	6	86 %	0	0 %	13	62 %

able to successfully feed castings with an identical modulus for the M08 and M15 castings.

It was observed that only the M08 and M15 size casting had feeder combinations that resulted in porosities for the bottom control volume. Additionally, it should be noted that the large 1.25/1.27 M<sup>∞</sup> feeders were a common denominator for these feeder combinations. Thus, a large 1.2x M<sup>∞</sup> upper or lower feeder might have entailed similar results for the M12 castings.

**Proportional Feeder Effects** Figure 12.12 on page 195 illustrate that the feeding of different modulus castings does not scale linearly. Additionally, it was also observed that while different combinations of upper and lower feeders do function, the feeders do not perform similarly if located at the upper position, as compared with the lower position.

As stated above, the non-linearity in the observed amount of porosities in combination with the different feeders, suggest that at least two different feeding mechanisms occur for the examined feeder combinations. In a few cases, good results were obtained with a feeder module larger than the module of the casting. However, especially for the M15 castings, it was shown that large feeders could in individual cases drastically increase the number and size of the porosities.

The other mechanism was found to yield the best results for a feeder that was smaller or equal to the modulus of the casting being fed. Per definition, these feeders should solidify before, or at the same time as, the last to freeze melt of the casting. Hence, the feeding paths should be closed at this point. Nonetheless, these proportionally smaller feeders influence the feeding efficiency of the castings.

### Sub Conclusion

Viewing fig. 12.12 on page 195 and the subsequent porosity distribution analysis it can be concluded that the top control volume is hardest of the three volumes to keep feed, but also yield comparable results for all three casting moduli. The middle control volume also yields porosities, though, the smaller moduli castings show more porosities than the large M15 castings. The bottom can be feed for all casting sizes.

This effect is not surprising as it is almost inherent in the chosen casting design; however, the analysis also shows that the larger M15 castings better fed at the centre control volume, and partially also at the top control volume, as compared to the smaller modulus castings.

### 12.2.5 Puncture at the Pre-Feeder Neck

As mentioned in section 12.1.1, on page 179, atmospheric punctures were observed for some of the castings during the ultrasound inspection. While no correlation between the atmospheric punctures and the number and size of porosities could be established, a further analysis did reveal some correlation between casting modulus and the choice of feeders, and the subsequent likelihood of atmospheric punctures. See table 12.4.

Of the 207 castings 43 % had the atmospheric puncture. However, none of the large castings, M15, had punctures. Of the medium sizes casting, M12, 61 % had a puncture, and for the smallest castings, M08, 67 % had a puncture.

While the M08 and M12 castings had roughly the same amount of castings with an atmospheric

puncture, the distribution of punctures between the two casting sizes was different. Of the 20 benchmark castings without feeders, 90 % of the M08 castings had an atmospheric puncture at the neck region. For the M12 castings, this number was only 45 %. However, it was found that for the castings that had a lower feeder, but no upper feeder, the percentages were 100 % for the M08 castings and 86 % for the M12 castings. Thus, the presence of a lower feeder, without an upper feeder, substantially increases the risk of an atmospheric puncture.

An analysis of the castings with upper feeders, both with and without a lower feeder, showed that presence of an upper feeder reduced the likelihood of a puncture from 90 % to 50 % for the small M08 castings. Thus, the analysis showed that the upper feeders could successfully change the heat distribution inside the casting to reduce the risk of punctures for the M08 castings, albeit the same analysis also showed that the upper feeders increased the risk of the punctures from 45 % to 64 %. Hence, the solidification pattern, heat distribution, and shell-forming of the two casting sizes progress differently.

Finally, a separation of the insulating and the exothermic upper feeder showed that significantly different performance for the M08 casting, while the influence on the M12 castings was marginal. 90 % of the M08 castings with insulating feeder had atmospheric punctures, while only 10 % of the M08 castings with exothermic upper feeders had this problem. For the M12 casting, the insulating upper feeders resulted in 67 % punctures, and the exothermic upper feeder yielded a similar 62 %. This correlation may be related to the overall proportionally of smaller feeders used for the M12 castings.

Hence, only the two smallest casting sizes had atmospheric punctures, but where the M08 castings were greatly influenced by both upper and lower feeders, the larger M12 castings were only significantly influenced by the lower feeder, while the presence of the upper feeder only had a small influence on the risk of punctures.

### 12.2.6 X-Ray Results Analysis

The ultrasound analysis was the most accurate method for estimating the size of the porosities available. The ultrasound analysis can detect smaller porosities than *eg* can be identified with x-ray imaging, and the sectioning of the castings yield no guarantee that the sectioning will reveal exactly the sought after porosities.

The radiation is emitted from the source, passes through the sample which absorbs some of the radiation, and the remaining radiation is then detected by a detector which turns the signal into a grey scale image. Cast iron is an excellent radiation absorbent, hence the more of the casting the radiation has to pass through, the darker the image. Thus, porosities appear lighter than the surrounding casting. However, the same phenomenon also applies to less massive casting sections and even the edges of the castings tend to brighten and become diffuse at increased radiation intensities due to diffraction of the x-rays. For this reason, it is difficult to capture large and small sections within the same image. To obtain detailed images of different modulus sections, they must be captured in multiple images with different exposures. Another effect of this absorption-contrast imaging is that only porosities of a certain size, relative to surrounding casting, will be visible in the image.

On the other hand, x-ray imaging also has some advantages compared with the ultrasound analysis. The x-ray imaging can be used for any geometry, with the above-mentioned limitations. Hence, the pre-feeder, the pre-feeder neck, and the feeders could be imaged and analysed.

#### Pre-Feeder Shrinkage

The pre-feeders were designed to handle the liquid shrinkage of the melt and then close off as the solidification of the bulk of the casting began, as described in section 11.1.2, on page 161. Thus, the initial liquid shrinkage of the entire castings should be subtracted from the pre-feeder volume, as well as the solidification shrinkage of the pre-feeder itself.

Analysing the x-ray images of the pre-feeders in fig. 12.13 on the next page the porosities are visible for the large M15 castings. A little variation can be found among the M15 pre-feeders, however no more than what was expected. No correlation was observed between the amount of shrinkage in the pre-feeders and the recorded porosities in the castings.

For the M12 castings, the pre-feeders displayed a similar amount of shrinkage, albeit the shrinkage in some cases were located more in the pre-feeder neck than in the pre-feeder itself. This can be seen in fig. 12.13 on the facing page (a,b,e,g). Figure 12.13 on the next page (c,d) show shrinkage in the pre-feeder, though the shrinkage in (c) is only slightly visible due to the contrast of the image. Note



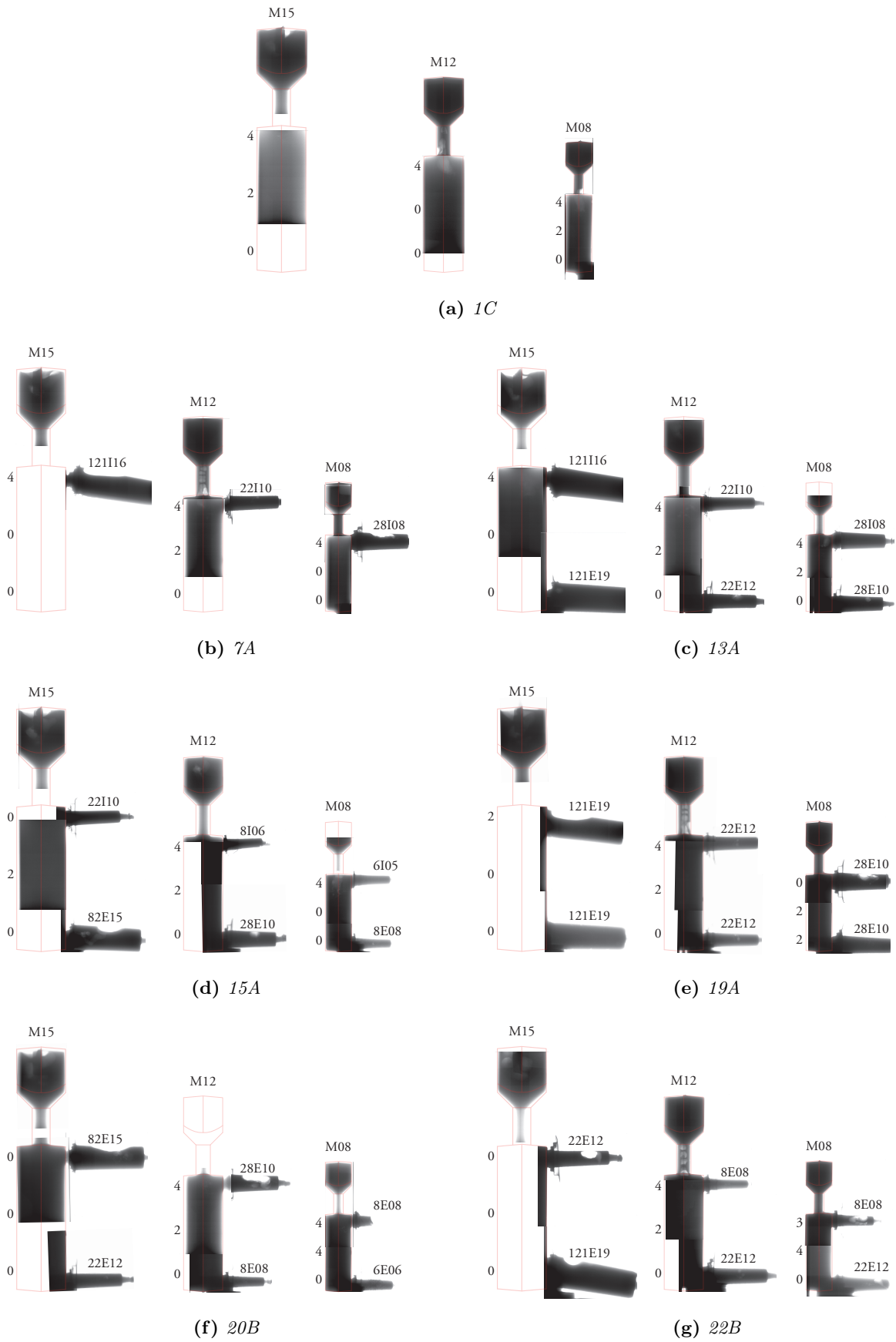


**Figure 12.13:** X-ray images of the select castings stitched together to provide context and overview. The casting modulus is shown at the top of each casting. The systematic name of each feeder is shown above it—volume, material, and modulus. The porosities sizes for each control volume, as recorded by the ultrasound analysis, is shown at the left of the castings.

that the difference between the location of the porosities in the pre-feeder and pre-feeder neck does not appear to yield any influence with regards to the recorded amount of porosities in the castings.

The pre-feeders and the pre-feeder necks of the M08 castings, on the other hand, did not yield a significant amount of shrinkage or porosities.

It could be argued that the upper feeders particularly, but in part also the lower feeders, prolong the closing time of the pre-feeder neck via the additional heat added to the casting. However, the simulation of the castings with feeders, upper and lower, suggests that the pre-feeder necks solidify shortly before the eutectic temperature was reached in the centre of the castings. Analysing the M12 castings and upper feeders in fig. 12.13 on page 201, no correlation was found between the upper feeder modulus and the location of the shrinkage in the pre-feeder neck. For instance fig. 12.13g on page 201 have an upper modulus of 8 mm feeder for the M12 castings and produces significant shrinkage in the pre-feeder neck, while the M12 castings in fig. 12.13c on page 201 was equipped with a more extensive 10 mm upper feeder and had no shrinkage at the pre-feeder neck.

The numerical fraction liquid analysis of the castings showed that the feeder does influence the solidification of the pre-feeder neck and that this might explain the pre-feeder neck shrinkage. See section 12.3.4, on page 212.

### Feeder Performance

The feeders themselves displayed two types of shrinkage: open shrinkage and internal porosities. The open shrinkage was characterised as shrinkage with an atmospheric puncture. These could be identified by the naked eye, albeit the true size of the shrinkage volume was only discovered when x-raying the feeder. The internal porosities were completely hidden from the outside and were only discovered via the x-ray analysis.

The direct performance of the individual feeders was challenging to access based on the shrinkage visible in the x-ray images in fig. 12.13 on page 201. Some feeders showed significant shrinkage, as the upper feeder of the M12 casting in 12.13f, without an apparent influence on the number and size of porosities recorded for the casting. Other feeders showed little, if any shrinkage, eg the upper and lower feeder of M15 in 12.13c while managing to feed part of the casting.

Regarding the question of the horizontal feeders being able to supply melt to the castings, the x-ray images show that many of the feeders, upper and lower, have succeeded in this respect. For example, the lower feeder of the M15 casting in 12.13d showed both sizeable open shrinkage and internal porosities. Hence, while gravity work against these feeders, rather than assisting the melt flow, as for standard feeders, other forces drive the melt from the feeders into the castings. The lower feeders had to overcome a more considerable ferrostatic pressure from the melt due to the lower position. However, no significant difference was observed between the amount of shrinkage found in the upper and the lower feeders.

## 12.3 Thermal Analysis

SHRINKAGE and porosity defects are, with the partial exception of inclusion related gas porosities, located near the last to freeze melt. Subsequently, thermal analysis of castings is a useful tool to identify the thermal behaviour of a casting, thus determining the progression of solidification for different sections. Additionally, the eutectic arrest is easily identified on a cooling curve and indicate the beginning and the end of solidifications.

Note that the melt will become increasingly more mushy as solidification progresses and that at some point, dependent on alloy composition and solidification conditions, the resistance of the mushy zone will surpass the driving forces attempting the feed melt through the zone. The end of feeding cannot be identified based on a cooling curve alone.

Nonetheless, a thermal analysis of the castings, the differences in modulus, and the influence of different feeder combinations is a valuable tool to understand the feeding behaviour recorded during the trials.

### 12.3.1 Numerical Simulations

The castings were simulated using a commercial numerical simulation software—MAGMASOFT 5.2 [69]. The material and process setup was adjusted and fine-tuned via several simulations on the benchmark casting without feeders. Subsequently, all simulations were individually set up to match their respective casting conditions as precisely as possible as described in chapter 11, on page 157, albeit the casting temperature was kept at 1380 °C for all simulations to ensure a simpler cause and

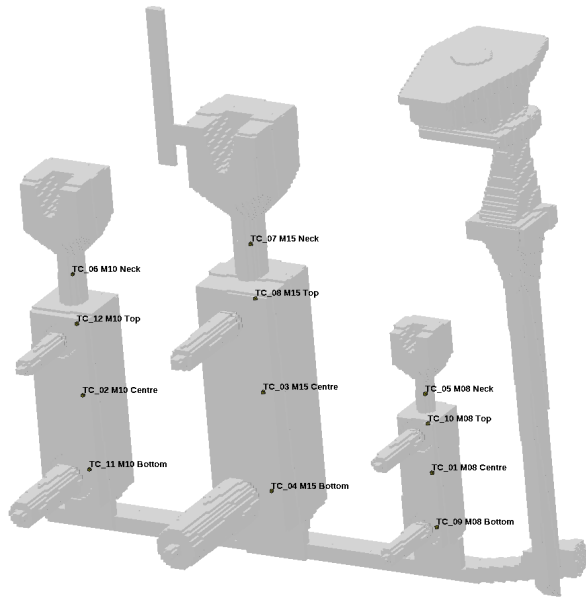


**Figure 12.14:** *Simulation mesh from MAGMASOFT showing thermocouple placement.*

effect analysis. The filling time was set at 6 s and was also kept constant despite the slight variation in volume between the combinations due to changes to the feeder setup.

### Geometry Modelling

The CAD-model for the simulations was based on the CAD-model developed in section 11.1.2, on page 161, as this CAD-model also made the basis for the manufacturing of the trial patterns. The gating system and the atmospheric vents were modelled based on technical drawings for the patterns.

The simulations used a 10 PPI Sedex ceramic foam filter from the FOSECO filter database in MAGMASOFT, albeit a different type of 10 PPI ceramic filter was used during the trials [118].

Note that the simulations of porosities to some extent deviated from this simulation setup, as described in section 12.4.1, on page 222.

**Mesh Generation** The meshes for all simulations, except one, was generated as an equidistant mesh cell of 2 mm without subdivisions. This size was assigned to all part of the mesh, including the mould. This approach resulted in meshes of approximately 21 million cells with approximately 320 000 cavity cells depending on the number and size of the feeders. See fig. 12.14.

The exception was a simulation without feeders that required a finer mesh division to provide sufficient spacing of the thermocouples. The virtual thermocouple simply logs the temperature of an assigned mesh cell. However, there can only exist one temperature per mesh cell; thus the measured temperatures become incremental. A finer mesh in itself does not change this, albeit it will decrease the increments. However, the mesh must have enough mesh cell to enable the thermocouples to be placed with a reasonable spacing. A too coarse mesh might result in thermocouples assigned to adjacent mesh cells resulting in an uneven thermocouple distance despite an accurate and equidistant placement within the geometry modelling. The worst-case scenario would be multiple thermocouples being assigned to the same mesh cell unintentionally.

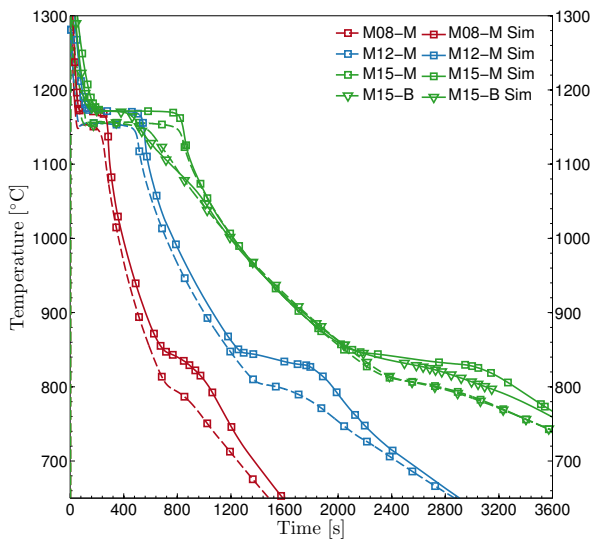
Thus, to ensure an equidistant placement of the virtual thermocouples a simulation was made with equidistant mesh cells of 1 mm, providing a total of 165 million cells and 2.5 million cavity cells. This division ensured 35 mesh cells across the width of the M08 casting. For 11 thermocouples spread across the width of the casting, this provided two or three mesh cell between each mesh cell assigned a thermocouple. The larger castings had more mesh cell; hence the M12 castings had four to five cells between each thermocouple cell, and for the M15 casting the numbers were five to six cells.

**Thermocouples** For all the regular simulations virtual thermocouples were placed at four locations in each of the three castings, M08, M12, and M15. See fig. 12.14.

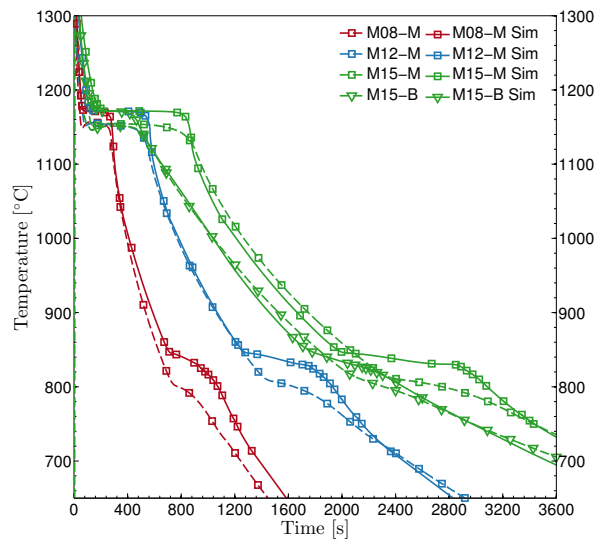
The particular simulation with the finer mesh had 11 thermocouples located equidistantly from edge to edge across the middle of the castings.

### Feeder Adaptation

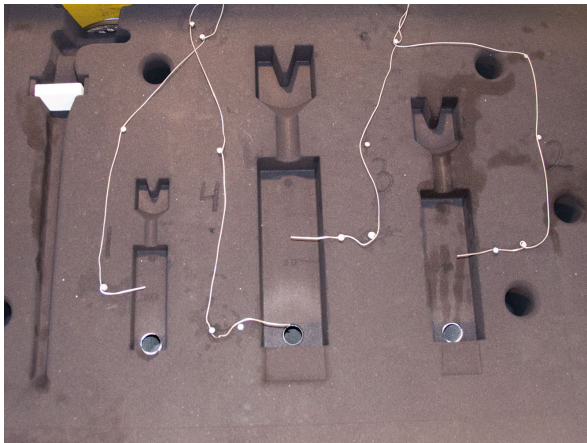
The feeders used during the trials were specially made for the experiment. The exothermic feeders, except the smallest one (6E06), are all stock products, though not as ram-up sleeves. The insulating feeders were prototype productions made with the same geometry as the corresponding exothermic feeders but with the insulating Kalminex material instead. In the simulations, the feeders have been used as they exist in the build-in FOSECO sleeve database, including the silica sand breaker cores [111]. The ram-up sleeves used in the trial had metal breaker cores.



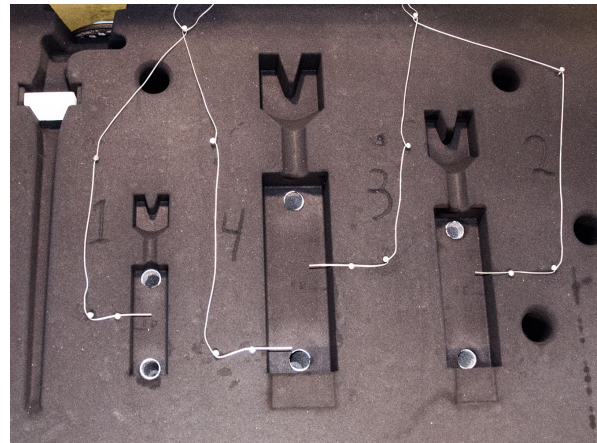
(a) 10A: Cooling Curves



(b) 17A: Cooling Curves



(c) 10A: Thermocouple Setup



(d) 17A: Thermocouple Setup

**Figure 12.15:** Comparison of the measured experimental cooling curves and the simulated cooling curves for the same feeder configuration.

#### Process Parameter Definitions

The general simulation setup and assumptions were the same as in section 5.2.1, on page 83. The significant changes in procedure are listed below.

**Material Definitions** All combinations were simulated using a custom material dataset calculated with JMatPro based on the average alloy composition in table 11.2 on page 167 [119].

**Melt Treatment** The graphite precipitation was set to 1 as this was the lowest possible setting. The simulations showed fewer porosities than was observed

in the ultrasound in section 12.1.1, on page 176 and x-ray analyses section 12.2.6, on page 200.

#### Experiment vs. Simulation

As described in section 11.4.1, on page 173 thermal measurements were made in four locations in two of the castings in the trial. These cooling curves present an opportunity compare simulated cooling curves with the measured cooling curves for the two different castings setups. See fig. 12.15.

The M08 castings are red, the M12 castings are blue, and the M15 castings are green. Solid lines

represent simulation data, while dashed represent measured data from the trials. The extra M15 curves represent the cooling at the bottom of the M15 casting next to the feeder.

The simulations and experimental data correspond very well. The measured cooling times for the three modulus castings, as well as at the bottom part of the M15 castings, were matched closely by the simulation. The only major differences were found at the temperature for the eutectic arrest, as well as at the austenite to ferrite phase transformation. Part of the shift in eutectic temperature can be explained by the algorithm used by MAGMASOFT. This algorithm is known to overestimate the eutectic temperature and has thus been updated for MAGMASOFT version 5.3 [79, 147]. The shift in the eutectic temperature was 8 °C for an alloy with 2.2% Si. The Si-content of the EN-GJS-500-14 used for the trials was measured to 3.81% just before the casting of the castings with the thermal measurements. As Si increases the eutectic temperature, as well as the eutectoid temperature, this difference in alloy composition might explain the differences observed in these areas of the cooling curves.

Similarly, the green sand water model in MAGMASOFT change from version 5.2 to 5.3 [147]. As with the eutectic temperature, the water model influences the cooling power of the green sand mould, thus affecting the cooling of the castings. The new water model increases the cooling power, resulting in lower temperatures. However, this does not change either the eutectic or the eutectoid transformation temperatures as these are alloy dependent.

Despite the differences in eutectic temperature between the measured data and the simulation data, the solidification times show minimal variation. The shift in eutectic temperature represents a minimal influence of the feeding of the castings, as the solidification time, in this respect, is the critical factor. Additionally, the measured cooling curves show a small undercooling at the initiation of solidification which is not matched by the simulated cooling curves. This difference should, however, not influence the feeding of the castings significantly. Thus, it is assessed that the simulation cooling curves are a good representation of the thermal conditions found in the trial castings.

### 12.3.2 Cooling Curve Analysis

As described in section 12.3.1, on page 204, six different feeder combinations were simulated. Four

cooling curves were recorded for each set of castings, with thermocouple locations in the model as shown in fig. 12.14 on page 203. The middle and bottom thermocouple locations correspond to those measured in production, as seen in section 11.4.1, on page 173. The cooling curves can be seen in fig. 12.16 on page 208. The six feeder combinations were; (C01) the benchmark castings without feeders, (C06) with 0.83/1.0 M<sup>∞</sup> upper feeders, (C07) with 1.00/1.25/1.27 M<sup>∞</sup> upper feeders, (C10) with 1.00/1.25/1.27 M<sup>∞</sup> lower feeders, (C17) with 0.66/0.75/0.80 M<sup>∞</sup> upper and lower feeders, and (C19) with 1.00/1.25/1.27 M<sup>∞</sup> upper and lower feeders.

#### Pre-Feeder Neck

The casting and pre-feeder were designed with the intent that the pre-feeder neck should be at least 95% solidified when the thermal centre (middle) of the casting reached the eutectic temperature. The lines marked with \* are the cooling curves at the thermal centre of the pre-feeder neck, while the lines marked with □ are the cooling curves at the thermal centre of the casting itself. For all 18 feeder and casting modulus combinations the pre-feeder neck ends solidification before the solidification of the main casting commences. Thus, the pre-feeder has solved the primary objective of preventing feeding of the solidification shrinkage in the main part, as described in section 11.1.2, on page 161.

The following objective of the pre-feeder neck was to solidify and close off at a time as close as possible to the main casting reaching the eutectic temperature. The graphs show that the end of the eutectic arrest for the pre-feeder neck cooling curves is relatively close to the initiation of solidification of the main casting. Additionally, though the pre-feeder neck closes off before the central part of the casting is cooled wholly to the eutectic temperature, the graphs show that the remaining superheat for all 18 combinations is in the range of 10 °C to 20 °C—with the smallest superheat for the M08 castings and the largest for the M15 castings. These closing temperatures correspond with the temperatures for the main part predicted in fig. 11.7a on page 166 for the pouring temperature of 1380 °C.

The premature close-off of the pre-feeder neck, concerning the main part reaching the eutectic temperature, allow for some liquid shrinkage within the castings. However, the amount was significantly reduced from the pouring temperature of 1380 °C

to the range of 1180 °C to 1190 °C. Note that the simulation in fig. 12.16 on page 208 were all set up with a pouring temperature of 1380 °C and thus do not illustrate the effect of varying production conditions.

### Influence of Feeders

The cooling curves can be divided into three groups. The pre-feeder neck (\*) which cools fast, the middle volume of the casting (□) which cools slowly, and the top (△) and bottom (▽) volumes of the casting which have intermediate cooling rates. The variations of the cooling curves for the top and bottom volumes show the thermal influence of the different feeder combinations.

Viewing the pre-feeder neck cooling curves, the graphs show that thermal behaviour of the pre-feeder neck was almost unaffected by the different feeder combinations. A minute shift in the cooling of the superheated melt in the pre-feeder neck can be detected as the cooling curves reach the eutectic arrest. However, note that this difference was equalised at the end of solidification and that eg C19 with two large feeders subsequently cool faster at the pre-feeder neck compared to the feederless castings.

The benchmark castings without feeders (C01) show that the top of the casting cools a bit slower than the bottom. As the castings were bottom filled, the bottom would naturally be the warmer part; thus the increased temperature at the top must be related to the thermal influence of the pre-feeder.

Combinations C06 and C07 show that the application of an upper feeder increases the thermal potential of the top part of the castings. Likewise, the C10 combination with a large lower feeder increases the thermal potential of the bottom volume to match the level of the upper volume. Hence, the largest of the examined feeder approximate the thermal influence of the pre-feeder. The C17 feeder combination also shows that a feeder smaller than the modulus of the casting can significantly influence the thermal gradients of the casting, albeit the main difference was observed as a reduced cooling rate after ended solidification.

This effect corresponds well with the cooling curves shown in fig. 12.15a on page 204. Here the bottom volume of the M15 casting had a large feeder but still solidified significantly before the centre of the casting. However, the feeder continues to heat the bottom volume, thus enabling it to align with

the temperature at the centre of the casting. The same phenomenon is seen in fig. 12.16 on page 208 where the combinations with feeders decrease the cooling rate at the volumes where they are located.

As this thermal effect occurs after the end of solidification, this effect will of course not influence the feeding of the local volume. However, the changes in thermal gradients will influence the cooling and solidification of other sections of the castings, as also the middle volume was affected by the presence of feeder at the upper and lower volumes.

### Scalability of the Castings

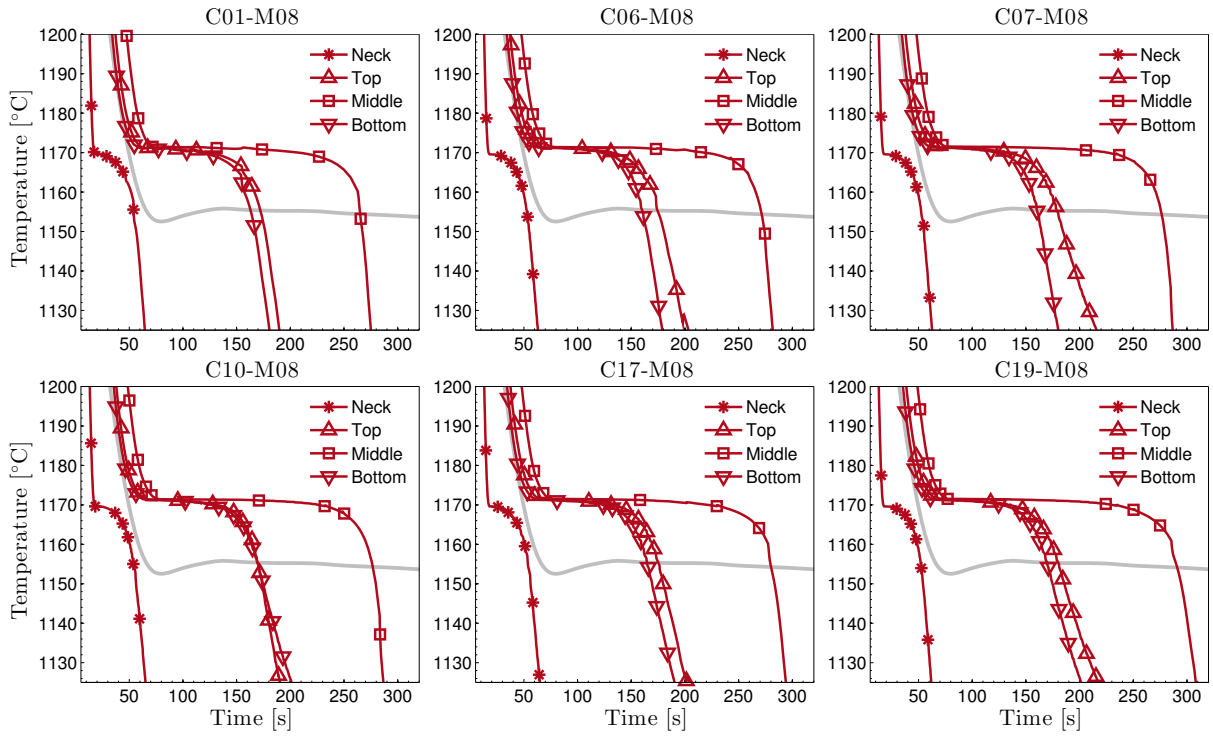
Viewing the cooling curves in fig. 12.16 on page 208 the similarities between the three different modulus castings are evident. The x-axes are scaled so that the M12 x-axis is approximately twice as long as the M08 x-axis, and the M15 x-axis is approximately three times as long as the M08 x-axis. Note the light grey cooling curve of the C10-M12 that is plotted as a reference on all the graphs.

Analysing the feeder combinations across the three modulus castings, M08, M12, and M15, the graphs show that the feeders influence the castings in a similar way for all three modulus castings. The changes to thermal gradients described in the previous section can be found for all three examined casting moduli; thus the proportional modulus feeders had a proportional influence on the thermal gradients of the castings, can be found.

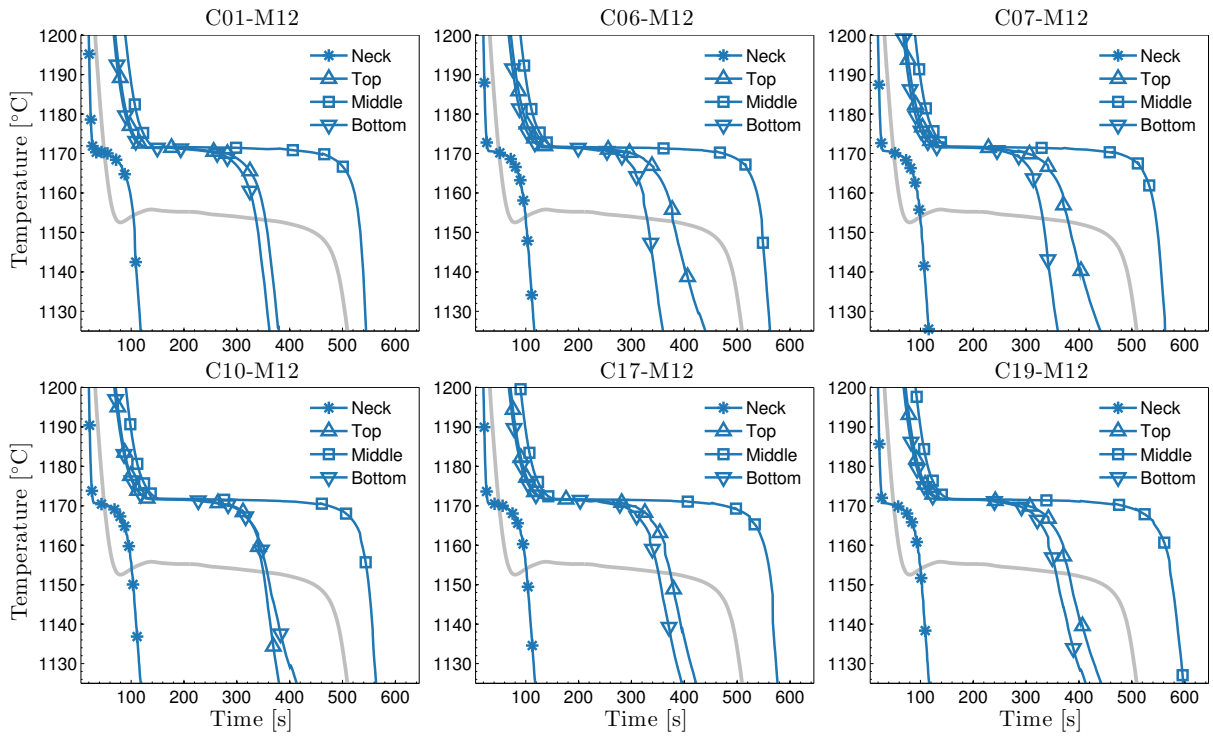
The cooling curves resemble a 1:2:3 pattern. This was matched by the cooling times calculated based on the casting moduli, which display the same direct correlation. Adapting eq. (2.4) on page 20 to a relation between the solidification time,  $t$ , and the modulus,  $M$ , of two different castings.

$$\frac{t_1}{t_2} = \frac{\mathcal{C} \times M_1^2}{\mathcal{C} \times M_2^2} \quad (12.2)$$

The mould-metal constant,  $\mathcal{C}$ , is reduced from the equation. The results of the moduli ratios and the corresponding cooling time ratios are shown in table 12.5 on page 208. The cooling times defined as the time in seconds of the first recorded temperature to be reached below 1170 °C for the numerical simulations, and the first recorded temperature below 1150 °C for the measured values. The difference between the two temperatures relates to the difference in the measured and the calculated eutectic temperature, as described in section 12.3.1, on page 204.

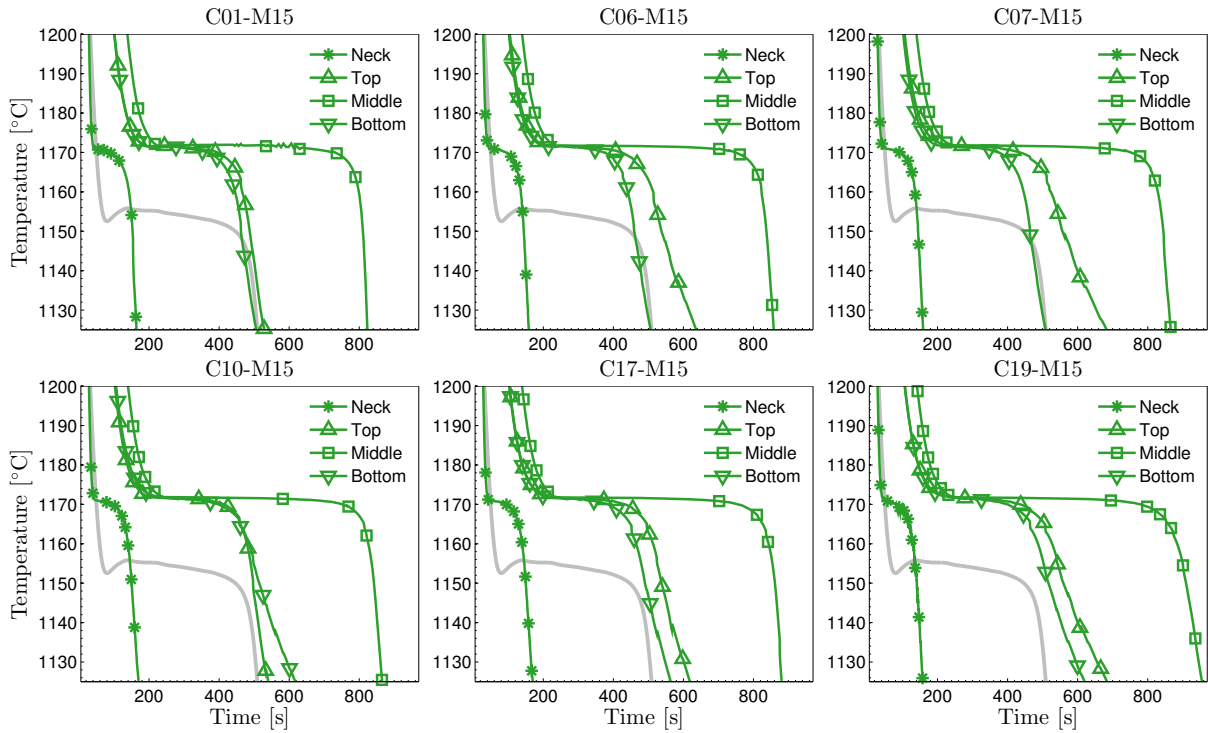


(a) M08: Simulation cooling curves.



(b) M12: Simulation cooling curves.

**Figure 12.16:** Comparison of the simulated cooling curves for six different feeder combinations. Each modulus, M08, M12, and M15, is shown in its own subfigure. For comparison, a reference cooling curves, C10A-M12, is shown in all plots as a light grey line.



(c) M15: Simulation cooling curves.

**Figure 12.16:** Comparison of the simulated cooling curves for six different feeder combinations. Each modulus, M08, M12, and M15, is shown in its own subfigure. For comparison, a reference cooling curves, C10A-M12, is shown in all plots as a light grey line.

**Table 12.5:** Modulus Scaling Ratios: Theoretical and recorded via numerical simulations. Calculated based on eq. 12.2.

Modulus			C10A, Measured			C17A, Measured				
$M_1$ [mm]	$M_2$ [mm]	$M_1^2 : M_2^2$	$t_1$ [s]	$t_2$ [s]	$t_1^2 : t_2^2$	$t_1$ [s]	$t_2$ [s]	$t_1^2 : t_2^2$		
M08	8.01	1.00	M08	183	183	1.00	M08	253	253	1.00
M12	12.00	2.24	M12	448	183	2.45	M12	410	253	1.62
M15	15.00	3.51	M15	776	183	4.24	M15	682	253	2.70

C01, Sim.			C10, Sim.			C17, Sim.				
$t_1$ [s]	$t_2$ [s]	$t_1^2 : t_2^2$	$t_1$ [s]	$t_2$ [s]	$t_1^2 : t_2^2$	$t_1$ [s]	$t_2$ [s]	$t_1^2 : t_2^2$		
M08	211	1.00	M08	227	227	1.00	M08	223	223	1.00
M12	456	2.16	M12	476	227	2.10	M12	477	223	2.14
M15	731	3.46	M15	751	227	3.31	M15	757	223	3.39

Table 12.5 shows that the three modulus scale close to the 1:2:3 rule with a ratio of 1.00:2.24:3.51. The M12 to M15 ratio was 1:1.56, where the perfect ratio according to the 1:2:3 rule would be 1:1.50. The ratio for the simulated castings without feeders (C01), shows comparable results—1.00:2.16:3.46, with a 2:3-ratio of 1:1.60.

The deviation of the 2:3-ratio from the ideal 1:1.50 can be related to the cooling time of all three modulus castings. As the M08 casting is used as a benchmark, a change in its recorded cooling time would affect the ratio towards both the M12 and the M15 castings. Likewise, a change in the cooling time of either M12 or M15 would also directly



influence the 2:3-ratio. Hence, the ratio provides no information about the origin of the deviation, if indeed it was a deviation and not the actual ratio.

The simulated cooling times for the C10 and C17 castings also adhere to the 1:2:3 rule as C10 had the ratios 1.00:2.10:3.31, with a 2:3 ratio of 1:1.58. The C17 had the ratios of 1.00:2.14:3.39, with a 2:3-ratio of 1:1.59. Note that the presence of feeders prolongs the cooling times compared with the feederless C01 casting. However, the cooling times were not prolonged according to the 1:2:3 rule. Instead, the cooling times of all three modulus castings, M08, M12, and M15 alike, were prolonged by ~20 s. Thus, the resulting ratios were decreased according to the M08 benchmark, though the 2:3-ratios show that the overall scalability still adheres to the 1:2:3 rule.

The measured cooling times displayed a greater variation. The C10A castings had shorter cooling time for the M08 casting, but longer cooling times for the M12 and M15 castings. This changing cooling time resulted in ratios of 1.00:2.45:4.24, with a 2:3-ratio of 1:1.73. For the C17A castings, the cooling times were reversed. The M08 casting displayed a longer cooling time, and the M12 and M15 castings had shorter cooling times compared with the other castings. Consequently, the ratios were 1.00:1.62:2.70, with a 2:3-ratio of 1:1.66.

The cooling time ratios show that there was a higher variation among the measured castings, with significant changes in the ratios between C10A and C17A, compared with the more uniform simulations. However, the comparison of the 2:3-ratios shows that the measured ratios of 1:1.73 and 1:1.66 both were relatively close to the ideal 1:1.50 ratio. Note also that the module-ratio of 1:1.56, as well as the simulated ratios of 1:1.58, 1:1.59, and 1:1.60, were all above the ideal ratio. The differences can be related to differences between the performance of the feeder in the experiment and the simulations. However, a more thorough cooling curve analysis that identifies the end of solidification based on the derived cooling curves may yield better results. A small change in the cooling time for the small M08 casting has a significant impact on the ratios. A likely explanation could also be variations in the pouring temperature due to pauses caused by the setup of the experiment. This change in the pouring temperature of the melt can explain the rapid cooling of the M08 casting in the C10A combination, though it does not explain why the M12 and M15 casting experience longer solidification times, or why the effect is opposite for the C17A casting.

Differences in eutectic temperature between the measured and the simulated results can potentially be assigned to a range of different mechanisms and measurement errors, a few of which are mentioned above. For example, the thermocouple in itself can influence the cooling rate, reducing the temperature in the casting, and thus de facto measuring temperatures lower than what would have been without the presence of the thermocouple. This phenomenon was described by describing for thin-walled ductile cast iron by Pedersen and Tiedje [136], and correlated to the simulation data by the same authors [137]. Additionally, Vedel-Smith explained the influence of mesh cell size and thermocouple placement for the numerical simulations [92]. Another difference can be the idealised cooling and solidification observed for simulation cooling curves. Pedersen and Tiedje found that the measured curves showed initial eutectic undercooling, resulting in nucleation that controls and influence the subsequent solidification much more than was predicted by the model [136, 137]. This effect is seen in fig. 12.15 on page 204, where the simulated cooling curves experience a sharper end of solidification, compared with the gradual temperature drop measured at the end of solidification.

However, the size of even the smallest M08 casting should be large enough to negate the effects reported by Pedersen and Tiedje for thin-walled castings, as well as the mesh cell size influences reported by Vedel-Smith. It should also be noted that if the thermocouples had a significant cooling influence on the C10A-M08 casting, then the cooling times should be equally reduced for the C17A-M08 casting. This change to the cooling curve was not observed. A more likely scenario was that eutectic temperature was miscalculated. However, the calculation of the eutectic temperature based on the alloy composition shown that the solidification should occur close to the prediction arrived by the numerical simulation. Several different equations can be used to calculate the iron-graphite eutectic. The equation used here was derived by Heine [139].

$$\begin{aligned} T_{EG} &= 1153 + 4.865 \times W_{Si} \\ &= 1171.20 \text{ } ^\circ\text{C} \end{aligned} \quad (12.3)$$

where  $T_{EG}$  is the equilibrium iron-graphite eutectic temperature, and  $W_{Si}$  is the weight percent of Si. This calculation only takes into account the Si content, and all the other alloying elements also influence the eutectic temperature, though most of them

can be negated due to their limited effect. However, the calculated  $T_{EG}$  indicate that it may be the measured temperature that is wrong. The probability of this is reduced by the fact that the simulated and measured cooling curves do match very well for all other parts than the eutectic solidification, and that all eight thermocouples measured the low eutectic temperature. A calibration of the measurement equipment may provide further answers.

The variation in cooling times for the C10A and C17A castings may be related to processing variations. Not enough data was available to fully explain this difference. Keeping the limited amount of data in mind, it should, however, also be noted the 2:3-ratios for both castings were still reasonably close to the ratios found for the moduli comparison and simulated temperatures.

### 12.3.3 Thermal Gradients

The cooling curves presented in the previous section provide information about the solidification time and cooling rate for selected locations at the centre of the castings. However, the cooling rate from the mould wall towards the centreline of the castings also provide important information about how solidification of the melt progresses.

To provide an adequate description of the thermal gradient across the centre of the castings, a numerical simulation was set up using the fine mesh described in section 12.3.1, on page 203 and the virtual thermocouples described in section 12.3.1, on page 203. The resulting thermal gradients can be seen in fig. 12.17 on the next page.

#### Method

The gradients were plotted using the cooling curves recorded with MAGMASOFT. These were then extrapolated to ensure a uniform and arbitrary time step for all cooling curves. This step was necessary because the thermal data exported by MAGMASOFT do not have a mutual or linear time increment. The extrapolated functions were then plotted as a function of two parameters; cooling time in seconds and centreline distance in millimetres.

The plots are viewed as a time lapse of the thermal gradients. Hence, the topmost line is the first time step, the next is the second, and so forth. The time steps are indicated by the colour gradient, with the first step being full colour, and the subsequent lines fading towards light grey. The topmost and lowest gradient lines are spherical indicating the natural

thermal gradient across the casting. At the eutectic temperature, the lines flatten out across the centre due to the latent heat released during solidification.

As the thermal gradient is steepest nearest the surface of the casting, in the solidified layer, the edges of the casting line are the first to solidify and continue its cooling. Note, however, that the cooling rate at this point was reduced due to the latent heat of the solidifying melt at the centre, which has to be transported through the outer zones. Finally, as the last melt has solidified, the cooling of the casting resumes its natural gradient and cools comparatively rapidly.

#### Adapted Distance and Time Step (12.17a-c)

The first row (a-c) of fig. 12.17 on the facing page shows the gradients with adapted centreline distance and adapted time increment. The adaptation was made manually by locating the initiation and end of solidification. The three modulus castings display very similar generic thermal gradients and can be said to be comparable. Note also that the time steps used are 25 s, 50 s, and 75 s, corresponding with the 1:2:3 rule described in section 12.3.2, on page 206.

#### Uniform Distance and Adapted Time Step (12.17d-f)

The second row (d-f) illustrate the thermal gradients adjusted according to the relative width of the castings. The small M08 casting displays a steeper gradient, meaning that the temperature difference per distance was greater for smaller modulus castings, compared with the larger. The intermediate performance of the M12 castings confirms the linear correlation. In terms of solidification, this means a shorter more defined solidification front for the smaller modulus castings.

#### Uniform Distance Time Step (12.17g-i)

The final row (g-i) shows the thermal gradients with uniform centreline distance and uniform time step. The time increments of the M12 castings were used as the common denominator. In addition to the steeper thermal gradients for, the smaller modulus castings, the uniform time step illustrate that the solidification progresses much faster for the M08 casting than for the M15 castings. The M08 casting has begun solidification at the mould-metal interface after 100 s, while simultaneously the interface of the M12 had just reached the eutectic

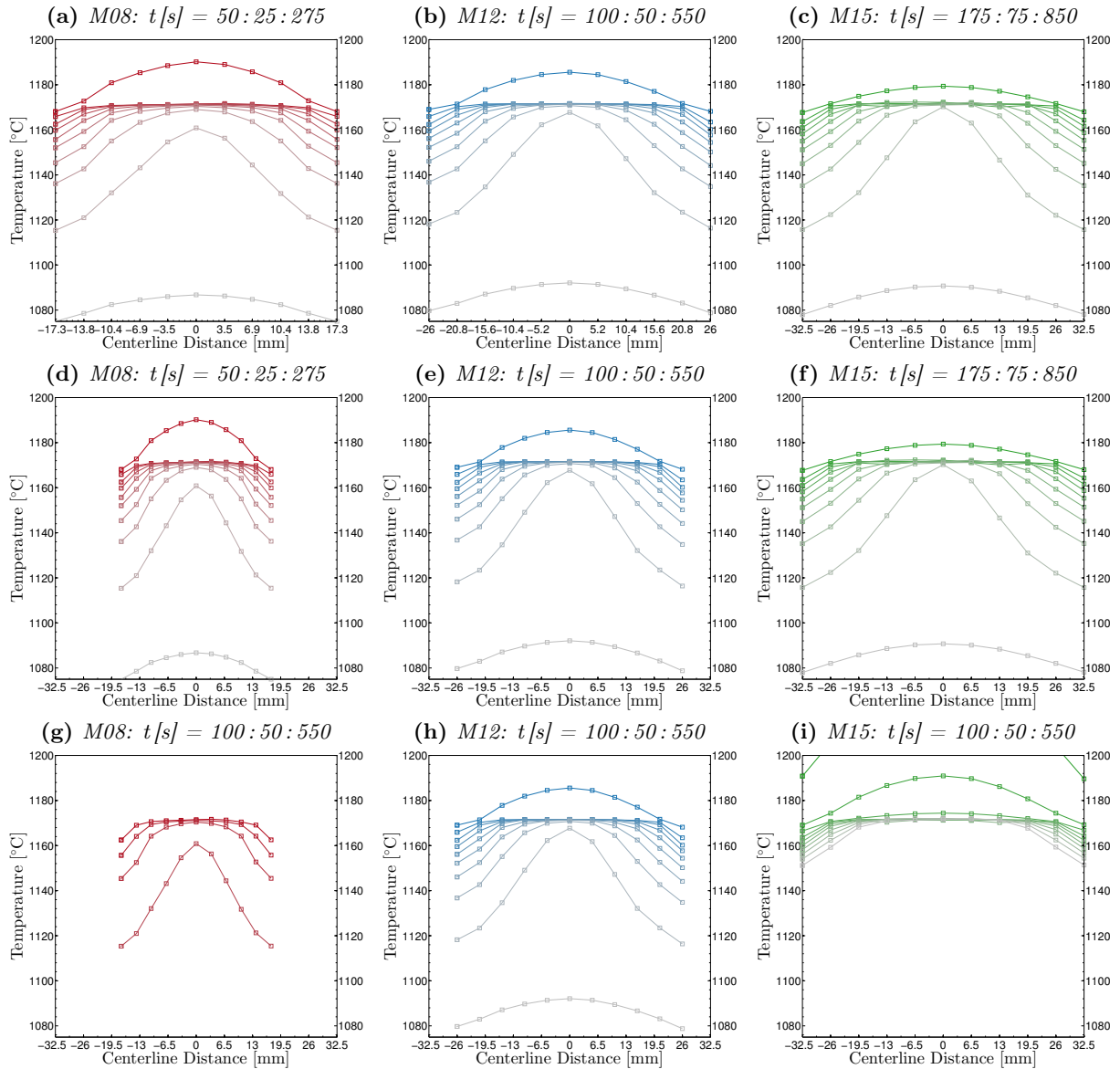


**Figure 12.17:** Temperature gradients for the M08, M12, and M15 castings without feeders. The gradients were extrapolated from 11 virtual thermocouples, equidistantly placed in a horizontal line across the middle of each casting, from edge to edge. The gradients are plotted as a function of time. The range and increments are indicated above each figure, in the format: Start Time : Time Increment : End Time. The top row (a-c) shows the gradients for adapted distance and time range, the second row (d-f) shows the thermal gradients with uniform distance on the x-axis, while the final row (g-i) shows uniform distance and uniform time range.  $t = 0$ s reference the initiation of the mould filling, the solidification simulation initiated at  $t = 6$ s.

temperature, and the interface of the M15 casting was still  $20^{\circ}\text{C}$  above the eutectic temperature. This difference in cooling rate continues throughout the solidification and cooling. The M08 casting was completely solidified at the fourth time step at 250s, while the M15 casting never completes solidification with the 550s shown on the graph. Consulting

table 12.5 on page 208 it is seen that the M08 casting had cooled below that eutectic temperature after 211s, while the M12 casting required 456s to achieve the same centreline temperature, and the M15 casting required 731s.

Additionally, the uniformity of the gradients from

one mould-metal interface to the other proves that the castings have cooled and solidified without any significant thermal influence from the other modulus castings. Had this been the case, this would have shown on the graphs as temperature increase on one of the edges.

### 12.3.4 Fraction Liquid Analysis

Similar to the thermal analysis described in section 12.3.3, on page 210, a fraction liquid analysis can also be performed, as the virtual thermocouples provide this information. See fig. 12.18 on the facing page. Fraction liquid is the inverse of fraction solid. It is a measure of the percentage of the mesh cell that is still liquid. Thus, the mesh cell is 100% liquid before solidification commences, and 0% liquid at the end of solidification.

The graphs were made in the same way as the thermal gradients in section 12.3.3, on page 210. Note that the time-increments are the same as for fig. 12.17 on page 211; however, the range has been shifted to provide a complete image of the process.

There are two main reasons to complement the thermal gradient analysis with a fraction liquid gradient analysis: (1) While the thermal gradient shows that temperature at different locations across the centre of the casting, temperatures below the eutectic temperature is not a guaranty that the melt has also solidified. Especially at the edges where high cooling rates can occur, the constitutional undercooling will be more pronounced. (2) The fraction liquid gradient graphs illustrate on a scale from 0% to 100% what occurs at the eutectic arrest, thus expanding the narrow temperature range near the eutectic arrest to a fully scaled graph.

The three rows of graphs in fig. 12.18 on the next page are arranged in the same manner as fig. 12.17 on page 211. Hence, the first row (a-c) displays adapted centreline distances and adapted time increments. The second row (d-f) shows uniform centreline distances with adapted time increments. Finally, the third row (g-i) shows the fraction liquid gradients with uniform centreline distances and time increments.

#### Adapted Distance and Time Step (12.18a-c)

Analysing the top row (a-c), the three modulus castings in this setup, solidification appears to progress in the same way in all three castings. Focusing on the few differences, the graphs can be viewed as if the edges cool faster the larger the modulus of the

casting is. This interpretation is not true. It is an effect of the adapted time increment. Hence, the fourth time step of the M08 casting should be compared to the second time step of the M15 casting. Comparing these two gradient lines, it was found that the small M08 casting solidifies faster than the large M15 casting. The edge of the M08 casting has solidified faster than the larger M15 casting.

Note though, that the limited resolution of the 11 thermocouple measurement across the width of the castings also entails a reduced resolution for the more massive castings. Hence, the distance between the measurements for the M08 casting was approximately half the distance between the measurement distance of the M15 casting. Additionally, the inherent limitation of the mesh can also distort the local measurement as described in section 12.3.1, on page 203.

#### Uniform Distance and Time Step (12.18g-i)

The third row (g-i) shows the gradients with uniform centreline distances and uniform time increments. This view supports the above conclusions that the smaller modulus castings do in fact solidify faster than, the larger modulus casting. The small M08 casting solidifies faster at both the edges and the centre. At the second time steps, the edge of the M08 casting had a fraction liquid of ~10%, while the M12 casting had a fraction liquid of ~55%. The M15 casting had not even begun to solidify at this point.

Analysing the subsequent time step as well, the M08 casting had now solidified to a fraction liquid of ~2%, while the M12 casting had a fraction liquid of 20%. The M15 casting had now reached a fraction liquid of ~55%. The fourth increment reveals that the M08 casting had a completely solidified shell, while the M12 casting had a fraction liquid of ~10%. The mould-metal interface of the M15 casting had now reached a fraction liquid of ~22%. Note that the two first gradients of the M15 casting can be difficult to distinguish because they are overlapping.

The analysis shows that the M08 casting solidifies much faster than the larger castings; however, it also shows that the solidification rate at the edge decreases as time progresses. Viewing the graphs in the final row (g-i), the decreased solidification rate can be observed for the M08 casting; however, the flow of the latent heat from the centre of the casting quickly ceases, and a solid shell was formed. The solidification of the casting centre followed shortly

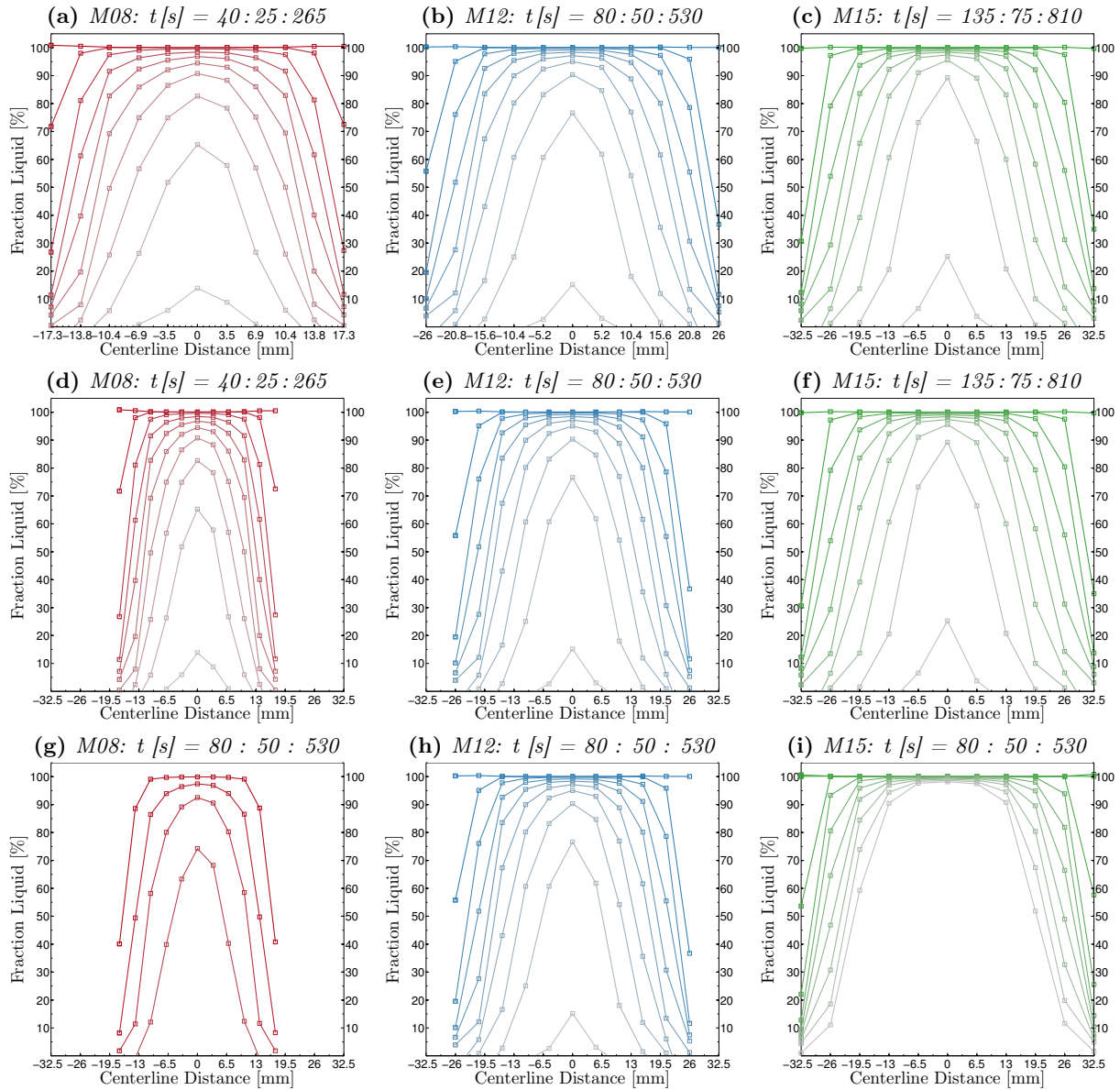


**Figure 12.18:** Fraction liquid gradients for the M08, M12, and M15 castings without feeders. The gradients were extrapolated from 11 virtual thermocouples, equidistantly placed in a horizontal line across the middle of each casting, from edge to edge. The gradients are plotted as a function of time. The range and increments are indicated above each figure, in the format: Start Time : Time Increment : End Time. The top row (a-c) shows the gradients for adapted distance and time range, the second row (d-f) shows the thermal gradients with uniform distance on the  $x$ -axis, while the final row (g-i) shows uniform distance and uniform time range.  $t = 0$  s reference the initiation of the mould filling, the solidification simulation initiated at  $t = 6$  s.

after that. For the M15 casting, the edge does not solidify completely within the unified time range, though it is very close at the end. However, the casting centre is also completely liquid at this point for the M15 casting, where the centre of the M08 casting had begun to solidify before the edge was

completely solidified.

Thus, the small modulus M08 casting showed a small but limited effect of the latent heat from the casting centre slowing the complete solidification of the shell. However, at the time the shell has formed entirely, the centre of the casting has also begun

to solidify making the remaining melt mushy and tough to feed through.

The M15 casting releases a lot more latent heat during solidification, as compared with the M08 casting. The effect of this can be seen by the slowed down solidification of the shell, which is caused by the latent heat of the centre being transported through the outer zones of the castings, thus retaining the eutectic temperature for a prolonged period. This effect is further enhanced by the heating of the mould, reducing its cooling power, and subsequently further slowing the heat extraction from the casting. However, the M15 casting achieves a state with a solid shell and a liquid centre which is not found in the M08 casting. As a result, the M15 centre will solidify and contract slowly encased in a solid shell. The slow uniform cooling of the centre enables the formation of equiaxed dendrites that, having a higher density than the surrounding melt, will fall to the bottom.

The M08 casting does not achieve this effect as the two edges continue their growth towards the centre until they meet at the centre.

The M12 casting shows an intermediate solidification pattern, where the uniform solidification of the centre commences just before the shell is completely solidified.

As 12.18i shows, the M15 is the only casting modulus to exhibit a liquid centre at the time when the shell is also completely solidified—hence the M15 castings are the only ones that can be categorised as shell-forming. This phenomenon is also supported by the smaller amount of porosities found in the M15 castings as shown in section 12.1, on page 175, and is additionally supported by the models described in chapter 13, on page 231.

### 12.3.5 Geometric Solidification Analysis

The previous three thermal analyses—the cooling curve analysis, the thermal gradient analysis, and the fraction liquid analysis—are all measurement point based. The two gradient analyses analyse a cross-section, and the cooling curve analysis analyses four different measurement positions, however, none of the analyses comprises the entire casting geometry.

The geometric solidification analysis is based on selected time steps from the solidification of four selected feeder combinations.

### The Selected Feeder Combinations

Based on the numerical simulation described in section 12.3.1, on page 202, four feeder combinations were selected and analysed using geometric representations of the numerical simulation results. The four different feeder combinations were synchronised so that the results were saved at the same time step in all simulations. The percentage presented for each time step is the fraction liquid of the C10 casting converted to a liquid percentage. Note that the total fraction liquid of the three other casting combinations can vary accordingly because of the differences in total melt volume and differences in feeder configurations.

Details about the four feeder combinations can be found in table 12.1 on page 180.

**C01: Benchmark without feeders** The basic casting geometry without either upper or lower feeders. This setup provides a reference to the natural solidification of the casting geometry, enabling a more precise estimate of the influence of the different feeder combinations.

**C06: Medium upper feeders** The C06 feeder combination shows the functioning of upper feeders without lower feeders. Additionally, the feeders of the M08 and M15 castings were  $1.00 M^\infty$ , while the M12 casting feeder was  $0.83 M^\infty$ . Thus, the feeder combination shows the performance of feeders with the same, or smaller, modulus than the casting modulus itself.

**C10: Large lower feeders** The C10 feeder combination comprises the largest of the feeder used in the experiment, located in the lower part of the casting. The proportional moduli of the feeders were  $1.25 M^\infty$  for the M08 casting,  $1.00 M^\infty$  for the M12 casting, and  $1.27 M^\infty$  for the M15 casting. Additionally, the location at the bottom serves to show the influence of a lower feeder on solidification and closing time if the pre-feeder neck. If the influence is thermal, the distance should negate the effect. If the influence is caused by a volume change, the lower feeder should display the same results as the upper feeder.

**C19: Large upper and lower feeders** This final combination shows the maximum influence exerted onto the castings during the trial, applying both an upper and a lower feeder. Both feeders were the largest used during the experiment and the same as used

in feeder combination C10. This C19 feeder combination shows the influence of a large feeder close to the pre-feeder neck, and the thermal influence of two feeders combined.

### Image Analysis Guide

The simulations show the casting geometries of the four feeder combinations, from left to right. The solidification progresses from top of the page to the bottom.

The colour gradient used is a widespread gradient. Hence, the nuances of green represent any part of the casting with a fraction liquid between 0% to 100%. This fraction liquid corresponds to the solidification progressing at the eutectic temperature. The parts of the casting that are above the eutectic temperature that is still liquid and have not yet begun to solidify are shown in red. However, note that the superheated melt can only be shown where it is in contact with the mould. While the inside of the casting will stay superheated for an extended period, the superheated red melt will be encased in solidifying green melt representing solidifying mushy zone.

In addition to the visible colour gradients in the images, what is not visible is also essential. The images are viewed in a so-called x-ray mode. Hence, all that has completely solidified becomes transparent, or invisible, allowing observation of the solidification process underneath. Note that as a consequence of the images showing only liquid and partly liquid melt, porosities within the casting are not shown as they, per definition, do not contain any fraction of liquid metal.

### Pre-Feeder Neck Solidification (12.19)

As described in section 11.1.2, on page 161 the pre-feeder neck was designed to solidify shortly before the thermal centre of the casting reached the eutectic temperature. This design, however, was made without the influence of a feeder. Speculations have been raised in section 12.2.6, on page 200, about how the feeders influenced the solidification of the pre-feeder neck. While section 12.3.2, on page 205 have shown that the presence of feeders did not have any significant influence on the temperature at the centre of the pre-feeder neck, this thermal analysis does not explain the large porosities observed at some of the pre-feeder necks.

Additionally, the analysis of the feeders influence on the pre-feeder neck is of interest because of the geometric resemblance to a secluded section, connected to another part of the casting by a narrow intermediate section. Hence, the interaction between the feeders and connecting section may be of interest to make optimal use of the ram-up sleeve feeders and to avoid unintended casting defects at other parts of the castings.

**M08: 90 s** The small M08 pre-feeder neck has just closed for the C01 benchmark castings. The distance between the two ends of the remaining melt is almost touching. Viewing the C06 feeder combination with a  $1.00 M^\infty$  upper feeder, it is observed that the distance between the two fingers of the remaining melt is greater than for the feederless C01 casting. Note that it is only the lower finger of the connecting melt that has changed shape between the two feeder combinations.

Analysing the C10 casting, it was observed that the M08 pre-feeder neck is comparable to the pre-feeder neck of the C01 casting. Finally, the M08 pre-feeder neck of the C19 casting displayed an even greater distance between the two fingers of the remaining melt. Both C10 and C19 used  $1.25/1.27 M^\infty$  feeders.

**M12: 100 s** The second row shows the time of solidification for the M12 pre-feeder neck. The C01 and C10 castings display a thin but still connected string of melt from the pre-feeder to the casting. The C06 and C19 castings have a very similar geometry of the melt in the pre-feeder neck; however, a closer inspection reveals the presence of the first transparent mesh cell at the centre of both the C06 and C19 pre-feeder necks, indicating the breaking of the connection.

That the difference between the combination with and without upper feeders is less pronounced for the M12 castings than for the M08 castings may be related to the time step used for the analysis. The images were saved for every  $\frac{1}{200}$  steps of the solidification. Hence, the analysed is incremental and not step-less. Only the pre-selected steps were available for analysis afterwards; hence, it was not possible to investigate the solidification progresses between two pre-selected solidification steps.

Additionally, note that the proportional modulus of the M12 feeders was only  $0.83 M^\infty$  and  $1.00 M^\infty$  which would have reduced the influence of the feeders.

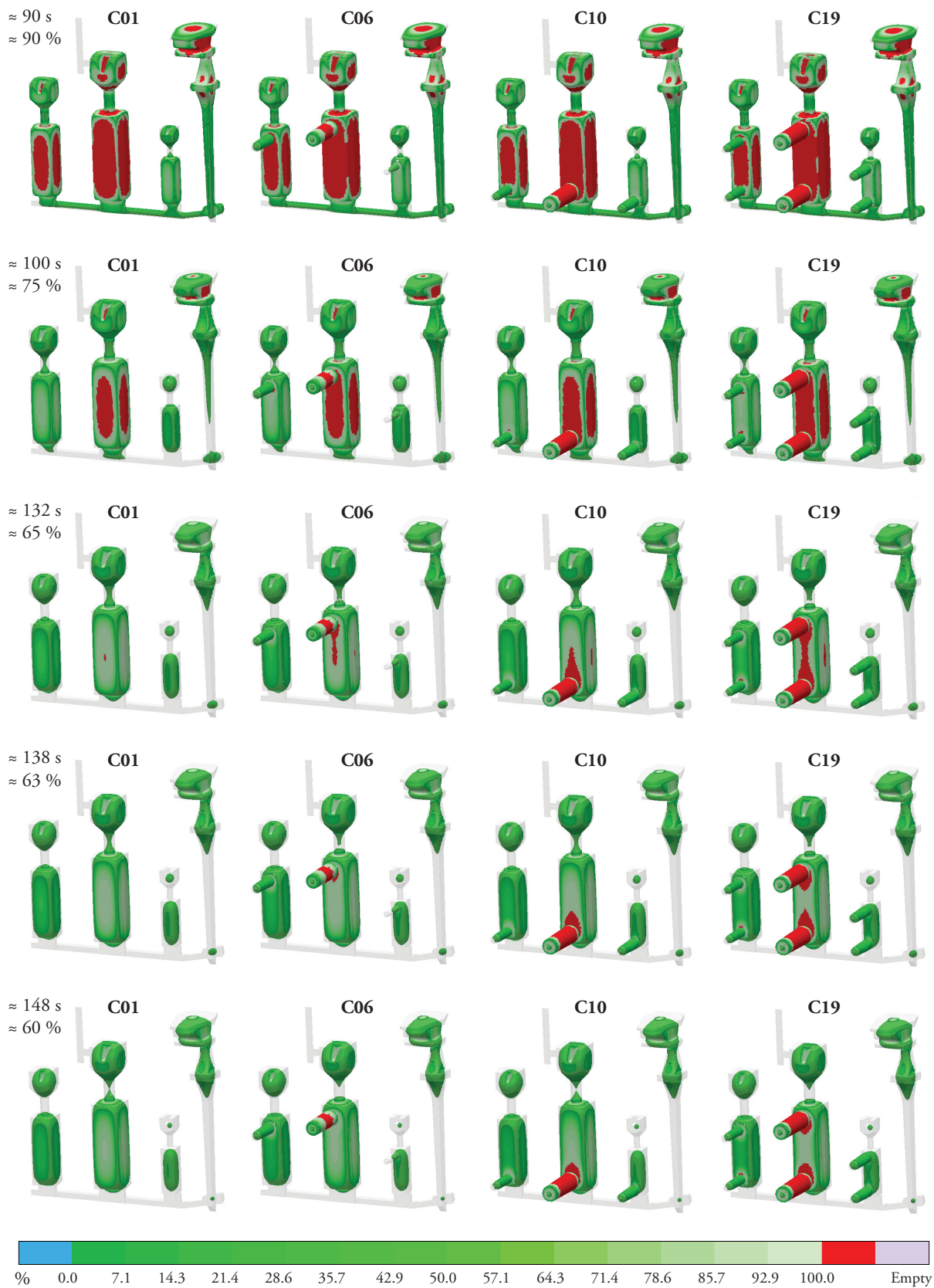


**Figure 12.19:** Pre-feeder neck solidification. The figure shows fraction liquid for four simulated casting with feeder combinations C01, C06, C10, and C19. Percent liquid varies a little between the castings. Time is the common denominator.



**M15: 132s to 148s** Due to the greater volume of the M15 castings, and subsequent later solidification, the solidification of the pre-feeder neck progresses over a longer time, allowing for a more detailed analysis. Thus, row 3-5 all show the solidification of the M15 pre-feeder necks.

At 132s it is observed that the pre-feeder necks of both the C06 and the C19 castings have already separated. Again it is observed that it is the lower finger of melt that sinks down and loses the connection to the upper finger. This effect is even more expressed for at 138s. Note that at this point the pre-feeder necks of C01 and C10 castings are still connected by melt. Finally, at 148s the pre-feeder necks of the C01 and C10 castings disconnect. Observing the two pre-feeder necks, the C10 casting with a lower feeder appear to display a longer distance between the two solidifying fingers than the feederless casting of C01.

Note that the pre-feeder necks of the C06 and C19 castings at this increment have not only disconnected by are almost without remaining melt. Additionally, the melt at the bottom of the pre-feeder neck seems to have fallen, resembling the emptied out pre-feeder necks observed in section 12.2.6, on page 200.

#### M08 Solidification (12.20)

The C01 combination shows the natural geometrical solidification without feeder of the M08 casting—it solidified as an ellipsoid towards the centre of the casting. At 272s the M08 casting has solidified completely. See fig. 12.20 on the following page.

The C06 feeder combination uses a  $1.00 M^\infty$  upper feeder. While the presence of the feeder prolongs solidification of the geometrically inherent ellipsoid, it is observed that the melt in the casting and the melt in the feeder disconnect at an early stage, preventing complete feeding. The disconnection occurs between 234s to 259s, while the final solidification of the casting occur between 272s to 291s. The M08 casting with the C06 feeder combination was found to have large (4) porosities in the middle control volume, as seen in table 12.1 on page 180. This finding corresponds with the disconnected feeding of the last to freeze melt.

By incomplete feeding is meant that the last to freeze melt is disconnected and cannot be fed. However, this does not rule out that a larger or smaller part of the casting is feed by the feeder. The fraction liquid analysis does not show the melt movement

or the porosity formations. It only shows the progression of the solidification.

The C10 feeder combination had a large  $1.25 M^\infty$  lower feeder. The larger feeder, compared with the C06 castings, managed to retain contact with the solidifying ellipsoid throughout the solidification. This prolonged melt connection in the casting would indicate that the last to freeze melt was moved towards the bottom of the casting enabling the formation of porosities at this location. However, no porosities were found in the bottom control volume of the any of the M08 castings with only a lower feeder; indicating that the last to freeze melt in the casting managed to feed off the lower feeder, thus preventing porosities. This thesis is supported by the porosities observed in the lower feeders in the x-ray analysis in section 12.2.6, on page 200.

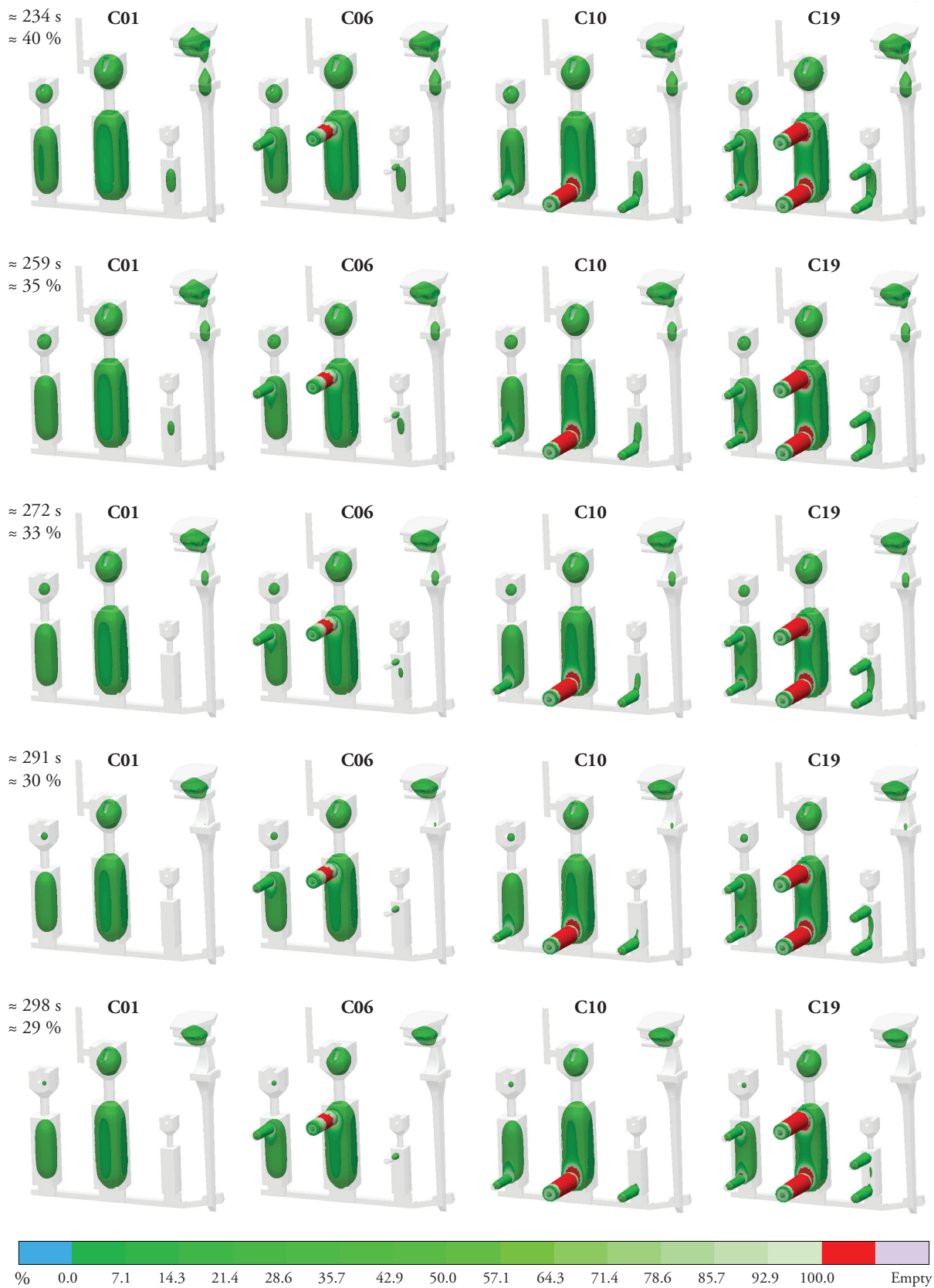
The final feeder combination uses two large  $1.25 M^\infty$  feeders. The geometrical representation of the solidifying melt shows that the ellipsoid of the natural solidification is changed to a banana-shaped geometry facing towards the two feeders. For the M08 casting, it was observed that the combination of two equally sized feeders created a long thin opening of remaining melt connecting the two feeders, albeit the last to freeze melt in the casting was eventually disconnected from both feeders.

Table 12.1 on page 180 shows that the M08 castings with the C19 feeder combination have small (2) porosities at the middle control volume, flanked by a small (2) porosity either at the top or bottom control volumes. This data corresponds well with the secluded residual melt at the casting centre and the connection to the feeder at both the top and the bottom. The porosity results suggest that the porosities can be moved between the top and the bottom control volume.

#### M12 Solidification (12.21)

The M12 castings solidify similarly to the M08 castings. The benchmark casting without feeders solidifies with the natural ellipsoid inherent in the geometry. See fig. 12.21 on page 219.

The C06 casting, though, retain the connection between the feeder and the melt in the casting almost to the end of solidification, as seen in the last row—551s. Note that the proportional modulus of the feeder for the M12 casting is only  $0.83 M^\infty$  where the similar feeder of the M08 casting had a proportional modulus of  $1.00 M^\infty$ . However, the proportionally smaller feeder of the M12 casting still retains the connection to the melt in the casting



**Figure 12.20:** M08 solidification. The figure shows fraction liquid for four simulated casting with feeder combinations C01, C06, C10, and C19. Percent liquid varies a little between the castings. Time is the common denominator.

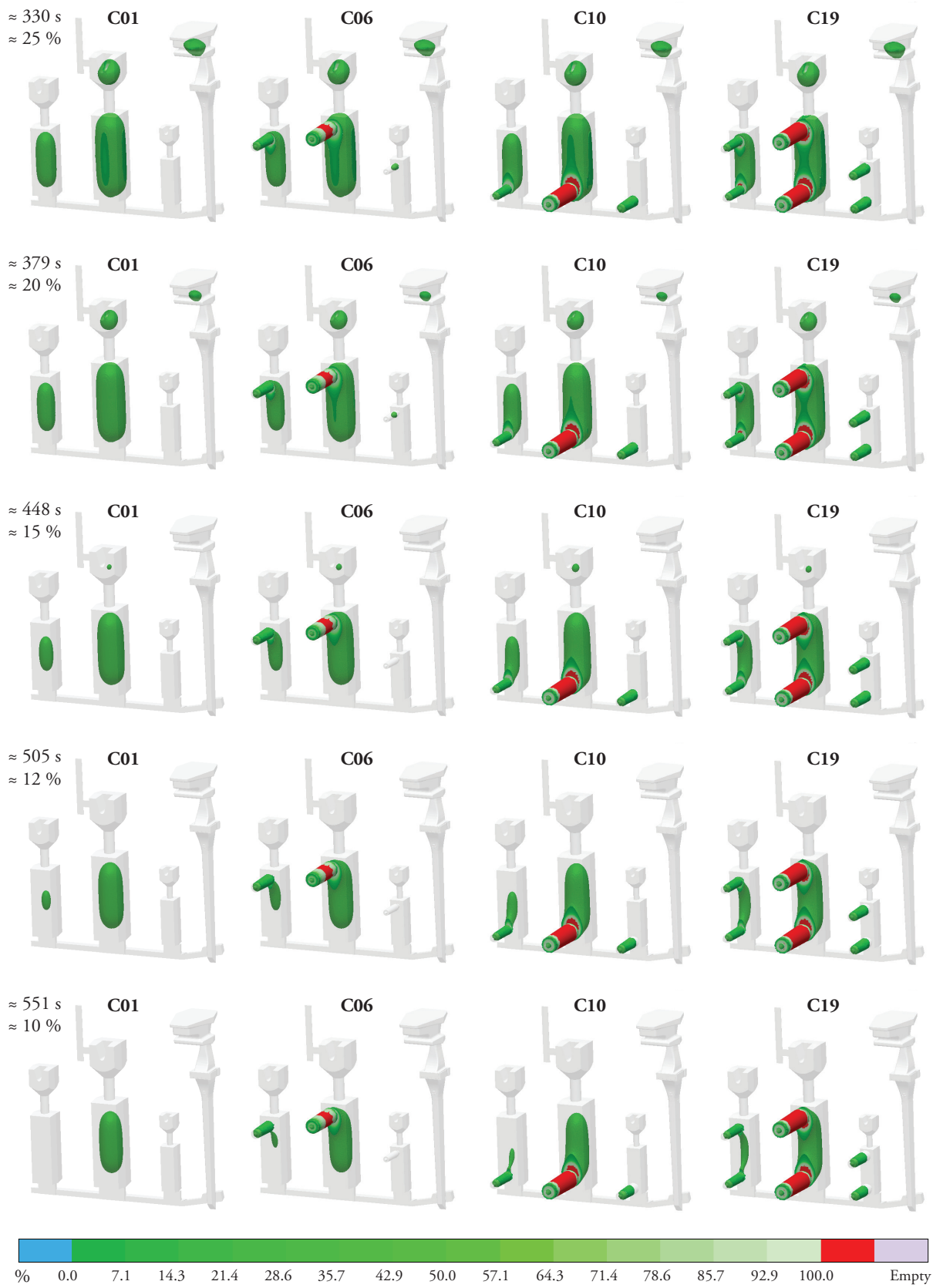


**Figure 12.21:** *M12 solidification.* The figure shows fraction liquid for four simulated casting with feeder combinations C01, C06, C10, and C19. Percent liquid varies a little between the castings. Time is the common denominator.

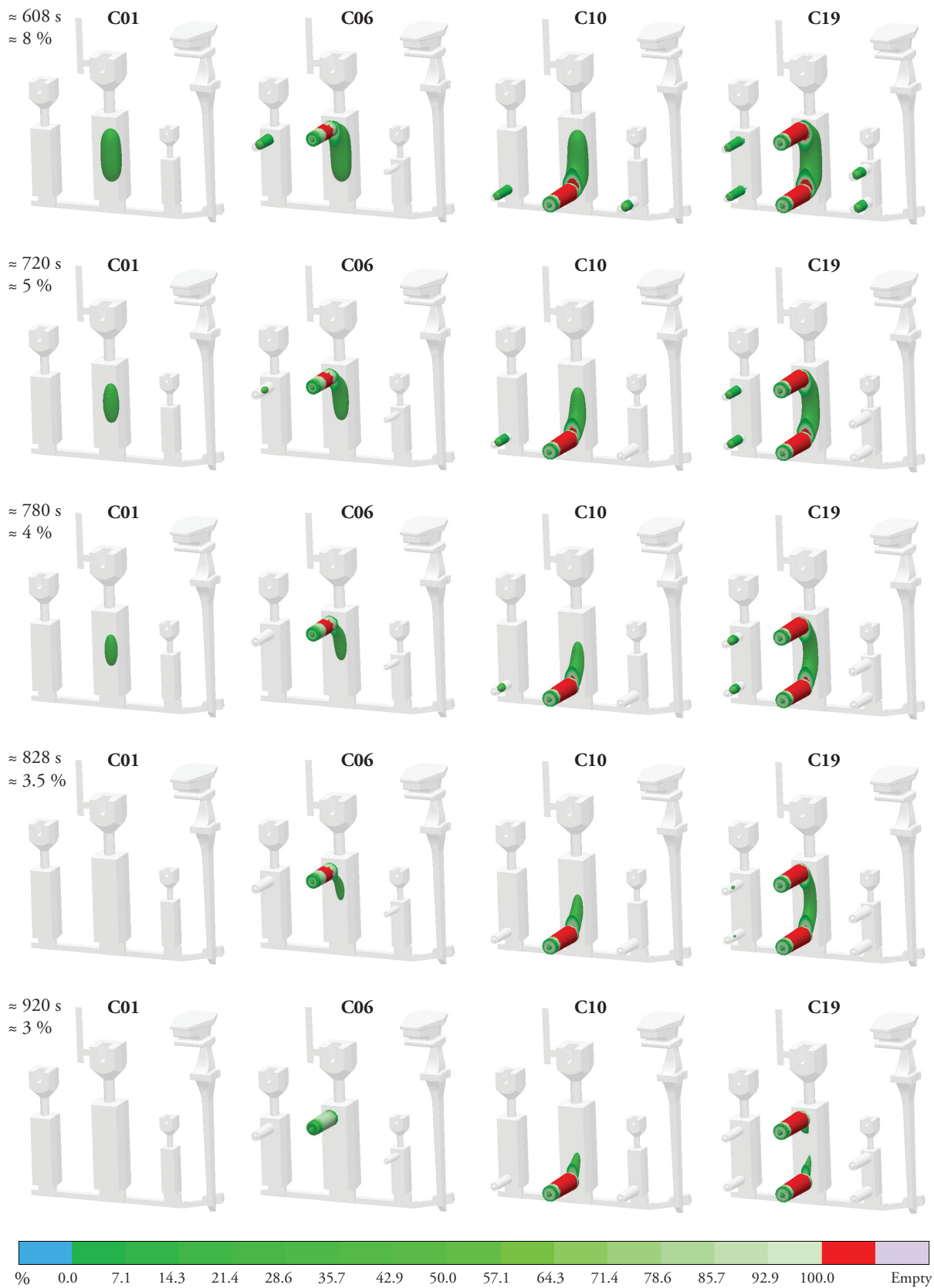


**Figure 12.22:** *M15 solidification.* The figure shows fraction liquid for four simulated casting with feeder combinations C01, C06, C10, and C19. Percent liquid varies a little between the castings. Time is the common denominator.

longer than was the case for the M08 casting. None of the three M12 castings with the C06 feeder combination had any porosities at the middle control volume, as seen in table 12.1 on page 180. This result corresponds with the observation of the feeder retaining contact with the solidifying melt in the casting almost until the end of solidification.

The C10 casting performs very similarly to the C06 castings, though the thermal gradient and solidification face towards the bottom of the casting where the feeder is located. However, the C10 feeder is a  $1.00 M^\infty$  and thus larger than the  $0.83 M^\infty$  of the C06 casting. The larger feeder was naturally expected to have a greater influence on the geometry of the remaining liquid. However, the upper part of the casting had a longer cooling time due to the presence of the pre-feeder as was concluded in section 12.3.2, on page 205. On the other hand, if this thermal influence was the cause of the similarity of the two feeders performance, then the same thermal effect should have been visible for the other castings and other feeders as well. This similarity in results was not the case.

The C19 feeder combination provided a banana-shaped geometry of remaining melt connecting the two feeders. Similar to the solidification observed for the M08 casting.

#### M15 Solidification (12.22)

The C01 feeder combination also solidify as an ellipsoid for the M15 modulus casting. See fig. 12.22 on page 220.

The C6 feeder combination for the M15 casting solidifies similar to the M12 casting, though the M15 casting uses a larger proportional feeder of  $1.27 M^\infty$ . The M08 casting used a similar proportionally sized feeder of  $1.25 M^\infty$  but was disconnected from the last to freeze melt during solidification. However, while the solidification was similar to the M12 casting, the M15 had a significant amount of porosities at the middle control volume. Here the M12 casting was porosity-free. Albeit, the performance was also better than the M08 casting that had large porosities at both the top and middle control volumes. The M15 castings had a variety of different porosity sizes at both the top and the middle volume.

The C10 and C19 feeder combinations for the M15 casting show that the combination of two identical feeders, in this case, two large  $1.27 M^\infty$  exothermic feeders, do change the total effect of the feeders. All three feeders, the one from the C10 cast-

ing and the two from the C19 casting, stay connected to the remaining melt in the casting throughout the solidification. However, while the casting with the C19 feeder combination had only small (2) porosities at the top control volume, the casting with the C10 feeder combination had large (4) porosities at all three control volumes. See table 12.1 on page 180. Hence, in this specific case, the addition of an extra identical feeder reduces the porosity sum of the casting by 10.

## 12.4 Numerical Porosity Analysis

THE thermal gradients and the illustrations of the geometrical solidification analysis are great tools for analysing the solidification mechanisms found in a casting. The information they provide is, however, seldom what is sought for. Users of MAGMASOFT and other numerical simulation software are interested in the properties of their castings; ultimate tensile strength, pearlite content, nodule count, sand burn on, and porosities. As described in section 3.4.3, on page 54, properties like temperature and thermal gradients are part of the basis for the numerical simulations. They do, however, in themselves not reveal anything about the mechanical properties of the casting. Whatever knowledge a viewer gain about the mechanical properties of a casting from the thermal gradients, is based on the observer's empirical knowledge and interpretation of the presented data.

Criteria functions are models describing correlations between the basic physical data—temperature ( $T$ ), thermal gradient ( $G$ ), cooling rate ( $\dot{T}$ ), feeding velocity ( $u$  or sometimes  $v$ ), solidification shrinkage ( $\beta$ ), freezing range ( $\Delta T_f$ ), and critical pressure drop ( $\Delta P_{cr}$ ) to list some of the most used parameters. The criteria functions provide a number based on the physical conditions which describing the material properties. For porosities this is often described via a threshold value—values above are sound, values below tend to form porosities—greater or smaller. Using criteria functions is thus an empirical analysis based on data obtained from numerical modelling software.

The actual criterion function used in MAGMASOFT to predict the formation of porosities in cast iron is not known, as described in section 3.4.3, on page 54. Neither is it possible to choose which criteria are taken into consideration or with which exponent. Thus, to calibrate the simulations to match the casting results, it is necessary to adjust

the process conditions and particularly the properties of the cast alloy.

The goal is to calibrate the simulation setup to match a given alloy under a set of known processing conditions. Hence, when the simulations have been calibrated, and the processing conditions—pouring temperature, mould stability, and alloy—are kept constant, then the simulation of a new geometry should yield credible results.

### 12.4.1 Simulation Setup and Calibration

Calibration of the simulation setup has been performed as an iterative process, changing one parameter at the time. The calibration setup for the thermal analysis, as described in section 12.3.1, on page 202 was used as the starting point of the parametric iteration. Additionally, a range of parameters was kept constant throughout the parametric iterations.

The geometry modelling and general setup were unchanged throughout the iterations. All simulations used the extended feeding algorithm, considered the water content of the mould and the mould permeability, and considered the microstructure of the iron. The HTC selections were unchanged throughout, which for the casting meant dynamic temperature HTC called ‘TempIron’, and the pouring time was kept at 6.0 s. The treatment yield was kept at 80 %, though it should be noted that the inoculation method was changed for one of the simulations. Additionally, the alloy composition was kept constant, as according to table 11.2 on page 167. Note, however, that the material itself was changed between three different alloys. The first was the GJS-500 iron alloy standard to MAGMASOFT, while the second and third alloys were alloys explicitly calculated for this project—namely the GJS450\_JT which is the  $\beta$ -alloy from Part I, and GJS500\_JT which in this case it the high Si alloy used in Part II. Both of these unique alloys were calculated by MAGMA GmbH using JMat Pro [119].

Table 12.6 on page 224 lists the parameters used for each iteration in the calibration process. Figure 12.23 on the facing page shows selected results from the simulation combinations in 12.6.

Most of the parameters varied are straightforward and will only be discussed briefly. The material is varied between MAGMASOFT’s build-in GJS-500 iron and two especially calculated for the alloys used in this project. MAGMASOFT offers three types of moulds for the simulation—Die, Stable, or Weak. As the castings were cast in green sand moulds, the

very rigid die option was not evaluated. However, both the stable and weak mould options were analysed. The graphite precipitation, as described in chapter 3, on page 39, is a factor that can be varied between 1 and 10. Only seven levels were analysed in this analysis, as there was a general problem with predicting enough porosities; hence, the more pronounced graphite expansion from 8 to 10 was not evaluated. The inoculation method was changed from ‘Very Good’ to ‘Good’ for a single iteration. Finally, the pouring temperature was analysed to understand its influence on the porosity formation.

Two of the varied parameters, do, however, require some additional explanation. The feeding effectivity, as described in section 3.4.4, on page 56 is not supposed to be used in correlation with cast iron. The MAGMASOFT manual describes that the value should be kept at 100 % [69]. The feeding effectivity describes the materials feeding property, in the sense of feedability through the mushy zone. In short, it defines the threshold for when it is no longer possible to feed through a section that has solidified a given percentage.

The mesh-factor listed in table 12.6 on page 224 list the equidistant dimension of the mesh cells in mm. Hence, the mesh generated with a cell size of 2×2×2 mm yielded approximately 21 million cell in total, and 325 000 metal cells. For the 5×5×5 mm mesh this number was approximately 1.4 million mesh cells in total, of which 20 000 were metal cavity cells. Thus, the coarse 5.0 mesh yields only ~6 % of the cells used in the fine 2.0 mesh. Including the mesh as a factor is a bit controversial as this is a simulation parameter and not a factor describing a physical phenomenon. It has, however, been shown that the mesh cell size matters for the porosity prediction showed in the simulation results, as described in section 3.4.2, on page 52 and reported by Vedel-Smith [92].

#### Parametric Iteration

The parameters described above was used to vary the simulations to find the best possible fit between the predicted porosities of the simulation and the porosities recorded in the porosity quantification in section 12.1, on page 175. The following section will address the individual iterations shown in fig. 12.23 on the facing page and the results they yielded.

First row (# 1,3,5,7) The top row (# 1,3,5,7) show a decrease of the graphite precipitation factor from

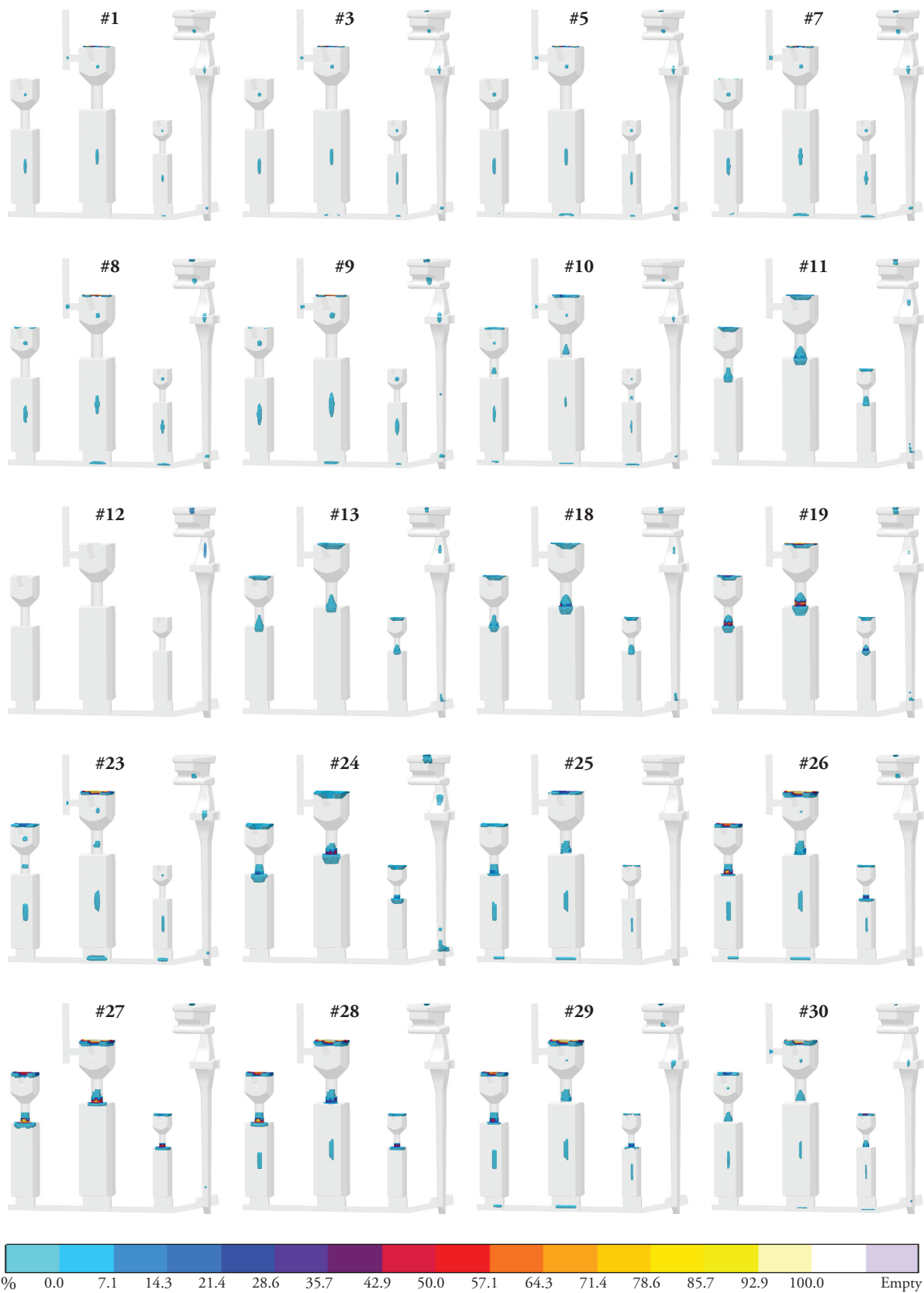


**Figure 12.23:** Calibration simulation setups and their resulting porosity predictions for the benchmark casting, C10. The numbers correspond to a simulation setup shown in table 12.6 on the following page. The predicted porosities should be compared with the porosities found in the section castings in fig. 12.6 on page 182 and in the ultrasound analysis shown in table 12.1 on page 180.

**Table 12.6:** Overview of parameter variation for numerical simulation of porosity probabilities. Text in **bold** shows parameter change since previous step. The two iterations framed by lines are the setups used by the thermal analysis (#15) and porosity analysis (#29) respectively.

#	Version	Material	Feeding Effectivity [%]	Mould	Mesh	Graphite Precipitation	Inoculation Method	Temp [°C]
1	v07	GJS-500	100	Stable	2.0	<b>7</b>	Very Good	1380
2	v01	GJS-500	100	Stable	2.0	<b>6</b>	Very Good	1380
3	v02	GJS-500	100	Stable	2.0	<b>5</b>	Very Good	1380
4	v03	GJS-500	100	Stable	2.0	<b>4</b>	Very Good	1380
5	v04	GJS-500	100	Stable	2.0	<b>3</b>	Very Good	1380
6	v05	GJS-500	100	Stable	2.0	<b>2</b>	Very Good	1380
7	v06	GJS-500	100	Stable	2.0	<b>1</b>	Very Good	1380
8	v08	<b>GJS450_JT</b>	100	Stable	2.0	1	Very Good	1380
9	v09	GJS450_JT	100	Stable	2.0	1	<b>Good</b>	1380
10	v10	GJS450_JT	<b>30</b>	Stable	2.0	1	Very Good	1380
11	v11	GJS450_JT	<b>0</b>	Stable	2.0	1	Very Good	1380
12	v14	<b>GJS500_JT</b>	0	Stable	2.0	1	Very Good	<b>1200</b>
13	v15	GJS500_JT	0	Stable	2.0	1	Very Good	<b>1300</b>
14	v16	GJS500_JT	0	Stable	2.0	1	Very Good	<b>1350</b>
15	v12	GJS500_JT	0	Stable	2.0	1	Very Good	<b>1380</b>
18	v17	GJS500_JT	0	Stable	2.0	1	Very Good	<b>1400</b>
19	v18	GJS500_JT	0	Stable	2.0	1	Very Good	<b>1450</b>
20	v19	GJS500_JT	0	Stable	2.0	1	Very Good	<b>1500</b>
21	v13	GJS500_JT	0	Stable	2.0	1	Very Good	<b>1600</b>
22	v22	GJS500_JT	<b>50</b>	Stable	<b>5.0</b>	1	Very Good	<b>1380</b>
23	v23	GJS500_JT	50	Stable	5.0	<b>5</b>	Very Good	1380
24	v24	GJS500_JT	<b>0</b>	Stable	5.0	5	Very Good	1380
25	v25	GJS500_JT	<b>20</b>	Stable	5.0	5	Very Good	1380
26	v26	GJS500_JT	20	<b>Weak</b>	5.0	5	Very Good	1380
27	v27	GJS500_JT	<b>10</b>	Weak	5.0	5	Very Good	1380
28	v28	GJS500_JT	<b>15</b>	Weak	5.0	5	Very Good	1380
29	v29	GJS500_JT	<b>25</b>	Weak	5.0	5	Very Good	1380
30	v30	GJS500_JT	25	Weak	<b>2.5</b>	5	Very Good	1380

7 through 5 and 3 to 1. The decreased graphite precipitation yield only the smallest visible effect between the extremes shown here. The porosities at the centre of the castings correspond well with the small (2) porosities found in most of the casting for the middle control volume. The porosities found in the top control volume in the castings, are, however, missing in the simulations.

Second row (# 8,9,10,11) Simulation #8 is different from #7 concerning the material, which has been changed to the custom GJS450\_JT, rather than the standard GJS-500. The change yielded a minimal effect. #9, on the other hand, had decreased inoculation methods, which was changed from ‘Very Good’ to ‘Good’. This change showed a small in-

crease in porosities, though the porosity location was unchanged.

Simulation #10 featured a change of the feeding effectivity from 100 % to 30 %. This change resulted in a relocation of the porosities, where a significant part was now predicted to be located at the bottom of the pre-feeder neck. At the same time, the probability of porosities at the centre of the casting was significantly reduced as well. A final interesting fact about this change in this simulation is the first in the iteration that shows any deviation between the three different castings, as the sizeable M15 casting has the smallest centre porosity, the small M08 casting the next smallest centre porosity, and the medium M12 casting showed the most extensive centre porosity.



The tendency of simulation #10 is continued in simulation #11, which was run with a feeding effectivity of 0%. This setup causes all the porosities to be agglomerated at the lower part of the pre-feeder neck. Though the feeding effectivity factor is described as an adjustment of the feeding flow through the mushy zone, the overall amount of porosities also seem to increase. The flow through the mushy zone should in principle only change the position of the porosities, not the number and size of porosities; hence, the feeding effectivity seems to influence more than this. One explanation could be the threshold limit for porosities in the single mesh cells, as discussed in section 3.4.2, on page 52. As the feedability of the material is decreased, the porosities will agglomerate in larger concentrations causing more mesh cells to exceed the porosity threshold of the single mesh cell. If this is the case, a coarser mesh should be able to adjust the porosity predictions.

Third row (# 12,13,18,19) The porosity results in the third row (# 12,13,18,19) are all simulated with the GJS500\_JT alloy, and show varying pouring temperatures; 1200 °C, 1300 °C, 1400 °C, and 1500 °C. It is seen that simulation #12 with a pouring temperature of only 1200 °C is virtually porosity-free, except for the pouring cup and down sprue before the filter. This simulation result indicates that the alloy, with the given setup, should be self-feeding as long as the liquid shrinkage is small enough. The subsequent simulation, #13, shows a medium amount of porosities at the bottom of the pre-feeder neck corresponding to a pouring temperature of 1300 °C. The porosity size is gradually increased by simulations #18 and #19; with pouring temperatures of 1400 °C, and 1500 °C respectively.

Fourth row (# 23,24,25,26) Simulation #23 reset several parameters to previous analysed settings. The graphite precipitation is set as 5, the feeding efficiency is set at 50%, the pouring temperature is back at 1380 °C, and additionally, the mesh cell size was changed to an equidistant 5×5×5 mm. This setting yield small porosities at the pre-feeder neck of the M12 and M15 castings, as well as medium porosities at the centre. Changing the feeding effectivity to 0%, in #24 showed a large concentration of porosities at the lower part of the pre-feeder neck and in the top control volume. The centre porosities disappeared on the other hand. Thus, simulations #25 adjusted this parameter further,

setting the feeding effectivity to 20%. This parameter adjustment was assessed to provide a more accurate balance between the two porosity centres, though the simulation again, as with #23, do not predict porosities at the pre-feeder neck/top control volume of the small M08 casting.

The following simulation, #26, introduces the weak mould to the simulations, which results in a general increase in the number and size of the porosities. The weaker mould is less effective in containing the volume expansion of the graphite resulting in an expanded volume, which in turn causes more porosities, as described in section 2.3.7, on page 29. How this feature is simulated in MAGMASOFT is not known; however, it is probably a factor influencing the porosity criterion function directly, rather than influencing the actual simulation. Evidence for this can be seen by the weak effect of the graphite precipitation factor on this particular alloy.

Last row (# 27,28,29,30) Simulations # 27, #28, and #29 all test the threshold of the feeding effectivity setting. #27 show that a feeding effectivity of 10% will remove the centre porosities as was also seen with the 0% setting analysed in #11. Simulation #28 shows that a feeding effectivity of 15% return the centre porosities to M12 and M15 respectively, whereas the M08 casting remains porosity-free at the middle control volume. The final setting of the feeding effectivity is set at 25%, which yield an acceptable balance between the centre porosities and the porosities located the bottom of the pre-feeder neck.

The final simulation, #30, is identical with #29 except for the mesh cell size which was adjusted to an equidistant side length of 2.5 mm. Eventually, it was decided that the more extensive overall amount of porosities found in simulation #29 be more accurate than the finer mesh version of #30.

#### Porosity Prediction Accuracy

So, how accurate are the porosity predictions when comparing the final setup, #29, with the recorded porosities in fig. 12.6 and table 12.1 on page 180 and on page 182?

The simulation predicts a probability for porosities at the centre of the casting for all three modulus sizes. The most common porosity sizes recorded for the middle control volume of the benchmark castings are microporosities (1) and small (2) porosities.

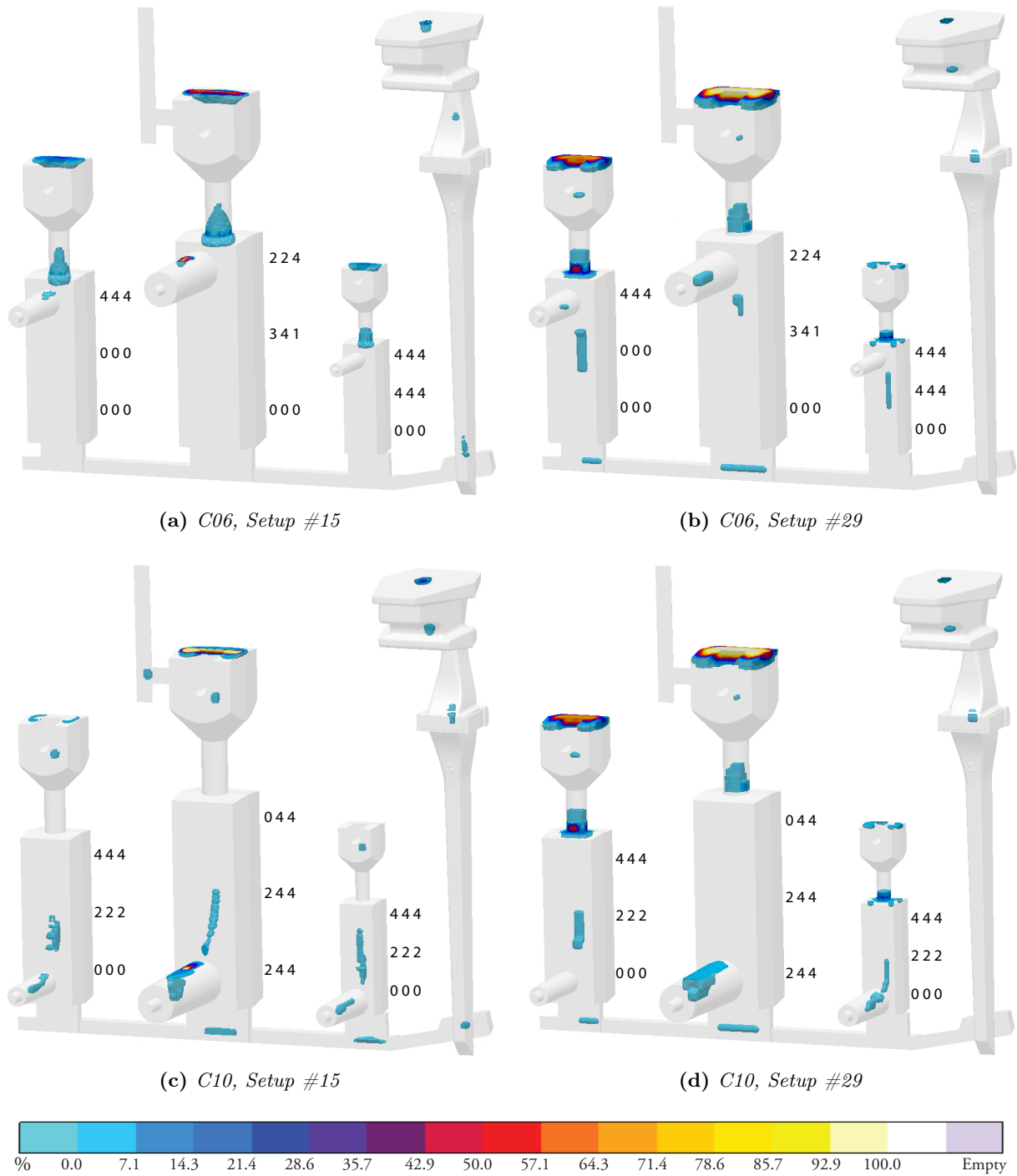


**Figure 12.24:** Porosity results for feeder configurations C06, C10, and C19. The simulations in the left shows simulations run with the parameters specified in #15 in 12.6, and the right side shows simulations run with the parameters specified in #29 in table 12.6 on page 224. The numbers next to each of the castings correspond to the recorded porosity sizes found with the ultrasound analysis listed in table 12.1 on page 180.

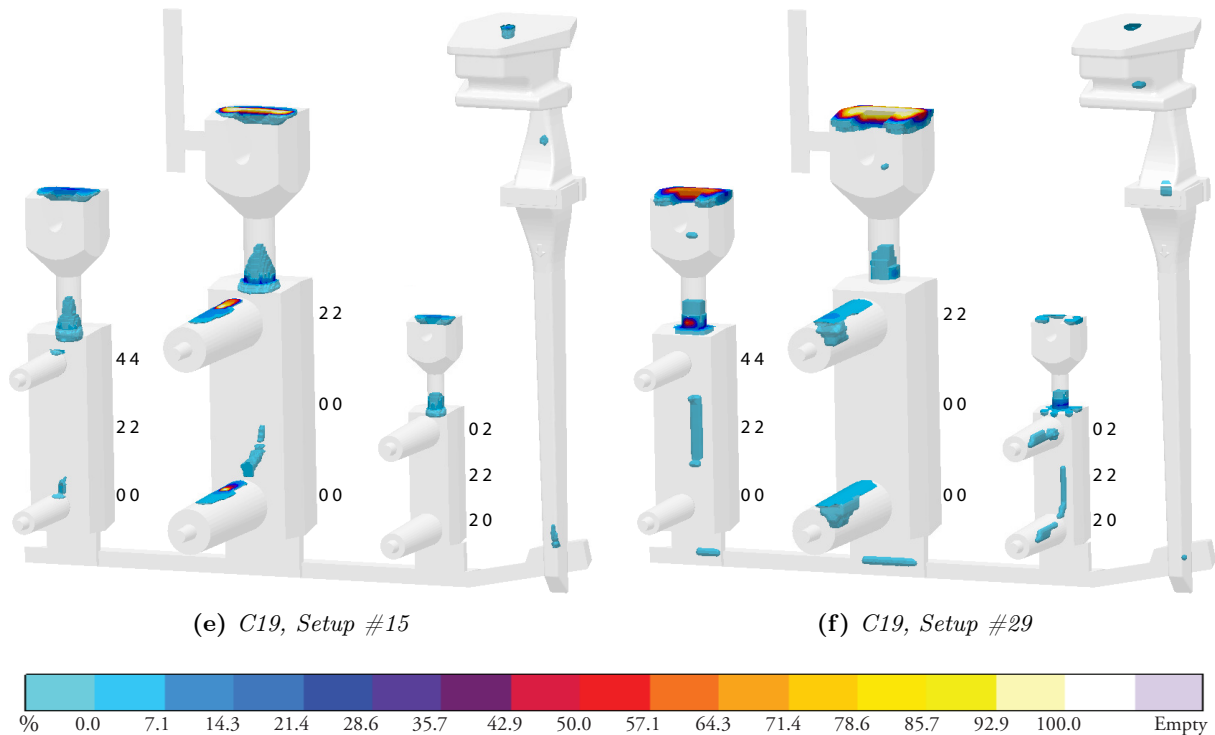


**Figure 12.24:** Porosity results for feeder configurations C06, C10, and C19. The simulations in the left shows simulations run with the parameters specified in #15 in 12.6, and the right side shows simulations run with the parameters specified in #29 in table 12.6 on page 224. The numbers next to each of the castings correspond to the recorded porosity sizes found with the ultrasound analysis listed in table 12.1 on page 180.

In this respect, the simulated predictions seem to indicate larger porosities in this region. However, no simulation parameter combination was found that predicted smaller porosities at the centre without also reducing the size of the porosities at the bottom of the pre-feeder neck considerably.

Note that the porosity prediction indicated by MAGMASOFT should be viewed as probabilities. There is a certain probability that a porosity will be located in the given area. Thus, for instance, the elongated porosity prediction found at the centre should be interpreted as an area in which one or more porosities of a given size may form.

The porosities at the top control volume are the next issue. The size of the porosities is deemed to be a good approximation of the porosities shown in fig. 12.6 on page 182. The predicted location, however, is not spot on. The simulations showed a tendency to have the porosities located inside the bottom part of the pre-feeder neck, while the sectioned castings in fig. 12.6 on page 182 show the porosities located inside the upper part of the casting below the pre-feeder neck, with the pre-

feeder neck itself apparently porosity-free.

Keeping these reservations about the porosity predictions in mind, the next step is to analyse how the simulations predict porosities for castings with feeders.

#### 12.4.2 Porosity Simulation Results

Figure 12.24 on page 226 and on this page shows the porosity results for the castings with feeder configuration C06, C10, and C19. All three are simulated with simulation setups #15 and #29 as described in table 12.6 on page 224. Next to each of the castings are listed the porosity sizes recorded in the ultrasound analysis. Hence, each of the columns of numbers represents a casting duplicate from table 12.1 on page 180.

##### C06 (12.24a,b)

Reviewing the porosity prediction in 12.24a the correlation between the measured and simulated porosities are not perfect. Remember that, follow-

ing the analysis in section 12.4.1, on page 222, the porosity prediction in the pre-feeder neck can be assumed to be found in the top control volume instead. Given this, the simulation predicts large (4) porosities in the top control volume which matches the ultrasound results. The ultrasound results, however, also show large (4) and medium (3) porosities in the middle control volume, which is not matched by the simulation. For the bottom control volume, both ultrasound analysis and simulation agree that this area is porosity-free.

The same feeder configuration, but with the other simulation setup is shown in 12.24b. Retaining the premiss of the pre-feeder porosities, this simulation predicts porosities at the top control volume. Note that the prediction shows a smaller amount of porosities at the pre-feeder neck for the sizeable M15 casting, which in part matches the ultrasound results. In addition to the simulation in 12.24a, this simulation also shows porosity probabilities at the centres of the three castings. Note, however, that the most massive porosity prediction is found in the M12 casting, which as the only one did not show porosities in that area in the ultrasound analysis. Finally, both ultrasound results and simulation agree that the bottom control volume is free of porosities.

#### C10 (12.24c,d)

The simulation in 12.24c is a partial success at best. In none of the three castings are the porosities at the top control volume predicted, though all except one of the castings in the ultrasound analysis had large (4) porosities in the area. The centre porosities are, however, predicted for all three castings. Also the prediction for the bottom control volume agrees that this area is porosity-free, except for the M15 casting which showed small (2) and large (4) porosities in this area. Note though, that the M15 casting of the C10 feeder combination was found to exhibit some casting defect, as shown in fig. 12.7b on page 184. What the simulation did show, however, is the tendency to form a porosity with contact to the surface, right above the bottom feeder, which is very similar to the open porosity formation found in both C10 B and C, and shown in fig. 12.7b on page 184.

The simulation of the C10 castings with the #29 parameter setup showed a better prediction of the porosities in the top control volume, though the prediction of the centre porosities for the M08 and M12 castings are similar to the other simulation. For

the sizeable M15 casting the porosity results predict no porosities at all, where the ultrasound showed large (4) porosities; though it should be remembered that some of these porosities may have had other causes than purely thermal and volumetric—likely inclusions or melt impurities as described in section 12.1.4, on page 181. For the bottom control volume, the porosity results show that the small M08 casting may have porosities in this area. Note, however, that this porosity is connected with the middle control volume as well, and maybe the probability definition is located in this area instead.

#### C19 (12.24e,f)

The final feeder configuration is the C19, which has feeders at both the upper and lower feeder position. Figure 12.24e on page 227 shows a good correlation between the ultrasound results and the simulation for the top control volume. The size of the pre-feeder neck shrinkage roughly accounts for the large (4) porosities observed in the ultrasound analysis. The same pre-feeder neck shrinkage for the M08 and M15 castings are assessed to be too large to correspond to the small (2) porosities found with the ultrasound. The prediction of the centre porosities is not very good. M08 and M12 are predicted to be porosity-free; however, these are the only two casting sizes that show porosities in the ultrasound analysis. The M15 casting, on the other hand, is predicted to have porosities at the centre, though, this was the only casting size that was found *not* to have porosities in this area. For the bottom control volume, the ultrasound results show an indication of porosities in the M08 casting, which is not mirrored by the simulations. Subsequently, the M12 and M15 castings are predicted to show porosities but yielded none in the ultrasound analysis. Additionally, it should be noted that the simulation predicts an open porosity over the lower feeder of casting M15, as was also seen in 12.24c. In this case, however, this open porosity—or any other porosity in this control volume for that matter—was not observed in the ultrasound analysis.

In the final simulation, shown in 12.24f, all three castings are predicted to have porosities at the top control volume. The scaling of the predicted porosities seem to match for the M12 casting, and with a small exaggeration also for the M15 casting. The M08 casting is predicted to have a little more porosities than was recorded by the ultrasound analysis. The middle control volume predicts porosities for

castings M08 and M12 which matches the ultrasound results. Additionally, the simulation predicts a porosity-free centre for the sizeable M15 casting, which is supported by the ultrasound results. The size of the predicted porosities may be a bit large, but not overly large compared with the ultrasound records. Finally, for the bottom control volume, the castings are predicted to be porosity-free for the M12 and M15 castings, while the small M08 casting was predicted to have a small (2) porosity in the area. All three of these predictions match the results of the ultrasound analysis. In general, the 12.24f can be said to have the best correlation between casting results and simulation of all the porosity results presented here.

### 12.4.3 Sub Conclusions

There has been a good correlation between the simulated results and those recorded as part of the porosity quantification analysis in section 12.1, on page 175 in a few cases. Moreover, this is the general problem. If it is not possible to set up a simulation with a fixed set of simulation parameters, then it becomes retrofitting rather than predicting. The simulation needs to be set up and calibrated properly. However, this should be a one time job as long as the processing conditions are kept constant.

The difficulties of simulating this particular alloy and setup can be multiple. First of all, it is assessed that the main issue is with the criteria functions, rather than the underlying simulation itself. Thus, if trouble like these arises with the porosity results, it is suggested that one revert to analysing other simulation results like temperature, thermal gradients, and fraction liquid.

It is believed that one of the significant issues with the constancy of the simulated predictions relates to the alloy itself. It seems as if the alloy exhibits freezing and feeding properties usually related to steel and Al alloys. This behaviour is indicated by the influence of the feeding effectivity factor had on the simulated results in correlation to the analysis of the castings. This influence, again, indicates that alloy had a reduced feedability which is not typical of cast iron.

The need of activating the feeding effectivity parameter may very well hinder the proper function of the feeding algorithm use in MAGMAiron, thus making it impossible for the simulation to yield the right results. However, this also relates to the amount of porosity achievable with the feeding effectivity

set to 100%. The graphite precipitation factor yielded almost no change in the amount or location of the porosities. Even with a graphite precipitation factor of 1, the simulated amount and location of porosities were very different from what was found in the porosity quantification of the castings.

Thus, this may be a case where one factor being off, and the subsequent correction of this by adjusting a different parameter, just destabilises the house of cards further, forcing new adjustments, and so forth.

One parameter that should, in principle, be independent of all the other parameters is the mesh cell size. For cases where casting results and porosity predictions do not match up, a quick simulation with a coarser mesh may solve this, though this break with the principle that a single simulation, when setup correctly, will yield all answers in one go. Simulating different versions of the same casting geometry, with different simulation setups, to faithfully predict different categories of results is not a favourable solution—however it may be what is necessary until the state-of-the-art of casting simulation has progressed further.

Whether or not other simulation software than MAGMASOFT will yield the same problems as described above remains to be tested. Ultimately it depends on the assumption made in the underlying modelling, the definition of the criteria functions in that particular software, as well as the threshold values delimiting the property handling of the individual cells. Software based on a fundamentally different modelling approach may very well be free of the above mentioned issues, though it is equally likely that the software has other challenges of its own.

## References

- [24] John Campbell. *Casting Practice - The 10 Rules of Casting*. Linacre House, Jordan Hill, Oxford OX2 8DP, 30 Corporate Drive, Burlington, MA 01803: Elsevier Butterworth-Heinemann, 2004. ISBN: 0 7506 4791 4.
- [27] PD Lee, A Chirazi and D See. “Modeling Microporosity in Aluminum-Silicon Alloys: A Review”. In: *Journal of Light Metals* 1.1 (2001), pp. 15–30.
- [69] MAGMASOFT 5.2 by MAGMA GmbH. [http://www.magmasoft.com/en/solutions/MAGMA\\_5.html](http://www.magmasoft.com/en/solutions/MAGMA_5.html). Program. 2014.

- [79] MAGMASOFT *5.3* by Magma GmbH. [http://www.magmasoft.com/en/solutions/MAGMA\\_5.html](http://www.magmasoft.com/en/solutions/MAGMA_5.html). Program. 2015.
- [92] Nikolaj Kjelgaard Vedel-Smith. “Obtaining Comparable Simulation and Thermal Measurement Results in Sand Moulds”. In: Presented at the Nordic MAGMASOFT User Meeting , Svedala, Sweden, 2012.
- [111] MAGMASOFT, FOSECO *Sleeve Database*. [http://www.magmasoft.com/en/solutions/MAGMA\\_5.html](http://www.magmasoft.com/en/solutions/MAGMA_5.html). Database. 2012.
- [118] MAGMASOFT, FOSECO *Filter Database*. [http://www.magmasoft.com/en/solutions/MAGMA\\_5.html](http://www.magmasoft.com/en/solutions/MAGMA_5.html). Database. 2012.
- [119] *JMatPro* by Sente Software Ltd. <http://www.sentesoftware.co.uk/jmatpro.aspx>. Program.
- [136] K.M. Pedersen and N.S. Tiedje. “Temperature Measurement During Solidification of Thin Wall Ductile Cast Iron. Part 1: Theory and Experiment”. In: *Measurement* 41.5 (2008), 551–560. ISSN: 0263-2241. DOI: {10.1016/j.measurement.2007.05.002}.
- [137] K.M. Pedersen and N.S. Tiedje. “Temperature Measurement During Solidification of Thin Wall Ductile Cast Iron. Part 2: Numerical Simulations”. In: *Measurement* 41.4 (2008), 341–348. ISSN: 0263-2241. DOI: {10.1016/j.measurement.2007.05.003}.
- [139] R.W. Heine. “The Fe-C-Si Solidification Diagram for Cast Irons”. English. In: *AFS Proceedings* 94 (1986), pp. 391–402.
- [145] *An Introduction to Ultrasonic Material Analysis*. <http://www.olympus-ims.com/en/applications-and-solutions/introductory-ultrasonics/introduction-material-analysis/>. Program.
- [146] *X-Ray Systems for Universal Deployment in 2D and CT Inspection*. <http://www.yxlon.com/Products/X-ray-systems>. Machine.
- [147] Guido Busch. “What’s New In MAGMA Release 5.3”. In: Presented at the International MAGMASOFT User Meeting , Potsdam, Germany, 2014.

## Discussion

<b>13.1 Introduction</b> . . . . .	<b>232</b>	<b>13.6 Effects of Feeding Parameters</b> . . . . .	<b>244</b>
13.1.1 Definition of Terms . . . . .	232	13.6.1 Feeder Modulus . . . . .	244
<b>13.2 Purpose and Objectives</b> . . . . .	<b>232</b>	13.6.2 Sleeve Material . . . . .	246
13.2.1 Feeding Requirement and Modulus Relationship . . . . .	232	13.6.3 Feeder Location . . . . .	248
13.2.2 Grading the Feeder Efficiency . . . . .	233	<b>13.7 Solidification Behaviour</b> . . . . .	<b>251</b>
13.2.3 Simulate Feeding of Secluded Sections . . . . .	233	<b>13.8 Driving Forces</b> . . . . .	<b>252</b>
13.2.4 Feeder Location . . . . .	233	13.8.1 Graphic Explanation . . . . .	253
13.2.5 Multiple Feeders . . . . .	234	13.8.2 Volume Contraction . . . . .	254
13.2.6 Design for Analysis . . . . .	235	13.8.3 Shell Compression . . . . .	254
<b>13.3 Process Stability</b> . . . . .	<b>236</b>	13.8.4 Graphite Expansion . . . . .	255
13.3.1 Statistical Porosity Sum Analysis . . . . .	236	13.8.5 Other Forces . . . . .	257
<b>13.4 Scalability of the Experiment</b> . . . . .	<b>239</b>	13.8.6 Pressure Loss . . . . .	257
13.4.1 Scalability of the Castings . . . . .	239	13.8.7 Feeding Requirement . . . . .	260
13.4.2 Scalability of the Feeders . . . . .	240	13.8.8 Other Factors . . . . .	261
13.4.3 Influence of Scaling Error . . . . .	242	<b>13.9 Feeding Regimes</b> . . . . .	<b>265</b>
<b>13.5 Shrinkage Defect Identification</b> . . . . .	<b>242</b>	13.9.1 Initial Feeding . . . . .	266
13.5.1 Centreline Porosities . . . . .	243	13.9.2 Expansion Feeding . . . . .	266
13.5.2 Surface Shrinkage . . . . .	243	13.9.3 Directional Feeding . . . . .	267
		<b>References</b> . . . . .	<b>267</b>

» DISCUSSION of the validity of the experiment and the limitations of the porosity analyses. The process stability is evaluated based on the recorded porosities, and a comparison of the feederless benchmark castings and the castings with feeders is presented. Subsequently, the effect of the different feeding parameters examined in the experiment is discussed, and the underlying driving forces that transport the melt is also dissected, analysed, and explained. This includes the influence of the pressure loss caused by the solidification of the casting and the influence of feeding requirement. Finally, the three stages of the basic feeding regime is described.

Keywords: . . . . . Discussion, Experiment Design, Statistical Process Stability, Scalability, Feeder Location, Multiple Feeders, Solidification, Modulus, Feeding Forces, Feeding Requirement, Pressure Loss, Feeding Factors, and Feeding Regimes.

Chapter findings reported in: . . Supplement IV, on page 337

Computer Aided Design (CAD), Compacted Graphite Iron (CGI), Coordinate Measurement Machine (CMM),

Heat Transfer Coefficient (HTC), Modulus Extension Factor (MEF), Magnesium (Mg), Spherical Graphite Iron (SGI)

## 13.1 Introduction

---

THIS chapter comprises the discussion of the second part of the dissertation and will address the most important parts of the method, the experimental design, the results, and the subsequent implications and hypotheses. The discussion will mainly be based on the information given in the two previous chapters, chapter 11, on page 157 and chapter 12, on page 175, as well as chapter 2, on page 13, and chapter 3, on page 39. However, where it is necessary to support the validity of the arguments, additional theories and references are presented.

The discussion is divided into subsections, each addressing different aspects of the research.

The focus of the discussion will start at the basics of the experimental setup and scientific method, then continue to evaluation of the results and their implications, and finish with the proposal of a theoretical explanation of the observed phenomenon.

### 13.1.1 Definition of Terms

---

To avoid confusion in the subsequent discussion and theory proposal, a few terms have to be defined.

**Driving Forces** are all the forces acting on the feed material to transport this from one position to another. The forces can act in the same direction adding up, or working against each other to limit each others effect. An unmoving feed material is a result of the driving force sum being zero.

**Feed Material** encompasses all material that is moved in the casting. Typically this would be liquid, but it can also be a semi-solid slurry or a solid. Feed material is used as a term because it encapsulates all five feeding mechanisms in one term without specifying one over the other.

**Feeding Mechanism** relates to the five mechanisms of feeding described by Campbell [25], and described in section 2.4, on page 30.

**Feeding Regime** as a term encompasses the entire feeding event, including the available conditions, the driving forces, and the mechanisms. Here the feeding regimes are used to describe the correlation between the conditions, the driving forces, and the feeding mechanisms.

## 13.2 Purpose and Objectives

---

THE success of the experiment should be judged based on the results concerning the purpose of the investigation. At the beginning of chapter 11, on page 157, six requirements were defined for the design and construction of the generic, scalable castings which was to substantiate the trials, which further relates to hypothesis 5: *The side feeder modulus necessary to feed SGI is not a linear function of the casting module, and traditional methods overestimate the feeder size.* Hence, the requirements can be seen as an outline for the experiment as a whole, and not just the casting design alone. Note, however, that while the casting design may fulfil the requirements, the experiment may not, and vice versa.

The six requirements were:

1. Feedability and feeding requirement for different modulus sections
2. Grade the feeder efficiency
3. Simulate feeding of secluded sections
4. Importance of feeder location (pressure height)
5. Influence of multiple feeders
6. Designed for easy and accurate analysis

### 13.2.1 Feeding Requirement and Modulus Relationship

---

The casting design completely conforms to the requirements of scalability. The casting design was developed and tested before the experiment, and the subsequent analysis of the castings, both with and without feeders, has shown a precise scaling of the casting modulus. The solidification of the pre-feeder neck was also shown to scale with the casting and to close off at the intended time. The cooling curves of the three modulus castings had a good coherence with the simulated results, and the additional simulations indicated that the cooling times scaled reasonably both for the measured cooling curves, as well as the simulated cooling curves.

The unintended scaling of the middle modulus casting described in section 11.2, on page 167 prevented a full comparison of the three modulus castings. However, the feeders used for the M12 casting did still overlap the proportional modulus ( $M^\infty$ ) ratio decided for the castings. Thus, additional information was gained about the very low  $M^\infty$  feeders for the M12 casting, while the large  $M^\infty$  feeders were



missing. Some scalability was lost; however, the M12 data are not invalid although conclusions of the scalability should consider the influence of the absent data.

### 13.2.2 Grading the Feeder Efficiency

---

The casting design, as well as the choice of feeder sizes and casting alloy, was focused on ensuring that porosities would remain after feeding. This experimental design approach was based on the experiences from Part I, where the efficiency of some of the feeder combinations could not be rated, simply because the scale was insufficient. If both solutions provide porosity-free castings, then the solutions cannot be distinguished. Thus, the design was intended to ensure that all feeder combinations would retain some measure of porosities.

In this respect, the casting design failed. Two of the 207 castings were found to be porosity-free. However, as none of the combination groups was without porosities, it can be assumed that the porosity-free castings were close to the limit of the feeder. In this respect, the correlation between the number and size of the porosities and the feeders ability to feed the casting was perfectly adjusted.

The other aspect of the grading was the evaluation of the number and size of porosities. While the scale of 0-4, from porosity-free (0) to large (4) porosities, was a convenient and straightforward way to quantify the number and size of the porosities found in each casting, it could have been supported by another quantification of the porosities. This additional scale would possibly have provided additional nuances to the experimental data. Depending on the method chosen, this might also have provided a better quantification of the large (4) porosities.

The open-ended nature of the 0-4 grading scale made it difficult to precisely quantify the number and size of porosities with and without feeders. The large (4) porosities classification was the most used grade of the scale. In hindsight, the scale should have been more refined, especially for the large porosities. How this scale was to be divided and distributed is unanswered. The same goes for how the analysis should be performed. A more detailed analysis using ultrasound could be performed. However, the nature of the analysis limits how detailed the size of the porosities can be judged. A more refined scale would thus also increase the risk of misjudged or misinterpreted porosities, which would be even worse than a coarse scale.

### 13.2.3 Simulate Feeding of Secluded Sections

---

The casting design with the pre-feeder was, as a secondary priority, designed with the intent to simulate secluded casting sections, separated from the regular feeding path by a thin-walled section that solidifies early in the process.

There are no direct criteria by which this requirement can be assessed. The pre-fed main part of the casting was subjected to the same type of primarily solidification shrinkage, that might be found in secluded sections. This behaviour, however, was part of the design and has not been tested as part of the trials or analyses.

What is of interest regarding secluded sections, though, is the correlation between the type, size, and location of the feeders, and the solidification of the pre-feeder neck. Here it was found that the upper feeder directly influenced the feeding path through the pre-feeder neck. Interestingly, though, it was found that the feeding path closed off sooner with the presence of an upper feeder. The implications of this are discussed further in section 13.6.3, on page 248.

### 13.2.4 Feeder Location

---

Two different feeder locations were used during the experiments; an upper location close to the pre-feeder neck, and a lower location close to the ingate. As the casting geometry and solidification is similar at the top and the bottom, the main difference between the feeding conditions of the two locations was the difference in ferrostatic pressure. Hence, the lower feeder had to overcome the entire ferrostatic pressure of the casting, while the upper feeder only had to overcome the influence of the pre-feeder. Note that the solidification of the pre-feeder neck would negate the pressure; hence the upper feeder would operate under a neutral pressure state. This pressure, however, is still less than a traditional gravity feeder that uses gravity to move the melt into the casting.

The analyses have shown that the secondary feeding mechanisms can make use of a lower feeder. The lower feeder functioned best for, the larger M15 castings; the lower feeder was less efficient for the M08 and M12 castings. When used without a supporting upper feeder, the best results were achieved

with the lower feeders that had a proportional modulus of  $1.00 M^\infty$ . However, the lower feeders were also found to be able to increase the number and size of porosities in the casting. This side-effect was seen for the M15 casting with a large  $1.27 M^\infty$  lower feeder, with no upper feeder for support. See figs. 12.10 and 12.12 on page 190 and on page 195. This casting had large (4) porosities at all three control volumes for two of the three castings in the group.

What happened was that the casting fed the feeder, rather than the other way around. See table 12.1 on page 180.

What is interesting is that, regarding the modulus ratio between the casting and the feeder, the feeder should stay liquid longer and thus being able to feed the casting as it solidifies. Similarly, it is interesting that the feeder with equal or smaller proportional modulus can feed the casting; which should solidify later than these smaller feeders. It should also be noted that the solidification time of the feeders is of course also affected by the presence of the casting. However, the cooling surface of the sleeved feeders is relatively smaller, hence the total cooling time of a sleeved feeder with a proportional modulus, do solidify later than the casting. This is seen for the C06 feeder combination in figs. 12.20 to 12.22 on pages 218–220.

The casting modulus was observed to play an essential role in the success of a single lower feeder. Only the sizeable M15 casting showed any promising results with these feeder combinations. Additionally, the  $1.00 M^\infty$  lower feeder performed very well while smaller proportional moduli were insufficient, and the larger  $1.27 M^\infty$  had the effect of creating porosities in the castings. Note, however, that the same feeder located at the upper part of the large M15 casting did not perform nearly as well as when located at the lower position. Hence, differences occur that significantly change the feeding conditions between the upper and lower feeder locations.

For the specific conditions examined in this research, it can be said to be possible to feed from the bottom up against gravity and the ferrostatic pressure of the casting. However, it was also found that the ‘window for feeding’ was very narrow and a specific set of conditions probably have to be present to enable this feeding opportunity.

### 13.2.5 Multiple Feeders

The combined efficiency of multiple feeders feeding

the same section was also part of the experiment. The intent was to examine the co-functioning of two feeders to obtain a better understanding of the fundamental feeding mechanisms governing the process. Additionally, it was sought to investigate if combinations of different modulus upper and lower feeders could achieve improvements not achievable with a single feeder solution.

Figures 12.20 to 12.22 on pages 218–220 illustrate how the combination of two feeders changes the solidification of the casting. The shape of the solidifying melt was changed. Viewing the castings with a single upper or lower feeder, the natural ellipsoid of the base casting was retained but drawn towards the feeder. However, the solidification mostly progresses uniformly from all sides, except the feeder. The result was similar to a deflating balloon. The castings with two feeders, on the other hand, they had a solidifying geometry similar to a tube, connecting the two feeders.

According to the geometric solidification analysis, the total solidification time was only marginally prolonged for the casting with two feeders, as compared with the single feeder combinations of the same or similar modulus. However, the centre of the casting was held liquid longer, providing a more directional solidification from the surface of the casting towards the centreline. This central channel of liquid melt was kept open for feeding almost to the end of solidification, thus allowing the upper feeder to reach the entire length of the casting at the end of solidification. This prolonged opening of the feeding path is supported by the x-ray analysis which shows that the lower feeder of casting C19A had a solid lower feeder and a well emptied upper feeder. See fig. 12.13 on page 201. However, the casting only had a small (2) porosity at the top control volume. It is proposed that the lower feeder has assisted the upper feeder by extending the feeding length and ensuring an open feeding path along the length of the casting until the end of solidification.

While the castings with the C19 feeder combination illustrated the co-functioning of the two large feeders, the best results were achieved with two smaller feeders and of different sizes. Both the C20 and C22 groups had castings that were classified as porosity-free. As for the C19 feeder combination, both the C20 and C22 feeder combinations featured feeders of different sizes: A  $1.00 M^\infty$  upper feeder and a  $0.80 M^\infty$  lower feeder for the M15-C20, and a  $0.80 M^\infty$  upper feeder and a  $1.27 M^\infty$  lower feeder for the M15-C22. Note that the C20 combination

had the large feeder at the upper position, while the C22 combination had the large feeder at the lower position.

Comparing this with the geometric solidification analysis of the C19 castings, the optimal feeder combination appears to be two feeders of different modulus size. Apparently, this combination ensures a prolonged feeding path, which stays open almost until the end of solidification; but also retain some direction of solidification towards the largest of the two feeders, enabling the large feeder to feed the last part of the casting that solidifies. Note, that the interchangeable positions of the large and the small feeder indicate that the driving forces that move the melt function independently of both gravity and the ferrostic pressure.

Viewing the solidification pattern shown in figs. 12.20 to 12.22 on pages 218–220 the changed direction of solidification aids the formation of a solid shell surrounding a liquid centre. Hence, it can be speculated that the feeding effect is, in part, achieved by the changed thermal gradients provided by the second feeder, rather than the feed material it provides. The changed gradients aid shell-forming, which in turn strengthen the impact of the driving forces.

While the large M15 castings showed promising feeding results with a combination of two feeders, the smaller M08 and M12 castings were less convincing. See figs. 12.11 and 12.12 on page 192 and on page 195. An effect of two feeders was observed for both the M08 and the M12 castings, note however that none of the smaller castings was found to be porosity-free.

The best results for the small M08 casting was achieved with either two large  $1.25 M^\infty$  feeders, or with two small feeders. The combinations of promising small feeders were with a  $0.63 M^\infty$  upper feeder, and either a  $0.75 M^\infty$  or  $1.00 M^\infty$  lower feeder. Again note that the largest feeder was located at the lower position. The inverse combination with a  $1.00 M^\infty$  upper feeder and a  $0.75 M^\infty$  lower feeder produced significant extra porosities. Hence, for the M08 casting, the feeders were not interchangeable, indicating a complex feeding mechanism with a narrow window for feeding.

The M12 casting had no feeders larger than the castings modulus. Of the feeder combinations tested, the combinations without a lower feeder functioned best. Only one combination with a lower feeder managed to reduce the overall porosity sum. This was the  $0.50 M^\infty$  upper feeder combined with

the  $0.66 M^\infty$  lower feeder. Hence, the two smallest feeders tested for the M12 casting.

The differences in function of the feeder combinations across the three modulus castings indicate that the solidification of the three castings progresses significantly different and that the same approach to feeding cannot be expected to yield comparable results. As the horizontal spot feeders depend on internal forces to drive the melt from the feeder into the casting, these differences in solidification would be expected to be more pronounced for these feeders than for their traditional gravity driven counterparts.

This statement is not to say that a two feeder combination cannot function for the smaller modulus castings. Figures 12.11 and 12.12 on page 192 and on page 195 show some effects. However, these smaller modulus castings require different feeder combination than for the larger M15 castings, and possibly also more exact feeder modulus combinations. Another observation made during the geometrical solidification analysis was that while the M15 exothermic feeders stayed liquid until almost all of the casting had solidified, the proportionally equivalent feeder of the M08 casting had begun to form a shell already at the initiation of the solidification process. See figs. 12.19 to 12.22 on page 216 and on pages 218–220. While the M08 feeders remained liquid until the casting had solidified, the shell-forming may prevent a free flow of the melt into the castings while there is still a liquid zone at the centre of the feeder. Once the centre of the feeder begins to solidify, the partially solidified melt would require a larger force to move it from the feeder and into the casting.

### 13.2.6 Design for Analysis

The analyses of the castings, both ultrasound, x-ray, and sectioning, worked well. The square design enables easy porosity detection using ultrasound, including the possibility to analyse the porosities from two perspectives. The pre-feeder neck, the pre-feeder, and the feeders were not suitable for ultrasound analysis. They were, however, never designed to be and this limitation was known at the time of the casting design. This limitation of the ultrasound analysis was, however, made up for by the x-ray analysis and the sectioning of select castings.

The geometry functioned well for the x-ray analysis. However, the vast difference in thickness

between the pre-feeder neck and the casting itself required multiple images to analyse all parts of the casting properly. The same was the case for some of the feeders. The x-ray had two main drawbacks: (1) The M15 casting was too thick to transilluminate appropriately, and (2) the resolution (sharpness) of the images did not allow for detection of small porosities. Both of these limitations relate to the equipment and the technology itself; hence it cannot be a shortcoming of the casting design.

A useful addition to the casting design would have been a ruler engraved into the corner of the casting. The ruler would have provided a direct visible reference on all castings that could easily be used as a size and location indication. Additionally, the different control volumes could be marked in the same manner to ensure a definite distinction between the control volumes, rather than a subjective assessment made for each casting.

### 13.3 Process Stability

THE experimental setup was centred around the scalable geometry for testing the performance of different modulus castings, or sections. The main purpose of the casting design was to produce castings with a comparable amount of porosities regardless of pouring temperature. 57 of the 60 castings cast without any feeders had large (4) porosities at the top control volume. Two had a small (2) and a medium (3) porosity at the top control volume instead, while the final casting was porosity-free at the top, but had a large (4) porosity at the middle control volume.

As described by Kainzinger, the porosity location can vary within the volume of the thermal centre [117]. Though, Kainzinger's experiments were horizontal Y-blocks, where the porosities shifted mainly along the length of the block and did not display considerable variation in the height location. However, the casting geometry was designed to produce a comparable amount of total shrinkage, hence sum of porosities was chosen as the best representation of the performance of the castings, in terms of stability.

#### 13.3.1 Statistical Porosity Sum Analysis

The castings were divided into two groups: The C01 without feeders, and the C02-C22 with feeders. A statistical comparison of the sum of porosities for castings with and without feeders, for each of the

three different casting modulus sizes, was then used to evaluate the stability of the benchmark castings, and subsequently the influence of the feeders. Note that the statistical analysis was based on a limited population.

The statistical analysis of the porosity sum of the different modulus castings can be found in fig. 13.1 on the facing page for the benchmark castings without feeders, and in fig. 13.2 on page 238 for all the castings with one or two feeders.

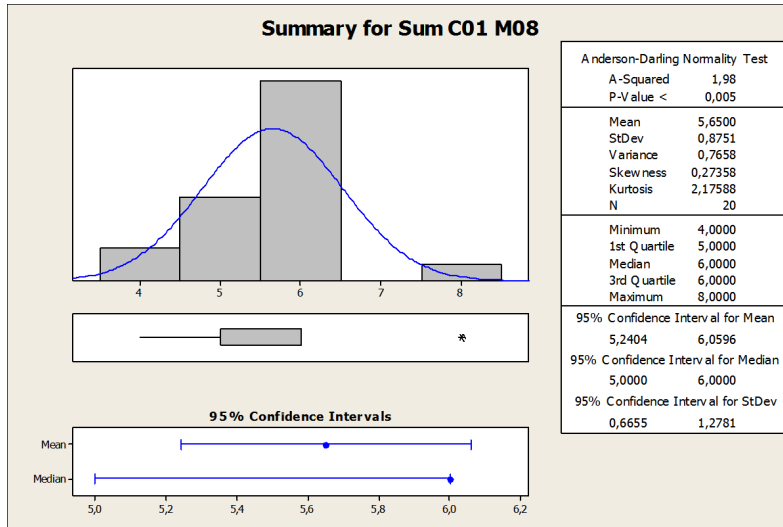
#### Castings without feeders (C01)

The statistical analysis of the benchmark castings shows that the three modulus castings had a porosity sum of 5.65, 5.30, and 5.15 respectively for the M08, M12, and M15 castings. Hence, the larger the casting modulus, the lower the average (mean) porosity score. As the porosity evaluation scale was absolute concerning porosity sizes, this indicates that the larger casting moduli do not naturally produce larger porosities. However, the estimate of the porosity sizes as they were recorded was subjective and performed by a human operator. The scalability of the castings considered, it would be an easy mistake for the operator to unknowingly evaluate porosities for the larger castings, as relatively smaller due to the comparison of the porosity size to the size of the castings. This said about scalability, a small relative difference caused by an evaluation error, do not change the general comparison of the scalable castings. Note that the comparison between the castings of the same size is unaffected by this. Additionally, larger modulus casting and sections are known to exhibit a greater graphite expansion due to the prolonged graphite precipitation [23]. See fig. 2.7 on page 22.

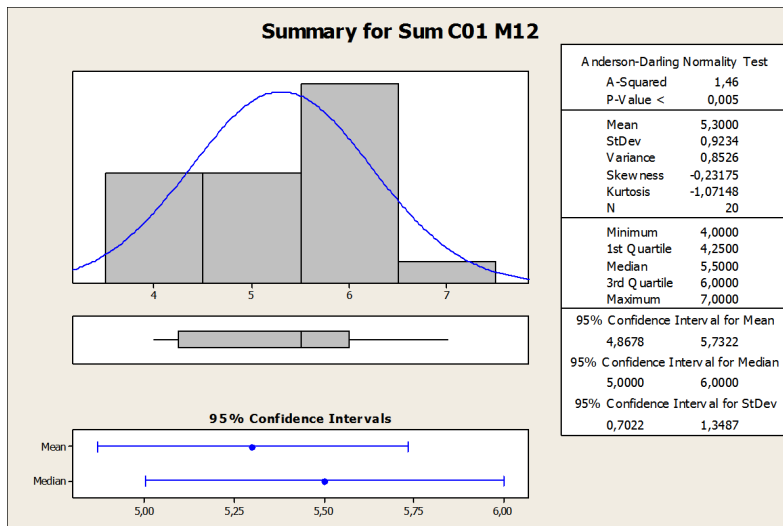
The three casting moduli produced a comparable amount of porosities, though the dispersion of the data varied between the different casting sizes. The feederless castings did also produce castings with either increased or decreased amounts of porosities. The variation for the castings without feeders was used to evaluate the likelihood of a similar porosity sum to occur for a casting with feeders, and thus supported the porosity evaluation of castings with similar or identical feeder combinations.

#### Castings with one or two feeders (C02-C22)

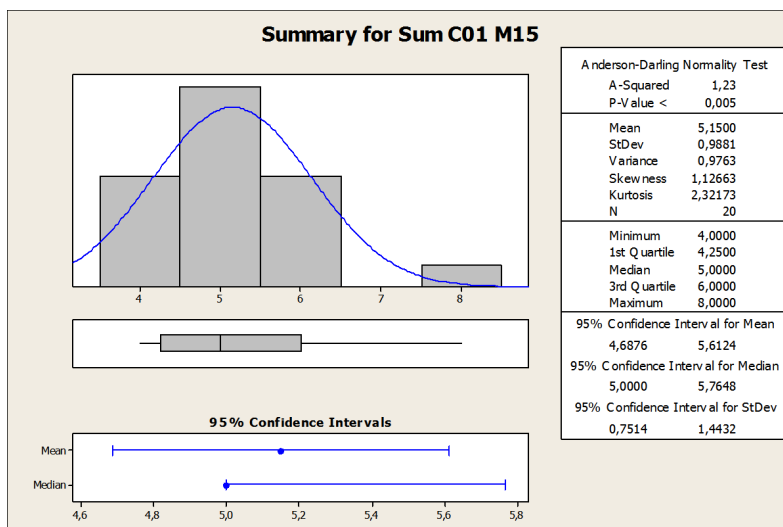
The castings with feeders have comparable porosity sum averages for the M08 and M12 castings, with



(a) C01-M08: Porosity Statistics

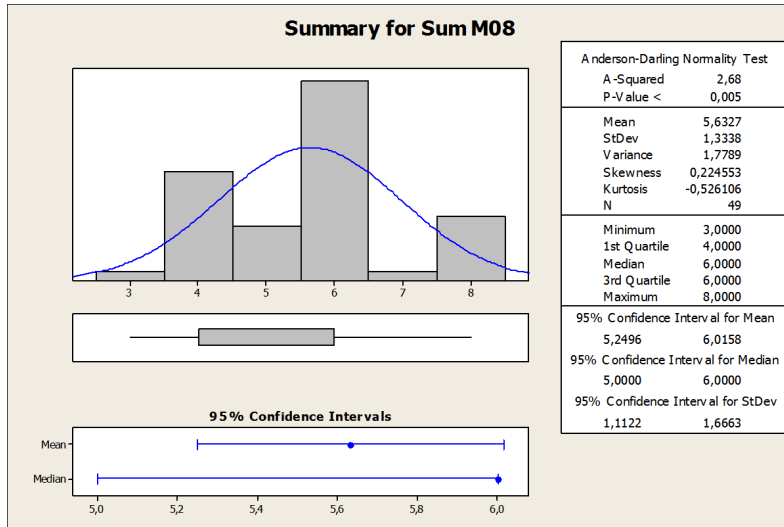


(b) C01-M12: Porosity Statistics

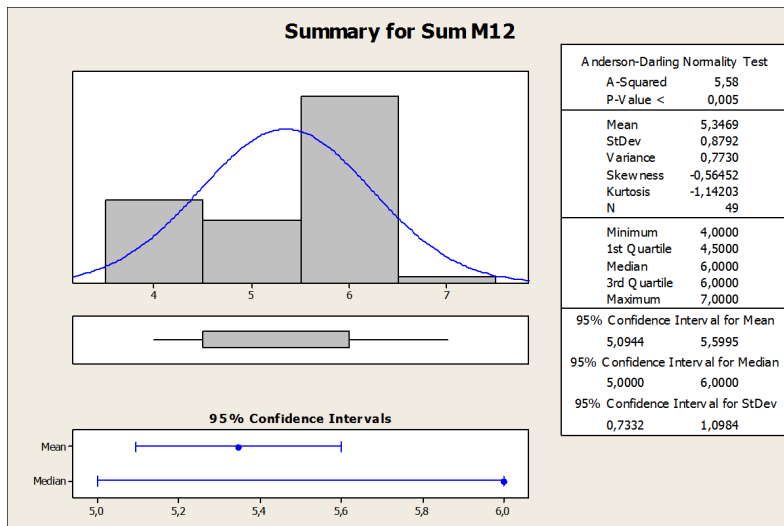


(c) C01-M15: Porosity Statistics

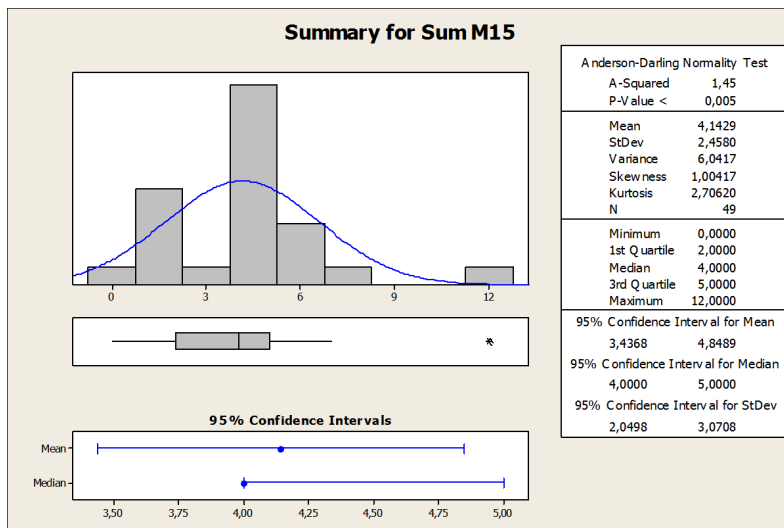
Figure 13.1: Porosity Statistics: Benchmark castings without feeders (C01).



(a) M08: Porosity Statistics



(b) M12: Porosity Statistics



(c) M15: Porosity Statistics

Figure 13.2: Porosity Statistics: Castings with feeders (C02-C22).

5.63 and 5.35 respectively. The M12 castings had more porosities on average, for the castings with feeders. The M15 casting had a significant reduction in the average sum of porosities from 5.15 to 4.14. However, the average is not an adequate measure of the effect of the feeders, as several different configurations were examined during the trials. The dispersion of the data of the castings with feeders was much more significant for the M08, and M15 castings, which is also indicated by the increased the variance ( $\sigma^2$ ) in fig. 13.2 on page 238. The M12 castings, on the other hand, had a smaller standard deviation and less variance with feeders, then without, though only a little. The difference, however, is not significant.

In fact, the distribution plots in fig. 13.1 on page 237 and in fig. 13.2 on page 238 show that the castings with a lower porosity sum were counterbalanced by castings with more porosities. This opposed feeding behaviour underlines that feeders can have an unintended and unwanted porosity increasing effect if not used correctly. Additionally, the relatively narrow range of feeders examined during the trials emphasises that the difference between a successful feeding of a casting, and a feeding that will introduce additional porosities, is small.

#### Evaluation of Process Stability

A control group without variation would be fantastic; however, this is seldom the case. In the case of castings and porosities, in particular, these have an in-built uncertainty which is expressed in fig. 13.1 on page 237. Designing castings to avoid porosities can be difficult; however, these casting designs can make use of a safety factor to ensure within a specified confidence interval, that the casting should be porosity-free. Even then, that is not always the case. To design a casting to produce the same amount of porosities every time can be said to be the same task, without the possibility of a safety factor.

The statistical analysis in fig. 13.1 on page 237 is considered a valid indication of the variation that must be expected for the given castings, at the given production conditions. Note, however, that none of the six groups can satisfy the null hypothesis of a normal distribution of the number and size of the porosities, as the P-Values are all below 0.005. The population of 20 castings per group may be too low to accurately establish if the variation of the porosities adheres to the normal distribution, or another type of distribution for

that matter. Especially not for a population that comprises so many different process variables, from castings conditions to the porosity analysis.

The increased stability of the M12 casting with feeders may be related to the proportional scaling of the feeder for this castings. As shown in chapter 12, on page 175, the large feeders had a significant influence on the castings, both regarding reducing, but also by introducing, porosities. This effect is supported by the M12 casting being the only casting that has less variation with feeders than without.

It is evaluated that the experimental setup and the analysis results are valid as an evaluation of the number and size of the porosities in the castings. However, the process variation should be noted and considered when concluding on the findings.

## 13.4 Scalability of the Experiment

THE experiment was designed to investigate the feeding of different modulus sections to better understand how the feeding mechanisms function with respect to the solidification differences occurring as a consequence of the inherently different cooling conditions. This understanding is important in order to optimise feeders and their application with respect to both process stability and energy savings.

Subsequently, the deductions made from the experiments must be based upon a valid assumption of the scalability and actual scaling of the castings and feeders.

### 13.4.1 Scalability of the Castings

The scalability of the castings was based on a generic geometry scaled according to a modulus governed solidification time. This setup was chosen to ensure correct scaling and ensure that the geometric influences in cooling could be negated. On the other hand, this in some respect also limits the experiment to the given generic geometry. Other geometries with the same moduli as the ones used in the experiment, may scale differently with regard to feeding performance as described by Hansen et al and Tiryakioğlu et al [22, 39]. The present research has not included different geometrical combinations; other geometries with the same modulus as the castings tested, may perform in a different manner as relayed by Chovorinov and Hansen et al [21, 22] and described in section 3.4.3, on page 54. Though other

castings with similar modulus may perform differently; the alloy composition and general process conditions will probably have a greater influence on the result than the geometry itself. With the exception of geometries that greatly differ from the basic geometries.

The thermal analysis of the three different casting sizes demonstrated an excellent thermal scalability of the castings. The thermal comparison of the measured and simulated cooling curves shown in fig. 12.15 on page 204 confirmed the validity of the numerical simulations thermal results. Subsequently, the thermal analysis of the numerical data was used to illustrate the similarity between the thermal performance of the three modulus castings.

Figure 12.16 on page 208 showed that the three castings cool in a similar manner, and that the influence of the different feeder combinations on the cooling curves, was very similar. The subsequent analysis of the scaling ratios in table 12.5 on page 208 showed a few minor discrepancies, mainly between the measured and the simulated data. Generally, however, the modulus scaling ratios also showed that the castings adhered to the 1:2:3 rule and that the intended scalability of the castings' cooling times was intact.

Probably most illustrating of the scalability of the castings were the two gradient analyses: The thermal gradient analysis is shown in fig. 12.17 on page 211 and the fraction liquid gradient analysis shown in fig. 12.18 on page 213. The graphs show that the cooling and solidification of the casting, in terms of gradients scale nicely. The graphs with adapted time step and adapted centreline distance (a-c) show clear similarities. Hence, the natural cooling and solidification are comparable for the three modulus castings, as expected. The graphs also show how cooling and solidification progresses with uniform centreline distance scales and synchronised time increments.

It should be noted, however, that even though the cooling of the three modulus castings progress in a similar way, the shell-forming abilities varied significantly between the three casting sizes, with the large M15 casting showing the greatest shell forming ability. Figure 12.18 on page 213 shows how the sizable M15 casting as the only one achieves a fully solidified shell while at the same time retaining a fully liquid centre.

## 13.4.2 Scalability of the Feeders

The feeder sizes were chosen based on the traditional  $M_f = 1.2 \times M_c$  assumption, as described in section 1.3.1, on page 9. It was the intent to test a range of different feeders to achieve a better understanding of the borders of sufficient and insufficient feeding. Therefore, additional two proportional feeder sizes were chosen for the experiment; the  $0.80 M^\infty$  and  $1.00 M^\infty$ . This provided a linear feeder modulus distribution around the casting modulus. The subsequent feeder moduli are shown in table 11.1a on page 167.

While commercial feeders could be found for most of the requested feeder sizes, they could not be found within a single feeder type. To retain the best possible comparison between the different feeders, it was chosen to adhere to a single feeder type, the Feedex HD V, though this meant that the scaling of the feeder modulus between the different casting sizes would not be exact. This was chosen because it was assessed that a known modulus difference was better than an unknown geometric difference.

The same principle was upheld for the insulating feeders. Rather than selecting commercially available insulating feeders, it was chosen to retain the geometry of the Feedex HD V feeders, but exchange the exothermic material with the insulating Kalmin 250 C2 instead. The only feeders that did not follow this pattern were the two smallest feeders; the 6E06 and subsequent also 6I05. These feeders were so small that they were outside the commercial program, and had to be specially manufactured for the trials.

The commercially available feeders, though, provided some restriction to the scalability. The geometry of the feeders changed between the different feeder moduli. That largest difference was between the 28E10 and 22E12. In this case, the latter has a higher modulus (12) but with a smaller melt volume (22). See table 11.4 on page 169. Hence, the increased modulus was achieved by a thicker sleeve.

The changed geometry and volume of the feeders may influence the cooling of the feeders differently. The feeders are affected by the thermal influence of the casting, as they themselves influence the casting. However, a different melt volume has a different potential for absorbing the heat from the casting.



Likewise, the cooling surfaces are different and while the thermal modulus of the feeders can be expected to adhere to the table values, it is uncertain if the prolonged solidification time of a given modulus sleeved feeder would be the same as a geometric feeder with the same modulus. It is uncertain how the sleeves feeder handles the excess thermal influence from the casting itself, as compared with the geometrical feeder, as the reservoir for heat storage is smaller, and the cooling conditions changed. The same principle applies to the two exothermic feeders with different sleeve thicknesses and melt volumes.

Additionally, this phenomenon may be dependent on the casting modulus as well. The potential to store thermal energy depends on the melt volume, as melt has a different heat capacity than both the insulating and the exothermic materials. The heat transfer from the melt to the sleeve material, and back again, also pose a difference. However, the temperature will go towards thermal equilibrium, though the continued cooling from the surface prevents this equilibrium to be reached before the casting has reached the ambient temperature. As the cooling conditions may change during cooling and solidification as a consequence of the different HTC between metal and mould, and metal, sleeve, and mould, as described in section 3.3.3, on page 43. In this special case the melt in the feeder could be heated by the casting at the early stages of cooling, and then later in the cooling and solidification process, the feeder could feed and heat the casting due to the differences in cooling rate. Subsequently, it may also be of importance how much heat energy from the casting, the feeder can absorb and store.

Following this train of thought through, the performance mentioned above is also dependent on the pouring temperature and the feeder locations as both influences the initial thermal gradients of the casting and the feeders subsequent placement according to these initial gradients. The release of thermal energy from the exothermic sleeve material to the melt and the timing of this also matters, as does the subsequent insulating properties of the burnt out exothermic material.

An additional aspect is the influence of the melt contraction and graphite expansion. A larger melt volume has a greater potential to precipitate graphite due to the prolonged solidification time and subsequently enforce a volume expansion that will aid the movement of the remaining melt. This effect is shown in fig. 2.7 on page 22 as reported by Brown [23]. The melt contraction during cooling and so-

lidification provides the same type driving force for the melt, but with opposite direction as relayed by Stefanescu [26] and discussed in section 2.2.1, on page 17. Hence, the melt volume of the feeder may influence the driving forces for feeding as well. It should, however, also be noted that the timing of these driving forces is essential and that a smaller melt volume, encased in a sleeve, may have a more uniform transformation resulting in eg a more concentrated graphite expansion that progresses over a shorter time. Again the contraction during cooling and solidification has the same influence, though pulling rather than pushing the remaining melt.

Returning to the much-used feeder sizing rule of  $M_f = 1.2 \times M_c$ , Kotas states that the origin of the factor relates to a 20% safety margin to allow for the differences between modulus and actual freezing time [20]. Chvorinov's modulus criteria were meant as an estimate and Tiryakioğlu et al confirmed the validity of the estimates for both geometry and volume [37, 39]. Note, however, that the modulus criteria remains an estimate with some measure of uncertainty.

Thus, there are a number of effects and phenomena to take into account when analysing the feeding performance of the different combinations. Each influencing the cooling, solidification, and feeding in a different manner. However, the influence of many of the above-mentioned factors may be negligible. The scalability of the castings was discussed in section 13.4.1, on page 239 and the castings are considered to perform according to their designed modulus. Hence, the uncertainty of the ratios between castings and feeder are focused on the feeders themselves. Regarding the modulus of the commercially available feeders, this is likely adapted based on the freezing time and not the other way around, though no literature has been found on the subject. Regarding the cooling rate and thermal energy storage potential of the sleeved feeders, this may play a small role regarding the thermal development of the casting. On the other hand, many of the factors influencing this behaviour are not related to the modulus criteria (position and pouring temperature), or should rightly be taken into consideration as part of the interface constant,  $C$ , addressing some of these factors.

When this has not been made as a part of the research, it relates to two conditions: (1) The modulus of the castings and the feeders have adhered to the same geometric basis throughout the experiment, hence any inherent uncertainty related the

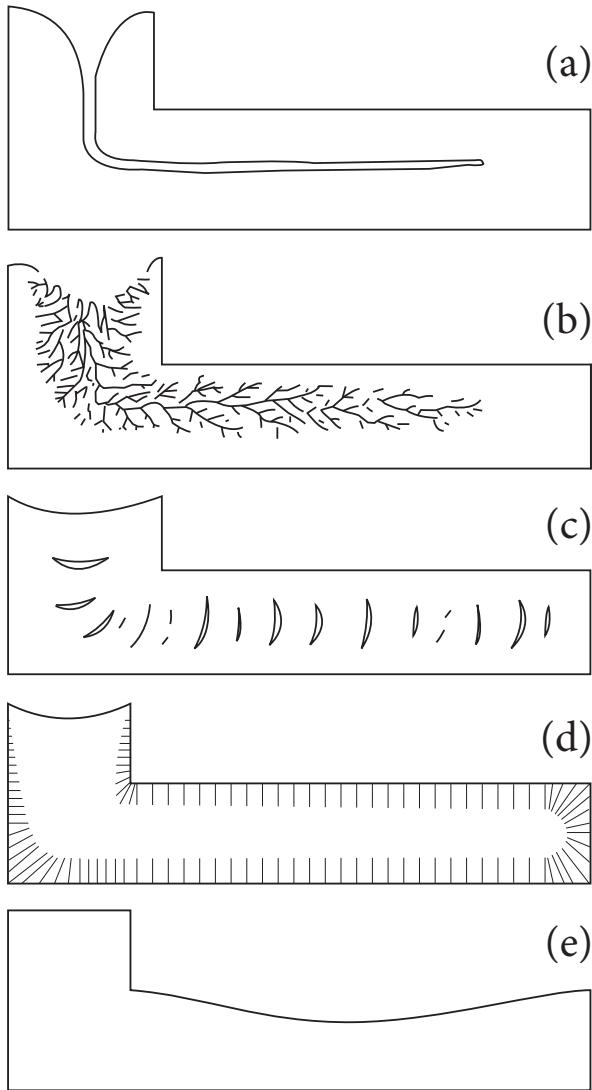


**Figure 13.3:** Five major porosity types: (a) Centreline porosity, (b) Sponge porosity, (c) Layer porosity, (d) Surface initiated porosity, and (e) Surface shrinkage. Courtesy of Campbell [25].

modulus should scale equivalently. Thus, the uncertainty of the absolute values may increase; however, the proportional comparison of the castings and feeders remain intact. (2) The potential differences in freezing time, thermal storage potential, and subsequent influence on feeding performance is assessed as undetectable compared with the overall process variation and resolution of the porosity quantification.

### 13.4.3 Influence of Scaling Error

A scaling ‘inaccuracy’ that is not negligible is the unintended scaling error of the middle modulus casting from an M10 casting to an M12 casting, as described in section 11.2, on page 167. The mistake in itself does not render the experiment, nor even the results from the M12 casting invalid or useless. The scaling error does, however, reduce some of the scalability of the experiment, as some feeder sizes were not examined for the middle modulus casting. On the other hand, even smaller modulus feeders were examined. The planned, supposed, and the actual casting and feeder modulus combinations are shown in table 11.1 on page 167.

### 13.5 Shrinkage Defect Identification

THE question of porosity quantification has already been answered in part in section 13.2.2, on page 233. However, the grading of the size of the porosities does not provide much information about the porosities themselves, or other shrinkage defects related to insufficient feeding. Campbell describes five major types of shrinkage defects related to insufficient feeding [25]. These are centreline porosity, sponge porosity, layer porosity, surface-initiated porosities, and surface shrinkage (surface sink). See fig. 13.3.

The sponge and the surface-initiated porosity defects, seen in figs. 13.3b and 13.3d on the current page, are types found in long freezing range alloys. The EN-GJS-500-14, as most cast iron alloys, had a relatively short freezing range. As these types of porosities were not identified during the analysis, they will not be considered further in this analysis. The layered porosity type, seen in fig. 13.3c on this page, indicates impurities in the melt and a poor thermal gradient, as well as feeding barrier growth in the solidifying melt (dendrites, precipitates, grains, and inclusions). The thermal analyses of the castings, measured and simulated, indicate that the EN-GJS-500-14 under the given production conditions have a flat thermal gradient which could provoke layered porosities. However, the EN-GJS-500-14 had a short freezing range and was assessed to form grains rather than dendrites in the melt, subsequently limiting the risk of an entangled mushy zone which can lead to these layered porosities. Note, however, that casting 10B manifested porosities resembling porosities found in long freezing range alloys.

See fig. 12.7b on page 184. The melt quality was assessed as good and the foundry did not report problems with melt impurities, so had it not been for the porosities found in castings 10B and 10C this porosity type could also have been ruled out without further analysis. However, as described in section 12.1.4, on page 181, the porosities in these two castings were assessed to be linked with the cleanliness around the pouring cup and vent opening in relation to the installation of the thermocouples in the subsequent mould. With respect to the further analysis, it is assumed that the irregular size and location of the porosities in castings 10B and 10C were caused by either an inclusion or a melt impurity. An inclusion or melt impurity would aid the nucleation of either ruptures or gas porosities, as described by Stefanescu and relayed in section 2.2.1, on page 17.

### 13.5.1 Centreline Porosities

---

The remaining porosity types are centreline and surface shrinkage. Both are mostly found in short freezing range alloys with good melt quality. The centreline porosities are described in detail in section 2.2.1, on page 17, and the underlying mechanism of surface shrinkage is described in section 2.4.5, on page 33.

Based on the ultrasound and x-ray porosity analyses, and particularly the sectioning of the castings, it was found that the porosities formed in the trial castings resembled the typical centreline porosities described by Campbell [25]. This assessment was based on the location and size of the porosities found in the sectioned castings. By comparing the porosity indication from the ultrasound analysis with the sectioned castings, it was assessed that the yellow markings made during the ultrasound analysis were viable for extending the analysis of the sectioned castings to a general assumption about the porosity formation, aided by the ultrasound results and the x-ray analysis. See figs. 12.1, 12.6 and 12.7 on page 176, on page 182 and on page 184.

### 13.5.2 Surface Shrinkage

---

As shown in Part I, surface shrinkage can occur under the given process conditions and with a similar alloy, EN-GJS-450-10. However, the geometry of the disc casting in Part I was significantly different from the cuboid shape of the casting geometry

used in Part II. The corners cool faster providing a rigid frame for the large flat surface. The section thickness was greater for all three modulus castings, compared with the disc castings. Additionally, four sides were equally prone to succumb to the solid feeding, distributing the volume displacement across a much larger area.

The castings were analysed for surface shrinkage via a visual inspection, which did not find evidence of surface shrinkage. Unlike the castings in Part I, the cuboid casting in Part II has not been measured using a CMM to establish the difference between the CAD-model and the final casting. Hence, small indents or sinks distributed across a large surface may have escaped detection.

On the other hand, if the castings were in a condition to solid feed itself, then this effect should be equally present for all trial combinations. Also the castings with detected porosities. These castings experienced an internal rupture of the melt, resulting in internal porosities as opposed to surface shrinkage. Had the porosity-free casting been a result of solid feeding alone, then the volume of the surface shrinkage would have been visible. A rupture can be described as a tear, rift, or parting of the melt to form a melt-free cavity or bubble inside the melt itself as described in section 2.2.1, on page 17. A further description is found in section 13.8.8, on page 262.

The investigations performed on the castings do not provide sufficient information to completely reject the possibility of partial solid feeding in some of the castings. For example, the difference between 20A and 20B, and 22A and 22B may be solid feeding. However, solid feeding of the castings is considered highly unlikely due to the recorded rupture of the melt in the feeders, releasing the internal tension. Additionally, the castings that were most exposed to solid feeding, castings with two large feeders, did not show signs of surface shrinkage or solid feeding. The combination of the two feeders kept the surface area between the two feeders heated for an extended period, as shown in figs. 12.20 to 12.22 on pages 218–220. However, these feeder combinations did not display fewer porosities than similar feeder combinations.

Subsequently, the primary volume of the porosities can be considered centreline porosities. The mutual origin of the porosities reduces the feeding effect analysis, as only one major porosity type have to be considered during the analysis.

## 13.6 Effects of Feeding Parameters

THE different feeder combinations examined during the trials yielded a measure of the feeding efficiency based on the size of the remaining porosities as compared with the feederless benchmark castings. The analysis showed that two or more feeding regimes were active for different feeder combinations. Hence, the different regimes were not necessarily active at the same time or for the same castings. The term ‘feeding regime’ is in this respect is used as a denotation of different methods of moving the liquid, semi-liquid, or solid to feed the casting, as described in section 13.1.1, on page 232.

As all castings were manufactured under constant production conditions and with the same alloy, three parameters were varied during the experiment: Feeder modulus, sleeve material, and feeder location. The feeder modulus and sleeve material were interdependent and cannot be completely separated. The feeder location was independent, however, as the experiment did not encompass a full factorial trial design some combination have not been part of the performed experiment. For example, only exothermic feeders have been used for the lower feeder location.

Another aspect that should also be noted was the geometrical differences and general scalability of the feeder, as discussed in section 13.4.2, on page 240.

### 13.6.1 Feeder Modulus

The feeding analysis showed that there was no linear correlation between larger feeders and fewer porosities, regardless of the casting modulus.

#### M08

For the small M08 castings the best of the analysed feeding combinations were either a small  $0.63 M^\infty$  upper feeder in combination with a  $0.75 M^\infty$  or  $1.00 M^\infty$  lower feeder, or a combination with two large  $1.25 M^\infty$  feeders at both the upper and lower location. Hence, while a few other combination with only upper feeders also yields reduced porosities, the best combinations all include two feeders. See fig. 12.12 on page 195. This indicates that a two feeder combination, with either small or large feeders, provides the best feeding regime. For energy savings, the choice of feeder should be  $0.63 M^\infty$  as the upper feeder and  $0.75 M^\infty$  as the lower feeder. Note, however, that none of these feeder combinations yielded porosity-free castings.

**A Single Upper Feeder** The upper feeders with a proportional modulus of less than one should traditionally not be able to feed the casting. However, as several castings show this tendency the feeding regime must be another functional regime than the traditional thermal gradient regime. It is proposed that the recorded feeding is the result of one or more effects creating a pressure difference great enough to move the liquid or semi-liquid melt from the feeder into the casting, as described in section 2.4, on page 30.

The pressure difference can be created both by the casting and by the feeder. The cooling, solidification, and shrinkage of the melt create a tension in the residual melt which, if in liquid connection with the melt in the feeder, can draw this melt into the casting before either the feeder or the casting solidifies. In this case, the feeding occurs early in the solidification and can only compensate the shrinkage that has occurred until then. Note that the shrinkage during solidification in the feeder will resist the movement, similar to the formation of porosities described in section 2.2.1, on page 17. Hence, the feeding regime would benefit by a feeder that retains an atmospheric puncture until late in the solidification or can initiate a rupture resulting in the formation of a porosity in the melt, which will locate the subsequent porosity in the feeder rather than the casting.

Another aspect that can influence the pressure difference in the feeder and the casting is the contraction of the already solidified shell. As the shell cools and gains mechanical strength, the contraction will also increase the pressure on the residual melt inside the feeder and the casting. However, as the feeder and the casting have different cooling rates and geometries, one is bound to contract before the other. If the feeder contracts first, which may be the case for the smaller proportional feeders, this contraction may, in turn, squeeze the remaining liquid or semi-liquid into the castings. In principle, the same could also occur if the centre of the feeder had solidified, as a form of solid feeding.

Note that the contraction of the shell is relatively small, as the total pattern maker’s shrinkage for cast iron is typically ranging from 1% to 3% for SGI [140]. Hence, only a small pressure can be exerted by the shell compression itself. However, it should also be remembered that the pressure balance in the casting, both with respect to the formation of porosities, as well as moving the melt,

is also relatively small and that the total feeding requirement for cast iron is also often equal to 1% to 3% of the casting volume. Thus, the small shell compression can influence the driving forces to a significant level.

In addition to the contraction, also the strength of the formed shell matter. If the shell yields, the plastic strain,  $\varepsilon^{Pl}$ , can be described by eq. (3.34) on page 60 [70]:

$$\dot{\varepsilon}^{Pl} = \frac{E_T - E}{E E_T} \frac{\partial \sigma_\gamma}{\partial T} \dot{T}$$

assuming that the yield stress increment,  $\dot{\sigma}_\gamma$ , is set as zero.

Equation (3.36) on page 60 yields additional information about the thermo-elasto-plastic deformation of castings [70]: (1) As the tangent modulus,  $E_T$ , is smaller than the Young's modulus,  $E$ , the yield stress decreases with increasing temperature. (2) The mechanical strain increment,  $\varepsilon^{Mech}$ , and the plastic strain increment,  $\varepsilon^{Pl}$  are equal as the elastic strain increment,  $\varepsilon^{El}$  is zero (assuming that Young's modulus,  $E$ , is equal for both temperature states). A great challenge with the application of this equation is the availability of material data describing the mechanical properties of a given cast iron alloy, or any alloy for that matter, at these elevated temperatures close to the melting point.

Additionally, a more general assessment can be made, describing the different partial strains that constitute the total strain,  $\varepsilon^{Tot}$  as it develops in the forming shell as described by Denis et al in eq. (3.37) on page 61 [102]:

$$\varepsilon^{Tot} = \varepsilon^{El} + \varepsilon^{Pl} + \varepsilon^{Th} + \varepsilon^{Tr} + \varepsilon^{Tp}$$

where  $\varepsilon^{El}$  is the elastic strain,  $\varepsilon^{Pl}$  is the plastic strain,  $\varepsilon^{Th}$  is the thermal strain,  $\varepsilon^{Tr}$  which is transformation strain, and  $\varepsilon^{Tp}$  which is the transformation plasticity strain. The transformation strain,  $\varepsilon^{Tr}$ , here relating to the solidification. The elevated temperature promotes plastic strain and deformation, however, the more elastic strain that the shell can retain, the more pressure it can exert on the melt subsequently.

In addition to the pressure differences mentioned above is the graphite expansion. Where the other pressure causes are general and can be found in other alloys as well, the graphite expansion is only found in cast iron. As with the compression pressure described above, the graphite expansion occurs as a function of the cooling and solidification of the melt. In some respect, the graphite expansion can

support the contraction, as the solidified shell will have had its graphite expansion at a different time than graphite expansion occurs at the solidifying centre. Note, however, that at the time the centre experiences the graphite expansion the solidification is per definition already in progress. Hence, the graphite can only aid semi-liquid or solid feeding, unless it can push melt closer to the casting that has not commenced solidification yet.

To complicate matters further the three different mechanisms—volume contraction, shell compression, and graphite expansion—developing pressure differences at different intervals during the cooling and solidification of the melt, all three mechanisms can occur for the same casting. Hence, the feeding of a casting is not only a question of which of the three driving force mechanisms are active, but also which mechanisms are active at the right time and how the three mechanisms support or oppose each other. For example, if the shell-contraction of the feeder occurred simultaneous with the volume contraction of the melt in the casting, then the tension of the volume change would be aided by the shell compression squeezing on the melt in the feeder. However, the opposite can also occur, eg if the graphite expansion of the solidifying melt of the casting occurs at the same time as volume contraction of the melt in the feeder, then both driving forces would move the remaining feed material (liquid, semi-liquid, and moveable solid) towards the feeder instead.

The proposed feeding regimes are discussed in detail in section 13.8, on page 252.

**Combination of Two Feeders** The successful two feeder combinations managed to feed the middle control volume of the M08 casting. While this was also achieved by the single large 1.25 M<sup>∞</sup> upper feeder, this combination resulted in porosities at the bottom control volume instead for one of the duplicates. The 0.63 M<sup>∞</sup> upper feeder performed well with all other combinations other than the large 1.25 M<sup>∞</sup> lower feeder.

As with the single upper feeder combinations, the successful feeder combinations with two feeders generally had a proportional smaller modulus than the casting itself at one of the feeder locations. This strengthens the theorem that other feeding regimes were in operation for these cases. Additionally, the low threshold between successful and unsuccessful feeding indicates that the process only functions optimally within specific boundaries.

The main difference between the single and two-feeder solution was the extended feeding channel kept open by the two feeders, allowing for a late feeding of the middle control volume. According to the feeder moduli, the direction of solidification should move towards the lower feeder as this had the largest modulus of the two. Note the opposite combination, with the larger feeder at the upper position did not yield a favourable outcome. Hence, it was indicated that the location of the feeders was significant, though it should also be noted that the  $0.63 M^\infty$  feeder was only examined at the upper location.

Additionally, it has been suggested in section 12.3.5, on page 214 that the application of two feeders alters the thermal gradients in a way that promote shell-forming, which in turn influences the magnitude of the driving forces for feeding.

#### M12

The M12 castings showed comparable feeding performances for the small upper feeders, compared with the M08 castings. The combinations of two feeders did not yield similar promising results. The large feeders were not examined for the M12 castings.

As with the M08 castings, the smallest of the upper feeders, in this case, a  $0.50 M^\infty$  feeder, performed well. The same was the case for the  $0.83 M^\infty$  upper feeder. Both feeders managed to secure a porosity-free middle control volume when used without a lower feeder. The  $0.50 M^\infty$  feeder in combination with the  $0.66 M^\infty$  feeder also performed better than average, though not as good as without the lower feeder. This is the opposite behaviour of the M08 casting, which benefited from a lower feeder to better feed the middle control volume. The difference in feeding regimes cannot be attributed to the scaling of the casting, as the feeder combination with a proportional modulus less than one was covered in full. Thus, it is proposed that the solidification regime of the casting, as described by the modulus, directly influence the feeding of the castings.

The influence of solidification is discussed further in section 13.7, on page 251.

#### M15

The large M15 castings were easier to feed by the chosen feeder combinations. However, the best performing feeders for the M15 casting were those with  $M^\infty$  of one or larger. The proportional  $1.00 M^\infty$

lower feeder displayed promising results. The combinations of a proportional  $1.00 M^\infty$  feeder together with a  $0.80 M^\infty$  functioned well regardless of feeder location. Also, the  $1.00 M^\infty$  lower feeder together with a  $0.60 M^\infty$  upper feeder, or entirely without an upper feeder, performed well.

The combination of two large  $1.27 M^\infty$  feeders also yielded good results. The same was the case for the  $0.80 M^\infty$  upper feeder combined with a large  $1.27 M^\infty$  lower feeder.

Overall a larger variety of different feeder combinations performed well for the large M15 castings, compared with the smaller castings. Additionally, note, that where the proportionally smaller feeders yielded the best results for the M08 and M12 castings, the proportional and larger than proportional feeders performed best for the large M15 castings. The proportionally small feeder only yielded good results in combination with other feeders.

The evidence of the complex feeding regimes is perhaps best illustrated by the combination with only a lower feeder. The  $0.80 M^\infty$  feeder performs comparably to the benchmark castings. The proportional feeder  $1.00 M^\infty$  performs very well with a microporosity (1) and a medium (3) porosity at the middle control volume as the only porosities recorded. Hence, when the feeder size increase from  $0.80 M^\infty$  to  $1.00 M^\infty$  yielded improvements. However, the further increase of the lower feeder modulus to  $1.27 M^\infty$  resulted in castings with large (4) porosities at all three control volumes.

The regimes behind the driving forces that move the melt into the casting are non-linear.

### 13.6.2 Sleeve Material

The experiment comprised two different sleeve materials; the insulating ‘Kalmin 250’ and exothermic ‘Feedex HD V’. As described in section 13.4.2, on page 240, the geometry was retained as the constant, leaving the change in sleeve material to be the factor that determines the modulus of the feeder,  $M_I$ , as a function of the different MEF of the two materials. See eq. (2.6) on page 20.

Figures 12.9 and 12.11 on page 188 and on page 192 show the performance of the two sleeve materials compared. Note that the insulating feeder sleeves were not tested at the lower feeder position, hence nothing can be concluded regarding this configuration. The insulating feeder sleeves were tested as single upper feeders, and as upper feeders in combination with a lower exothermic feeder.

Note that the term *stable* in this context refers to the different feeder combinations resulting in the same amount of porosities. Hence, stable cannot be said to be better. As different feeder moduli are compared, a stable process in principle means that the feeders have less influence on the number and size of the porosities (positive or negative), then an unstable process.

### Upper Feeder Only

The insulating feeder that is shown in fig. 12.9 on page 188 displayed a more stable feeding; with less variation. Though the insulating feeders also had a smaller modulus, compared with their exothermic counterpart, the differences in moduli were generally small, and the ranges overlapped by most of the range. For instance, the M08 insulating feeders covered the modulus range from 5 mm to 8 mm, while the exothermic feeders covered the range from 6 mm to 10 mm. The overlapping ranges were similar for the M12 and M15 castings.

It is unlikely that the moduli with insulating feeders were, by coincidence, the feeder combinations that nullified the feeding regimes else displayed by the exothermic feeder moduli. As the insulating feeders were prototypes made especially for the experiment, it is possible that the moduli were not exact—not as much due to the prototype production as the estimated calculation of the modulus. However, even if the moduli of the insulating feeders were off, the range would still be overlapping and some effect would likely be visible in the porosity results.

Another difference between the insulating and exothermic feeder experiments was the date of production. The combinations with exothermic upper feeders were produced in February 2014 (session I and II), and the combinations with insulating upper feeders were produced in March 2014 (session III and IV). The alloy compositions and pouring temperatures from the four sessions are shown table 11.2 on page 167. While neither the alloy composition nor the pouring temperatures can explain the difference in feeder performance, it may be possible that impurities in the melt have caused performance instability, as described in section 2.2.1, on page 17. In this case, it is plausible to assume that the impurities would have been present at the first production data, with the exothermic feeders, as these feeders display the greatest dispersion in the porosity results, as described by Stefanescu in

eq. (2.3) on page 18 [26]:

$$P_{\gamma} = \frac{2\gamma_{LG}}{r}$$

where  $P_{\gamma}$  is the pressure induced by the tension acting on the surface of the pore,  $\gamma_{LG}$  is the gas/liquid surface energy, and  $r$  is the radius of the pore. Thus the melt impurities may act a nucleation sites for porosities, creating ruptures in the melt. If a rupture has formed, then the tension on the surface of the pore,  $P_{\gamma}$ , is reduced greatly changing the balance of the pore formation as described in eq. (2.1) on page 18 [26]:

$$P_{gas} + P_{shr} > P_{amb} + P_{st} + P_{exp} + P_{\gamma}$$

where  $P_{gas}$  is the gas evolution,  $P_{shr}$  is the negative pressure from resistance to shrinkage induced flow,  $P_{amb}$  is the ambient pressure applied to the mould,  $P_{st}$  is the ferrostatic pressure, and  $P_{exp}$  is the expansion pressure caused by phase transformations.

If the proposed scenario with melt impurities was the cause of the exothermic feeder instability for the upper feeder, then a similar instability would be expected for the exothermic lower feeder cast on the same date. This is not the case as can be seen in fig. 12.10 on page 190. The M08 and M12 castings with exothermic lower feeders shown a very stable performance, similar to the performance observed for the insulating upper feeders in fig. 12.9 on page 188. The M15 castings display significant variation; however, this variation is matched by the insulating feeder combinations with two feeders. While the stability of the lower feeders can be assumed to relate to their physical location, this was categorised as less plausible.

Another explanation is proposed instead. The insulating feeders formed a solid shell early in the process. This is plausible because the geometry of the feeders was designed to be used for exothermic feeders, but was adapted to use an insulating sleeve material as part of the experiment. The geometry was without a William's wedge to ensure an atmospheric puncture of the feeder. A solid shell would then entail a negative pressure differential in the feeder working against the movement of the melt into the casting. This is also supported by eq. (2.1) on page 18, where the ambient pressure,  $P_{amb}$ , also play a role in internal pressure balance of the casting.

The exothermic feeders which were designed to stay liquid at the surface for a longer time would not suffer this problem. Again it can be argued

that this theory is disproved by the successful feeding of the insulating feeders. However, different feeding regimes have been identified and some of these would actually benefit from an early shell formation. These are described in detail in section 13.8, on page 252.

### Upper and Lower Feeder

Analysing the difference between an insulating upper feeder with an exothermic lower feeder versus an exothermic upper feeder also with an exothermic lower feeder, it is less easy to conclude on the effect of the insulating feeders because none of the combinations is free from exothermic feeders.

The M08 castings with an insulating upper feeder in fig. 12.11 on page 192 show greater stability compared with the castings with an exothermic upper feeder. Two of the smaller modulus sums yielded improved feeding results, however, the rest of the combinations were close to the benchmark castings.

For the M12 castings, the results were the opposite. Here the feeder combination with an exothermic upper feeder was most stable. In fact, this combination group yielded no variance in the porosity sum at all. The insulating upper feeders performed better than the exothermic feeders in half of the cases, and again the smaller feeder modulus sums yielded the best results.

The M15 castings did not show the same clear difference between the insulating upper feeder and the exothermic upper feeder. Both combinations yielded good variation in the sum of porosities recorded for the castings. This indicates that the feeding regimes shift between the smaller M08 and M12 castings, and the larger M15 castings.

### 13.6.3 Feeder Location

For all of the feeder combinations, two feeder locations were possible, providing in total three combinations; a single upper feeder, a single lower feeder, or a feeder at both locations at the same time. The intent with the two different locations was to investigate the influence of ferrostatic pressure on the feeding regimes, but also to evaluate the efficiency of two feeders combined. The effect is best analysed with table 12.2 and fig. 12.12 on page 194 and on page 195, as these provide an overview of the effect of both locations in the same table/figure.

Note that the larger range of upper feeder moduli was examined. This results in graphs that have 1-2

additional modulus sizes on the y-axis. Hence, comparing the upper and lower feeder location efficiency, the  $0.63 M^\infty$ ,  $0.50 M^\infty$ ,  $0.60 M^\infty$ , and  $1.07 M^\infty$  feeders were not examined at the lower feeder position, hence the axes are not completely invertible.

### Upper or Lower Location

The combinations using a single feeder can be compared with regards to the performance of the upper feeder location versus the lower feeder location.

**M08** For the M08 castings the upper feeders yielded some improvements of the porosity sum for the  $0.63 M^\infty$ ,  $0.75 M^\infty$ , and  $1.25 M^\infty$  feeders. The proportional  $1.00 M^\infty$  feeder, on the other hand, caused an increase in porosities in the casting. The same increase for the  $1.00 M^\infty$  was not found for the lower feeder location. However, the improved feeding of the  $0.75 M^\infty$  and  $1.25 M^\infty$  for the upper position was not reflected for the lower position either. In fact, all three feeder combinations for the lower feeder location yielded slightly increased porosities compared with the benchmark castings. Hence, it is concluded that the examined modulus sizes, without the support of an upper feeder, did not improve the feeding of the casting. Subsequently, it can also be concluded that for the M08 casting, the feeder setup was favoured by the upper location.

**M12** The M12 casting displayed a pattern similar to the smaller M08 casting. The single upper feeder all yielded significant feeding improvements, while the lower feeder was less impressive in their performance. The  $0.66 M^\infty$  lower feeder yielded a small feeding improvement, while the larger  $0.83 M^\infty$  and  $1.00 M^\infty$  feeder displayed a small increase in porosities compared to the benchmark castings. Again it is concluded that the upper feeder location is favourable for the examined modulus range.

**M15** The large M15 castings showed a similar effect of the upper feeders, as for the smaller M08 and M12 castings. All upper feeders, with the exception of the  $1.00 M^\infty$ , yielded improved feeding. The  $1.00 M^\infty$  upper feeder resulted in a slight increase in porosities, however, not as significant as for the M08 casting. Note that the  $1.07 M^\infty$  upper feeder yielded a porosity result slightly better than the benchmark castings, though not as good as the  $0.60 M^\infty$ ,  $0.80 M^\infty$ , or the  $1.27 M^\infty$  feeders. The performance of the  $1.07 M^\infty$  feeder was closer to the



1.00 M<sup>∞</sup> feeder and the benchmark castings than the other feeders. This is of interest because the 1.00 M<sup>∞</sup> feeder was an exothermic feeder, while the 1.07 M<sup>∞</sup> feeder was an insulating feeder. Hence, this indicates that the governing factor was the modulus, with little or no influence from the sleeve material.

The lower feeder location for the M15 casting showed very different results than for the lower feeder of the two smaller modulus castings. The 0.80 M<sup>∞</sup> lower feeder performs marginally better than the benchmark castings, which is comparable with the performance of the 0.66 M<sup>∞</sup> lower feeder for the M12 castings. However, the 1.00 M<sup>∞</sup> lower feeder yielded castings that were close to porosity-free. They had a microporosity (1) and a medium (3) porosity at the middle control volume respectively. Hence, the single lower feeder managed to feed the top control volume that typically displayed large (4) porosities.

While the proportional 1.00 M<sup>∞</sup> lower feeder performed very well, the larger 1.27 M<sup>∞</sup> lower modulus had the opposite effect. Two of the three duplicates with this feeder combination displayed large (4) porosities at all three control volumes. Hence, the casting feeds the feeder instead of the other way around.

The difference between the 1.00 M<sup>∞</sup> and the 1.27 M<sup>∞</sup> lower feeder for the M15 casting, compared with the smaller M08 and M12 castings showed that the different casting moduli solidified in significantly different ways.

The massive porosities for the 1.27 M<sup>∞</sup> lower feeder indicate that the core of the M15 casting remained fully liquid until very late in the solidification process and that the feeder has kept a feeding path open for the casting to feed the feeder. This is supported by the geometric solidification analysis, which shows the solidification sequence of the C10 casting in fig. 12.22 on page 220. The geometrical solidification analysis also identifies a major difference between the large 1.27 M<sup>∞</sup> of the M15 and the 1.25 M<sup>∞</sup> of the small M08 casting. The 1.27 M<sup>∞</sup> feeder for the M15 casting remains completely liquid until the casting has solidified completely. This is not the case for the 1.25 M<sup>∞</sup> of the M08 casting. Here, the shell of the feeder has commenced solidification right after ended pouring. See fig. 12.19 on page 216.

The good performance of the proportional 1.00 M<sup>∞</sup> lower feeder, however, indicated that for the M15 casting an optimum was achieved with

a feeder of the same modulus as the casting. As the feeder was located at the lower feeder position, gravity cannot have aided the feeding process. In fact, the feeding had to overcome the ferrostatic pressure exerted by the remaining melt in the casting. Hence, the driving forces acting on the melt had to be 'internal' effects supplied by the casting and the feeder themselves. Additionally, the driving forces had to be strong enough, at the right time, for a sufficient period, to move the melt into the casting where needed.

The difference between the number and size of the porosities for the 0.80 M<sup>∞</sup>, 1.00 M<sup>∞</sup> and the 1.27 M<sup>∞</sup> illustrate the narrow window of operation that has to be upheld to capitalise on the feeding abilities shown by the proportional 1.00 M<sup>∞</sup> feeder. As with the production of CGI where the Mg treatment has to comply with similar narrow operation parameters, great care and understanding of the casting, section, and feeder must be considered to select the best possible feeder.

Analysing the single upper and lower feeders, the upper feeders yielded better results, with the exception of the single proportional 1.00 M<sup>∞</sup> feeder for the M15 casting. In all other cases, the upper feeder fared better than their lower counterparts. As the main difference between the two combinations was the ferrostatic pressure height, partially aiding the upper feeders, and working against the lower feeders, this may have been the expected result. However, the difference between the 1.00 M<sup>∞</sup> upper feeder and the 1.00 M<sup>∞</sup> lower feeder of the M15 casting indicates that the ferrostatic pressure benefited the lower feeder. This conclusion, in turn, indicates that an increased pressure towards the feeder benefited the feeding regime as a whole. The ferrostatic pressure may also explain why the same feeding effect was not observed for the smaller castings, M08 and M12. The large M15 retain a volume of the fully liquid melt at the centre of the casting longer than the other castings, as shown in fig. 12.18 on page 213. Hence, the ferrostatic pressure would develop differently for the smaller M08 and M12 castings as these reach a solid or semi-solid core earlier in the solidification process. Subsequently, the ferrostatic pressure cannot act on the lower feeders, in the same manner, changing the feeding regime of the casting.

The solidification of the castings is discussed in section 13.7, on page 251 and the feeding regimes are discussed in section 13.8, on page 252.

## Upper and Lower Location

Where the lower feeders alone, with the exception of the  $1.00 M^\infty$  feeder for the M15 casting, did not yield great improvements in the feeding performance, the combination of two feeders was less straightforward.

Note again that the  $0.63 M^\infty$ ,  $0.50 M^\infty$ ,  $0.60 M^\infty$ , and  $1.07 M^\infty$  feeders were not examined at the lower feeder position. The x- and y-axes are not invertible (cannot be switched) for the fig. 12.12 on page 195. As a result, the graphs cannot be analysed as if they were mirrored along a diagonal axis. Additionally, the two smallest of the lower feeders were not examined together with the largest upper feeder.

**M08** Analysing the  $0.75 M^\infty$  and  $1.00 M^\infty$  feeder combinations, the combination with the  $1.00 M^\infty$  at the upper location and the  $0.75 M^\infty$ , noted as  $\frac{1.00}{0.75} M^\infty$ , at the lower location yielded greatly increased porosities, while the opposite combination,  $\frac{0.75}{1.00} M^\infty$ , resulted in an amount of porosities close to the benchmark castings. Hence, the small feeder at the upper location yielded the best result, through the absolute porosity value was the same as the feederless benchmark castings. If the lower feeder, though, was increased to the large  $1.25 M^\infty$  feeder this yielded similar porosity result as the  $\frac{1.00}{0.75} M^\infty$  combination. This indicates that a similar effect to the one that created the large porosities for the  $\frac{1.00}{0.75} M^\infty$  combination was activated for the  $\frac{0.75}{1.25} M^\infty$  combination, but also that to activate this feeding effect the lower feeder required a larger modulus.

**M12** For the M12 casting, the  $\frac{0.83}{0.66} M^\infty$  feeder combinations yielded slightly more porosities compared with the benchmark castings, while the reverse combinations,  $\frac{0.66}{0.83} M^\infty$ , yielded slightly fewer porosities. As with the M08 casting, increasing the lower feeder modulus resulted in an increase in the number and size of porosities, similar to the  $\frac{0.83}{0.66} M^\infty$  combination. This increase in porosities with increasing feeder modulus indicates that the effects observed for the small M08 casting are the same for the medium M12 casting. However, it should also be noted that the feeder used for the M12 casting were proportionally smaller, hence the relative feeder sizes that trigger the effect was smaller for the M12 casting indicating a slightly different solidification scheme.

**M15** The differences in solidification are empathised by the M15 feeder combinations. The  $\frac{1.00}{0.80} M^\infty$  feeder combination thus yielded one porosity-free

casting and one with a single microporosity at the top control volume. The opposite combinations,  $\frac{0.80}{1.00} M^\infty$ , displayed almost as promising results. For the smaller M08 and M12 casting the combination with the smaller feeder modulus at the upper locations provided Three castings with a microporosity (1), a small (2) porosity, and a large (4) porosity at the middle control volume, and one casting with a microporosity (1) at the top control volume. See table 12.1 on page 180. Note that both C12 and C21 have this feeder combination. The C12 with the insulating upper feeder, and C21 with the exothermic upper feeder.

The  $\frac{0.80}{1.27} M^\infty$  feeder combination also yielded very good results with one casting being porosity-free and the other having only a microporosity (1) at the middle control volume. The  $\frac{1.07}{1.27} M^\infty$  combination, on the other hand, was found to have almost as many porosities as the benchmark castings. This behaviour was also the opposite of the behaviour observed for the M08 casting.

It is proposed that this difference in behaviour is related to the differences in solidification schemes between the different modulus castings. The smaller castings perform better with the larger feeder at the upper position, where large M15 castings benefit from having the larger feeder at the lower position. For the M08 and M12 castings, it was favourable to have the thermal gradient, and thus also the direction of solidification, going towards the large upper feeder. The smaller lower feeder extended the liquid zone, the feed path, at the centre of the casting enabling the upper feeder to better reach the middle control volume. The reduced volume of the M08 and M12 casting cannot build up enough tension in the remaining melt to benefit from the melt reserve in the lower feeder.

The sizeable M15 casting, on the other hand, has a significant melt volume late in the solidification, and the more uniform cooling narrows the time frame for the tension, thus increasing the maximum tension achieved. This larger melt tension then draws the melt from the lower feeder. This mechanism would function equally good for the large feeder placed at the upper position. When it does not, this is believed to relate to the difference in ferrostatic pressure, and possibly the difference in initial temperature due to the filling conditions.

The solidification of the castings is discussed further in section 13.7, on the next page and the feeding regimes are discussed in section 13.8, on page 252.

## Pre-Feeder Neck

Finally, the location of the feeder also influences the solidification of the pre-feeder neck. The x-ray analysis showed that some of the castings had pre-feeder necks partly empty. See section 12.2.6, on page 200. This finding was subsequently supported by the geometrical solidification analysis in section 12.3.5, on page 215.

The geometrical solidification analysis showed that the castings with a proportionally medium or large feeder at the upper feeder location had a changed solidification scheme, compared with the benchmark castings. This could potentially be related to the extra volume added by the feeder, which in turn would yield a larger volume change as the casting cools. If this was the case, however, the effect should be the same for C10 feeder combination with the feeder at the lower position. This was not the case. The C10 combination had a pre-feeder neck solidification that resembled that of the feederless benchmark castings.

Instead, it is proposed that the thermal influence of the upper feeder increases the temperature for the lower part of the pre-feeder neck. This extra heat to the critical pre-feeder neck region, in turn, increases the fluidity of the melt allowing the melt in the lower part of the pre-feeder neck to sink into the melt basin of the casting. The increased fluidity allow the melt to separate at the middle of the pre-feeder neck, breaking the tension and releasing the melt in the lower half of the pre-feeder neck. This is supported by the relatively quick separation of the melt in the middle of the pre-feeder neck.

Concluding that the thermal field created by the upper feeder influences the solidification of the pre-feeder neck, the feeder location is naturally also concluded to influence this. However, it should also be noted that the pre-feeder neck according to the geometrical solidification analysis still solidifies and closes off at the middle point according to the intentions in the design.

Subsequently, the thermal influence of the upper feeder must be larger than the largest examined feeder,  $1.27 M^\infty$ , to keep the pre-feeder neck open to enable feeding this way through. Additionally, constructors must be careful not to introduce porosities in small sections located above a larger secluded section by placing a large feeder close to the small section.

## 13.7 Solidification Behaviour

THE feeding results showed differences between the performance of the different proportional feeders for the three modulus castings. This indicates significant changes to the solidification of the castings as a consequence of the modulus change, as solidification is the main governing factor for the feeding of the castings. Solidification influences the shell forming, the solidification contraction, the graphite expansion, the build-up of tension in the melt, the viscosity of the melt, and the thermal gradient of the castings.

As the castings had the same alloy composition and the same cooling conditions, the only influential difference between the three castings were their differences in modulus. The alloy composition for the slightly hypereutectic alloy is found in table 11.2 on page 167. The alloy, as a function of being near eutectic, is a short freezing range alloy, which can also be described as endogenous shell-forming. See section 2.3.5, on page 26.

The formation and growth of the casting shell are directly linked to the cooling rate and the heat transport through the shell region. Hence, the larger the casting, the longer and slower is the formation and growth of the casting shell. However, at the same time, the cooling of the liquid centre is even slower for the large M15 castings indicating the formation of a solid shell at a time where the centre volume is still fully liquid.

Analysing figs. 12.17 and 12.18 on page 211 and on page 213 together with figs. 12.19 to 12.22 on page 216 and on pages 218–220 it is found that the solidification of the small M08 casting progresses much faster than the larger castings. This corresponds with the solidifications times recorded in table 12.5 on page 208, showing the castings total solidification progressing according to the 1:2:3 rule. This ratio upholds the experimental scaling according to modulus as developed by Chvorinov [37] and confirmed for scaled geometries by Tiryakioğlu et al [39]. The deviation measured and calculated was well within the 20 % uncertainty described by Kotas [20], though this was also expected exactly because of the scaled geometry.

The smaller castings, by definition, have a smaller cooling surface. However, the increased cooling

power of the larger castings was matched by an exponentially larger melt volume, hence, larger castings cool slower even though their larger cool surface. Cooling power is also a bulk property. This ratio is what Chvorinov described in his modulus criterion. See section 2.3.2, on page 20. Note, however, that the modulus criterion describes the total solidification time, and do not consider the progression of solidification.

The smallest M08 casting solidifies fast due to the low ratio between the melt volume and the cooling surface. This results in a rapid directional solidification towards the centre of the casting. As a result, the residual melt volume is relatively small by the time the increased latent heat from the solidification overcomes the cooling power of the surface, slowing down the continued solidification process. Hence, only a small core volume is kept liquid long enough to precipitate equiaxed dendrites and graphite nodules in the residual melt. As a result, a large part of the driving forces that has to move melt from the feeder into the castings come from the initial directional solidification.

The large M15 casting solidifies in a different manner. The growth rate of the shell progress further than the growth rate of the shell in the small M08 casting, within the time frame that the centre volume remains liquid. See fig. 12.18 on page 213. The slow cooling provides sufficient time for the casting centre to reach a uniform temperature, levelled out by the latent heat. Hence, the cooling and solidification of the large castings progress with a flat thermal as well as solidification gradient. The slow solidification promotes graphite precipitation and subsequent expansion, but also the formation of grains and equiaxed dendrites. As these particles are heavier than the melt, they will sediment towards the bottom of the casting, but can also inhibit the continued feeding process as described in section 2.4, on page 30. However, free graphite or graphite nodules encased in an austenite shell may be buoyant or even float towards the top. The EN-GJS-500-14 is hypereutectic, hence the formation of dendrites is limited. Note also, that this potential movement of solidified particles in the melt as a function of their density,  $\rho$ , and through this act as a heat transport within the casting. The phenomenon is called advection and described in section 13.7:

$$q = -vA\rho C_p \frac{\partial T}{\partial x}$$

where  $q$  is the heat flow,  $v$  is the velocity of the melt

flow,  $A$  is the area through which the melt flows,  $\rho$  is the density of the melt,  $C_p$  is the specific heat capacity of the melt, and  $x$  is the descriptive space parameter perpendicular to the cross-section area. Note also that, though the specific heat capacity of graphite is higher than that of austenite, the austenite has a significantly greater density, hence, being able to transport more heat.

As a consequence of the differences in solidification, the driving forces act differently on the different modulus castings. The M12 castings are intermediary in the behaviour of the M08 and the M15 castings.

The solidification of the castings can be described as a combination of type (a) and (c) described by [46] and seen in fig. 2.12 on page 26, where the small modulus castings primarily exhibit type (a) behaviour, and the larger modulus castings primarily exhibit type (c) behaviour.

## 13.8 Driving Forces

**F**EEDING is the transport of material from one place to another. Preferably from the feeder into the casting. As described in section 2.4, on page 30 there exist five basic feeding mechanisms ranging from liquid to solid. The mechanisms describe how the feed material can be transported, however, the mechanisms do not elaborate on the driving forces necessary to perform any of the five mechanisms.

The seven rules of feeding described in section 2.3, on page 19, indirectly consider the driving forces. The seven feeding rules are made to ensure that the required conditions for feeding are present. Through this effort, some of the driving forces are addressed. Rule six and seven address the *pressure gradient* and the internal melt *pressure*. However, the driving forces moving the feed material for the castings analysed in this work were found to be more complex and non-linear than described in the literature review. Hence, to better explain the findings of the feeding analysis additional elaboration is needed regarding the driving forces feeding the casting.

As defined in section 13.1.1, on page 232, the driving forces are forces acting on the feed material resulting in a transport of material. Moving the feed material from one location to another requires a sum of forces driving the material in the right direction to its final destination.

The primary driving force for feeding most castings is gravity. However, gravity is also the sole

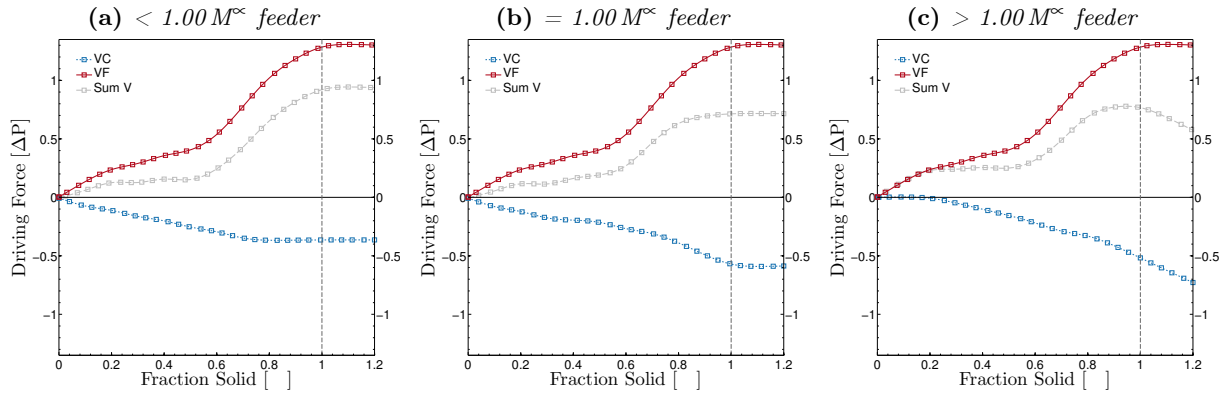


**Figure 13.4:** *Driving Force, Volume Contraction: Overview of the pressure difference created at the feeder and at the casting as a function of the volume contraction that occur during cooling and solidification. VF is the driving force, as a pressure difference, caused by the volume contraction in the feeder. VC is the same for the volume contraction in the feeder. Sum is the resulting driving force. The figure shows the scenarios for (a) a feeder smaller modulus than the casting, (b) where the feeder and casting have the same modulus, and (c) where the feeder modulus exceeds modulus of the casting. The x-axis shows the fraction solid of the casting. The y-axis shows the driving force for feeding, where positive is aiding feeding of the casting, and negative resist feeding of the casting. The scale is arbitrary.*

external force driving the feed material, not considering advanced methods as actively pressurised feeders or magnetic and electrically induced forces.

The feeder setup examined in the present experiment, on the other hand, is almost free from the influence of gravity, with the exception of the internal ferrostatic pressure. This is the case for most applications of horizontally mounted ram-up sleeves. Hence, the present experiment is a study in the manifestation of the internal driving forces and their correlation.

The internal forces act on the feed material as pressure difference. The feed material will then move from the higher pressure potential towards the lower. As the casting solidify the resistance towards moving the feed material will increase. However, different forces develop and diminish during the solidification and cooling of the casting. Hence, if the conditions are right the combined pressure difference of multiple forces may move the feed material unmovable by each of the forces by themselves.

### 13.8.1 Graphic Explanation

Each of the identified major driving forces is described below with respect to how they occur and how they influence the feeding of the casting. Each driving force is elaborated separately even though they are all interdependent to a smaller or larger degree. However, a strict distinction between them

is necessary with respect to the resulting forces. If this distinction is not made it entails the risk of assigning the same effect to multiple forces. For example are volume contraction and graphite expansion opposites, where the graphite expansion will counteract the volume contraction to some degree. Thus, the volume contraction must be narrowed to display the pure volume contraction, not including the graphite expansion. If this is not the case, then the effect of the graphite expansion would appear twice.

The graphs show fraction solid of the casting on the x-axis. Hence, the feeders may solidify completely before or after final solidification of the castings. This is also part of the reason that the graphs are extended beyond the solidification of the casting. The other reason is to illustrate the potential solid feeding occurring at this point, though the effect is estimated as minimal for the examined castings.

The y-axis shows the driving force as a pressure difference,  $\Delta P$ . Positive  $\Delta P$  indicate that a feeder improves feeding of the casting, while a negative  $\Delta P$  means that feeding is reduced and porosity formation promoted. The scale is arbitrary and meant to provide a comparison of the magnitudes of the different forces. The different forces are estimated for the given scenario. The graphs are made to illustrate the correlation and combination between different forces in the casting and the feeder. The graphs should not be taken as calculated or meas-

ured representations of the driving forces. Positive in the y-axis indicates a force moving the feed material towards the casting. Negative on the y-axis means the force draws the feed material towards the feeder.

The feeders are assumed to be insulated ram-up sleeves of the type used for the experiment. These have a cylindrical geometry, a relatively small melt volume due to the insulating or exothermic sleeve. Subsequently, these feeders display a reduced contraction and graphite expansion as a function of the limited melt volume, and the shell-forming is likewise delayed due to the thermal barrier of the sleeve.

### 13.8.2 Volume Contraction (13.4)

---

Analysing fig. 13.4 on page 253 the three subfigures illustrate the cooling and solidification of the same arbitrary casting. The figure shows the pressure difference between the casting and the feeder. For the volume contraction, the negative pressure created in the casting by the contraction draws melt into the casting itself, thus creating a positive feeding force. The three subfigures show the pressure increase as a function of the continued contraction of the casting. The contraction created a reduced pressure, which tries to draw in new feed material to compensate for the shrinkage. At the same time, however, the feeder is also cooling and solidifying, resulting in the same effects. Hence, the feeder also creates a negative feeding pressure, trying to draw the feed material into the feeder.

The force acting on the feed material is the sum of the two individual pressures. As with any tug of war, the balance shifts during the battle as the sides gain and lose momentum.

Note that while the casting is kept constant for all three subfigures, the counter pressure from the different modulus feeders significantly changes the timing and magnitude of resulting force. The  $< 1.00 M^\infty$  feeder in 13.4a solidifies early in the process, exercising an early counter pressure, keeping the resulting force close to negligible for the first half of the solidification of the casting. At this point the feeder is almost completely solidified, hence no further volume contraction occurs, and the feeder remains at this level for the remainder of the solidifications. However, as the casting continues to solidify and contract, the feeding force increases subsequently.

Note that positive feeding force at the end can only be utilised if feed material is available.

The  $= 1.00 M^\infty$  feeder in 13.4b solidify and contract similar to the casting, exercising its negative pressure at roughly the same time as the casting. However, the smaller volume of the feeder reduces its impact.

The  $> 1.00 M^\infty$  feeder in 13.4c cool and solidify slower than the casting. Hence, the feeder remains partly liquid at the time the casting is fully solidified and has reached its full contraction potential. The delayed solidification and contraction of the large feeder enable the contraction of the casting to establish a positive feeding force at the beginning of solidifications, which is retained throughout the solidification. Only when the casting is almost solidified do the pressure decrease. However, at this late stage, the transport of any further feed material is limited.

Of the three scenarios, the large  $> 1.00 M^\infty$  feeder yielded the best feeding scheme.

### 13.8.3 Shell Compression (13.5)

---

Shell compression is the pressure created by the contraction of the already solidified shell. Hence, the pressure cannot build until the shell has solidified and formed enough strength to pressurise the residual feed material. Subsequently, shell compression is a late developing driving force that is very geometry and cooling rate dependent. The geometry determines the surface area for cooling, but also the geometrical strength of the shape. The cooling rate, together with the heat transfer rate of the cast material, determines the thermal gradient from the mould-metal interface towards the thermal centre of the casting. A higher cooling rate of the mould, and a lower heat transfer rate of the metal will increase the shell compression force before the volume contraction negates the effect.

The  $< 1.00 M^\infty$  shown in 13.5a illustrates that the smaller feeder solidifies before the casting, and subsequently the shell around the feeder contracts early and squeezes the feed material into the casting. The shell contraction ceases as the feeder is completely solidified. Not because the contraction has stopped, but because then there is no more feed material to pressurise. The casting also contracts and squeezes the feed material inside the casting at the same time, and as the volume of the casting is greater than the feeder, the shell compression is also greater.

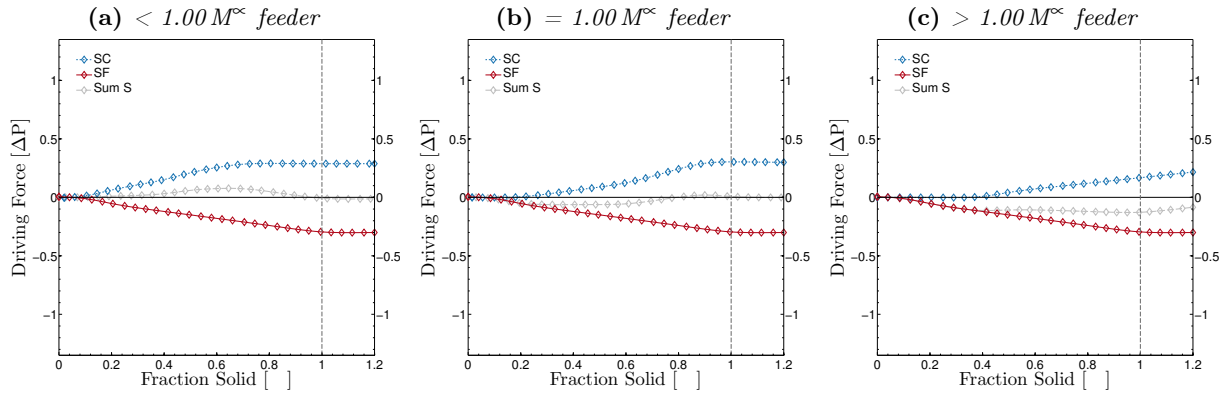


**Figure 13.5:** *Driving Force, Shell Compression: Overview of the pressure difference created at the feeder and at the casting as a function of the shell compression that occur during cooling and solidification. SF is the driving force, as a pressure difference, caused by the shell compression in the feeder. SC is the same for the shell compression in the feeder. Sum is the resulting driving force. The figure shows the scenarios for (a) a feeder smaller modulus than the casting, (b) where the feeder and casting have the same modulus, and (c) where the feeder modulus exceeds modulus of the casting. The x-axis shows the fraction solid of the casting. The y-axis shows the driving force for feeding, where positive is aiding feeding of the casting, and negative resist feeding of the casting. The scale is arbitrary.*

It is estimated that the shell compression is generally weaker than the volume contraction and that the different factors determining the development of the shell compression balance each other out during the course of the solidification. For instance, it is assumed that the heating of the mould, resulting in reduced cooling rate, will be balanced by the reduced latent heat at the end of solidification.

Note, however, that the shell compression is more sensitive to the casting modulus than the volume contraction. Where the volume contraction scales with the volume of the casting, the shell compression is dependent on the heat transport of both the mould and the metal, as well as the amount and timing of the release of the latent heat of solidification from the residual melt. This sensitivity to the thermal conductivity of the alloy itself is as described in eq. (3.4) on page 44:

$$q = -kA \frac{\partial T}{\partial x}$$

where  $q$  is the diffusive heat flow (heat flux) perpendicular to the surface,  $k$  is the thermal conductivity,  $A$  is the area of the surface,  $T$  is the temperature, and  $x$  is the descriptive space component perpendicular to the surface. However, the transport of thermal energy to the surface is only part of the phenomenon, the transport to the mould from the metal, as well as the continued transport of heat away from the castings is just as important. Hence,

the mould-metal interface, as described in section 3.3.3, on page 43, is of great importance for the shell-forming and shell contracting abilities. Note also, that the liquid and solid metal have different thermal conductivities,  $k$ , resulting in a differentiated thermal transport rate.

The  $= 1.00 M^\infty$  feeder case illustrated in 13.5b display a resulting force that remains close to neutral. This is similar to the scenario with the smaller feeder, though the oscillations are opposite. The large  $> 1.00 M^\infty$  feeder, on the other hand, display a negative feeding force for the entire range. This is due to the late shell forming and contraction of the large feeder.

### 13.8.4 Graphite Expansion (13.6)

As the liquid metal solidifies graphite nucleates and precipitates to form graphite nodules (for SG1). The examined alloy composition is slightly hypereutectic, so initially, graphite will precipitate in the liquid. However, as soon as the temperature reaches the eutectic temperature the remainder of the melt will also begin to solidify, as shown by Lesoult et al in fig. 3.6 on page 48.

The nodularity of the graphite nodules is related to the quality of the Mg treatment, while the amount of nodules formed is related to the quality and amount of the inoculant and the cooling rate, as well as the alloy composition. A greater cooling

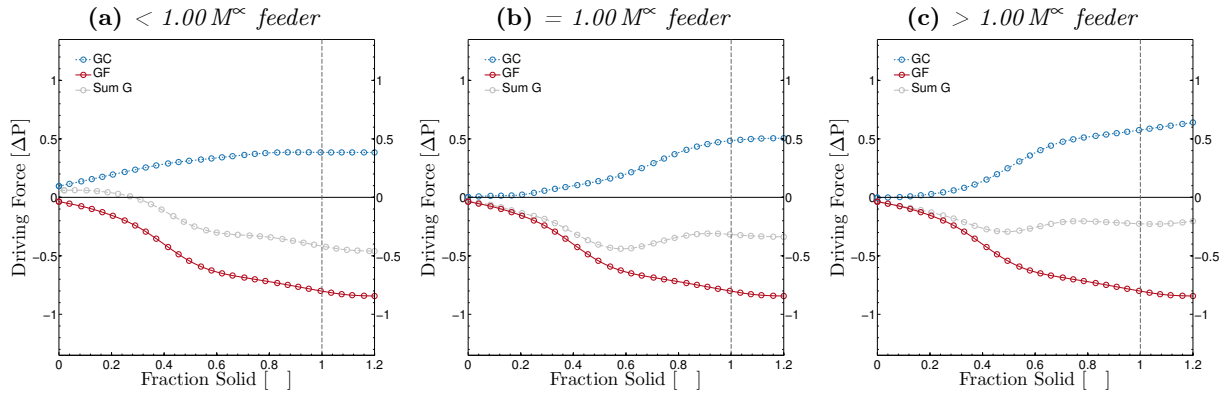


**Figure 13.6:** *Driving Force, Graphite Expansion: Overview of the pressure difference created at the feeder and at the casting as a function of the graphite expansion that occur during solidification and cooling. GF is the driving force, as a pressure difference, caused by the graphite expansion in the feeder. GC is the same for the graphite expansion in the feeder. Sum is the resulting driving force. The figure shows the scenarios for (a) a feeder smaller modulus than the casting, (b) where the feeder and casting have the same modulus, and (c) where the feeder modulus exceeds modulus of the casting. The x-axis shows the fraction solid of the casting. The y-axis shows the driving force for feeding, where positive is aiding feeding of the casting, and negative resist feeding of the casting. The scale is arbitrary.*

rate will result in a larger undercooling, which in turn will increase the nodule count; and reduce the average nodule size by increasing the overall nodule count. For SGI this phenomenon is described by Lesoult et al in eq. (3.12) on page 49 [80]:

$$dN = A_n (\Delta T_L^g)^{n-1} (g^l V^{off}) \frac{d(\Delta T_L^g)}{dt} dt$$

when  $\frac{d(\Delta T_L^g)}{dt} > 0$

and

$$dN = 0$$

when  $\frac{d(\Delta T_L^g)}{dt} < 0$

where  $dN$  is the change in number of graphite particles (nodules) for the time step  $dt$ ,  $n$  is an inoculation efficiency constant,  $A_n$  is an inoculation constant,  $\Delta T_L^g$  is the undercooling relative to the graphite liquidus,  $g^l$  is the liquid fraction of off-eutectic volume,  $V^{off}$ . Thus,  $(g^l V^{off})$  describes the volume of the remaining liquid and its limiting influence on nucleation sites as the solidification progresses.

Besides the influence of undercooling, Lesoult's equation also describes the influence of inoculation,  $A_n$  and  $n$ —inoculation amount and inoculation efficiency.

As the shell compression will counter the volume contraction from the outside by reducing the overall volume of the casting, the graphite expansion will reduce the volume contraction by increasing the material volume.

Additionally, the effect of the graphite expansion is greatly dependent on the solidification time, as a slower cooling and solidification allow for more nodules to be formed and for the graphite precipitation to grow the nodules for a longer period. The relationship between modulus and graphite expansion is shown in fig. 2.7 on page 22.

For the < 1.00 M<sup>∞</sup> feeder in 13.6a the nucleation of graphite nodules has already started in the feeder at the time when the casting started to solidify. However, the reduced volume and small modulus of the feeder yields a relatively limited graphite expansion which reaches its maximum as the feeder solidifies completely. Continued precipitation of graphite is possible after solidification, however, the process is slow even at temperatures close to the melting point. Larger sections benefit more from this than smaller sections, hence, the effect for the < 1.00 M<sup>∞</sup> feeder is assumed negligible.

The = 1.00 M<sup>∞</sup> feeder in 13.6b cool and solidify similar to the casting, hence the precipitation and expansion of the graphite are also comparable. Note, however, that the magnitude of the graphite expansion for the feeder is less than the casting. This is due to the reduced volume of the feeder as



a function of the feeder sleeve. The volume change as a function of the graphite expansion is slow in the beginning. This is because the nodules have to nucleate before the growth can commence. The effect of this is governed by the undercooling and the melt treatment. The initial phase is followed by a growth phase governed by the graphite growth kinetics and the diffusion of graphite through the liquid and solid material. As this progresses the local graphite resources are depleted and the graphite atoms have to travel further to reach the growing nodules. Additionally, the material is more and more solidified, which also slow down the process. Hence, as a consequence of these mechanisms, the graphite growth slows down towards the end of solidification [32].

The  $> 1.00 M^\infty$  feeder in 13.6c is similar to  $= 1.00 M^\infty$  feeder. The main difference is the delayed nucleation and growth of the nodules in the beginning and the prolonged graphite expansion towards the end of the casting solidification. This relates to the slower cooling and solidification of the feeder, compared with its smaller counterparts. The increased overall graphite expansion due to the larger modulus is not effected before after the casting is completely solidified.

### 13.8.5 Other Forces

---

Most traditional feeders capitalise on gravity to move the feed material from the feeder into the casting. This is a simple and reliable method, though elevating the feeder above the casting is not per definition a complete solution. Figure 2.13 on page 27 shows that even gravity driven feeders require that atmospheric pressure acts on the liquid in the feeder to ensure the internal forces, particularly the negative pressure in the feeder caused by volume contraction, retains the feed material within the feeder. Hence, the internal forces are known to overpower the influence of gravity if not negated by a pressure release as the atmospheric vent.

When gravity feeding is so widely used, and a very reliable approach to feeding, it relates to the unchanging nature of gravity and the simplicity and if used together with an atmospheric pressure vent it can negate a major part of the effects created by the internal pressure forces.

#### Ferrostatic Pressure

Gravity, however, also influence the melt in the material regardless of the presence of a pressure

release. It is this effect that allows the mould to be filled via a bottom filling gating system. The melt diverges towards a level height of the liquid, regardless of the volume of the melt in the gating system vs. the casting. The ratio between the gating system and the casting determines the filling rate, especially toward the end of filling.

The ferrostatic pressure is dependent on the melt height as it is governed by gravity. Subsequently, the surfaces of connected melts will be level if the system has an atmospheric contact at both ends. As long as the system remain open there is no difference in the static pressure head, as the system is in equilibrium.

As the gating system and ingate solidify and close off, the counter-pressure provided by this system disappears. Subsequently, the pressure is increased on the lower part of the casting. Gravity will act on the melt, pulling it downwards. However, as the internal forces are more powerful the gravity pull is not the governing force of the feeding regimes.

While the ferrostatic pressure on its own is not one of the strongest feeding forces, the experimental results indicate that it still influences the feeding regimes. This is seen by the differences in porosities observed with castings identical feeders at opposite positions. Hence, the influence of the ferrostatic pressure should be remembered when analysing complex feeding regimes. Additionally, as described by Stefanescu in eq. (2.1) on page 18, the ferrostatic pressure,  $P_{st}$ , is a factor aiding the cohesiveness of the melt and preventing the formation of porosities [26].

The ferrostatic pressure is different from the pressure based feeding forces. The ferrostatic pressure will remain constant as long as the liquid height remains the same. However, the solidification of an intermediary section may abruptly reduce the ferrostatic pressure at the bottom of the casting. This feature is greatly geometrically dependent and may result in abrupt changes to the ferrostatic pressure during solidification, and in change influence the effect of the internal pressure feeding forces.

### 13.8.6 Pressure Loss

---

While the main different feeding forces and their origins have been described in section 13.8, on page 252, other factors influence the outcome of forces acting on the feed material.

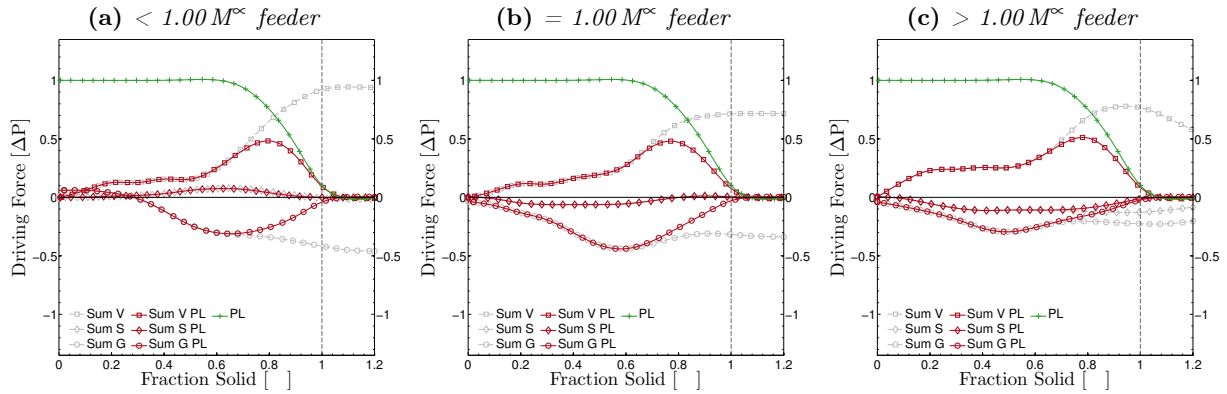


**Figure 13.7:** *Driving Force, Pressure Loss: Overview of the pressure loss effect. The grey and red lines are the sums of the three different feeding forces; Volume Contraction (V)  $\square$ , Shell Compression (S)  $\diamond$ , and Graphite Expansion (G)  $\circ$ . The grey lines show the distribution of the forces without the pressure loss factor, and the red lines show the effect of the forces including the pressure loss effect. The pressure loss factor (PL) + is illustrated by the green line. Note that the pressure loss is a factor and not a pressure in itself. The x-axis shows the fraction solid of the casting. The y-axis shows the driving force for feeding, where positive is aiding feeding of the casting, and negative resist feeding of the casting. The scale is arbitrary.*

### Influence of Feeding Flow

A phenomenon that influences the distribution of the feeding forces is the dynamics of the melt. Liquid iron in motion can carry a great amount of inertia. Hence, melt already in motion may be carried further than force itself justify. This effect may particularly be visible for horizontal feeding distances and with respect to burst feeding as described in section 2.4.4, on page 32. However, the effect is not considered a major influencing factor.

The inertia of liquid iron is well known from the studies of gating systems, as described by Larsen [148] and Skov-Hansen [149]. The EN-GJS-500-14 alloy has liquid density of  $\sim 6.6 \text{ kg m}^{-3}$  [150]. While the velocity, and subsequently also the inertia, is much greater during mould filling, the density of the cast iron melt ensures a high inertia even for the melt in the filled casting. The results in one particular effect; a resistance towards acceleration and deceleration. Hence, the forces required to accelerate and decelerate the melt must either be greater or act on the feed material for a longer time.

Likewise, the movement of the melt entails a flow regime; laminar flow, non-turbulent flow, or turbulent flow [148]. The shift between these flow schemes are described by the Reynolds number,  $Re$ , where a flow with a  $Re$ -value of  $< 2300$  remains laminar, a flow with a  $Re$ -value between 2300 and 13800 is considered non-turbulent, and a flow with a  $Re$ -value of  $> 13800$  is considered turbulent. The

Reynolds number can be calculated by the following equation:

$$Re = \frac{\rho V D}{\mu} \quad (13.1)$$

where  $\rho$  is the density of the liquid,  $V$  is the flow velocity,  $D$  is the characteristic distance, and  $\mu$  is the dynamic viscosity of the liquid.

All of the above factors influence the flow of melt in the casting during feeding. Note that the system is doubly dynamic as both the medium (liquid) and the boundary conditions change during the feeding sequence. The melt cools, which increases both the density and the viscosity of the residual liquid. Similarly, the ‘tubes’ will narrow and change shape as the casting solidifies inwards. Depending on the alloy composition and the cooling rate the surface roughness of the inner wall of the flow tube may also influence the melt flow. Additionally, the velocity of the melt flow is likely to be non-constant. The difference feeding forces will push the melt back and forth accelerating and decelerating the melt along the way. In the same manner, ruptures in the melt caused by tension build up in the melt may also influence the flow with sudden and abrupt movements of the melt. Campbell estimated that these ruptures developed with the speed of sound [25]. Hence, even if the ruptures are less violent than described by Campbell, this type of ruptures must result in sudden movements of the melt, further influencing the flow characteristics.

Another aspect of the melt flow is the venturi effect described by Bernoulli's principle. The principle states that for an inviscid flow of a non-conducting liquid, an increase in velocity will yield a reduction in pressure. While liquid cast iron is neither inviscid nor non-conductive, a pressure drop can still be expected as a function of the melt velocity. This is what happens when the melt passes a narrow section, eg a feeder neck. The velocity of the melt is increased with a decreased pressure in return. The influence of this phenomenon is, however, considered negligible as the melt velocities are expected to be relatively low with respect to the venturi effect.

The dynamic and flow forces are not estimated in the present work.

Campbell also describe the pressure loss experienced as the melt has to feed through an interdendritic structure. This is described in eq. (2.10) on page 32 [25]:

$$\Delta P = 32\eta \left( \frac{\alpha}{1-\alpha} \right) \frac{\lambda^2 L^2 d^2}{R^4 D^2} \quad (13.2)$$

where  $\Delta P$  is the pressure drop across the mushy zone in question,  $\eta$  is the viscosity of the melt,  $\alpha$  is the coefficient of thermal expansion of the liquid,  $L$  is the length of the capillary flow through the mushy zone,  $d$  is the dendrite arm spacing,  $R$  is the radius of the capillaries, and  $D^2$  is the area of the mushy zone the melt must travel through. The actual flow resistance may be even higher than predicted by eq. (2.10) on page 32, as this assumes straight channels and aligned flow.

However, as the EN-GJS-500-14 alloys is hyper-eutectic and for very few dendrites, the dendrite arm spacing used in eq. (2.10) on page 32 can be difficult to use correctly. For eutectic and hyper-eutectic cast irons it may thus be better to use Darcy's law of flow through a porous medium to describe the feeding flow, as these alloys do not form dendrites but solidify as grains [68, 70]:

$$\frac{dp}{dx} = \frac{\mu(1-f_s)}{K} v \quad (13.3)$$

where  $dp/dx$  is the incremental pressure change per distance,  $\mu$  is the viscosity of the liquid metal,  $f_s$  is the fraction of solid,  $K$  is the permeability of the porous region being fed, and  $v$  is the velocity of the liquid metal. Darcy's law shows how the pressure loss increase for each increment towards the 'back' of the mushy zone which is being fed. It also shows that the feeding is very dependent on the permeability of the mushy zone, naturally,

but also that both viscosity, velocity, and fraction solid matter. Note that while most of the factors in Darcy's law are conditions influencing feedability, the melt velocity,  $v$ , is a direct derivative of the driving forces.

### Pressure Loss Factor (13.7)

The pressure loss caused by increased viscosity,  $\mu$ , and reduced permeability,  $K$ , is only part of the pressure loss experienced by the feed material. The solidification of the casting limits the pressure distribution through the feed material. The closer to complete solidification the casting becomes, the greater force is required to feed the remaining feed areas. The total pressure loss of the feeding channel increases, hence, the feeding force requirement also rise. Eventually, the solidification of the casting will terminate the feeding process. The point at which this happens, and how fast, depends on the development and direction of the feeding forces as solidification commences, the condition of the feed path and feed material.

A narrow feeding path may remain easy to feed through until late into solidification of the casting, if the alloy solidifies as an endogenous shell-forming alloy, and if a thermal gradient can keep the melt from becoming too mushy. The latter was seen for some of the castings with two feeders and shown in figs. 12.20 to 12.22 on pages 218–220. On the other hand, an exogenous alloy with a long freezing range may close off very early in the solidification process. This is aided by a high cooling rate.

The pressure loss can be described as a factor influencing all feeding forces. The factor ranges from 1 to 0; where 1 signifies that there is no pressure loss in the casting, and 0 signifies that all feeding forces are negated by the pressure loss. The relatively loss-free feeding ranges from the beginning of solidification until the solidifying casting in one way or another begins to hamper the free flow of feed material. From this point onward the solidification of the casting will increase the pressure loss. The progression of this may be linear or it may be non-linear. This depends on which mechanisms develop and hinder the free flow, and this again is dependent on the alloy composition, the cooling conditions, and the geometry. Finally, as the casting solidifies completely the pressure loss factor diverges towards 0. Note that the pressure loss may not be absolute at the point of complete solidification. Again depending on the magnitude of the feeding forces,

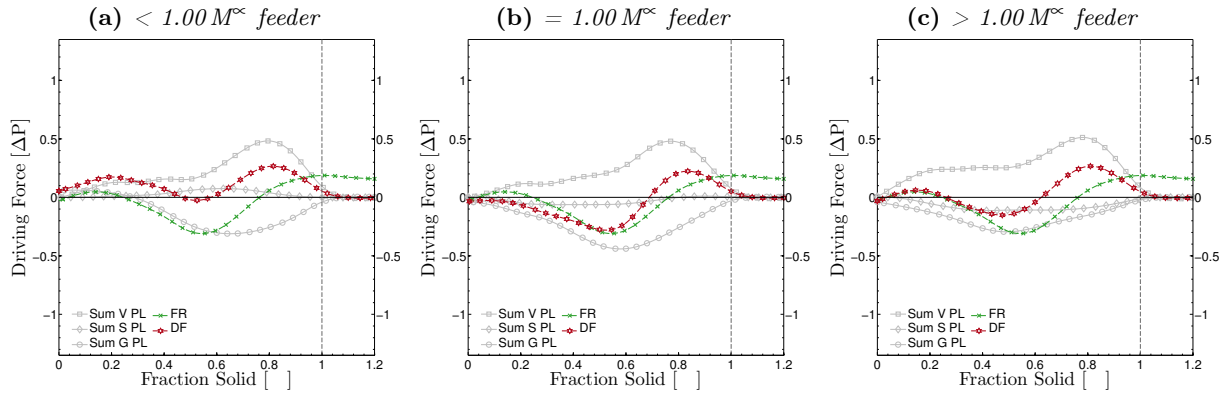


**Figure 13.8:** *Driving Force, Feeding Requirement: Overview of the need for feeding. The grey and red lines are the sums of the three different feeding forces; Volume Contraction (V)  $\square$ , Shell Compression (S)  $\diamond$ , and Graphite Expansion (G)  $\circ$ . The grey lines show the distribution of the driving forces (DF)  $\star$  with the pressure loss factor. The red line shows the sum of the forces including the pressure loss effect. The feeding requirement (FR)  $\times$  is illustrated by the green line. Note that the feeding requirement is not a pressure but a volume. Here it is shown on the same scale to illustrate the correlation. A positive feeding requirement equals a shrinkage that needs filling, a negative feeding requirement illustrate a reduction of the volume to be filled. The graphite expansion is the primary cause of the expansion effect, hence a negative feeding requirement is seldom seen for alloys other than cast iron. The x-axis shows the fraction solid of the casting. The y-axis shows the driving force for feeding, where positive is aiding feeding of the casting, and negative resist feeding of the casting. The scale is arbitrary.*

the strength of the solidified metal, which again is temperature dependent, the casting may be subject to solid feeding, as described in section 2.4.5, on page 33. In principle the pressure loss factor never reaches 0. Cold forging can, for instance, be viewed as a form of solid feeding with external forces, so the effect can occur at lower temperatures if only the forces are great enough. The same can be said for the Hot Isostatic Pressing (HIP) process. For any practical purpose regarding feeding, the pressure loss factor can be assumed to reach 0 shortly after the complete solidification of the casting.

The effect of the pressure loss effect is shown in fig. 13.7 on page 258. The figure shows that the feeding forces have a great efficiency at the beginning of solidification. However, as the casting solidifies the influence of the feeding forces diminish as the increasing pressure loss negates the possibility for feeding. As a result, the feed material is most easily moved at the beginning of solidification.

Note that the pressure loss reduces both the positive and the negative feeding forces, hence the pressure loss does not influence the balance directly. However, as the different forces display their effect at different times during the solidification of the casting, the pressure loss effect may very well indirectly influence some forces more than others.

### 13.8.7 Feeding Requirement (13.8)

The feeding forces describe the ability to move the melt and the pressure loss describe how the feeding forces are overpowered by the increasing flow resistance towards the end of solidification. The feeding requirement, on the other hand, describe the need for feeding which entails both volume and time. Successful feeding requires that the feeding forces can transport a sufficient amount of feed material into the casting at the time it is needed.

Figure 13.8 shows the correlation between the feeding forces and the feeding requirement. Note that the two lines are closely related. This is because the origin of some of the feeding forces is the feeding requirement itself—in this case, shown as the volume contraction, shell compression, and graphite expansion. The sum of the feeding forces are shown in a red line, and display the sum of the three estimated feeding forces assessed in figs. 13.4 to 13.7 on page 253, on page 255, on page 256 and on page 258.

The feeding requirement, shown in green in fig. 13.8, is calculated as the sum of the volume contraction, shell compression, and graphite expansion of the casting itself. Note that some of these have a negative attribution to the sum, as eg the graphite expansion will reduce the need for feeding.

The feeding requirement is a volume requirement and the graph shows pressure difference, hence, it should be noted that the feeding requirement can be used to assess the timing of the feeding forces in accordance to the shrinkage in the castings. However, the scales are not the same and only a relative comparison can be made.

### Early Solidification

Analysing the feeding requirement in 13.8 it was found that the dominant contribution at the beginning of solidification was the volume contraction of the solidifying melt. This results in a feeding requirement, which may be filled by a flow of feed material into the casting from the feeder if the driving forces are strong enough and there is melt enough available. At this point, the small  $< 1.00 M^\infty$  feeder provides the greatest feeding pressure, followed by the large  $> 1.00 M^\infty$  feeder with a slightly smaller pressure, and finally, the proportional  $= 1.00 M^\infty$  feeder which yields almost no feeding pressure at this early stage of solidification.

### Intermediate Solidification

Following the initial increase in the feeding requirement, the growing contribution from the shell compression and the graphite expansion overpowers the volume contraction, resulting in a net expansion of the volume of the casting. The expansion can either squeeze the melt out of the casting, contain the pressure build up, or expand the mould cavity.

Squeezing the melt out of the casting can move the melt into the feeders or into the gating system, or in case of a more complex casting into other casting sections. If this is not possible because the gating system is already solidified and the feeder already full, the combined strength of the casting shell and the mould determines what happens.

If the shell and mould are strong enough to withstand the pressure build up, then the pressure is stored inside the melt. This will be released as the feed requirement increases again, at which time the stored pressure will manifest as a prolonged expansion, further reducing the feeding requirement.

If however, the shell and mould together cannot contain the pressure build up, the casting and mould cavity deforms as shown in fig. 2.14 on page 28. This is unintentional for several reasons. The dilation changes the geometry of the casting, resulting

in castings that do not match the intended shape or volume. Additionally, the dilation expands the volume of the casting but not the available melt. Hence, the increased volume will manifest itself as porosities in the casting. Similarly, the pressure builds up that would otherwise have reduced the feeding requirement was released in the mould and casting dilation. On the other hand, the subsequent volume contraction is also increased and some of the lost feeding force may be regained this way.

### End of Solidification

Towards the end of solidification, the volume contraction again overtakes as the dominant force, resulting in an increase in both feeding force and feeding requirement. Note though, that the pressure loss reduces the effect of the feeding forces towards the end, while the pressure loss naturally has no influence on the feeding requirement. This, however, is not a complete description of the final stage of solidification and feeding. If the feeding system has been correctly designed for the casting—according to the seven rules of feeding—the feeding path will solidify towards the feeder in a manner that keeps the path open to feed itself as it solidifies. Hence, the pressure loss in the feeding channel may be much lower than the graphs in figs. 13.7 and 13.8 on page 258 and on page 260 might indicate. Controlling the direction of solidification, as thus also the pressure loss towards the end of solidification may be very important to utilise as much of the feeding forces as possible. Additionally, also the feeding distance and the related pressure loss is increasingly significant towards the end of solidification, as the feeding path gets less permeable and the melt becomes more viscous.

Another aspect of the final stages of solidification and feeding is the availability of feed material. Though the required feeding forces are present at the same instance as the feeding requirement requires melt, the demand can only be met if feed material is available, as described in section 2.3.3, on page 21.

### 13.8.8 Other Factors

---

In addition to the feeding forces, the pressure loss factor, and the feeding requirement, other factors may also have a significant influence on the feeding success.

## Melt Cohesiveness

The cohesiveness of the melt is important with regard to maintaining a pressure differential through the melt, as described in section 2.2.1, on page 17. The tension in the melt can be released by the melt moving to ease the tension, or by the melt breaking apart so that a porosity is created. When the feed material is moved by a negative pressure a tension is created in the melt. If the melt is cohesive and without weak points (impurities) that can initiate a fracture, the melt will remain a unit. If the cohesiveness of the melt is not strong enough, then the melt will break apart, creating a porosity.

With eq. (2.1) on page 18 Stefanescu shows that the gas evolution,  $P_{gas}$ , and the resistance to shrinkage induced flow,  $P_{shr}$ , are the driving forces for pore formation. The nucleation of pores is governed by the relationship between the maximum solubility of gas in the melt,  $C_L$ , and the amount of gas in the melt,  $C_L^{max}$ . See fig. 2.6 on page 18. The stability of the pore after it is formed is given by [26]:

$$P_\gamma = \frac{2\gamma_{LG}}{r}$$

where  $\gamma_{LG}$  is the gas/liquid surface energy, and  $r$  is the radius of the pore. As discussed previously in this chapter, as well as in section 2.2.1, on page 17, this equation shows that a very small initial radius of the pore results in a very large surface tension, making it unlikely that homogeneous nucleation will occur, which in turn will open further as a rupture if the melt is under tension.

To distinguish ruptures from other types of porosities, ruptures can be defined as porosities created by the tension in the melt in combination with the lack of cohesiveness in the melt.

Note that both outcomes—rupture or no rupture—may be advantageous or disadvantageous. It depends on the location of the rupture. If the melt displays a high cohesiveness the feeding pressure can be transferred to the melt in the feeder, pulling the feed material towards the casting. This transfer of pressure, however, is only advantageous if the pull from the casting is stronger than the pull from the feeder. A casting where the pressure buildup is small enough to not cause ruptures (porosities) in either the casting or the feeder is very uncommon. Hence, most castings will experience melt ruptures. Thus, the location of the rupture becomes important, and subsequent also the potential location of impurities. A rupture can behave similarly to an atmospheric puncture in the sense that it can release

the tension in the melt. If the rupture is located in the casting the melt may retract into the feeder. If the rupture is located at the feeder it may ease the transport of feed material into the casting. Note, however, that the melt on the far side of the rupture is, momentarily at least, cut off from the feeding forces, and thus cannot be pulled into the casting. Hence, a rupture at the feeder reduces the available feed material.

Impurities in the melt are uncontrollable and are known to cause melt ruptures [24]. Hence, if these were the only origin of fractures in the melt, feeding would be a very random process—some might say this is actually the case. However, ruptures in the melt are also temperature dependent. The cohesiveness of the melt is reduced with increasing temperature [32]. Hence, the hot melt in the feeder is more likely to rupture than the cooling melt inside the casting, assuming the melt is free of impurities.

## Pouring Temperature

The pouring temperature controls more than the liquid volume shrinkage. The initial temperature of the melt as it enters the mould cavity greatly influences the thermal gradients of the casting. While a higher temperature will result in a greater liquid shrinkage, reducing the remaining liquid in the feeder, it will also ensure the intended thermal gradients with a hot feeder and a colder casting. This is because feeders are designed as low modulus geometries that cool slowly, hence the casting will if the feeder is designed correctly, cool faster than the feeder.

However, these changes also influence the development of the feeding forces. A hotter feeder will display larger liquid shrinkage. However, as this occurs early in the process, no shell has formed and no negative pressure is created as a function of the volume contraction. Later in the solidification process, the reduced volume will yield a belated graphite expansion because of the hotter feeder, and an overall reduced graphite expansion due to the reduced melt volume contained in the feeder. Note that this is not the case for horizontally mounted spot feeder as used in the experiment. Here the increased liquid shrinkage is absorbed elsewhere in the casting.

Generally, as the thermal gradients of the casting changes, the sequence of the feeding forces also shift. A relatively colder casting will form a shell earlier, the volume contraction will happen earlier, and the

graphite expansion will occur earlier. The opposite is true for the relatively hotter feeder. Here all the forces will be delayed. Hence, the pouring temperature is a simple way to adjust the shift between the feeding forces of the casting and the feeder. Unfortunately, it is more difficult to conclude which direction—hotter or colder pouring—is preferable, as this is dependent on both the casting and feeder geometry, the feeder type (geometrical, insulating, or exothermic), the alloy composition, the cooling rate, and the stability of the mould. For instance, the initial liquid shrinkage may be compensated by the graphite expansion, which in a weak mould would else have caused mould dilation.

For the scalable castings used in the experiment, it would be advantageous to increase the pouring temperature for all three feeder sizes. The main reason for this is, that the driving force analysis that is shown in figs. 13.4 to 13.6 on page 253, on page 255 and on page 256 show that this will benefit the shift between the casting and feeder feeding forces. Hence, the initial volume contraction of the casting will be countered less by the forces generated by a hot feeder enabling better early feeding. The subsequent graphite expansion will then be partly absorbed by the simultaneous initiation of the volume contraction of the melt in the feeder. The same is partly true for the shell compression. Finally, the postponement of the driving forces origination from the feeder is then utilised at the final stages of solidification for the casting.

It is difficult to assess the exact temperature difference between the casting and the feeder that is required to achieve the full effect of the above example. In most cases the thermal gradient created may shift the initiation of the different feeding forces, though it is unlikely that the full effect can be achieved only based on varying the pouring temperature.

It should also be noted that the sleeved feeder does not scale in the same manner as the casting or a geometrical feeder. Where the casting and the geometrical feeder have the same cooling conditions from the mould, the insulating sleeve cools slower due to the insulating material. However, the melt volume is also reduced, hence the extra heat energy provided to the feeder is also less than a similar geometrical feeder. In this case, the net cooling time for the casting may increase more than the insulated feeder. The feeders with exothermic sleeves may be even more sensitive towards this change in pouring temperature. The volume of the feeder is, for the

same modulus, even smaller than the insulating feeders, hence, the extra thermal energy contributed to the feeder by the melt is relatively smaller. At the same time, the thermal addition to the feeder by the sleeves remains the same, though it should also be noted that the exothermic sleeves provide some insulating abilities besides the exothermic reaction.

In summary, the simplest solution seems to be to use feeders with extra exothermic material. This will prolong the cooling of the feeder without changing the volume, and would also benefit the melt cohesiveness to rupture at the feeder. At the same time, it will not require a hotter pouring temperature, as this would only negate the effect of the exothermic feeder by increasing the temperature of the casting. However, it should also be noted that this would only have an effect if the melt volume of the feeder was still large enough to meet the mass-transfer criteria described in section 2.3.3, on page 21, and had enough melt to successfully utilise the driving forces generated by the feeder.

The 22E12 feeder had a design with a thicker sleeve and smaller melt volume, compared with the design of the other sleeves used during the experiment. Viewing table 12.1 on page 180 it was found that this feeder design yielded average results for the M12 casting and the M15 casting by itself. The M15 casting where it was used in combination with other feeders yielded above average porosity results.

#### Effect of Multiple Feeders

The examples describing the interaction of the feeding forces are simplified to some degree. One of the aspects that are not included in the feeding force analysis is the possibility of using multiple feeders, as was also part of the experiment.

The geometric solidification analysis shown in figs. 12.20 to 12.22 on pages 218–220, illustrate the difference in solidification between the single feeder combinations and the multiple feeder combinations.

The additional feeder extends the heated zone at the centre of the casting. As a result, the central feeding channel is kept open until a late stage of the casting solidification. The solidification of the casting grows inwards, reducing the diameter of the feeding channel. However, it is proposed that the connection between the two feeders result in a convection effect with hot melt rising at the centre of the feeding channel—a piping effect. This in turn normally change the thermal gradient of the feeding channel keeping it open for feeding long as this would also reduce the pressure loss at the

centre. Without two feeders the thermal gradient will be towards either the top or the bottom of the casting. The piping effect created by two connected feeders will result in a rising hot centre, with cold melt sinking towards the bottom on the outside close to the solidification front. Hence the piping effect changes the thermal gradient from a vertical gradient to a horizontal gradient.

Additionally, as the solidification of the casting progresses longer before the final stages of feeding are initiated, the feeding forces would have reached a greater magnitude at this stage, further assisting the feeding process.

Analysing the porosities of the casting in table 12.1 on page 180 it was found that not all feeder combinations benefited from an additional feeder. The lower feeder may easily become a sink fed by the casting instead of the feeder feeding the casting. This is seen for the C05 and C17, for the M15 casting. However, the same combination improves with an extra feeder for the small M08 casting. The effect depends on the combination of feeding forces, as shown in fig. 13.8 on page 260, as well as the modulus of the casting. Adding an extra feeder to the casting will introduce a new set of driving forces; volume contraction, shell compression, and graphite expansion. Are the feeders of the same modulus and volume, the effects can be expected to appear almost simultaneously, especially at the beginning of the solidification process. The further the solidification progresses the more will the melt be moved around inside the casting. Some melt may be drawn from the top feeder early in the solidification process, as indicated in fig. 13.8 on page 260. Subsequently, the melt may be pushed back into the feeder by the graphite expansion. The lower feeder, on the other hand, will naturally be kept full at the early stages of solidification. The initial volume contraction cannot draw melt from the lower feeder, as this would require a negative pressure buildup, which in turn would require a casting shell to be formed first.

The difference between the castings with a single feeder and multiple feeders relate to both the changed geometry of the solidifying melt and the addition of an additional set of feeding forces. While not all feeder combinations with two feeders yielded improved feeding results, the best results recorded all used two feeders, with the exception of C09 for the M15 casting. Here the lone lower feeder managed to feed the casting very well. The same feeder, aided by different upper feeders—C12, C15, and

C21—performed as well or better. Only the C18 combination performed a little worse than the C09 with only the lower feeder. The combination that performed less well than the other was the combination that had the same feeder at both the upper and the lower location. As concluded previously this indicates that the best results can be achieved by using different modulus feeders to ensure a direction of solidification. At least for the large M15 castings, though it should also be noted that one feeder combination, the C16, using identical feeder did perform for the large M15 casting. The small M08 castings showed the best results with identical or close to identical feeders, as seen with the C05, C08, C11, C14, C17, and C20 in table 12.1 on page 180.

**Convection, Advection, and Segregation** To explain this phenomenon it is proposed that the cause is to be found in the differences in solidification behaviour of the different modulus castings. The small M08 casting, as described in section 13.7, on page 251, solidify fast with little time to form grains or equiaxed dendrites that can sediment towards the bottom. This is not the case for the larger M15 castings, as shown in figs. 12.17 and 12.18 on page 211 and on page 213. For the smaller castings, the two feeders will ensure a directional solidification towards the centre of the feeding channel connecting the two feeders. Hence, the feeders provide the required feed material to substitute the volume shrinkage inside the casting. Some convection, and possibly also advection, may occur in the residual melt, however, the solidification is too rapid to be significantly influenced by segregation effects. The sizable castings, on the other hand, will solidify slowly enough to cause segregation of grains and dendrites in the residual melt. Graphite segregations will then settle towards the bottom as they are heavier than the surrounding melt. This will happen close to the edges of the channel as hot melt will be rising at the centre due to convection effects, as is also the case for the small M08 castings.

For the small castings that solidify without the segregation effects the main influence of the second feeder is to ensure a directional solidification, both inwards towards the centre of the feeding channel, but also towards one of the feeders. As the combinations with identical feeders yield promising results for the small castings, this indicates that small castings may develop a small gradient naturally. However, as the geometry is a scaled-down version of the large castings, this effect should also



be observable for the larger castings if this was the case. In fact, it may actually be but muffled or obscured by other effects present in the larger castings. Another explanation could be the combined feeding forces of the two identical feeders managed to feed one half of the casting each towards the end of solidification. When the feeding channel connecting the two feeders eventually closes off, some residual melt will still remain in the casting, though the final amount requiring feeding may be smaller than for the single feeder option. Hence, for the small castings, the optimal feeding scenario may be to reduce the remaining melt volume as much as possible before each feeder feeds a separate final volume.

The segregation of the larger castings eliminate the ability to have two identical feeders solidify in the same manner at the end of solidification. The sedimentation of the segregated grains and dendrites sediment towards the bottom, or with containing enough graphite raise to the top, subsequently cooling the lower section of the casting and the lower feeder or vice versa. The advection effect can in principle also be found in the small castings. Here, however, the rapid cooling limits the effect. It is proposed that the additional feeder is beneficial for the feeding of large sections, partly because of the same reasons that apply to the smaller modulus castings, but also because it counters some of the sedimentation of grains and dendrites caused by the slower solidification. A large casting with only an upper feeder will have a shorter and relatively wider residual melt volume. This is because of the solidification moving upwards from the bottom, hence the volume will experience a reduced length earlier in the process before the inward solidification has progressed as far. This results in an ellipsoid geometry similar to the natural solidification geometry of the casting, as was shown in the geometrical solidification analysis in section 12.3.5, on page 214. For this scenario, if the thermal gradient is not great enough, the sedimentation of the grain and dendrites may result in a large mushy zone, that in turn would be difficult to feed as there are few driving forces to push the feed material into the sedimented mushy zone. The lower feeder, if large enough, is an effective way to keep the feeding channel open for longer and reducing the volume of the sedimenting mushy zone. The feeding distance between the fully liquid melt and to the fully eutectic end of the interdendritic feeding is greatly reduced. See fig. 2.18 on page 32. The reduced distance, in turn, reduces

the pressure loss, which means the feeding requires a smaller feeding force. Possibly the capillary forces may be enough to draw the melt into the dendritic structure by itself if the distance is small enough.

## 13.9 Feeding Regimes

THE progression of the feeding can be divided into multiple stages of feeding. These stages are governed by the feeding requirement, shown in fig. 13.8 on page 260 and the success of the feeding is decided by the feeding forces and other influencing factors. The feeding regime changes with feeder combinations, casting geometries, alloy composition, and cooling conditions to list the major factors. Hence, two castings may be close to similar, in geometry or casting conditions, and one will yield a successful porosity-free casting, while the other yield a very high scrap rate. Due to the multitude of factors influencing the feeding regime, even small changes may be significant. Regarding the experimental castings, this was best illustrated by combinations C09 and C10 for the large M15 casting. Both were equipped with a single lower feeder. The C09 combination had a  $1.00 M^\infty$  feeder and yielded few porosities at the middle control volume. The C10 combination had the same setup, but with a  $1.27 M^\infty$  feeder, which resulted in large (4) porosities for all three control volumes. In principle melt impurities and inclusions, causing porosities can also be viewed as part of the feeding regime.

Analysing and identifying issues with the feeding regime of a casting is difficult. Process variation, large or small, occur constantly and the feeding result may also be influenced by random factors as eg melt impurities. Hence, a proper feeding regime encompasses a safety margin that can secure a stable feeding performance taking into account the reasonable process variations expected in the foundry. In this respect note that the safety margin cannot be treated as a simple factor to enlarge the feeder volume or modulus at the end. The important part is to ensure that the sum of feeding forces corresponds to the feeding requirement and that there is enough feed material available at the required time. Hence, if one feeding force is reduced or shifted, it may be compensated by other forces, yielding a similar outcome.

The challenge is to identify and quantify the feeding force, feeding requirement, and how they are influenced by the casting conditions. An approach can be made by macro modelling, though this is

beyond the scope of this project, and while modelling can provide useful insight and found the basis of the numerical simulations of tomorrow, a modelling approach is not viable to the foundry engineer troubled by porosities. Numerical simulation software, like eg MAGMASOFT [69], Novacast [151], and Flow-3D [152], are widely used in foundries around the world and provide valuable input to casting designers and foundry engineers about the casting process. Numerical simulation cannot, at the time of writing, provide information about the feeding forces directly. However, the information provided can be very useful in analysing the behaviour of the casting. Knowledge of the thermal gradient of a casting is for example important to any feeding analysis, and thermal measurement on the actual casting can only provide a partial picture. Thus, calibrated numerical simulations are the basis for analysing the feeding regime of a casting.

For the scalable casting used in the experiment, the analysis is simplified by the simple geometry. As the feeding force and the feeding requirement are all assessed, the analysis is not an exact display of the actual feeding regime. However, the understanding of feeding as an entire regime consisting of multiple interdependent factors is used as a mindset to interpret the experimental results. This approach, as stated at the beginning of the section, have shown that the feeding is governed by the feeding requirement and the success determined by the feeding forces, factors and availability of feed material.

The feeding regime of the scalable casting can be divided into three stages; initial feeding, expansion feeding, and directional feeding. Note that the subsequent feeding regime analysis is a general analysis encompassing many different feeder combinations that, per definition, all have different feeding regimes.

### 13.9.1 Initial Feeding

---

Initial feeding describes the early stage of feeding. This covers feeding liquid shrinkage as a result of a superheated melt and the initial stages of volume contraction experienced by the casting. The phase is characterised by occurring at the early stage of solidification, hence the feed material is still completely liquid and easily transported. Subsequently, gravity and the volume contraction itself is almost always sufficient to transport the feed material into the casting, filling the vacancy of the contracting

melt. For the experimental castings, the feeder combinations with only a lower feeder may experience a rupture in the melt, resulting in an empty unfilled volume at the upper part of the casting. Though the build up tension in the melt is still small at this early stage, the melt is also hotter and will more easily rupture—assuming that the rupture is not gas related. Note, however, that ruptures formed at this early stage can be re-closed during at later feeding stage as long as the porosity has not had contact with the atmospheric air.

If the cohesiveness of the melt is sufficient, the casting may pull the required melt from the lower feeder, assuming this has retained a pressure release vent to the atmosphere. It is not advantageous that a rupture forms in the volume of the casting, however, at this early stage the damage can be repaired at a later stage of feeding. Note that the required negative pressure build up to pull the melt from the lower feeder is dependent on the strength of the formed shell.

The initial feeding stage is governed by the volume contraction as both the primary feeding force and the feeding requirement.

### 13.9.2 Expansion Feeding

---

The second feeding stage is called expansion feeding, as the combined forces reduce the feeding requirement to a negative entity. The main driver is the graphite expansion, which as it nucleates and grows to increase the total volume of the solidifying melt. In principle the feed requirement can also be reduced shell compression, however, this entails that both the HTC of the mould-metal interface is high and that the mould has a good thermal conductivity or heat capacity. Additionally, the shell compression would favour an exogenous alloy to help form a strong shell at an early stage of solidification. An endogenous shell-forming alloy like most cast iron alloys does form a shell. However, the latent heat from the eutectic solidification of the short freezing range is not favourable in terms of making the casting contract on itself to reduce the required amount of feeding.

Even though cast iron does not rely on shell compression to generate a negative feeding requirement, the shell and the mould are very important at this stage, as well a pressure relief in form of a partly empty feeder. As the expansion feeding occur the combined strength of the weak shell and the relatively weak green sand mould has to contain the

pressure build up that cannot be diverted to the feeder.

For the experimental casting the final shape of the castings, which resemble the pattern without bulging, indicate that the combined strength of the shell and mould could retain the pressure build up. The expansion was greatest in the large M15 casting as the slower solidification allowed for a greater graphite expansion as shown in fig. 2.7 on page 22 and the less steep thermal gradient resulted in a more concentrated volume expansion.

A more describing name for the phenomenon may be *self-feeding* as this concept encompasses both shell compression and graphite expansion. This name was used by Karsay to describe the workings of feederless casting designs [19] However, self-feeding is also used as a term for solid feeding, hence, to avoid confusion the term *expansion feeding* was chosen. An alternative that encompasses both mechanisms may be *negative feeding* or *mould feeding*.

### 13.9.3 Directional Feeding

The final feeding is the most important stage of the feeding regime. It may be aided by the expansion feeding, however, the feeding requirement at the end of solidification must still be met in order to avoid porosities in the casting. Figure 13.8 on page 260 shows that the feeding requirement increases again towards the end of solidification, while at the same time the pressure loss begins to inhibit the transport of feed material into and through the casting. The combination of reduced driving forces at the time of an increasing feeding requirement is what makes this part of the feeding regime so difficult.

However, this is also the feeding part that is addressed in most of the literature. The feeding mechanisms described in section 2.4, on page 30 all apply to the final stages of feeding, though it should be noted that the five mechanisms are not limited to the final stages of solidification. The seven rules of feeding described in section 2.3, on page 19 address how to ensure that the casting and feeder solidify in a manner that allows for feeding at this final stage. This has also given rise to the name of the final feeding stage—*directional feeding*. The reason is that the pressure loss effect will eventually overpower the feeding forces and negate further feeding. This, however, is a gradual phenomenon that progresses through the casting as the different sections solidify. Securing a feeding path that can

be kept open long enough is key to ensuring that feeding continues until the end of solidification. This was found in the analysis of the effect of using multiple feeders in section 13.8.8, on page 263.

Except for the difference in graphite expansion, the main difference in the feeding regimes between the three different modulus castings relate to segregation effects.

## References

- [19] Stephen I. Karsay. “Rising Methods for Gray and Ductile Iron Castings”. In: *Int. Cast Met. J.* 5.4 (1980), pp. 45–51.
- [20] Petr Kotas. *Integrated Modeling of Process, Structures and Performance in Cast Parts*. DTU Mechanical Engineering, 2011. ISBN: 978-87-90416-54-6.
- [21] N Chvorinov. “Solving Feeders and Sink-heads”. In: *Proceedings of the 30th International Foundry Congress*. 1963.
- [22] PN Hansen, PR Sahm and E Flender. “How to Select and Use Criterion Functions in Solidification Simulation”. In: *Transactions of the American Foundrymen’s Society*. 101 (1993), pp. 443–446.
- [23] John R. Brown. “FOSECO Ferrous Foundryman’s Handbook”. In: FOSECO International Ltd., 2000. Chap. 19, pp. 296–310.
- [24] John Campbell. *Casting Practice - The 10 Rules of Casting*. Linacre House, Jordan Hill, Oxford OX2 8DP, 30 Corporate Drive, Burlington, MA 01803: Elsevier Butterworth-Heinemann, 2004. ISBN: 0 7506 4791 4.
- [25] John Campbell. *Castings, 2nd Ed*. Linacre House, Jordan Hill, Oxford OX2 8DP, 30 Corporate Drive, Burlington, MA 01803: Elsevier Butterworth-Heinemann, 2003. ISBN: 0 7506 4790 6.
- [26] DM Stefanescu. “Computer Simulation of Shrinkage Related Defects in Metal Castings—A Review”. In: *International Journal of Cast Metals Research* 18.3 (2005), pp. 129–143.
- [32] David A. Porter, Kenneth E. Easterling and Mohamed Y. Sherif. *Phase Transformations in Metals and Alloys*. 3rd ed. CRC Press, Taylor & Francis Group, 6000 Broken Sound Parkway NW, Suite 300, Boca Raton, FL 33487-2742, 2009. ISBN: 978-1-4200-6210-6.

- [37] Nicolas Chvorinov. “Theory of the Solidification of Castings”. In: *Giesserei* 27 (1940), pp. 177–186.
- [39] M. Tiryakioğlu, E. Tiryakioğlu and D.R. Askeland. “The Effect of Casting Shape and Size on Solidification Time: A New Approach”. In: *International Journal of Cast Metals Research* 9. (1997), 259–267.
- [46] M. Petrič, J. Medved and P. Mrvar. “Effect of Grain Refinement and Modification of Eutectic Phase on Shrinkage of AlSi9Cu3 Alloy”. In: *Metallurgija* 50.2 (2011), 127–131. ISSN: 0543-5846.
- [68] Jonathan A Dantzig and Michel Rappaz. *Solidification*. EPFL press, 2009.
- [69] MAGMASOFT 5.2 by MAGMA GmbH. [http://www.magmasoft.com/en/solutions/MAGMA\\_5.html](http://www.magmasoft.com/en/solutions/MAGMA_5.html). Program. 2014.
- [70] Jesper Henri Hattel et al. *Fundamentals of Numerical Modelling of Casting Processes*. Polyteknisk Forlag, 2005. ISBN: 978-87-502-0969-0.
- [80] G Lesoult, M Castro and J Lacaze. “Solidification of Spheroidal Graphite Cast Irons—I. Physical Modelling”. In: *Acta materialia* 46.3 (1998), pp. 983–995.
- [102] S Denis, S Sjöström and A Simon. “Coupled Temperature, Stress, Phase Transformation Calculation”. In: *Metallurgical Transactions A* 18.7 (1987), pp. 1203–1212.
- [117] Paul Kainzinger. “Utilizing Casting Simulation for the Fatigue Design of Wind Turbine Components”. In: Presented at the International MAGMASOFT User Meeting, Hannover, Germany, 2012.
- [140] H.T. Angus. *Cast Iron - Physical and Engineering Properties*. Butterworth & Co (Publishers) Ltd., 1976.
- [148] Per Leif Larsen. *Iron Melt Flow in Thin-Walled Sections Cast in Vertically Parted Green Sand Moulds*. DTU, IPL, 2004.
- [149] Søren Skov-Hansen. *Reduced Energy Consumption for Melting in Foundries*. DTU, IPL, 2007. ISBN: 978-87-91035-63-5.
- [150] *Aid to Calculate Sprues, Ingates and Runners for Castings in the Foundry - Density Data List*. <http://homepage.ntlworld.com/oxfordtours/workitoutnet/castaid/spruecalculator/decinote.htm>. Calculator.
- [151] *Novacast*. <http://novacast.se/>. Program.
- [152] *Flow-3D Cast*. <http://www.flow3d.com/home/industries/metal-casting>. Program.



Part Summary

<b>14.1 Summary</b> . . . . .	<b>269</b>	14.1.4 Porosity Analysis . . . . .	271
14.1.1 Experimental Setup . . . . .	269	14.1.5 Results Analysis and Discussion . . . . .	271
14.1.2 Porosity Quantification and Results . . . . .	270	<b>References</b> . . . . .	<b>271</b>
14.1.3 Thermal Analysis . . . . .	270		



**S**HORT summary of the investigations, results, and findings reported in part II.

Keywords: Summary, Experimental Setup, Scalability, Porosity Quantification, Ultrasound Analysis, X-Ran Analysis, Thermal Analysis, Numerical Simulation.

Chapter findings reported in: . . Supplement IV, on page 337

14.1 Summary

**T**HE proposed methodological approach was described and developed. A test geometry has been developed which has subsequently been used in a full-scale experiment with a wide range of different feeder combinations. The produced castings were analysed using ultrasound and x-ray imaging to quantify the amount and location of the remaining porosities. The results were analysed with the aid of numerical simulation data. Finally, the methodology and results have been discussed and the feeding regimes and underlying feeding forces have likewise been discussed and explained.

14.1.1 Experimental Setup

The six specified requirements for the casting design formed the basis for the development of the final casting design and pattern layout. The casting design was aided by analytical solutions and numerical simulations to ensure that the final design would perform as intended. A key point of the design was the construction of the pre-feeder neck. The design required the pre-feeder to limit the influence of pouring temperature and subsequent liquid shrinkage. The construction of the pre-feeder neck was paramount in ensuring that it stopped the feeding of the casting from the pre-feeder at the correct

time and that this timing was scalable with the rest of the casting design. The subsequent analysis of the castings, aided by the numerical simulations, showed that the pre-feeder neck had performed as intended.

The design for easy and accurate analysis was also considered successful, though improvements could be made as mentioned in the discussion. The potential inaccuracies regarding the location and particularly regarding the size of porosities were related to the grading scale rather than the casting design itself. Additional examinations of the castings could possibly have provided more data and better insight into the size and distribution of the porosities.

A wide range of different modulus feeders was tested as part of the trials. The feeders were selected based on the commercially available exothermic feeder which best covered the range in question. The insulating feeder sleeves were then prototyped to the same geometry as the exothermic feeders to keep the geometry constant. The exothermic feeders were selected to be  $0.80 M^\infty$ ,  $1.00 M^\infty$ , and  $1.20 M^\infty$  in relation to the respective casting. By error, the M10 casting was scaled to an M12 casting on the pattern. As a result, the proportional modulus of the feeder for the M12 casting was shifted. As a consequence the M12 casting was cast without proportionally larger feeders, but with a larger range of different smaller feeder.

The process stability discussion and analysis showed that the benchmark castings produced a comparable amount of porosities. The analysis also showed that the feeders significantly changed the number and size of porosities found in the castings, though it should be noted that the average porosity amount was only markedly reduced for the large M15 castings. Additionally it was examined and discussed if solid feeding of the castings could have influenced the porosity results. It was concluded that this was not the case.

### 14.1.2 Porosity Quantification and Results

The castings were analysed with ultrasound by an experienced operator who also quantified the size and location of porosities. The results were structured in a series of tables focussing on different aspects of the combination between casting size, feeder size, and feeder location. An analysis showed that the observed atmospheric punctures at the pre-feeder neck did not affect the amount of poros-

ities recorded, though it was shown that sensitivity towards forming these atmospheric punctures was greatest for the M08 casting and that the insulating feeders at the upper locations were nine times as likely to cause a punctures as the exothermic feeders at the same location.

The x-ray analysis and sectioned castings were used to confirm the findings of the ultrasound analysis. Additionally, the x-ray imaging of the castings was used to show the porosities in the pre-feeder, pre-feeder neck, and the feeders. This information was used in the subsequent analysis of the solidification and porosity formation of the castings.

To provide an overview of the porosity results, the data listed in the tables were illustrated as graphs. This approach provided an overview of the correlations between the main factors of the experiment—casting modulus, feeder modulus, feeder location, and sleeve material. The graphs showed that the three different modulus castings performed differently with proportionally identical feeders. As a consequence, it was concluded that the traditional approach of scaling the feeders linearly according to the casting modulus is not sufficient or descriptive for the underlying feeding regime.

### 14.1.3 Thermal Analysis

Temperature measurements were conducted as part of the trials and the thermal data obtained from these measurements was used to assess the accuracy of the numerical simulations. This was done by comparing the cooling curves and by comparing the solidification times of the three different modulus castings.

Having confirmed the validity of the simulation setup, the data from the numerical simulations were used to analyse the influence of the different feeder combinations in the cooling curves. Again it was concluded that the scalability of the casting and experiment design was satisfactory. Additionally, the thermal data from the simulations were used to analyse the cooling and solidification behaviour of the three modulus castings. This was achieved by plotting the gradient across the centre of the casting and illustrating how this developed during the solidification of the casting.

Finally, a geometrical analysis was performed to investigate the influence of the different feeder combinations and locations on the casting solidification pattern. It was found that combinations with two feeders significantly changed the geometry of the

residual melt at the later stages of solidification. Subsequently, in the discussion, it was proposed that the extra feeder creates a feeding channel connecting the two feeders, thus ensuring an open feed path along the entire length of the casting until late in the solidification process. Additionally, the feeding channel created by the two feeders reduced the distance of the interdendritic feeding reducing the required feeding pressure to achieve a successful feeding.

#### 14.1.4 Porosity Analysis

---

A parametric iteration was performed to establish the simulation parameters that yielded the most accurate porosity predictions. This showed that the porosity results from the benchmark casting could only be matched partially and that this required the use of the feeding efficiency factor, which is

not intended to be used for cast iron. The two best of the calibrated simulation setups were afterwards tested on three different feeder configurations. These porosity prediction results matched in some cases only. A simulation result that cannot be used without trial confirmation is of little use.

#### 14.1.5 Results Analysis and Discussion

---

The cause and formation of porosities in relation to solidification patterns have been discussed. It was concluded that the analysed alloy composition solidified in an endogenous shell-forming manner, resulting in either centreline porosities or surface shrinkage caused by solid feeding. The combinations of the different feeders and varying casting sizes showed some of the complexity involved in feeding cast iron castings, especially without the aid of gravity.







Part **III**  
Dissertation  
Summary

Conclusion 15

Future Work and 16  
Application of Findings

“**T**HE most exciting phrase to hear in science, the one that heralds the most discoveries, is not ‘Eureka!’ (I found it!) but ‘That’s funny...’ ”

---

—Isaac Asimov





## Conclusion

---

<b>15.1 Introduction</b> . . . . .	<b>275</b>	<b>15.3 Impact</b> . . . . .	<b>279</b>
15.1.1 Purpose and Objective . . . . .	275	15.3.1 Energy Savings . . . . .	280
<b>15.2 Conclusions</b> . . . . .	<b>276</b>	<b>References</b> . . . . .	<b>280</b>
15.2.1 Feeding Guidelines . . . . .	278		

---



**C**ONCISE listing of the dissertation findings, followed by an estimation of the potential impact and energy savings.

Keywords: . . . . . Conclusions, Feeding Guide, Impact, Energy Savings.

Chapter findings reported in: . . . Supplement I, on page 301  
Supplement II, on page 315  
Supplement III, on page 325  
Supplement IV, on page 337

---

### 15.1 Introduction

---

**T**HIS chapter presents the major findings of the dissertation in a condensed and resynthesized manner, structured according to the seven hypotheses described in chapter 1.1, on page 3.

The findings are listed with respect to each hypothesis and according to category and correlation. The conclusions are not sorted specifically according to a chapter or part order.

#### 15.1.1 Purpose and Objective

---

The purpose and intent of this dissertation is to contribute to the advance of casting technology, specifically in the field of feeding vertically cast SGI

casting with spot feeders.

Casting has been used as a manufacturing process for more than 7000 years. If this is to continue, foundry technology must advance and progress to be able and capable of supplying customers with high quality, precision manufactured castings with an outstanding balance between cost and properties.

The findings presented here is a contribution to this continued development.

Professor Stefanescu has described how casting has transformed from a witchcraft to an engineering science [2]. A field of science that has seen great discoveries over the past century or so, but to this day still retains many of its secrets and mysteries.

---

Coordinate Measurement Machine (CMM), Silicon (Si)

In these years foundries are embracing new and emerging technologies as never before. Additive manufacturing, optical 3D-scanning of castings, and numerical simulations are only some of the digital advances many foundries have already taken to retain their competitive edge. However, among these novel technologies, there should also be a focus on improving the technological core of casting. Not in competition with, but in collaboration with new technologies.

The findings, conclusions, and proposals listed in the following section are aimed at furthering the understanding of cast iron feeding, and how this can be used to improve casting yield, reduce scrap rate, save energy, reduce production cost, and make cast products a better choice. However important or inconsequential the findings may turn out to be they constitute a piece of the greater puzzle.

## 15.2 Conclusions

THE conclusions are based on the work and findings presented in the previous chapters. The findings rely on specific casting geometries and alloy compositions, hence not all of the conclusions can be extended to general casting conclusions. This reservation does not mean that the conclusions cannot be of a more general nature, only that further investigations are required to conclude that it is so.

**Hypothesis 1: Spot feeders can (effectively) feed secluded sections located away from the parting line in vertically parted moulds**

1.1 Spot feeders can feed secluded sections reliably.

- (a) All examined feeder combinations managed to successfully feed the boss section for the less demanding low Si  $\alpha$ -alloy (EN-GJS-500-7).
- (b) The exothermic feeder combination managed to successfully feed the boss section for the more demanding high Si  $\beta$ -alloy (EN-GJS-450-10).
- (c) The other feeder combinations were unsuccessful in feeding the boss section for  $\beta$ -alloy.
- (d) It is proposed that the reduced feeding efficiency of the insulating centre feeder is related to an early shell-forming inside the feeder, without an atmospheric vent, causing the solidification contraction to

build up a negative pressure in the feeder, impeding optimal feeding.

**Hypothesis 2: The location and amount of porosities can successfully be predicted via numerical simulation when spot feeding SGI**

2.1 Numerical simulation can be used to predict porosities in SGI casting in relation to spot feeding, for some castings and alloys.

- (a) The porosity results for the disc castings were found to be reliable and useful in predicting the amount and location of the porosities.

2.2 For other alloys and geometries the numerical simulations can be set up to provide a partial prediction, but with significant limitations.

- (b) The simulation setup had trouble predicting a large enough amount of porosities for the block castings.
- (c) The simulation setup had trouble predicting the location of the porosities in the block castings.
- (d) It was not possible to find a single common simulation setup that satisfied both the prediction of amount and location of porosities.
- (e) The feeding effectivity factor, which is not supposed to be used in cast iron, was the only means to significantly influence the location of the porosities. This indicates that the alloy behaves similarly to eg steel or aluminium.
- (f) The feeding effectivity factor was also the only parameter that showed a significant influence on diversifying the porosities prediction for each of the three modulus castings.
- (g) It is proposed that the porosity prediction issues relate more to the simulation of the alloy properties, rather than the feeding algorithm itself.
- (h) The mesh cell size matter with regards to the size of the predicted porosities.

**Hypothesis 3: Exothermic sleeve materials do not significantly influence the casting microstructure**

3.1 No significant differences in microstructure were observed for the insulating and exothermic feeders, except what ensued of the modulus differences.

3.2 A prolonged solidification time locally influence solidification and segregation. The prolonged solidification reduces Si segregation and increase the yield of the local graphite precipitation potential.

Hypothesis 4: Thermal deformation is significantly influenced by spot feeders and can (to some degree) be controlled by choice of feeders

4.1 The thermal influence of a feeder can significantly change the dimensional accuracy of a casting.

- (a) Thermal deformation differences can be attributed to differences in feeder configuration.
- (b) The  $\alpha$ - and  $\beta$ -alloys were considered statistically identical with respect to average deformation ( $f_v$ ).
- (c) The modulus of the centre feeder displayed a significant influence of the casting deformation.
  - i. For the  $\alpha$ -alloy a high modulus centre feeder lead to greater deformation ( $f_v$ ). The feeders with smaller modulus displayed less deformation.
  - ii. For the  $\beta$ -alloy varying the module for the centre feeder caused no significant difference in  $f_v$ .
  - iii. The  $\beta$ -alloy with the low moduli centre feeders was found to have the best reproducibility of all casting combinations.
- (d) No statistical evidence was found that proved that the top feeder alone could significantly influence the thermal deformation.
  - i. No statistical difference was found between the two top feeder moduli examined—neither for the  $\alpha$ - nor  $\beta$ -alloys.
- (e) Castings without both feeders showed significantly more thermal deformation than castings with one or two feeders. Feeders reduce surface shrinkage due to solid feeding and stabilise the thermal gradients of the casting.
- (f) The high Si  $\beta$ -alloy displayed much less variance, leading to a better manufactur-

ing precision and greater potential for production optimisation.

- i. the  $\alpha$ - and  $\beta$ -alloy was considered statistically identical with respect to average deformation ( $f_v$ ),
- ii. the high Si  $\beta$ -alloy displayed much less variance, leading to a better manufacturing precision and greater potential for production optimisation.

(g) Risk of internal porosities can be detected by identifying micro-sinks on the casting surface.

4.2 Casting deformations are governed by thermal gradients and eutectoid phase transformations.

- (a) The casting deformation valley is caused by small thermal gradients during solidification and cooling.
- (b) The thermal gradients during solidification control the Si segregation, which in turn influence the pearlite formation at the eutectoid phase transformation.
- (c) The subsequent formation of pearlite, following the austenite to ferrite phase transformation, prolong the overall transformation and increase the deformation variation.
- (d) The order of solidification and the order of eutectoid phase transformations are not necessarily the same. The thin-walled section solidifies first, while the rim of the casting undergoes the eutectoid phase transformation first.
- (e) The fully ferritic alloy and the pearlitic-ferritic alloy showed insignificant differences in average deformation.
- (f) The pearlitic-ferritic alloy showed significantly greater deformation variance, compared with the high Si  $\beta$ -alloy.
- (g) If sufficient care was taken to control the production parameters, the variation in deformation is small enough for the pattern itself to be altered in order to compensate for some of the deformation. This would make possible a reduction in machining allowance, reducing the melt requirement.

4.3 The casting deformations observed in this work cannot be predicted by the current numerical simulation models.

Hypothesis 5: The side feeder modulus necessary to feed SGI is *not* a linear function of the casting module, and traditional methods overestimate the feeder size

#### 5.1 Application of a single horizontal spot feeder.

- (a) The optimum feeder modulus does *not* scale linearly with casting modulus.
- (b) The optimum feeder is dependent on alloy, modulus, casting geometry, cooling rate, sleeve material, and melt quality.
- (c) Less is more. For some combinations, a smaller feeder will clearly outperform a larger modulus feeder.
- (d) Larger modulus castings require relatively smaller modulus feeders.
- (e) A horizontal spot feeder can successfully be applied to both the upper and lower part of a casting or section.
- (f) It is possible in special cases to successfully feed a casting or section against the pull of gravity.
- (g) The feeder performance may vary between feeder locations. Hence, a different feeder may be a better choice if the feeder location is moved.

Hypothesis 6: Multiple smaller feeders can, for elongated sections, provide better feeding of a single casting section than a single large feeder

#### 6.1 Application of a multiple thermally connected feeders.

- (a) Feeders can be thermally connected across thin-walled sections that prevent a direct liquid connection.
- (b) The centre feeder influences the thickness of the upper part of the thin-walled section, hence it is a thermal influence and not a ferrostatic influence.
- (c) The application of multiple feeders yield synergy effects.
- (d) Two feeders connected via a liquid connection can change the inherent thermal gradients of the casting via convection effects.
- (e) Combinations of multiple feeders can improve feeding. Though an incorrect application, it can also increase the prevalence and size of the porosities.

Hypothesis 7: The feed material movement in spot feeding can be described by the sum of driving forces

#### 7.1 Identification of driving forces for feeding and the understanding of feeding regimes.

- (a) Each casting has its own feeding regime, which describes all things influencing the feeding application; alloy, casting geometry, feeder sleeve, pouring temperature, melt purity, mould stability, cooling rate, and more. Even small changes can significantly change the feeding regime from successful to unsuccessful.
- (b) The transport of the feed material is governed by external forces like gravity and the internal forces like volume contraction, shell compression, and graphite expansion for the major part.
- (c) It is proposed that feeding forces are considered to explain the movement of the melt, for horizontal as well as vertical feeders.
- (d) Three stages of feeding are proposed to explain the progression of feeding during the casting solidification; initial feeding, expansion feeding, and directional feeding.
- (e) It is proposed that melt cohesiveness, and subsequent melt purity and the local melt temperature play an important role regarding the location of ruptures and subsequently the formation of porosities. Note that these ruptures are wanted as long as their location and timing can be controlled.
- (f) It is proposed that the pressure loss caused by solidification overpower the feeding forces as the casting solidify.
- (g) It is proposed that the feeding requirement governs the three stages of feeding and through local solidification and segregational differences make the transition between stages fluent.

### 15.2.1 Feeding Guidelines

---

One of the aims of the work is to improve casting yield and reduce energy costs by improving feeder technologies for cast iron foundries. However, the above findings can only have effect if they are implemented and used.

This is a short simplified guide towards implementing better feeding practices in the foundries, and how to optimise feeder solutions for specific castings.

**Ensure a stable process:** It is important to be able to reproduce the castings with a high level of accuracy. If different process parameters vary too much, the outcome will be castings that behave differently. A 5% scrap rate signifies a process variation for which 5% of the castings has exceeded the threshold for that particular casting. This can be solved by better process control, reducing the process variations, or the casting design (gating, feeders, cores, etc.) can be changed to encompass a larger safety margin towards these process variations. Note that the variation may be contributed to several correlated process variables. The smaller the controllable process variation, the less safety margin is required, and the better the yield that can potentially be achieved.

**Identify the optimisation objective:** Casting effects are all related to some degree, hence optimising and solving all issues at once can easily complicate the problem beyond what can be handled and analysed. Focus on one issue at the time. What yield the best overall improvement? Reduced feeder size, reduced scrap rate, or reduced machining allowance. As the effects are linked, solving one issue may solve other as well. If possible determine an acceptable scrap rate and use this to determine a target safety factor.

**Understand the casting's thermal history:** Do numerical simulations of the casting, possibly varying different casting parameters to learn their influence on the particular casting. If the castings are already in production then analyse the current defects and try to locate the origin (this is easier say than done). Many foundries have access to CMM or optical 3D-scanners. Use these to identify variations between sound and unsound castings.

**Test multiple feeder combinations:** If using ram-up sleeves it is very easy to cast castings with several different feeder combinations. However, also for traditional geometrical feeder and parting line feeders with sleeves, it can be valuable to investigate the influence

of different feeders. Investigate a range of feeders, and possibly also feeders that are considered outside the range that would typically be chosen. Analyse the trial castings for porosities and dimensional accuracy, and select configuration that provides the best yield with a reasonable safety factor. Estimating the safety factor can be very difficult and will rely on empirical knowledge, potentially supported by numerical simulations.

**Prioritise to solve the problem:** Castings have delivery dates and there is seldom if ever, time to optimise existing castings. If a delivery is upcoming it may be necessary to produce with high scrap rate to ensure that the contracted castings can be delivered in time. That is the nature of the foundry industry. When the deadline has been met, then it is important to prioritise to solve the known problems. Problem analysis, tests, simulations, and pattern changes require time. Hence, if it is not prioritised the problem will never be solved. The importance is determined by the severity of the problem and the number of castings produced. To aid the prioritisation calculate the cost of the existing scrap rate vs an improved scrap rate an estimate the time it will take before the one time cost of optimising the casting will have repaid itself.

## 15.3 Impact

ONLY time can show the impact of the dissertation findings will be. Some of the findings can be implemented immediately, though it is expected that the foundries will implement the applications and methods slowly in the beginning. If and when the foundries have tested spot feeders with success, they are likely to turn to this solution again for other troublesome castings, and hopefully, with time these methods will be an implemented part of casting design.

It is assessed that the methods will become more and more relevant as castings become more complex and the requirements increase. It is also important to remember that the driving force behind the implementation is reduced production cost, primarily by reduced energy consumption, hence the foundries should implement these solutions to reduce production cost. However, this also means that the

driving factor is related to the cost of electricity and changeover required for each foundry.

The impact of the feeding forces will hopefully be a new mindset and a new approach to understanding spot feeding. When these forces can be modelled and implemented into numerical simulation software, then it will be possible truly optimise the feeding applications. This ability to simulate and optimise, is, however, not expected in the near future, as it requires completely new and complicated features to be added to the numerical simulation algorithms.

### 15.3.1 Energy Savings

---

It is assessed that the impact of the dissertation findings in total, within a foreseeable future, can reduce the energy consumption for cast iron foundries in EU27 with 300 GWh per annum.

The annual cast iron tonnage for EU was 13.5 Mt in 2005. Assuming a casting yield of 50 % and a total melting energy yield of 50 %, the yearly energy consumption is 32 238 GWh, with a melting energy of 1194 kWh/kg.

Improvements of numerical simulations are as-

essed to yield 25 GWh per annum. New implementations of horizontal spot feeders are assessed to potentially yield savings for 60 GWh each year. The estimation is based on new approaches to solving feeding problems and making use of the ability to feed up-hill by optimising the internal feeding forces. The greatest impact is estimated to come from an increased application of ram-up sleeves to solve and improve feeding problems with existing and new castings. This is assessed to contribute an annual saving of 145 GWh. Finally, it is estimated that reduced machining allowance and reduced tool wear can save 70 GWh per annum. The impact here will be greatest for high volume castings like eg break discs.

## References

- [2] Doru Michael Stefanescu. "Introduction to the Science and Engineering of Cast Iron". In: Presented at the Metallurgy, Solidification, and Modelling of Cast Iron Castings, Jönköping, Sweden, 2013.





## Future Work and Application of Findings

---

<b>16.1 Technology Roadmap</b> . . . . .	<b>281</b>	<b>16.4 Feeding Forces</b> . . . . .	<b>283</b>
<b>16.2 Spot Feeding</b> . . . . .	<b>281</b>	16.4.1 Pouring Temperature . . . . .	283
16.2.1 Applied Investigation in Production . . . . .	282	16.4.2 Active Cooling . . . . .	283
16.2.2 Pressurised Feeding . . . . .	282	<b>16.5 Casting Production Statistics</b> . . . . .	<b>284</b>
16.2.3 Active Pattern . . . . .	282	16.5.1 Casting Research . . . . .	284
<b>16.3 Thermal Deformation</b> . . . . .	<b>282</b>	<b>References</b> . . . . .	<b>284</b>

---



**P**LANNED and suggested work for the continuation of the research, and proposed applications of the dissertation findings.

Keywords: . . . . . Work to Come.      Chapter findings reported in: . . . . . Not reported.

---

### 16.1 Technology Roadmap

HAVING concluded on the findings constituting the dissertation, the next step is to consider where these findings lead us. The reported findings can influence the application of feeders, as well as the construction and design of castings with respect to feeding. However, the dissertation also leaves questions unanswered; to be investigated further before the reported findings can be utilised in full.

The next sections point to a few important tasks to address to further the science and technology of feeding and casting in general. However, part of the technology roadmap also addresses the industry and how the most mature parts can be implemented.

### 16.2 Spot Feeding

IT was shown that spot feeders as ram-up sleeves can feed secluded sections successfully. Additionally, the feeding forces driving the feeding of horizontally mounted spot feeders was elaborated. The study showed that the driving forces governing feeding are complex processes that is difficult to predict with the modelling and numerical simulations solutions available.

---

Coordinate Measurement Machine (CMM), Future Process for Casting (FPC)

### 16.2.1 Applied Investigation in Production

---

As a consequence further investigations are required to expand the understanding of these feeding effects. Fortunately, ram-up sleeves by definition can easily be changed, hence a wide range of feeder solutions can be tested without extensive altering of the pattern. Thus, it is suggested that foundries, possibly as a joint research project, will investigate the application of ram-up sleeves to improve their yield on difficult castings, or possibly be able to manufacture them at all.

Hopefully, a successful investigation of how spot feeders can be applied to their own castings will encourage the foundries to extend the use to other castings as well. Together this will generate knowledge about the possibilities and limitations of spot feeder until these become a common tool in the foundry engineer's toolbox that is used as natural part of the casting design—when it is the best solution.

It requires a lot of different castings and different solution to build an empirical knowledge for spot feeding similar to that of traditional gravity driven feeders.

### 16.2.2 Pressurised Feeding

---

An essential part of successful feeding, and especially regarding feeding yield, is the feeding forces. Previous investigations have addressed active feeding in different ways. The application of these active feeding methods is, to the author's knowledge, limited to large hand moulded castings.

For high volume production, such as vertical moulding lines, the active feeding methods have not caught on. Thus, it is proposed that passive-active spot feeder may provide a solution. Passive-active means a feeder that supplies pressure but function as a discreet solution that does not require external power or control during operation. The idea is to develop a controlled pressure on the melt in the feeder, at the time when it is needed. Both parts may present difficulties, as safe and disposable pressure system in itself will require a considerable development. Ensuring that the pressure does not develop too early may be equally difficult, and the solution has to be cheap enough to be a disposable one-use application.

However, if a solution like this could be developed, it would revolutionise the feeding possibilities. The cost, in turn, would determine if it would also revolutionise the industry.

### 16.2.3 Active Pattern

---

An alternative to ram-up sleeves could be active patterns. The term active pattern is here used to describe patterns with inserted parts that can change shape during moulding. This could eg be a spot feeder away from the parting line on vertically parted moulds. The idea is that the geometry, that would normally not be mouldable due to negative draft constrictions, is inflated during moulding. The geometry is then deflated before demoulding, to avoid the draft issues. In addition to spot feeder, other geometries could also be created. This would limit the restrictions the foundry engineers face when determining the best orientation for complex castings. In addition, this may help avoid cores that previously could not be avoided due to the orientation restrictions.

Active patterns do exist today, though their application is limited and often only involve simple geometries. However, as casting geometries increase in complexity, the additional degree of freedom may be a competitive advantage.

## 16.3 Thermal Deformation

---

IT has been shown that foundries that control their process parameters can produce castings with a very high repeatability. The machining allowance chosen for the different surfaces of different castings should correlate to the process repeatability the foundry is capable of achieving. This is not to say that there should be no safety factor, only that the safety factor should be chosen deliberately based on the actual casting deformation variation.

Numerical simulations cannot yet predict thermal casting deformation with enough accuracy to adjust for the fraction of a mm that the correction should be. However, simulations and casting analysis can provide some answers, and the final detailing of the pattern compensation may very well be achieved by an iterative process where the test castings are made at the foundry, measured with a 3D optical scanner or a CMM, and these measurements subsequently are used to correct the shape of the pattern.

In terms of casting and solidification research, it would be of interest to pursue the origin of these thermal deformations further, to eventually be able to make better predictions, models, and numerical simulations.

## 16.4 Feeding Forces

---

It is also proposed that focus is given to obtaining a better understanding of the non-gravitational feeding forces. This dissertation has shown the complexity of the feeding forces, even for a simple casting geometry with a single feeder. To truly benefit from the possibilities of using these forces to aid the feeding of the casting in an optimal way it is necessary to achieve two things: (1) to measure quantify the magnitude and timing of the different forces, and (2) to model the phenomena so that it can be applied to numerical simulations. The complexity and multitude of factors require the application of process optimisation tools to be used to identify the optimal solution. The findings of the dissertation have shown that this is not just a question of choosing a large enough feeder.

### 16.4.1 Pouring Temperature

---

A more practical application of some of the findings may be to control the pouring temperature to ensure the optimal thermal gradient in the casting at the end of filling. These findings have shown that even small changes to the thermal gradients may influence the direction of solidification for the entire solidification process.

One approach could be to have two sources of melt, held at different temperatures. The initial melt is poured from the hottest source to avoid cold runs and to have the hottest melt be cooled by the mould. As pouring continues the melt source is shifted to the colder source, which in turn will fill the final part of the mould. In principle, this should achieve some of the same advantages as the Cosworth process benefits from [25].

As it may be expensive and difficult to install two separate sources of melt, which can be kept at different temperatures, a similar effect can possibly also be achieved with a single pouring station. Basically, the idea is to divide the melt flow as it leaves the basin. One flow is insulated to retain the heat, and other is allowed to cool as much as necessary. Hence, by the time the two streams of melt are poured into the mould, they may very well have the required temperature difference to ensure the thermal gradient in the casting that was needed.

### 16.4.2 Active Cooling

---

Another similar approach to improve the thermal

gradients of the castings, with respect to improving the feeding yield, could be to actively cool the mould and thus also the castings as they are transported along the cooling line by the Automatic Mould Conveyor (AMC) [17]. The cooling should be initiated immediately after the filling of the mould, as the cooling effect must affect the melt temperature before the solidification of the casting progresses too far.

The cooling effect is limited by the insulating effect of the sand mould, which also causes latency to the system because of the time required to transfer the heat through the mould. Additionally, the system would require being designed in a manner that itself do not require a large amount of energy or upkeep to ensure a great enough cooling power to have a useful effect.

The extracted heat can, for some foundries be deployed to the local heating system, or it could potentially be used to internally for heating or to preheat the metal scraps before melting, to reduce the required energy for melting. Another advantage would be the reduced cooling time of the castings. This could either be used to increase the cycle time resulting in an increased production capacity because the castings reach the safe shake-out temperature faster, or it could be used to reduce the length of cooling line which would free out additional space in the foundry production floor.

An active cooling system provides an additional process parameter to use for optimising the performance of the foundry, but also for optimising the casting layout of the castings and to influence the microstructure formation of the casting during solidification and cooling. The latter though is strongly dependent on the cooling power that can be applied to the system. However, a similar process, Future Process for Casting (FPC), has been developed and is today in use at Volvo AB's foundry in Skövde, as described by Diószegi [153].

A fast cooling of cast iron, assuming it is not rapid enough to reach the meta-stable phase diagram and solidify as white cast iron, will increase the pearlite content. However, many castings and alloys today are made to be close to fully ferritic to ensure a high elongation. This material requirement, however, may also be possible with an active cooling system, if the system is constructed to take advantage of this. Most cooling systems based on the flow of a liquid to transport the heat away has the advantage that they can be reversed. Hence, if the system is constructed in sections, and the different sections

can be coupled, the heat can be moved from one part of the mould to another, or from one end of the cooling line to another, or even from one cooling line to another. The latter could potentially be used if pearlitic castings were produced on one line, while fully ferritic castings were produced on another line, hence the transfer of heat from the pearlitic to the ferritic line would benefit the microstructure of both castings.

Finally, with a better understanding of the thermal deformations caused by the eutectoid phase transformations, this technology may also be used to reduce the deformation of the castings by changing the cooling rate during the phase transformation.

## 16.5 Casting Production Statistics

A wider approach to casting production improvements in the foundries, as well as a solid base for casting research, can be achieved by improved traceability of the castings if this traceability is subsequently linked to all the recorded process conditions. The problem has three stages: (1) to sequentially mark the casting, (2) to record and store all the relevant process data, and (3) to statistically find the influence of the significant process variables, including identifying which variables are most vital.

A method for sequential part marking of casting on vertically parted moulding lines was proposed by Vedel-Smith and Lenau [154], and at least one foundry do use part marking for all their casting [155].

To decide which process parameters to record, where to record them, and how often to record them, can in itself be difficult. However, many factors influence to a greater or lesser degree the properties of the final casting. However, if the significant process parameter is recorded, these can provide a unique opportunity to improve process stability and casting quality.

Correlation of effect is the key to finding the hidden causes for casting defects. This may require a long time of continued data recording to establish a database with sufficient data to find the underlying causal effects for different casting defects. In foundries with many active patterns, this may take even longer. However, building a database of traceable data may be an invaluable source for the foundry to discover process variations and to determine the acceptable process parameters.

The direct outcome of this would hopefully be an increased yield and a significant reduction in scrap percentage. Another aspect would be the aid such a statistical database could provide in terms of process optimisation and during the development of new castings.

### 16.5.1 Casting Research

With respect to casting research, the access to relatively complete and traceable process data can possibly provide a whole new pillar for foundry and casting research. The possibilities can potentially change the pace of improvement and discoveries simply because of the availability of complete process data on a large scale. This availability of ‘big data’, in turn, may be a solid foundation for the development of numerical simulation models, which again will improve the foundry engineers work conditions.

## References

- [17] *Application Manual: DISAMATIC MK2, Sand moulding System*. Manual. 1995.
- [25] John Campbell. *Castings, 2nd Ed.* Linacre House, Jordan Hill, Oxford OX2 8DP, 30 Corporate Drive, Burlington, MA 01803: Elsevier Butterworth-Heinemann, 2003. ISBN: 0 7506 4790 6.
- [153] Attila Diószegi. “Casting Process Development at Volvo Foundry”. In: Presented at 3rd Metallurgy, Solidification, and Modelling of Cast Iron Castings course, Jönköping, Sweden, 2013.
- [154] Nikolaj Kjelgaard Vedel-Smith and Torben Anker Lenau. “Casting Traceability with Direct Part Marking using Reconfigurable Pin-Type Tooling based on Paraffin-Graphite Actuators”. In: *Journal of Manufacturing Systems* 31.2 (2012), 113–120. ISSN: 0278-6125. DOI: {10.1016/j.jmsy.2011.12.001}.
- [155] *Conversation with Professor Doru Michael Stefanescu at the 10th International Symposium on the Science and Processing of Cast Iron, Mar del Plata, Argentina, Nov. 2014*. Conversation.



# Backmatter

Bibliography

Appendix A

“THE road to wisdom? Err but less  
Well, it’s plain and and err and less  
simple to express: and err again and less.”

—Grook,  
*Piet Hein*



# Bibliography

- [1] Lars Gierke. *Instrumentarium zur Planung und Umsetzung von Zulieferer-Hersteller-Netzwerken*. Peter Lang GmbH, Eurpaischer Verlag der Wissenschaften, Frankfurt am Main, 1999. ISBN: 3-631-34507-0.
- [2] Doru Michael Stefanescu. “Introduction to the Science and Engineering of Cast Iron”. In: Presented at the Metallurgy, Solidification, and Modelling of Cast Iron Castings, Jonkoping, Sweden, 2013.
- [3] DISA Industries A/S, *Internal Report*. . Data.
- [4] *Worldwide Casting Tonnage Slowed by Recession*. <http://www.afsinc.org/content.cfm?ItemNumber=7613>. Data.
- [5] David Joop. “Fabrication of Hybrid HPDC-Structures with Perforated Sheet Metal Inserts”. In: Presented at the International MAGMASOFT User Meeting , Potsdam, Germany, 2014.
- [6] Jakob Olofsson. *Simulation of Microstructure-based Mechanical Behaviour of Cast Components*. School of Engineering, Jonkoping University, 2014. ISBN: 978-91-87289-04-0.
- [7] David Bue Pedersen. *Additive Manufacturing Multi Material Processing and Part Quality Control*. DTU Mechanical Engineering, 2012. ISBN: 978-87-7475-384-1.
- [8] *Sand Casting With PolyJet and FDM Patterns*. <http://www.stratasys.com/solutions-applications/digital-manufacturing/tooling/sand-casting>. Production.
- [9] *Additive Manufacturing for Metal Casting*. <http://www.voxeljet.de/en/services/>. Production.
- [10] *Additive Manufacturing for Metal Casting*. <http://www.exone.com/Services/3D-Printing-Services>. Production.
- [11] *Additive Manufacturing for Investment Casting*. <http://envisiontec.com/castable-materials/>. Production.
- [12] *CO<sub>2</sub>-emission per kWh*. <http://www.ens.dk/info/tal-kort/statistik-nogleletal/nogleletal/danske-nogleletal>. Data.
- [13] Kim Vedel Pedersen. *Elforsyning - Opgaver og cases*. Dansk Energi, 2010. ISBN: 978-87-91326-07-3.
- [14] Foundry Practice by FOSECO Ltd. “The Application of Compressor Core Technology for Feeding Systems in a Mass Iron Automotive Foundry”. In: 248 (2008), pp. 1–3.
- [15] Foundry Practice by FOSECO Ltd. “An Advanced Breaker Core System with Enhanced Knock Off Properties for High Pressure Moulding Applications”. In: 244 (2006), pp. 1–7.
- [16] Jorg Daier et al. *Manual of Casting Defects—Incidence and Avoidance of Defects Attributable to Moulding Sands*. 3rd ed. S&B Industrial Materials GmbH, 2011.
- [17] *Application Manual: DISAMATIC MK2, Sand moulding System*. Manual. 1995.
- [18] AFS Molding Methods & Materials Division. *Mold & Core Test Handbook*. 4th ed. American Foundry Society, 2014.
- [19] Stephen I. Karsay. “Rising Methods for Gray and Ductile Iron Castings”. In: *Int. Cast Met. J.* 5.4 (1980), pp. 45–51.
- [20] Petr Kotas. *Integrated Modeling of Process, Structures and Performance in Cast Parts*. DTU Mechanical Engineering, 2011. ISBN: 978-87-90416-54-6.
- [21] N Chvorinov. “Solving Feeders and Sinkheads”. In: *Proceedings of the 30th International Foundry Congress*. 1963.

- [22] PN Hansen, PR Sahn and E Flender. “How to Select and Use Criterion Functions in Solidification Simulation”. In: *Transactions of the American Foundrymen’s Society*. 101 (1993), pp. 443–446.
- [23] John R. Brown. “FOSECO Ferrous Foundryman’s Handbook”. In: FOSECO International Ltd., 2000. Chap. 19, pp. 296–310.
- [24] John Campbell. *Casting Practice - The 10 Rules of Casting*. Linacre House, Jordan Hill, Oxford OX2 8DP, 30 Corporate Drive, Burlington, MA 01803: Elsevier Butterworth-Heinemann, 2004. ISBN: 0 7506 4791 4.
- [25] John Campbell. *Castings, 2nd Ed.* Linacre House, Jordan Hill, Oxford OX2 8DP, 30 Corporate Drive, Burlington, MA 01803: Elsevier Butterworth-Heinemann, 2003. ISBN: 0 7506 4790 6.
- [26] DM Stefanescu. “Computer Simulation of Shrinkage Related Defects in Metal Castings—A Review”. In: *International Journal of Cast Metals Research* 18.3 (2005), pp. 129–143.
- [27] PD Lee, A Chirazi and D See. “Modeling Microporosity in Aluminum-Silicon Alloys: A Review”. In: *Journal of Light Metals* 1.1 (2001), pp. 15–30.
- [28] Doru Michael Stefanescu. “Modeling of cast iron solidification- The defining moments”. In: *Metallurgical and Materials Transactions A-Physical Metallurgy and Materials Science* 38A.7 (2007). Symposium on Solidification Modeling and Microstructure Formation held at the 2006 TMS Annual Meeting, San Antonio, TX, MAR 13-16, 2006, 1433–1447. ISSN: 1073-5623. DOI: {10 . 1007 / s11661 - 007 - 9173 - y}.
- [29] Doru Michael Stefanescu. *Science and Engineering of Casting Solidification, 2nd ed.* Springer Science+Business Media, LLC, 233 Spring Street, New York, NY 10013, USA: Springer, 2009. ISBN: 978-0-387-74609-8.
- [30] Nikolaj Kjelgaard Vedel-Smith et al. “Quantification of Feeding Effects of Spot Feeding Ductile Iron Castings made in Vertically Parted Molds”. English. In: *AFS Proceedings* (2013).
- [31] N. K. Vedel-Smith and N. S. Tiedje. “Effect of Feeder Configuration on the Microstructure of Ductile Cast Iron”. English. In: *TMS Proceedings—Shape Casting: 5th International Symposium 2014* (2014), pp. 113–120.
- [32] David A. Porter, Kenneth E. Easterling and Mohamed Y. Sherif. *Phase Transformations in Metals and Alloys*. 3rd ed. CRC Press, Taylor & Francis Group, 6000 Broken Sound Parkway NW, Suite 300, Boca Raton, FL 33487-2742, 2009. ISBN: 978-1-4200-6210-6.
- [33] Attila Diószegi et al. “Defect Formation at Casting of Gray Iron Components”. In: (2009).
- [34] Attila Diószegi, Tobias Björklind and Zoltán Diószegi. “Surface Turbulence at Flow of Gray Cast Iron”. In: *Key Engineering Materials*. Vol. 457. Trans Tech Publ. 2011, pp. 422–427.
- [35] R Monroe. “Porosity in Castings”. In: *AFS Transactions* 113 (2005), pp. 519–546.
- [36] Vasilios Fournalakidis. “A Study on Ductile Iron Production without the Use of Feeders”. In: *Science and Processing of Cast Iron IX*. Ed. by Nofal, A and Waly, M. Vol. 457. Key Engineering Materials. 9th International Symposium on Science and Processing of Cast Iron, Luxor, Egypt, Nov. 10-13, 2010. Central Metallurg Res & Dev Inst. 2011, 499–504. DOI: {10.4028/www.scientific.net/KEM.457.499}.
- [37] Nicolas Chvorinov. “Theory of the Solidification of Castings”. In: *Giesserei* 27 (1940), pp. 177–186.
- [38] P. Jelínek and T. Elbel. “Chvorinov’s Rule and Determination of Coefficient of Heat Accumulation of Moulds with Non-Quartz Base Sand”. In: *Archives of Foundry Engineering* 10.4 (2010), 77–82.
- [39] M. Tiryakioğlu, E. Tiryakioğlu and D.R. Askeland. “The Effect of Casting Shape and Size on Solidification Time: A New Approach”. In: *International Journal of Cast Metals Research* 9. (1997), 259–267.
- [40] Merton C. Flemings. *Solidification Processing*. New York: McGraw-Hill, 1974.



- [41] K. Weiß and C. Honsel. “New Algorithm to Calculate Liquid - Solid Shrinkage and Graphite Expansion”. In: *Solidification and Gravity IV*. Ed. by R. Roos, M. Rettenmayr and Z. Gacsi. Vol. 508. Materials Science Forum. 4th International Conference on Solidification and Gravity, Miskolc Lillafured, Hungary, Sep.06-09, 2004. Univ Miskolc, Mat & Met Engr Fac, Phys Met & Metalforming Dept; Hungarian Acad Sci, Res Grp Mat Sci; NASA MSFC; HAS, Miskolc Comm; Hungarian Space Off; Assoc Hungarian Foundries. 2006, 509–514. ISBN: 0-87849-991-1.
- [42] Q.M. Chen, E.W. Langer and P.N. Hansen. “Influence of the Process Parameters on the Volume Change during the Eutectic reaction of SG Cast Iron: A Computer Simulation”. In: *Journal of Materials Science* 32.5 (1997), 1239–1248. ISSN: 0022-2461. DOI: {10.1023/A:1018592120197}.
- [43] Lennart Elmquist, Attila Diószegi and Tobias Björklind. “On the Formation of Shrinkage in Grey Iron Castings”. English. In: *Key Engineering Materials* 457 (2011), pp. 416–421.
- [44] W.S. Pellini. “Factors Influencing Riser Range and Feeding Adequacy—Part II”. In: *American Foundryman*. (1953), 62–71.
- [45] Carolin Körner. *Integral Foam Molding of Light Metals*. Berlin: Springer—Verlag Berlin Heidelberg, 2008. ISBN: 978-3-540-68838-9.
- [46] M. Petrič, J. Medved and P. Mrvar. “Effect of Grain Refinement and Modification of Eutectic Phase on Shrinkage of AlSi9Cu3 Alloy”. In: *Metallurgija* 50.2 (2011), 127–131. ISSN: 0543-5846.
- [47] Q.M. Chen, E.W. Langer and P.N. Hansen. “Stable Solute Boundary Layer for Liquid and Volume Change during Eutectic Solidification of Spheroidal Graphite Iron”. In: *Journal of Materials Science Letters* 16.4 (1997), 249–252. ISSN: 0261-8028. DOI: {10.1023/A:1018572211806}.
- [48] R. Siclari et al. “Micro-Shrinkage in Ductile Iron—Mechanism and Solution”. In: *Proceedings*. 66th World Foundry Conference. Istanbul. World Foundry Organisation. 2004, 863–873.
- [49] T. Skaland. “A New Method for Chill and Shrinkage Control in Ladle Treated Ductile Iron”. In: *Proceedings*. 66th World Foundry Conference. Istanbul. World Foundry Organisation. 2004, 975–986.
- [50] I. Jimbo and A.W. Cramb. “The Density of Liquid Iron-Carbon Alloys”. In: *Metallurgical Transactions B-Process Metallurgy* 24.1 (1993), 5–10. ISSN: 0360-2141. DOI: {10.1007/BF02657866}.
- [51] J.T. Berry, J. Shenefelt and R. Luck. “Presurised Feeding Systems”. In: *International Journal of Cast Metals Research* 14.6 (2002), 365–370. ISSN: 1364-0461.
- [52] N.W. Rasmussen, R. Aagaard and P.N. Hansen. “Gating and risering in vertical green sand moulds”. In: *International Journal of Cast Metals Research* 14.6 (2002), 355–363. ISSN: 1364-0461.
- [53] G. Alonso. et al. “Kinetics of Graphite Expansion during Eutectic Solidification of Cast Iron”. In: *International Journal of Cast Metals Research* 27.2 (2014), 87–100. ISSN: 1364-0461. DOI: {10.1179/1743133613Y.0000000085}.
- [54] Jafar Khalil-Allafi and Behnam Amin-Ahmadi. “Effect of Mold Hardness on Microstructure and Contraction Porosity in Ductile Cast Iron”. In: *Journal of Iron and Steel Research International* 18.4 (2011), 44+. ISSN: 1006-706X.
- [55] Nikolaž Kjelgaard Vedel-Smith. “Feeding Against Gravity with Spot Feeders in High Silicon Ductile Iron”. In: *Science and Processing of Cast Iron X*. Vol. 10th International Symposium on the Science and Processing of Cast Iron, Mar Del Plata, Argentina, Nov. 10-13, 2014. 2014,
- [56] G. Alonso et al. “Kinetics of Graphite Expansion during eutectic Solidification of Lamellar and Spheroidal Graphite Iron”. In: *AFS Proceedings 2014*. AFS Conference. Schaumburg, IL, USA. American Foundry Society. 2014, 1–12.
- [57] Q.M. Chen, E.W. Langer and P.N. Hansen. “Modelling Volume Change during Solidification of SG Cast Iron with Eutectic Composition”. In: *Scandinavian Journal of Metallurgy* 24.2 (1995), 48–62. ISSN: 0371-0459.

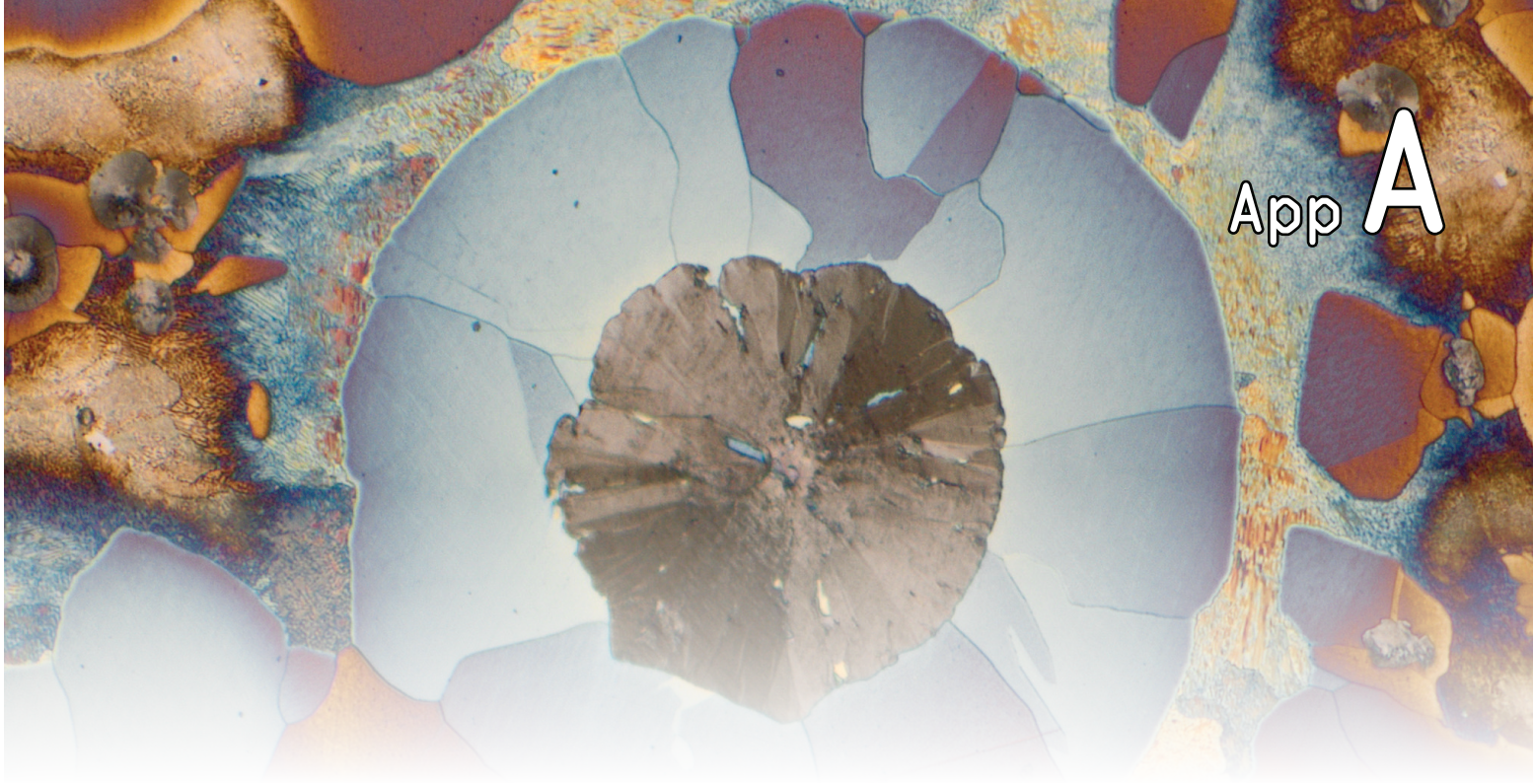
- [58] Q.M. Chen. “Influence of C, Si on Volume Change of SG Iron during Solidification—Computer Modelling for Hypereutectic and Hypoeutectic Compositions”. In: *Journal of Materials Science Letters* 16.15 (1997), 1288–1290. ISSN: 0261-8028. DOI: {10.1023/A:1018583110183}.
- [59] Rohallah Tavakoli and Parviz Davami. “Optimal Feeder Design in Sand Casting Process by Growth Method”. In: *International Journal of Cast Metals Research* 20.5 (2007), 288–296. ISSN: 1364-0461. DOI: {10.1179/136404607X268238}.
- [60] Rohallah Tavakoli and Parviz Davami. “Automatic Optimal Feeder Design in Steel Casting Process”. In: *Computer Methods in Applied Mechanics and Engineering* 197.9-12 (2008), 921–932. ISSN: 0045-7825. DOI: {10.1016/j.cma.2007.09.018}.
- [61] Rohallah Tavakoli and Parviz Davami. “Feeder Growth: A New Method for Automatic Optimal Feeder Design in Gravity Casting Processes”. In: *Structural and Multidisciplinary Optimization* 39.5 (2009), 519–530. ISSN: 1615-147X. DOI: {10.1007/s00158-008-0340-6}.
- [62] A. Muumbo, H. Nomura and M. Takita. “Casting of Semi-Solid Cast Iron Slurry using combination of Cooling Slope and Pressurisation”. In: *International Journal of Cast Metals Research* 17.1 (2004), 39–46. ISSN: 1364-0461. DOI: {10.1179/136404604225020533}.
- [63] J.J. Sobczak, L. Drenchev and R. Asthanas. “Effect of Pressure on Solidification of Metallic Materials”. In: *International Journal of Cast Metals Research* 25.1 (2012), 1–14. ISSN: 1364-0461. DOI: {10.1179/1743133611Y.0000000016}.
- [64] Krzysztof Jakub Fidkowski. *A Simplex Cut-Cell Adaptive Method for High-Order Discretizations of the Compressible Navier-Stokes Equations*. Massachusetts Institute of Technology, Department of Aeronautics and Astronautics, 2007.
- [65] *Die Rechenmaschine des Johann Helfrich Müller aus Darmstadt*. <http://www.fbi.fh-darmstadt.de/fileadmin/vmi/darmstadt/objekte/rechenmaschinen/mueller/index.htm>. History.
- [66] *The Analytical and Difference Engines*. <http://www.computerhistory.org/babbage/>. History.
- [67] Alan Mathison Turing. “On computable numbers, with an application to the Entscheidungsproblem”. In: *J. of Math* 58.345-363 (1936), p. 5.
- [68] Jonathan A Dantzig and Michel Rappaz. *Solidification*. EPFL press, 2009.
- [69] MAGMASOFT 5.2 by MAGMA GmbH. [http://www.magmasoft.com/en/solutions/MAGMA\\_5.html](http://www.magmasoft.com/en/solutions/MAGMA_5.html). Program. 2014.
- [70] Jesper Henri Hattel et al. *Fundamentals of Numerical Modelling of Casting Processes*. Polyteknisk Forlag, 2005. ISBN: 978-87-502-0969-0.
- [71] Richard Aagaard. *Ductile Iron—Solidification Shrinkage Simulation*. DTU, Institute of Manufacturing Engineering, 1997.
- [72] Autodesk Inc., *Finite Element vs Finite Volume*. <http://knowledge.autodesk.com/support/cfd/learn-explore/caas/CloudHelp/cloudhelp/2015/ENU/SimCFD-Learning/files/GUID-12A9AED8-2047-4D3A-BC80-82BE9CF47517-htm.html>.
- [73] CG Mingham and DM Causon. “High-Resolution Finite-Volume Method for Shallow Eater Flows”. In: *Journal of Hydraulic Engineering* 124.6 (1998), pp. 605–614.
- [74] David M Ingram, Derek M Causon and Clive G Mingham. “Developments in Cartesian Cut Cell Methods”. In: *Mathematics and Computers in Simulation* 61.3 (2003), pp. 561–572.
- [75] Richard Aagaard et al. “Simulation vs. Reality of an Industrial Ductile Iron Casting”. In: *Transactions of the American Foundrymen’s Society* 104 (1996), pp. 659–667.
- [76] M. Lipinski, W. Schaefer and S. Andersen. “Modeling of Combined heat and Fluid Flow for Determination of Filling Sequence for Real Complex shaped Castings”. In: *Modeling of casting, welding and advanced solidification processes. TMS, Warrendale, PA* (1991), pp. 185–211.

- [77] D.M. Lipinski, W. Schaefer and E. Flender. “Numerical Modelling of the Filling Sequence and Solidification of Castings”. In: *The Minerals, Metals & Materials Society(USA)*, (1993), pp. 389–396.
- [78] *Scheil or Lever Rule*. Presentation by Markus Rettenmayr, Friedrich-Schiller-University Jena, Institute of Materials Science and Technology. 2008.
- [79] MAGMASOFT 5.3 by MAGMA GmbH. [http://www.magma-soft.com/en/solutions/MAGMA\\_5.html](http://www.magma-soft.com/en/solutions/MAGMA_5.html). Program. 2015.
- [80] G Lesoult, M Castro and J Lacaze. “Solidification of Spheroidal Graphite Cast Irons—I. Physical Modelling”. In: *Acta materialia* 46.3 (1998), pp. 983–995.
- [81] W Oldfield. “A Quantitative Approach to Casting Solidification: Freezing of Cast Iron”. In: (1966).
- [82] Karl Martin Pedersen and Niels Tiedje. “Nucleation and Solidification of Thin Walled Ductile Iron—Experiments and Numerical Simulation”. In: *Materials Science and Engineering: A* 413 (2005), pp. 358–362.
- [83] K.M. Pedersen and N.S. Tiedje. “Undercooling and Nodule Count in Thin Walled Ductile Iron Castings”. In: *International Journal of Cast Metals Research* 20.3 (2007). 5th Decennial International Conference on Solidification Processing, University of Sheffield, Sheffield, England, Jul. 23-25, 2007, 145–150. ISSN: 1364-0461. DOI: {10.1179/136404607X239816}.
- [84] Roy Elliott. *Cast Iron Technology*. Butterworth-Heinemann, 1988.
- [85] S E Wetterfall, H Fredriksson and M Hillert. “Solidification Process of Nodular Cast Iron”. In: *Journal of the Iron and Steel Institute* 210.5 (1972), pp. 323–333.
- [86] J Lacaze, M Castro and G Lesoult. “Solidification of Spheroidal Graphite Cast Irons—II. Numerical Simulation”. In: *Acta materialia* 46.3 (1998), pp. 997–1010.
- [87] J Lacaze. “Solidification of Spheroidal Graphite Cast Irons—III. Microsegregation Related Effects”. In: *Acta materialia* 47.14 (1999), pp. 3779–3792.
- [88] Karl Martin Pedersen. *Simulation and Microstructure of Thin Walled Ductile Cast Iron*. DTU Mechanical Engineering, 2006. ISBN: 87-91035-42-2.
- [89] DM Stefanescu et al. “Use of Combined Liquid Displacement and Cooling Curve Analysis in Understanding the Solidification of Cast Iron”. In: *Transactions of the American Foundrymen’s Society* 120 (2012), pp. 365–374.
- [90] G. Alonso. et al. “Understanding Graphite Expansion During the Eutectic Solidification of Cast Iron Through Combined Linear Displacement and Thermal Analysis”. In: *International Foundry Research* 66.4 (2014), 2–12.
- [91] Doru M Stefanescu. “Solidification and Modeling of Cast Iron—A Short History of the Defining Moments”. In: *Materials Science and Engineering: A* 413 (2005), pp. 322–333.
- [92] Nikolaj Kjelgaard Vedel-Smith. “Obtaining Comparable Simulation and Thermal Measurement Results in Sand Moulds”. In: Presented at the Nordic MAGMASOFT User Meeting , Svedala, Sweden, 2012.
- [93] H.F. Bishop and W.S. Pellini. “The Contribution of Risers and Chill-Edge Effects to Soundness of Cast Steel Plates”. In: *AFS Transactions* 58 (1950), pp. 185–197.
- [94] Rouhollah Tavakoli. “On the Prediction of Shrinkage Defects by Thermal Criterion Functions”. In: *The International Journal of Advanced Manufacturing Technology* 74.1-4 (2014), pp. 569–579.
- [95] E Niyama et al. “A Method of Shrinkage Prediction and its Application to Steel Casting Practice”. In: *Int. Cast Met. J.* 7.3 (1982), pp. 52–63.
- [96] PN Hansen and PR Sahm. “How to Model and Simulate the Feeding Process in Casting to Predict Shrinkage and Porosity Formation”. In: *Modeling and Control of Casting and Welding Processes. IV* (1988), pp. 33–42.
- [97] X. Xue. *M.Sc. Thesis from Shenyang Research Institute of Foundry, Shenyang, China*. Shenyang Research Institute of Foundry, Shenyang, China, 1985.

- [98] YW Lee, E Chang and CF Chieu. “Modeling of Feeding Behavior of Solidifying Al-7Si-0.3 Mg Alloy Plate Casting”. In: *Metallurgical transactions B* 21.4 (1990), pp. 715–722.
- [99] RM Pillai, V Panchanathen and UD Mallya. “Chilled Influence on Feeder Dimensions of Long-Freezing-Range Aluminum Alloys”. In: *AFS Trans* 86 (1978), pp. 103–112.
- [100] Kent D Carlson and Christoph Beckermann. “Prediction of Shrinkage Pore Volume Fraction Using a Dimensionless Niyama Criterion”. In: *Metallurgical and Materials Transactions A* 40.1 (2009), pp. 163–175.
- [101] Mayur Sutaria and B Ravi. “Computation of Casting Solidification Feed-Paths using Gradient Vector Method with Various Boundary Conditions”. In: *The International Journal of Advanced Manufacturing Technology* 75.1-4 (2014), pp. 209–223.
- [102] S Denis, S Sjöström and A Simon. “Coupled Temperature, Stress, Phase Transformation Calculation”. In: *Metallurgical Transactions A* 18.7 (1987), pp. 1203–1212.
- [103] R.S. Jackson. “Factors Determining Dimensional Accuracy of Castings”. English. In: *The British Foundryman* 56 (1963), pp. 332–336.
- [104] C. S. E. Mkumbo et al. “Linear Contraction of Grey Iron Sand Castings”. English. In: *Applied Mathematical Modelling* 14.6 (2002), pp. 225–234.
- [105] Yuichi Motoyama et al. “Dynamic Measurements of the Load on Castings and the Contraction of Castings During Cooling in Sand Molds”. English. In: *Journal of Materials Processing Technology* 213.2 (2013), pp. 238–244.
- [106] J. W. Kang et al. “Evaluation of Distortion of Castings”. English. In: *International Journal of Cast Metals Research* 24.3 (2011), pp. 228–232.
- [107] Anthony Chang and Jonathan Dantzig. “Improved sand surface element for residual stress determination”. English. In: *Applied Mathematical Modelling* 28.6 (2004), pp. 533–546.
- [108] U. C. Nwaogu, N. S. Tiedje and H. N. Hansen. “A Non-Contact 3D Method to Characterize the Surface Roughness of Castings”. English. In: *Journal of Materials Processing Technology* 213.1 (2013), pp. 59–68.
- [109] A. D. Sosa, M. D. Echeverria and O. J. Moncada. “Machining and Heat Treatment Effects on Distortion and Residual Stresses in an Industrial Application of ADI”. English. In: *ISIJ International* 44.7 (2004), pp. 1195–1200.
- [110] *Founding: Spheroidal Graphite Cast Irons*. Norm. 2012.
- [111] MAGMASOFT, FOSECO *Sleeve Database*. [http://www.magmasoft.com/en/solutions/MAGMA\\_5.html](http://www.magmasoft.com/en/solutions/MAGMA_5.html). Database. 2012.
- [112] MAGMASOFT 5.1 by MAGMA GmbH. [http://www.magmasoft.com/en/solutions/MAGMA\\_5.html](http://www.magmasoft.com/en/solutions/MAGMA_5.html). Program. 2012.
- [113] *Mail correspondence with Christof Volks, International Product Manager—Feeding Systems*, FOSECO International Limited, 2015. Mail correspondence.
- [114] *ATAS MetStar, by Novacast Systems AB*. <http://novacast.se/products/atasmeststar/>. Adaptive Thermal Measurement System.
- [115] *DasyLab by Measurement Computing*. <http://www.dasylab.com/>. Program.
- [116] *Founding: Liquid Penetrant Testing—Sand, Gravity Die, and Low Pressure Die Castings*. Norm. 2011.
- [117] Paul Kainzinger. “Utilizing Casting Simulation for the Fatigue Design of Wind Turbine Components”. In: Presented at the International MAGMASOFT User Meeting, Hannover, Germany, 2012.
- [118] MAGMASOFT, FOSECO *Filter Database*. [http://www.magmasoft.com/en/solutions/MAGMA\\_5.html](http://www.magmasoft.com/en/solutions/MAGMA_5.html). Database. 2012.
- [119] *JMatPro by Sente Software Ltd*. <http://www.sentesoftware.co.uk/jmatpro.aspx>. Program.
- [120] J. M. Motz. “Microsegregations easily unnoticed influencing variable in the structural description of cast materials”. In: *Prac.Met.* 25.6 (1988), pp. 285–293.

- [121] Sadaf Vazehrad, Jessica Elfsberg and Attila Diószegi. “Study on microstructure in cast iron using color etching and electron microprobe analysis”. English. In: *Materials Characterization* (2015). DOI: {10.1016/j.matchar.2014.09.008}.
- [122] Sadaf Vazehrad. *A Study on Factors Influencing the Microstructure and Shrinkage Porosity Formation in Compacted Graphite Iron*. School of Engineering, Jönköping University, 2014. ISBN: 978-91-7595-275-8.
- [123] Françoise Condet and Alain Reynaud. *Metallographic Atlas of Cast Iron*. ETIF, 2007.
- [124] Janina M. Radzikowska. *Metallography and Microstructures of Cast Iron*. ASM International.
- [125] Ugochukwu Chibuzoh Nwaogu. *New Sol-Gel Coatings to Improve Casting Quality*. DTU Mechanical Engineering, 2011. ISBN: 978-87-90416-82-9.
- [126] Zeiss OMC 850 by Carl Zeiss AG and Schott AG. [http://www.zeiss.co.uk/industrial-metrology/en\\_gb/metrology-solutions/machinery.html](http://www.zeiss.co.uk/industrial-metrology/en_gb/metrology-solutions/machinery.html). Instrument.
- [127] Leonardo De Chiffre. *Geometrical Metrology and Machine Testing: Textbook*. DTU Mechanical Engineering, 2011. ISBN: 978-87-7078-155-8.
- [128] Calypso by Carl Zeiss AG. [http://www.zeiss.dk/industrial-metrology/da\\_dk/produkter/software/calypso.html](http://www.zeiss.dk/industrial-metrology/da_dk/produkter/software/calypso.html). Program.
- [129] MiniTAB 16 by Cleverbridge AG. <http://www.minitab.com/en-us/>. Program.
- [130] Ductile Iron Data. *Ductile Iron Data - for Design Engineers*. Rio Tinto Iron & Titanium Inc., 1990.
- [131] Flemming Hjelmberg. *Calibration Certificate - Carl Zeiss OMC 850 3D Coordinate Measuring Machine*. Tech. rep. Brock and Michelsen A/S, Industriel Måleteknik, 2011.
- [132] *ISO/DTR 14253-2:1997(E): Geometrical Product Specifications (GPS)—Inspection by Measurement of Workpieces and Measuring Equipment—Part 2: Guide to the Estimation of Uncertainty of Measurement, in Calibration of Measuring Equipment and in Product Verification*. Norm. 1997.
- [133] Giulio Barbato, Alessandro Garmak and Gianfranco Genta. *Measurements for Decision Making: Measurements and Basic Statistics*. Società Editrice Esculapio, 2013. ISBN: 978-88-7488-575-6.
- [134] C. Labrecque and M. Gagne. “Interpretation of cooling curves of cast irons: A literature review”. In: *Transactions of the American Foundrymen’s Society, Vol. 106*. Vol. 106. Transactions of the American Foundrymen’s Society. 102nd Annual Meeting of the American-Foundrymen’s-Society, Atlanta, GA, May 10-13, 1998. American Foundrymen’s Society. 1998, 83–90. ISBN: 0-87433-195-1.
- [135] Conrad Vogel, Celia Juhl and Ernst Maahn. *Metallurgi for ingeniører*. Polyteknisk Forlag, 2009. ISBN: 978-87-502-0930-0.
- [136] K.M. Pedersen and N.S. Tiedje. “Temperature Measurement During Solidification of Thin Wall Ductile Cast Iron. Part 1: Theory and Experiment”. In: *Measurement* 41.5 (2008), 551–560. ISSN: 0263-2241. DOI: {10.1016/j.measurement.2007.05.002}.
- [137] K.M. Pedersen and N.S. Tiedje. “Temperature Measurement During Solidification of Thin Wall Ductile Cast Iron. Part 2: Numerical Simulations”. In: *Measurement* 41.4 (2008), 341–348. ISSN: 0263-2241. DOI: {10.1016/j.measurement.2007.05.003}.
- [138] Lennart Elmquist and Attila Diószegi. “Shrinkage Porosity and its Relation to Solidification Structure of Grey Cast Iron Parts”. English. In: *International Journal of Cast Metals Research* 23.1 (2010), pp. 44–50.
- [139] R.W. Heine. “The Fe-C-Si Solidification Diagram for Cast Irons”. English. In: *AFS Proceedings* 94 (1986), pp. 391–402.
- [140] H.T. Angus. *Cast Iron - Physical and Engineering Properties*. Butterworth & Co (Publishers) Ltd., 1976.
- [141] *EN ISO 8062-3:2007: Geometrical Product Specifications (GPS)—Dimensional and Geometrical Tolerances for Moulded Parts—Part 3: General Dimensional and Geometrical Tolerances and Machining Allowances for Castings*. Norm. 2007.

- [142] Rio Tinto Iron & Titanium Inc. *Ductile Iron—The Essentials of Gating and Riser Design*. 770 Sherbrooke Street West - Suite 1800, Montréal (Québec) Canada: Rio Tinto Iron & Titanium Inc., 2000.
- [143] Hasse Fredriksson and Ulla Åkerlind. *Materials Processing during Casting*. English. Wiley, 2006, 434 blz. ; ISBN: 0470015136, 9780470015131.
- [144] Rune Engelbert Hansen. *Design of Experimental Method for Feeding*. Special Course. Technical University of Denmark, Department of Mechanical Engineering, 2013.
- [145] *An Introduction to Ultrasonic Material Analysis*. <http://www.olympus-ims.com/en/applications-and-solutions/introductory-ultrasonics/introduction-material-analysis/>. Program.
- [146] *X-Ray Systems for Universal Deployment in 2D and CT Inspection*. <http://www.yxlon.com/Products/X-ray-systems>. Machine.
- [147] Guido Busch. “What’s New In MAGMA Release 5.3”. In: Presented at the International MAGMASOFT User Meeting , Potsdam, Germany, 2014.
- [148] Per Leif Larsen. *Iron Melt Flow in Thin-Walled Sections Cast in Vertically Parted Green Sand Moulds*. DTU, IPL, 2004.
- [149] Søren Skov-Hansen. *Reduced Energy Consumption for Melting in Foundries*. DTU, IPL, 2007. ISBN: 978-87-91035-63-5.
- [150] *Aid to Calculate Sprues, Ingates and Runners for Castings in the Foundry - Density Data List*. <http://homepage.ntlworld.com/oxfordtours/workitoutnet/castaid/spruecalculator/decinote.htm>. Calculator.
- [151] *Novacast*. <http://novacast.se/>. Program.
- [152] *Flow-3D Cast*. <http://www.flow3d.com/home/industries/metal-casting>. Program.
- [153] Attila Diószegi. “Casting Process Development at Volvo Foundry”. In: Presented at 3rd Metallurgy, Solidification, and Modelling of Cast Iron Castings course, Jönköping, Sweden, 2013.
- [154] Nikolaj Kjelgaard Vedel-Smith and Torben Anker Lenau. “Casting Traceability with Direct Part Marking using Reconfigurable Pin-Type Tooling based on Paraffin-Graphite Actuators”. In: *Journal of Manufacturing Systems* 31.2 (2012), 113–120. ISSN: 0278-6125. DOI: {10.1016/j.jmsy.2011.12.001}.
- [155] *Conversation with Professor Doru Michael Stefanescu at the 10th International Symposium on the Science and Processing of Cast Iron, Mar del Plata, Argentina, Nov. 2014*. Conversation.



## Appendix

---

### Appendix A: Colour Etching Guidelines for Picric Acid . . . . . 296

- I: Quantification of Feeding Effects of Spot Feeding Ductile Iron Castings Made in Vertically Parted Molds . . . . . 301
- II: Effect of Feeder Configuration on the Microstructure of Ductile Cast Iron 315

- III: Thermal Distortion of Disc-Shaped Ductile Iron Castings in Vertically Parted Moulds . . . . . 325
- IV: Feeding Against Gravity with Spot Feeders in High Silicon Ductile Iron 337

∴ Colour etching with picric acid, user guide. ∴

Keywords: . . . . . Colour Etching Chapter findings reported in: . . . Supplement II, on page 315

---

## Color Etching

---

**USE PROTECTIVE CLOTHING, EYE PROTECTORS AND GLOVES  
PICRIC ACID IS UNHEALTHY AND MUST HANDLED CAREFULLY**

### Preparation of etching solution

It is suitable to prepare an amount 5 times the recipe.

Store the solution in a bottle marked with your name and the date.

The solution is prepared in a big beaker (e.g. the coffee pot)

### Recipe

10 g Sodium hydroxide (NaOH)

40 g Potassium hydroxide (KOH)

10 g Picric acid

50 ml Distilled water

At preparation:

*Use protective clothing, eye protectors and gloves*

- Pour the distilled water into the beaker
- Weigh the chemicals
  - Put a beaker on the weighing machine
  - Never pour the chemicals back into their containers. It is better to use smaller amounts during the weighing
  - Do not use the same spoon for different chemicals (unless it is washed in between)
  - Never use unwashed tools
- Do not pour all the chemicals into the water at the same time, only small amounts. Because of heat evolution – stir thoroughly all the time.
  - Stir until the chemicals are dissolved – this may take some time
  - Start with NaOH
  - Then KOH
  - Picric acid is last

### Etching procedure

The sample must be cut, ground, polished and possibly also mounted before etching

Cover the working area with paper towels all the way from the hot plate to the water tap – reduces problems with dripping

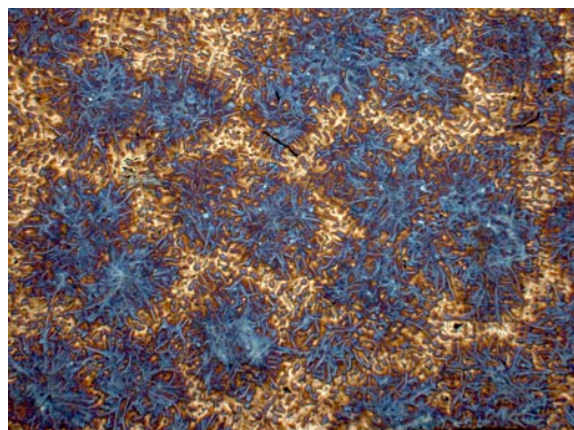
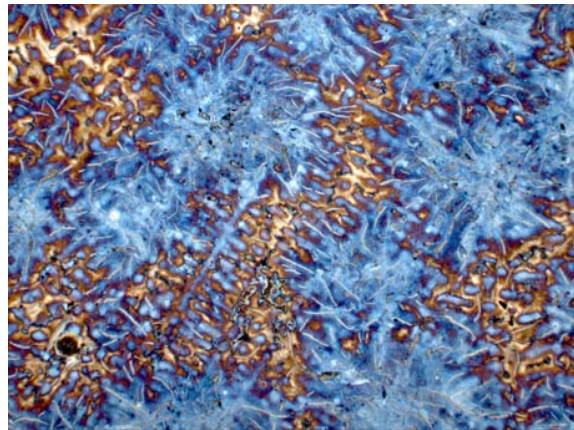
- Pour the etching solution into the beaker
  - When re-using previously heated solution: Use one bottle for already heated solution and another for newly mixed solution. Mix the old solution with the new one and then after 2-3 times through it away. Remaining or old solution is poured into the container used for that purpose. Sometimes it is appropriate to add more distilled water into the solution, especially if the solution has been boiling.
- Heat the solution to 109°C
  - Place the thermocouple almost on the bottom of the beaker
- During etching – hold the sample upside down with the sample surface at the same level as the thermocouple – hold it with a tong or the magnetic device,



avoid contact with the bottom of the beaker (may introduce scratches on the sample)

- Keep the sample in the solution for approximately 2 minutes the first time
- After etching – rinse in water as quickly as possible – then use ethanol
  - Examine the result in the microscope
  - These steps should be done as quick as possible to avoid that the sample loses to much heat before eventually further etching.
- If etched too long and too much – re-polish and etch ones again

There are no general rule for how long time it takes before etching is complete. It depends on factors such as sample size, whether being mounted or not, and how stable the temperature is. It is therefore a good way to etch for short times, investigate the result and if necessary continue the etching procedure, or stop if the result is good enough. Skill comes with experience and after practicing, one gets a feeling for how long times should be used. The pictures below shows how the sample can look like when the etching is enough.





PICRIC ACID is toxic at inhalation, skin contact and consuming and explosive at stroke, friction, fire or another cause of ignition.

Use it very carefully and wash the spoon or other equipments when being in contact with picric acid.

Never let it be dry!



# Part IV Supplements

AFS 2013 I

TMS 2014 II

JMPT 2014 III


SPCI 2014 IV

“**P**ROGRESS is made by trial and failure; the failures are generally a hundred times more numerous than the successes; yet they are usually left unchronicled.”

---

—*William Ramsay*






# Supplement I

## Quantification of Feeding Effects of Spot Feeding Ductile Cast Iron Made in Vertically Parted Moulds

Published  
AFS Proceedings 2013 @  
American Foundry Society, St. Louis, MO USA

“If your experiment needs statistics,  
you ought to have done a better experiment.”

—Ernest Rutherford



## Supplement I

---

### Quantification of Feeding Effects of Spot Feeding Ductile Iron Castings Made in Vertically Parted Molds

N.K. Vedel-Smith  
N.S. Tiedje  
J. Sällström  
K.T. Maza

Technical University of Denmark, Department of Mechanical Engineering  
Technical University of Denmark, Department of Mechanical Engineering  
Foseco Sweden AB  
Valdemar Birn  $\frac{1}{2}$

Vedel-Smith was the main author. Tiedje contributed with review and evaluation. Vedel-Smith, Sällström, and Maza performed the experimental part.

Vedel-Smith presented the paper at the 2013 AFS conference in St. Louis, MO.  
Paper was awarded the *Best Paper Award* at the 2014 AFS conference in Schaumburg, IL.

*Published*  
AFS Proceedings 2013 © American Foundry Society, St. Louis, MO USA

---

## Quantification of Feeding Effects of Spot Feeding Ductile Iron Castings Made in Vertically Parted Molds

N.K. Vedel-Smith, N.S. Tiedje  
Technical University of Denmark, Kgs. Lyngby, Denmark

J. Sällström  
FOSECO Sweden, Åmål, Sweden

K.T. Maza  
Vald.Birn A/S, Holstebro, Denmark

Copyright 2013 American Foundry Society

### ABSTRACT

In vertically parted molds it is traditionally difficult to feed heavy sections that cannot be reached by traditional side/top feeders or other conventional methods. This project aims at quantifying the effects of using molded-in ram-up spot feeders as a means of feeding isolated sections in castings made in vertically parted molds and it gives directions towards the effectiveness of this technology.

The casting examined is a disc-shaped casting with an inner boss and an outer ring, separated by a thin walled section. Thus, both boss and ring are prone to porosities.

The experimental work analyzes the effect of different exothermic and insulating spot feeders and their interaction with traditional parting line feeders, with respect to porosities and surface shrinkage. Experiments were performed using EN-GJS-500-7 and EN-GJS-450-10 alloys.

The experiment shows that the geometry cannot be cast successfully without the use of both a top and a spot feeder. Leaving out one or both feeders, results in porosities and surface shrinkage. For EN-GJS-500-7, any combination, with both feeders present, produced sound castings. For the more demanding EN-GJS-450-10 the exothermic spot feeder produced sound castings. All other combinations displayed some degree of porosities.

**Keywords:** Spot feeding, porosities, surface shrinkage, ductile iron, sleeves, ram-up sleeves, vertically parted molds, porosity

### INTRODUCTION

As the price of energy is rising, and will continue to rise in coming years, melt reduction has become a significant parameter with which to improve a foundry's business. It has been shown that great savings in raw materials energy and money can be achieved by optimizing feeding methods<sup>1</sup>. Proper feeding of the castings gives an

improved yield, which in return saves energy for melting, and thus money.

While there still may be room for further optimization of traditional feeders, the larger gains are achieved by new approaches to the feeding challenge. New opportunities present themselves to the designer of the cast layout, enabling otherwise difficult castings to be produced with a profit.

Spot feeders, on vertically parted molds, enable feeding of areas located away from the parting line of the mold, much like the feeder placement known from horizontally parted molds. The spot feeders are sleeves of insulating or exothermic material or a combination material. They provide melt and heat for the chosen area, thus changing the overall thermal gradients of the casting and the local direction of solidification.

This paper is the result of an ongoing project, involving several companies, working towards characterizing, quantifying and understanding the effect of various feeder applications.

### RAM-UP SLEEVES

The spot feeder is molded into the sand mold using the ram-up sleeve system. The sleeve is made of exothermic, insulating or a combined exothermic-insulating material. Traditionally sleeves are inserted into the molded sand on vertically parted molds. The ram-up sleeves, though, are mounted onto a specially designed pin which holds the sleeve in place while the mold is compacted. The pin is placed on the pattern at the location where the feeder is to be located (Fig. 1).

The ram-up sleeves have a collapsible steel neck, which enable them to collapse and compact the sand around the feeder neck while protecting the sleeve itself during the molding operation.

The solution with the ram-up pin enables the feeder to be placed away from the parting line, making it possible to

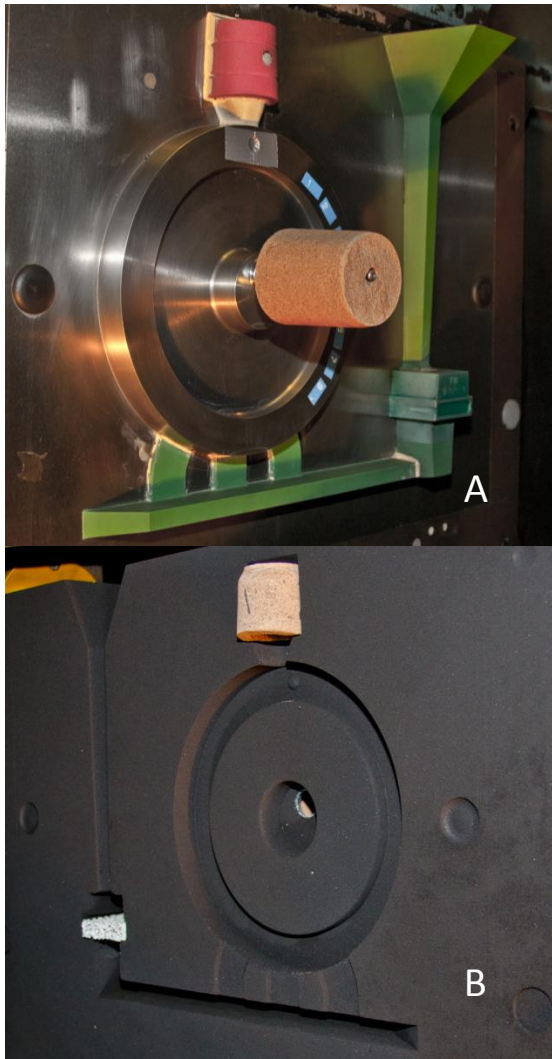


**Fig. 1.** These are photos of A) pattern plate with gating system (green), top feeder geometry (red), the casting geometry and pin with Ram-Up Sleeve (at the center) and B) molded in Ram-Up Sleeve spot feeder (center), 10 PPI foam filter and top feeder sleeve.

apply spot feeders on vertically parted molds. The only major restriction is that the ram-up pin and sleeve must be aligned with the direction of mold compression.

## EXPERIMENTAL SETUP

### THE CASTING GEOMETRY

The test geometry used for this experiment consists of a disc with an inner boss and an outer ring, separated by a thin plate like section. The geometry is designed to display casting problems similar to those found on disc-brakes, fly-wheels and other castings with higher modulus sections, isolated from feeding by in between low modulus sections (Fig. 2). The casting's design dimensions can be found in Table 1 alongside the

calculated modulus and feed modulus for the different sections of the casting.

$$M_f = 1.2 \cdot M_c \quad \text{Equation 1}$$

where  $M_c$  is the modulus of the casting section in question calculated as volume divided by cooling area<sup>2</sup>.

**Table 1. Casting Geometry Dimensions and Modulus (mm) (Section Overview Found in Fig. 3)**

	III	IV	V	VI	VII
Height	25	55	50	55	25
Thickness	20	10	30	10	20
Modulus	6	5	9	5	6
Feed Modulus	7	6	11	6	7

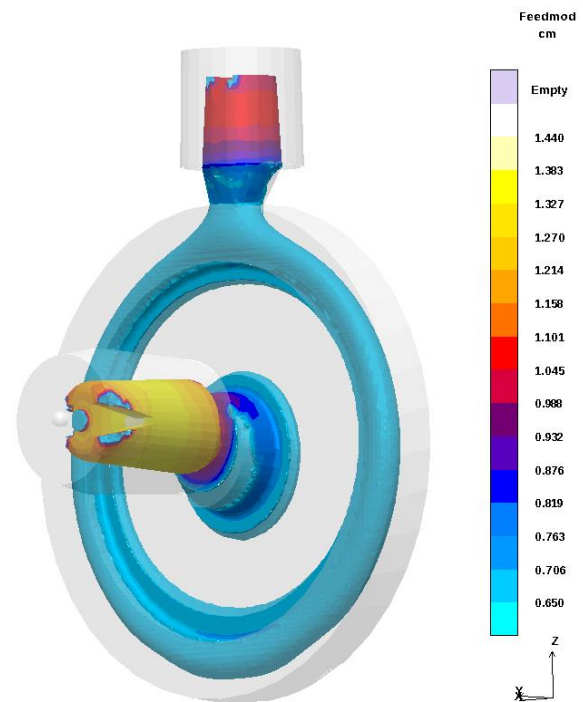


**Fig. 2.** This is a feeding modulus for casting geometry. The out ring and inner boss show higher modulus than the section in between. The highest modulus is found in the feeders with the center feeder as the greater.

The downsprue, runner and gating design are all of conventional design. A foam filter (10 pores per inch [PPI]) was placed at the bottom of the downsprue to reduce turbulence and capture inclusions in the melt (Fig. 1).

The poured weight is approx. 8 kg (18 lb) and the casting itself weighs 4 kg (9 lb).



## ALLOYS

Two different cast irons were used in the experiment. The first alloy was a traditional EN-GJS-500-7<sup>3</sup> ( $\alpha$ ), which is a commonly used cast iron with little shrinkage. The other alloy was an EN-GJS-450-10<sup>3</sup> ( $\beta$ ) with high silicon content, displaying close to fully ferritic structure with better elongation and machinability. The alloys chemical compositions are shown in Table 2.

**Table 2. Alloy Compositions [wt%]**

	C	Si	Mn	P	S	Mg	Cu
EN-GJS-500-7 ( $\alpha$ )	3.67	2.73	0.50	0.015	0.005	0.049	0.025
EN-GJS-450-10 ( $\beta$ )	3.35	3.48	0.34	0.017	0.003	0.046	0.010

The lower carbon content makes the alloy more prone to shrinkage and porosity defects.

Both alloys are near eutectic and are, as such, expected to solidify in a similar manner. Thus, the main difference between the alloys can be contributed to the higher C content and thus greater graphite expansion of the EN-GJS-500-7 alloy.

## FEEDER SLEEVES

The experiment made it possible to vary the thermal (or true) modulus ( $M_t$ ) without changing the geometric modulus ( $M_g$ ).

$$M_g = \frac{V}{A} \quad \text{Equation 2}$$

Thus, the results are free from changes in hydrostatic pressure caused by a larger liquid volume, but retain the effects related to solidification time.

The sleeve material provides a Modulus Extension Factor<sup>2</sup> (MEF) which is material specific. The MEF is an addition to the geometric modulus. The MEF is determined by the material properties and the geometry—i.e. thickness—of the sleeve walls.

All feeders have the same geometric modulus. Thus, they cannot be meaningfully compared based on this figure alone. Instead the different feeder sleeves are compared using the thermal modulus<sup>2</sup>.

$$M_t = \text{MEF} \cdot M_g \quad \text{Equation 3}$$

## Feeder Placement

The casting is designed with two feeders—1) a top feeder placed on top of the outer ring at the mold parting line, and 2) a center feeder placed away from the parting line using a Ram-Up Sleeve. The top feeders used here were made from either insulating ( $M_t$  9 mm [.035 in.]) or exothermic and insulating ( $M_t$  10 mm [.039 in.]) material. The center feeder sleeves were made from exothermic ( $M_t$  12 mm [.047 in.]); insulating ( $M_t$  11 mm [.043 in.]) or a mixture of exothermic/insulating ( $M_t$  11 mm [.043 in.]) materials.

## Feeder Combinations

The trials were comprised of 18 combinations of feeders and cast-alloys. However, this paper only presents data from 8 of those trials. The 8 triplicate casting groups are systematically numbered from  $\alpha$ 1-5 for the EN-GJS-500-7 alloy, and  $\beta$ 1-3 for the EN-GJS-450-10 alloy. Each triplicate copy is denoted A, B or C.

The feeder combinations examined are shown in Table 3. The combinations are designed to give insight into the effect of the different feeder types, as well as the absence of the one or both feeders. Castings  $\alpha$ 1-5 were cast with EN-GJS-500-7 alloy, whereas  $\beta$ 1-3 were cast with the EN-GJS-450-10 alloy.

**Table 3. Feeder Combinations**

	$\alpha$ 1	$\alpha$ 2	$\alpha$ 3	$\alpha$ 4	$\alpha$ 5	$\beta$ 1	$\beta$ 2	$\beta$ 3
Top	E/I	Ins	E/I	-	-	E/I	Ins	E/I
Center	Exo	Ins	-	E/I	-	Exo	Ins	-

Exo stands for exothermic,  
 Ins stands for insulating and  
 E/I stands for exothermic-insulating

## CASTING CONDITIONS

The trials were made under production conditions at Vald.Birn Iron Foundry A/S in Holstebro, Denmark. The experimental castings were cast using a vertical molding line—DISAMATIC 2013. The castings were made during two separate trials in June 2011 and January 2012. Both experiments used the same vertical molding line with identical machine settings for each trial. All molds were green sand molds.

All castings were made using a heated pouring station, keeping the melt temperature constant between the first and the last poured casting. The castings were cast in three sequences; 1<sup>st</sup> and 2<sup>nd</sup> in June 2011 with the EN-GJS-500-7 alloy. First sequence was cast at 1,401±5C (2,554±10F). Second sequence was cast within an hour of the first sequence, and was cast at 1,408±5C (2,566±10F). The 3<sup>rd</sup> and final sequence was cast in January 2012 with the EN-GJS-450-10 alloy at 1,392±5C (2,538±10F). The chemical composition shown in Table 2 was determined with optical emission spectroscopy. The pouring times for all castings were approx. 3.5 s.

The castings were separated from the production at the shake-out station to preserve the gating systems intact. Afterwards the castings were shot blast.

## LIQUID PENETRANT TEST

All castings were sectioned through the vertical centerline to allow for thorough examination for macro and micro porosities as close to the center as possible. A 5 to 10 mm (0.2 to 0.4 in.) thick slice was cut from each casting, and

the center surface of the slice was then ground to achieve a smooth surface (Fig. 3). The slices were then etched with oxalic acid dihydrate—approx. 25 g (.06 lb) and

500 ml (17 oz) water per casting—at room temperature for 24 h. The etching was done to remove material that the grinding might have smeared over the surface, potentially blocking porosities, thus obscuring the results.

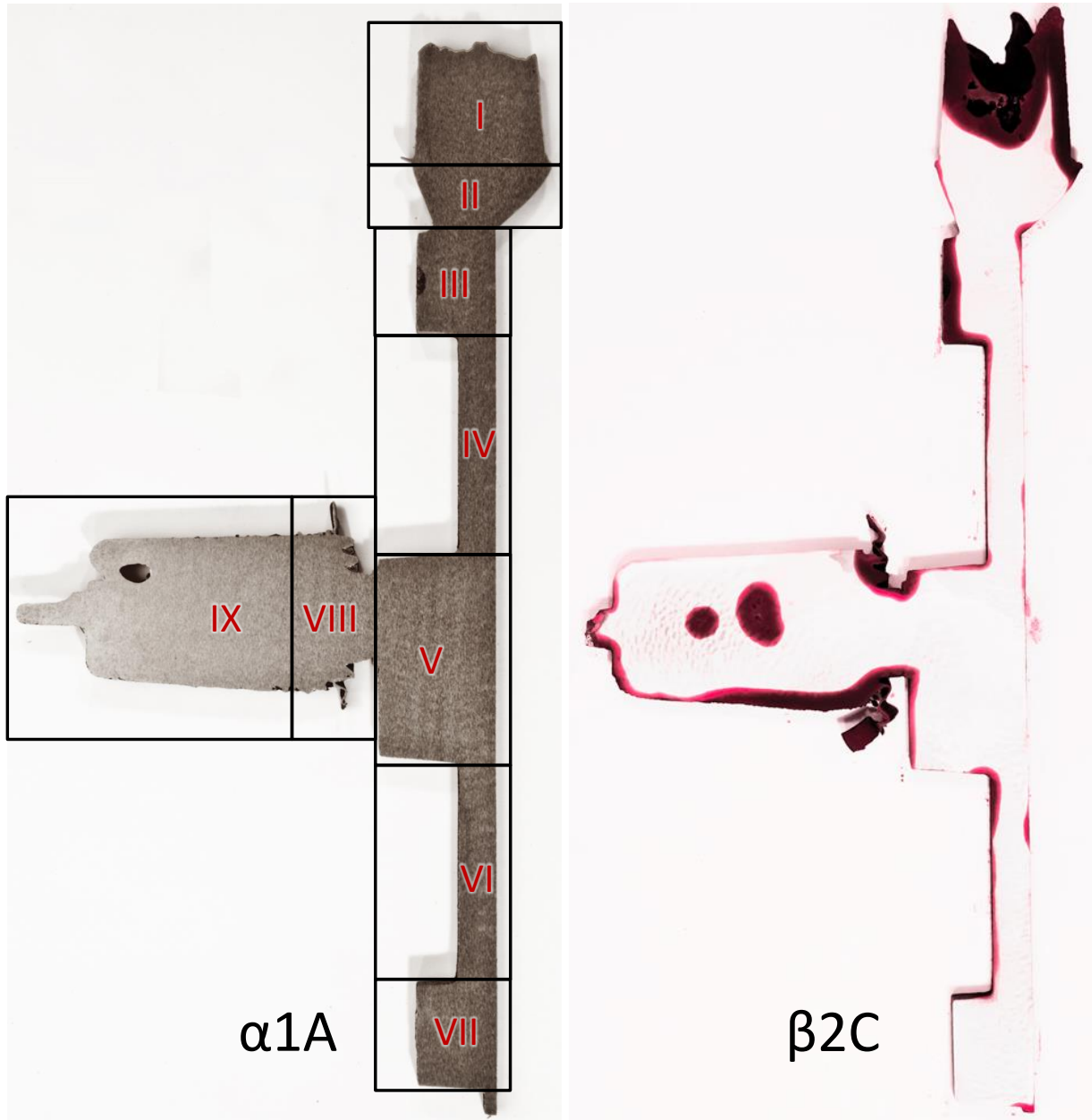


**Fig. 3.** Left—The nine non-overlapping areas examined for porosities are shown on casting  $\alpha 1A$  before the liquid penetrant test. Right—These are the results of liquid penetrant test for casting  $\beta 2C$ . Area III is classified with a SP1 defect and area IX is classified with a CP3 defect.

The etched castings were rinsed carefully, then sprayed with dye penetrant, allowed to rest for 5-10 min., rinsed again and finally sprayed with the liquid penetrant developer. All castings were photo-documented within 20 min. of the liquid penetrant development. The liquid penetrant tests were performed according to European Standard EN 1371-1:2011. The visual evaluation and classification of the porosities also conferred with the descriptions in the standard.

The casting slices were each divided into nine non-overlapping areas, as seen in Fig. 3. Each area was evaluated for size and type of porosities. Also the feeders and feeder necks were evaluated. Porosities are expected in the feeders and do not influence the quality of the casting. Likewise, porosities in the feeder neck do not influence the casting quality, but porosities here indicate that the feeder is close to the limit of its abilities. Thought should then be given to the possibility of choosing a feeder with a higher modulus.

#### SURFACE DEFORMATION MEASUREMENTS

Insufficient feeding can cause not only porosities, but also surface shrinkage. To be able to evaluate the different feeder combinations influence on surface shrinkage and geometric stability, the plane surface of all castings were measured using a Coordinate Measuring Machine (CMM). The CMM maps the back surface of the castings with a probe, using a pre-programmed measuring layout. A probe with a head diameter of 3 mm (0.19 in.) was used to ensure a suitable mechanical filter against the roughness of the surface itself. The program ensures identical and comparable measurements between all castings. The 3D-coordinate map is then used to evaluate the flatness of the casting. The flatness value ( $f_v$ ) is given as a simple measure of the largest difference in height measured across the surface. A perfectly flat surface is equivalent to an  $f_v$  of 0.00 mm.

The  $f_v$  in itself gives no definite proof of surface shrinkage. Castings can, for various reasons, warp as part of solidification and cooling. However, surface shrinkage will normally exist as a local depression of the surface.

#### NUMERICAL SIMULATION

All feeder combinations have been simulated and examined using a commercial numerical simulation software—MAGMASOFT 5.2. The simulation setups were configured to mirror the conditions present during the three casting sequences, as best as possible. The simulations were used to evaluate the amount and location of the porosities and provide the opportunity to see where porosities have a higher probability of forming. Also, porosities located away from the centerline can be identified. Moreover, it is possible to see how porosities

develop during solidification, as well as disappear again due to graphite expansion when the casting cools. This is done by analyzing the porosities during solidification in addition to the fully solidified casting.

#### RESULTS

The castings were evaluated according to several parameters—porosities, porosity location and surface deformation—to properly identify if they would qualify as sound or unsound. As it is not the intent of the present paper to set standards for evaluating sound castings, the defect types are listed for the different areas. The acceptable amount, size and placement of casting defects are very dependent on application.

#### POROSITIES

Reviewing the nine areas for all eight feeder and alloy combinations, all defects were classified as either non-linear isolated indications (SP) or non-linear clustered indications (CP) in accordance to EN 1371-1:2011 (C, D).

Areas II, IV and VI displayed no defect indication for any of the 24 castings. Area II is the feeder neck of the top feeder, and concludes that the top feeder is feeding sufficiently for all castings. Areas IV and VI are the thin walled sections in between the boss and the outer ring. For casting  $\beta 3C$ , an SP1 defect was identified for area VII—the bottom ring. For all other of the 24 castings area VII was defect free. Therefore, with focus on the areas III, V and VIII, it is possible to analyze the different feeders' ability to sufficiently feed the casting.

#### Reference Castings

In order to quantify the effect of the different feeders, reference castings without the feeders were needed. Casting groups  $\alpha 3$  and  $\beta 3$  were cast without the center feeder. Casting group  $\alpha 4$  was cast without the top feeder, and casting group  $\alpha 5$  was cast without either of the feeders.

Casting group  $\alpha 3$  displays SP1 or CP1 defects in area V. Casting group  $\alpha 4$  displays SP1 defects in area III. Castings  $\alpha 5A$  and C display SP1 and CP1 defects in area III and V, while casting  $\alpha 5B$  displays a SP1 defect in area III. None of the reference castings are without defects. These nine castings are all cast as EN-GJS-500-7 iron.

Casting group  $\beta 3$  is without center feeder—like casting group  $\alpha 3$ —but as EN-GJS-450-10 iron. All three castings have defects classified as SP1, CP2 or CP3 in areas III and V. Again all reference castings contain defects.

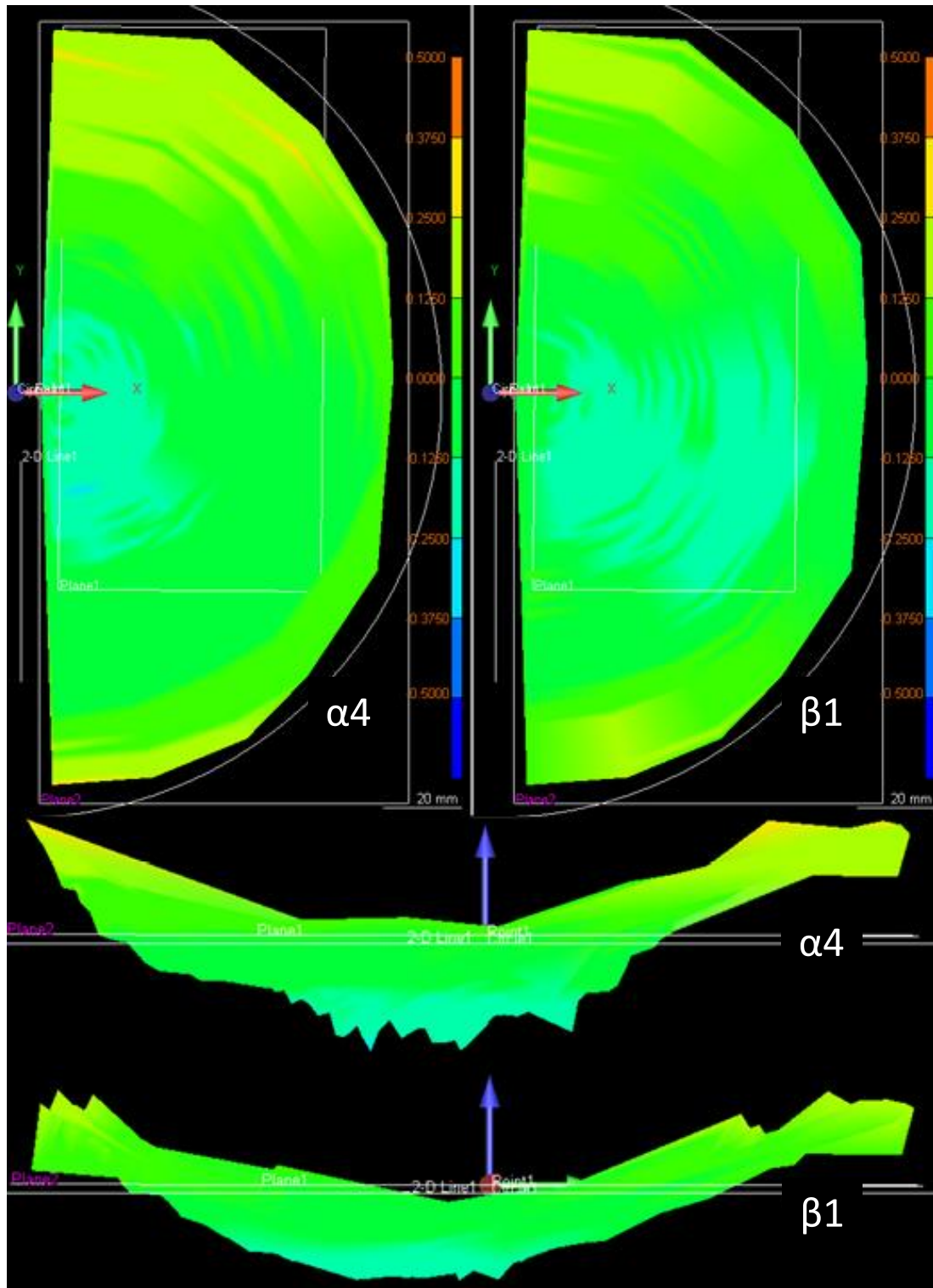


**Fig. 4.** The photo shows the flatness of castings  $\alpha_4A$  and  $\beta_1A$ . The halved castings are viewed from the top and the side. All four representations adhere to the same scale. 0.00 is the mean value and the color scale covers  $\pm 0.50$  mm. (Note: the warp-effect for both castings are large enough to obscure the effect of surface shrinkage.)

### EN-GJS-500-7 Castings

Casting groups  $\alpha 1$  and  $\alpha 2$  are cast as EN-GJS-500-7 iron with a fairly high graphite precipitation. For the three areas in focus, for all six castings, only the feeder neck—area VIII—for casting  $\alpha 2B$  displayed an SP1 defect.

### EN-GJS-450-10 Castings

Casting groups  $\beta 1$ , and  $\beta 2$  were equipped with the same feeders as casting groups  $\alpha 1$  and  $\alpha 2$  respectively, but cast with a different alloy. For the three areas in focus casting group  $\alpha 1$  displays no defects. Casting  $\beta 2A$  displays an SP1 defect in area VIII. Casting  $\beta 2B$  displays an SP2 defect in area V and an SP1 defect in area VIII. Finally, casting  $\beta 2C$  displays an SP1 defect in area III.

The results of the liquid penetrant test are summarized in Table 4.

### SURFACE DEFORMATION

Of the 24 castings, 20 have a flatness value between 0.33 and 0.53 mm (0.01 and 0.02 in.) with a maximum difference between castings  $\alpha 1B$  and  $\alpha 2B$  of 0.2 mm (0.008 in.). Casting group  $\alpha 5$  has a far greater  $f_v$  ranging from 0.82 to 0.97 mm (0.03 to 0.04 in.). Casting groups  $\alpha 3$  and  $\alpha 4$  have comparable flatness values even though they lack either the top or the center feeder. The absence of both feeders about doubles the height difference measured across the surface, compared to all the other castings (Fig. 5).

As shown in Fig. 5, there is some difference in flatness related to the combination of feeders used. The exothermic feeders of casting group  $\alpha 1$  have an  $f_v$  approx. 25% larger than the purely insulating feeders used for casting group  $\alpha 2$ . The same effect is not seen for the EN-GJS-450-10 alloy where  $f_v$  varies between 0.39 and 0.41 mm (0.015 and 0.016 in.).

The flatness value, though, cannot directly be linked to surface shrinkage. The variation in height difference across the back surface of the casting can also be related to a warping caused by thermal stresses that occur during cooling (Fig. 4). All castings show warping. It is impossible from the data at hand to conclude how large a part of the surface un-flatness that is shrinkage related. In some castings—like  $\alpha 4A$ —a low area is located close to the boss, while others—like  $\beta 1A$ —show a low area covering the larger part of the middle section of the casting.

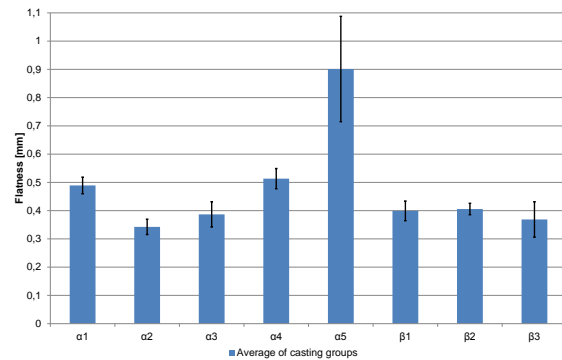


**Fig. 5. This graph indicates the Flatness Value ( $f_v$ ) as an average for each casting group, with 95% confidence  $T$  interval marked by the error bars.**

Another feature observed for all castings are ripples that radiate from the center boss towards the outer ring. The ripples are differences in height, and the height differences between ripple peak and valley are in most cases less than 0.1 mm (0.004 in.). Nevertheless, the ripples are present for all castings and do vary slightly with respect to amplitude and wavelength.

### SIMULATIONS

#### Porosity Analysis

Analyses of the porosity formation during solidification show that the main difference between the two alloys is indeed the better recuperation of the EN-GJS-500-7 alloy. This was expected as the EN-GJS-500-7 has a higher C content, and thus a greater graphite expansion, compared to the EN-GJS-450-10.

The simulations show a few areas with possibility for minor porosities. The feeders with exothermic sleeves show areas with intensive porosity formation, indicated by the red and yellow colors in Fig. 6,  $\alpha 1$ . The feeders with insulating sleeves display areas with potential porosity formation, but on a different level than the feeders with exothermic sleeves, indicated by blue in Fig. 6,  $\alpha 2$ .

The changes in alloy also resulted in change to the size and location of the porosities. The EN-GJS-450-10 showed increased tendency for porosities compared to the EN-GJS-500-7, using the same graphite expansion factor. The EN-GJS-500-7 is simulated with a graphite precipitation factor of 8. Simulating several different graphite precipitation factors with the EN-GJS-450-10 and comparing these to the results of the liquid penetrant test, the best matching graphite expansion factor is between 6 and 7 (Fig. 6,  $\beta 1$  and  $\beta 2$ ).



**Fig. 6.** These are porosity simulations for casting groups  $\alpha 1$ ,  $\alpha 2$ ,  $\beta 1$  and  $\beta 2$ . The 3D model is sectioned through the vertical centerline, exactly as the real castings were. The simulations of  $\alpha 1$  and  $\alpha 2$  apply a graphite precipitation factor of 8, and the simulations of  $\beta 1$  and  $\beta 2$  apply a factor of 6.

Examining the thermal gradients produced by the different types of feeder sleeves, it is clear that the exothermic and exothermic-insulating sleeves have a significantly higher modulus than the insulating sleeves (Fig. 7).

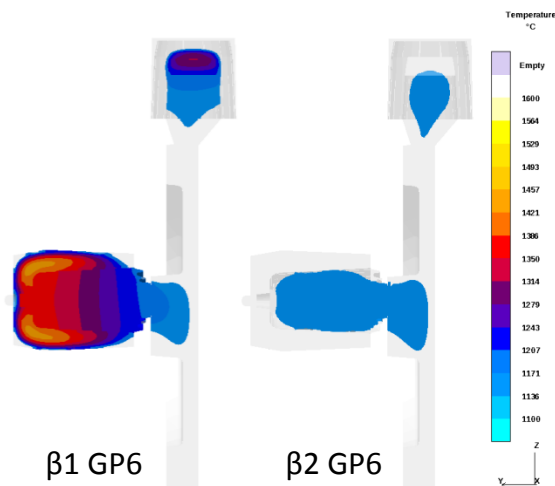


**Fig. 7.** The simulation of thermal gradients at the center cross-section of the casting includes feeder sleeves. By comparing exothermic and exothermic-insulating sleeves on  $\beta 1$  (left) with insulating sleeves on  $\beta 2$  (right), both simulations show at 85% solidified.

## DISCUSSION

### POROSITIES EN-GJS-500-7

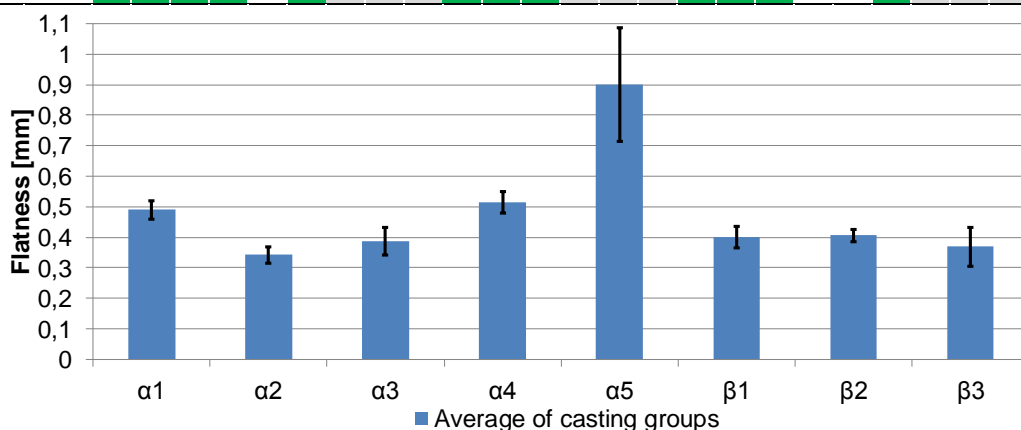
The casting porosity analysis shows almost no defects for casting groups  $\alpha 1$ ,  $\alpha 2$  and  $\beta 1$ . The one defect identified in these nine castings is found in  $\alpha 2$ B area VIII and classified SP1. It is a very small non-linear porosity in the feeder neck of the center feeder. Thus, all nine castings are sound for all categories according to the EN 1371-1:2011.

Compared to the casting groups  $\alpha 3$ ,  $\alpha 4$  and  $\alpha 5$ , which were cast with the same alloy as above, but cast without one or both feeders, all of these nine castings display SP1 or CP1 defects in one or more areas. Casting group  $\alpha 3$  directly shows the effect of not using a spot feeder. The  $\alpha 3$ A and B display SP1 defects at area V, while  $\alpha 3$ C displays a CP1 defect in the same area. As the design of the casting was made to provoke these types of defects, this is not surprising, but it proves that both the exothermic and the insulating spot feeders provide the conditions needed to produce defect free castings. The spot feeders supply melt, heat and pressure sufficient for the boss to be porosity free.

Casting group  $\alpha 4$ —center feeder and no top feeder—displays no defects in area V, but SP1 defects in area III. This corresponds with the intension of the casting design. Likewise, casting group  $\alpha 5$  displays SP1 or CP1 defects in area III and V, respectively. The only exception is  $\alpha 5$ B, area V, which is defect free.

**Table 4. Summation of Results Comparing Feeder Sleeve Material (and Modulus) with Type and Size of Both Alloys (Exo = exothermic; Ins = insulating and E/I = exothermic-insulating)**

	GJS-500-7					GJS-450-HS																	
	α1			α2		α3		α4		α5			β1			β2			β3				
Top Feeder Sleeve Material	E/I			Ins		E/I		N/A		N/A			E/I			Ins			E/I				
Top Feeder Sleeve Thermal Modulus	10 mm			9 mm		10 mm		N/A		N/A			10 mm			9 mm			10 mm				
Center Feeder Sleeve	Exo			Ins		N/A		E/I		N/A			Exo			Ins			N/A				
Center Feeder Sleeve Thermal Modulus	12 mm			11 mm		N/A		11 mm		N/A			12 mm			11 mm			N/A				
	A	B	C	A	B	C	A	B	C	A	B	C	A	B	C	A	B	C	A	B	C		
Areas of the Castings examined for porosities	III									SP1	SP1	SP1	SP1	SP1	SP1						SP1		
	V						CP1	CP1	SP1				CP1		CP1				SP2		CP2	SP1	CP3
	VIII				SP1													SP1	SP1				



**EN-GJS-450-10**

The more shrinkage prone, high silicon alloy EN-GJS-450-10 displays more severe porosities than the EN-GJS-500-7. Only casting group β1 is defect free. Casting group β1 applies an exothermic/insulating top feeder sleeve and an exothermic center feeder sleeve. Casting group β2 displays defects, though to a varying degree. Casting β2A displays an SP1 defect in area VIII—the center feeder, feeder neck—and the casting itself is thus without defects. This defect is similar to the same area of casting α2B, which is cast with the exact same feeder configuration. The difference is that while α2B displayed the only defect of the whole casting group, β2A is the only casting of the group that is not flawed with defects inside the critical areas. Thus, the EN-GJS-450-10 has shown that there is a functional difference between the insulating and exothermic feeders, where the extended M<sub>1</sub> of the exothermic feeder sleeve made all the difference.

Finally, as a reference to casting group α3, casting group β3 tests the effect of an absent center feeder with the EN-GJS-450-10 alloy. As with casting group α3, the affected area is area V. The severity of the defects is just greater than with the EN-GJS-500-7 alloy.

**Potential Process Errors**

Porosities may as well be located 5 mm (0.2 in.) away from the centerline of the casting, as it may be exactly where the cut was made. Therefore, it is certain that the porosities that are found are there, whereas other porosities may be located just below the surface escaping detection.

The test has been conducted with ground and etched castings to minimize the effects of machining on the castings. It is unlikely that any significant defects were obscured from the liquid penetrant test by this.

Potentially some minor defects may have escaped detection due the choice of photo documenting the castings, rather than evaluating them in quick succession of the penetrant development. Direct evaluation of the castings would have allowed use of a 3x magnification during examination in accordance with EN 1371-1:2011. Even though it cannot be ruled out completely that more defects may have been found, all of these would have been microscopic and probably well outside the detection capabilities of both x-ray and ultrasound. On the other hand the digitalization of the liquid penetrant tests allowed for different digital filters to be used for processing the images, enhancing different features of the images and therefore ensuring that all parts of the images were given the optimum display conditions. Moreover,

the digitalization enables continued analysis and allows for several people to review and classify the results.

Finally, the dye on the sides of the casting that was not efficiently rinsed away during the rinsing process slowly dissipates into the area of interest. Throughout the analysis these false positives have been omitted from the results, but it is possible that small porosities that would normally have been identified have been obscured by the coloring from the edges. As the porosities are most likely to form at the center of a section, away from the edges, it is less likely that this phenomenon has influenced the results. Albeit, the sections are small and the edge-penetrant may very well reach parts of the casting, it can be expected to have porosities.

#### Porosity Simulation

The analysis of the porosity formation during solidification showed that the centerline is the most likely place to find porosities for this casting geometry. Though porosities can be located off center, the simulation also shows that these have a size that is unlikely to show up on either x-ray or ultrasound analyses. Especially the bottom part of the outer ring may be prone to these off-center porosities. The simulations show good correspondence with the size and location of the porosities found in the liquid penetrant test.

The analysis of the thermal gradients related to the different feeder sleeves show that the exothermic sleeves not only retain the temperature of the melt for an extended period, it raises the temperature inside the feeder, thereby making the thermal gradient steeper than that produced by the insulating feeder sleeves.

#### **SURFACE DEFORMATION**

The deformation of the back surface of the casting is expected to have two origins: the shrinkage of the surface due to decreasing volume during solidification and cooling and the warping of the casting due to thermal stresses deforming the casting during solidification and cooling.

#### Reproducibility

The measurements show great reproducibility between the different casting groups as can be seen in Fig. 5. The 95% confidence interval is overlapping for casting groups  $\alpha_2$ ,  $\alpha_3$ ,  $\beta_1$ ,  $\beta_2$  and  $\beta_3$ . Casting groups  $\alpha_1$  and  $\alpha_4$  are slightly higher than aforementioned groups, but overlap with each other. The final group— $\alpha_5$ —clearly differentiates itself from the other groups. Casting group  $\alpha_5$  displays clear signs of surface shrinkage at the back surface of the boss, which adds additional height difference to the already warping surface. Remember that group  $\alpha_5$  is the one cast without either of the feeders.

#### Feeder Interaction

Comparing the surface shrinkage at the boss for casting group  $\alpha_5$  with the other groups, casting groups  $\alpha_3$  and  $\beta_3$

show interesting results. Neither group  $\alpha_3$  nor group  $\beta_3$  displays any great surface shrinkage near the boss. This is interesting because these two groups, like casting group  $\alpha_5$ , were cast without the center feeder. However, the presence of the top feeder seems to be sufficient to avoid gross surface shrinkage at the center boss, despite the thermal division caused by the thin walled low modulus section separating the two. Instead the top feeder manages to influence the solidification at the center boss. The influence can come from change to the thermal gradients of the casting or by increased ferrostatic pressure. The authors expect the ferrostatic pressure as the prime influence, albeit, more tests are required to conclude as to which amount the effect can be contributed—change to thermal gradients or ferrostatic pressure.

It must be noted, though, that the feeding is still not sufficient to a degree that the center feeder can be avoided. Group  $\alpha_3$  displays larger and more severe internal porosities at the boss, thus the reduced surface shrinkage does not ensure a sound casting.

#### Ripples

The surface flatness measurements showed a ripple-like effect radiating as circular waves from the boss at the center outward towards the outer ring. All 50 casting parts of the experiment display this feature.

As many of the ripple peaks and valleys consist of multiple measurement points, it is highly unlikely that the measurements are coincidental. Moreover, the ripples seem to have fairly the same wavelength depending on feeder combination. Some groups like  $\alpha_1$ ,  $\alpha_2$  and  $\alpha_3$  display shorter wavelengths, while group  $\alpha_4$  displays longer ripple wavelengths.

While the ripples appear to be consistent and linked, the graded color scale used to illustrate the surface flatness also obscure the accuracy of the ripple. The stepwise colors make it impossible to determine the exact height of a given point. Therefore, two points with the same green color may have a height difference of as much as 0.125 mm [0.005 in.], while at the same time two other points—having different colors—may be as little as 0.001 mm [0.00004 in.] apart.

New, more detailed measurements, must be made before conclusions can be drawn, though present results suggest a clear interdependency between modulus and deformation. It seems likely that the ripples are a result of the inner boss, outer ring construction. Determining how different geometries behave during these sinusoidal contractions may help improve dimension stability and a give better understanding of how feeder potentially can help change or avoid these features.



## CONCLUSION

The experimental castings were made with great reproducibility and show that the ram-up spot feeders provide sufficient feeding to successfully cast a casting that is otherwise deemed unsound.

The casting geometry was cast without the center feeder as a reference. This showed porosities at the center boss for all three castings of each alloy. For the EN-GJS-500-7 alloy with a standard ductile iron graphite precipitation, any combination of two feeders proved to produce sound, defect free castings. With the more shrinkage prone EN-GJS-450-10 alloy, only the feeder combination with the high  $M_t$  exothermic and exothermic/insulating feeders proved sufficient. The combination with solely insulating sleeves produced only one of the three castings that displayed no defects in the critical areas.

It was found that the top feeder did influence the solidification in the boss area, even though the boss was isolated from the top feeder by the thin walled section in between. Moreover it was also found that the feeder modulus affected the flatness value of the casting's back surface and that the deviation with each casting group was insignificant compared to the overall warp of the casting.

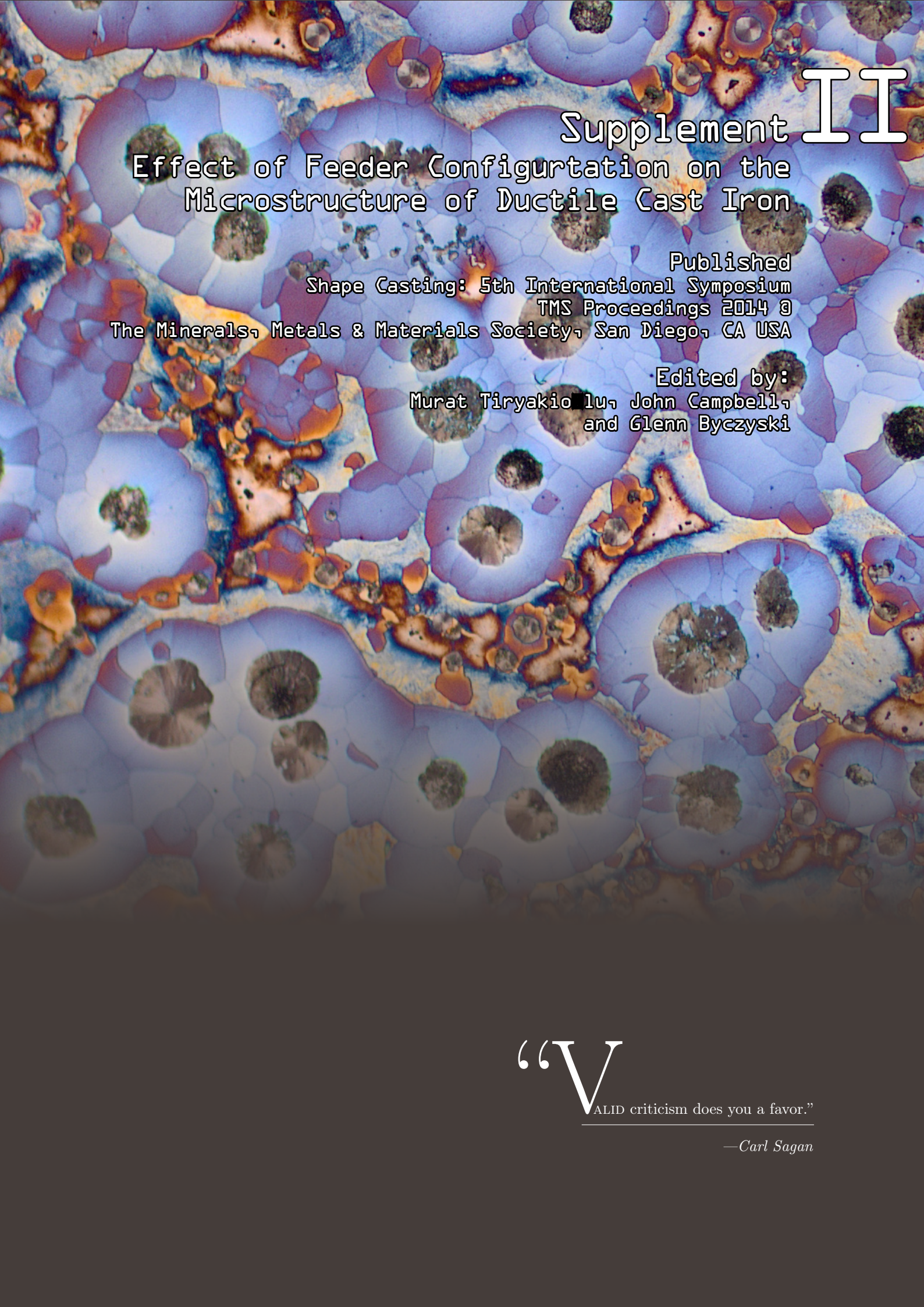
## ACKNOWLEDGMENTS

Thanks are due to the funding body of the project; the PSO funds from the Danish government. Moreover, the project comprises the collaborating effort of FOSECO Ltd., MAGMA GmbH, DISA Industries A/S, Vald.Birn A/S and The Technical University of Denmark, department of Mechanical Engineering. All have been engaged in the work and were helpful in their contributions to the results presented in this paper.

## REFERENCES

1. Tiedje, N.S., "Resource Savings by Optimising Process Conditions in Foundries," World Foundry Congress (2008).
2. Brown, J.R., *Foseco Ferrous Foundryman's Handbook*, Foseco International (2000).
3. <http://www.ductile.org/didata/section12/12intro.htm> (September, 2012).





# II

## Supplement Effect of Feeder Configuration on the Microstructure of Ductile Cast Iron

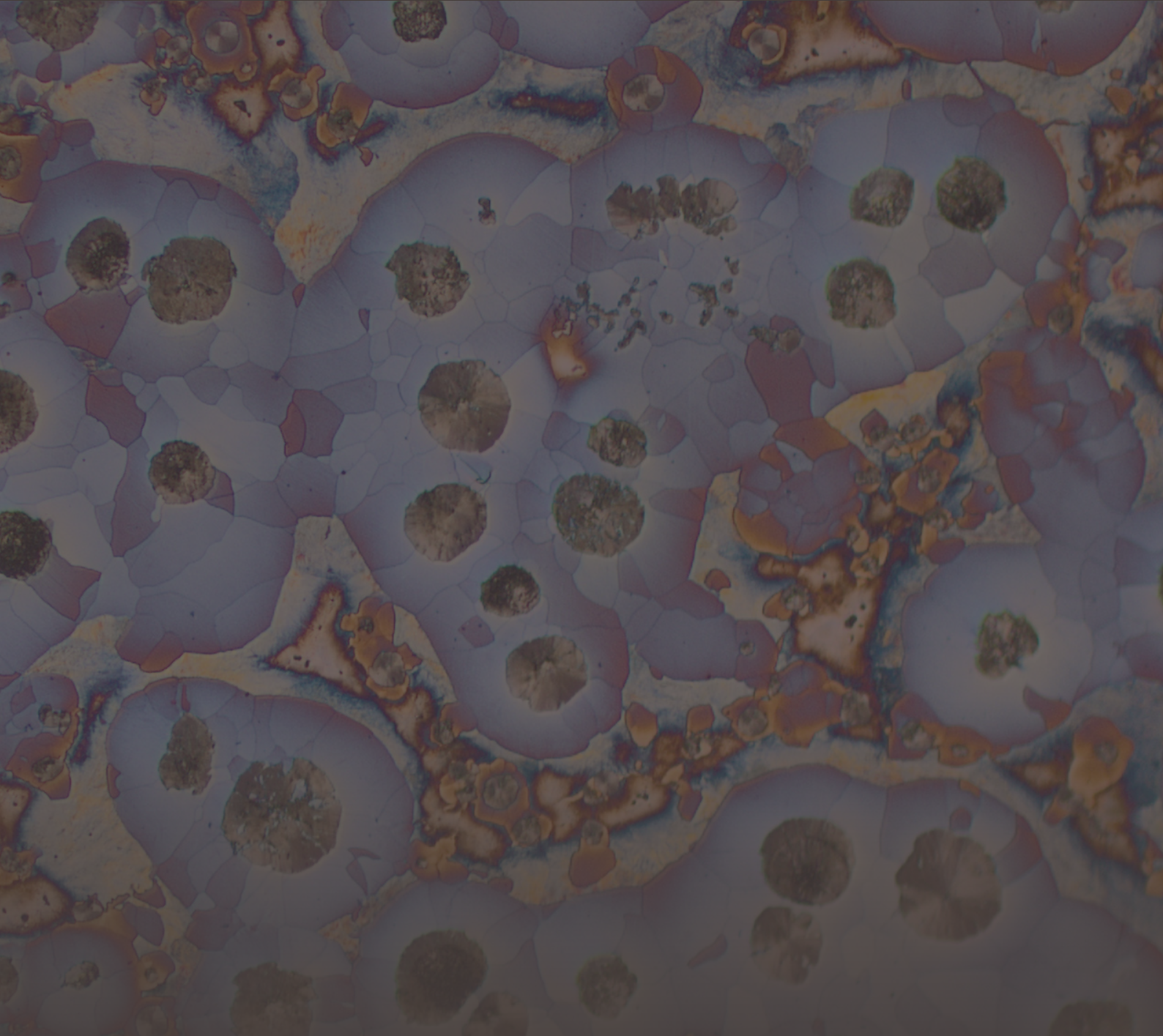
Published  
Shape Casting: 5th International Symposium  
TMS Proceedings 2014 @  
The Minerals, Metals & Materials Society, San Diego, CA USA

Edited by:  
Murat Tiryakioğlu, John Campbell,  
and Glenn Byczyski

“V

ALID criticism does you a favor.”

—Carl Sagan

A micrograph showing the microstructure of ductile cast iron. The image displays a complex, interconnected network of dark, irregular shapes (likely graphite nodules) embedded within a lighter, matrix-like structure. The overall appearance is highly textured and porous, characteristic of a ductile cast iron microstructure.

## Supplement II

---

### Effect of Feeder Configuration on the Microstructure of Ductile Cast Iron

N.K. Vedel-Smith  
N.S. Tiedje

Technical University of Denmark, Department of Mechanical Engineering  
Technical University of Denmark, Department of Mechanical Engineering

Vedel-Smith was the main author. Tiedje contributed with review and evaluation. Vedel-Smith performed the experimental part.

Vedel-Smith presented the paper at the 2014 TMS conference in San Diego, CA.

*Published*  
*Shape Casting: 5th International Symposium*  
*TMS Proceedings 2014 © The Minerals, Metals & Materials Society, San Diego, CA USA*  
*Edited by: Murat Tiryakioğlu, John Campbell, and Glenn Byczynski*

---

## **Effect of Feeder Configuration on the Microstructure of Ductile Cast Iron**

Nikolaj Kjelgaard Vedel-Smith<sup>1</sup>, Niels Skat Tiedje<sup>1</sup>

<sup>1</sup>Technical University of Denmark, Department of Mechanical Engineering,  
Produktionstorvet Building 427A, 2800 Kgs. Lyngby, Denmark

Keywords: SG Iron, Color Etching, Feeder, Porosities, Dimensional Accuracy, Hot spot

### **Abstract**

Feeding and microstructure of a test casting rigged with different feeder combinations was studied. Castings were examined and classified by soundness and microstructure. Subsequently the casting macro- and microstructure was analyzed to study how differences in solidification and segregation influence the soundness of different sections of the castings. Moreover, the microstructural changes due to variations in thermal gradients are classified, and the variations in the mushy zone described.

The paper discusses how solidification and segregation influence porosity and microstructure of ductile iron castings. The goal is to enable metallurgists and foundry engineers to more directly target mushy zone development to prolong the possibility to feed through this section. Keeping smaller section open for an extended period will make it possible to use fewer or smaller feeders, with reduced energy consumption and cheaper products as a result.

### **Introduction**

Energy for melting is a significant expense and represents approx. one quarter of the production cost for cast iron foundries. New applications for ductile iron (DI) increase the requirements for improved mechanical properties, and some of these alloys show significant problems with shrinkage and porosities. Larger modulus feeders and better designs are required to successfully cast sound castings. The changes in alloy composition also entail a different behavior of the primary and secondary graphite expansion making it difficult to feed secluded sections of the casting.

This paper is the result of an ongoing project, involving several companies, working towards characterizing, quantifying and understanding the effect and functioning of various feeder applications.

On vertically parted molds it can be difficult to place feeders freely. Traditional feeders are geometrically restrained to the upper half of the parting line. Spot feeders, on vertically parted molds, enable feeding of secluded sections located away from the parting line. The spot feeders can be insulation, exothermic or a combination, and provide heat and melt to a given section.

## Experimental Setup

### Casting Geometry

The test geometry used for the experiments consist of a disc with an inner boss and an outer ring, separated by a thin plate like section. The geometry is designed to display the same problems as found in disc brakes, flywheels and other castings with combinations of small and large modulus sections. The casting layout and feeder location is seen in Fig. 1. For more details please refer to [1].

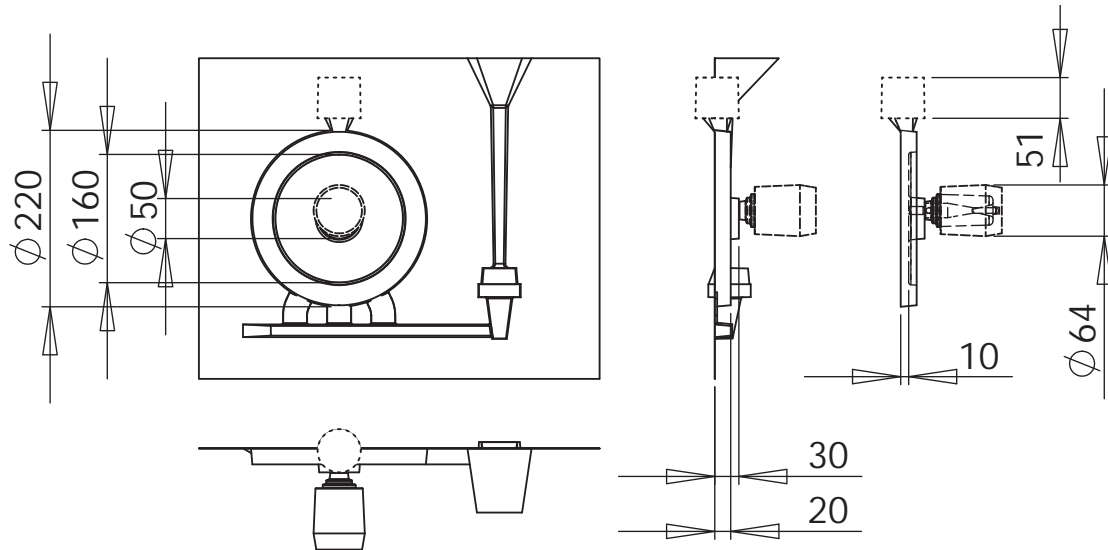


Figure 1: Overview of casting geometry and feeder placement. The dotted lines indicate the top feeder, and the dashed lines indicate the centre feeder. Measurements are in mm.

All feeders used where sleeved and had the same geometric modulus ( $M_g$ ), calculated as  $M_g = \frac{V}{S}$ , where  $V$  is the volume of the feeder and  $S$  is the cooling surface. By changing the sleeve material, the thermal (or true) modulus ( $M_t$ ) was increased without changing the geometry—thus keeping the ferrostatic pressure constant. The modulus of the feeders change because of the thermal properties of the chosen sleeve material. This multiply the size of the geometric modulus with a Modulus Extension Factor (MEF) specific for each sleeve material. Thus, the true modulus becomes  $M_t = \text{MEF} \times M_g$ .

### Alloys and Combinations

Two different alloys for three different feeder combinations were cast in triplicates. The alloys were a pearlitic-ferritic EN-GJS-500-7 and a fully ferritic EN-GJS-450-10 [2]. Both alloys were spheroidal graphite irons (SGI), and their chemical composition is shown in Tab. 1(a). The combination of alloy, sleeve material and feeder modulus can be seen in Tab. 1(b). The castings are identified by alloy ( $\alpha$  or  $\beta$ ), feeder combination (1, 2 or 3) and triplicate copy (A, B or C). E.g.  $\beta$ 3A is EN-GJS-450-10 fully ferritic alloy cast with a combined material feeder sleeve for the top feeder, and no center feeder.

**Table A: Dimension and  $M_g$  in mm**

	I	III	IV	V	VI	VII	IX
w	ø32	20	10	30	10	20	ø40
h	40	30	55	50	55	30	60
$M_c$	7	6	5	9	5	6	8

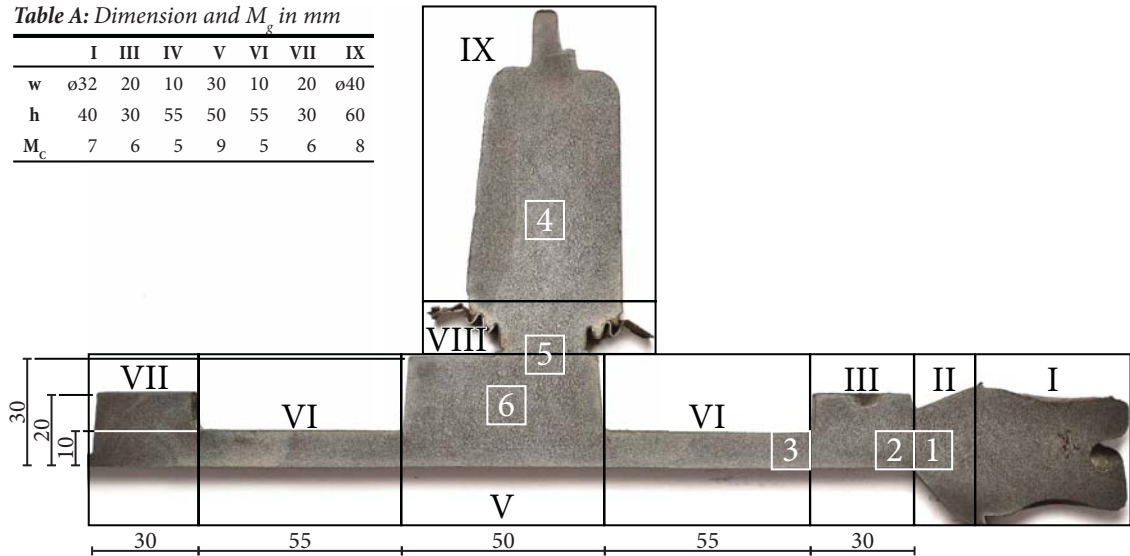


Figure 2: Overview of sectioned casting ( $\alpha 2A$ ). Etched with 1% Nital for 600s. The casting is divided into 9 non-overlapping areas (Roman numerals) for quantification and analysis of porosities. 6 sections (Arabic numerals) of 10 x 10 mm were cut and color etched. The inserted table (Table A) shows the dimensions and geometric modulus ( $M_g$ ) of the different areas. All measurements are in mm.

Table 1: Alloy compositions and feeder combinations used.

(a) Alloy compositions in wt%.  $\alpha$  is the EN-GJS-500-7 pearlitic-ferritic alloy, and  $\beta$  is the EN-GJS-450-10 fully ferritic alloy.

	CE	C	Si	Mn	P	S	Mg	Cu
$\alpha$	4.6	3.69	2.75	0.50	0.015	0.005	0.044	0.25
$\beta$	4.5	3.35	3.48	0.34	0.017	0.003	0.046	0.10

(b) Sleeve materials: Exothermic (Exo), insulating (Ins) or combined (E/I). Parenthesis shows the true modulus ( $M_t$ ) in mm.

	$\alpha 1$	$\alpha 2$	$\alpha 3$	$\beta 1$	$\beta 2$	$\beta 3$
Top	E/I (10)	Ins (9)	E/I (10)	E/I (10)	Ins (9)	E/I (10)
Center	Exo (12)	Ins (11)	-	Exo (12)	Ins (11)	-

## Production

$\alpha 1$  and  $\alpha 2$  was cast at  $(1401 \pm 5)^\circ\text{C}$ ,  $\alpha 3$  was cast at  $(1408 \pm 5)^\circ\text{C}$  and the  $\beta$ -series was cast at  $(1392 \pm 5)^\circ\text{C}$ . The poured weight was 8 kg with a pouring time of 3.5s and a casting weigh of 4 kg. All castings were made on the same vertical molding line. For more details please refer to [1].

## Methods

### Liquid Penetrant Test

The porosities in the sectioned castings were examined using liquid penetrant testing and classified according to the European Standard EN 1370-1:2011 [3]. The analysis of each casting was divided into 9 areas as seen on Fig. 1, and was evaluated for size and type of porosities. The process is fully described here [1].

## Deformation Measurements

The deformation of the reverse side of the castings is in this paper described by its flatness value ( $f_v$ ). In simple terms the  $f_v$  is the difference between the highest and lowest point on the surface. The  $f_v$  was measured using a Zeiss OMC 850 mechanical Coordinate Measuring Machine (CMM) with a resolution of 0.2  $\mu\text{m}$ . The measurements were made using a 3 mm prob which acted as a mechanical filter with respect to the surface roughness. For more detail see [1].

## Etchings

Macro Etching All analyzed discs were sectioned using a cold saw, after which the sectioned piece was ground plane. The newly ground surface was etched for 600 s in a 20 °C 1% Nital solution—99 mL Ethyl alcohol and 1 mL Nitric acid ( $\text{HNO}_3$ ). After etching the sectioned casting was cleaned in ethanol and left to dry in a hot air oven at 110 °C for 1800 s. The macro etched castings were analyzed using a magnifying glass—see Fig. 1.

Color Etching The cut out sections (1-6) from castings  $\alpha 1$ ,  $\alpha 2$  and  $\beta 1$  was color etched with a picric acid—50 ml Distilled water, 10 g Sodium hydroxide (NaOH), 40 g Potassium hydroxide (KOH) and 10 g Picric Acid ( $\text{C}_6\text{H}_3\text{N}_3\text{O}_7$ ). After mixing the mounted and polished pieces were etched at 105 °C. Most pieces required an etching time around 330 s, but some required more. Each piece was analyzed in an optical microscope after etching, and then etching again if the etching was not fully developed.

## **Results**

### Porosities

For all 18 castings areas II, IV, VI and VII display no sign of porosities in any of the casting. Area II is the feeder neck of the top feeder, and areas IV and VI are the thin walled sections between the outer ring and the center boss. Area VII is the ring section at the bottom of the casting. Areas I and IX are the feeders and are excluded from the porosity analysis. Thus, the analysis focus on the remaining three areas—III, V and VIII—and the results are shown in Tab. 2.

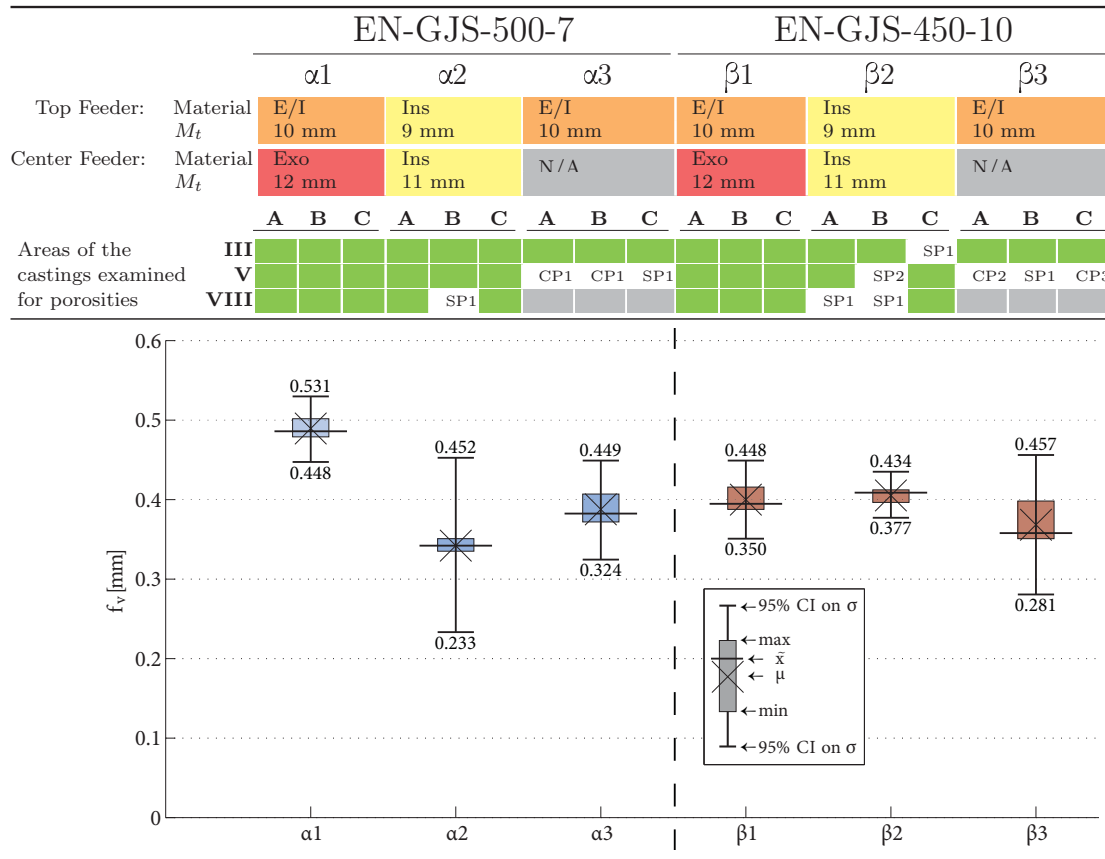
All 6 castings that used the exothermic sleeves ( $\alpha 1$  and  $\beta 1$ ) displayed no porosities in the areas analyzed. Of the three castings with insulating sleeves and the EN-GJS-500-7 alloy, the  $\alpha 2\text{B}$  showed the smallest category of non-linear isolated porosities (SP1). The same feeder configuration with the fully ferritic EN-GJS-450-10 alloy showed SP1 porosities in 2 of 3 feeder necks (VIII), a single more severe SP2 porosity at the boss (V) and a single SP1 porosity at the upper ring (III). The reference castings without center feeder all displayed porosity defects at the boss (V).

### Casting Flatness

All 18 castings have a flatness value ( $f_v$ ) between 0.33 and 0.50 mm. The results are shown in Tab. 2, displaying each casting configuration as separate bar graphs. The



Table 2: Feeder types and modules are shown in red, orange and yellow boxes. Soundness of individual castings is shown in the bottom section. Green means no porosities. SP indicate non-linear isolated porosities and CP indicate non-linear clustered porosities. The suffix indicate severity—higher is more severe [3]. The graph show the  $f_v$  of the different casting groups.



bar ends show the highest and lowest value measured.  $\times$  mark the arithmetic mean of the population, and  $-$  mark the median value. The error bars mark a 95% confidence interval assuming a Gaussian distribution. Using an outliers factor of 3, no outliers were found. There was a greater variation in the pearlitic-ferritic  $\alpha$ -alloy, compared to the fully ferritic  $\beta$ -alloy, but only  $\alpha 1$  and  $\beta 2$  can be identified as statistically different. All other groups have overlapping confidence intervals and cannot be concluded to be different.

### Etchings

Macro Etchings The macro etching had little or no effect on the fully ferritic  $\beta$ -alloy. The lack of reaction showed that these castings contained very little or no pearlite. The analysis of the pearlitic-ferritic  $\alpha$ -alloy showed evenly distributed pearlite in all areas of the castings. Dendrite structures were visible to the naked eye in areas I, II, III, V, VIII and IX. Areas IV, VI and VII do not have visible dendritic structures. All  $\alpha$ -castings showed clear signs of directional dendrite growth across areas I, II and III. The dendrites

in areas V, VIII and IX did not show a clear direction of solidification.  $\alpha 2A$  after etching with Nital can be seen in Fig. 1.

Color Etchings Comparing the microstructures of the  $\alpha$ - and  $\beta$ -alloys it was seen that the  $\beta$ -alloy display a greater nodule count. All three castings displayed good nodularity in all of the etched sections. The thin walled section (3) showed directional solidification from the edge and towards the center of the section. Dendrites were found in sections 3, 4, 5 and 6 for all three castings. Dendrites were not identified in etchings of section 1 and 2.

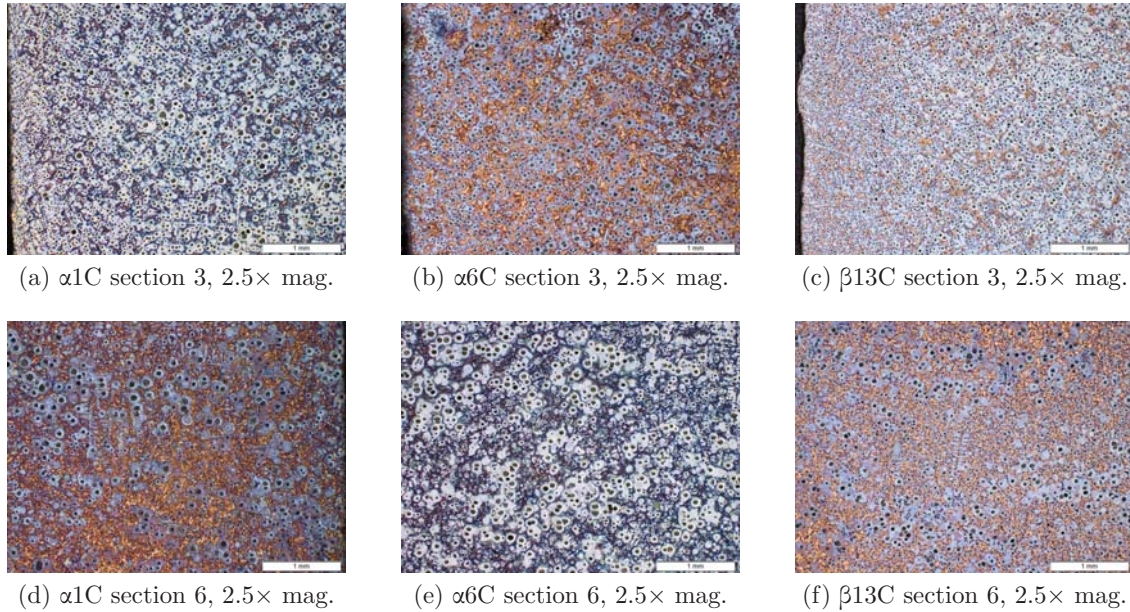


Figure 3: Color etchings: Si segregation gives a blue tint. Brown areas are low Si regions.

$\alpha 1C$  and  $\beta 1C$  with the exothermic sleeves contained a large fraction of low Si eutectic segregation in section 6.  $\alpha 2C$  with the insulating sleeves, showed a large fraction of low Si eutectic segregation in sections 3, 4 and 5. Furthermore, sections 4 and 5 for castings  $\alpha 1C$  and  $\beta 1C$  showed alignment of the graphite nodules according to the dendritic structure, while the same section for  $\alpha 2C$  was less orderly and displayed a larger fraction of non-linearized nodules. For section 6 none of the three castings showed a high degree of linearized nodules.

## Discussion

### Porosities and Deformation

First of all the results show that the test casting could not be cast porosity free without the center feeder. All six castings from  $\alpha 3$  and  $\beta 3$  displayed porosities at the boss (V). The porosity analysis also showed that the  $\beta$ -alloy was more prone to porosities, as also the  $\beta 2$  configuration displayed porosities in the boss (V), the top ring (III) and on two

occasions at the feeder neck (VIII) close to the boss. In comparison the  $\alpha$ 2 castings that had the same feeder configuration showed only a single porosity defect, namely at the feeder neck (VIII). Porosities in the feeder neck do not deem the casting itself unsound, but it indicates that the given feeder is close to the limit of how much it can feed. For both the  $\alpha$ - and the  $\beta$ -alloy the feeder configuration using exothermic sleeves showed no sign of porosities at the examined areas.

There were no direct correlation between the flatness value  $f_v$  of the castings and the porosities. Comparing the two alloys it was shown that the pearlitic-ferritic  $\alpha$ -alloy displayed a greater variance than the fully ferritic  $\beta$ -alloy. The higher Si content of the  $\beta$ -alloy increase the austenite to ferrite transformation temperature [4], which result in an earlier graphite expansion, which again occur at a time where the casting has regained less strength compared with the low Si  $\alpha$ -alloy. The pattern plate was measured to have a  $f_v$  of 16.4  $\mu\text{m}$ —approx. 20-30 times smaller than the flatness measured on the castings and is thus concluded to have no significant influence on the results.

### Solidification and Microstructure

The greater nodule count in the  $\beta$ -alloy cannot be contributed to the difference in alloying elements. Increased Mn content can increase the nodule count, but the  $\beta$ -alloy have a lower Mn content than the  $\alpha$ -alloy, and should thus have a lower nodule count. However, the two alloys were cast at different dates and the inoculation procedure may have changed in between. The castings with the exothermic sleeves ( $\alpha$ 1C and  $\beta$ 1C) both showed a large fraction of low Si eutectic solidifying in between the nodules at the boss (6). The insulating sleeves showed the opposite effect, having low Si eutectic at the feeder neck and in the feeder it self. Before making final conclusions in this matter, further color etchings should be made. The etchings are very sensitive with respect to etching time, and the lack of brown areas in section 6 of  $\beta$ 6C may be due to under etching. Assuming the etchings are reliable, the phenomena may be explained by the delayed graphite expansion of the exothermic feeders. The boss section (V) will have expanded and pushed out a portion of the low Si eutectic, after which the graphite expansion in the feeder (IX) will push back the last to freeze melt—the low Si eutectic.

The greater tendency to shrink found in the  $\beta$ -alloy may be, in part, related to an improved inoculation procedure, as has previously been shown in gray cast iron [5]. While under-inoculation will result in a decreased graphite expansion, over-inoculation can advance the occurrence of the graphite expansion resulting in a decreased expansion later in the process. Another phenomena that influence the movement of the last to freeze melt through the mushy zone is the thermal center. The movement of the thermal center during solidification—a so called migrating hot spot—has been shown to play a significant role in the development and location of porosities [5, 6]. A migrating hot spot can also be part of the explanation for the different locations of the last to freeze melt, as the not only the different  $M_t$  of the different feeders will influence the development and movement of the global and local hot spots, the differences in sleeve material will likewise also influence the migration of the hot spots.

## Conclusions

The results showed that the high Si  $\beta$ -alloy was more prone to porosities than the low Si  $\alpha$ -alloy, and that the exothermic feeder sleeves could feed both alloys while the insulating sleeves was insufficient for the  $\beta$ -alloy. The measurement of the castings showed that the two alloys had close to the same average  $f_v$ , but that the  $\beta$ -alloy displayed a smaller variance. This is suspected to be related to the elevated austenite to ferrite transitions temperature controlled by the Si content. Finally, the color etchings indicated that the low Si segregation of the last to freeze melt were located differently in the castings with exothermic feeders, as compared to the castings with insulating feeders. It is suspected that this is related to the shift in graphite expansion due to the changed  $M_t$  and the effect of the migrating hot spot.

## Acknowledgments

This work is funded by the PSO funds from the Danish Government, and is performed in collaboration with FOSECO Ltd., MAGMA GmbH, DISA Industries A/S, Vald. Birn A/S and the Technical University of Denmark, Department of Mechanical Engineering. A special thanks to Professor Attila Diószegi and Sadaf Vazehrad at Jönköping University, School of Engineering, Sweden, for their kind assistance with color etching the cut sections.

## References

- [1] N. K. Vedel-Smith, et al. Quantification of Feeding Effects of Spot Feeding Ductile Iron Castings made in Vertically Parted Molds. *AFS Proceedings*, (1310), 2013.
- [2] EN 1563:2012-3—Founding: Spheroidal Graphite Cast Irons, 2012.
- [3] EN 1371-1:2011—Founding: Liquid Penetrant Testing—Sand, Gravity Die, and Low Pressure Die Castings, 2011.
- [4] Ductile Iron Data. *Ductile Iron Data - for Design Engineers*. Rio Tinto Iron & Titanium Inc., 1990.
- [5] Lennart Elmquist, et al. On the Formation of Shrinkage in Grey Iron Castings. *Key Engineering Materials*, 457:416–421, 2011.
- [6] Lennart Elmquist and Attila Diószegi. Shrinkage Porosity and its Relation to Solidification Structure of Grey Cast Iron Parts. *International Journal of Cast Metals Research*, 23(1):44–50, 2010.

A large Zeiss industrial microscope is the central focus of the image. It features a tall, light-colored vertical column and a dark, heavy granite table. The microscope's head is positioned above the table, and a control console with a keypad and joysticks is attached to the right side. In the background, a computer workstation with a monitor and keyboard is visible on a desk. The setting appears to be a clean, well-lit laboratory or industrial environment.

# Supplement III

## Thermal Distortion of Disc-Shaped Ductile Iron Castings in Vertically Parted Moulds

Published  
Journal of Materials Processing Technology

“GREAT scientific discoveries have been made by men seeking to verify quite erroneous theories about the nature of things.”

—Aldous Huxley  
*Wordsworth in the Tropics*



## Supplement III

---

### Thermal Distortion of Disc-Shaped Ductile Iron Castings in Vertically Parted Moulds

N.K. Vedel-Smith  
J. Rasmussen  
N.S. Tiedje

Technical University of Denmark, Department of Mechanical Engineering  
Technical University of Denmark, Department of Mechanical Engineering  
Technical University of Denmark, Department of Mechanical Engineering

Vedel-Smith was the main author. Tiedje contributed with review and evaluation. Vedel-Smith and Rasmussen performed the experimental part.

Additional material available online at <http://dx.doi.org/10.1016/j.jmatprotec.2014.11.025>

*Published*  
*Journal of Materials Processing Technology*

---



Contents lists available at ScienceDirect

## Journal of Materials Processing Technology

journal homepage: [www.elsevier.com/locate/jmatprotec](http://www.elsevier.com/locate/jmatprotec)

## Thermal distortion of disc-shaped ductile iron castings in vertically parted moulds



N.K. Vedel-Smith\*, J. Rasmussen, N.S. Tiedje

Technical University of Denmark, Department of Mechanical Engineering, Produktionstorvet, Building 427A, DK-2800 Kgs Lyngby, Denmark

## ARTICLE INFO

## Article history:

Received 26 March 2014

Received in revised form 15 October 2014

Accepted 11 November 2014

Available online 20 November 2014

## Keywords:

Dimensional accuracy

SG iron

Feeder and riser

Machining allowance

Si content

Thermal gradient

## ABSTRACT

A disc-shaped casting with an inner boss and an outer rim, separated by a thin walled section, was examined. This measurable deformation varied with the feeding modulus. The influence of alloy composition, particularly Si content, was examined with a pearlitic ductile iron (EN-GJS-500-7) and a fully ferritic ductile iron (EN-GJS-450-10).

The experiment showed that both the alloy composition and choice of feeder influenced the degree of deformation measured in the finished casting. It was found that the deformation of the pearlitic alloy was influenced controllably by changing the feeder modulus, whereas the deformation of the fully ferritic alloy was less affected by a change in thermal gradient. Both alloys underwent comparable deformations with respect to size, shape, and location.

© 2014 Elsevier B.V. All rights reserved.

### 1. Introduction

Working with grey cast iron and steel, Jackson (1963) showed why casting precision was more than just a distance between a finite number of working faces, but more importantly also a concern with regards to eliminating excess machining and grinding. Jackson's paper also discussed the influence of alloy composition, casting geometry, and thermal gradients on the dimensional variation of the castings. Demonstrating that free linear contraction was inversely related to the section modulus, Mkumbo et al. (2002) also reported a correlation between the modulus and shape of the casting and modelled how flanges affected this. Likewise, Motoyama et al. (2013) examined the effect of flanges and showed how residual stress and distortion develop during solidification and cooling of the casting, and that these were affected by the casting geometry and the strength of the sand mould.

The idea of counteracting distortion by modifying the pattern geometry was suggested by Kang et al. (2011) who also proposed

machining allowance as a parameter for distortion reduction. This requires precise measurements and an understanding of the casting's dimensional change and surface finish. As part of their development of an improved model for a sand surface element, Chang and Dantzig (2004) described how the green sand mould itself was deformed by the contraction of the casting, and how that left the casting unconstrained by the mould. Subsequently, Nwaogwu et al. (2013) described how to characterise the surface of ductile iron castings, and provide some guidance as to which types and sizes of surface roughness can be expected with and without coating.

Mkumbo et al. (2002) showed that ductile iron, even with a higher CEV, displayed greater contraction than grey iron, and variations in dimensional change between pearlitic and ferritic alloys were demonstrated by Sosa et al. (2004). They worked with ADI to show that a ferritic microstructure displayed greater dimensional stability than a pearlitic microstructure, and that a ferritic-pearlitic structure was even more prone to dimensional change.

Distortion of castings made under production conditions were investigated to quantify the reproducibility of large scale manufacturing facilities.

This paper presents a detailed analysis of the changes in thermal distortion of a disc-shaped casting, examined with respect to a number of different spot feeder and top feeder combinations, tested for both a ferritic-pearlitic and a fully ferritic alloy, and correlated to the cooling curves and austenite to ferrite phase transformation at various measurement positions (MP) in the casting.

Abbreviations: ADI, austempered ductile iron; CEV, carbon equivalent value; CMM, coordinate measuring machine;  $M_g$ , geometric modulus; LGI, Lamellar graphite iron; MP, measurement position; MEF, modulus extension factor; PPI, pores per inch; SGI, spheroidal graphite iron; TC, thermo couple;  $M_r$ , thermal modulus.

\* Corresponding author. Tel.: +45 45 25 47 14; fax: +45 45 93 01 90.

E-mail addresses: [nikvs@mek.dtu.dk](mailto:nikvs@mek.dtu.dk) (N.K. Vedel-Smith), [nsti@mek.dtu.dk](mailto:nsti@mek.dtu.dk) (N.S. Tiedje).

<http://dx.doi.org/10.1016/j.jmatprotec.2014.11.025>

0924-0136/© 2014 Elsevier B.V. All rights reserved.

**Table 1**  
Casting geometry in mm and moduli in mm.

Section	T.Rim	U.Sec	Boss	L.Sec	B.Rim
Height	27.5	55	55	55	27.5
Thickness	20	10	30	10	20
Modulus	6	5	9	5	6
Feed modulus	7	6	11	6	7

**Table 2**  
Material and modulus for the feeders used as top and centre feeder respectively.

Feeder	Top		Centre					
	1	2	1	2	3	1s	2s	3s
Material	Ins	E/I	Ins	E/I	Exo	Ins	E/I	Exo
Modulus [mm]	9	10	11	11	12	9	10	11

## 2. Methods

### 2.1. Casting geometry

The casting design was circular with a diameter of 220 mm, with an outer rim and an inner boss. See Figs. 1 and 2. The circular design provided a casting that was mirrored thermally about a vertical plane through its centre, so that any distortions that were not symmetrical must originate from the thermal imbalance in the casting caused by the feeders and the filling. See Table 1 for the dimensions and moduli of the different casting sections.

### 2.2. Feeder placement and modulus

One feeder was mounted at the mould parting line, at the top of the casting. See Fig. 1. The second feeder was mounted onto the centre boss, and placed slightly above the centre to provide better ferro-static pressure for feeding. Ram-up sleeve feeders were used for the centre feeder.

In the experiment, different sleeve materials were used for the feeders—insulating (1), exothermic-insulating (2), or purely exothermic (3). Using sleeves made from different materials (1,2,3) it was possible to change the modulus of the feeder while maintaining a constant geometric size and ferro-static pressure. It was also possible to remove the feeder altogether, but this change also entailed a change in ferro-static pressure. An overview of the feeder moduli is given in Table 2.

Distinction was made between the geometric modulus ( $M_g$ ) of the feeder and the thermal (or true) modulus ( $M_t$ ) of the feeder. This distinction was required because the sleeves covering the melt in the feeders changed the basic modulus relation  $M_g = V/A$ , with the addition of the Modulus Extension Factor (MEF). As described by Brown (2000), the modulus equation for the feeders could thus be stated as  $M_t = \text{MEF} \times M_g$ , allowing changes to the thermal modulus while keeping the geometric modulus and the ferro-static pressure constant.

### 2.3. Alloys and feeder combinations

The 16 different combinations were distinguished by four parameters; (1) alloy, (2) top feeder (or parting line feeder), (3) centre feeder (or boss feeder), and (4) size variations for the centre feeder. This gave 36 possible combinations, of which 16 were cast as part of the experiment. See the combinations in Table 4. Each of the combinations were cast in triplicate for statistical analysis. Additionally two castings were fitted with 11 thermo couples (TC) to measure the temperature of the different areas of the casting during solidification (TC-castings). The four parameters are elaborated below:

**Table 3**  
Alloy compositions for  $\alpha$  (EN-GJS-500-7),  $\beta$  (EN-GJS-450-10), and  $\tau$  (Temperature Measurements) [wt%].

Alloy	C	Si	Mn	P	S	Mg	Cu
$\alpha$	3.67	2.73	0.50	0.015	0.005	0.049	0.025
$\beta$	3.35	3.48	0.34	0.017	0.003	0.046	0.010
$\tau$	3.20	3.71	0.27	0.044	0.028	0.048	0.081

**Table 4**  
The 16 combinations sorted by alloy, top feeder, centre feeder. (x) indicate  $M_t$  in mm.

Alloy	Top Feeder		Centre Feeder		Size	
$\alpha$	0	(0)	0	(0)		
$\alpha$	0	(0)	2	(11)		
$\alpha$	1	(9)	1	(11)		
$\alpha$	1	(9)	2	(11)		
$\alpha$	1	(9)	3	(12)		
$\alpha$	2	(10)	0	(0)		
$\alpha$	2	(10)	1	(11)		
$\alpha$	2	(10)	2	(11)		
$\alpha$	2	(10)	3	(12)		
$\beta$	1	(9)	1	(11)		
$\beta$	1	(9)	2	(10)	s	(Small)
$\beta$	2	(10)	0	(0)		
$\beta$	2	(10)	1	(9)	s	(Small)
$\beta$	2	(10)	3	(12)		
$\beta$	2	(10)	3	(11)	s	(Small)
$\tau$	2	(10)	3	(12)		

- (1) The castings were made using three different alloys—one pearlitic EN-GJS-500-7 (labelled  $\alpha$  in Table 4) and one purely ferritic EN-GJS-450-10 (labelled  $\beta$  in Table 4), both as defined by EN 1563:2012-3 (2012). The alloy used for the TC-castings was made to be a fully ferritic alloy (labelled  $\tau$ ). See alloy composition in Table 3.
- (2) The top feeders were all identical in size and were only varied by using either insulating (labelled 1 in Table 4) or exothermic-insulating material (labelled 2 in Table 4) for the sleeve. In one experiment this feeder was removed altogether, indicated as 0 in Table 4.
- (3) The centre feeders had the same basic options as the top feeder (0,1,2), but could also be purely exothermic (3). The geometric moduli of the top and centre feeders are different, thus the number-designation indicates sleeve material and not moduli as is shown in Table 2.
- (4) Additional information regarding the centre feeder configuration. When appended with an s for small, it indicates that the feeders' geometric modulus was reduced to the same size as that of the top feeder, which in turn also reduced the thermal modulus compared to the other centre feeders using the same sleeve material.

### 2.4. Production

The castings were produced on a vertically parted moulding machine—Disamatic 230A—as part of a production run in an operating foundry.

The poured weight was approximately 8 kg and the castings themselves weighed 4 kg. The pouring time was approximately 3.5 s and the three series were poured at; (1)  $1401 \pm 5^\circ\text{C}$ , (2) at  $1408 \pm 5^\circ\text{C}$ , and (3) at  $1392 \pm 5^\circ\text{C}$ .

The castings solidified and cooled in the mould for approximately 1 h and were then separated from the other goods at the



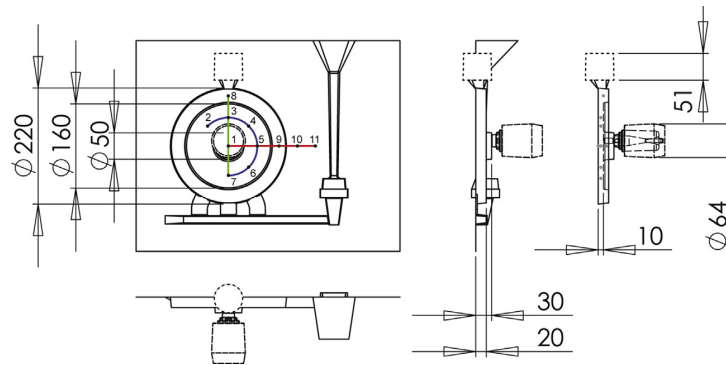


**Fig. 1.** Overview of casting geometry and feeder placement. The dotted lines indicate the top feeder, and the dashed lines indicate the centre feeder. Measurements are in mm. No. 1–11 indicate the measurement position (MP) of the thermo couples (TC) for the temperature measurements. All TCs were placed at the centre of the section as indicated with grey dots on the draft on the right.

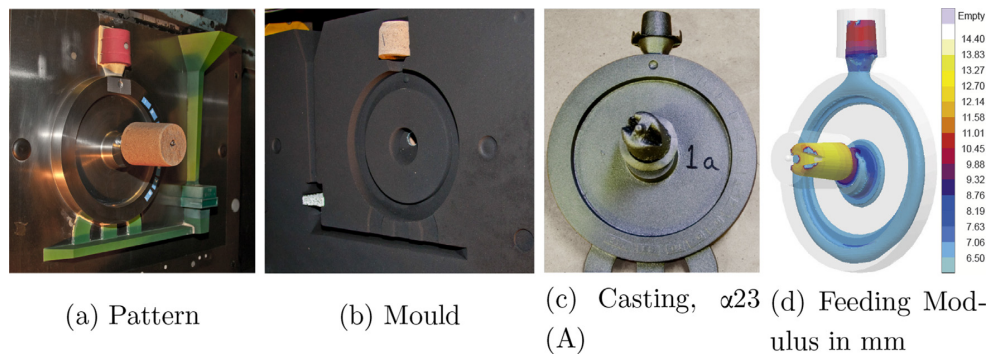


**Fig. 2.** Production overview: (a) the pattern with a ram-up sleeve mounted at the centre, (b) the mould with a top feeder sleeve mounted at the top, a ram-up sleeve moulded in at the centre, and a 10 PPI foam filter mounted at the bottom of the down sprue, (c) casting  $\alpha$  23 (A) after shot blasting, and (d) numerical simulation of the feeding modulus of the different sections of the casting.

shake-out station. The castings then cooled in air to room temperature, after which they were cleaned by shot blasting.

The TC-castings were produced on a vertically parted moulding machine—Disamatic 2110—at a small scale research facility.

The poured weight and pouring time were identical to the process parameters for the other castings. The pouring temperature was  $1385 \pm 5^\circ\text{C}$ .

TCs 1–9 were type K and were placed inside the casting. TCs 10 and 11 were type N and were placed in the mould. See Fig. 1. TCs 1–9 were mounted through the mould perpendicular to the reverse side of the casting. TCs 10 and 11 were mounted vertically parallel to the mould parting line. The data were sampled at 100 Hz.

### 2.5. Numerical simulation

Numerical simulations were made using the a commercial simulation software—MagmaSoft v5.2.0. The simulations were setup to resemble the casting conditions in the best possible way. Another commercial simulation software—JMatPro—was used to calculate the thermo-physical properties of the  $\alpha$  and  $\beta$ -alloys. These thermal datasets were used in the numerical casting simulation. The simulations with the  $\tau$ -alloy used the  $\beta$ -alloy dataset, albeit with  $\tau$ -alloy composition.

The simulations were used to (1) visually evaluate the thermal gradients of the casting during filling and solidification, and (2) export TC-measurement data at the 11 measurement positions (MP) of the trial TCs for comparison of the simulation and the trial

measurements. The simulations were made using finite volume method with an equidistant mesh.

### 2.6. Cooling curves

The cooling curves from the trial measurements were plotted and analysed using the second derivative of the cooling curve to identify the start and end points of the austenite to ferrite phase transformation, as seen in Fig. 8a. The same procedure was followed for the simulated cooling curves, albeit sixth degree polynomial fits were used to describe the simulated cooling curves when derived. The latter was necessary due to time steps of the simulated data.

The derived cooling curves were smoothed using a gaussian distribution filter.

### 2.7. Colour etching

Sections were cut from the vertical centre line of selected castings. The cut pieces were resin mounted, polished, and colour etched with a picric acid solution—50 ml Distilled water, 10 g Sodium hydroxide (NaOH), 40 g Potassium hydroxide (KOH) and 10 g Picric Acid ( $\text{C}_6\text{H}_3\text{N}_3\text{O}_7$ ). The picric acid was kept at  $105^\circ\text{C}$  during the etching. Most pieces required an etching time around 330 s, but some required more. Each piece was analysed in an optical microscope after etching, and then etching again if the etching was not fully developed, as described by Vedel-Smith and Tiedje (2014).

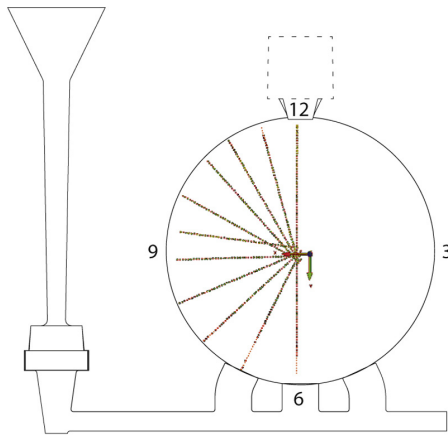


**Fig. 3.** Overview of the individual points measured by the automated measurement program used for all castings—here showing  $\alpha$  23A. The measurements were made on the flat reverse side of the casting, on the half closest to the down sprue.

### 2.8. Surface deformation measurements

The reverse, plane side of each casting was measured with a mechanical Coordinate Measuring Machine (CMM)—Ziess OMC 850—with a resolution of  $0.1 \mu\text{m}$ . A probe with a diameter of  $3 \text{ mm}$  was used, acting as a mechanical filter with respect to the roughness of the surface itself. This corresponded to the measurements presented by Nwaogu et al. (2013) which provided guidelines to typical surface roughness characteristics and sizes for cast iron castings in green sand moulds. This mechanical filter ensured that the measurements displayed the deformation of the casting and not random dimples in the surface caused by its general surface roughness.

All castings were measured using an automated measurement program. The multi-point measurements were arranged in a polar grid as shown in Fig. 3. The same program was used for all castings, thus securing identical and repeatable measuring conditions.

The castings had previously been sectioned through the vertical centreline to investigate porosity formation at different locations in the castings, as described by Vedel-Smith et al. (2013). Thus only the half part of the casting closest to the down sprue was measured—the part from 06:00 to 12:00 h when viewed from the reverse side, with the top feeder located at 12:00 h and the in-gate at 06:00 h. See Fig. 3.

The resulting 3D-coordinate map can be represented as a topographic image of the reverse side of the casting showing the differences in height across the surface.

The characteristics of the topographic maps were separated into six parameters that together describe the surface of each of the castings. (1) *SV*—the curvature of the casting was analysed as viewed from the side at 09:00 h towards the centre, assigning values of high (H), mean (M), and low (L) to the top, centre, and lower part of the casting. Likewise, (2) *Cen*—the centre area at the boss was analysed and assigned a H-, M-, or L-value. (3) *Dir*—the valley (or low area) of the casting was described by its clockwise location relative to the centre of the casting. (4) *Ang*—the width of the valley was indicated by the angle it covers seen from the centre of the casting. (5) *Vol*—the volume (or indent) of the valley was graded from 1 to 3 (3 being the largest) indicating how large the valley was. And, (6) *Dist*—the distance the valley reaches from the centre towards the rim was indicated as  $x/3$ .

Quantification of the casting deformation was made using the difference between the highest and lowest measured point—called

the flatness value ( $f_v$ ). A perfectly flat surface has an  $f_v$  of  $0.00 \text{ mm}$ —as the reverse plane side of the casting was designed to be.

## 3. Results

### 3.1. Surface deformation measurements

#### 3.1.1. Deformation topography

The first comparison between the different castings was the topographic analysis that revealed the size and location of the deformation. A topographic map generated from the 3D coordinate measurements is shown in Fig. 4a–d. Fig. 4a and c shows a view perpendicular to the reverse side surface (half circle) for a casting from alloy  $\alpha$  and  $\beta$  respectively. Fig. 4b and d have the same castings viewed from the side (crescent), as viewed from 09:00 h and towards the centre. The variation in height is indicated by the colour—red is high (peaks), green is the mean, and blue is low (valleys). In the side view the same colour scheme applies, though it is more easily seen by the crescent shape of the topographic image. The vertical line indicates the mean value for the measurement. The view perpendicular to the reverse side gives an overview of both height and location, and the colours convey the magnitude.

In the side view the colour scheme is the same, though the main information is conveyed by the thickness of the crescent shape itself—a perfectly flat plane would be a vertical line. The crescent shape itself gives indications of the difference between the maximum and minimum of the deformation. A thin crescent (or part of the crescent) indicates a unidirectional deformation along the vertical axis with little deformation along the horizontal axis. A thickened crescent shape indicates a greater distortion along the horizontal axis. The more curved the crescent appears to be, the greater the deformation along the vertical axis.

All castings deformed in the same manner, displaying the highest values at 12:00 and 06:00 h, indicating the main deformation is along the vertical axis. While the two peaks that make out the high points are clearly defined for all castings, the location of the valley is described in detail in Table 5.

Table 5 shows that the variation between castings made with the same feeder configuration was generally small. While the size, angle, and distance of the valley may vary from group to group, the direction of the valley from the centre outwards was always between 09:00 and 11:00 h.

#### 3.1.2. Statistical representation of $f_v$

The flatness values ( $f_v$ ) are presented here as box plot graphs. See Fig. 5 and 6.  $\times$  indicates the average of the group, — indicate the median of the group, the bars indicate the spread from min. to max. measured value, the whiskers (or error bars) indicate a 95% confidence interval assuming a Gaussian distribution. Outliers are defined as  $>3 \times \sigma$  and indicated as \* but is only found in Fig. 6a.

The bars are coloured blue for casting sequence (1), grey for sequence (2), and red for sequence (3). Thus the blue and grey are pearlitic and the red are ferritic. Each bar represents a casting group. Group  $\alpha$  13 consist of one casting, groups  $\alpha$  11,  $\alpha$  12, and  $\beta$  23s each consist of two castings. The remaining 11 groups all consist of three castings. An overview of all casting groups displayed in the order in which they were cast is given in Fig. 5, excluding the TC-castings.

*Influence of alloy.* The analysis of the flatness,  $f_v$ , showed that the flatness of the ferritic  $\beta$ -alloy displayed a narrower confidence interval and little variance between the groups of castings. The castings made with the pearlitic  $\alpha$ -alloy had both the highest and lowest values measured. The average  $f_v$  of all the castings cast with two feeders was  $0.417 \text{ mm}$ . Compared to this, the average  $f_v$  of the  $\alpha$  group alone with both feeders was  $0.413 \text{ mm}$  with a standard

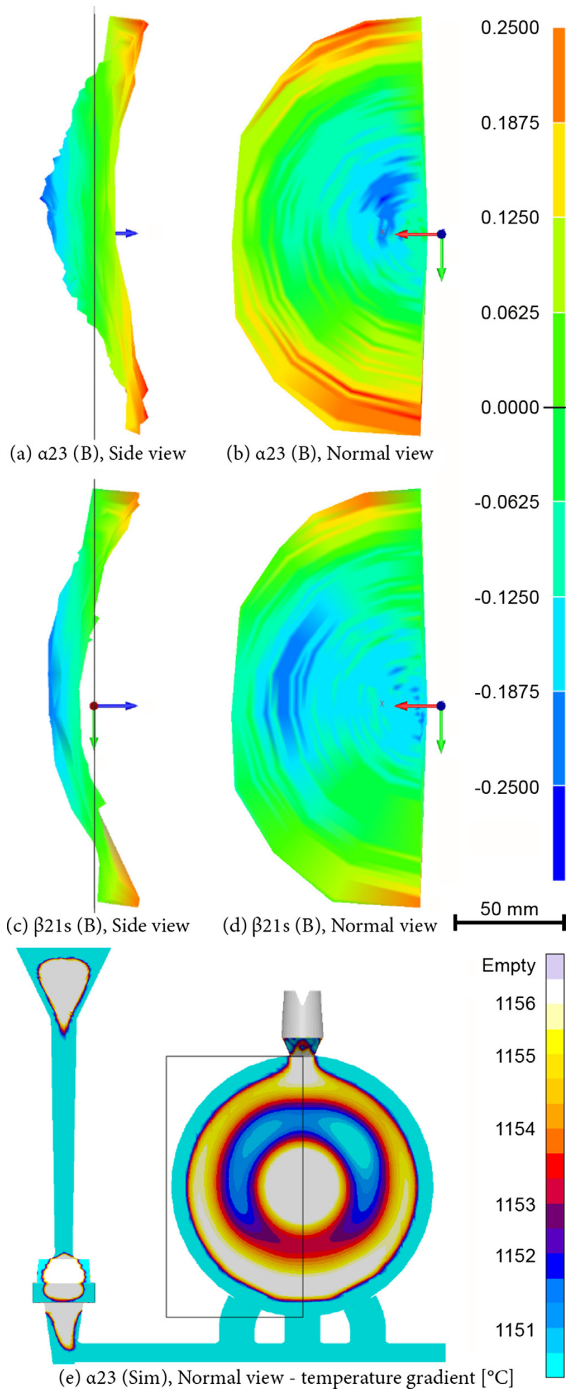


**Fig. 4.** Measured casting topography amplified 100 times. Scale in mm. Sub-figures (a) and (b) are the same casting,  $\alpha$  23 (B), viewed perpendicular and perpendicular to the measured surface. Sub-figures (c) and (d) are the same, but for casting  $\beta$  21s (B). The black horizontal line on (a) and (c) indicates the mean of the measured values (0.0000 on the scale) for the respective casting. (b) Shows a mean (M) centre area, and (d) shows a low (L) centre area. (e) Show the thermal gradients at 50% solidified for  $\alpha$  23. The black box frame the area viewed in (b) and (d). (For interpretation of the references to color in text near the reference citation, the reader is referred to the web version of this article.)

**Table 5**

Topography Overview; where  $f_v$  is the flatness value measured,  $SV$  is a low, mean, high evaluation (L,M,H) of the central area of the crescent,  $Por$  indicates porosities (Y = yes—porosities were found, N = no—porosities were not found) in the boss as examined by Vedel-Smith et al. (2013),  $Cen$  is a low, mean, high evaluation (L,M,H) of the boss area at the centre,  $Dir$  is an hours indication of the direction of the valley,  $Ang$  is an angle degree width indication for the valley,  $Vol$  is a 1–3 scale volume indication for the valley, and  $Dist$  is a  $\times/3$  indication of the distance the valley reaches from the centre.

Grp	Id	$f_v$	SV	Por	Cen	Dir	Ang	Vol	Dist
$\alpha$ 23	A	0.486	M	N	M	10:30	75°	2	2/3
	B	0.502	H	N	M	11:00	65°	2	1/3
	C	0.479	M	N	M	10:30	75°	2	2/3
$\alpha$ 22	A	0.359	M	N	M	10:00	75°	1	2/3
	B	0.337	M	N	M	10:00	65°	1	2/3
	C	0.364	M	N	M	10:00	75°	2	2/3
$\alpha$ 21	A	0.367	M	N	M	10:30	75°	1	2/3
	B	0.316	M	N	M	10:30	65°	1	2/3
	C	0.424	L	N	M	10:00	90°	2	3/3
$\alpha$ 13	A								
	B	0.520	M	N	M	09:00	75°	3	3/3
	C								
$\alpha$ 12	A	0.375	M	N	M	09:30	65°	1	2/3
	B	0.428	L	N	M	09:30	75°	2	3/3
	C								
$\alpha$ 11	A								
	B	0.335	M	N	M	10:00	65°	1	2/3
	C	0.350	M	N	M	10:30	50°	1	2/3
$\alpha$ 20	A	0.406	M	Y	L	09:30	65°	2	2/3
	B	0.371	L	Y	L	10:00	65°	2	2/3
	C	0.383	M	Y	L	09:30	65°	2	2/3
$\alpha$ 02	A	0.505	M	N	L	11:00	65°	2	1/3
	B	0.530	M	N	L	11:00	65°	2	2/3
	C	0.505	M	N	L	11:00	65°	2	1/3
$\alpha$ 00	A	0.915	L	Y	L	09:30	75°	3	3/3
	B	0.969	L	N	L	09:30	75°	3	3/3
	C	0.820	L	Y	L	09:30	75°	3	3/3
$\beta$ 23	A	0.415	M	N	M	10:00	65°	2	2/3
	B	0.388	H	N	M	10:30	50°	1	1/3
	C	0.395	M	N	M	10:30	65°	1	1/3
$\beta$ 11	A	0.412	M	N	L	10:30	65°	2	2/3
	B	0.409	M	Y	L	10:30	65°	2	2/3
	C	0.396	M	N	L	10:30	75°	2	2/3
$\beta$ 23s	A	0.452	L	Y	L	10:00	75°	2	2/3
	B								
	C	0.487	L	N	L	09:30	75°	2	2/3
$\beta$ 12s	A	0.430	M	Y	L	10:00	65°	2	2/3
	B	0.437	M	Y	L	10:00	75°	2	2/3
	C	0.424	M	Y	L	10:00	65°	2	2/3
$\beta$ 21s	A	0.396	M	Y	L	10:30	65°	2	2/3
	B	0.423	L	Y	L	10:00	65°	2	3/3
	C	0.403	M	Y	L	10:30	65°	2	2/3
$\beta$ 20	A	0.358	M	Y	L	09:30	65°	1	2/3
	B	0.398	M	Y	L	10:00	65°	1	2/3
	C	0.351	M	Y	L	09:30	65°	1	2/3

deviation ( $\sigma$ ) of 0.069 mm. See Fig. 6a. For the  $\beta$  group it was 0.423 mm with a standard deviation of 0.032 mm. The average flatness of the  $\alpha$ -castings was smaller; it was closer to the overall average, but the variation was greater. The ferritic  $\beta$ -alloy was more consistent in its deformation regardless of feeder configurations.

Sorting the groups according to alloy, including all casting groups and only including the groups with two feeders (wF) as shown in Fig. 6a, it was clear that the ferritic  $\beta$ -alloy displayed only half as wide a confidence interval as the  $\alpha$ -alloy, meaning that it had twice as good manufacturing precision as the pearlitic  $\alpha$ -alloy. The graph shows that all  $f_v$  were above 0.31 mm and that both alloys

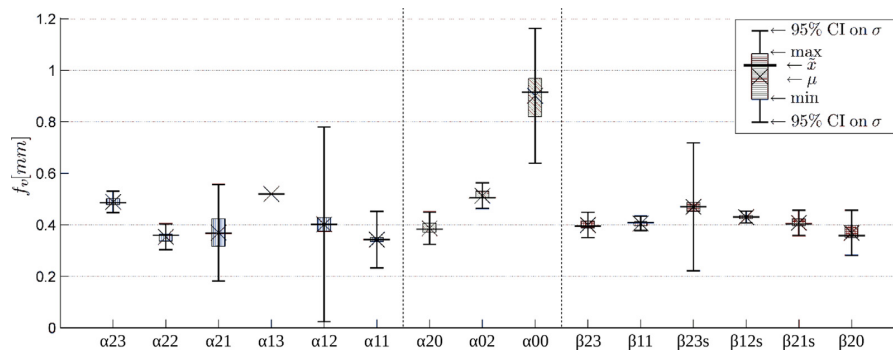


Fig. 5. Flatness values ( $f_v$ ) for each separate casting group, sorted by order of casting. Group  $\alpha$  13 consist of one casting, groups  $\alpha$  11,  $\alpha$  12, and  $\beta$  23s consist of two castings. The remaining 11 groups all consist of three castings.

displayed little variation in minimum measured  $f_v$ . The bars show that the pearlitic  $\alpha$ -alloy group included values almost twice the size of the ferritic  $\beta$ -alloy. Comparing with Fig. 5 it was clear that group  $\alpha$  00 was the main source of the variation.

**Influence of top and centre feeder.** Sorting the castings produced with two feeders according to the type of centre feeder, as shown in Fig. 6b, a statistical difference in  $f_v$  was found between the castings made with high modulus (12) centre feeder and the two groups of lower modulus (11) feeders, with a difference in  $f_v$  of approximately 0.15 mm. The same comparison for the ferritic  $\beta$ -alloy showed that the two group averages were only 0.014 mm apart. It is worth noting that the deviation of the high modulus feeder group was more than twice the range of the low modulus group.

Rearranging the groups to be sorted by type of top feeder, show that the average of all groups were just above 0.4 mm, and that all four groups may be considered statistically inseparable. See Fig. 6c. Again, as with the centre feeders, the pearlitic  $\alpha$ -alloy castings displayed greater variance. For the pearlitic  $\alpha$ -alloy the exothermic-insulating top feeder resulted in a marginally better confidence interval compared to the insulating top feeder. For the ferritic  $\beta$ -alloy the insulating top feeder resulted in the best confidence interval.

### 3.2. Microstructure analysis

Previous studies have shown that the  $\alpha$ - and  $\beta$ -alloys have similar microstructures but that the ferritic  $\beta$ -alloy had a greater nodule count compared to the pearlitic  $\alpha$ -alloy, as reported by Vedel-Smith and Tiedje (2014). The greater nodule count for the  $\beta$ -alloy was despite the higher Mn content of the  $\alpha$ -alloy.

Fig. 7a shows the microstructure of the thin walled section for the  $\alpha$ -alloy with the graphite nodules surrounded by the ferrite shell, and in between pearlite. In comparison the  $\beta$ -alloy from the same section, Fig. 7b, also display graphite nodules surrounded by ferrite. However, very little pearlite was found in the last to freeze eutectic of the latter.

The microstructures at the higher modulus boss section showed larger graphite nodules in the pearlitic  $\alpha$ -alloy (Fig. 7c), compared to the ferritic  $\beta$ -alloy (Fig. 7d). As with the thin walled section, pearlite was found at the edge of the ferrite in the last to freeze eutectic, as seen in Fig. 7c.

No significant difference was found between the microstructures of the castings made with the exothermal feeder sleeves compared to the casting made with the insulating feeder sleeves.

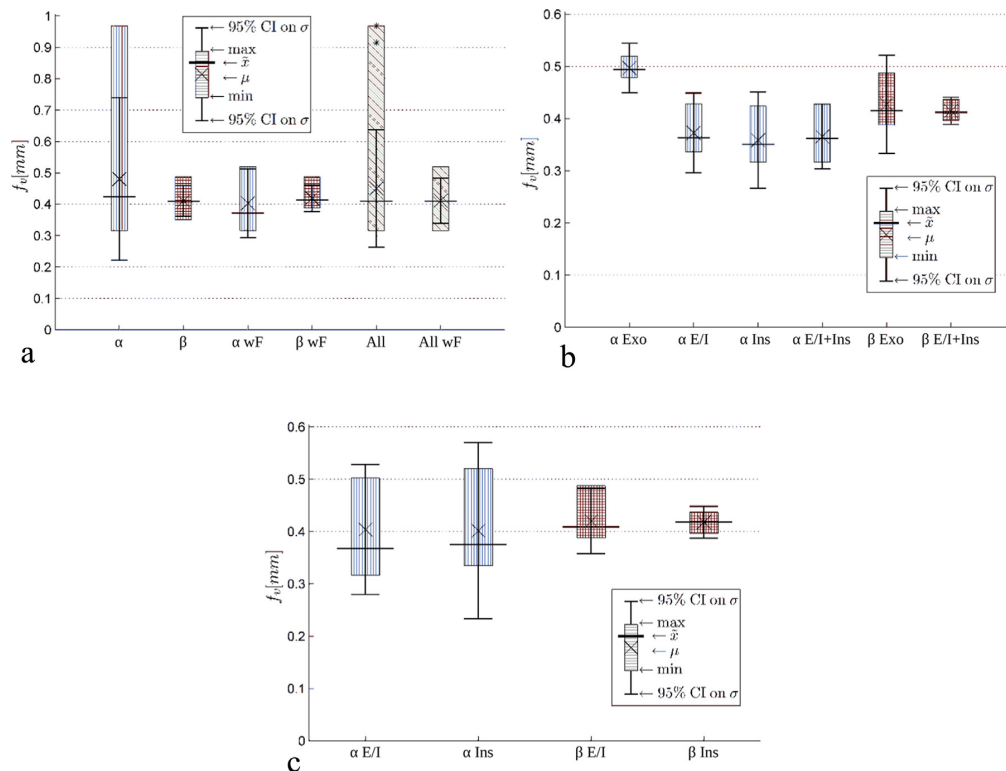
### 3.3. Thermal analysis

Fig. 8a shows that the difference between cooling curves for two castings made under similar conditions was small. The two castings solidify and cool in an identical fashion. The austenite to ferrite phase transformation was shifted 40 s, but the difference in the duration of the phase transformation was only 4 s. The duration of the phase transformation were within a 10 s timeframe for six of the nine MPs. The largest measured difference was 25 s at MP 9.

The cooling and solidification times and temperatures were similar for both the measured and simulated results. In the trial castings and for the simulations it was found that the thin walled section (MP 2–7) solidified before the rim (MP 8 and 9). However, after solidification this changed so that the rim cooled faster than the thin walled section. Thus, the rim was the first section of the casting to go through the austenite to ferrite phase transformation followed by the thin walled section, and ending with the boss (MP 1). Fig. 8b shows how long time it took before the MP was half way through the austenite to ferrite phase transformation (full lines at the top). The duration of the phase transformation is also shown (dashed lines at the bottom). For the trial castings the rim right below the top feeder also cooled faster than the thin walled section. All three simulations showed a greater effect of the heat from the top feeder on the top part of the rim (MP 8) and on the top most part of the thin walled section (MP 3).

The top feeder was also found to influence the duration of the phase transformation for the upper part of the thin walled section (MP 2–4) for the numerical simulations. All three alloy simulations showed a prolonged phase transformation duration at MP 2 and 4, while the centre point between the two displayed a decreased duration of the phase transformation. See Fig. 8b. In comparison the trial measurements did not show a similar effect. The simulations showed increased duration of the phase transformation at MP 2 and 4, and decreased duration close to the feeders at MP 1 and 3, although the duration at MP 8 was unaffected when compared to MP 9. The duration of the phase transformation was longest at the boss (MP 1). The thin walled measurements (MP 2–7) was slightly shorter and all within an 18 s timeframe. Finally the fastest phase transformation was found for the rim (MP 8 and 9). Measurements and simulations showed that the eutectoid transformation begins at the rim and travels through the thin walled section to the boss at the centre.

The duration of the phase transformation for the trial measurements (A and B) only varied by 80 s from MP 1 to 9 in an almost linear fashion. The duration of the phase transformation of the high Si alloys ( $\beta$ ,  $\tau$ ) simulations varied by 130 s with peaks at MP 2 and 4.



**Fig. 6.** Flatness values ( $f_v$ ) for sorted groups. (a) Flatness values ( $f_v$ ) for all  $\alpha$ -castings, all  $\beta$ -castings, all castings, and all castings with two feeders (wF). (b) Flatness values ( $f_v$ ) for each alloy ( $\alpha, \beta$ ) and sorted by centre feeder. (c) Flatness values ( $f_v$ ) for each alloy ( $\alpha, \beta$ ) and sorted by top feeder. (For interpretation of the references to color in text near the reference citation, the reader is referred to the web version of this article.)

The pearlitic low Si alloy ( $\alpha$ ) varied by 200 s and also showed peaks at MP 2 and 4. The duration of the phase transformation for the pearlitic-ferritic alloy ( $\alpha$ ) was found to be approximately twice as long as for both the trial measurements and the high Si alloy simulations. This prolonged duration was related to two-step phase transformation that was found for all MPs for the pearlitic-ferritic  $\alpha$ -alloy.

The temperature distribution in the casting during the solidification and cooling from 0% to 100% solidified was analysed. It was found that there was a non-uniform temperature distribution in the casting. This was particularly clear in the thin section of the plate, and is illustrated in Fig. 4e. The figure shows two colder areas located at approximately 02:00 h and 10:00 h respectively. Those two areas remained 5–10 °C colder than the rest of the thin-walled section until 85% of the entire casting was solidified. The local solid-fraction was at this point 100% and the local temperature approximately 1050 °C. Since this temperature variation was observed during eutectic solidification, where that solidification interval was small, it means that there was a large local variation in solid fraction and strength of the casting.

Likewise it was found that the inside of the rim and outside of the boss, where the geometry retains the heat so that circular hotspots are formed, solidification was markedly slower than for the remaining casting. In these hotspots, heat was retained on the front side of the casting, while on the reverse, flat, side cooling was more efficient. As a result the temperature gradient from one side of the casting was in the order of 10 °C over a distance of 10 mm. It was also found from the simulations that this picture was common for all three alloys.

## 4. Discussion

### 4.1. Surface deformation measurements

#### 4.1.1. Deformation topography

The topography of all 40 castings were found to be similar. Casting group  $\alpha$  00 displayed a far greater distortion than the other 14 groups, but as shown in Table 5 the  $\alpha$  00 displayed the same valley direction and angle, though the volume and distance of the valleys were more pronounced in the other 13 casting groups. All 40 castings displayed a valley with a centreline located between 09:00 and 11:00 h, with an angular width between 50° and 90°. Almost 3/4 of the castings featured a valley reaching 2/3 of the distance from the centre to the edge of the rim. The last 1/4 was divided into two small groups either reaching all the way to the edge of the rim (3/3), or only reaching a small distance outwards from the centre (1/3). A similar pattern was found for the depth of the valleys. See Fig. 6a.

Within each group of castings it was seen that the direction of the valley varied not more than 30 min. For six of the groups the valley ran in the same direction in all three castings. The total variation in the direction of the valley was within 1 h and 30 min. This indicated that the direction of the valley was indeed influenced by the feeder combination, and that it could be controlled by the choice of feeder modulus. Likewise, there was an indication that for the pearlitic  $\alpha$ -alloy a high modulus centre feeder resulted in a more pronounced (larger) valley. This was in good agreement with the  $f_v$  measurements. On the other hand no correlation between the range and the volume of the valley was found; meaning that a

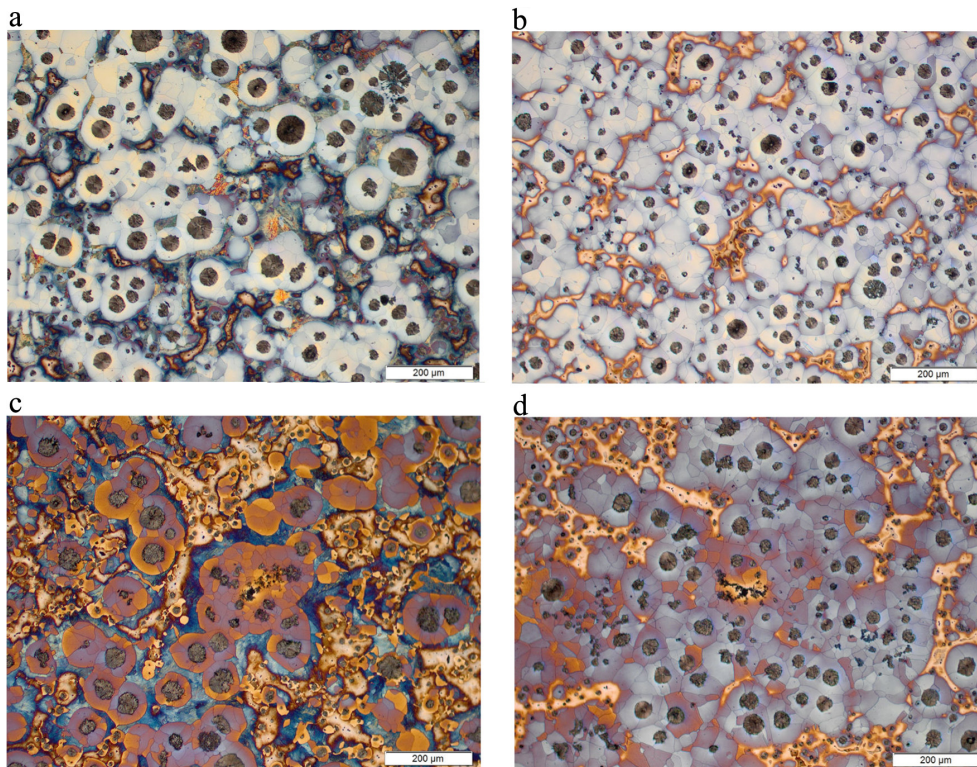


**Fig. 7.** Microstructures from castings  $\alpha$  23 (C) (a and c) and  $\beta$  23 (C) (b and d). Both castings were made with an insulating-exothermic top feeder and an exothermal centre feeder. Microstructures (a) and (b) were from the thin walled section at the vertical centre line just below the upper rim. Microstructures (c) and (d) were from the centre of the boss section. (a)  $\alpha$ -alloy, microstructure from thin walled section [ $\times 10$ ]. (b)  $\beta$ -alloy, microstructure from thin walled section [ $\times 10$ ]. (c)  $\alpha$ -alloy, microstructure from centre of boss section [ $\times 10$ ]. (d)  $\beta$ -alloy, microstructure from centre of boss section [ $\times 10$ ].

change in area did not entail a change in valley depth. Hence the volume of the valley was not constant.

The consistency of the castings, especially within each casting group, showed high reproducibility and indicated that production conditions were uniform. If the distortion had been variable, an effective adaptation to the pattern would be impossible, or in the best case have a limited effect. The consistency that has been demonstrated here may lead to an adaptation that not only reduces the machining allowance considerably, but also counters the inherent distortion so that the cooled casting becomes much more flat than at present. Changing the pattern, however, requires either a sufficiently good optimisation simulation or an iterative trial and error development of the casting pattern. This is because the added and removed padding in various areas of the pattern also changes the thermal gradients and the strength of the sections, thus slightly affecting the distortion of the casting. Additionally the casting deformation must be viewed as an interval not an exact value, since variation will always occur—especially over time. A narrow confidence interval for the casting deformation indicates a stable production and thus accordingly allow for a greater casting optimisation with smaller tolerances.

Though the analysis of the casting's topography showed consistency in the distortion between the different castings, it must also be noted that the graphical representation of the measured results was less well defined than the  $0.1 \mu\text{m}$  resolution of the CMM. The colour scale was discontinuous and comprises only nine colours from orange to blue as seen in Fig. 4.

As the geometric modulus ( $M_g$ ) of the casting was identical in all directions from the centre outward, the placement, range, size, and

direction of the valley must be the product of the filling conditions and the thermal influence provided by the feeders. Alternatively it could be an inaccuracy in the pattern itself. The flatness of the entire 400 by 500 mm pattern was measured and found to have a  $f_v$  of  $16.4 \mu\text{m}$ —approximately 20–30 times smaller than deformations measured on the casting. Thus, pattern distortion was negligible.

**Porosities.** None of the 17 castings that were given the mean height indication (M) at the boss contained internal porosities. For the 23 castings designated low (L), 16 had internal porosities. Four of the seven that were designated (L), but displayed no porosities were castings without the top feeder. The three remaining castings were all in casting groups where other castings displayed porosities, and can thus be said to be prone to porosities. In these cases, the porosities may be present, but located away from where the casting was sectioned. The porosities in the boss were all classified as small non-linear isolated porosities (SP) or non-linear clustered (CP) porosities as defined by EN 1371-1:2011 (2011).

#### 4.1.2. Solidification and deformation sequence

The following mechanisms are proposed for solidification and deformation of the castings. The reverse, plane side of the casting was more uniformly cooled; it formed a solid shell that contracted uniformly during and immediately after solidification. On the front there were areas on the inside of the rim and along the outside of the boss that remained hot so that the strength was reduced locally.

The casting was initially pulled backwards as it solidified and cooled. As the hot areas on the front of the casting gained strength additional stresses build up around the now relatively strong thin walled section. At the point where the eutectoid transformation

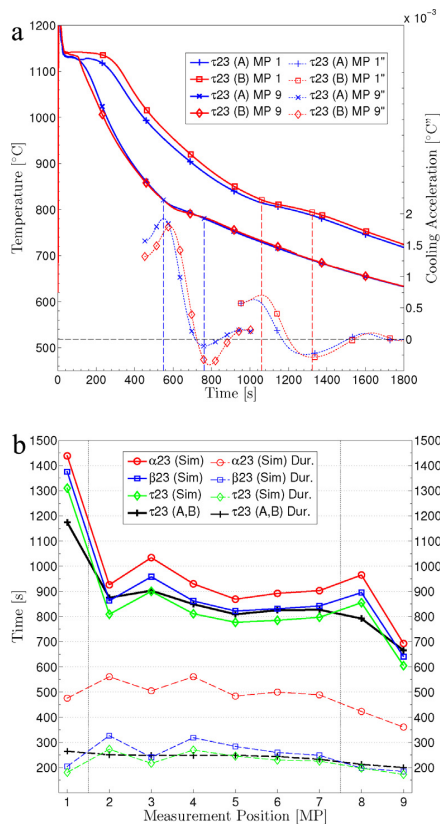


**Fig. 8.** Results of the thermal analysis. (a) Cooling curves from the trial castings. Comparison of MP 1 and 9 for the two castings. The dashed lines show the second derivative of the cooling curves. The vertical lines show how the beginning and end of the austenite to ferrite phase transformation has been identified. (b) The full lines show the mean time of the austenite to ferrite phase transformation for all 9 MPs inside the casting. The dashed lines show the duration of the phase transformation for each MP. The black lines marked with + display the average of the experimental measurements. The three other curves were obtained via numerical simulation.

began, the temperature distribution in the casting had changed so that the rim now became the coldest part of the casting. As the transformation took place from the rim through the thin walled section to the boss, further stresses build up, adding to the deformation. The shape of the reverse, plane side was affected by the following four mechanisms.

(1) *Backwards deformation:* The two sides were not equally stable. The hotspots created at the corners of the boss and rim remained hot for an extended period, thus postponing contraction and recovery of strength. This effect is illustrated by the feeding modulus in Fig. 2d, showing the location of the last melt to solidify. The reverse plane side on the other hand was planar and cooled faster without less pronounced hotspots, and thus contract sooner and regain strength sooner than the front.

(2) *Location of the valley:* The cold spot was pushed upward due to the bottom filling that heated the lower part of the mould more than the upper part. Because the rim had a greater modulus than the thin walled section, the upper half of the thin walled section was initially the coldest area of the casting. Again with the reverse planar side being colder than the front side. As the last volume of the mould to be filled was directly at the centre, the largest melt flow during filling was at the vertical centre line. This heated the vertical centre line more than the sides of the casting,

creating a hotspot here, pushing the cold spot at the upper part of the thin walled section towards the sides. Afterwards this centre line hotspot was maintained by the top feeder. A hot top feeder will eventually counter the heating effect of the in-gate, albeit the shift of the hotspot from below the boss to above the boss was only fully in effect at the end of solidification. Thus the coldest area was where the valley would form. Reversing the argument, a valley at the centre thus indicate that this area was cold during solidification. This is supported by the correlation between low areas at the centre (Cen) and the porosities found inside the boss (Por) shown in Table 5.

(3) *Silicon (Si) content:* A significant difference between the two alloys was the Si content. Si is a graphitizer and suppresses the formation of pearlite. Although increased Si content leads to greater graphite expansion, and thus a potential for greater deformation, the main effect of Si was to increase the temperature for the transformation from austenite to ferrite, as described in *Ductile Iron Data (1990)*. The higher temperature means that all parts of the casting had recovered less strength to withstand the graphite expansion. The higher temperature of the metal at the time of the transition made it softer and less likely to have build up unreleased stresses. The greater influence of Si, though, comes from its ability to suppress the formation of pearlite. The combined austenite to ferrite and pearlite phase transformation was shown to significantly increase the total duration of the transformation by comprising two consecutive phase transformations in the  $\alpha$ -alloy.

(4) *Inoculation:* The  $\beta$ -alloy castings had a finer microstructure when compared to the  $\alpha$ -alloy castings, as described by *Vedel-Smith and Tiedje (2014)*. *Elmquist et al. (2011)* reported that over-inoculation could advance the effect of the primary graphite expansion, but would in turn also lessen the effect of the secondary graphite expansion. For LGI this follows that over-inoculation could have caused increased shrinkage but also decreased deformation variation because the main graphite expansion occurred at a higher temperature and more uniformly. For SGI, however, *Chen et al. (1997)* reported that the increased nodule count ease the deposition of graphite excreted from the austenite and inhibit the formation of pearlite. Additionally better inoculation reduce the amount of undercooling during solidification limiting the formation of cementite and prompt a more uniform solidification.

#### 4.1.3. Statistical comparison of $f_v$

The variation in flatness within each group of castings was very small compared to the total variation in the experiments. This showed that the experimental conditions were stable and uniform. The only group that was markedly different was  $\alpha$  00 which exhibited a distortion that was twice as large as that of the other 14 groups. See Fig. 5. The castings in group  $\alpha$  00 were significantly different from all other castings. Applying at least one feeder to the casting, regardless of whether it was applied to the top or the centre boss or both, reduced  $f_v$  in comparison to the castings without feeders. There was no statistically significant difference between the groups of castings to which feeders were applied.

As  $\alpha$  00 displayed the inherent deformation of the casting geometry itself, influenced only by the heated area at the in-gate, it was concluded that both feeders, together or separately, minimise the deformation of the casting by changing the cooling conditions to create a temperature field that reduces thermal stress by allowing castings to maintain a more uniform temperature gradient during cooling.

*Influence of alloy.* Both materials were near-eutectic in composition. However, there were significant differences in how they responded to cooling. Most significantly, the high Si-alloy was less likely to form pearlite at the solid state transformation when cooled from 900 to 600 °C. It is known that this transformation is accompanied by a change in specific volume. The size of the volume change

depends on the pearlite content in the finished casting, as described in *Ductile Iron Data* (1990), so that the higher the pearlite content, the larger the volume change, even though the austenite to ferrite phase transformation would by itself cause a volume change.

Since the high Si  $\beta$ -alloy was a fully ferritic alloy, it would be less subject to deformation due to the reduced graphite expansion at the time of the solid state phase transformation. On the other hand, pearlite formed in the low Si  $\alpha$ -alloy. The amount of pearlite will depend on local cooling conditions so that the pearlite content would vary between groups of castings and also between specific locations within the individual casting. As a result it was seen that the high Si  $\beta$ -alloy castings that are pearlite free were more consistent in their dimensions.

This means that in this alloy, it is easier to compensate for thermal deformation by modifying the pattern.

In terms of production, the correction should be aimed at the average deformation measured, adding a machining allowance to ensure that the confidence 95% (or possibly 99%) interval is covered. By adapting the tolerances required based on the reproducibility demonstrated in this paper, any traditional machining allowance as described by Angus (1976) and defined by EN ISO 8062-3:2007 (2007), specifying machining allowance for castings, can be minimised considerably. This will only be feasible if sufficient process control is achieved.

*Influence of top and centre feeder.* The feeders, besides fulfilling their primary job of feeding, alter the thermal gradients of the casting. Vedel-Smith et al. (2013) showed that both top and centre feeders were required to produce sound, porosity free castings. In terms of the deformation of the casting, it was not the actual feeding of melt to the casting that influence the final result, but the change in the thermal gradients of the casting. Thus, deformation could be changed and countered by increasing or decreasing the  $M_f$  of the feeder, providing  $M_f$  and the melt volume were still sufficient to provide adequate feeding.

## 5. Conclusions

- Alloy—moderately high Si content reduced deformation.
  - the  $\alpha$  and  $\beta$  alloy was considered statistically identical with respect to average deformation ( $f_v$ ),
  - the high Si  $\beta$  alloy displayed much less variance, leading to a better manufacturing precision and greater potential for production optimisation.
- Moduli of the centre feeder.
  - For the  $\alpha$ -alloy high modulus centre feeder lead to greater deformation ( $f_v$ ). The feeders with smaller modulus displayed less deformation.
  - For the  $\beta$ -alloy varying the module for the centre feeder caused no significant difference in  $f_v$ .
  - The  $\beta$ -alloy with the low moduli centre feeders was found to have the best reproducibility of all casting combinations.
- Modulus of the top feeder.
  - No statistical difference was found between the two top feeder moduli examined—neither for  $\alpha$ - nor  $\beta$ -alloys.
- Porosity tendency indicated by micro-surface shrinkage at the boss.
  - Micro-surface shrinkage was a viable indication of internal porosities for the bulk boss section.

## 5. Pattern adaptation for production optimisation.

- If sufficient care was taken to control the production parameters, the variation in deformation is small enough for the pattern itself to be altered in order to compensate for some of the deformation. This would make possible a reduction in machining allowance, reducing the melt requirement.

## Acknowledgements

This project was funded by the Danish Public Service Obligation (PSO) (Project no. 342-050) funds. It was a collaboration between FOSECO Ltd., MAGMA GmbH., DISA Industries A/S, and Vald.Birn A/S. Casper Petersen made the representation of the flatness values. The colour etching of the microstructures were made in collaboration with Professor Attila Diószegi and Sadaf Vazehrad at Jönköping University, School of Engineering, Sweden.

## Appendix A. Supplementary Data

Supplementary data associated with this article can be found, in the online version, at <http://dx.doi.org/10.1016/j.jmatprotec.2014.11.025>.

## References

- Angus, H., 1976. *Cast Iron – Physical and Engineering Properties*. Butterworth & Co (Publishers) Ltd., London.
- Brown, J.R., 2000. *Foseco Ferrous Foundryman's Handbook*. Foseco International Ltd., Oxford, pp. 296–310, Ch. 19.
- Chang, A., Dantzig, J., 2004. Improved sand surface element for residual stress determination. *Appl. Math. Model.* 28 (6), 533–546.
- Chen, Q.M., Langer, E.W., Hansen, P.N., 1997. Influence of the process parameters on the volume change during the eutectic reaction of SG cast iron: a computer simulation. *J. Mater. Sci.* 32 (March (5)), 1239–1248.
- Ductile Iron Data, 1990. *Ductile Iron Data – for Design Engineers*. Rio Tinto Iron & Titanium Inc.
- Elmqvist, L., Diószegi, A., Björklind, T., 2011. On the formation of shrinkage in grey iron castings. *Key Eng. Mater.* 457, 416–421.
- EN 1371-1:2011, 2011. *Founding: Liquid Penetrant Testing—Sand, Gravity Die, and Low Pressure Die Castings*.
- EN 1563:2012-3, 2012. *Founding: Spheroidal Graphite Cast Irons*.
- EN ISO 8062-3:2007, 2007. *Geometrical Product Specifications (GPS)—Dimensional and Geometrical Tolerances for Moulded Parts. Part 3: General Dimensional and Geometrical Tolerances and Machining Allowances for Castings*.
- Jackson, R., 1963. Factors determining dimensional accuracy of castings. *Br. Foundrym.* 56, 332–336.
- Kang, J.W., Long, H.M., Wang, T.J., Huwang, T.Y., Liu, B.C., 2011. Evaluation of distortion of castings. *Int. J. Cast Metals Res.* 24 (3), 228–232.
- Mkumbo, C.S.E., Nyichomba, B.B., Campbell, J., Tiryakioglu, M., 2002. Linear contraction of grey iron sand castings. *Appl. Math. Model.* 14 (6), 225–234.
- Motoyama, Y., Takahashi, H., Inoue, Y., Shinji, K., Yoshida, M., 2013. Dynamic measurements of the load on castings and the contraction of castings during cooling in sand molds. *J. Mater. Process. Technol.* 213 (2), 238–244.
- Nwaogu, U.C., Tiedje, N.S., Hansen, H.N., 2013. A non-contact 3D method to characterize the surface roughness of castings. *J. Mater. Process. Technol.* 213 (1), 59–68.
- Sosa, A.D., Echeverra, M.D., Moncada, O.J., 2004. Machining and heat treatment effects on distortion and residual stresses in an industrial application of ADI. *ISIJ Int.* 44 (7), 1195–1200.
- Vedel-Smith, N.K., Tiedje, N.S., 2014. Effect of feeder configuration on the microstructure of ductile cast iron. In: *TMS Proceedings – Shape Casting: 5th International Symposium 2014*, pp. 113–120.
- Vedel-Smith, N.K., Tiedje, N.S., Sällström, J., Maza, K.T., 2013. Quantification of feeding effects of spot feeding ductile iron castings made in vertically parted molds. In: *AFS Proceedings*.





IV

Supplement  
Feeding Against Gravity  
with Spot Feeders  
in High Silicon Ductile Iron

Published  
10th International Symposium on  
the Science and Processing of Cast Iron  
SPCI10, Mar del Plata, Argentina, 2014

“EQUIPPED with his five senses, man explores the universe around him and calls the adventure Science.”

—Edwin Powell Hubble



## Supplement IV

---

### Feeding Against Gravity with Spot Feeders in High Silicon Ductile Iron

N.K. Vedel-Smith  
N.S. Tiedje

Technical University of Denmark, Department of Mechanical Engineering  
Technical University of Denmark, Department of Mechanical Engineering

Vedel-Smith was the main author. Tiedje contributed with review and evaluation. Vedel-Smith performed the experimental part.

Vedel-Smith presented the paper at the 10<sup>th</sup> SPCI conference in Mar del Plata, Argentina, 2014.

*Published*  
*10<sup>th</sup> International Symposium on the Science and Processing of Cast Iron*  
*SPCI10, Mar del Plata, Argentina, 2014*

---

## Feeding Against Gravity with Spot Feeders in High Silicon Ductile Iron

N.K. Vedel-Smith<sup>1\*</sup> and N.S. Tiedje<sup>1</sup>

<sup>1</sup>Department of Mechanical Engineering, Technical University of Denmark, Kgs. Lyngby, Denmark

A test pattern, with three different moduli castings was developed to investigate methods to optimise feeding of high silicon ductile cast irons. Different feeder types, modulus, and locations were investigated using both an insulating and an exothermal sleeve material. Porosities were analysed and classified using X-ray imaging and ultrasound analysis. The effect of the different feeder configurations were classified in reference to defect location, sleeve material, and feeder type, modulus, and location.

The analysis showed that exothermal feeder sleeves with the right configurations can feed uphill against gravity. This effect may contribute to the thermal expansion created by the exothermal reaction. It was also found that the optimum feeder size does not scale linearly with the casting modulus but that larger casting modulus requires relatively smaller modulus feeders. The thermal gradient created by the feeders made with the insulating sleeve material was not sufficient to significantly improve feeding.

**Keywords:** ductile iron, spot feeding, risering, solidification, high silicon, ram-up sleeves.

### Introduction

Feeding complex castings with different moduli sections is a challenge for the foundries, as customers require improved yield, less machining, and sound castings. Optimisation of cast components is an essential driver for many industries in order to improve their products. Thus the foundries are met with an ever growing requirement to improve methods and increase yield. The location and orientation of the casting is determined by casting geometry, location of cores and feeders. However, new designs with great variation between thin and thick walled sections, and highly complex designs limit the use of traditional feeders.

In vertically parted moulds geometrical feeders are normally located at the top of the casting on the parting plane. All feeders require an unbroken feeding path from the feeder to the section that must be fed. This makes it difficult, if not impossible, to feed heavy sections that are disconnected from the feeding path by a low modulus section. Additionally, the feeder requires a driving force to move the melt from the feeder into the casting. Traditionally this driving force is gravity, but other forces also act on the melt during solidification. E.g. solutions like the William wedge and similar geometries are a part of almost all feeder designs to ensure that the feeder is kept open to the atmosphere (punctured) and thus prevent the negative pressure gradient retaining the melt inside the feeder. Other natural forces working on the melt can be the contraction and expansion of the melt itself as different sections of the casting goes through the different stages of solidification at different intervals depending on the modulus, cooling rate, and alloy composition. The movement, deformation, expansion, and the reduction in strength of the green sand mould also influence these factors.

Descriptions and guidelines to the application and effect of feeders that make use of these naturally occurring driving forces to move the melt from a feeder located at the bottom of the casting into a section at a higher elevation are sparse at best. The study presented in this paper represents an experimental design comprising 9 different feeder configuration tested on a scalable casting geometry in three different sizes of casting moduli—8 mm, 10 mm and 15 mm. The study quantified the effect of different modulus spot feeders for different modulus castings. The trial was made with different insulating and exothermic ram-up sleeves together with high silicon ductile iron castings.

### Experimental Procedure

#### Casting Geometry and Pre-feeder Design

The casting geometry was designed to be parametric in order to represent different moduli sections with the same geometry (see Figure 1). The casting itself was a rectangular cuboid. A square footprint was chosen because the square design allow for a high geometrical modulus and was better suited than a round design for ultrasound and x-ray analysis. The height of the casting was chosen as 3 times the width and depth of the casting. The basic idea with the design was to have one uniform section that would create a significant amount of shrinkage by itself. The height of the casting should be great enough that a feeder at the top and a feeder at the bottom would influence the casting differently due to the difference in ferrostatic pressure. For steel bars cast in a horizontal orientation the maximum feeding distance between two feeders was reported as varying between 1-4 times the thickness of the bar<sup>1</sup>. Though the trial castings are

---

\* Corresponding author, email: nikvs@mek.dtu.dk

cast vertically and in SGI, it was chosen to uphold as great a distance between the two feeders on the casting as possible. The height of the bar was governed by the pattern size and allowed for a bar length of 3 times the thickness (a). In turn this allowed for a feeder distance of approximately 2.5 times the thickness (a).

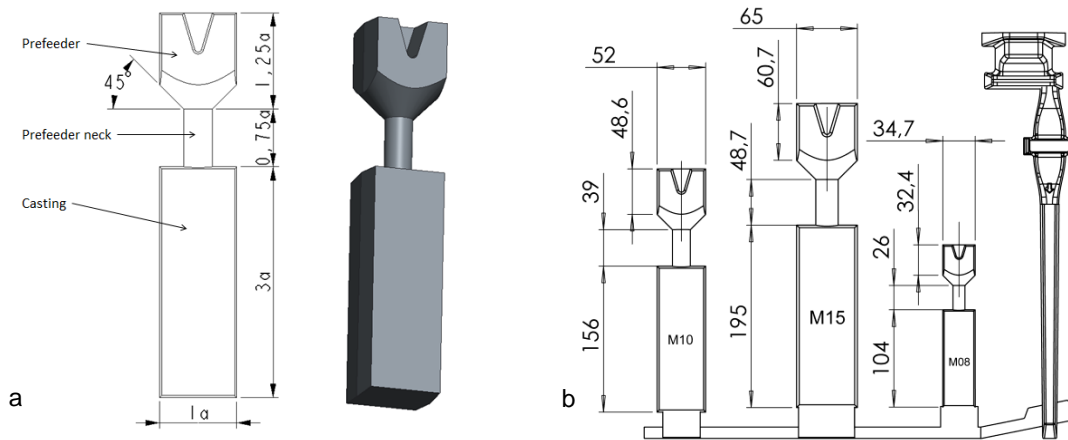


**Fig.1:** Schematic of the parametric casting design (a), and pattern layout (b). Measurements in mm.

A pre-feeder was placed on top of the casting—designed to compensate for the liquid shrinkage that occur as the casting cools from the pouring temperature to the solidus temperature, so that the variations in pouring temperature on total shrinkage are eliminated. The design had to ensure an identical amount of shrinkage in all castings, regardless of pouring temperature. If not done properly it would afterwards be impossible to prove that changes in porosities in the castings were related to changes in feeder configurations and not attributable to a smaller or greater liquid shrinkage caused by varying pouring temperatures.

The size of the pre-feeder neck was determined so that it closes and blocks feeding at the point in time where solidification begins in the casting itself. Based on Chvorinov's modulus law<sup>2</sup> equation (1) was derived:

$$D_{neck} = 4M_{neck} = \frac{c_p(T_{start}-T_{eut})}{(-\Delta H)+c_p(T_{start}-T_{eut})} M_{casting} \quad (1)$$

where  $D_{neck}$  was the diameter of the pre-feeder neck,  $M_{neck}$  was the modulus of the pre-feeder neck, and  $M_{casting}$  was the modulus of the casting.  $H$  was the enthalpy of the system,  $c_p$  was the heat capacity,  $T_{start}$  was the pouring temperature and  $T_{eut}$  was the eutectic temperature for the given alloy. Equation (1) gives the diameter of the pre-feeder neck. However, the equation does not take into account the heat flux from the casting and pre-feeder but assume unidirectional solidification. To determine the optimum pre-feeder neck height, which would reduce the amount of liquid shrinkage as much as possible while still allowing for a timely solidification of the neck, numerical simulations of the different pre-feeder neck geometries were used (see Figure 2).

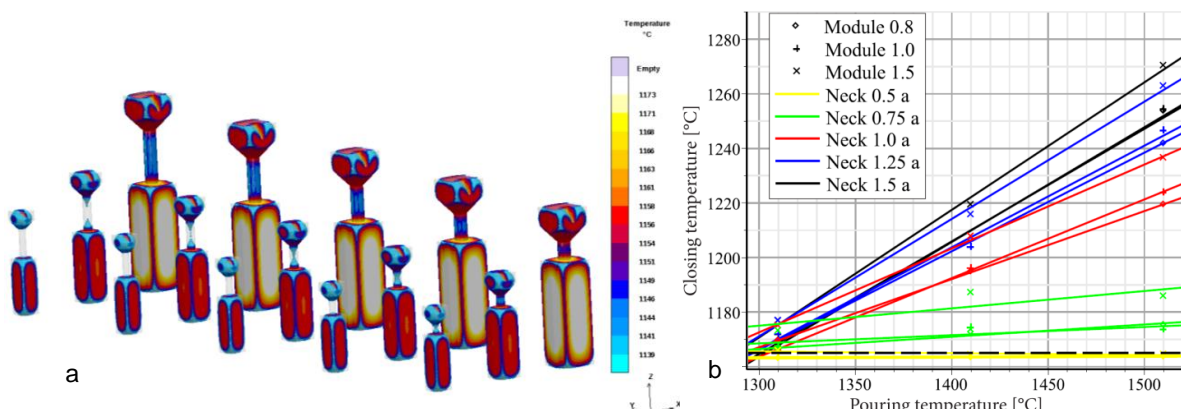


**Fig.2:** (a) Parametric study of varying pre-feeder neck lengths from 0.5a to 1.5a, and (b) a graph showing the temperature at the centre of the casting (Closing temperature) as a function of the pouring temperature for three different moduli castings and five different pre-feeder neck lengths. The dashed line indicates the eutectic temperature of the alloy.

The solidification times obtained from the numerical simulation of the different parametrical geometries, at different pouring temperatures, were plotted in Figure 2(b). The graph shows that the yellow line representing the shortest pre-feeder neck was below the eutectic temperature line. This means that the solidification of the casting had begun before the neck had closed off. All other pre-feeder neck lengths closed off before the casting centre reaches the eutectic temperature. Hence the pre-feeder neck length of 0.75a was chosen because that length allowed for the best prevention of liquid shrinkage and for the most uniform performance across all casting temperatures. Additionally, this analysis was repeated for another alloy with a different eutectic temperature to make sure the design would function with different alloy compositions.

**Feeder Placement, Modulus, and Combinations**

The trial setup consisted of 6 different feeder geometries, using either an insulating or an exothermic sleeve material, and applying feeders to two different locations on the casting—at the top near the pre-feeder neck (upper) and at the bottom near the ingate (lower). The possibility of placing feeders either at the top or bottom of the casting, or at both locations simultaneously, enabled an analysis of the feeders’ performance in relation to the pressure height of the location. The feeders themselves were mounted horizontally, which minimises the feeders own influence on the ferrostatic pressure. The driving force for moving the melt from the spot feeder into the casting required other forces than gravity to act on the liquid in order to feed the casting. The horizontal orientation also minimised the difference between the upper and lower spot feeder location.

The different spot feeders were mounted onto the three different modulus castings as shown in Table 1. The first group (0) was a control group without any spot feeders. Groups 1 and 2 had only feeders at the upper location, groups 3 and 4 only at the lower location. The remaining groups (5-9) all had feeders at both the upper and the lower location. All combinations were cast in 2-3 duplicates to ensure repeatability.

**Table 1:** Trial combination overview. Numbers before the letter indicate melt volume [cm<sup>3</sup>], letters indicate I for insulating and E for exothermic, and numbers after the letters indicate feeder modulus [mm].

#	0	1	2	3	4	5	6	7	8	9	Feeder Types	
Dup.	3	3	3	2	3	2	2	2	2	2	Ins	Exo
M08	U	28I08	28E10			28I08	07I05	28E10	08E08	07E06	07I05	07E06
	L			08E08	28E10	28E10	08E08	28E10	07E06	28E10	08I06	08E08
M10	U	22I10	22E12			22I10	08I06	22E12	28E10	08E08	28I08	28E10
	L			28E10	22E12	22E12	28E10	22E12	08E08	22E12	22I10	22E12
M15	U	12I116	12I19			12I116	22I10	12I19	82E15	22E12		82E15
	L			82E15	12I19	12I19	82E15	12I19	22E12	12I19	12I116	12I19

The spot feeders used in the study were so called ram-up sleeves which are mounted on a pin on the pattern before the moulding process begins. After the moulding process the ram-up sleeves are located inside the green sand mould as described by Vedel-Smith et.al.<sup>3</sup> Figure 3 show the spot feeders from group 6 mounted on the pattern, ready for moulding.

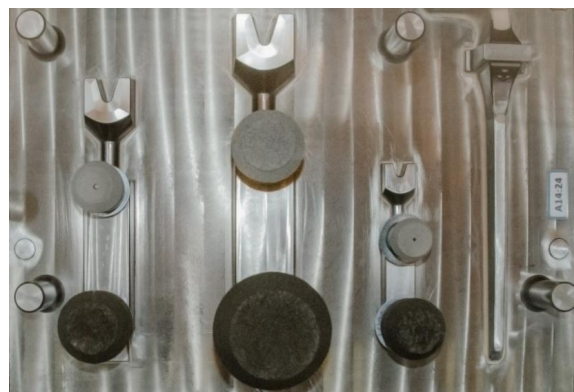


**Fig.3:** Spot feeders from group 6 mounted on the pattern, ready for moulding. Insulating spot feeders on the top. Exothermic spot feeders at the bottom.

**Production, Alloy and Thermal Measurements**

The castings were produced on a vertically parted moulding machine—Disamatic 240B—as part of a production run in an operating foundry. The mould size was 775 x 600 x 300 mm. The poured weight of the casting without any spot feeders was approx. 16 kg—whereof the M08 weights ~1.1 kg, M10 ~3.7 kg, and M15 ~7.3 kg. The pouring time was around 6 s. The castings were made with an EN-GJS-500-14<sup>4</sup> alloy and four alloy composition analyses were made during the duration of the trails. See Table 2.

**Table 2:** Alloy composition [wt%] and casting temperature [°C] variation during the trials.

	CE	C	Si	Mn	P	S	Mg	Cr	Ni	Mo	Cu	Sn	Temp [°C]
I	4.60	3.31	3.91	0.31	0.015	0.003	0.051	0.047	0.021	0.001	0.09	0.004	1,398 (±5)
II	4.57	3.31	3.81	0.31	0.015	0.003	0.045	0.046	0.023	0.001	0.09	0.005	1,387 (±5)
III	4.54	3.35	3.61	0.25	0.015	0.004	0.042	0.051	0.026	0.001	0.06	0.005	1,380 (±5)
IV	4.54	3.34	3.64	0.25	0.015	0.004	0.039	0.050	0.025	0.001	0.06	0.005	1,361 (±5)
Avg	4.56	3.33	3.74	0.28	0.015	0.004	0.044	0.049	0.024	0.001	0.08	0.005	1,382 (±5)

Four temperature measurements were made in one of the castings—4A—which was cast immediately before the series II castings listed in Table 2 were made. Three thermo couples were placed at the centre of each parametric casting, and a single thermo couple was placed at the lower spot feeder of the M15 parametric casting (see Figure 4). All thermo couples were K-type and the data were recorded at a sampling rate of 1 Hz with a stand-alone 4-channel thermo couple data logger.

The castings solidified and cooled in the mould for approx. 1½ hours, and were thereafter removed manually from the moulds at the shake-out station. This ensured that all spot feeders remained attached to the castings. When the castings had air cooled to room temperature they were cleaned by shot blasting.

**Ultrasound Analysis and X-ray Analysis**

All castings were analysed with ultrasound by the same, experienced operator using a Karl Deutsch Digital-Echograph. The location and size of the porosities were painted on the castings. This gave a detailed picture of the size, location, and direction of the porosities. All castings were photo documented for later analysis.

Following the ultrasound analysis selected groups of castings were analysed using x-ray imaging. The x-ray imaging focussed on confirming the results obtained by the ultrasound analysis, but also on documenting the porosities located in areas not suitable for ultrasound analysis—the pre-feeder neck and the spot feeders. Several images were taken of each of the castings and then assembled into an overview, allowing for a more holistic analysis of the x-ray imaging results.

**Results**

**Ultrasound Analysis**

The findings from the ultrasound analysis were classified with respect to porosity size (0-4 where 0 is no porosities and 4 is large porosities), porosity location (top, middle, bottom), and if porosities at different locations were connected or disconnected. Additionally it was also registered when the porosities had an opening out unto the surface of the casting (**bold**). See Table 3.

**Table 3:** Results of the ultrasound analysis

#	0			1			2			3			4			5			6			7			8			9			Nomenclature		
	A	B	C	A	B	C	A	B	C	A	B	C	A	B	C	A	B	C	A	B	C	A	B	C	A	B	C	A	B	C			
M8	T	4	4	4	4	4	4	4	4	4	4	4	4	4	4	4	4	4	4	4	4	4	4	4	4	4	4	4	4	4	3	0	No porosity
	M	2	2	2	2	2	0	0	0	0	2	2	2	2	2	2	2	2	2	2	2	2	0	0	2	2	4	4	4	4	4	1	Micro Porosities
	B	0	0	0	0	0	0	0	0	0	4	0	0	0	0	0	0	0	0	0	0	0	0	0	2	0	0	0	0	0	0	2	Small Porosities
M10	T	4	4	4	4	4	4	4	4	4	4	4	4	4	4	4	4	4	4	4	4	4	4	4	4	4	4	4	4	4	4	4	Large Porosities
	M	2	2	2	1	0	1	2	2	0	2	2	2	2	2	2	2	2	2	2	2	2	2	2	2	2	2	2	2	2	2	2	
	B	0	0	0	0	0	0	0	0	0	0	0	0	0	0	0	0	0	0	0	0	0	0	0	0	0	0	0	0	0	0	0	
M15	T	4	4	4	4	4	4	4	4	4	0	0	0	4	4	4	4	4	0	0	0	2	2	1	0	0	0	0	0	0	0	0	Connected
	M	0	4	2	0	2	1	0	0	0	1	3	2	4	4	0	2	2	1	0	0	0	2	1	0	0	0	1	0	Disconnected			
	B	0	0	0	0	0	0	0	0	0	0	0	2	4	4	0	0	0	0	0	0	0	0	0	0	0	0	0	0	0	0	0	Puncture at neck

The quantified results of the ultrasound analysis indicated that many of the different castings, especially the two smallest modulus castings, displayed the same amount of porosity as the reference casting groups (0) without any spot feeders. This was partly true, however it should be noted that the large porosity (4) indication has no upper limit, meaning that the same indication can cover great differences (see Figure 4).

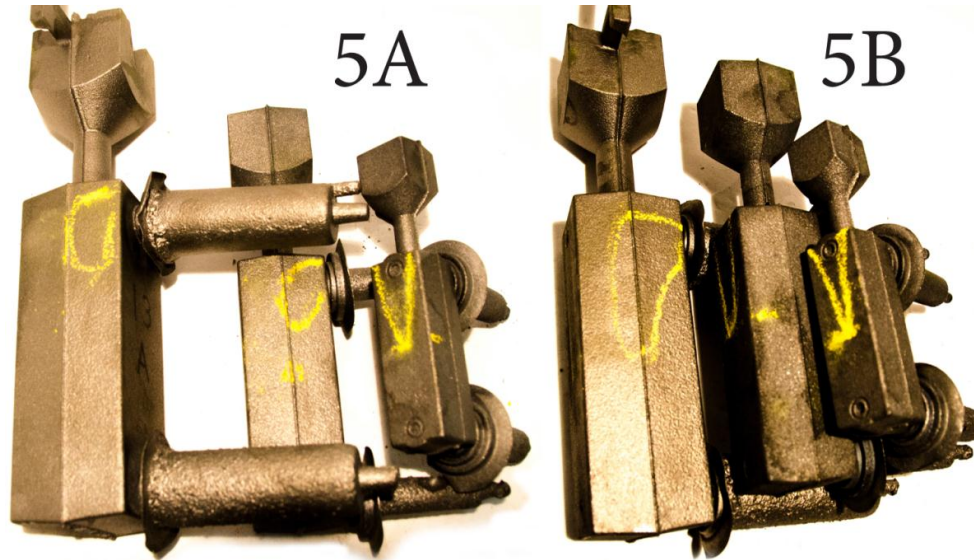


**Fig.4:** Porosity markings from the ultrasound analysis of casting groups 5A and 5B.

Additionally, some of the reference castings without spot feeder displayed clear signs of surface shrinkage, indicating that some of the shrinkage for these castings have occurred in location that have not been covered by this analysis. Surface shrinkage was not observed in any of the castings with spot feeders.

### X-Ray Imaging and Analysis

The x-ray images are greyscale images produced by irradiating the casting from one side, and recording the radiation that reaches the sensor at the opposite side. This gives an image that in greyscale contrast show areas with little material in between (light), and areas with a lot of material in between (dark). Porosities show up because they are holes in the bulk material, and thus areas with porosities absorb less radiation, resulting in a brighter area of the image. However, the radiation does scatter and diffuse, rendering the images a little fuzzy at the edges. Because of this effect there was a limit to the difference between the size of the casting and the size of the porosity that could be imaged. This made it difficult to obtain good images of the defects in the M15 castings (see Figure 5).

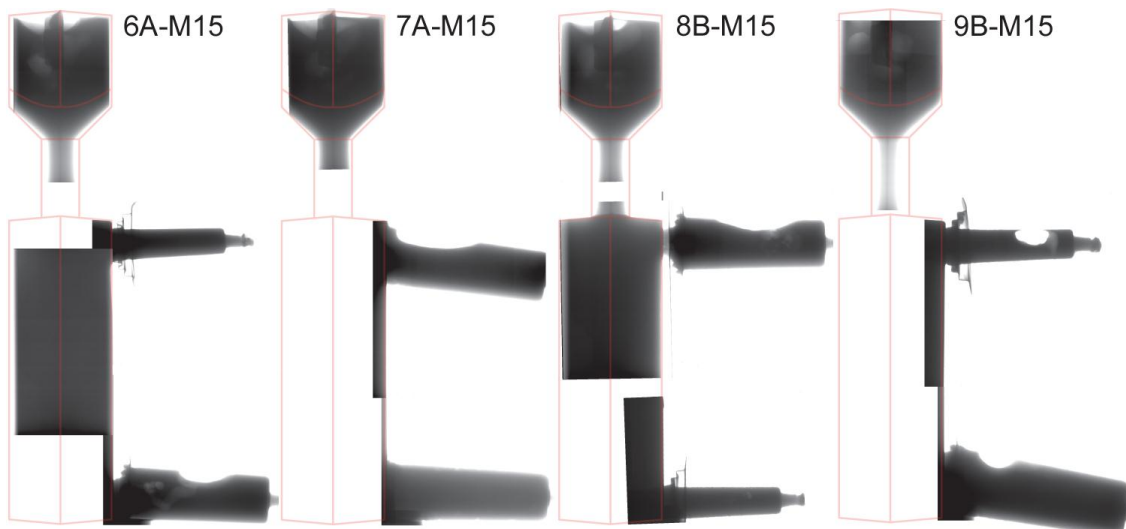


**Fig.5:** X-ray images of casting 6A, 7A, 8B, and 9B—all that largest casting with a modulus of 15 mm.

### Thermal Measurements and Cooling Curves

The cooling curves showed that the three parametric castings solidified and cooled in a comparable manner, confirming that the parametric design provide the intended comparison between the different moduli castings (see Figure 6). The maximum temperature measured was  $1,325 \pm 5$  °C indicating that the gating filling of the mould has lowered the temperature of the melt by  $62 \pm 10$  °C from the pouring temperature of  $1,387 \pm 5$  °C. However, the specified temperature limit of 1.300 °C for the K-type thermo couples for short duration readings should be taken into consideration<sup>5</sup>.

The cooling curves showed that in the bottom part of the M15 casting ended solidification approx. 320 s before the centre of the casting, albeit 400 s later the curves met again. This was caused by the thermal influence of the spot feeder, and the area between the two curves indicates the energy that the spot feeder provides transferred to the casting.

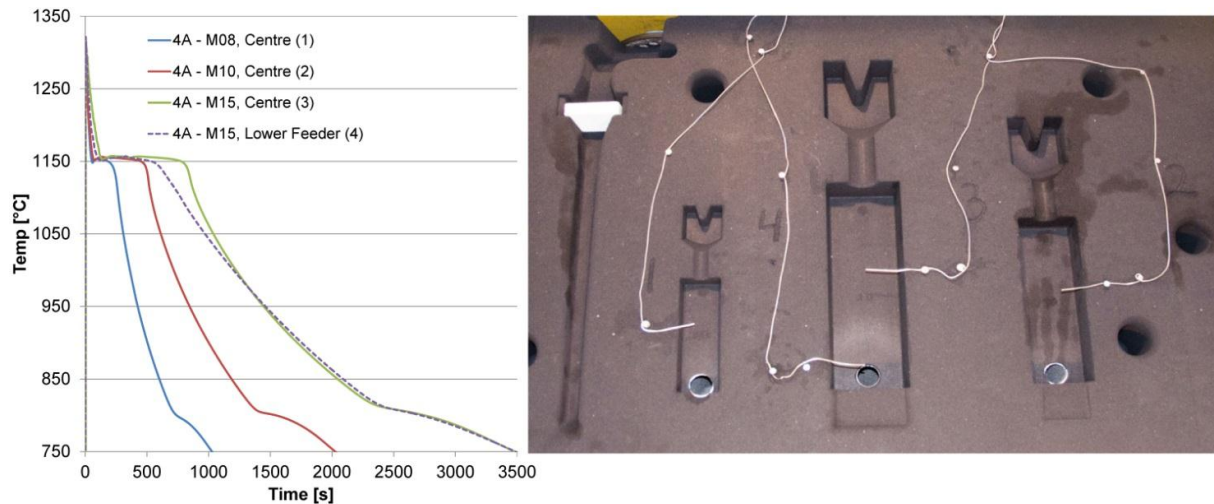


Fig.6: Thermal measurement of the casting, cooling, and solidification of casting group 4A.

### Discussion

Examining Table 3 it was seen that most of the castings, regardless of modulus size and spot feeder combinations, had a large (size 4) porosity at the top and a small (size 2) porosity at the middle. As mentioned in the results section the large porosity characteristic was open ended, and covered many gradually increasing porosities. However, the consistent results show the stability of the model and the production conditions. Thus, the most interesting castings were the ones that differentiate from the stable and repeatable porosities formed in the other castings.

Castings 8B-M15 and 9B-M15 were classified as porosity free and the castings with the same spot feeder configuration—8A-M15 and 9A-M15—only displayed micro (size 1) porosities. 7A-M15 and 7B-M15 were classified with small porosities at the top, but no porosities at the middle. Finally, 3A-M15 and 3B-M15 only displayed porosities at the middle of the casting—ranging from micro (size 1) to medium (size 3) porosities.

The smaller castings—M08 and M15—did not show the same effect for these feeder configurations even though the modulus of the spot feeders were scaled according to the changes in casting modulus. This indicated that the solidification of the three different modulus castings was different as well. These changes in solidification can be caused by the slower solidification of the large modulus castings, which provide the longer time for the graphite nodules to grow and inhibit pearlite formation which would have reduced the effect of the graphite expansion. However, the high Si content of the alloy greatly limits pearlite formation already, and none of the three castings are small enough to be considered thin walled sections. Hence other factors were needed to fully explain the solidification differences between the different modulus castings.

Additionally several of the castings had ‘punctures’ at the bottom of the pre-feeder neck, opening into a large porosity in the casting. This effect seemed to have been dominant for the smaller modulus castings, but it also seemed to be unrelated to the amount of porosities recorded and the effectiveness of the spot feeders.

The most likely explanation was that the large modulus castings had a greater tendency to form a solid shell early during solidification, so that the low pressure that occurred inside the casting towards the end of solidification had enough force to move the melt from the spot feeders and into the casting itself.

Some melt may have been provided by the pre-feeder regardless of the intention that this should not happen. The x-ray images showed that the pre-feeders contained porosities. It was not possible to determine how much of the porosities in the pre-feeders that was a result of feeding and how much were related to the liquid shrinkage that the pre-feeders were designed to handle. However, it was noted that most pre-feeders displayed the some amount of porosities.



## 10<sup>th</sup> International Symposium on the Science and Processing of Cast Iron – SPC110

No correlation was found between the amount of porosities in the pre-feeder and the amount of porosities in the casting itself.

However, the negative pressure gradient from the casting itself could completely explain the results shown in Table 3. If group 3 and 4 were compared for the M15 castings it was noted that the first displayed a few and small porosities whereas the latter displayed more and larger porosities. However, it was the latter—group 4—that had the largest spot feeder. If the main driving force for feeding from the spot feeder into the casting was the negative pressure in the casting, then the larger spot feeder should have produced a porosity free casting. Instead it was seen that the smaller spot feeder reduced the porosities in the casting significantly compared to the large one.

To explain this phenomenon other forces than a negative pressure caused by shrinkage of the material in the casting must be taken into account. The graphite expansion was assumed to be the same for both configurations as they were cast with the same alloy, and only minor differences would occur as an effect of the small changes in solidification between the two spot feeder configurations. However, the timing of the graphite expansion, and particularly in relation to the timing of the negative pressure inside the casting, seemed to reach an optimum for this configuration. Thus, the two different forces come to act together, rather than against each other. If so, this could be seen as a special case of John Campbell's feeding rule no. 6 regarding the pressure gradient requirement<sup>6</sup>.

External forces can also have occurred and gas development from exothermic feeder sleeves was a known concern. However, if gas development from the exothermic material was a significant driving force for the movement of the melt, then group 4 and 5 should have displayed fewer porosities than what was recorded.

Finally, examining the results of the M15 casting groups 3, 6, 8, and 9, in comparison with the other five groups, it was shown that a feeder located at the lower part of a casting section can feed the section with equal efficiency compared the same feeder located at the upper part of the casting section. This showed that the horizontally oriented spot feeders with exothermic sleeve material depend little upon the gravity as a driving force for feeding.

### Conclusions

1. The optimum feeder size did not scale linearly with casting modulus. Larger casting modules required relatively smaller modulus feeders.
2. The timing of the negative pressure from solidification shrinkage combined with the timing of the graphite expansion seemed to be important in order to achieve the best possible feeding conditions. Similarly a larger feeder may shift the time enough for the effects to counteract each other and thus cancel most of the feeding effect if not directly developing more shrinkage.
3. The location for horizontally oriented spot feeders was relatively unaffected by the difference between the high and low location. The spot feeders that functioned at one location also functioned at the other location. The spot feeders that did not function at one location did not function at the other location either. In special cases it was possible to feed against gravity.

### References

1. ASM International: Casting Design and Performance—Part II: Process Design, Riser Design, 2009, 61-72.
2. N. Chvorinov: Theory of the Solidification of Castings, *Giesserei*, Vol. 27, 1940, 177-186.
3. N.K. Vedel-Smith, N.S. Tiedje, K.T. Maza, and J. Sällström: Quantification of Feeding Effects of Spot Feeding Ductile Iron Castings made in Vertically Parted Molds, AFS Proceedings, 13-1310, 2013.
4. EN 1563:2012-3: Founding: Spheroidal Graphite Cast Irons, 2012.
5. L. Michalski, K. Eckersdorf, J. Kucharski, and J. McGhee: Temperature Measurements, 2<sup>nd</sup> Edn, 2001 John Wiley & Sons Ltd.
6. J. Campbell: 'Casting Practice – The 10 Rules of Castings', 120-156, 2004, Burlington, Elsevier Butterworth-Heinemann.

### Acknowledgement

This work was funded by the Public Service Obligation (PSO) funds made available by the Danish Government. The project was made in collaboration with FOSECO Ltd., MAGMA GmbH, DISA Industries A/S, and Vald. Birm A/S. Rune Engelberth Hansen carried out the development of the parametric casting geometry.



“O HNE dich kann ich nicht sein  
Ohne dich

Mit dir bin ich auch allein  
Ohne dich

Ohne dich zähl ich die Stunden ohne dich

Mit dir stehen die Sekunden  
Lohnen nicht ohne dich”

---

—Ohne Dich, Rammstein  
2004

This manuscript was typeset by the author with the L<sup>A</sup>T<sub>E</sub>X 2<sub>ε</sub> Documentation System on a PC running Windows 7 64-bit (stable).

Text editing was done in *TeXworks* using the CTAN- $\TeX$  package depository. The illustrations and graphs were created with *Microsoft Excel*, *plot.ly*, and *MathWorks MatLab*, respectively. The chapter layouts were made with *Adobe InDesign*.

The body was typeset in 10 point Computer Modern Roman. Section titles were typeset in various sizes of Computer Modern Sans. Chapter titles were typeset in various sizes of OCR A Std Regular. The monospace typeface used for figures was Eras Medium ITC, and the serif font was Garamond. The cover text was typeset in Neo Sans Std and Minion Pro.

A digital copy of the dissertation can be found at  
[http://download.vedel-smith.com/PhD\\_Dissertation\\_Nikolaj\\_Vedel-Smith.pdf](http://download.vedel-smith.com/PhD_Dissertation_Nikolaj_Vedel-Smith.pdf)

The PhD Defence presentation can be viewed at  
<http://vedel-smith.com/PhD/PhD-Defence.html>

**DTU Mechanical Engineering**  
**Section of Manufacturing Engineering**  
Technical University of Denmark

Produktionstorvet, Bld. 427S  
DK-2800 Kgs. Lyngby  
Denmark  
Phone (+45) 4525 4763  
Fax (+45) 4593 0190  
[www.mek.dtu.dk](http://www.mek.dtu.dk)  
ISBN: 978-87-7475-452-7